



# TURKISH JOURNAL OF ENGINEERING

## **EDITOR IN CHIEF**

*Prof. Dr. Murat YAKAR*  
Mersin University Engineering Faculty  
Türkiye

## **CO-EDITORS**

*Prof. Dr. Erol YAŞAR*  
Mersin University Faculty of Art and Science  
Türkiye

*Prof. Dr. Cahit BİLİM*  
Mersin University Engineering Faculty  
Türkiye

*Assist. Prof. Dr. Hüdaverdi ARSLAN*  
Mersin University Engineering Faculty  
Türkiye

## **ADVISORY BOARD**

*Prof. Dr. Orhan ALTAN*  
Honorary Member of ISPRS, ICSU EB Member  
Türkiye

*Prof. Dr. Armin GRUEN*  
ETH Zurich University  
Switzerland

*Prof. Dr. Hacı Murat YILMAZ*  
Aksaray University Engineering Faculty  
Türkiye

*Prof. Dr. Artu ELLMANN*  
Tallinn University of Technology Faculty of Civil Engineering  
Estonia

*Assoc. Prof. Dr. E. Çağlan KUMBUR*  
Drexel University  
USA

## **TECHNICAL EDITORS**

*Prof. Dr. Roman KOCH*  
Erlangen-Nurnberg Institute Palaontologie  
Germany

*Prof. Dr. Hamdalla WANAS*  
Menoufyia University, Science Faculty  
Egypt

*Prof. Dr. Turgay CELIK*  
Witwatersrand University  
South Africa

*Prof. Dr. Muhsin EREN*  
Mersin University Engineering Faculty  
Türkiye

*Prof. Dr. Johannes Van LEEUWEN*  
Iowa State University  
USA

*Prof. Dr. Elias STATHATOS*  
TEI of Western Greece  
Greece

*Prof. Dr. Vedamanickam SAMPATH*  
Institute of Technology Madras  
India

*Prof. Dr. Khandaker M. Anwar HOSSAIN*  
Ryerson University  
Canada

*Prof. Dr. Hamza EROL*  
Mersin University Engineering Faculty  
Türkiye

*Prof. Dr. Ali Cemal BENİM*  
Duesseldorf University of Applied Sciences  
Germany

*Prof. Dr. Mohammad Mehdi RASHIDI*  
University of Birmingham  
England

*Prof. Dr. Muthana SHANSAL*  
Baghdad University  
Iraq

*Prof. Dr. Ibrahim S. YAHIA*  
Ain Shams University  
Egypt

*Assoc. Prof. Dr. Kurt A. ROSENTRATER*  
Iowa State University  
USA

*Assoc. Prof. Dr. Christo ANANTH*  
Francis Xavier Engineering College  
India

*Prof. Dr. Bahadır K. KÖRBAHTİ*  
Mersin University Engineering Faculty  
Türkiye

*Assist. Prof. Dr. Akın TATOGLU*  
Hartford University College of Engineering  
USA

*Assist. Prof. Dr. Şevket DEMİRCİ*  
Mersin University Engineering Faculty  
Türkiye

*Assist. Prof. Dr. Yelda TURKAN*  
Oregon State University  
USA

*Assist. Prof. Dr. Gökhan ARSLAN*  
Mersin University Engineering Faculty  
Türkiye

*Assist. Prof. Dr. Seval Hale GÜLER*  
Mersin University Engineering Faculty  
Türkiye

*Assist. Prof. Dr. Mehmet ACI*  
Mersin University Engineering Faculty  
Türkiye

*Dr. Ghazi DROUBI*  
Robert Gordon University Engineering Faculty  
Scotland, UK

#### **JOURNAL SECRETARY**

*Aydin Alptekin*  
aydinalptekin@mersin.edu.tr

#### **TURKISH JOURNAL OF ENGINEERING (TUJE)**

Turkish Journal of Engineering (TUJE) is a multi-disciplinary journal. The Turkish Journal of Engineering (TUJE) publishes the articles in English and is being published 4 times (January, April, July and October) a year. The Journal is a multidisciplinary journal and covers all fields of basic science and engineering. It is the main purpose of the Journal that to convey the latest development on the science and technology towards the related scientists and to the readers. The Journal is also involved in both experimental and theoretical studies on the subject area of basic science and engineering. Submission of an article implies that the work described has not been published previously and it is not under consideration for publication elsewhere. The copyright release form must be signed by the corresponding author on behalf of all authors. All the responsibilities for the article belong to the authors. The publications of papers are selected through double peer reviewed to ensure originality, relevance and readability.

#### **AIM AND SCOPE**

The Journal publishes both experimental and theoretical studies which are reviewed by at least two scientists and researchers for the subject area of basic science and engineering in the fields listed below:

- Aerospace Engineering
- Environmental Engineering
- Civil Engineering
- Geomatic Engineering
- Mechanical Engineering
- Geology Science and Engineering
- Mining Engineering
- Chemical Engineering
- Metallurgical and Materials Engineering
- Electrical and Electronics Engineering
- Mathematical Applications in Engineering
- Computer Engineering
- Food Engineering

#### **PEER REVIEW PROCESS**

All submissions will be scanned by iThenticate® to prevent plagiarism. Author(s) of the present study and the article about the ethical responsibilities that fit PUBLICATION ETHICS agree. Each author is responsible for the content of the article. Articles submitted for publication are priorly controlled via iThenticate ® (Professional Plagiarism Prevention) program. If articles that are controlled by iThenticate® program identified as plagiarism or self-plagiarism with more than 25% manuscript will return to the author for appropriate citation and correction. All submitted manuscripts are read by the editorial staff. To save time for authors and peer-reviewers, only those papers that seem most likely to meet our editorial criteria are sent for formal review. Reviewer selection is critical to the publication process, and we base our choice on many factors, including expertise, reputation, specific recommendations and our own previous experience of a reviewer's characteristics. For instance, we avoid using people who are slow, careless or do not provide reasoning for their views, whether harsh or lenient. All submissions will be double blind peer reviewed. All papers are expected to have original content. They should not have been previously published and it should not be under review. Prior to the sending out to referees, editors check that the paper aim and scope of the journal. The journal seeks minimum three independent referees. All submissions are subject to a double blind peer review; if two of referees gives a negative feedback on a paper, the paper is being rejected. If two of referees gives a positive feedback on a paper and one referee negative, the editor can decide whether accept or reject. All submitted papers and referee reports are archived by journal Submissions whether they are published or not are not returned. Authors who want to give up publishing their paper in TUJE after the submission have to apply to the editorial board in written. Authors are responsible from the writing quality of their papers. TUJE journal will not pay any copyright fee to authors. A signed Copyright Assignment Form has to be submitted together with the paper.

### **PUBLICATION ETHICS**

Our publication ethics and publication malpractice statement is mainly based on the Code of Conduct and Best-Practice Guidelines for Journal Editors. Committee on Publication Ethics (COPE). (2011, March 7). Code of Conduct and Best-Practice Guidelines for Journal Editors. Retrieved from [http://publicationethics.org/files/Code%20of%20Conduct\\_2.pdf](http://publicationethics.org/files/Code%20of%20Conduct_2.pdf)

### **PUBLICATION FREQUENCY**

The TUJE accepts the articles in English and is being published 4 times (January, April, July and October) a year.

### **CORRESPONDENCE ADDRESS**

Journal Contact: [tuje@mersin.edu.tr](mailto:tuje@mersin.edu.tr)

# CONTENTS

*Volume 8 – Issue 1*

## ARTICLES

- A review on application areas and surface geometry in superhydrophobic materials**  
Serhat Akinci, Filiz Karaömerlioğlu, Emre Kaygusuz ..... 1-10
- Analysis of temperature and precipitation series of Hirfanli Dam Basin by Mann Kendall, Spearman's Rho and Innovative Trend Analysis**  
Fatma Gunduz, Utku Zeybekoglu ..... 11-19
- Assessment of engineering geology and grouting applications in Yalnızcı Dam Site (Antalya, Türkiye)**  
Ömür Çimen, Halil İbrahim Günaydın ..... 20-30
- Machine learning empowered prediction of geolocation using groundwater quality variables over YSR district of India**  
Jagadish Kumar Mogaraju ..... 31-45
- Application of a new fuzzy logic model known as "SMRGT" for estimating flow coefficient rate**  
Ayse Yeter Gunal, Ruya Mehdi ..... 46-55
- Prediction of elevation points using three different heuristic regression techniques**  
Vahdettin Demir, Ramazan Doğu ..... 56-64
- Comparison of CNN-based methods for yoga pose classification**  
Vildan Atalay Aydın ..... 65-75
- Counterface soil type and loading condition effects on granular/cohesive soil – Geofom interface shear behavior**  
Tanay Karademir ..... 76-91
- Optimal power flow analysis with circulatory system-based optimization algorithm**  
Hüseyin Bakır ..... 92-106
- Solution-based fabrication of copper oxide thin film influence of cobalt doping on structural, morphological, electrical, and optical properties**  
Samed Çetinkaya ..... 107-115
- Investigating best algorithms for structural topology optimization**  
Sohayb Abdulkarim ..... 116-126
- Drought analysis based on SPI and RDI drought indices in the Burdur Basin**  
Nazire Göksu Soydan Oksal, Neslihan Beden ..... 127-138
- Cotton yield estimation using several vegetation indices**  
Bakhtiyar Babashli, Aytaj Badalova, Ramis Shukurov, Agil Ahmadov ..... 139-151
- Energy capable protocol for heterogeneous blue brain network**  
Rajesh Dennison, Giji Kiruba Dasebenezer, Ramesh Dennison ..... 152-161
- A lasso regression-based forecasting model for daily gasoline consumption: Türkiye Case**  
Ertugrul Ayyıldız, Mirac Murat ..... 162-174



### A review on application areas and surface geometry in superhydrophobic materials

Serhat Akinci <sup>1</sup>, Filiz Karaömerlioğlu <sup>1,2</sup>, Emre Kaygusuz <sup>3</sup>

<sup>1</sup>Mersin University, Nanotechnology and Advanced Materials, Türkiye, serhatakinci1903@gmail.com

<sup>2</sup>Mersin University, Department of Electrical and Electronics Engineering, Türkiye, filizkrm@mersin.edu.tr

<sup>3</sup>Bingöl University, Department of Mechanical Engineering, Türkiye, emreyguz03@gmail.com

Cite this study:

Akinci, S., Karaömerlioğlu, F., & Kaygusuz, E. (2024). A review on application areas and surface geometry in superhydrophobic materials. Turkish Journal of Engineering, 8 (1), 1-10

#### Keywords

Superhydrophobic Materials  
Icing  
Friction  
Water Repellent

#### Review Article

DOI: 10.31127/tuje.1127095

Received:06.06.2022

Revised: 01.09.2022

Accepted:06.09.2022

Published:15.09.2023



#### Abstract

Superhydrophobic surfaces offer many advantages beyond just being hydrophobic (water repellent) to the surface. The superhydrophobic property can be achieved by artificially creating geometric structures on the material surface. These geometric structures reduce the contact area between the liquid and the surface. The contact angle between the liquid and the surface gives rise to two conditions: hydrophobic and hydrophilic. If the contact angle between the surface and the liquid is above 90 degrees, a hydrophobic state occurs. If the angle is below 90 degrees, the surface is in a hydrophilic state. One of these two states is determined depending on the need and provides alternative solutions for many problems that currently await engineering interventions. Scientific studies in the field of superhydrophobia are increasing day by day. Interest in superhydrophobia is expected to grow further, as it offers environmentally friendly and economical solutions to ongoing challenges in various sectors. Superhydrophobic materials also offer a method of preventing icing due to their ability to prevent liquid retention on the material surface through their water repellent properties. Since the reduction of the contact area between the liquid and the material surface on superhydrophobic surfaces leads to a decrease in the friction factor, the friction of the flow on the material will also decrease. These properties of superhydrophobic materials generate interest in sectors such as aviation and marine. This study describes the properties of superhydrophobic surfaces created through various methods on materials, focusing on applications such as anti-icing and reduction of friction factor.

#### 1. Introduction

With the widespread use of the internet recently, access to technological and scientific studies and research and development opportunities are increasing. For this reason, the development of computers, which are increasing day by day and almost becoming an indispensable part of our lives, is accelerating. The use of developed microelectronics in every field is the event that triggers the development of computer technology [1].

In the last quarter of the 20<sup>th</sup> century, the developments in the world of science have realized that material properties at the nanometer (billionth of a meter) level have become quite important. With scanning tunnel microscopes that can directly view atoms and the atomic force microscope derived from this microscope, the first stage of producing artificial materials has been realized, while providing the opportunity to examine atoms one by one and being able to be transported to the desired location in a controlled

manner. Since the desired physical and chemical materials can be produced in artificial materials designed in nanometer sizes, more functional, stronger and faster processes can be produced. These new types of materials also open the doors of savings in many areas. Producing materials that consume less energy, take up less space and are smaller will also solve the problems in many sectors [2].

Quantum laws seem to be valid in atomic dimensions. The material can show visible changes depending on the arrangement of the atoms. For example, when an atom is removed from a molecule or an atom is added, the properties may change partially or completely, and many properties of the molecule such as physical, chemical, mechanical and conductivity properties may become different. This changes the feature in nano-structures and creates different opportunities for many technological applications [3].

Micro-electro-mechanical system (MEMS) is a process technology comprising miniaturized mechanical and electro-mechanical parts made using micro-

fabrication methods [4-7]. Microfluidics is the science and technology of systems that process or manipulate small amounts of fluids (10<sup>-9</sup> to 10<sup>-18</sup>L), using channels measuring from tens to hundreds of micrometers [8]. Branson et. al. [9] studied Superhydrophobic Surface Coatings for Microfluidics and MEMs.

Yu et al. [10] presents a controllable superhydrophobic helix capable of directional bubble distribution. In the liquid, the bubble tends to stay above the helical structure and cooperates with the helical rotation. The speed of bubble delivery can be easily adjusted in terms of the spacing length of the helix. Continuous bubble collection and distribution was accomplished by integrating the helix with a gas needle, and the anti-flotation transport of the air bubble was demonstrated using an oblique superhydrophobic helix.

In recent years, scientists have focused on superhydrophobic surfaces for its non-wetting effect, corrosion resistance, friction factor, anti-icing, anti-fogging, anti-bacterial and self-cleaning properties. Superhydrophobic coated materials can be used at marine and aerospace industry areas. A major difference of the properties of a hydrophobic surface and a hydrophilic surface is given in Figure 1 and Figure 2.



Figure 1. Hydrophilic and hydrophobic surface properties [5].

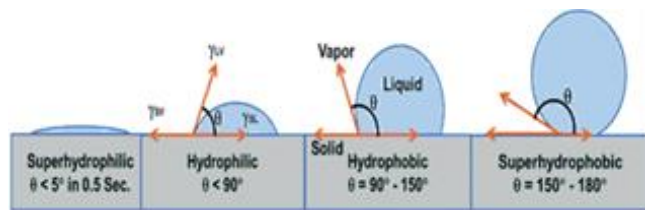


Figure 2. Various conditions according to contact angle of the drop of liquid on the surface [11].

Dou et al. [12] developed a prototype anti-icing coating with cross-linked hygroscopic polymers grafted into photolithographically prepared micropores on a silicon wafer surface. This method greatly reduces the ice bond strength and there are no durability problems as water can be reclaimed from moisture or melted ice. However, this prototype coating is of limited use because it is impractical to prepare micropores and graft cross-linked hygroscopic polymers in micropores on different solid substrates. Therefore, it is more preferable to have a mechanically sound coating with a durable lubricating aqueous layer, and most importantly, the coating can be applied directly over a variety of solid surfaces. Finally, it

is crucial for the practical application of anti-icing coatings.

Materials that control ice buildup are important for aircraft efficiency, highway and power line maintenance, and building construction. Most current defrosting systems involve the physical or chemical removal of both energy and resource-intensive ice. A more desirable approach would be to prevent ice buildup rather than to end ice buildup. Recently, much attention has been paid to the freezing of static water droplets resting on supercooled surfaces. However, ice accumulation begins with droplet/substrate impact followed by freezing. Here, the focus is on the behavior of dynamic droplets affecting supercooled nanostructured and microstructured surfaces. Detailed experimental analysis of the temperature-dependent droplet/surface interaction shows that highly ordered superhydrophobic materials can be designed to remain completely ice-free down to approximately -25 to -30°C due to their ability to repel water acting before ice nucleation. Ice accumulated below these temperatures can be easily removed. The factors contributing to droplet retraction, needling, and freezing are combined with the heat transfer and wetting dynamics of classical nucleation theory, laying the foundation for the development of rationally designed anti-icing materials. In particular, the potential of hydrophobic polymeric coatings containing cell and closed cell surface microstructures suitable for enhanced mechanical and pressure stability, easy replication and large-scale fabrication, and opportunities for better tuning of materials and chemical properties are highlighted [11].

Atmospheric icing from supercooled droplets in the atmosphere can have catastrophic consequences for man-made structures built in cold climates and high-altitude regions, resulting in both socioeconomic losses and loss of human life. To reduce the icing problem, active deicing has been developed, which includes chemical, thermal and mechanical techniques to remove the ice that has already accumulated. However, these techniques are sub-optimal as they face problems such as high energy consumption, environmental hazards, high economic costs, and the need for frequent reapplications [11,12].

Most research in the field of superhydrophobicity focuses on surfaces with open cell structures, eg; column-like surfaces and surfaces containing mounds and valleys. Closed-cell surfaces have been reported to have a comparative advantage in that they are better at holding their hydrophobic properties under pressure. Using LAMMPS simulations in the work of Boinovich and Emelyanenko [13], the wetting properties of closed-cell structures (often closely linked to the syphobic properties of ice) were further investigated. The simulations show that the wetting of these surfaces meets the known Wenzel and Cassie-Baxter theories. However, at the small scale where simulations are made, the effect of adjusting the roughness scale is not as predicted by theory. Also, no comparative advantage could be demonstrated for closed cell surfaces versus open cell constructs. A physical experiment was also conducted; here the density of water droplets on the dynamic behavior of an almost superhydrophobic black

silicon surface is tested. The results confirm a well-known problem: Condensation severely impairs the waterproofing of hydrophobic surfaces.

Literature review and experiments in the study of Boinovich and Emelyanenko [13] show that superhydrophobic surfaces have great potential for use in anti-icing applications, with delayed freezing, reduced ice accumulation and reduced ice adhesion. However, major problems remained unresolved, including de-icing from mechanical damage and reduced icing in humid conditions.

Ice formation and accumulation reduces the efficiency of infrastructure components, mechanisms and machinery, including aircraft, ships, offshore oil platforms, wind turbines, dams, power stations, power lines and telecommunications equipment, heat pumps, refrigerators and air conditioners. In recent years, efforts have been made to develop a more detailed understanding of the physicochemical phenomena that regulate icing processes and to develop more efficient systems for icing prevention and/or reducing its consequences [14].

The most popular defrosting strategies are generally power-consuming and not always efficient and environmentally safe. For example, mechanical and electrothermal methods are used to combat factors that adversely affect the operation of overhead transmission lines under propeller conditions. The effectiveness of these methods in preventing wet snow collection, icing, and freezing rain or frost accumulation has been repeatedly discussed in the literature. Mechanical action in an overhead transmission line creates conditions that disrupt the normal operation of a repaired section. Also, many of the mechanical methods even create additional mechanical stress. This stress can cause failure in some cases. In addition, the application of mechanical methods to combat icing of power lines generally requires access to the line and direct transport of wires and electrical transmission towers. Electrothermal methods are based on the use of heat developed during the passage of current through an object protected against icing [15].

In recent years, many electrothermal methods have been proposed to prevent ice formation or accelerated ice melting on structural parts subjected to ice formation. However, these methods require additional power consumption and expensive equipment. The use of electrothermal methods of transporting electrical energy is either accompanied by a redistribution of electrical flow in networks, and in some cases, a temporary blackout of some consumers or a more complex network configuration that allows the network scheme is required, or the parameters of electromagnetic wave propagation will be changed. Therefore, the application of electrothermal methods results in considerable appreciation of the manufacture and process of an icing protected object. In some cases, the use of such methods has adverse effects, such as a reduction in the working life of an object and an automated system that monitors its state [13].

Ice-repellent coatings can have a significant impact on global energy savings and improve safety in many infrastructure, transportation and refrigeration systems. In the development of ice-repellent surfaces, the use of

superhydrophobic surfaces most often inspired by lotus leaves has been avoided in recent years, but these surfaces fail in high humidity conditions due to water condensation and frost formation, and even cause increased ice adhesion due to the large surface area. A radically different type of ice-repellent material has been reported based on slippery liquid-filled porous surfaces (SLIPS), in which a stable, smooth, low-hysteresis lubricant top layer is retained by flowing a water-immiscible liquid onto a chemically functionalized nanostructured surface [15,16].

A direct fabrication method has been developed on industrially relevant metals, especially aluminum, one of the most widely used lightweight construction materials. It has been shown that SLIPS-coated Al surfaces not only suppress ice/frost build-up by effectively removing condensed moisture, but also exhibit an order of magnitude lower ice adhesion than state-of-the-art materials. On the basis of a theoretical analysis following extensive icing/de-icing experiments, the particular advantages of SLIPS as anti-icing surfaces due to very low contact angle hysteresis are discussed, with highly reduced floating droplet sizes. Our surfaces have been shown to be non-freezing, antifreeze, where conventional materials accumulate ice. These results show that SLIPS is a promising candidate to develop robust anti-icing materials for wide applications such as refrigeration, aerospace, roofs, wires, outdoor signage, railings and wind turbines [16].

Chen et al. [17] produced an aqueous lubricating layer with an anti-icing coating. This anti-icing coating can be applied directly to various surfaces that needs treatment. Adhesion strength can be reduced on coated surfaces to a greater extent than on uncoated surfaces. It has been proven for the first time that the ice formed on the anti-icing coating can be formed by a wind movement in the wind tunnel with controllable temperature and wind speed. In addition, even the ice grip of the low anti-icing coating can be maintained when the temperature drops to  $-53^{\circ}\text{C}$ . The strength and durability of the anti-icing coating has been proven by icing/ defrosting experiments. The results show that an anti-icing coating with an aqueous lubricating layer is of great importance for practical applications. The accumulation of ice on various surfaces causes serious problems in our daily life. In some cases, it causes catastrophic events such as plane crash and power grid collapse, resulting in severe economic impacts and loss of lives.

In Kibar et al. [18]'s study, the diffusion profiles of liquid jets hitting superhydrophobic/hydrophobic surfaces were examined and the data to be obtained as a result of the experiments were estimated. A liquid jet was sent using a 1.75 mm inner diameter glass tube nozzle on the hydrophobic surfaces with flat and smooth 93, 104 and  $117^{\circ}$  contact angles. The angles of inclination between the liquid jet and the surface are in the range of  $15-45^{\circ}$ . As a result of the experiment, it was observed that the azimuth angles, where the widest widths occur, are only affected by the inclination angle. The forward length of the spreading profile of the imping liquid jet increases accordingly with the increase of the inclination angle and becomes higher than at a critical angle. It decreases as the angle of inclination increases. This

critical angle is also not affected by the weber number. The theory in the literature is in good agreement with the equation predicted in the study for the azimuth angle at which the largest widths occur.

Allred et al. [19]’s study, hydrophilic surfaces showed promise in capillary wicking and boiling applications, as they increase the maximum heat flow that can be dispersed. Conversely, highly non-wetting (superhydrophobic) surfaces have been found to be largely ignored for these applications, as they have been shown to promote the formation of insulating vapor film, which greatly reduces heat transfer efficiency.

## 2. Method

With the development of nanotechnology day by day, the range of fields and sectors affected by the studies in this field is expanding. The increase in scientific studies in this field paved the way for new scientific studies and provided the opportunity to work in more specific areas. With the development of nanotechnology, it has become easier to understand the superhydrophobic structures already found in nature, and this advantage has opened the way to be designed and used in line with the needs. The hydrophobic and self-cleaning feature of the leaf of the Lotus flower in nature has increased the interest in hydrophobic and superhydrophobic, and studies in this field have shown that hydrophobic surfaces have many advantages besides being non-wetting and self-cleaning. An exemplary hydrophobic surface is shown in Figure 3.

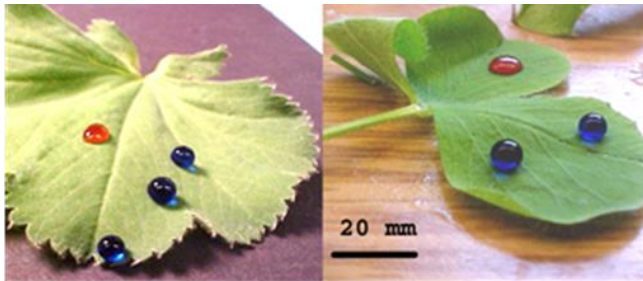


**Figure 3.** Leaves of *Alchemilla vulgaris* (a) and crimson clover *Trifolium incarnatum* (b) have a hairy surface that traps aqueous Methylene Blue solution in superhydrophobic drops and ethanolic Sudan Red solution in hydrophilic drops [20].

It has been determined that a hydrophobic surface provides the opportunity to prevent icing together with its non-wetting property. It is very interesting that a surface being hydrophobic causes non-wetting, preventing icing and also reducing friction between the liquid surface.

### 2.1 The non-wetting effect of superhydrophobicity

The most important parameter that determines the wettability or non-wetting property of a solid surface is the contact angle resulting from the bark free surface energy. The spreading area on the surface of a drop of liquid and the equilibrium at the contact line are defined by Young's Equation (1) [21,22].

$$\cos\theta_E = (\gamma_{SG} - \gamma_{LS}) / \gamma_{GL} \quad (1)$$

In Equation (1),  $\theta_E$  represents the equilibrium contact angle of the water drop, and  $\gamma_{SG}$ ,  $\gamma_{LS}$  and  $\gamma_{GL}$  represents the surface tensions between solid-gas, solid-liquid, liquid-gas phases.

The contact angle obtained by Young's equation gives information about the wettability properties of the surface. If the contact angle obtained is less than 90 degrees, it is called a wetted surface (hydrophilic), if it is greater than 90 degrees but less than 150 degrees, it is called a non-wetted surface (hydrophobic), and if it is greater than 150 degrees, it is called a super-non-wet (superhydrophobic) surface. General view of liquid drop on hydrophilic, hydrophobic and super hydrophobic surfaces are shown in Figure 4.

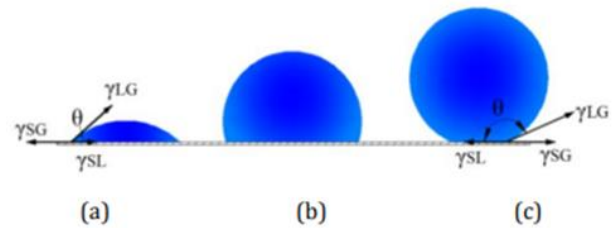


**Figure 4.** General view of liquid drops on (a) hydrophilic, (b) hydrophobic, (c) super hydrophobic surfaces [23].

The contact angle can reach up to 120° on a solid and smooth surface [22,23]. This contact pain can only be seen in materials such as teflon with very low surface energy. If we want to obtain a larger contact angle, the surface must be rough in micro or nano size [22,23]. This roughness has 2 consequences. The first of these is called the Wenzel state because if the liquid drop fills the micro and nano-sized spaces on the surface, since this increases the contact area of the liquid with the surface, the other is called the Cassie state because it does not fill the micro or nano-sized spaces on the surface, and if air sacs are trapped in these spaces, the contact area of the liquid with the surface decreases considerably [23]. Water drops on hydrophobic surface with regular micro surface is shown in Figure 5.

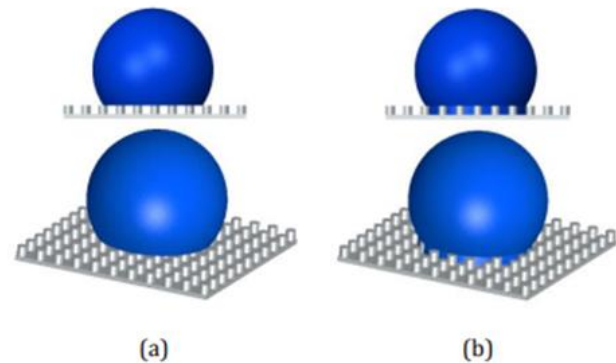


**Figure 5.** Water drops on hydrophobic surface with regular micro surface (a): Situation on pillars (Cassie Condition), (b): Situation where it penetrates between pillars (Wenzel case) [23].

The achievement of a hydrophobic surface is achieved using many methods, such as micro surface treatment

and regular surface fabrication, spray or coating [24]. In the studies carried out by obtaining a regular surface on a smooth surface, the roughness on the surface is obtained by creating regular and repeating columns. Hydrophobic surfaces with different properties can be obtained by changing parameters such as the shape, size, distance between these columns and the applied material.

## 2.2. Application areas of hydrophobic surfaces

### 2.2.1. Marine applications

Reducing the drag of a liquid is very important for materials whose surface comes into contact with the liquid, such as ship submarine pipelines and torpedoes [25]. In this direction, in some previous studies, continuous air bubbles were sent on solid surfaces, thereby reducing the contact area between the liquid and solid surface and thus reducing the drag resistance [26]. Today, with the development of nanotechnology, it has been observed that superhydrophobic surfaces appear to be covered with a thin layer of air film when immersed in water. As a result of this observation, having a superhydrophobic surface for surfaces that have to move in the liquid will provide a great advantage as it will reduce the viscous surface friction [25].

### 2.2.2. Aerospace applications

Brown et. al [27] studied durability of superhydrophobic duplex coating systems for aerospace applications. Superhydrophobic surfaces, have been shown to offer improvements to heating-based anti-icing and de-icing systems, reducing energy requirements for ice prevention and facilitating ice removal.

## 2.3 Superhydrophobic materials' icing prevention

The materials used in the construction industry, power lines, aviation industry and many other areas are exposed to icing and this creates many disadvantages. In these sectors, materials that are not exposed to icing are of great interest and demand. Defrosting or de-icing methods used today require high amounts of energy or harm the environment. In many studies, it has been investigated how to overcome this problem by examining the dynamics of various cold surfaces and water droplets hitting these surfaces. As a result of the experiments, it was concluded that the superhydrophobic surfaces to be formed with nanostructures can prevent the initial growth of ice. Test of anti-icing properties of superhydrophobic coated material is shown in Figure 6.

While the destruction of ice spread in a thin layer, which may occur as a result of natural or artificial reasons in many materials used today, is unpredictable, the extent of the danger it may pose is also quite large.

Melting removal, which is used as a de-icing method, causes damage to the material and the time this process will take is unpredictable. Melting with salt, which is used as another method, causes corrosion on the material. In addition, ethylene glycol, which is used as another method, is a highly toxic substance.

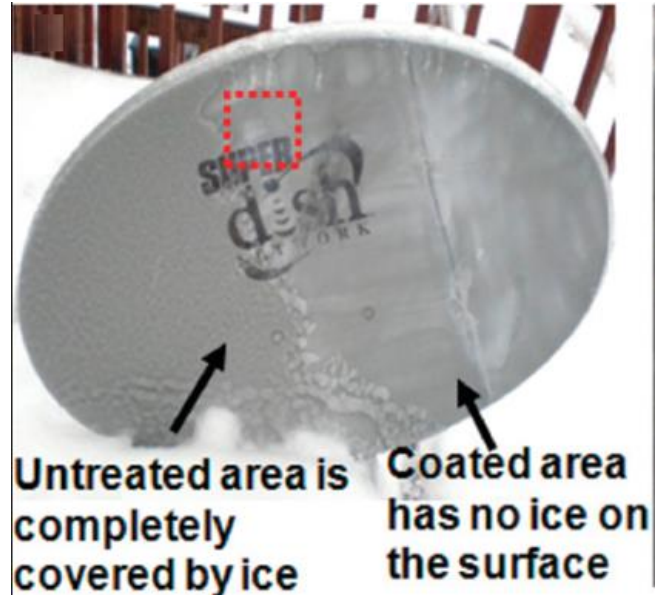


**Figure 6.** Test of anti-icing properties of superhydrophobic coated material [28].

Scientists are working to eliminate the threat of ice in areas where it is needed, and they are doing many studies to develop more environmentally friendly methods with less energy. Many studies by scientists show that surface geometry can be a solution to the problem of icing formation. Mishchenko et. al. [29] investigated the collision dynamics of the water droplet with a superhydrophobic surface at plus and minus temperatures. According to the results obtained as shown in Figure 7, they hypothesized that a superhydrophobic surface could repel water down to  $-30^{\circ}\text{C}$  and thus prevent ice formation.

Mishchenko et. al. [29] created various geometric structures, various types of nanostructures and superhydrophobic surfaces of various sizes on a fluoride-based silicon. They carried out a series of experiments by dropping water droplets in a volume of  $15\ \mu\text{l}$  (a few millimeters in radius) onto the silicon surface from a height of 10 cm, with temperatures ranging from  $+20^{\circ}\text{C}$  to  $-35^{\circ}\text{C}$ . Droplets ranged between  $-5^{\circ}\text{C}$  and  $+60^{\circ}\text{C}$ .

As a result of the experiment, the researchers came to the following conclusions:

On an ordinary, untreated rough aluminum surface, the shrinkage of the drop after expansion does not matter:  $r_{\text{max}} = r_{\text{min}}$ . This result leads to a wide field of interaction and as a result, the freezing of the drop occurs within a few seconds (Figure 8).

Although the droplets contract strongly on a smooth silicone hydrophobic surface, they still maintain a non-zero contact area and will freeze sooner or later at any negative substrate temperature (few seconds if the temperature is lower than  $-10^{\circ}\text{C}$ ) (Figure 8).

In droplets, the superhydrophobic nanostructured surface has a complete contraction ( $r_{\text{min}} = 0$ ) for surface temperatures down to minus  $25\text{--}30^{\circ}\text{C}$  (Figure 8). Simply put, after hitting the surface, the droplets bounce off so fast that they don't have time to solidify. This can be verified by monitoring the behavior of the droplets for all three substrate types. Thus, icing does not occur on the surface.

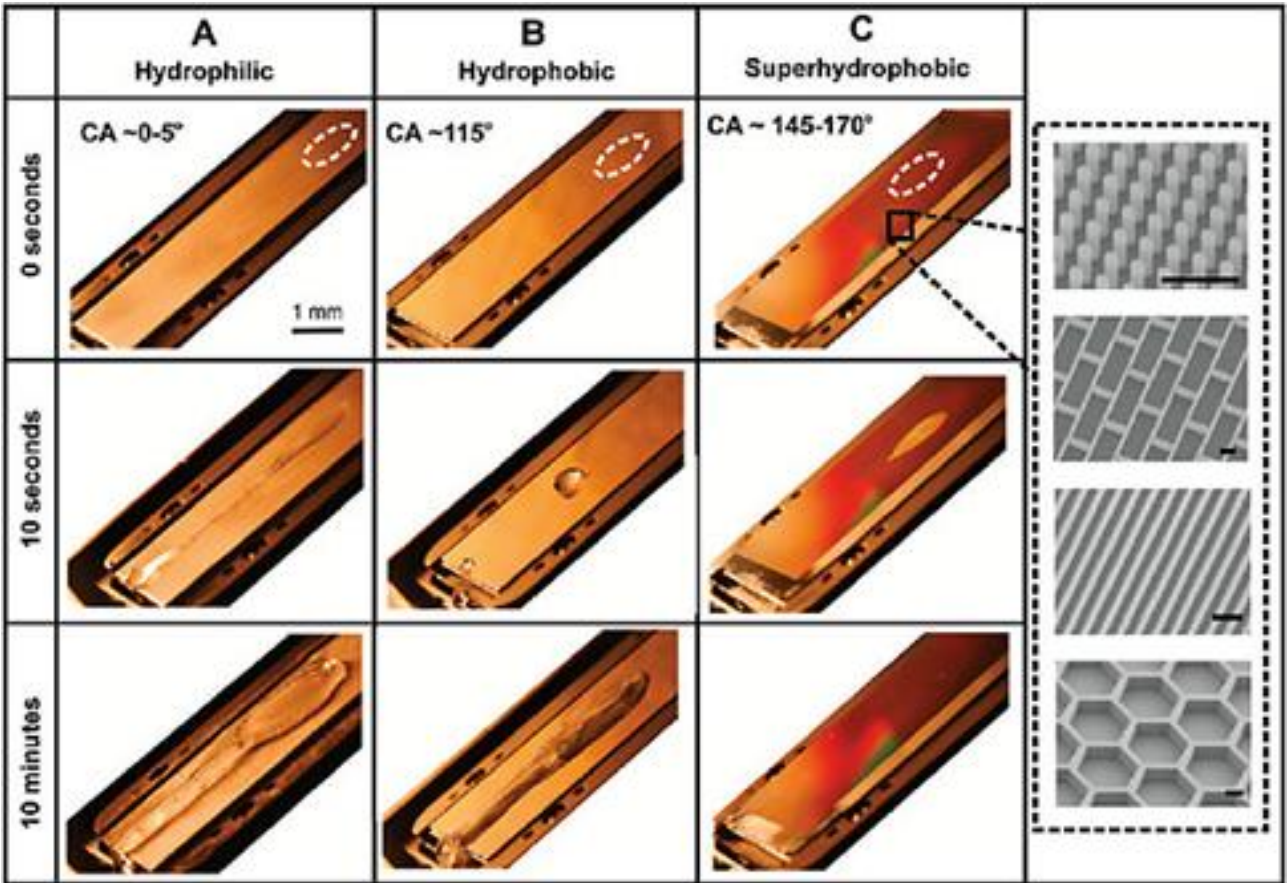


**Figure 7.** Ice accumulation on flat aluminum (A), smooth fluorinated Si (B), and microstructured fluorinated Si (C) surfaces. The advancing contact angle (CA) of the water droplets on these surfaces is indicated [29].

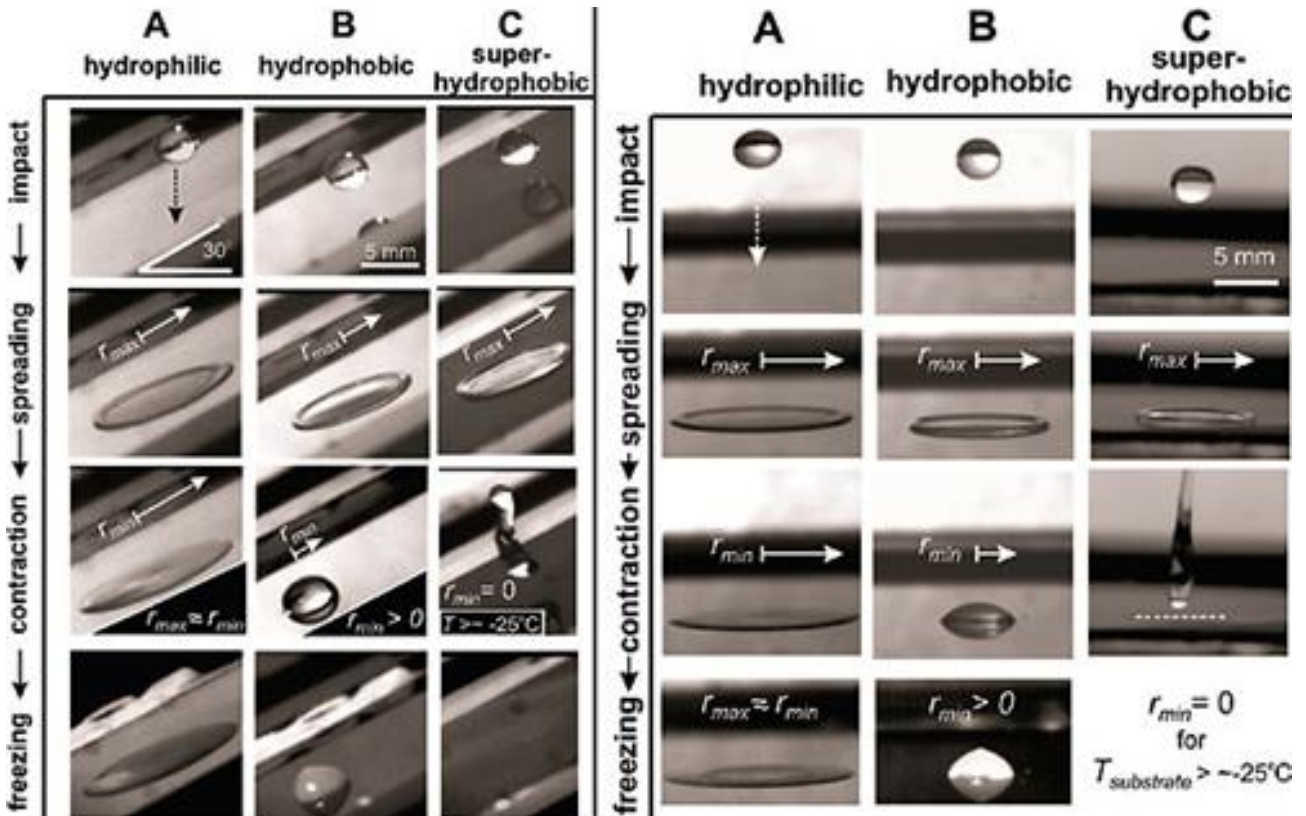


**Figure 8.** Dynamics of droplet behavior on hydrophilic, hydrophobic and superhydrophobic surfaces placed at an angle of 30° (left) and horizontal (right). The temperature of all surfaces is below zero. Drop temperature 0°C. The top-down photos describe the collision of the drop, the moment of maximum expansion ( $r_{max}$ ), followed by compression ( $r_{min}$ ), and freezing. For superhydrophobic surfaces, the compression radius is zero if its temperature is above minus 25 - minus 30°C [29].

During the experiments, scientists achieved a very important result. It has been determined that superhydrophobic surfaces can be an alternative to prevent ice as well as repel water as shown in Figure 7. In the Cassie case, the decrease in the contact area between the liquid and the surface minimizes the contact between the surface and the liquid, thus reducing the contact time of the water with the surface so that the water does not have a chance to freeze. In this way, ice will be prevented from forming without the need for any de-icing method. With superhydrophobic materials, it will be possible to solve engineering problems in many fields, save energy and eliminate the damage to the environment.

### 2.4 Effect of superhydrophobicity on friction

The advantages of hydrophobic surfaces are seen as a solution to many problems in the field of engineering. For example, the transmission of a fluid from one place to another requires solving many engineering problems. While transporting the fluid from one place to another is carried out with pumps, these pumps constitute 20% of the electricity consumption [30]. Today, with the increase in the need for energy, the use of fossil fuels creates the necessity of being economical in terms of both the greenhouse gas it creates and the unity of being depleted. Reducing friction losses can be a solution to both increasing efficiency and reducing the energy used in pump systems. With the developing surface coating technologies, materials with low surface energy can be produced and superhydrophobic surfaces can be created. In these created surfaces, the non-slip condition created by the fluid with the surface is eliminated, so the shear stress and friction force are reduced.

It is visualized that the flow in a pipe can be laminar and turbulent, with the help of a capillary tube placed in a transparent tube made by Osborne Reynolds and a colored liquid injected through this capillary tube. The line formed by the colored liquid injected through the capillary tube in the transparent tube gives us an idea about the type of flow. At low speeds and flow rates, the line formed by the colored liquid is seen as a straight and sharp line. In this case, the type of flow in the transparent pipe is called laminar flow. At high speeds and flow rates, the line formed by the liquid, on the contrary to appearing as a straight line, follows a random trajectory and its boundaries are broken. This type of flow is called turbulent flow. The transition to laminar flow followed by turbulent flow is called the transition regime [31]. Flow types are shown in Figure 9.

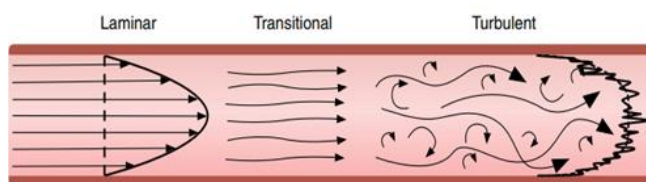


**Figure 9.** Schematic view of turbulent flow, transitional flow and laminar flow [32].

In many studies, the friction factor observed in laminar flow is higher than in turbulent flow. The reason

why it provides the non-slip condition on hydrophobic surfaces is that the area where the liquid contacts the existing hydrophobic surface is small and accordingly liquid drops can roll on the hydrophobic surface. Effect of hydrophobic property on velocity profile is shown in Figure 10. Drops of water that can roll on a solid surface reduce the frictional force on the surface [31].

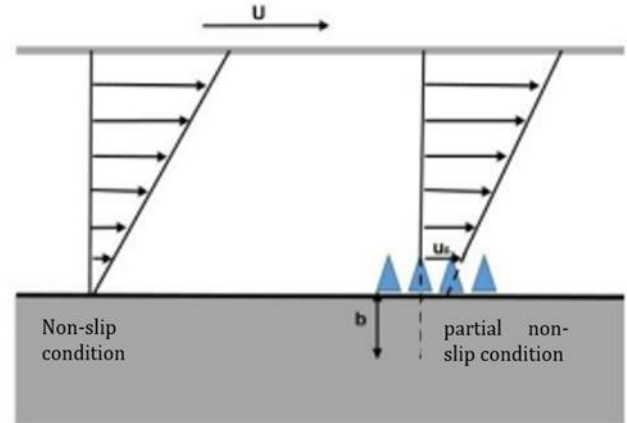


**Figure 10.** Effect of hydrophobic property on velocity profile [33].

Pehlivan et. al. [34] created turbulent flows between 5000 and 30000 Reynolds numbers from a 1 meter long and 15.8-millimeter diameter Flora polymer-based material (FEP, FEP-C, FEP-G) covered with hydrophobic copper pipe. Pressure losses and variation of friction factor were measured. While the contact angle of a water droplet with the copper surface without hydrophobic coating was 65°, the contact angle on the inner surface of the pipe where hydrophobic properties were obtained by coating FEP, FEP-C, FEP-G were measured as 93°, 96° and 102°. FEP with the lowest contact angle has the lowest reduction in friction factor compared to the uncoated copper pipe, while the pipe covered with FEP-G with the highest angle has the highest reduction in friction factor. It has been determined that the decrease in the friction factor on the inner surface of the pipe with the increase in hydrophobicity that occurs proportionally with the increase of the contact angle will cause a decrease in the energy that will be spent in the transmission of the fluid from one place to another.

Ou et al. [35] created Micro protrusions parallel to the flow direction on the superhydrophobic surface in microchannels, and this structure was measured with the Micro-PIV technique. The maximum shear velocity in the microchannel was determined to be 60% of the average flow velocity. They emphasized that superhydrophobicity is the most important factor for reducing the sliding friction factor on the surface.

Choi et al. [36] coated various sizes of grid patterns on a flat sheet. They stated that this process reduces the friction factor by 20-30%. In addition, they found that the friction factor decreased more in the flows parallel to the patterns on the nanostructure compared to the transverse flows. They explained this with the air layer formed between the grids.

Chinappi and Casciola [37] covered the uncoated smooth material surface with a hydrophobic coating and

calculated the slip lengths on these surfaces by molecular dynamic simulation (MD) method. According to the calculated results, the shift length, measured at 20 nm resulted in values of 0.2-0.5 nm when measured with the help of the MD technique. The reason for these two value differences is explained by the air layer formed between the liquid-solid surfaces.

Nouri et al. [38] analyzed the reduction of friction on hydrophobic surfaces using the Large Eddy Simulation (LES) equations in their study. They also confirmed the friction reduction value, which decreased by 30% in the results they found, with the numerical simulation method (DNS). They stated that the turbulent part of the flow near the wall changes with the shear rate on the surface. They stated that this effect occurs when the slip length exceeds a certain value.

Bidkar et al. [39] stated that there is friction reduction between 20% and 30% on hydrophobic surfaces in the turbulent flow regime. They stated that the higher the Reynolds number, the lower the ability of hydrophobic surfaces to hold air, and the decrease in friction accordingly.

### 3. Conclusion

Literature researches and studies show that nanotechnology is one of the strongest bridges that can be formed between the present and the future. With the inspiration taken from nature and the discoveries of science, it will become more possible with nanotechnology to meet the needs of humanity and our environment with more effective and more environmentally friendly methods using less energy. Superhydrophobic surfaces also play an important role in achieving this goal. It is quite clear that superhydrophobic surfaces offer more environmentally friendly engineering solutions with less energy, as they do not hold water, prevent icing and reduce friction losses. It is expected that the use of such designed surfaces and materials will become widespread in the future and will open the door to many more innovations.

There are low-cost applications of superhydrophobic materials with low water contact angle and slide angles [40].

### Author contributions

**Serhat Akinci:** Methodology, Writing-Reviewing, Writing-Original draft preparation. **Filiz**

**Karaömerlioğlu:** Methodology, Writing-Reviewing, Writing-Original draft preparation. **Emre Kaygusuz:** Writing-Reviewing and Editing.

### Conflicts of interest

The authors declare no conflicts of interest.

### References

1. Nosonovsky, M., & Bhushan, B. (2008). Lotus-Effect and Water-Repellent Surfaces in Nature. *Multiscale Dissipative Mechanisms and Hierarchical Surfaces: Friction, Superhydrophobicity, and Biomimetics*, 181-197. [https://doi.org/10.1007/978-3-540-78425-8\\_10](https://doi.org/10.1007/978-3-540-78425-8_10)
2. Whyman, G., Bormashenko, E., & Stein, T. (2008). The rigorous derivation of Young, Cassie–Baxter and Wenzel equations and the analysis of the contact angle hysteresis phenomenon. *Chemical Physics Letters*, 450(4-6), 355-359. <https://doi.org/10.1016/j.cplett.2007.11.033>
3. Özdoğan, E., Demir, A., & Seventekin, N. (2006). Lotus etkili yüzeyler. *Tekstil ve Konfeksiyon*, 16(1), 287-290.
4. Syms, R. R., & Wright, S. (2016). MEMS mass spectrometers: the next wave of miniaturization. *Journal of Micromechanics and Microengineering*, 26(2), 023001. <https://doi.org/10.1088/0960-1317/26/2/023001>
5. Iannacci, J. (2015). Reliability of MEMS: A perspective on failure mechanisms, improvement solutions and best practices at development level. *Displays*, 37, 62-71. <https://doi.org/10.1016/j.displa.2014.08.003>
6. Chai, J., Zhang, K., Xue, Y., Liu, W., Chen, T., Lu, Y., & Zhao, G. (2020). Review of MEMS based Fourier transform spectrometers. *Micromachines*, 11(2), 214. <https://doi.org/10.3390/mi11020214>
7. Ulkir, O., Ertugrul, I., Akkus, N., & Ozer, S. (2022). Fabrication and experimental study of micro-gripper with electrothermal actuation by stereolithography method. *Journal of Materials Engineering and Performance*, 31(10), 8148-8159. <https://doi.org/10.1007/s11665-022-06875-5>
8. Farré, M., Kantiani, L. & Barceló, D. (2012). Chapter 7 - Microfluidic Devices: Biosensors. *Chemical Analysis of Food: Techniques and Applications*, Academic Press, 177-217. <https://doi.org/10.1016/B978-0-12-384862-8.00007-8>
9. Branson, E. D., Singh, S., Houston, J. E., Swol, F. V. & Brinker, C. J. (2006). Superhydrophobic Surface Coatings for Microfluidics and MEMs. Sandia National Laboratories. Sandia Report SAND2006-7020. <https://doi.org/10.2172/1137218>
10. Yu, C., Zhu, X., Cao, M., Yu, C., Li, K., & Jiang, L. (2016). Superhydrophobic helix: controllable and directional bubble transport in an aqueous environment. *Journal of Materials Chemistry A*, 4(43), 16865-16870. <https://doi.org/10.1039/C6TA07318B>
11. Manoharan, K., & Bhattacharya, S. (2019). Superhydrophobic surfaces review: Functional application, fabrication techniques and limitations. *Journal of Micromanufacturing*, 2(1), 59-78. <https://doi.org/10.1177/2516598419836345>
12. Dou, R., Chen, J., Zhang, Y., Wang, X., Cui, D., Song, Y., ... & Wang, J. (2014). Anti-icing coating with an aqueous lubricating layer. *ACS applied materials & interfaces*, 6(10), 6998-7003. <https://doi.org/10.1021/am501252u>

13. Boinovich, L. B., & Emelyanenko, A. M. (2013). Anti-icing potential of superhydrophobic coatings. *Mendelevov Communications*, 23(1), 3-10. <https://doi.org/10.1016/j.mencom.2013.01.002>
14. Farhadi, S., Farzaneh, M., & Kulinich, S. A. (2011). Anti-icing performance of superhydrophobic surfaces. *Applied Surface Science*, 257(14), 6264-6269. <https://doi.org/10.1016/j.apsusc.2011.02.057>
15. Si, Y., & Guo, Z. (2015). Superhydrophobic nanocoatings: from materials to fabrications and to applications. *Nanoscale*, 7(14), 5922-5946. <https://doi.org/10.1039/C4NR07554D>
16. Kim, P., Wong, T. S., Alvarenga, J., Kreder, M. J., Adorno-Martinez, W. E., & Aizenberg, J. (2012). Liquid-infused nanostructured surfaces with extreme anti-ice and anti-frost performance. *ACS nano*, 6(8), 6569-6577. <https://doi.org/10.1021/nn302310q>
17. Chen, J., Li, K., Wu, S., Liu, J., Liu, K., & Fan, Q. (2017). Durable anti-icing coatings based on self-sustainable lubricating layer. *ACS omega*, 2(5), 2047-2054. <https://doi.org/10.1021/acsomega.7b00359>
18. Kibar, A., & Yiğit, K. S. (2018). The spreading profile of an impinging liquid jet on the hydrophobic surfaces. *Sigma Journal of Engineering and Natural Sciences*, 36(3), 609-618.
19. Allred, T. P., Weibel, J. A., & Garimella, S. V. (2018). Enabling highly effective boiling from superhydrophobic surfaces. *Physical review letters*, 120(17), 174501. <https://doi.org/10.1103/PhysRevLett.120.174501>
20. Stahlberg, R., Babauta, K. & Mayer, G. (2011). Superhydrophobic Hairy Leaf Surfaces: Are the Hairs Hydrophilic or Hydrophobic? *Proceedings of the ASME 2011 International Mechanical Engineering Congress & Exposition IMECE2011 2011, Denver, Colorado, USA, IMECE2011-6590*
21. Young, T. (1832). An essay on the cohesion of fluids. In *Abstracts of the Papers Printed in the Philosophical Transactions of the Royal Society of London* (No. 1, pp. 171-172). London: The Royal Society.
22. Erbil, H. Y., Demirel, A. L., Avci, Y., & Mert, O. (2003). Transformation of a simple plastic into a superhydrophobic surface. *Science*, 299(5611), 1377-1380. <https://doi.org/10.1126/science.1078365>
23. Kibar, A. (2016). Süperhidrofobik ve hidrofobik yüzeyler üzerinde sıvı damlası gaz kabarcığı ve sıvı jeti dinamiğinin incelenmesi. *Pamukkale Üniversitesi Mühendislik Bilimleri Dergisi*, 22(7), 613-619. <https://doi.org/10.5505/pajes.2016.07088>
24. He, Y., Jiang, C., Cao, X., Chen, J., Tian, W., & Yuan, W. (2014). Reducing ice adhesion by hierarchical micro-nano-pillars. *Applied Surface Science*, 305, 589-595. <https://doi.org/10.1016/j.apsusc.2014.03.139>
25. Aljallis, E., Sarshar, M. A., Datla, R., Sikka, V., Jones, A., & Choi, C. H. (2013). Experimental study of skin friction drag reduction on superhydrophobic flat plates in high Reynolds number boundary layer flow. *Physics of fluids*, 25(2), 5103. <https://doi.org/10.1063/1.4791602>
26. Merkle, C. L., & Deutsch, S. (1990). Drag reduction in liquid boundary layers by gas injection. *Progress in Astronautics and Aeronautics*, 123, 351-412.
27. Brown, S., Lengaigne, J., Sharifi, N., Pugh, M., Moreau, C., Dolatabadi, A., ... & Klemberg-Sapieha, J. E. (2020). Durability of superhydrophobic duplex coating systems for aerospace applications. *Surface and Coatings Technology*, 401, 126249.
28. Cao, L., Jones, A. K., Sikka, V. K., Wu, J., & Gao, D. (2009). Anti-icing superhydrophobic coatings. *Langmuir*, 25(21), 12444-12448. <https://doi.org/10.1021/la902882b>
29. Mishchenko, L., Hatton, B., Bahadur, V., Taylor, J. A., Krupenkin, T., & Aizenberg, J. (2010). Design of ice-free nanostructured surfaces based on repulsion of impacting water droplets. *ACS nano*, 4(12), 7699-7707. <https://doi.org/10.1021/nn102557p>
30. Yumurtaci, Z., & Sarigul, A. (2011). Santrifüj pompalarda enerji verimliliği ve uygulamaları. *Makina Mühendisleri Odası Tesisat Mühendisliği Dergisi*, 49-58.
31. Pehlivan, M. (2005). Hidrofobik Yüzeylerin Türbülanslı Boru Akımlarında Sürtünme Kayıplarına Etkisinin Deneysel İncelenmesi. Master's Thesis, Ondokuz Mayıs University.
32. McGurk, K. A., Owen, B., Watson, W. D., Nethononda, R. M., Cordell, H. J., Farrall, M., ... & Keavney, B. D. (2020). Heritability of haemodynamics in the ascending aorta. *Scientific Reports*, 10(1), 14356. <https://doi.org/10.1038/s41598-020-71354-7>
33. Wang, C., Tang, F., Li, Q., Zhang, Y., & Wang, X. (2017). Spray-coated superhydrophobic surfaces with wear-resistance, drag-reduction and anti-corrosion properties. *Colloids and surfaces A: Physicochemical and engineering aspects*, 514, 236-242. <https://doi.org/10.1016/j.colsurfa.2016.11.059>
34. Pehlivan, M., Karakurt, U., Özbey, M. & Gürbüz, M. (2019). Floro polimer kaplamanın bakır plaka üzerine uygulanması ve aşınma üzerine etkisinin incelenmesi. *3th ISAS Booklets*, 408-410
35. Ou, J., & Rothstein, J. P. (2005). Direct velocity measurements of the flow past drag-reducing ultrahydrophobic surfaces. *Physics of fluids*, 17(10), 103606. <https://doi.org/10.1063/1.2109867>
36. Choi, C. H., Ulmanella, U., Kim, J., Ho, C. M., & Kim, C. J. (2006). Effective slip and friction reduction in nanogated superhydrophobic microchannels. *Physics of fluids*, 18(8), 7105. <https://doi.org/10.1063/1.2337669>
37. Chinappi, M., & Casciola, C. M. (2010). Intrinsic slip on hydrophobic self-assembled monolayer coatings. *Physics of Fluids*, 22(4), 2003. <https://doi.org/10.1063/1.3394120>
38. Nouri, N. M., Sekhavat, S., & Mofidi, A. (2012). Drag reduction in a turbulent channel flow with hydrophobic wall. *Journal of Hydrodynamics, Ser. B*, 24(3), 458-466. [https://doi.org/10.1016/S1001-6058\(11\)60267-9](https://doi.org/10.1016/S1001-6058(11)60267-9)
39. Bidkar, R. A., Leblanc, L., Kulkarni, A. J., Bahadur, V., Ceccio, S. L., & Perlin, M. (2014). Skin-friction drag reduction in the turbulent regime using random-textured hydrophobic surfaces. *Physics of Fluids*, 26(8), 5108. <https://doi.org/10.1063/1.4892902>
40. Wang, Z., Li, Q., She, Z., Chen, F., & Li, L. (2012). Low-cost and large-scale fabrication method for an

environmentally-friendly superhydrophobic coating  
on magnesium alloy. Journal of Materials

Chemistry, 22(9),  
<https://doi.org/10.1039/C2JM14475A>

4097-4105.



© Author(s) 2024. This work is distributed under <https://creativecommons.org/licenses/by-sa/4.0/>



## Analysis of temperature and precipitation series of Hirfanli Dam Basin by Mann Kendall, Spearman's Rho and Innovative Trend Analysis

Fatma Gunduz<sup>1</sup> , Utku Zeybekoglu<sup>\*2</sup> 

<sup>1</sup>Sinop University, Property Protection and Security Department, Türkiye, fgunduz@sinop.edu.tr

<sup>2</sup>Sinop University, Construction Department, Türkiye, utkuz@sinop.edu.tr

Cite this study:

Gunduz, F., & Zeybekoğlu, U. (2024). Analysis of temperature and precipitation series of Hirfanli Dam Basin by Mann Kendall, Spearman's Rho and Innovative Trend Analysis. Turkish Journal of Engineering, 8 (1), 11-19

### Keywords

Temperature  
Precipitation  
Trend analysis  
Disaster management

### Research Article

DOI: 10.31127/tuje.1177522

Received:20.09.2022

Revised: 12.12.2022

Accepted:19.12.2022

Published:15.09.2023



### Abstract

In this study long-term trend analysis of precipitation and temperature series are determined in the Hirfanli dam basin of Turkey. Data is obtained from the Turkish State Meteorological Service for the period of 1968 to 2017 for Gemerek, Kayseri, Kirsehir, Nevsehir, Sivas and Zara. Mann-Kendall, Spearman's Rho and Innovative Trend Analysis are used for trend analysis with 95% confidence levels. According to the results of the temperature series upward trend were determined. The results of all methods are similar but increasing significant trends were determined by Mann Kendall and Spearman's Rho except Zara. According to the precipitation series results, with decreasing trends in Gemerek, Kirsehir, Nevsehir and Zara, increasing trends were determined in Kayseri and Sivas. The results of Mann Kendall and Spearman's Rho methods show parallelism with each other. Contrary to other methods, Innovative Trend Analysis determined a decreasing trend in Kayseri. As a result of the analysis, the trends in the precipitation series are not significant at the 95% confidence level. In addition to statistical analyzes, evaluations were made in terms of integrated disaster management for drought disaster in the basin with arid climate characteristics.

## 1. Introduction

Along with the global climate change, the causes of the events that adversely affect the climate are the irregularities in the precipitation regimes with the increase in temperatures. It is observed that global climate change affects hydrological and climatological parameters, such as the decrease in glacial masses in the world, changes in sea water levels and irregularities in precipitation [1].

As can be seen in the literature, the effects of global climate change on various hydro-meteorological parameters are being investigated [2-10].

Global climate change has become an important problem affecting civilization around the world. Global climate change manifests itself to different degrees in various geographies in Turkey. These effects were investigated using hydro-meteorological climate parameters [11-21].

Studies on climate and climate components have reported that temperatures have increased and precipitation has decreased in recent years [22].

Keskin et al. [23] examined the effects of global climate change on the Eastern Anatolia region by using precipitation and temperature parameters. Toros [24] evaluated low and high temperature data and precipitation data of 18 stations. Altin et al. [25] conducted trend analysis using rainfall and temperature series of 33 stations in the Central Anatolia region between 1975 and 2007 using the Mann Kendall test.

Drought disaster, which emerged with the oscillations in hydro-meteorological parameters with the effect of global climate change, is one of the main subjects of researchers today. This disaster, which is examined on a global and local scale, is also evaluated in terms of countries [26-36].

In this study, Hirfanli Dam basin, which is located in the semi-arid climate region where climate change can be

seen due to its location, was chosen as the study area. The drought situation in the basin and the Central Anatolia region, where it is geographically located, has been examined with different methods in the literature [37-42]. Temperature and precipitation series analyzes were made by using Mann Kendall (MK), Spearman's Rho (SR) and Innovative Trend Analysis (ITA). In addition, evaluations were made from the perspective of integrated disaster management for the basin's fight against drought.

## 2. Integrated Disaster Management

Disasters are events that affect every geography and every society. Disasters encountered in the developing and changing world have revealed the importance of the concept of integrated disaster management. Disaster management is one of the main areas of activity under the responsibility of the public administration. It is an interdisciplinary, transdisciplinary and transdisciplinary field of study that covers all processes from detection of risks, control of natural, social, human and technological conditions, education of decision makers and all stakeholders, creation of disaster awareness and disaster culture, and planning to control in management. The management model, which is called integrated disaster management today, is a strategic management system that aims to identify risks before disaster or emergency occurs, to prevent or minimize damages, to respond effectively and quickly when disaster occurs, and to carry

out post-disaster recovery efforts by providing integration. The phases of this strategic management system are mitigation, preparedness, response and recovery phases [43-45].

## 3. Material and Methodology

### 3.1. Study area and data

The sub-basin containing the Hirfanli Dam Basin, which is located between 33.3°E and 38.7°E longitudes and 38.3°N and 40.1°N latitudes, is within the Kizilirmak River Basin, and has a surface area of approximately 26700 km<sup>2</sup>. In the basin, the altitude varies between 799 and 3880 m (Figure 1). The east part of the basin is the hillest region of the basin, which consists of high peaks and is bordered by mountainous areas. Plateaus, wide plains, and meadows are more common in the west part of the basin [38-40].

Temperature and precipitation data between 1968 and 2017 were obtained from the Turkish State Meteorological Service. The mean temperature of the basin is 10.03 °C, and the mean annual precipitation value is 424.82 mm. In addition, geographical and meteorological details of the stations are given in Table 1. The temperatures in the basin decrease from west to east, and the distribution of precipitation increases from west to east contrary to temperatures. The spatial distribution of temperature and precipitation is given for the basin in Figures 2-3, respectively.

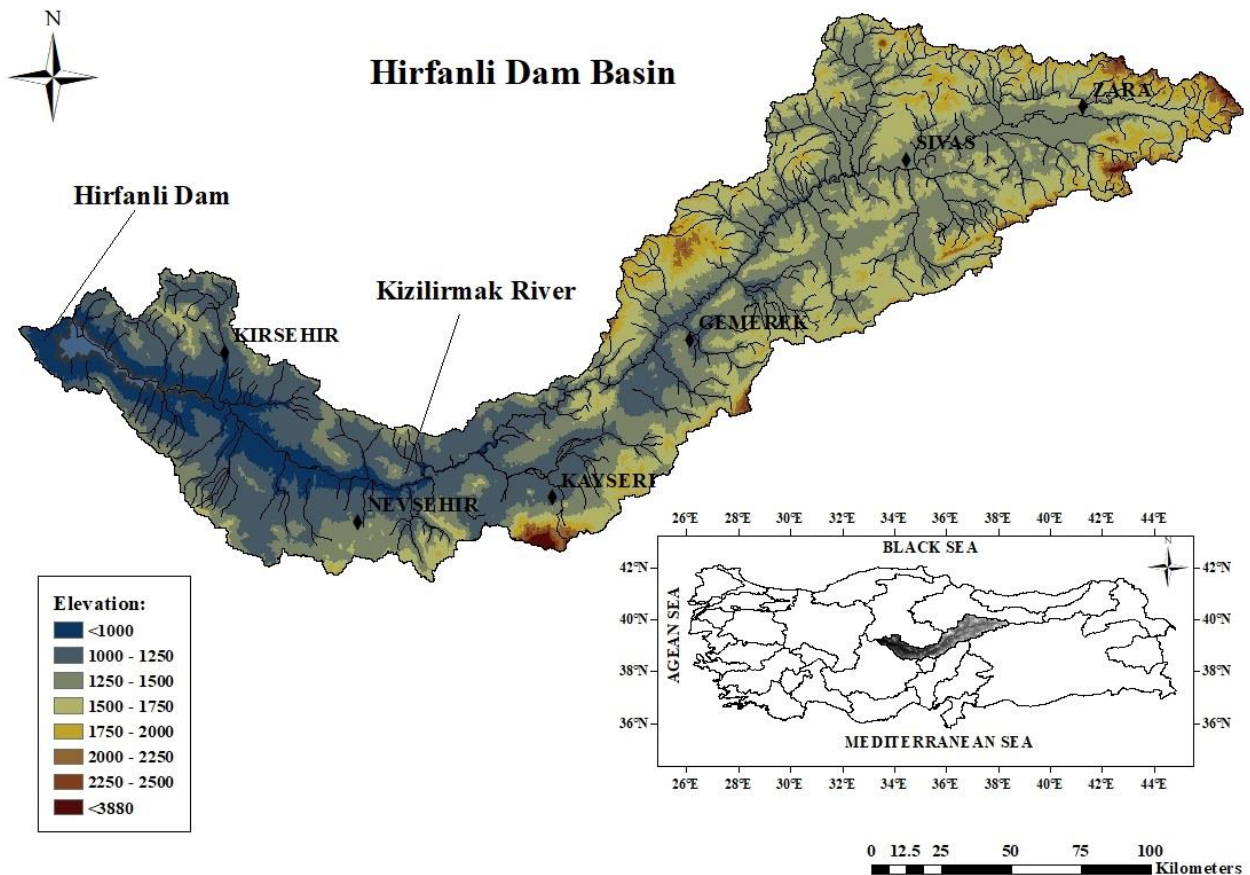
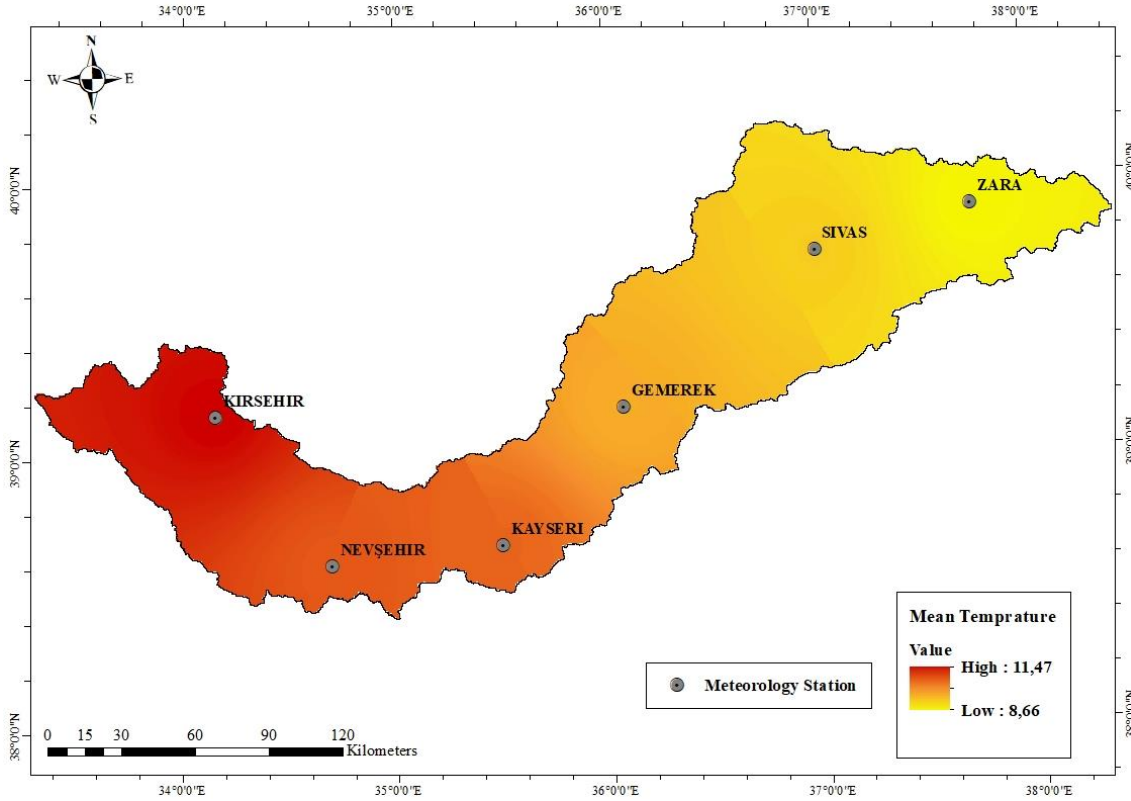


Figure 1. The geographical and topographical situation of the study area [41].

**Table 1.** Geographical and meteorological information of the stations.

Stations	Latitude (N)	Longitude (E)	Elevation (m)	P <sub>mean</sub> (mm/year)	T <sub>mean</sub> (°C/year)
Gemerek	39.11	36.04	1173	403.31	9.64
Kayseri	38.44	35.29	1093	390.13	10.54
Kirsehir	39.09	34.10	1007	383.49	11.47
Nevsehir	38.35	34.40	1200	413.20	10.70
Sivas	39.45	37.01	1285	443.70	9.19
Zara	39.54	37.45	1348	515.11	8.66



**Figure 2.** Spatial distribution of temperatures [42].

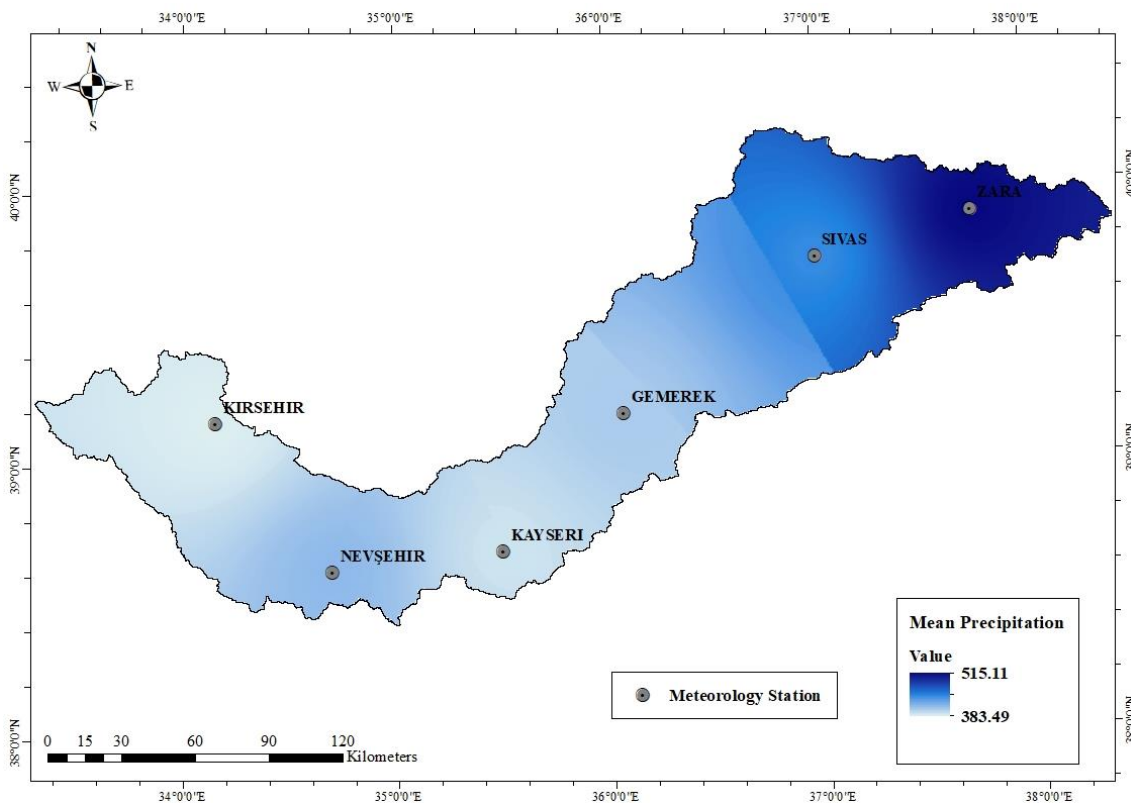


**Figure 3.** Spatial distribution of precipitation [42].

### 3.2. Mann Kendall (MK) trend test

The MK test is independent of the distribution of variables [46-47]. Whether there is a tendency in the time series is tested by the null hypothesis ( $H_0$ : no trend) [2, 48-49]. The pairs  $x_i, x_j$  in the series  $x_1, x_2, \dots, x_n$  are divided into two groups. The test statistic ( $S$ ) is expressed by Equation (1), where for  $i < j$  the number of pairs with  $x_i < x_j$  is  $P$  and the number of pairs with  $x_i > x_j$  is  $M$ . Kendall correlation coefficient with Equation (2); variance is calculated by Equation (3). If there are equal values in observations in the series, the variance value is calculated using Equation (4).

$$S = P - M \quad (1)$$

$$\tau = \frac{S}{\left[\frac{n(n-1)}{2}\right]} \quad (2)$$

$$\sigma_s = \sqrt{\frac{n(n-1)(2n+5)}{18}} \quad (3)$$

$$\sigma_s = \sqrt{\frac{n(n-1)(2n+5) - \sum t_i(t_i-1)(2t_i+5)}{18}} \quad (4)$$

Standardized MK test statistics are calculated by Equation (5).

$$\begin{array}{l} \frac{(S-1)}{\sigma_s} \quad ; \quad S > 0 \\ 0 \quad ; \quad S = 0 \\ \frac{(S+1)}{\sigma_s} \quad ; \quad S < 0 \end{array} \quad (5)$$

If the absolute Z obtained by Equation (5) is less than the critical Z of the normal distribution corresponding to the selected  $\alpha$  significance level, the  $H_0$  is accepted; otherwise, the existence of the trend is determined. Positive values indicate the presence of an increasing trend, while negative values indicate a decreasing tendency [50].

### 3.3. Spearman's Rho (SR) trend test

SR method is a simple and fast method used to investigate whether a linear trend exists. The purpose of the SR test is to investigate the existence of a linear relationship between the two-observation series [51-52]. Using Equation (6), the  $r_s$  value for the SR test statistic is calculated [53-54].

$$r_s = 1 - \frac{6\left[\sum_{i=1}^n (R(x_i) - i)^2\right]}{(n^3 - n)} \quad (6)$$

If the observation period ( $n$ ) exceeds 30 years, the Z value is calculated using Equation (7) [11, 55].

$$Z = r_s \sqrt{n-1} \quad (7)$$

If the Z value at a selected  $\alpha$  significance level is greater than the  $z\alpha$  value determined from the standard normal distribution table, the  $H_0$  (No trend) hypothesis based on the fact that the observation values do not

change over time is rejected and it is concluded that there is a certain trend.

### 3.4. Innovative trend analysis (ITA)

According to this approach proposed by Sen, the recorded set of hydrometeorological data is divided into two equal halves from the median year [56]. The trend was not observed above the 1:1 line, and it was observed that decreasing trend is observed when the data 1: 1 line is located in the lower triangular region, and there is an increasing trend when it is located in the upper triangular region [56]. Sen [57] provided statistical control of the statistical process and results with this method. The steps of the stated statistical process are given in Equations (8-13) [57-60].

$$E(s) = \frac{s}{n} [E(\bar{y}_2) - E(\bar{y}_1)] \quad (8)$$

$$\sigma_s^2 = \frac{4}{n^2} [E(\bar{y}_2)^2 - 2E(\bar{y}_2 \bar{y}_1) - E(\bar{y}_1)^2] \quad (9)$$

$$\rho_{\bar{y}_2 \bar{y}_1} = \frac{E(\bar{y}_2 \bar{y}_1) - E(\bar{y}_1)E(\bar{y}_2)}{\sigma_{\bar{y}_2} \sigma_{\bar{y}_1}} \quad (10)$$

$$\sigma_s^2 = \frac{8}{n^2} \frac{\sigma^2}{n} (1 - \rho_{\bar{y}_2 \bar{y}_1}) \quad (11)$$

$$\sigma_s = \frac{2\sqrt{2}}{n\sqrt{n}} \sigma (1 - \rho_{\bar{y}_2 \bar{y}_1}) \quad (12)$$

$$CL_{(1-\alpha)} = 0 \pm S_{critical} \sigma_s \quad (13)$$

In equations:  $\bar{y}_1$  average of first data,  $\bar{y}_2$ : the average of the second data,  $\rho$ : correlation between the first and second data,  $s$ : slope value,  $n$ : number of data,  $\sigma$ : standard deviation of all data,  $\sigma_s$ : slope standard deviation,  $S_{critical}$ : In the one-way hypothesis (for example 95% confidence level) Z shows critical values. The critical upper and lower limit values calculated by Equation 6 were established to determine the limits of the hypothesis test. Each station has a trend in the time series when the slope value  $s$  is outside the upper and lower confidence limits. The trend direction  $s$  depending on the sign. Slope value ( $s$ ) can be positive or negative. This means that there is an increasing (+) or decreasing (-) trend in the time series [57-62].

## 4. Results

The MK, SR and ITA were applied to identify the tendency in the Hirfanli Dam Basin stations recorded by TSMS in the period of 1968-2017. The results of the analyzes performed at 95% confidence levels are shown in the Tables 2 and 3 respectively. Graphical results of ITA also shown Figures 4-5.

According to temperature results (Table 2 and Figure 4), increasing trends were determined at all stations. Statistically significant trends of upward ( $Z > Z_{Cr}$ ) were designated in the Gemerek, Kayseri, Kirsehir, Nevsehir and Sivas pursuant to MK and SR. On the other hand, the ITA results of stations, a significant upward trend could not be determined but stations have upward trend. The findings of this results, obtained by MK, SR and ITA

methods for the Hirfanli dam basin, show parallelism for temperature series.

According to Table 3 and Figure 5, MK, SR and ITA results of the stations. According to the MK and SR results, a significant trend could not be determined. An upward trend detected Kayseri and Sivas. Gemerek, Kirsehir, Nevsehir and Zara have downward trend. For

ITA results, Gemerek Kayseri, Kirsehir, Nevsehir and Zara have downward trend. There is just Sivas has upward trend. The findings of precipitation results, obtained by MK, SR and ITA methods for the Hirfanli dam basin, show parallelism except Kayseri. The results of Kayseri have upward for MK and SR but ITA show downward trend.

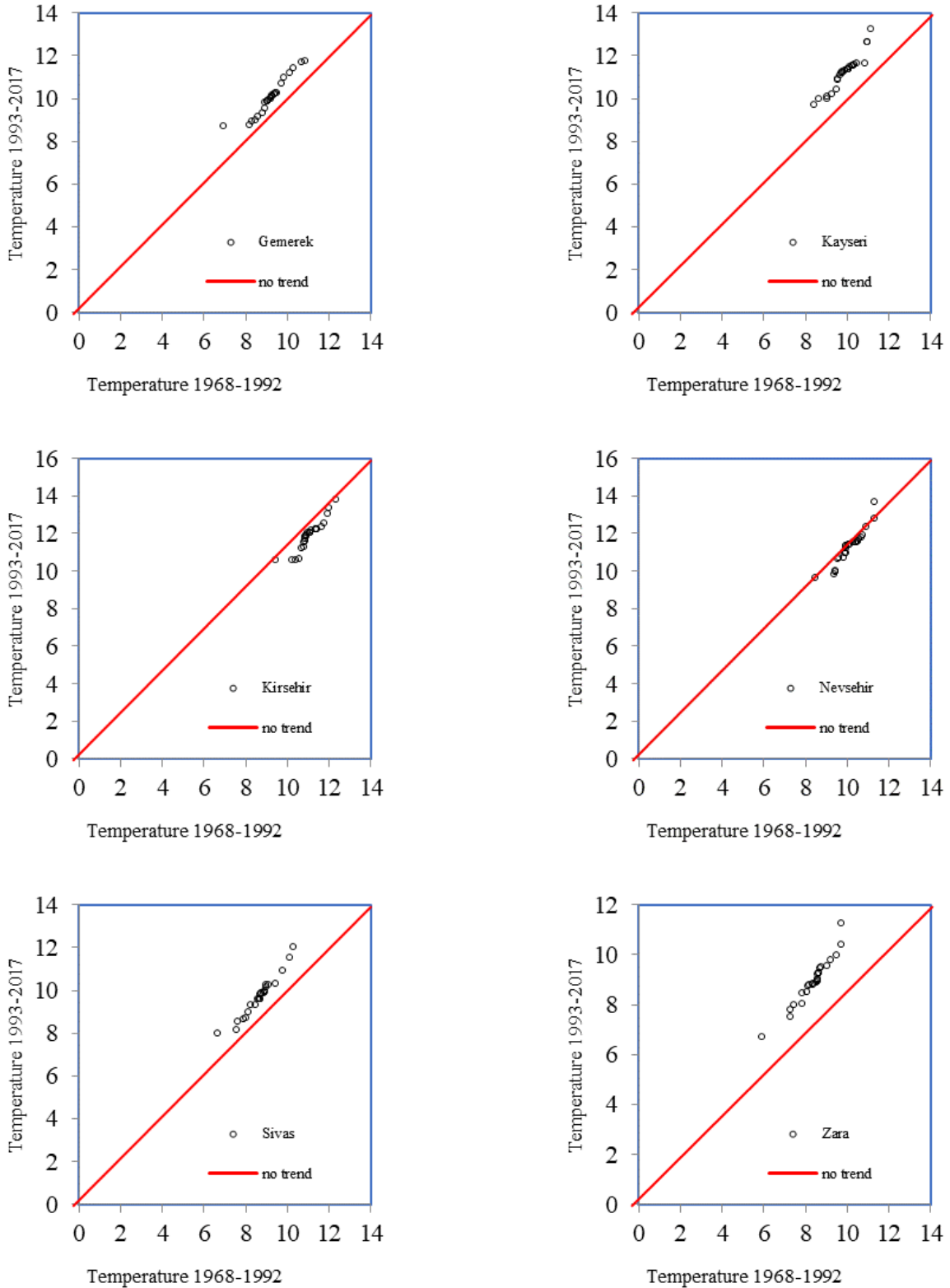
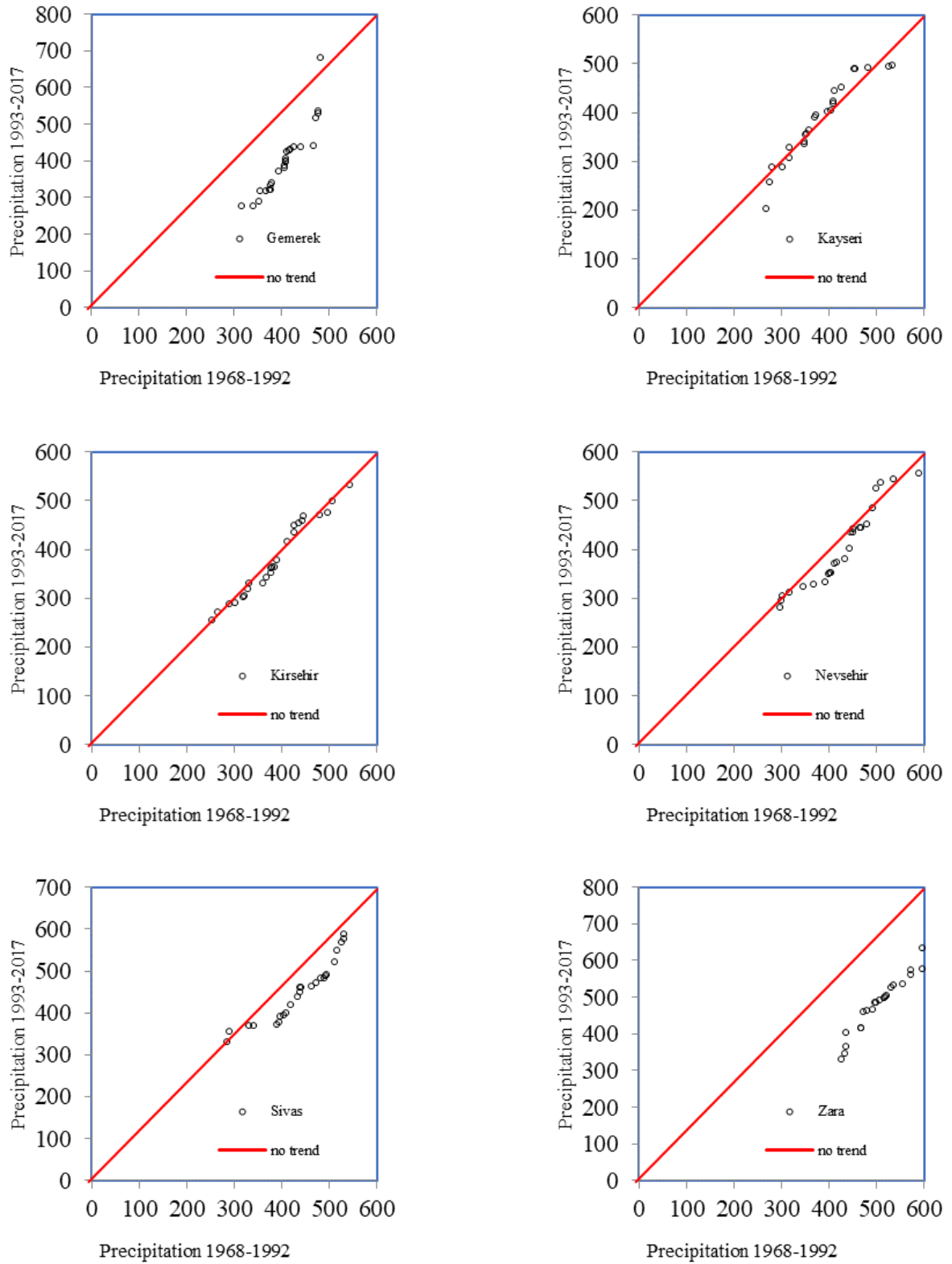


Figure 4. Graphical ITA results of temperature series.



**Figure 5.** Graphical ITA results of precipitation series.

**Table 2.** MK, SR and ITA results of temperature series.

Stations	$Z_{Cr}$	$Z_{MK}$	Trend	$Z_{SR}$	Trend	$CL_{ITA}$	s	Trend
Gemerek	$\pm 1.96$	<b>2.46</b>	<b>Significant upward</b>	<b>2.53</b>	<b>Significant upward</b>	$\pm 0.0568$	0.0341	Upward
Kayseri	$\pm 1.96$	<b>4.80</b>	<b>Significant upward</b>	<b>4.55</b>	<b>Significant upward</b>	$\pm 0.0695$	0.0526	Upward
Kirsehir	$\pm 1.96$	<b>3.35</b>	<b>Significant upward</b>	<b>3.40</b>	<b>Significant upward</b>	$\pm 0.0645$	0.0337	Upward
Nevsehir	$\pm 1.96$	<b>4.02</b>	<b>Significant upward</b>	<b>4.06</b>	<b>Significant upward</b>	$\pm 0.0673$	0.0457	Upward
Sivas	$\pm 1.96$	<b>3.36</b>	<b>Significant upward</b>	<b>3.36</b>	<b>Significant upward</b>	$\pm 0.0581$	0.0413	Upward
Zara	$\pm 1.96$	1.77	Upward	1.80	Upward	$\pm 0.0508$	0.0225	Upward

**Table 3.** MK, SR and ITA results of precipitation series.

Stations	Z <sub>Cr</sub>	Z <sub>MK</sub>	Trend	Z <sub>SR</sub>	Trend	CL <sub>ITA</sub>	s	Trend
Gemerek	±1.96	-0.08	Downward	-0.03	Downward	±1.1895	-0.2965	Downward
Kayseri	±1.96	1.14	Upward	1.05	Upward	±1.3414	-0.0810	Downward
Kirsehir	±1.96	-0.36	Downward	-0.25	Downward	±1.2302	-0.2707	Downward
Nevsehir	±1.96	-0.23	Downward	-0.19	Downward	±1.2699	-0.9218	Downward
Sivas	±1.96	0.86	Upward	0.79	Upward	±1.1621	0.5354	Upward
Zara	±1.96	-1.70	Downward	-1.72	Downward	±1.4146	-0.7675	Downward

## 5. Conclusion

In this study, the effect of global climate change on the temperature and precipitation series in the Hirfanli Dam Basin was investigated. The temperature and precipitation records measured by TSMS in the period 1968-2017 were used. An upward trend has been determined in the temperature values throughout the basin. For precipitation series downward and upward trends have been determined.

As a result of global climate change, drought in the basin is expected to increase even more in the future. In line with this expectation, it is important to identify risks and hazards, take all necessary precautions, take responsibility for disasters and to raise awareness in order to prevent and reduce damages within the scope of the modern disaster management approach [63]. In line with the disaster management approach, for the drought disaster and other possible disasters in the basin:

- Strategic disaster action plans should be prepared with a participatory understanding.
- Disaster management policies should be established with a culture of cooperation between central and local governments, non-governmental organizations, professional chambers and the private sector.
- In this context, all stakeholders, governorships, local governments, public institutions, development agencies, universities, city councils, professional chambers and non-governmental organizations should come together to prepare plans and share them with the public, knowing their responsibilities within the framework of cooperation.
- Short films and public service announcements should be created to inform about disasters.
- Disaster education issues should be reviewed and new topics should be strategically added. Disaster education should be given starting from primary school age and education should be repeated at regular intervals.

## Acknowledgement

The authors thank the Turkish State Meteorological Service for the data. The authors also thank the reviewers for their constructive criticisms which have considerably improved this manuscript.

## Author contributions

**Utku Zeybekoglu:** Conceptualization, Methodology, Analysis, Validation, Visualization, Writing-Original draft preparation, Editing. **Fatma Gunduz:** Conceptualization, Analysis, Investigation, Writing-Original draft preparation, Writing-Reviewing and Editing

## Conflicts of interest

The authors declare no conflicts of interest.

## References

1. Zeybekoğlu, U., Partal, T., (2018), Sinop iline ait aylık ve yıllık yağış yükseklikleri ile standart süreli yağış şiddetlerinin farklı trend analizi yöntemleriyle değerlendirilmesi. İklim Değişikliği ve Çevre, 3, (1) 1-8,
2. Partal, T., & Kahya, E. (2006). Trend analysis in Turkish precipitation data. *Hydrological Processes*, 20(9), 2011-2026. <https://doi.org/10.1002/hyp.5993>
3. Türkeş, M. (1996). Spatial and temporal analysis of annual rainfall variations in Turkey. *International Journal of Climatology*, 16(9), 1057-1076. [https://doi.org/10.1002/\(SICI\)1097-0088\(199609\)16:9<1057::AID-JOC75>3.0.CO;2-D](https://doi.org/10.1002/(SICI)1097-0088(199609)16:9<1057::AID-JOC75>3.0.CO;2-D)
4. Singh, S., & Kumara, S. (2021). Non-Parametric Trend Analysis in South-East Regions of Uttarakhand, India. *International Journal of Earth Sciences Knowledge and Applications*, 3(3), 301-304.
5. Jayasekara, S. M., Aeysingha, N. S., & Meegastenna, T. J. (2020). Streamflow trends of Kelani River basin in Sri Lanka (1983-2013). *Journal of the National Science Foundation of Sri Lanka*, 48(4), 449-462. <http://dx.doi.org/10.4038/jnsfsr.v48i4.9440>
6. Caloiero, T. (2020). Evaluation of rainfall trends in the South Island of New Zealand through the innovative trend analysis (ITA). *Theoretical and Applied Climatology*, 139(1-2), 493-504. <https://doi.org/10.1007/s00704-019-02988-5>
7. Cooley, A., & Chang, H. (2017). Precipitation intensity trend detection using hourly and daily observations in Portland, Oregon. *Climate*, 5(1), 10. <https://doi.org/10.3390/cli5010010>
8. Ribeiro, S., Caineta, J., Costa, A. C., Henriques, R., & Soares, A. (2016). Detection of inhomogeneities in precipitation time series in Portugal using direct sequential simulation. *Atmospheric Research*, 171, 147-158. <https://doi.org/10.1016/j.atmosres.2015.11.014>
9. Birsan, M. V., Micu, D. M., Nita, A. I., Mateescu, E., Szep, R., & Keresztesi, A. (2019). Spatio-temporal changes in annual temperature extremes over Romania (1961-2013). *Romanian Journal of Physics*, 64(7-8), 816.
10. Yacoub, E., & Tayfur, G. (2019). Trend analysis of temperature and precipitation in Trarza region of Mauritania. *Journal of Water and Climate Change*, 10(3), 484-493. <https://doi.org/10.2166/wcc.2018.007>

11. Zeybekoğlu, U., & Karahan, H. (2018). Standart süreli yağış şiddetlerinin eğilim analizi yöntemleriyle incelenmesi. Pamukkale Üniversitesi Mühendislik Bilimleri Dergisi, 24(6), 974-1004. <https://doi.org/10.5505/pajes.2017.54265>
12. Topuz, M., Feidas, H., & Karabulut, M. (2020). Trend analysis of precipitation data in Turkey and relations to atmospheric circulation:(1955-2013). Italian Journal of Agrometeorology, (2), 91-107. <https://doi.org/10.13128/ijam-887>
13. Ülke, A., & Özkoca, T. (2018). Sinop, Ordu ve Samsun illerinin sıcaklık verilerinde trend analizi. Gümüşhane Üniversitesi Fen Bilimleri Dergisi, 8(2), 455-463. <https://doi.org/10.17714/gumusfenbil.351294>
14. Zeybekoğlu, U., & Aktürk, G. (2022). Homogeneity and Trend Analysis of Temperature Series in Hirfanli Dam Basin. Türk Doğa ve Fen Dergisi, 11(1), 49-58. <https://doi.org/10.46810/tdfd.955393>
15. Haktanir, T., & Citakoglu, H. (2014). Trend, independence, stationarity, and homogeneity tests on maximum rainfall series of standard durations recorded in Turkey. Journal of Hydrologic Engineering, 19(9), 05014009. [https://doi.org/10.1061/\(ASCE\)HE.1943-5584.000097](https://doi.org/10.1061/(ASCE)HE.1943-5584.000097)
16. Keskin, A. Ü., Beden, N., & Demir, V. (2018). Analysis of annual, seasonal and monthly trends of climatic data: a case study of Samsun. Nature Sciences, 13(3), 51-70. <http://dx.doi.org/10.12739/NWSA.2018.13.3.4A0060>
17. Ay, M., & Kisi, O. (2017). Kızılırmak Nehrinde Bazı İstasyonlardaki Akımların Trend Analizi. Teknik Dergi, 28(2), 7779-7794. <https://doi.org/10.18400/tekderg.304034>
18. Bacanlı, U. G., & Tanrikulu, A. (2017). Ege Bölgesinde Buharlaşma Verilerinin Trend Analizi. Afyon Kocatepe Üniversitesi Fen ve Mühendislik Bilimleri Dergisi, 17(3), 980-987. <https://doi.org/10.5578/fmbd.66282>
19. Kadioğlu, M. (1997). Trends in surface air temperature data over Turkey. International Journal of Climatology: A Journal of the Royal Meteorological Society, 17(5), 511-520. [https://doi.org/10.1002/\(SICI\)1097-0088\(199704\)17:5<511::AID-JOC130>3.0.CO;2-0](https://doi.org/10.1002/(SICI)1097-0088(199704)17:5<511::AID-JOC130>3.0.CO;2-0)
20. Ceribasi, G. (2018). Analysis of meteorological and hydrological data of Iznik Lake Basin by using Innovative Sen Method. Journal of Environmental Protection and Ecology, 19(1), 15-24.
21. Yenigün, K., & Ülgen, M. (2016). İklim değişikliği ekseninde maksimum akım verilerindeki trendler ve baraj güvenliğine etkisinin izlenmesi. Dicle Üniversitesi Mühendislik Fakültesi Mühendislik Dergisi, 7(2), 343-353.
22. Kuyucu, H., Demir, V., Geyikli, M. S., & Citakoglu, H. (2017). Trend Analysis of Turkey Temperatures. 1st International Symposium on Multidisciplinary Studies and Innovative Technologies Proceedings. Tokat, 157-159.
23. Keskin, M. E., Çakto, İ., Çetin, V., & Bektaş, O. (2018). Doğu Anadolu Bölgesi yağış ve sıcaklık trend analizi. Mühendislik Bilimleri ve Tasarım Dergisi, 6(2), 294-300. <https://doi.org/10.21923/jesd.380963>
24. Toros, H. (1993). Klimatolojik Serilerden Türkiye İkliminde Trend Analizi. Master's Thesis, İstanbul Technical University
25. Altın, T. B., Barak, B., & Altın, B. N. (2012). Change in Precipitation and Temperature Amounts over Three Decades in Central Anatolia Turkey. Atmospheric and Climate Sciences, 2(1), 107-125. <https://doi.org/10.4236/acs.2012.21013>
26. Lloyd-Hughes, B., & Saunders, M. A. (2002). A drought climatology for Europe. International Journal of Climatology, 22 (13), 1571-1592. <https://doi.org/10.1002/joc.846>
27. Sirdas, S., & Sen, Z. (2003). Spatio-temporal drought analysis in the Trakya region, Turkey. Hydrological Sciences Journal, 48(5), 809-820. <https://doi.org/10.1623/hysj.48.5.809.51458>
28. Kömüşçü, A. Ü., Erkan, A., Turgu, E., & Sönmez, K. F. (2004). A new insight into drought vulnerability in Turkey using the standard precipitation index. Journal of Environmental Hydrology, 12(18), 1-17.
29. Sönmez, F. K., Koemuescue, A. U., Erkan, A., & Turgu, E. (2005). An analysis of spatial and temporal dimension of drought vulnerability in Turkey using the standardized precipitation index. Natural hazards, 35, 243-264. <https://doi.org/10.1007/s11069-004-5704-7>
30. Livada, I., & Assimakopoulos, V. (2007). Spatial and temporal analysis of drought in greece using the Standardized Precipitation Index (SPI). Theoretical and applied climatology, 89, 143-153. <https://doi.org/10.1007/s00704-005-0227-z>
31. Mishra, A. K., & Singh, V. P. (2010). A review of drought concepts. Journal of hydrology, 391(1-2), 202-216. <https://doi.org/10.1016/j.jhydrol.2010.07.012>
32. Yacoub, E., & Tayfur, G. (2017). Evaluation and assessment of meteorological drought by different methods in Trarza region, Mauritania. Water Resources Management, 31, 825-845. <https://doi.org/10.1007/s11269-016-1510-8>
33. Ionita, M., Scholz, P., & Chelcea, S. (2016). Assessment of droughts in Romania using the Standardized Precipitation Index. Natural Hazards, 81, 1483-1498. <https://doi.org/10.1007/s11069-015-2141-8>
34. Dabanli, I. (2018). Drought hazard, vulnerability, and risk assessment in Turkey. Arabian Journal of Geosciences, 11, 538. <https://doi.org/10.1007/s12517-018-3867-x>
35. Cebeci, İ., Demirkıran, O., Doğan, O., Sezer, K. K., Öztürk, Ö., & Elbaşı, F. (2019). Türkiye'nin iller bazında kuraklık değerlendirmesi. Toprak Su Dergisi, 169-176. <https://doi.org/10.21657/topraksu.655613>
36. Topçu, E. (2022). Appraisal of seasonal drought characteristics in Turkey during 1925-2016 with the standardized precipitation index and copula approach. Natural Hazards, 112(1), 697-723. <https://doi.org/10.1007/s11069-021-05201-x>
37. Bacanlı, Ü. G., Dikbaş, F., & Baran, T. (2011). Meteorological drought analysis case study: Central

- Anatolia. Desalination and Water Treatment, 26(1-3), 14-23. <https://doi.org/10.5004/dwt.2011.2105>
38. Yildiz, O. (2009). Assessing temporal and spatial characteristics of droughts in the Hirfanli dam basin, Turkey. *Scientific Research and Essays*, 4(4), 249-255. <https://doi.org/10.5897/SRE.9000212>
39. Yildiz, O. (2014). Spatiotemporal analysis of historical droughts in the Central Anatolia, Turkey. *Gazi University Journal of Science*, 27(4), 1177-1184.
40. Oguzturk, G., & Yildiz, O. (2016). Assessing hydrological responses to droughts in the Hirfanli Dam basin, Turkey. *International Journal of Advances in Mechanical and Civil Engineering*, 3(5), 116-123
41. Zeybekoğlu, U., & Aktürk, G. (2021). A comparison of the China-Z Index (CZI) and the Standardized Precipitation Index (SPI) for drought assessment in the Hirfanli Dam basin in central Turkey. *Arabian Journal of Geosciences*, 14(24), 2731. <https://doi.org/10.1007/s12517-021-09095-8>
42. Zeybekoglu, U. (2022). Spatiotemporal analysis of droughts in Hirfanli Dam basin, Turkey by the Standardised Precipitation Evapotranspiration Index (SPEI). *Acta Geophysica*, 70(1), 361-371. <https://doi.org/10.1007/s11600-021-00719-x>
43. Karaman, Z. T. (2016). Afet yönetimine giriş ve Türkiye’de örgütlenme. İlkem Yayıncılık.
44. Ekşi, A. (2016). Kamu Yönetiminde Değişimin Afet Yönetimi Uygulama Alanına Etkileri. *Hastane Öncesi Dergisi*, 1(1), 27-41.
45. AFAD. (2022). Afet Türleri. Ankara: Afet ve Acil Durum Yönetimi Başkanlığı
46. Mann, H. B. (1945). Nonparametric tests against trend. *Econometrica: Journal of the econometric society*, 13(3), 245-259. <https://doi.org/10.2307/1907187>
47. Kendall, M. G. (1975). Rank Correlation Method. London, Charles Griffin.
48. Bayazit, M. (1996). İnşaat Mühendisliğinde Olasılık Yöntemleri. İstanbul, İTÜ İnşaat Fakültesi Matbaası
49. Önöz, B., & Bayazit, M. (2003). The power of statistical tests for trend detection. *Turkish Journal of Engineering and Environmental Sciences*, 27(4), 247-251.
50. Yu, Y. S., Zou, S., & Whittemore, D. (1993). Non-parametric trend analysis of water quality data of rivers in Kansas. *Journal of Hydrology*, 150(1), 61-80. [https://doi.org/10.1016/0022-1694\(93\)90156-4](https://doi.org/10.1016/0022-1694(93)90156-4)
51. Yue, S., Pilon, P., & Cavadias, G. (2002). Power of the Mann-Kendall and Spearman's rho tests for detecting monotonic trends in hydrological series. *Journal of hydrology*, 259(1-4), 254-271. [https://doi.org/10.1016/S0022-1694\(01\)00594-7](https://doi.org/10.1016/S0022-1694(01)00594-7)
52. Yenigun, K., Gumus, V., & Bulut, H. (2008). Trends in Streamflow of Euphrates Basin Turkey. *ICE Water Management*, 161(4), 189-198. <https://doi.org/10.1680/wama.2008.161.4.189>
53. Sneyers R. (1990). On the Statistical Analysis of Series of Observations. World Meteorological Organization, Geneva, Switzerland. Technical Note no. 143, WMO-no. 415.
54. Kalayci, S., & Kahya, E. (1998). Susurluk havzası nehirlerinde su kalitesi trendlerinin belirlenmesi. *Turkish Journal of Engineering and Environmental Science*, 22, 503-514.
55. İçağa, Y., & Harmancıoğlu, N. (1995). Yeşilirmak havzasında su kalitesi eğilimlerinin belirlenmesi. *Türkiye İnşaat Mühendisliği XIII. Teknik Kongresi*, 20-22.
56. Şen, Z. (2012). Innovative trend analysis methodology. *Journal of Hydrologic Engineering*, 17(9), 1042-1046. [https://doi.org/10.1061/\(ASCE\)HE.1943-5584.0000556](https://doi.org/10.1061/(ASCE)HE.1943-5584.0000556)
57. Şen, Z. (2017). Innovative trend significance test and applications. *Theoretical and applied climatology*, 127, 939-947. <https://doi.org/10.1007/s00704-015-1681-x>
58. Demir, V., Zeybekoglu, U., Beden, N., & Keskin, A. U. (2018). Homogeneity and trend analysis of long term temperatures in the Middle Black Sea Region. 13th International Congress on Advances in Civil Engineering, 12-14 September 2018, Izmir, 1-8.
59. Zeybekoglu, U., Alrayess, H., & Keskin, A. U. (2018). Meteorological Drought Analysis in Sinop, Turkey. 13th International Congress on Advances in Civil Engineering, 12-14 September 2018, Izmir, 1-9.
60. Şen, Z. (2017). Innovative trend methodologies in science and engineering (pp. 1-349). New York: Springer International Publishing.
61. Alashan, S. (2020). Combination of modified Mann-Kendall method and Şen innovative trend analysis. *Engineering Reports*, 2(3), e12131.
62. Dabanlı, İ., Şen, Z., Yeleğen, M. Ö., Şişman, E., Selek, B., & Güçlü, Y. S. (2016). Trend assessment by the innovative-Şen method. *Water resources management*, 30, 5193-5203.
63. Gündüz, F. (2022). Afetlerde Kadın ve Toplumsal Cinsiyet Perspektifi ile Çıkarılması Gereken Dersler (Haiti ve Japonya Depremi Örneği). *IBAD Sosyal Bilimler Dergisi*, (12), 440-460.





# Assessment of engineering geology and grouting applications in Yalnızardıç Dam Site (Antalya, Türkiye)

Ömür Çimen<sup>1</sup>, Halil İbrahim Günaydın<sup>\*2</sup>

<sup>1</sup>Süleyman Demirel University, Department of Civil Engineering, Türkiye, omurcimen@sdu.edu.tr

<sup>2</sup>Akdeniz University, Vocational School of Technical Sciences, Türkiye, hgundaydin@akdeniz.edu.tr

Cite this study:

Çimen, Ö., & Günaydın, H. İ. (2024). Assessment of engineering geology and grouting applications in Yalnızardıç Dam Site (Antalya, Türkiye). Turkish Journal of Engineering, 8 (1), 20-30

### Keywords

Soil stabilization  
Permeability  
Grouting  
Seepage  
Dams

### Research Article

DOI: 10.31127/tuje.1221774

Received:20.12.2022

Revised: 13.03.2023

Accepted:16.03.2023

Published:15.09.2023



### Abstract

The Yalnızardıç roller compacted concrete (RCC) dam, constructed in 2015, is located in the Mediterranean region of Turkey, intended for electric power production. It is approximately 303 m long and 92 m in height. In this paper, it is aimed to determine the performance of the grouting method, conducted to control the water seepage and improve the foundation of the Yalnızardıç dam. The engineering properties of the site were introduced by geological mapping, drilling, and laboratory tests. The seepage of the foundation was determined by the in-situ Lugeon test method, also referred to as a water pressure test, which is estimate the mean hydraulic conductivity of rock mass. As a result of the tests, high-permeable and permeable zones were determined in the dam axis area. To make a barrier layer for these permeable zones, grout curtains were built in the left abutment, thalweg and right abutment with two lines of grouting holes which is proposed according to the Lugeon test and rock quality designation (RQD) results. Consolidation grouts were built to increase the density of the soil which makes the strength of the dam's foundation. After the groutings, check boreholes were drilled and water pressure tests were performed to control the seepage along the foundation and dam site. The results indicated that average Lugeon (LU) values reduced, and the values were within the recommended limit. The process shows considerable accuracy in evaluating grouting efficiency.

## 1. Introduction

Yalnızardıç Dam Hydroelectric Power Plant is located in the Mediterranean region within the borders of Antalya on the northeastern part of Alanya, Turkey (Figure 1). It is built to produce energy by utilizing the available water potential of the Gevne Stream that flows through the Göksu Basin. The research region is situated between the heights of 1385 m and 1205 m in the Göksu River Basin on the Gevne Stream, which is the source branch of the Ermenek Stream of this river. The installed capacity amounts to 33.13 MW, with an energy production of 90 GWh per year. The average annual discharge is 8.76 m<sup>3</sup>/s, and the average yearly water volume totals 276.10 hm<sup>3</sup>. The maximum water level of the dam lake reaches 1359.40 m, with a total storage volume of 109.525 hm<sup>3</sup>. A circular diversion tunnel with a diameter of 4 m and length of 230 m was constructed. A summary of the dam's characteristics includes a crest elevation of 1361 m, a crest length of 303 m, and a crest width of 12 m. The thalweg elevation is 1269 m, with a

foundation elevation of 1263 m. The dam's height from thalweg is 92 m, and its body fills volume totals 571,293 m<sup>3</sup>.

Seepage during reservoir impoundment is a common issue observed in many dams worldwide. Seepage in fractured or unconsolidated terrains can escalate to erosion, which ultimately leads to the formation of concentrated leakage pathways. This can jeopardize the stability of a dam and result in unforeseen dam failure. Therefore, the hydraulic and mechanical characteristics of the rock foundation are critical parameters in dam design [1]. Several methods have been developed to detect dam seepage. In addition to geophysical surveys such as ground-penetrating radar (GPR), self-potential (SP), and various types of logging (such as gamma-gamma, neutron-neutron, and caliper logging), permeability and pressure water tests are commonly used methods. The decision to install a grout curtain primarily depends on the results of these tests [2-3].

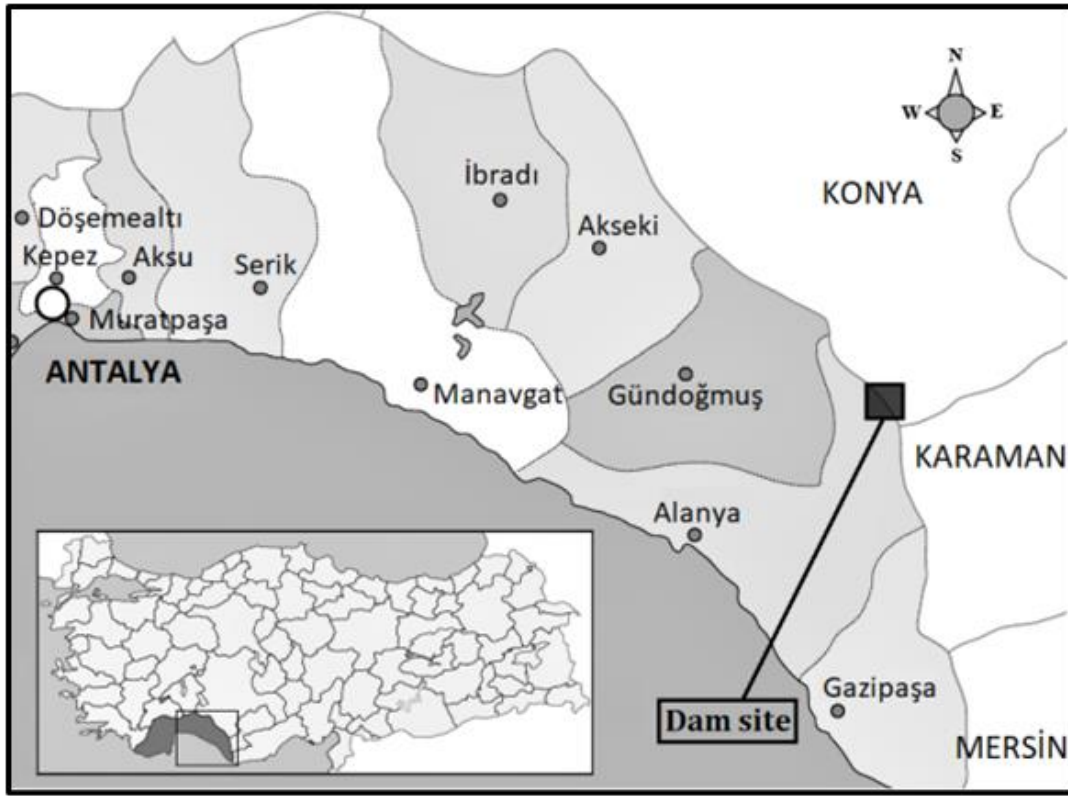


**Figure 1.** Location map of the Yalnızardıç Dam Site.

Grouting is one of the most common methods of foundation reinforcement, defined simply as the filling of fractures and gaps in the base rock with cement slurry, resulting in a relatively impermeable rock mass, greater strength, and reduced deformability. The success of this method depends on the overall properties of the ground, which include irregularities, apertures, and the space volumes of the fractures. These factors directly influence the grout mixture and quantity needed for effective application. Grouting is used in dam construction to reinforce the foundation of the dam. This is achieved by making the ground impermeable, preventing seepage through the foundation, reducing hydrostatic pressure on the downstream side, and obstructing the washout and erosion of fine-filling materials. Despite being designed to prevent leakage, dams may still experience seepage. In such cases, preventing piping is crucial, and this is achieved by grouting with appropriate materials based on the results of the Lugeon test. Grouting often constitutes a significant portion of the dam budget [1, 4-6].

Grouting in dam engineering has been extensively studied to enhance the strength and durability of weak soils while reducing permeability. Kocbay and Kilic [7] investigated the engineering geological properties of rock masses in the Obruk Dam region of Turkey. The study focused on various factors such as discontinuities, degree of weathering, strength, and hydraulic conductivities, to identify potential problems and necessary precautions for construction. However, no recommendations were provided regarding impermeability. Agan [8] suggested the use of grout at the Mezra Dam site in Turkey. However, the focus of the study was primarily on presenting the findings of site investigations, rock mechanics, and geological

assessments. Gürocak and Alemdağ [9] assessed the depth of grout and conducted seepage analyses using the finite element technique at the Atasu Dam site in Türkiye, based on the values obtained from Lugeon tests.

Kociánová et al. [10] focused on novel techniques for remediation grouting and examined the composition of grout mixtures. Lin et al. [5] developed a new grouting model for a super high arch dam, while Chhun et al. [11] investigated the impact of a newly developed cement grout on the strength of silty sand through a laboratory study.

The seepage of the dam foundation and body following impoundment, as well as the measures taken to prevent it, were examined in case studies by Turkmen [12], Chun et al. [13], and Ozcelik and Tuzlu [14].

Alkaya and Yeşil [15] investigated the grouting procedure of the Cindere Dam in Türkiye, while Ozcelik [16] examined the Deriner Dam in Türkiye.

Numerous studies have been conducted on specific aspects related to dams, such as the grouting procedures [15-16], case studies about seepage following dam impoundment [12-14], grout techniques and mixtures [5, 10-11], and geological properties of rock masses [7-9], including discontinuities, degree of weathering, strength, and hydraulic conductivities.

This study presents an analysis of the geotechnical properties of rock masses, including permeability and rock quality designation, at the Yalnızardıç Dam site in Turkey after grouting application in the foundation. The study provides a detailed description of the grouting application process based on the proposed method. The study uniquely assesses the effectiveness of the grouting application through a regional comparison of permeability before and after remediation, utilizing check boreholes.

## 2. Geological Characteristics of the Dam Site

The dam site is characterized by two primary geological structures dating back to the Triassic, Jurassic, and Cretaceous periods. The Derebucak Formation, depicted in Figure 2, is comprised of bituminous schist, limestones, carbonate cement conglomerate, sandstone, claystone, and limestone. This formation is composed of alternating thick and thin layers of sedimentary rocks, with a thick claypan layer on the surface in the upper zones. Additionally, conglomerates consisting of limestone, sandstone, and other materials of varying sizes can be found in this formation. The formation is situated to the north of the dam axis, and almost the entire dam lake area lies atop it. The Çamlık Formation, on the other hand, is composed of medium and thick-bedded Jura-Cretaceous dolomitic limestones and limestones. Petrographic analyses conducted on samples collected from the dam axis identified dolomitic

limestone. The limestone member of this formation is located on the dolomite limestone on the right and left slopes of the Gevne valley downstream of the dam site.

In the dam axis area, the bedrock on the right abutment has undergone significant alteration, particularly in the surface and fault zones. Laboratory analyses conducted on alteration materials obtained from drill cores revealed that the soil type was classified as CL, SM, and SC based on the Unified Soil Classification System. The Atterberg Limits of the clay component of these samples were assessed, and the swelling was evaluated through laboratory analyses. Specifically, the plasticity of the sample collected from the 11-12 m alteration zone of the SK-6 well was found to be 27% (indicating high swelling), as illustrated in Figure 3.

Based on the Turkish Earthquake Zoning Map provided by the Turkish General Directorate of Disaster Affairs, the Yalnızardıç dam site is located within the fourth-degree earthquake zone.

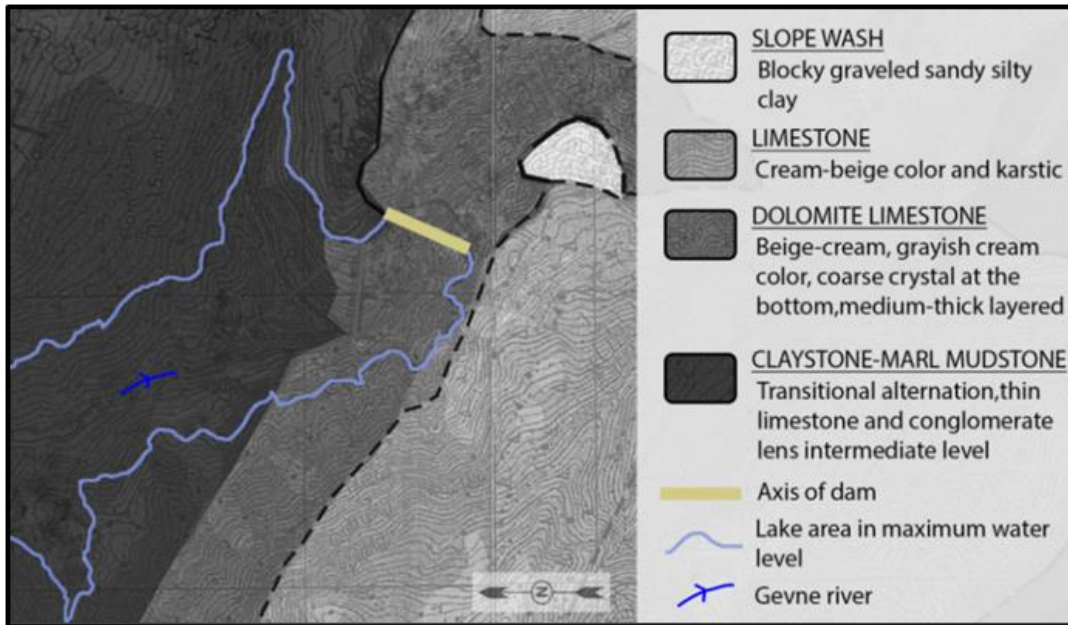


Figure 2. Geological map of the Yalnızardıç Dam.

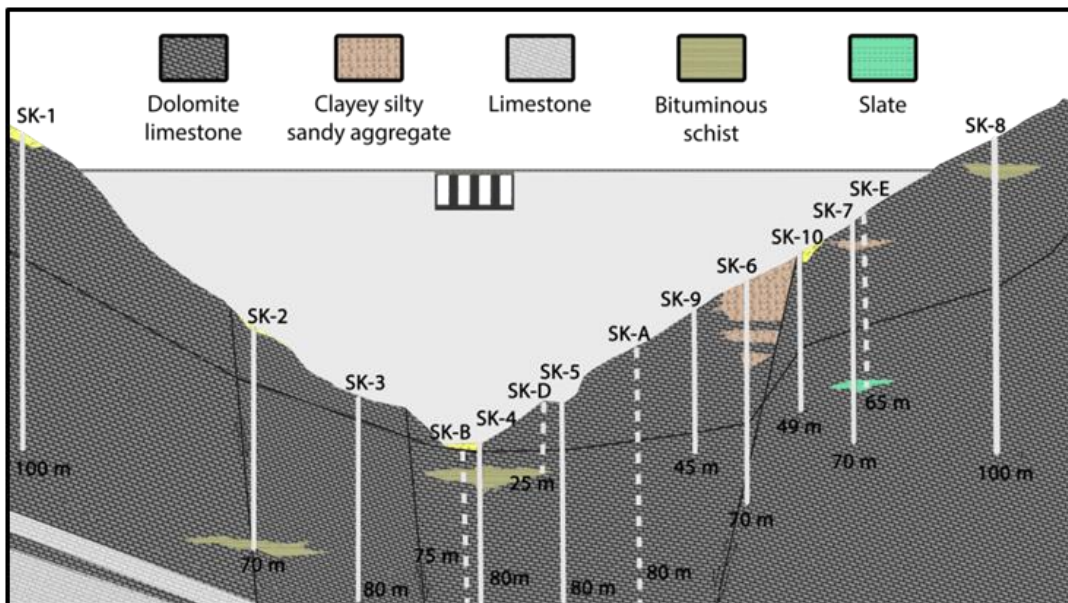


Figure 3. Geological profile of the dam foundation.

### 3. Engineering Geotechnical Investigations

Geotechnical properties of the dam area were examined through boreholes drilled in the river area and along the dam axis, as depicted in Figure 4. This investigation primarily focused on groundwater levels, Lugeon permeability parameters (Lu) of the zones, and Rock Quality Designation (RQD).

#### 3.1 Drillings

To identify key ground properties such as groundwater levels, permeability, and rock quality, boreholes were drilled before the dam's construction.

The grouting method was then prepared by these factors. The drilling process occurred in several locations, including the thalweg, riverbed, left and right abutments, and energy tunnel. The General Directorate of the State Hydraulic Works in Türkiye (DSI) carried out the drilling process, as shown in Figure 3 and Figure 4. During the drilling process, groundwater was observed in cracks, faults, and alteration zones of both the alluvial cover and bedrock. This groundwater flowed from the slopes towards the stream. Table 1 displays the results of Lugeon permeability, rock quality designation (RQD) and triaxial compression test values for the dam axis, including their mean values.

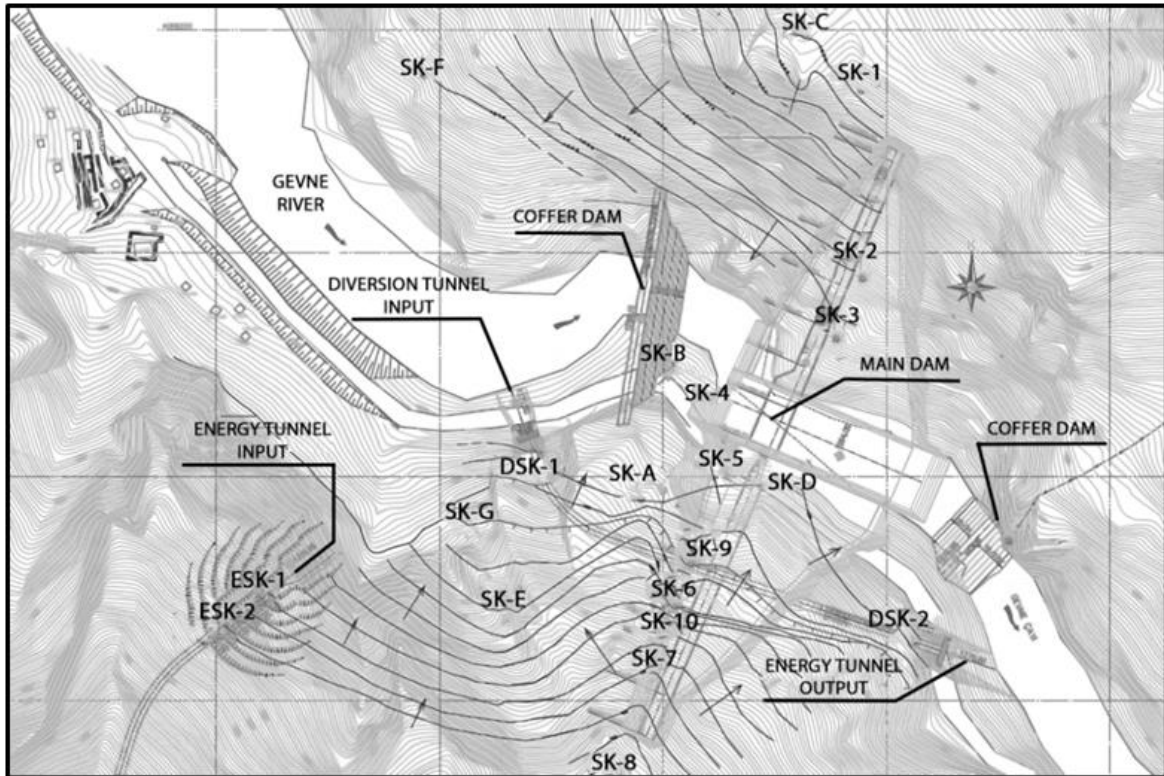


Figure 4. Location plan of the drillings

Table 1. Geotechnical parameters of the boreholes.

Location	Borehole Number	Depth (m)	Permeability (Lugeon)			RQD (%)		
			Min	Max	Ave	Min	Max	Ave
Left Abutment	SK-1	100	0,70	48,40	4,00	11	96	46
	SK-2	70	0,10	13,80	2,10	0.0	88	49
	SK-3	80	0,20	7,90	2,00	0.0	96	56
Thalweg	SK-4	80	0,30	25,10	4,40	4.0	88	50
Right Abutment	SK-5	80	0,60	60,60	5,50	29	95	75
	SK-6	70	0,10	13,80	3,20	0.0	91	45
	SK-7	70	0,50	10,30	2,00	0.0	90	55
	SK-8	100	0,00	14,20	2,70	12	98	80
	SK-9	45	0,30	8,90	1,30	0.0	93	50
	SK-10	49	1,00	12,10	4,10	0.0	60	27

The bedrock in the dam axis area was exposed to severe alteration, leading to the formation of alteration clay zones. Based on the Atterberg limits of samples taken from these clay zones, it was determined that the

clay materials, particularly in samples taken from the SK-6 borehole area on the right bank, exhibited a "high swelling" characteristic.

### 3.2 Permeability and rock quality designation (RQD)

The permeability of the base rock at the dam foundation was determined using pressured water-pumping tests (WPTs). In total, 247 WPTs were performed in the thalweg, left and right abutments. The

Lugeon values (Table 1) were used to explain the permeability. The results of the 247 WPTs showed that 37% of the base rock was impermeable, 45% was d-permeable, 16% was permeable, and 2% was highly permeable (Figure 5a).

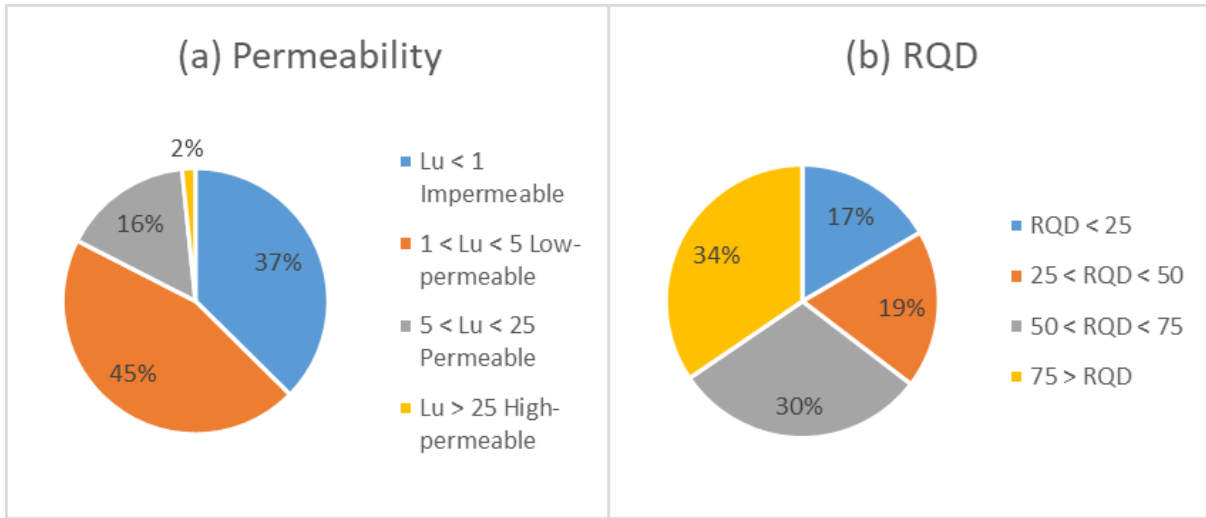


Figure 5. Results of the (a) WPTs and (b) the RQD for all drillings in the dam axis.

RQD is a value used to characterize the rock mass. It is defined as the total length of borehole stick samples over 10 cm identified as a percentage of the total core line length. RQD values range from 0 to 100 and have corresponding engineering quality categories. For example, an RQD value of 0-25 is considered very poor, while an RQD value of 90-100 is considered very good.

Generally, low RQD values indicate highly fractured rock requiring grouting [17]. The RQD values for all boreholes in the dam axis are shown in Figure 5b. The results show that 35% of the samples had very poor to poor RQD values, 30% had medium values, and 35% had good values.



Figure 6. (a) WPTs and (b) RQD values by location in the dam axis.

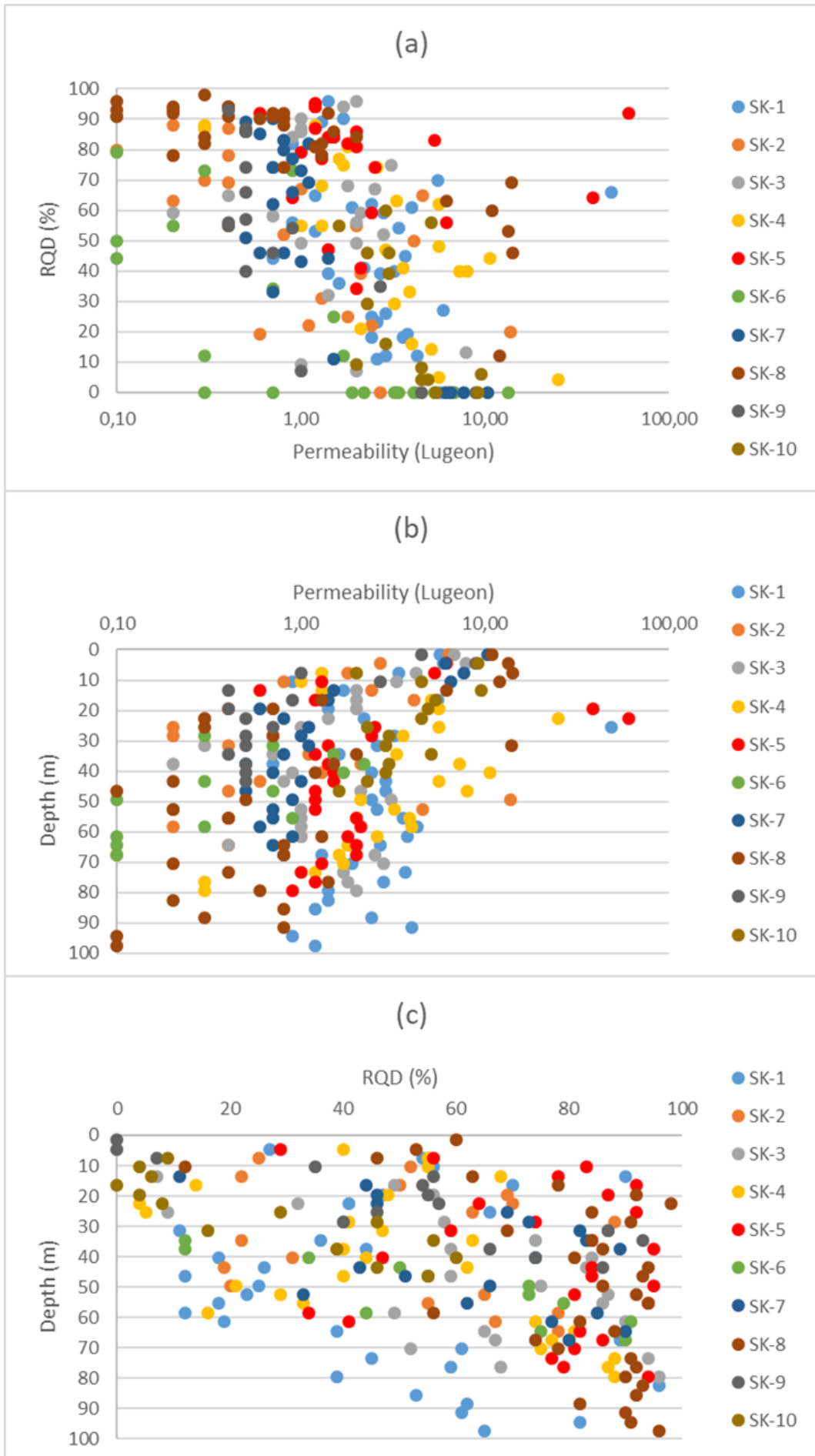


**Figure 7.** The correlations among (a) permeability and rock quality, (b) permeability and depth, and (c) rock quality and depth for rock units [23].

The WPTs results showed the presence of low-permeable and permeable zones at depths of 0-50 m. The Lu values of the rock mass went below 1, making it impermeable between depths of 50-100 m (Figure 6a). The RQD results showed poor values at depths of 0-25 m, with an increase in values as depth increased (Figure 6b). The occasional presence of permeable and high-permeable zones was observed at depths of 0-40 m (Figure 7b).

While many studies have reported that permeability generally decreases with depth, there are also exceptions to this trend [18-20]. Berhane and Walraevens [21] found that hydraulic conductivity tends to decrease with depth based on an analysis of borehole data. Interestingly, they also found no direct correlation between RQD and Lugeon values. However, in the case of the current study, it appears that permeability increases

with poor RQD (Figure 7a), but still decreases with depth overall (Figure 6a). On the other hand, RQD tends to increase with depth for the rock units examined in this study (Figure 7b, 7c).

### 3.3 Rock quality classification

The bedrock was classified according to the RMR (Rock Mass Rating) system, based on the information obtained within the scope of this study, taking into account the RQD value, groundwater conditions, crack spacing, crack characteristics, and the uniaxial compressive strength that represents the in-situ rock conditions as a mass. The sum of the RMR scores and rock quality classes for the bedrock were presented in Table 2, categorized by region.

**Table 2.** RMR and Rock quality classification.

Location	RMR Score				Total RMR score	Rock quality classification
	uniaxial compression	RQD	Crack spacing	groundwater		
Left abutment	12	8	8	4	32	IV- weak rock
Thalweg	12	8	8	4	32	IV- weak rock
Right abutment	12	13	18	7	50	III-medium rock

### 3.4 Grouting studies

The correlation between depth and permeability of the base rock at the dam axis is illustrated in Figure 6a. Generally, the conductivity of the units at depths of 0-50 meters is low, with permeability ranging from low to moderate levels. The shallow units of the base rock have the potential to cause leakage following the construction of the dam. Therefore, measures such as enhancer curtains and blanket grouts have been proposed to mitigate permeability beneath the left and right abutments, as well as along the thalweg.

Consolidation (blanket) grout is usually designed shallow and its aims to reinforcing faults by reduce permeability and increase rock strength [8]. In this study, blanket grout holes were built as 5 m deep, and with square pattern, and with 2 m intervals (Figure 8b). In the SK-6 borehole located at right abutment of the dam axis, alteration zones (0-18 m) were removed and replaced with backfill concrete. The multi-cracked bedrock between 18-27.5 meters was strengthened by the blanket grout.

Curtain grouts are designed to obstruct seepage and serve as a barrier beneath the dam axis prior to the construction of the dam body. They can also be used for repair purposes following construction. This process involves drilling vertical holes at intervals that intersect to form a curtain, which is then filled with pressurized grout [8]. Thus, the curtain grout holes were drilled to a depth of 30 m (front) and 70 m (back), using a double line pattern with 3-meter intervals (as shown in Figure 8a). As the existence of bituminous schists in the bedrock could lead to increased seepage when washed with pressurized water, the grout curtains were extended to deeper levels to prevent this issue. In areas of high permeability in the abutments, groundwater flows from the slopes towards the streams. To address these areas, grouting galleries were constructed, and the curtain

grouts were extended 37 m in the left abutment and 45 m in the right abutment towards the slopes. Grout boreholes were drilled using the shortened distance method and the grout area was divided into three-meter sections. The boreholes were grouted in the following sequence: A, B, C, and D.

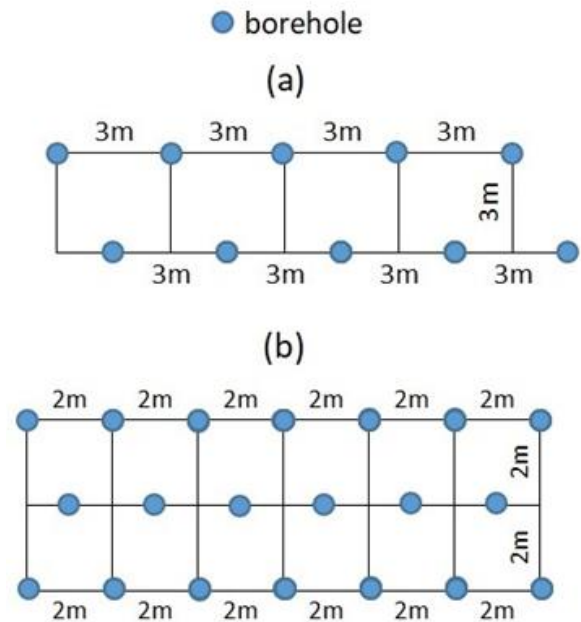


**Figure 8.** Details of (a) curtain grouts, (b) blanket grouts.

Moreover, inclined grouts were constructed to connect the curtain grouts that were vertically drilled. These inclined grouts were designed to be 3 meters apart and 15 meters deep at a 15-degree angle. Inclined radiating grouts were also built on both the right and left abutments' galleries, extending from the curtains. These grouts were drilled at specific angles and to a depth of 5 meters.

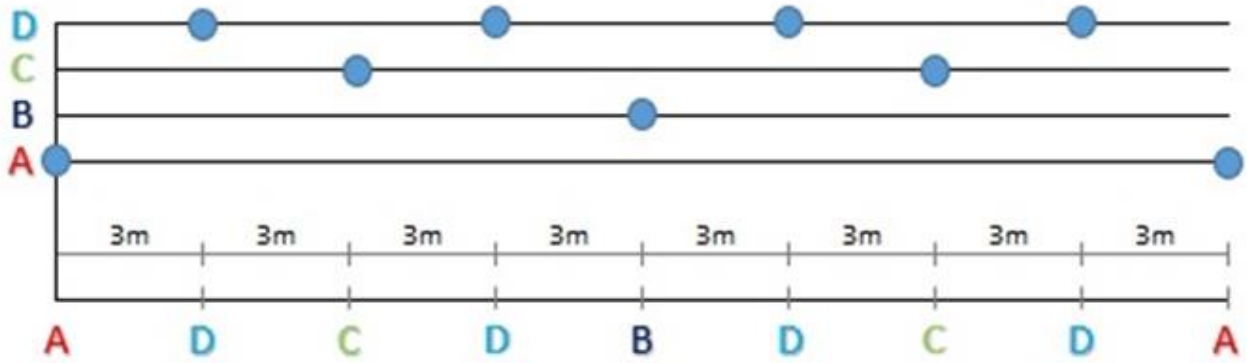


Figure 9. The drilling plan executed using the shortened distance method.

3.5 Performance evaluation of control boreholes

To assess the effectiveness of the grouting procedure after the completion of the curtain grouting structure, check boreholes were drilled to intersect multiple boreholes at various angles, and WPTs were performed. The depths of the check boreholes, which were drilled during the grouting works, varied between 75 m and 95 m, depending on the conditions of the area (as illustrated in Figure 10). Table 3 displays the permeability values and their mean values of the control boreholes in the dam axis. The results, as shown in Figure 11a, 11b, 11c,

demonstrate a decrease in permeability in the thalweg, left, and right abutments, indicating the effectiveness of the grouting process. In general, the Lugeon test results in the thalweg exhibited higher values than those of the right and left abutments.

The results demonstrate a reduction in permeability in the thalweg, left abutment, and right abutment, indicating the effectiveness of the grouting process (refer to Figure 11a, 11b, and 11c). Specifically, the Lugeon test results show higher permeability values in the thalweg compared to those of the right and left abutments.

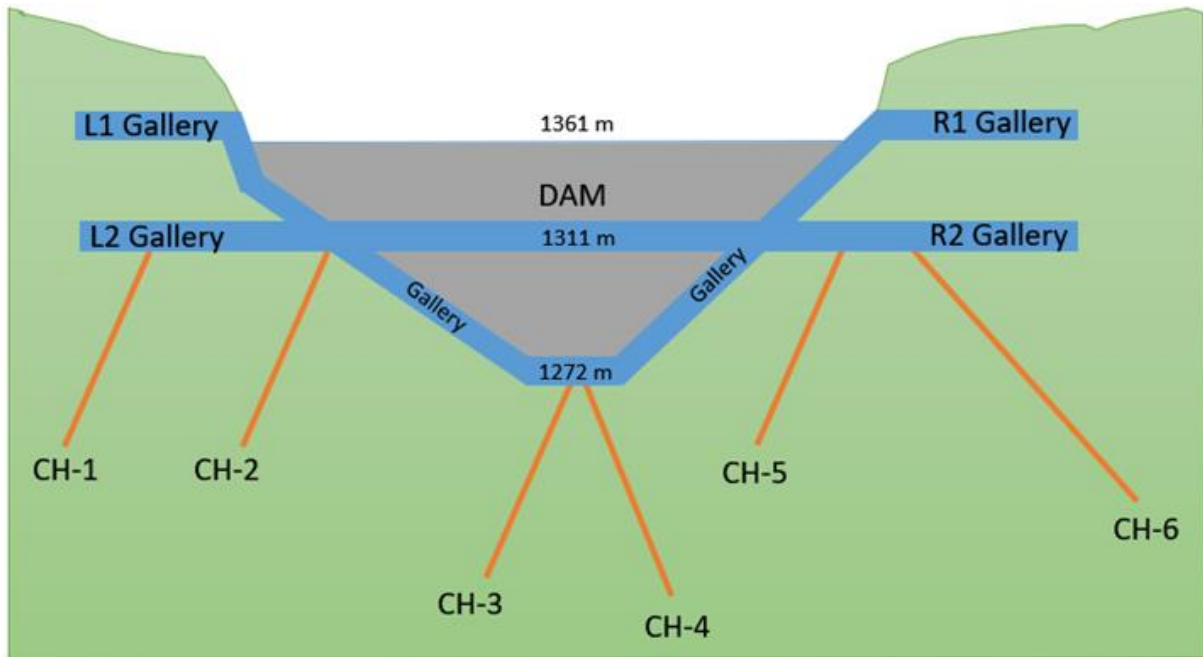
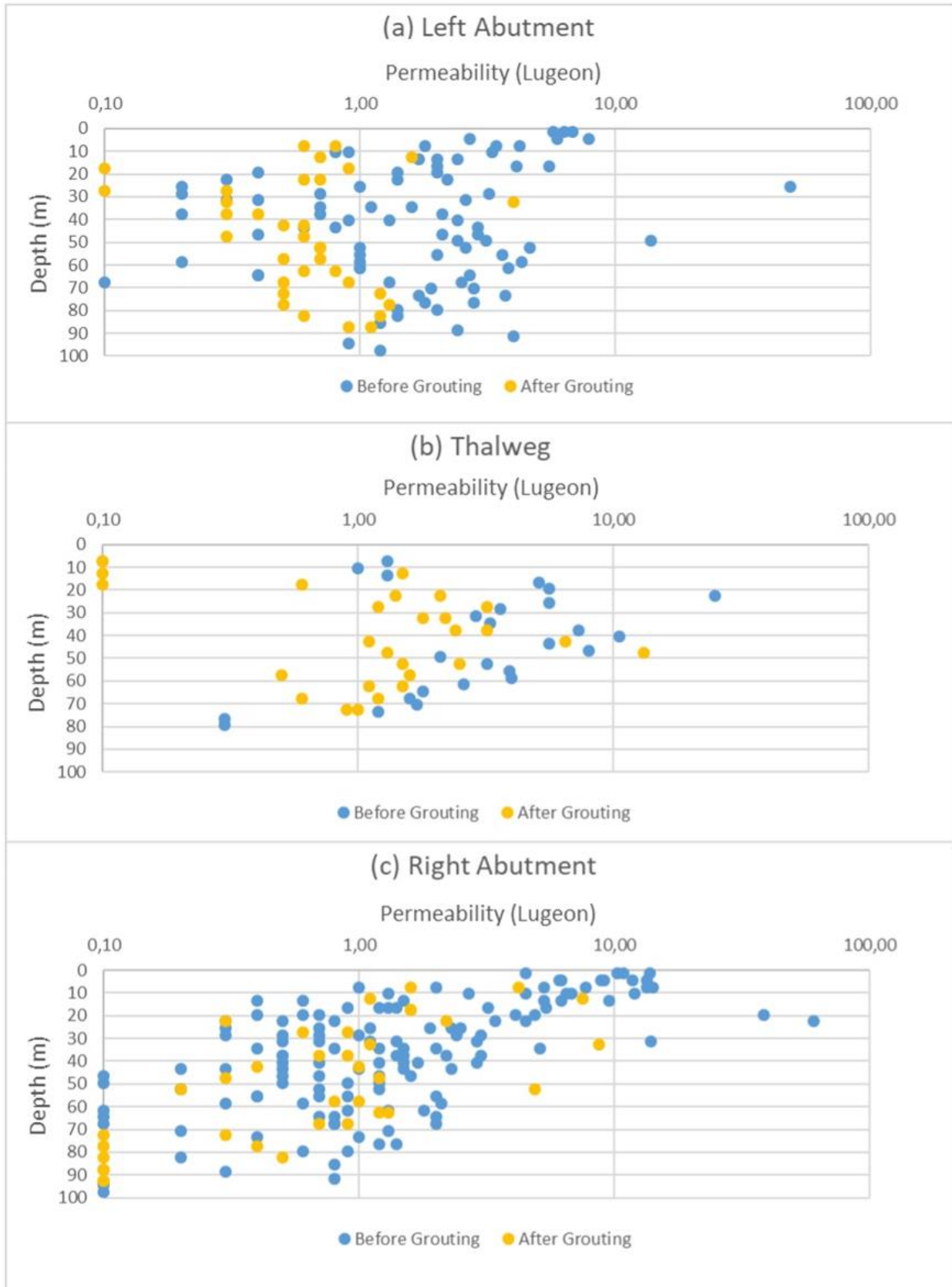


Figure 10. Location of control borehole.

Table 3. Geotechnical parameters of the check boreholes.

Location	Borehole Number	Depth (m)	Angle of Gradient (°)		Permeability (Lugeon)		
			Min	Max	Ave	Ave	
Left Abutment	CH-1	90	31	0,10	1,60	0,60	0,70
	CH-2	90	28	0,10	4,00	0,90	
Thalweg	CH-3	75	42	0,10	3,20	1,40	1,90
	CH-4	75	29	0,10	13,20	2,40	
Right Abutment	CH-5	95	37	0,10	8,70	2,00	1,30
	CH-6	95	32	0,10	1,60	0,70	



**Figure 11.** Comparing permeability before and after grouting at the dam axis [23].

**4. Conclusion**

This study focuses on the geological characteristics and engineering geological conditions of the Yalnızardıç dam site, which is located in an area underlain by the Derebucak Formation. This formation comprises various rock types, including bituminous schist, limestones,

carbonate cement conglomerates, sandstones, claystones, and limestone, all of which date back to the Triassic, Jurassic, and Cretaceous ages. Additionally, the site is situated in the Çamlık Formation, characterized by medium to thick-bedded Jura-Cretaceous dolomitic limestones and limestones.

Leakage and rock quality in the foundation are crucial design parameters for dam constructions. In particular, the construction of curtain and consolidation grouts can enable the creation of a stable and impermeable foundation structure. The geological investigation, drilling (including RQDs, borehole logs, etc.), and Lugeon tests have shown that it is necessary to treat the foundations. Based on the results of WPTs conducted at the 0-50m depth of the dam foundation, the bedrock was determined to have both low permeable and permeable characteristics. Additionally, occasional high-permeable zones were observed at depths of 0-40m, which indicates that excessive leakage through the rock foundations can be expected. The RQD analysis results indicate poor values at 0-25m depth, which increase linearly with depth. The relationship between depth and permeability for the base rocks of the dam area shows a reduction in permeability with increasing depth. Additionally, the RQD results indicate that there is an increase in permeability when RQD values are low.

During the grouting works, the alteration zones of the bedrock were removed and replaced with backfill concrete. Consolidation grouts were constructed at a depth of 5m in a square pattern, with 2m intervals throughout the dam foundation. Additionally, curtain grouts with two lines of grouting holes were built to a depth of 30m and 70m for the left abutment, thalweg, and right abutment.

The conclusions of this study are as follows:

- Prior to the grouting works, it was observed that 33%, 12%, 45%, and 37% of the sections at the left abutment, thalweg, right abutment, and total dam site, respectively, had LU values of less than 1, indicating nearly no flow records. Additionally, 58%, 54%, 36%, and 45% of the sections at the left abutment, thalweg, right abutment, and total dam site, respectively, had LU values ranging from 1-5, indicating low permeability. Finally, 8%, 31%, 18%, and 16% of the sections at the left abutment, thalweg, right abutment, and total dam site, respectively, had LU values greater than 5, indicating permeable and high permeable conditions.
- After the grouting works, it was observed that 84%, 32%, 64%, and 61% of the sections at the left abutment, thalweg, right abutment, and total dam site, respectively, had LU values less than 1. Additionally, 18%, 61%, 31%, and 35% of the sections at the left abutment, thalweg, right abutment, and total dam site, respectively, had LU values ranging from 1-5. Finally, 0%, 7%, 6%, and 4% of the sections at the left abutment, thalweg, right abutment, and total dam site, respectively, had LU values ranging from 5-25, and no values exceeding 25 LU were observed.
- After grouting, the mean LU values significantly decreased at all locations. Specifically, the mean LU values decreased from 2.80 to 0.70 at the left abutment, from 4.00 to 1.90 at the thalweg, from 4.00 to 1.30 at the right abutment, and from 3.20 to 1.30 at the total dam site.

The results indicate that the parameter values are within the advised limits by DSI [22]. Therefore, it can be concluded that the grouting process was appropriate and effective considering the geological structure.

### Acknowledgement

The field investigations described in this paper were conducted by the General Directorate of the State Hydraulic Works (DSI). The authors would like to express their sincere gratitude to the DSI staff who assisted in the research reported in this paper, as well as to the Editor. The views and opinions presented in this paper are solely those of the authors.

### Author contributions

**Ömür Çimen:** Literature review, Writing-Original draft preparation, **Halil İbrahim Günaydın:** Analysis and Evaluation of results, Writing-Reviewing and Editing.

### Conflicts of interest

The authors declare no conflicts of interest.

### References

1. Sohrabi-Bidar, A., Rastegar-Nia, A., & Zolfaghari, A. (2016). Estimation of the grout take using empirical relationships (case study: Bakhtiari dam site). *Bulletin of Engineering Geology and the Environment*, 75, 425-438. <https://doi.org/10.1007/s10064-015-0754-5>
2. Camilo Quinones-Rozo, P. E. (2010). Lugeon test interpretation, revisited. In: *Proceedings of the 30th Annual USSD Conference*, Sacramento, California, 12-16 Apr 2010, 405-414.
3. Ewert, F. K. (1997). Permeability, groutability and grouting of rocks related to dam sites, Part 3: hydrogeological regime around dams and reservoir. *Dam Engineering*, 8 (3), 215-248.
4. Houlsby, A. C. (1991). *Construction and design of cement grouting: a guide to grouting in rock foundations* (Vol. 67). John Wiley & Sons.
5. Lin, P., Zhu, X., Li, Q., Liu, H., & Yu, Y. (2016). Study on optimal grouting timing for controlling uplift deformation of a super high arch dam. *Rock mechanics and rock engineering*, 49, 115-142. <https://doi.org/10.1007/s00603-015-0732-z>
6. Mesci, B. (2006). *Examination of infiltrations and phreatic line in filler dam bodies: Seferihisar dam*. Master's Thesis, Istanbul Technical University
7. Kocbay, A., & Kilic, R. (2006). Engineering geological assessment of the Obruk dam site (Corum, Turkey). *Engineering Geology*, 87(3-4), 141-148. <https://doi.org/10.1016/j.enggeo.2006.04.005>
8. Agan, C. (2015). *Engineering geological and geomechanical assessments of the proposed Mezra dam site (Şanlıurfa, Turkey)*. *Arabian Journal of Geosciences*, 8(4), 2371-2381. <https://doi.org/10.1007/s12517-014-1317-y>

9. Gurocak, Z., & Alemdag, S. (2012). Assessment of permeability and injection depth at the Atasu dam site (Turkey) based on experimental and numerical analyses. *Bulletin of Engineering Geology and the Environment*, 71, 221-229. <https://doi.org/10.1007/s10064-011-0400-9>
10. Kociánová, M., Drochytka, R., & Černý, V. (2016). Technology of remediation of embankment dams by optimal grout. *Procedia Engineering*, 151, 257-264. <https://doi.org/10.1016/j.proeng.2016.07.370>
11. Chhun, K. T., Lee, S. H., Keo, S. A., & Yune, C. Y. (2019). Effect of acrylate-cement grout on the unconfined compressive strength of silty sand. *KSCE Journal of Civil Engineering*, 23, 2495-2502. <https://doi.org/10.1007/s12205-019-1968-z>
12. Turkmen, S. (2003). Treatment of the seepage problems at the Kalecik Dam (Turkey). *Engineering Geology*, 68(3-4), 159-169. [https://doi.org/10.1016/S0013-7952\(02\)00225-9](https://doi.org/10.1016/S0013-7952(02)00225-9)
13. Chun, B. S., Lee, Y. J., & Chung, H. I. (2006). Effectiveness of leakage control after application of permeation grouting to earth fill dam. *KSCE Journal of Civil Engineering*, 10(6), 405-414. <https://doi.org/10.1007/BF02823979>
14. Ozcelik, M., & Tuzlu, F. (2018). Leakage analysis of Deriner dam (Artvin-Turkey) using 3D modeling. *KSCE Journal of Civil Engineering*, 22(8), 2916-2922. <https://doi.org/10.1007/s12205-017-1793-1>
15. Alkaya, D., & Yesil, B. (2011). Grouting applications of grout curtains in Cindere dam and hydroelectric power plant. *Scientific Research and Essays*, 6(19), 4039-4047. <https://doi.org/10.5897/SRE11.103>
16. Özçelik, M. (2014). Foundation consolidation grouting applications in Deriner Dam and hydroelectric power plant (Artvin, Turkey). *Bulletin of Engineering Geology and the Environment*, 73, 493-498. <https://doi.org/10.1007/s10064-013-0547-7>
17. Deere, D. U. (1968). Geological considerations. In: Stagg RG, Zienkiewicz DC (eds) *Rock mechanics in engineering practice*. Wiley, New York, 1-20.
18. Lee, C. H., & Farmer, I. (1993). *Fluid flow in discontinuous rocks*. Chapman & Hall, New York
19. Nappi, M., Esposito, L., Piscopo, V., & Rega, G. (2005). Hydraulic characterisation of some arenaceous rocks of Molise (Southern Italy) through outcropping measurements and Lugeon tests. *Engineering geology*, 81(1), 54-64. <https://doi.org/10.1016/j.enggeo.2005.07.007>
20. Hamm, S. Y., Kim, M., Cheong, J. Y., Kim, J. Y., Son, M., & Kim, T. W. (2007). Relationship between hydraulic conductivity and fracture properties estimated from packer tests and borehole data in a fractured granite. *Engineering Geology*, 92(1-2), 73-87. <https://doi.org/10.1016/j.enggeo.2007.03.010>
21. Berhane, G., & Walraevens, K. (2013). Geological challenges in constructing the proposed Geba dam site, northern Ethiopia. *Bulletin of Engineering Geology and the Environment*, 72, 339-352. <https://doi.org/10.1007/s10064-013-0480-9>
22. DSI, (2013). *Geotechnical Report: Yalnızcı Dam and Berat Hydroelectric Power Plant*. Ankara, Turkey, 39-41.
23. Günaydın, H. İ. (2017). *Yalnızcı Dam and Berat Hydroelectric Power Plant implementation of grouting*. Master's Thesis, Süleyman Demirel University



© Author(s) 2024. This work is distributed under <https://creativecommons.org/licenses/by-sa/4.0/>



## Machine learning empowered prediction of geolocation using groundwater quality variables over YSR district of India

Jagadish Kumar Mogaraju \*<sup>1</sup> 

<sup>1</sup>Lovely Professional University, Department of Geography, India, jagadishmogaraju@gmail.com

Cite this study: Mogaraju, J. K. (2024). Machine learning empowered prediction of geolocation using groundwater quality variables over YSR district of India. Turkish Journal of Engineering, 8 (1), 31-45

### Keywords

Machine learning  
Haversine distance  
Prediction  
Extra trees regressor  
Groundwater quality

### Research Article

DOI: 10.31127/tuje.1223779

Received:24.12.2022

Revised: 01.04.2023

Accepted:12.04.2023

Published:15.09.2023



### Abstract

Machine Learning (ML) has been used in the prediction of geolocation with improved accuracies in this work. The pre-processed data was subjected to prediction analytics using 22 machine learning algorithms over regression mode. It was observed that Extra Trees Regressor performed well with better accuracies in predicting latitude, longitude, and Haversine distance, respectively. Regression models like CatBoost, Extreme Gradient boosting, Light Gradient boosting machine, and Gradient boosting regressor were also tested. The  $R^2$  values were computed for each case, and we obtained 0.96 (Longitude), 0.98 (Latitude), and 0.96 (Haversine), respectively. The evaluation of models was done using metrics like MAE, MASE, RMSE,  $R^2$ , RMSLE, and MAPE and  $R^2$  is considered most important than others. The effect of data point was calculated using Cooks' distance, and the variable fluoride has a significant impact on the prediction accuracy of Longitude followed by RSC, Cl, SO<sub>4</sub>, SAR, NO<sub>3</sub>, Na, Ca, EC and pH variables. In the prediction of latitude, the SAR variable played a significant role, followed by Na and TH. According to the t-SNE manifold, three longitude values were quite different from the others. This work is supported by some of the manifests like Cooks' distance outlier detection, feature importance plot, t-SNE manifold, prediction error plot, residuals plot, RFECV plot, and validation curve. This work is done to report that the challenge of predicting both latitude and longitude on a common ground is solved partially, if not completely, and machine learning tools can be used for this purpose. Haversine distance can be obtained from latitude and longitude and can be used in the prediction of geolocation.

## 1. Introduction

Groundwater is an essential source that needs to be protected from external and internal pollutants and its overexploitation to achieve the goals set by the United Nations through SDGs [1-2]. Machine learning tools can be effectively used in the prediction of environmental factors that can disturb the purity and extent of groundwater across the world [3]. Most of the modeling techniques that are considered predictive ML algorithms are adaptable and can simulate nonlinear and complicated interactions within a small window of time [4]. We can observe different hydrogeological environments that can also alter the availability of groundwater [5]. The availability of data is limited, and this is the main problem that hinders experimentation and analysis [6]. The prediction of groundwater levels was possible using simulation methods, and this has helped in groundwater management effectively [7-9]. Several numerical models were used in the prediction of

the quantity and quality of groundwater [10-11]. We can use Long Short-Term Memory (LSTM), Extreme Learning Machine (ELM), and Deep Learning (DL) methods for accurate and meaningful predictions [12-16]. The autoML frameworks can be used in handling the whole ML pipeline, starting from data input to the display of outputs in graphical modes and also solving other data-related problems [17]. AutoML tools were previously used in the investigation of drinking water quality [18]. Pycaret is one of the important libraries that can be used in the AutoML frameworks with appreciable results in the form of metrics and graphs [19]. Regression methods were used in the investigation of water quality to know correlation and other insights [20]. The latitude and longitude values can be merged in the form of Haversine distance, and it is being used for some of the location-based services [21]. Haversine distance is least affected by some of the features like the width of a valley, the height of a mountain, etc., and hence can be used in solving some of the navigation problems [22]. The

interpolation techniques based on deterministic geostatistical techniques and artificial neural networks were used to create digital elevation models [23]. The extent of solar radiation was forecasted/predicted using machine learning approaches [24]. The water levels in the surface water body like lake was predicted using neurocomputing intelligence methods [25]. The empirical equations that are associated with climatic regions were calibrated using genetic algorithm, particle swarm optimization techniques along with multi-gene genetic programming method [26].

There is some gap in research that embraces the fact that variables of groundwater quality can be used in the prediction of geolocation with reasonable accuracy. Though the attempt to achieve the same is naïve at this

point in time, considering data availability, this work might lead to higher enhancements in the future in solving navigation problems and improving location-based services.

## 2. Material and Method

### 2.1. Data

The datasets essential for this study were collected from the WRIS system of Government of India website [27] and Central Groundwater Control Board website [28].

The study area is shown in Figure 1. 1000 random points were selected for this study.

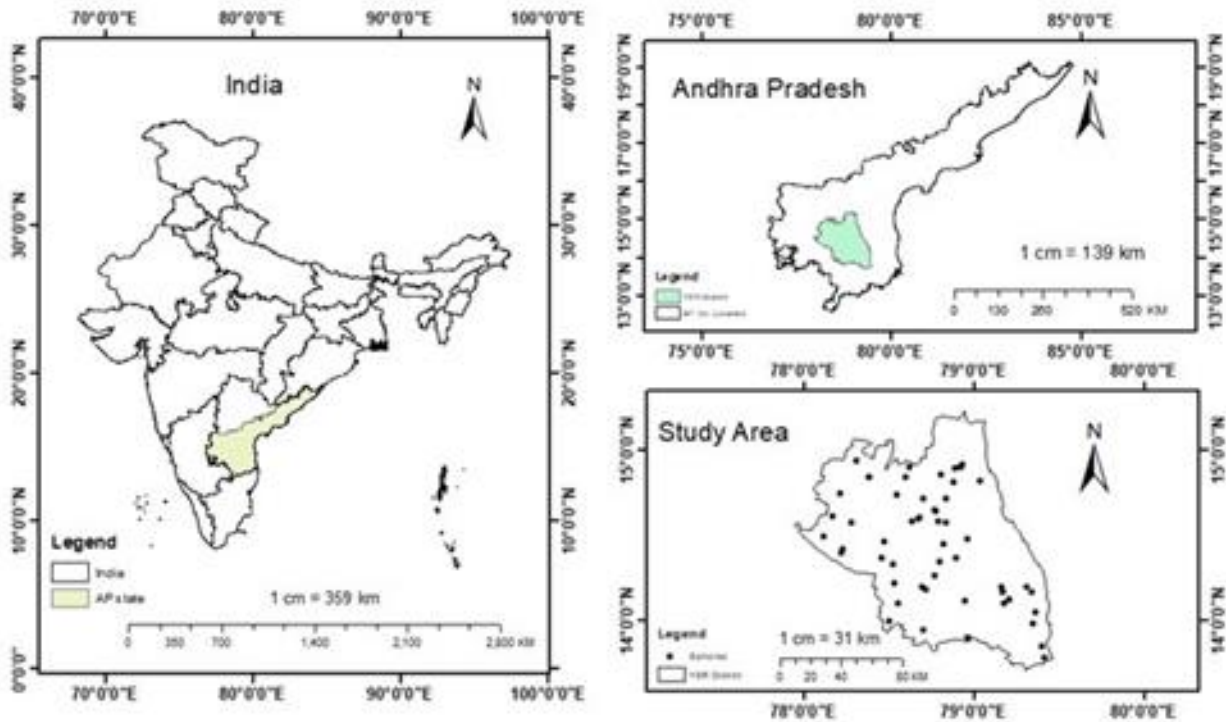


Figure 1. Study area.

### 2.2. Method

The models that were considered in this study are Extra Trees Regressor, CatBoost Regressor, Extreme Gradient Boosting, Light Gradient Boosting Machine, Random Forest, Gradient Boosting Regressor, Decision Tree, AdaBoost Regressor, k Neighbors Regressor, Ridge Regression, Linear Regression, Least Angle Regression, etc. Evaluation metrics like MAE, MSE, RMSE,  $R^2$ , RMSLE, and MAPE for each algorithm were considered. The datasets needed for this study were subjected to standard procedures that deal with data imbalance, missing values, and errors under the ML framework. The variables that were considered are  $HCO_3$ , Ca, Cl, F, K, Mg, Na,  $NO_3$ , pH, RSC, SAR,  $SO_4$ , TH (Total hardness), TA (Total alkalinity), and EC (Electrical conductivity). These variables were combined with latitude, longitude, and Haversine values separately, and they were considered as dependent or response variables, respectively. The combined datasets were passed onto the ML framework

separately, and prediction accuracies with evaluation metrics were reported. The methodology employed in this study is given in Figure 2. The python packages built-in H2O AutoML was used in this study. The information linked with the machine learning algorithms and H2O AutoML package can be viewed through the online sources i.e., [29] (for models/algorithms) and [30] (for H2O autoML).

The extra-trees regressor is a meta estimator that can fit randomized decision trees on sub-samples and averaging is done to enhance the prediction accuracy and regulates overfitting. CatBoost regressor relies on gradient boosted decision trees and a specific set of these trees will be built accordingly. Every tree that is built can be devoid of loss compared to the original ones. XGBoost or Extreme Gradient Boosting regressor can be scalable and it supplies parallel tree boosting. It can lower the error caused due to bias. Light Gradient Boosting Machine regressor uses traditional gradient boosting decision tree algorithms and also uses exclusive feature

bundling (EFB) and Gradient-based One-Side sampling (GBDT) algorithms. More information on the algorithms/regressors can be obtained from the aforementioned links.

Central Haversine distance can be calculated between two points using Equation 1.

Where 'r' is the radius of earth, 'd' is the distance between two points,  $\phi_1, \phi_2$  is the latitude of the two points and  $\lambda_1$  and  $\lambda_2$  are the longitudes of the two points.

$$\text{Haversine} (d/r) = \text{haversine} (\phi_1 - \phi_2) + \cos (\phi_1) \cos (\phi_2) \text{haversine} (\lambda_2 - \lambda_1) \tag{1}$$

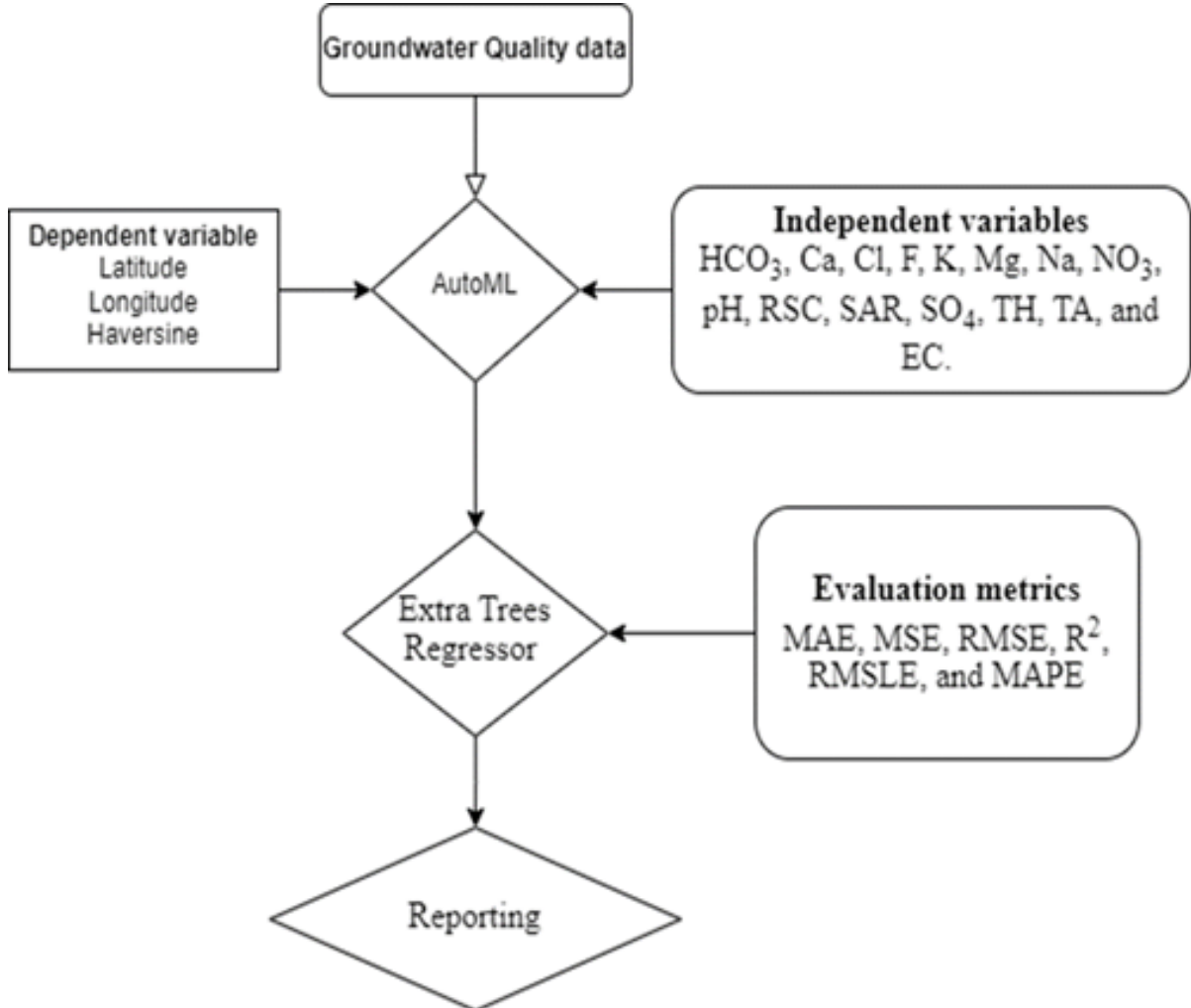


Figure 2. Methodology.

### 3. Results

#### 3.1 Prediction of longitude

The Extra Trees Regressor (et) performed better than other regressors like CatBoost, Extreme Gradient boosting, Light Gradient boosting machine, Gradient boosting regressor, etc., predicting the Longitude variable. The 'et' regressor yielded an R<sup>2</sup> value of 0.96 with MAE (0.0391), MSE (0.004), RMSE (0.062), RMSLE (0.0008), and MAPE (0.0005), showing that the model fitted well and is shown in Figure 3 and model metrics for 'et' are given in Figure 4. The Cook's Distance Outlier Detection plot (6.98%) is given in Figure 5, and it represents the importance of an instance that might affect the prediction. The feature importance plot (Figure 6) shows that the variable 'F' has more influence than other variables like RSC, Cl, SO<sub>4</sub>, SAR, NO<sub>3</sub>, Na, Ca, EC and pH. According to the t-SNE Manifold plot, the longitude

values 78.6, 78.4, and 78.2 are quite different from the others (Figure 7). The prediction error of the Extra Trees Regressor is shown in Figure 6, and we can observe an R<sup>2</sup> value of 0.965 with a best fit and identity (Figure 8). The residuals R<sup>2</sup> for training data is 1 and for test data, it is 0.965 (Figure 9). The Recursive feature elimination with cross-validation (RFECV) plot showed a score of 0.97 (Figure 10). The training score and the CV or cross-validation score are steadily increasing with each other, and it reflects that this model fitted well (Figure 11).

The plot given in Figure 3 shows the combined metrics of models used in this study. The dominance of R<sup>2</sup> metric is given in dark green.

#### 3.2 Prediction of latitude

The Extra Trees Regressor (et) performed better than other regressors like CatBoost, Extreme Gradient boosting, Light Gradient boosting machine, Random

Forest, etc., predicting the Latitude variable. The ‘et’ regressor yielded an R<sup>2</sup> value of 0.98 with MAE (0.0261), MSE (0.0019), RMSE (0.0419), RMSLE (0.0027), and MAPE (0.0018), showing that the model fitted well and is shown in Figure 12 and model metrics are given in Figure 13. The Cook’s Distance Outlier Detection (6.78%) is given in Figure 14. The feature importance plot shows that SAR highly influences the prediction, followed by Na, TH, Ca, Mg, SO<sub>4</sub>, NO<sub>3</sub>, EC, Cl, and RSC (Figure 15). The t-SNE Manifold plot shows that the latitude values 14.8, 114.6, and 14.4 differ from others (Figure 16). The prediction error plot shows that the R<sup>2</sup> value is 0.984 with best fit and identity (Figure 17). The predicted value versus Residuals is given in Figure 18 with Train R<sup>2</sup> of 1 and Test R<sup>2</sup> value of 0.984. RFECV plot scored 0.983 with 15 features (Figure 19). The validation curve showed that the training and cross-validation scores are growing gradually, reflecting that model performed well (Figure 20).

The plot given in Figure 12 shows the combined metrics of models used in this study. The dominance of R<sup>2</sup> metric is given in dark green.

### 3.3 Prediction of Haversine distance

The Extra Tress Regressor (et) performed better than other regressors like CatBoost, Extreme Gradient

boosting, Light Gradient boosting machine, Random Forest, etc., predicting the Haversine distance variable. The ‘et’ regressor yielded an R<sup>2</sup> value of 0.96 with MAE (4.235), MSE (47.2008), RMSE (6.7658), RMSLE (0.0008), and MAPE (0.0005), showing that the model fitted well and is shown in Figure 21 and model metrics are given in Figure 22. The outlier detection plot (7.22%) is shown in Figure 23. The feature importance plot showed that the F variable strongly influences prediction, followed by RSC, SO<sub>4</sub>, and Cl. SAR, Ca, NO<sub>3</sub>, Na, pH, and EC (Figure 24). The t-SNE Manifold showed that the values 8780, 8760, and 8740 of Haversine distance are quite different from others (Figure 25). The prediction error plot shows that the R<sup>2</sup> value is 0.963 with the best fit (Figure 26). The residuals plot showed a Train R<sup>2</sup> and Test R<sup>2</sup> of 1 and 0.963, respectively (Figure 27). The RFECV plot showed a score of 0.969 (Figure 28). The validation curve showed that the cross-validation and training scores grew gradually, showing that the model fits well (Figure 29).

The plot given in Figure 21 shows the combined metrics of models used in this study. The dominance of R<sup>2</sup> metric along with other metrics is given.

The evaluation metrics of all models considered in this study is given in Table 1.

**Table 1.** Evaluation metrics.

Model	Latitude (R <sup>2</sup> )	Longitude (R <sup>2</sup> )	Haversine (R <sup>2</sup> )
Extra Trees Regressor	0.9829	0.9697	0.9691
CatBoost Regressor	0.9814	0.9532	0.9537
Extreme Gradient Boosting	0.9691	0.9452	0.9427
Light Gradient Boosting Machine	0.9682	0.9322	0.9326
Gradient Boosting Regressor	0.9678	0.9072	0.9134
Random Forest	0.9646	0.9047	0.913
AdaBoost Regressor	0.9483	0.8322	0.8399
Decision Tree	0.9287	0.8279	0.8261
Linear Regression	0.9082	0.7606	0.7627
Ridge Regression	0.9059	0.7604	0.7624
Bayesian Ridge	0.9057	0.7579	0.76
TheilSen Regressor	0.9057	0.7306	0.7413
Random Sample Consensus	0.9049	0.7288	0.735
K Neighbors Regressor	0.9043	0.6856	0.7309
Elastic Net	0.8833	0.4237	0.6875
Lasso Regression	0.8725	0.3684	0.6766
Orthogonal Matching Pursuit	0.8467	0.3501	0.3658
Support Vector Machine	0.8112	0.3093	0.121
Lasso Least Angle Regression	0.6901	-0.0258	-0.001
Least Angle Regression	-0.0127	-4.799	-5.0102
Huber Regressor	-68.0315	-1740.73	-2006.42
Passive Aggressive Regressor	-554.398	-14405	-15444.1

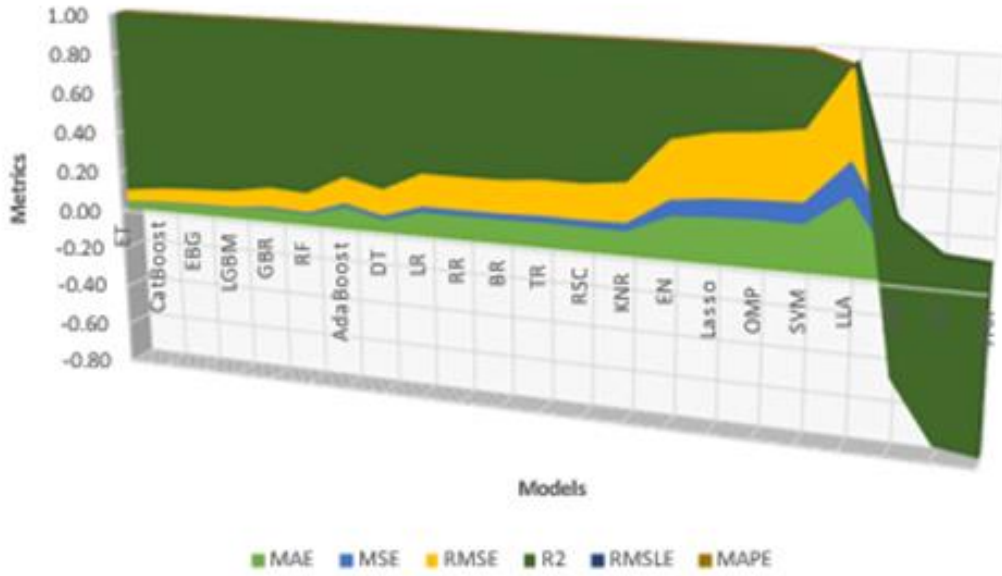


Figure 3. Model contrast (Longitude).

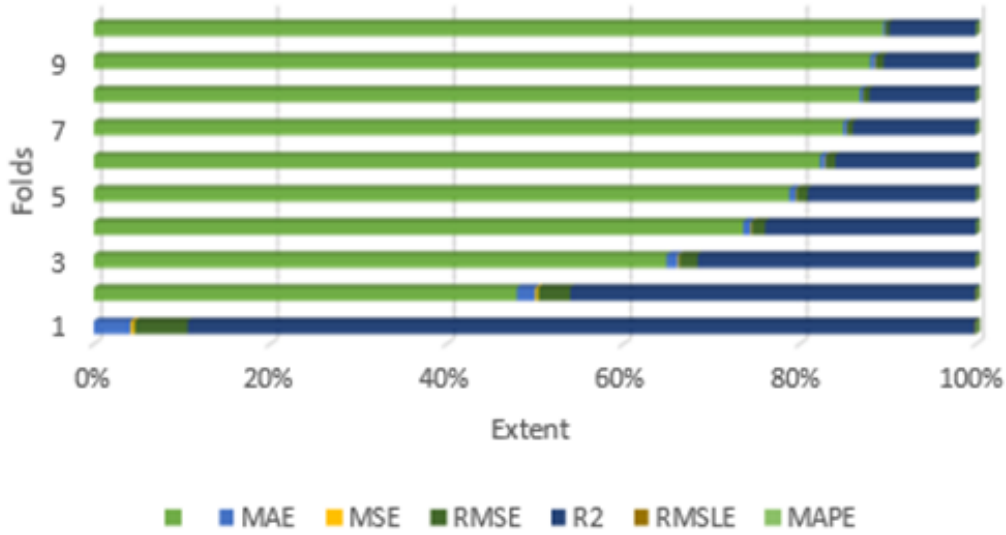


Figure 4. Model performance (Longitude).

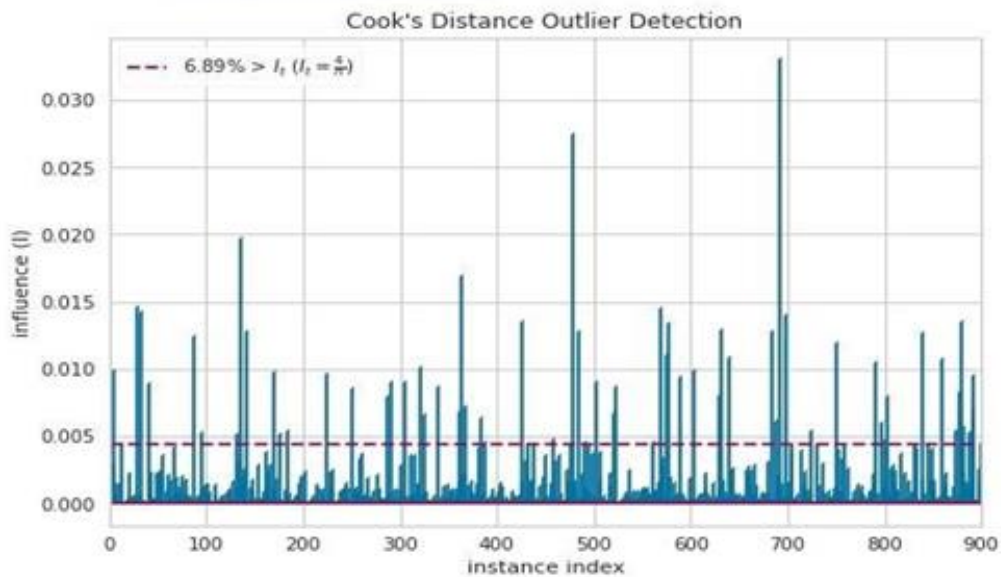


Figure 5. Outliers (Longitude).

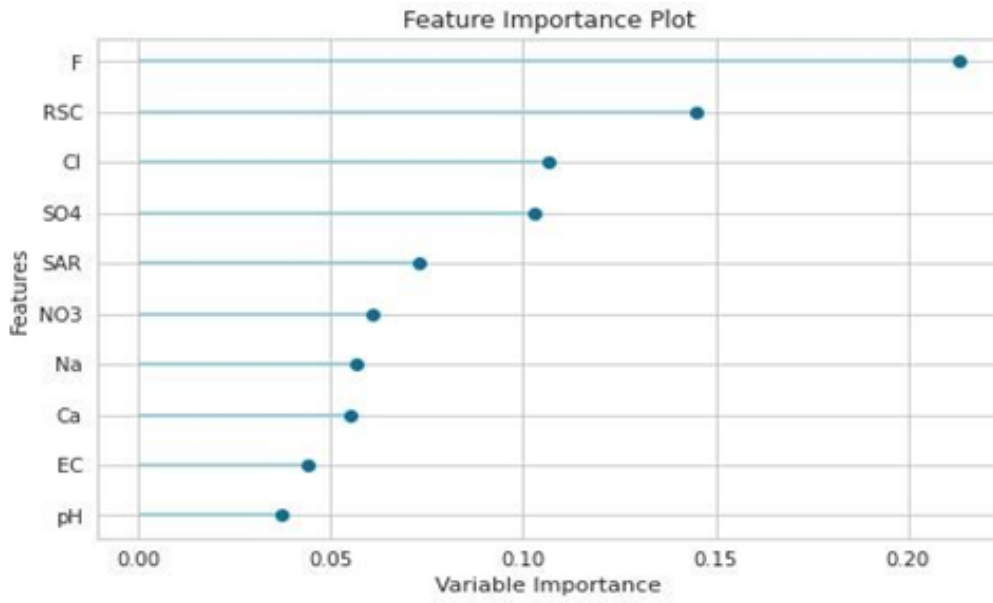


Figure 6. Feature importance (Longitude).

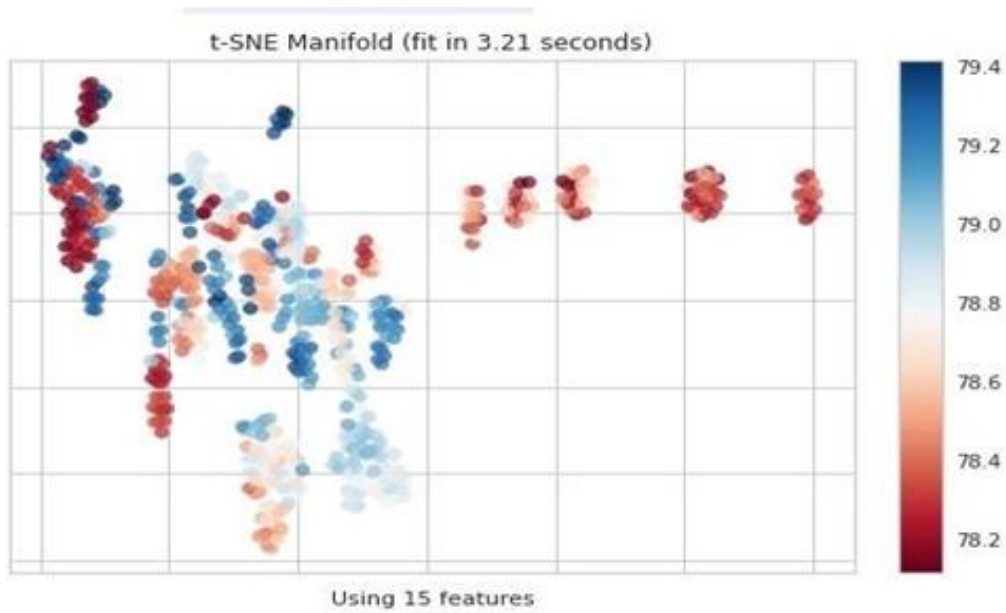


Figure 7. t-SNE Manifold (Latitude).

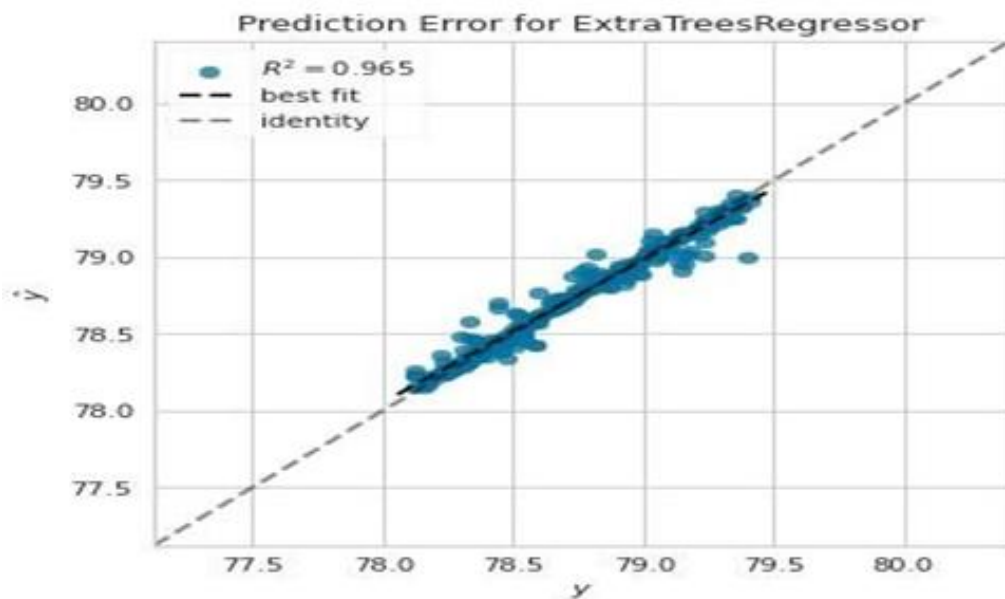


Figure 8. Prediction error (Longitude).

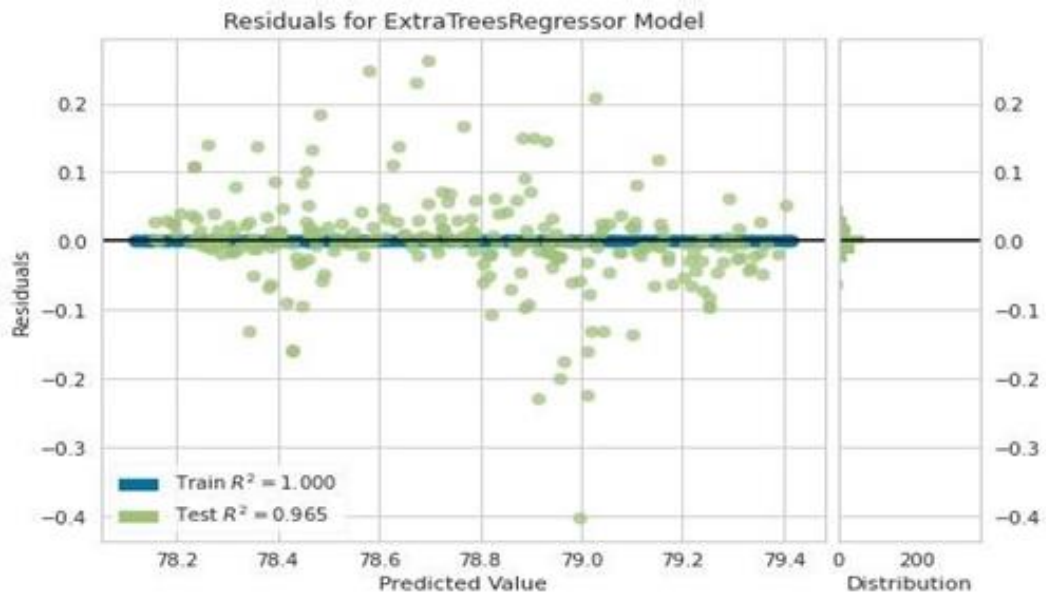


Figure 9. Residuals (Longitude).

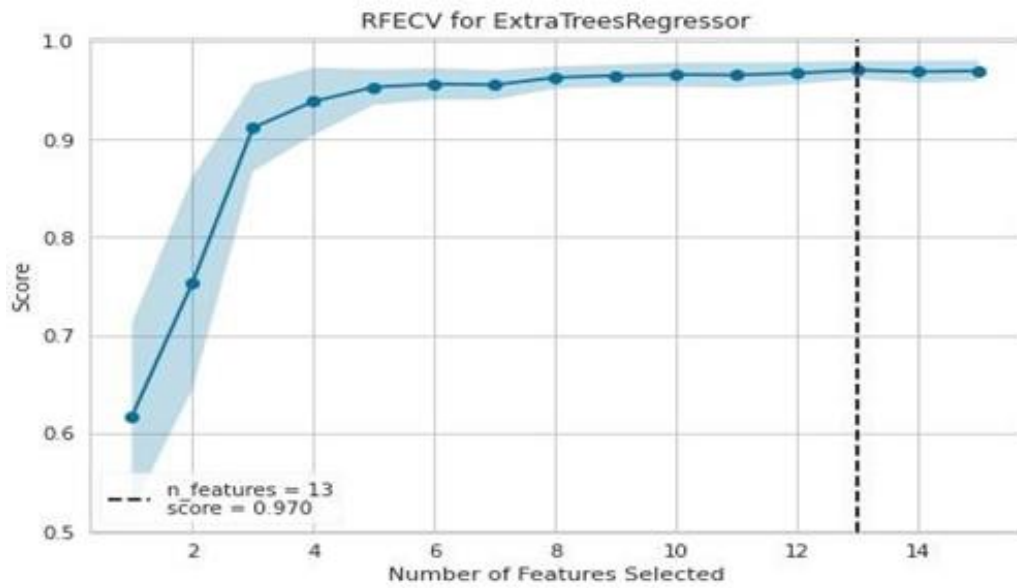


Figure 10. RFECV (Longitude).

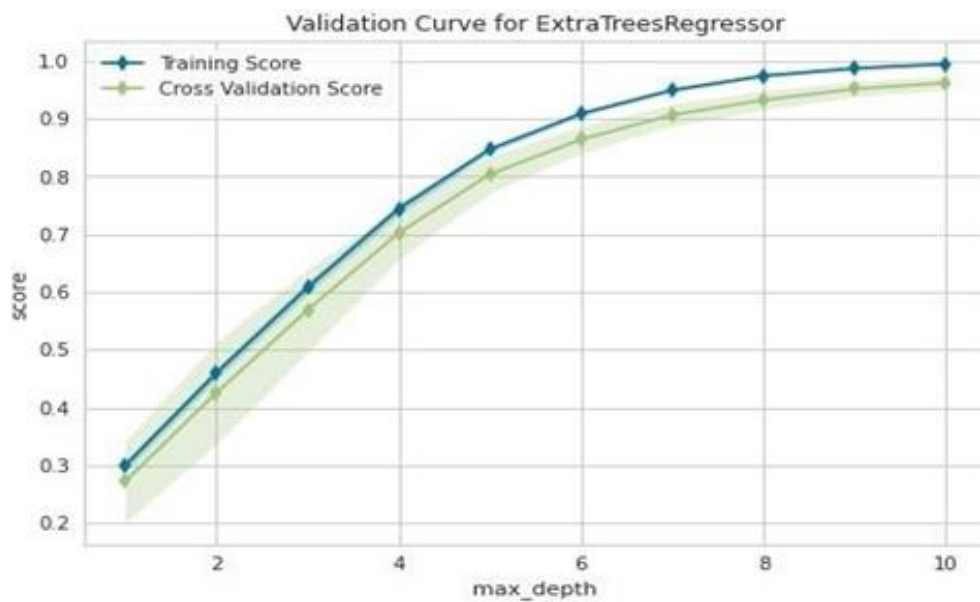


Figure 11. Validation curve (Longitude).

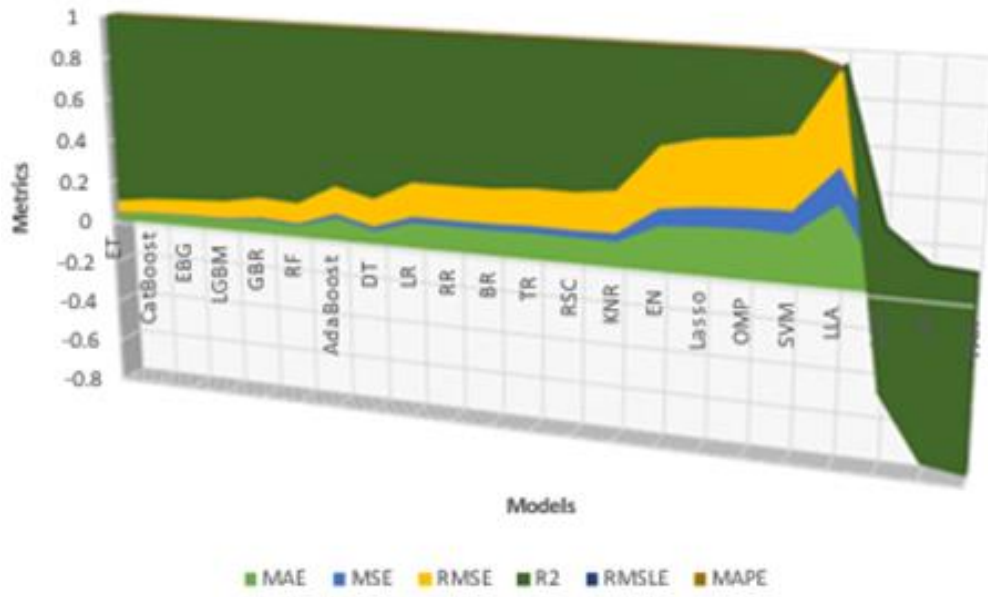


Figure 12. Model contrast (Latitude).

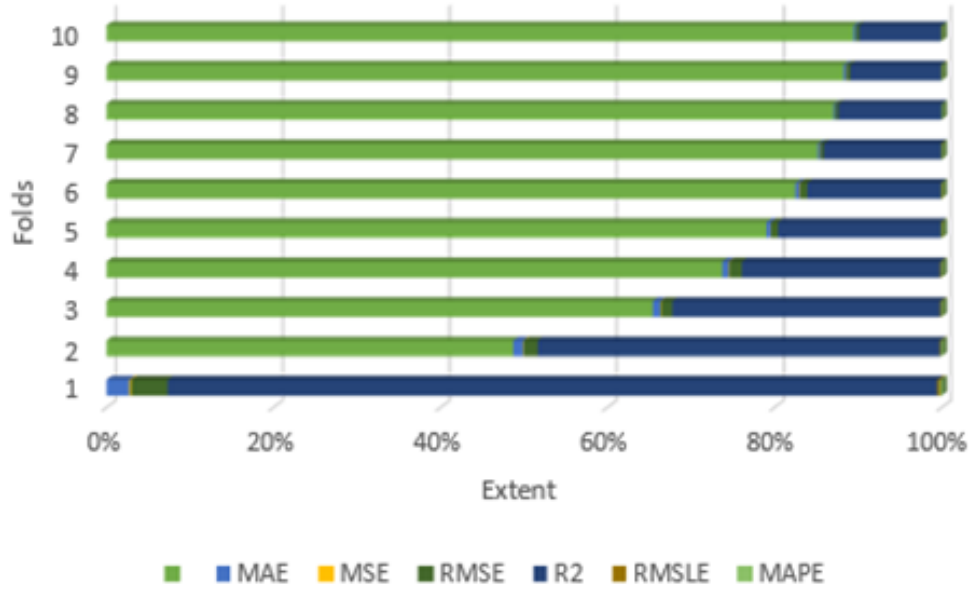


Figure 13. Model performance (Latitude).

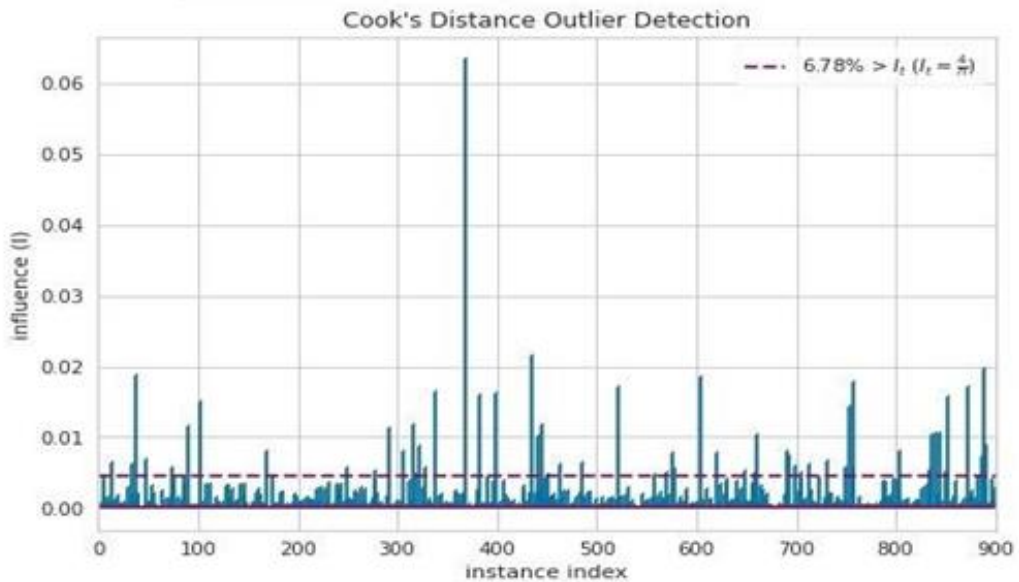


Figure 14. Outliers (Latitude).

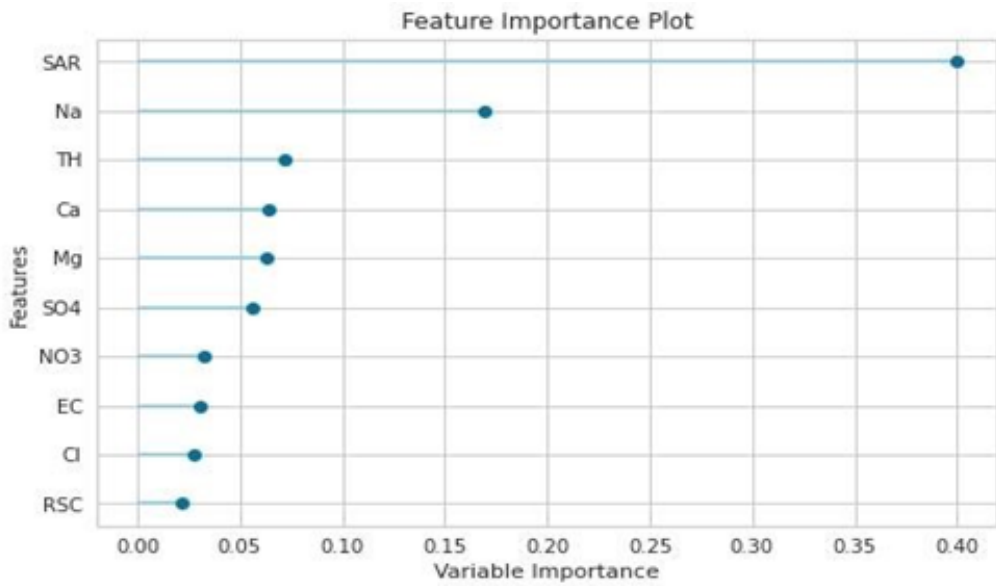


Figure 15. Feature importance (Latitude).

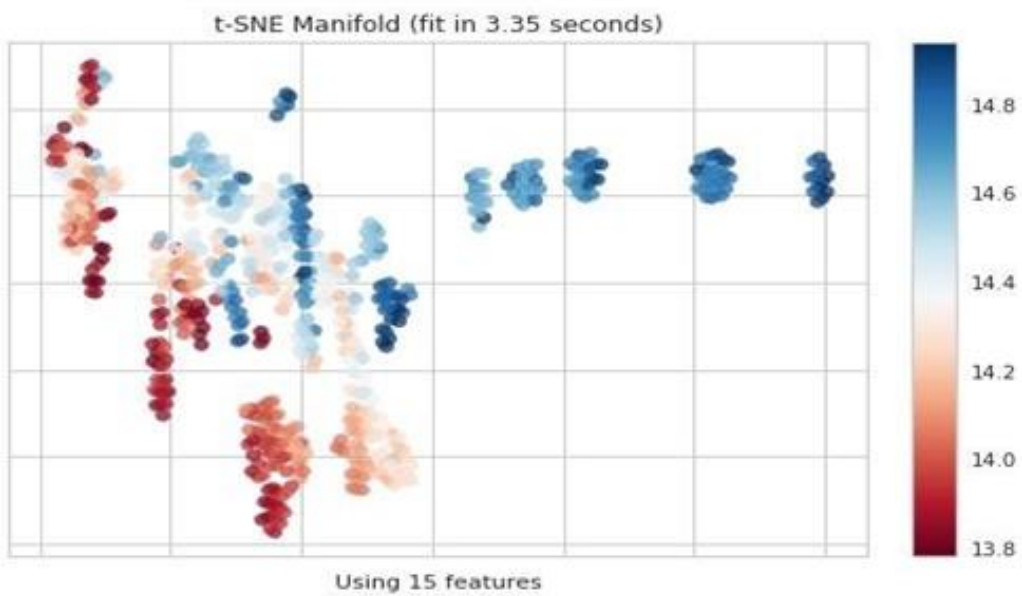


Figure 16. t-SNE Manifold (Latitude).

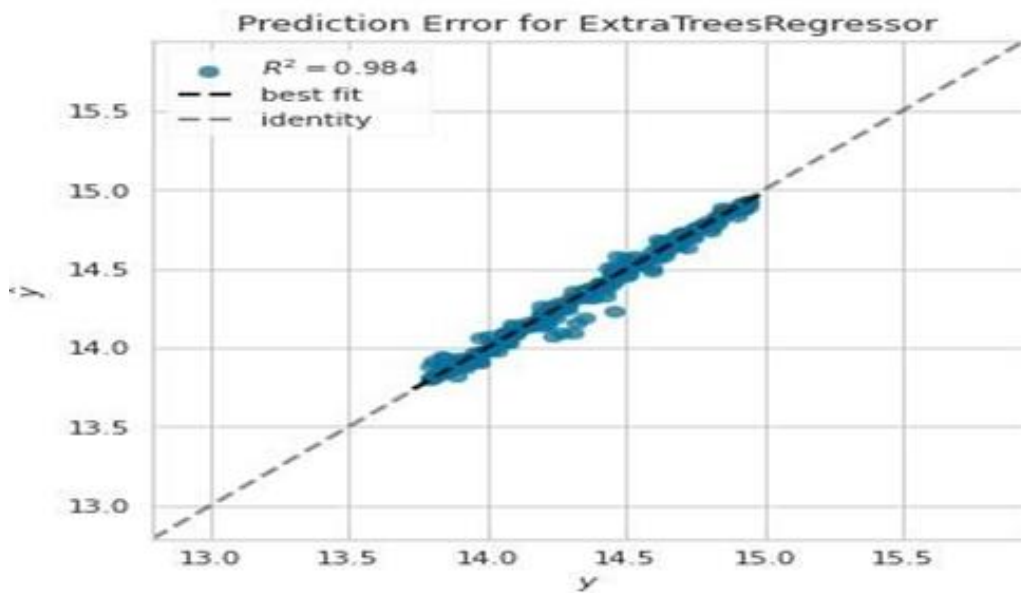


Figure 17. Prediction error (Latitude).

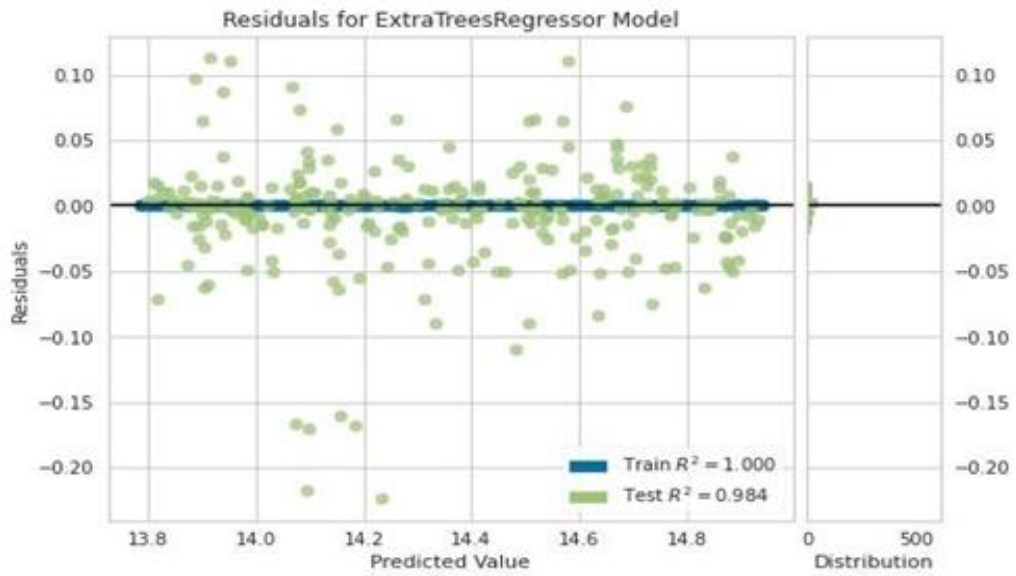


Figure 18. Residuals (Latitude).

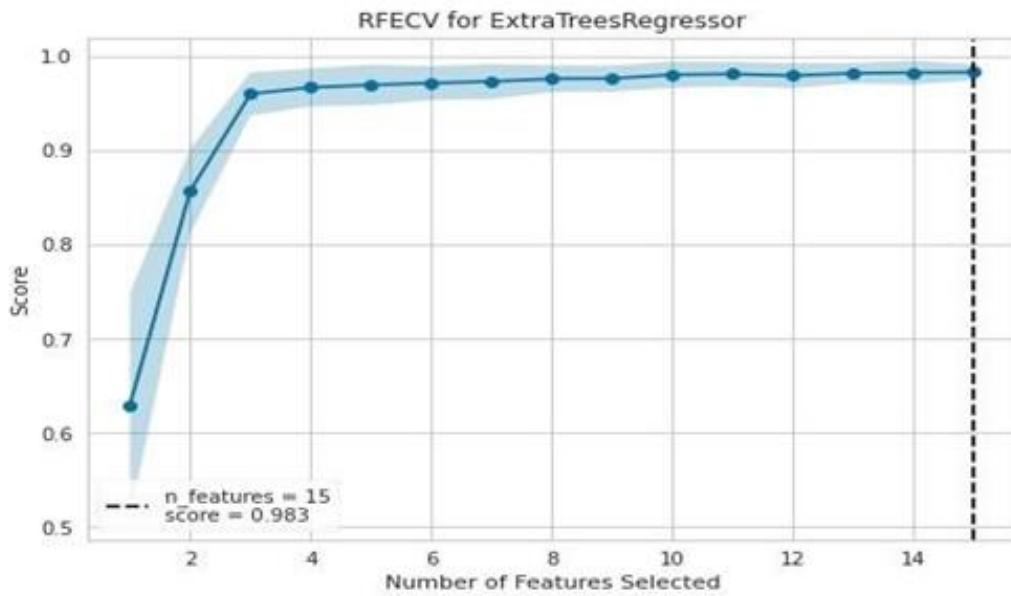


Figure 19. RFECV (Latitude).

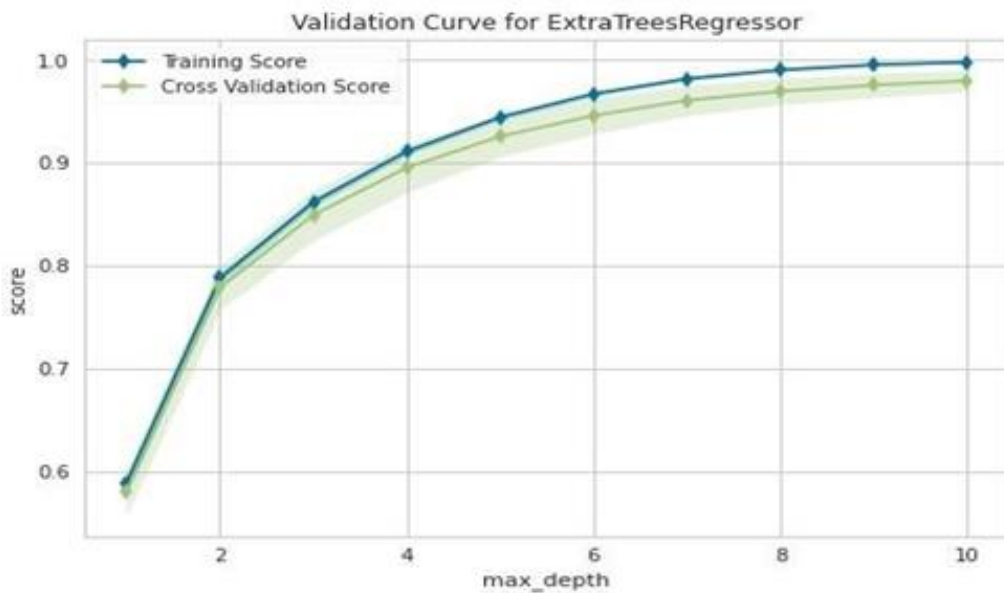


Figure 20. Validation curve (Latitude).

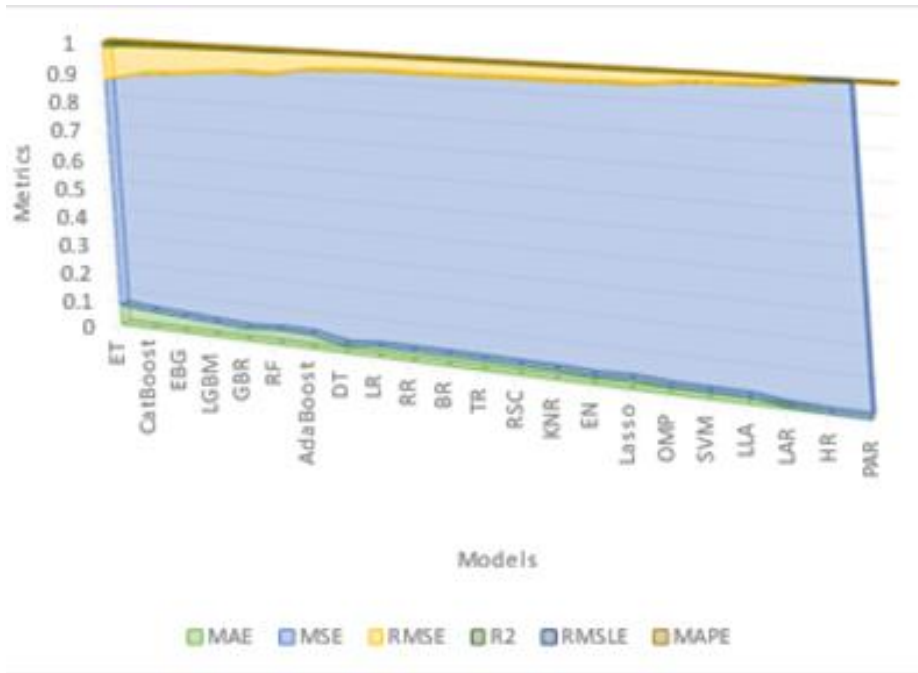


Figure 21. Model contrast (Haversine distance).

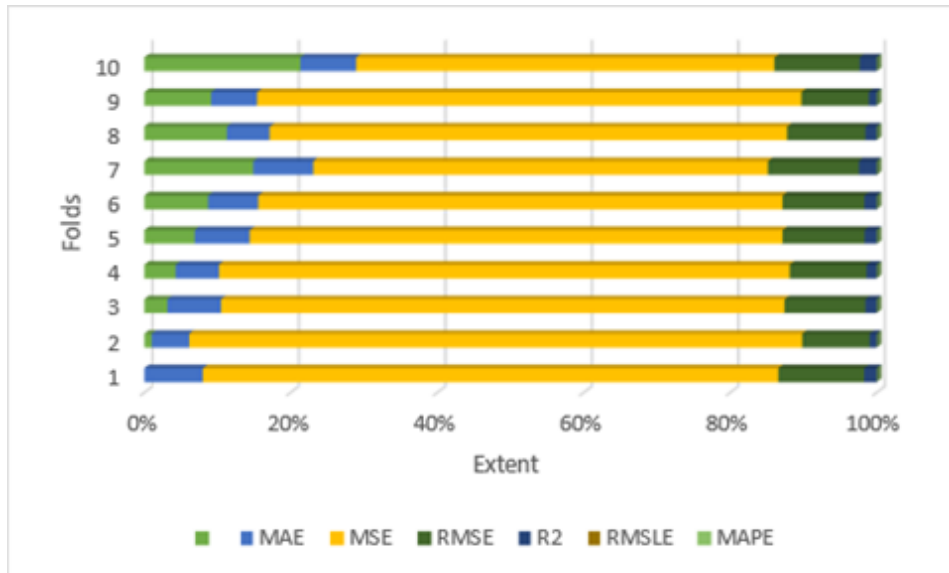


Figure 22. Model performance (Haversine distance).

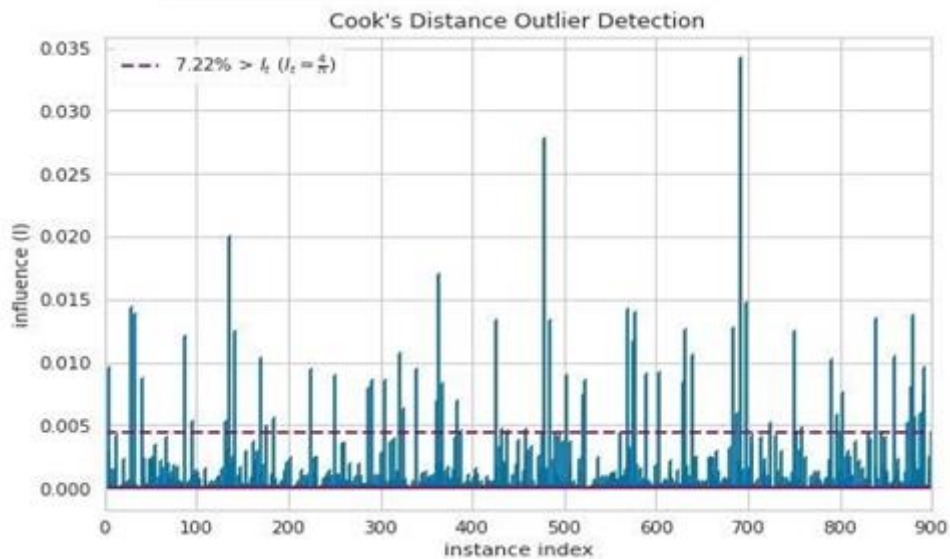


Figure 23. Outliers (Haversine distance).

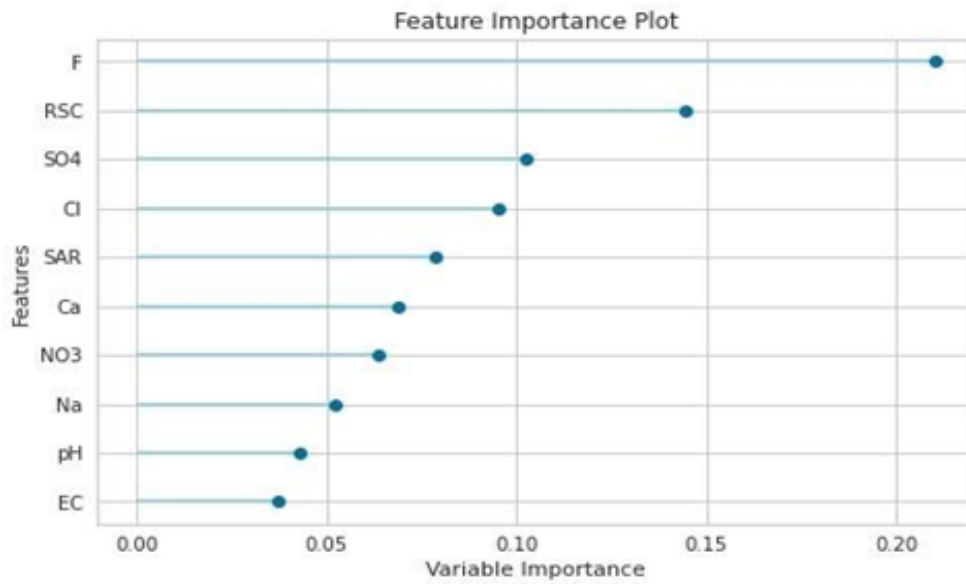


Figure 24. Feature importance (Haversine distance).

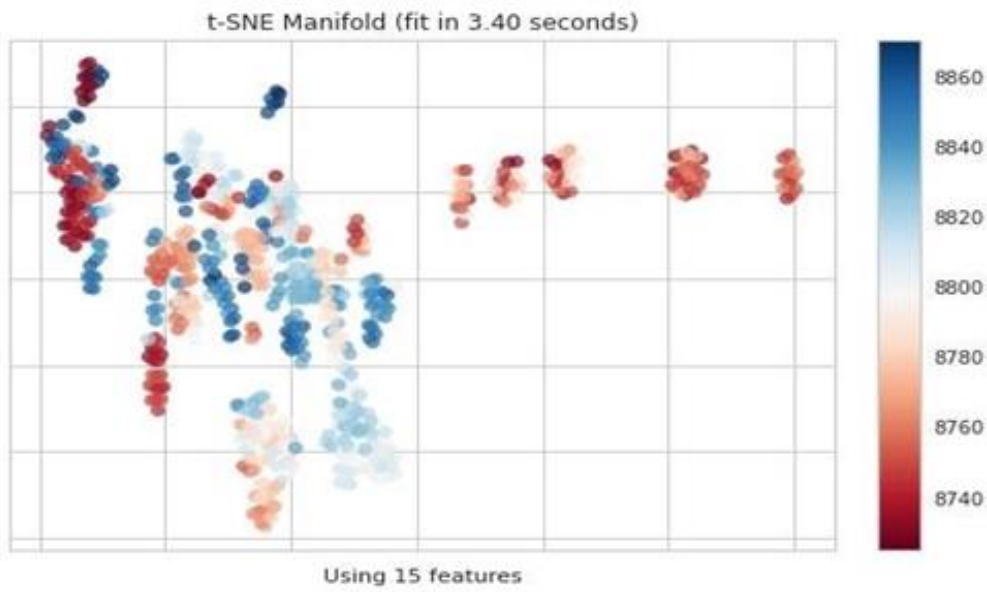


Figure 25. t-SNE Manifold (Haversine distance).

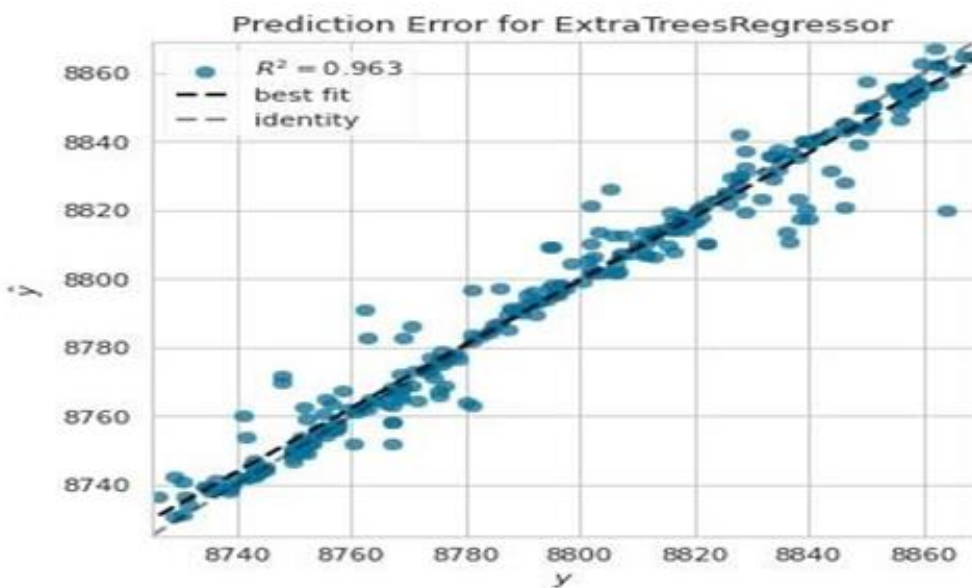


Figure 26. Prediction error (Haversine distance).

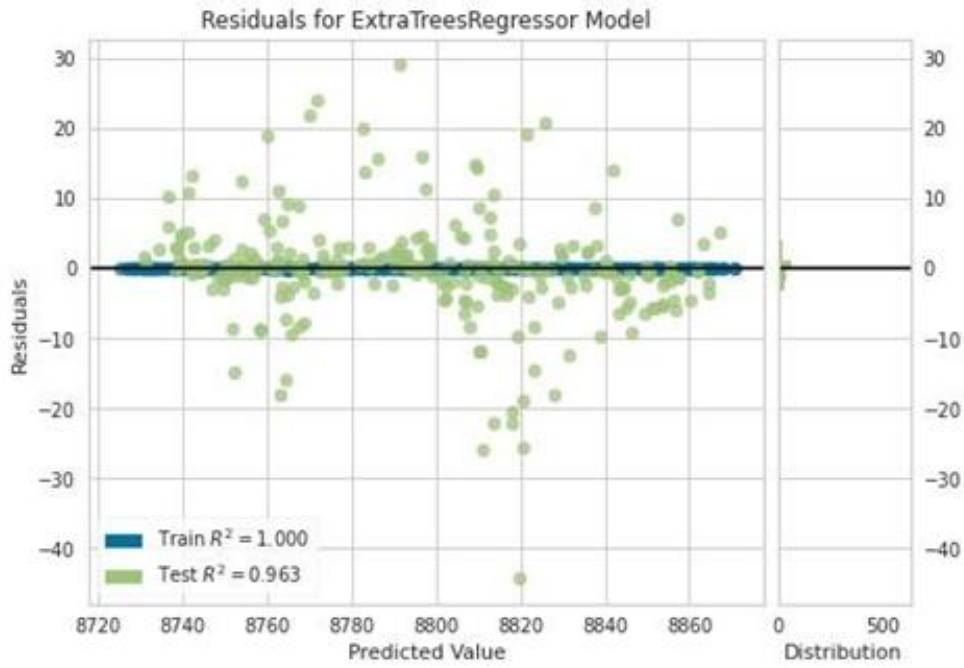


Figure 27. Residuals (Haversine distance).

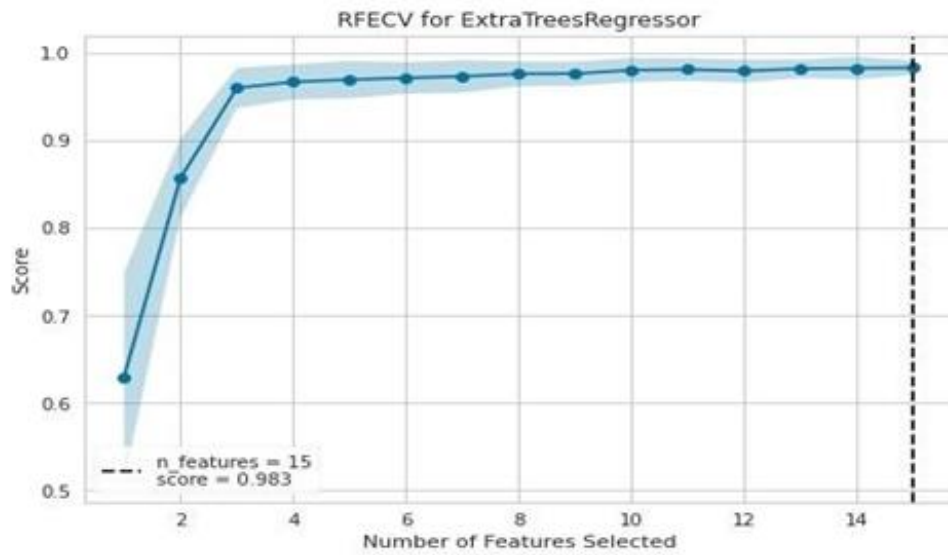


Figure 28. RFECV (Haversine distance).

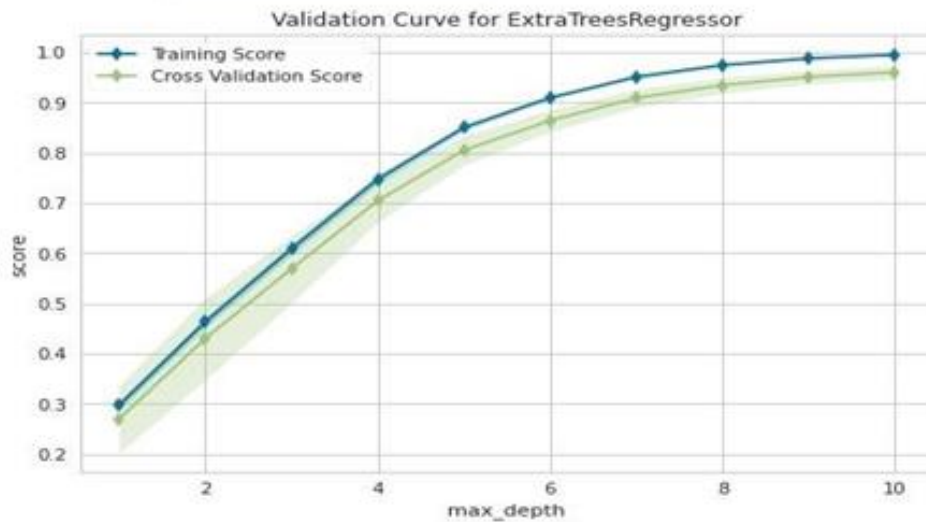


Figure 29. Validation curve (Haversine distance).

#### 4. Discussion

The Extra Trees Regressor (et) performed better than other regressors i.e., CatBoost, Extreme Gradient boosting, Light Gradient boosting machine, Gradient boosting regressor, etc., predicting the Longitude variable. The 'et' regressor yielded an  $R^2$  value of 0.96 reflecting that the model fitted well. Fluoride has more influence than other variables i.e., RSC, Cl,  $SO_4$ , SAR,  $NO_3$ , Na, Ca, EC and pH. The Extra Trees Regressor (et) responded well in predicting the Latitude variable. The 'et' regressor yielded an  $R^2$  value of 0.98 showing that the model fitted well. The SAR highly influenced the prediction, followed by Na, TH, Ca, Mg,  $SO_4$ ,  $NO_3$ , EC, Cl, and RSC. The Extra Trees Regressor (et) performed better than other regressors in predicting the Haversine distance. The 'et' regressor yielded an  $R^2$  value of 0.96 reflecting that the model fitted well. Fluoride strongly influenced prediction, followed by RSC,  $SO_4$ , and Cl. SAR, Ca,  $NO_3$ , Na, pH, and EC. The present observations obtained through this study suggests that the groundwater quality variables if collected at large from several points will aid in solving some of the navigation problems when there is no network and if satellite relay systems are impaired due to solar storms. This work shows that the prediction accuracy of the geolocation can be effectively improved if more data related with groundwater quality is available. The works cited in the introduction section may be viewed to know the navigation challenges. Though artificial networks and deep learning frameworks were used in estimation of groundwater and watershed components, the location-based applications were less studied and this work will add some information in this research area. AutoML tools like H<sub>2</sub>O can be used across various areas of scientific studies and cloud-based analytics can also aid us in lowering the cost of research.

#### 5. Conclusion

This work aimed to predict latitude, longitude, and haversine distance, and it is concluded that the Extra Trees Regressor model performed better than other models in all the three cases. This work can be used in various applications and preferably larger datasets with location components. This research helps solve location-based problems if for any reason satellite-based navigation becomes impaired due to unpredictable natural disasters. The present work can be also used to address several issues that helps in both ways i.e., in understanding the role of groundwater quality variables in locational intelligence and vice versa. Through the evolution of artificial intelligence and cloud-based analytics, the cost of understanding the local hydrology has drastically reduced, however the field-based investigations are still consuming excess human labor and money. The researchers in the fields of hydrology, pollution, and GIS can get benefitted from this work.

#### Acknowledgement

The authors would like to thank Central Groundwater Control Board, Government of India for making data available for this research work.

#### Conflicts of interest

The authors declare no conflicts of interest.

#### References

1. Afzaal, H., Farooque, A. A., Abbas, F., Acharya, B., & Esau, T. (2019). Groundwater estimation from major physical hydrology components using artificial neural networks and deep learning. *Water*, 12(1), 5. <https://doi.org/10.3390/w12010005>
2. Azdy, R. A., & Darnis, F. (2020, April). Use of haversine formula in finding distance between temporary shelter and waste end processing sites. In *Journal of Physics: Conference Series*, 1500(1), 012104. <https://doi.org/10.1088/1742-6596/1500/1/012104>
3. Ahmed, U., Mumtaz, R., Anwar, H., Shah, A. A., Irfan, R., & García-Nieto, J. (2019). Efficient water quality prediction using supervised machine learning. *Water*, 11(11), 2210. <https://doi.org/10.3390/w11112210>
4. Alizamir, M., Kisi, O., & Zounemat-Kermani, M. (2018). Modelling long-term groundwater fluctuations by extreme learning machine using hydro-climatic data. *Hydrological sciences journal*, 63(1), 63-73. <https://doi.org/10.1080/02626667.2017.1410891>
5. Alkan, H., & Celebi, H. (2019). The Implementation of Positioning System with Trilateration of Haversine Distance. 2019 IEEE 30th Annual International Symposium on Personal, Indoor and Mobile Radio Communications (PIMRC), 1–6. Istanbul, Turkey: IEEE. <https://doi.org/10.1109/PIMRC.2019.8904289>
6. Bowes, B. D., Sadler, J. M., Morsy, M. M., Behl, M., & Goodall, J. L. (2019). Forecasting groundwater table in a flood prone coastal city with long short-term memory and recurrent neural networks. *Water*, 11(5), 1098. <https://doi.org/10.3390/w11051098>
7. Dwivedi, P., Khan, A. A., Mudge, S., & Sharma, G. (2022). Explainable AI (XAI) for Social Good: Leveraging AutoML to Assess and Analyze Vital Potable Water Quality Indicators. In *Computational Intelligence in Data Mining: Proceedings of ICCIDM 2021* (pp. 591-606). Singapore: Springer Nature Singapore. [https://doi.org/10.1007/978-981-16-9447-9\\_45](https://doi.org/10.1007/978-981-16-9447-9_45)
8. Gupta, P. K., Yadav, B., & Yadav, B. K. (2019). Assessment of LNAPL in subsurface under fluctuating groundwater table using 2D sand tank experiments. *Journal of Environmental Engineering*, 145(9), 04019048. [https://doi.org/10.1061/\(ASCE\)EE.1943-7870.0001560](https://doi.org/10.1061/(ASCE)EE.1943-7870.0001560)
9. Izady, A., Davary, K., Alizadeh, A., Ziaei, A. N., Alipoor, A., Joodavi, A., & Brusseau, M. L. (2014). A framework toward developing a groundwater conceptual model. *Arabian Journal of Geosciences*, 7, 3611-3631. <https://doi.org/10.1007/s12517-013-0971-9>
10. Jamin, P., Cochand, M., Dagenais, S., Lemieux, J. M., Fortier, R., Molson, J., & Brouyère, S. (2020). Direct measurement of groundwater flux in aquifers within

- the discontinuous permafrost zone: an application of the finite volume point dilution method near Umiujaq (Nunavik, Canada). *Hydrogeology Journal*, 28(3), 869-885. <https://doi.org/10.1007/s10040-020-02108-y>
11. Kim, G. B. (2020). A study on the establishment of groundwater protection area around a saline waterway by combining artificial neural network and GIS-based AHP. *Environmental Earth Sciences*, 79(5), 117. <https://doi.org/10.1007/s12665-020-8862-3>
  12. Kuhn, M., & Johnson, K. (2013). *Applied predictive modeling*, 26, 13. New York: Springer.
  13. Larsen, E., Noever, D., MacVittie, K., & Lilly, J. (2021). Overhead-MNIST: Machine Learning Baselines for Image Classification. <https://doi.org/10.48550/ARXIV.2107.00436>
  14. Mallikarjuna, B., Sathish, K., Venkata Krishna, P., & Viswanathan, R. (2021). The effective SVM-based binary prediction of ground water table. *Evolutionary Intelligence*, 14(2), 779-787. <https://doi.org/10.1007/s12065-020-00447-z>
  15. Meyer, H., Reudenbach, C., Wöllauer, S., & Naus, T. (2019). Importance of spatial predictor variable selection in machine learning applications—Moving from data reproduction to spatial prediction. *Ecological Modelling*, 411, 108815. <https://doi.org/10.1016/j.ecolmodel.2019.108815>
  16. Moez, A. (2020). PyCaret: An open source, low-code machine learning library in Python. *PyCaret*, Apr.
  17. Mukherjee, A., Duttagupta, S., Chattopadhyay, S., Bhanja, S. N., Bhattacharya, A., Chakraborty, S., ... & Sahu, S. (2019). Impact of sanitation and socio-economy on groundwater fecal pollution and human health towards achieving sustainable development goals across India from ground-observations and satellite-derived nightlight. *Scientific Reports*, 9(1), 15193.
  18. Omar, P. J., Gaur, S., Dwivedi, S. B., & Dikshit, P. K. S. (2019). Groundwater modelling using an analytic element method and finite difference method: an insight into Lower Ganga River basin. *Journal of Earth System Science*, 128, 195. <https://doi.org/10.1007/s12040-019-1225-3>
  19. Pant, R. R., Zhang, F., Rehman, F. U., Wang, G., Ye, M., Zeng, C., & Tang, H. (2018). Spatiotemporal variations of hydrogeochemistry and its controlling factors in the Gandaki River Basin, Central Himalaya Nepal. *Science of the Total Environment*, 622, 770-782. <https://doi.org/10.1016/j.scitotenv.2017.12.063>
  20. Pham, B. T., Jaafari, A., Prakash, I., Singh, S. K., Quoc, N. K., & Bui, D. T. (2019). Hybrid computational intelligence models for groundwater potential mapping. *Catena*, 182, 104101. <https://doi.org/10.1016/j.catena.2019.104101>
  21. Xin, L., & Mou, T. (2022). Research on the Application of Multimodal-Based Machine Learning Algorithms to Water Quality Classification. *Wireless Communications and Mobile Computing*, 2022, 9555790. <https://doi.org/10.1155/2022/9555790>
  22. Xue, J., Huo, Z., Wang, F., Kang, S., & Huang, G. (2018). Untangling the effects of shallow groundwater and deficit irrigation on irrigation water productivity in arid region: New conceptual model. *Science of the Total Environment*, 619, 1170-1182. <https://doi.org/10.1016/j.scitotenv.2017.11.145>
  23. Çubukçu, E. A., Demir, V., & Sevimli, M. F. (2022). Digital elevation modeling using artificial neural networks, deterministic and geostatistical interpolation methods. *Turkish Journal of Engineering*, 6(3), 199-205. <https://doi.org/10.31127/tuje.889570>
  24. Demir, V., & Citakoglu, H. (2023). Forecasting of solar radiation using different machine learning approaches. *Neural Computing and Applications*, 35(1), 887-906. <https://doi.org/10.1007/s00521-022-07841-x>
  25. Demir, V., & Yaseen, Z. M. (2023). Neurocomputing intelligence models for lakes water level forecasting: a comprehensive review. *Neural Computing and Applications*, 35(1), 303-343. <https://doi.org/10.1007/s00521-022-07699-z>
  26. Citakoglu, H., & Demir, V. (2023). Developing numerical equality to regional intensity–duration–frequency curves using evolutionary algorithms and multi-gene genetic programming. *Acta Geophysica*, 71(1), 469-488. <https://doi.org/10.1007/s00521-022-07699-z>
  27. <https://indiawris.gov.in/wris/>
  28. <http://cgwb.gov.in/GW-data-access.html>
  29. [https://scikit-learn.org/stable/supervised\\_learning.html#supervised-learning](https://scikit-learn.org/stable/supervised_learning.html#supervised-learning)
  30. <https://docs.h2o.ai/h2o/latest-stable/h2o-docs/automl.html>



© Author(s) 2024. This work is distributed under <https://creativecommons.org/licenses/by-sa/4.0/>



### Application of a new fuzzy logic model known as "SMRGT" for estimating flow coefficient rate

Ayşe Yeter Gunal <sup>1</sup>, Ruya Mehdi <sup>\*1</sup>

<sup>1</sup>Gaziantep University, Department of Civil Engineering, Türkiye, [agunal@gantep.edu.tr](mailto:agunal@gantep.edu.tr); [ruya.mehdi1991@gmail.com](mailto:ruya.mehdi1991@gmail.com)

Cite this study:

Gunal, A. Y., & Mehdi, R. (2024). Application of a new fuzzy logic model known as "SMRGT" for estimating flow coefficient rate. *Turkish Journal of Engineering*, 8 (1), 46-55

#### Keywords

Fuzzy System  
SMRGT  
Flow Coefficient  
Mamdani theory  
Ambiguity

#### Research Article

DOI: 10.31127/tuje.1225795

Received:28.12.2022

Revised: 06.03.2023

Accepted:10.03.2023

Published:15.09.2023



#### Abstract

Since we all have our own set of limitations when it comes to perceiving the world and reasoning profoundly, we are constantly met with uncertainty as a result of a lack of information (lexical impression, incompleteness), as well as specific measurement inaccuracies. It has been found that uncertainty, which shows up as ambiguity, is the root cause of complexity, which is everywhere in the real world. Most of the uncertainty in civil engineering systems comes from the fact that the constraints (parameters) are hard to understand and are described in a vague way. The ambiguity comes from a number of sources, including physical arbitrariness, statistical uncertainty due to using limited information to estimate these characteristics, and model uncertainty due to using overly simplified methods and idealized depictions of actual performances. Thus, it is better to combine fuzzy set theory and fuzzy logic. Fuzzy logic is well-suited to modelling the indeterminacy and ambiguity that results from multiple factors and a lack of data. In order to improve upon a previous predictive model, this paper uses a smart model built on a fuzzy logic system (FLS). Precipitation, temperature, humidity, slope, and land use data were all taken into account as input variables in the fuzzy model. Toprak's original explanation of the simple membership function and fuzzy rules generation technique (SMRGT) was based on the fuzzy-Mamdani methodology and used the flow coefficient as its output. The model's results were compared to available data. The following factors were considered in the comparison: 1) The maximum, minimum, mean, standard deviation, skewness, variation, and correlation coefficients are the seven statistical parameters. 2) Four types of error criteria: Mean Absolute Relative Error (MARE), Mean Square Error (MSE), Mean Absolute Error (MAE), and Root Mean Square Error (RMSE). 3) Scatter diagram.

## 1. Introduction

"As a system learns, our ability to make accurate and consistent statements about its behaviour diminishes until a threshold is reached beyond which precision and significance (or relevance) become almost reciprocally inimitable features," writes Zadeh [1]. It is now evident that a plausible mathematical structure of any physical reality is often impossible to describe and generate. Fuzzy logic is the technological revolution in computer logic. It aids computers and logical applications similarly to how it aids human behaviour. In 1965, Lutfu Askerzade published the first information regarding fuzzy principles [1]. According to Zadeh, the majority of human thought is hazy and uncertain. In 1965, Zadeh initiated a new review of systems containing uncertainty. Limiting the properties of assets and objects to two values (0; 1), according to Zadeh, is insufficient, as the

real world consists of thousands of similarities, ranges, and opposites between 0 and 1. However, these ideas were criticized by the western world. This philosophy brought a simple and contemporary solution to difficult and complex problems in a vast array of applications and fields such as science, maths, and engineering [2,3]. For the frequency fuzzy logic theory, Freksa stated that the facts are fuzzy, but their rules cannot be disregarded [4]. In 1975, Mamdani and Assilian implemented the concept of fuzzy logic for the first time in the control system of a steam engine [5].

Events in the natural world that change and evolve together affect one another. Therefore, the number of factors that can affect an event, as well as the strength and scope of those factors' effects, can shift over time and space. It is also challenging to replicate observations made in nature under identical laboratory conditions or

to recreate conditions similar to those used in the original experiments. Factoring in measurement and observation errors increases the magnitude of the uncertainties. It can be challenging to incorporate the concepts and interpretations of the observed natural phenomenon into the model, even when these are complete. If that's the case, then people will always face a degree of uncertainty whenever natural disasters occur. It is exceedingly challenging to make accurate predictions or models of natural events because of these uncertainties. Given these data, it's reasonable to conclude that error exists in the supposedly error-free models' development. For the prediction of natural events, the exact reason is not known. These errors generally depend on the assumptions and omissions, in short idealizations, errors in the measurements and recordings, differences in the experimental or observational conditions, the quality and quantity of the parameters considered, and so on. The ambiguity remains, and computers are unable to resolve or interpret it. However, they do make it easier to process data that has been entered numerically quickly. Humans, in contrast to computers, are able, depending on their cognitive abilities, to perform operations and define concepts with limited, incomplete, and uncertain data and information. Human thought, description, and representation typically involve some degree of doubt (approximation). That is to say, fuzzy thinking is common, and similarly imprecise definitions are often used to describe how people think. What this means is that people are typically verbal rather than numerical thinkers and communicators. Due to idealizations, measurement and observation errors, and a lack of complete and accurate data about natural phenomena, scientific uncertainty has persisted. According to Sen [6], "fuzzy sources" are any information that is both complete and imprecise, such as complexity and uncertainty, and Zadeh [7] said that the more closely a real-world problem is examined, the less clear the solution becomes. Therefore, complexity and uncertainty are inherent to the field of science.

The primary purpose of this investigation is to provide evidence that the proposed fuzzy model has the ability to make accurate predictions regarding the flow coefficient. A complete comprehension of river flow is necessary for the effective management of water resources, the planning and construction of water infrastructure, and the mitigation of the effects of natural disasters. There are two scenarios in which the use of fuzzy logic systems can prove to be extremely beneficial: the first is when the performance of extremely complex systems is not completely understood, and the second is when an efficient and approximative solution is acceptable. The differences between a classical system and a fuzzy system are illustrated in Figure 1 and Figure 2, respectively. The optimal construction of membership functions (MFs) and fuzzy rules (FRs) is the primary concern in any fuzzy system. The question at hand is how to achieve maximum efficiency.

This paper proposes a straightforward technique to assist those who are uncertain about the number, shape, and logic of the MFs and FRs in any fuzzy system. For open canal flow modelling, Toprak [8] introduced Simple

Membership functions and the fuzzy Rules Generation Technique, which uses only a few key numbers to calculate all MFs of input and output variables. The MF shape (triangular, trapezoidal, etc.) and the defuzzification method determined the key numbers (centroid, maximum membership degree, etc.). This study favors the centre of gravity (centroid method) because it is more compatible with the fuzzy SMRGT method. The SMRGT model does not require any particular conditions. The user can specify the minimum and maximum values for the model. This is also the range of values for which the model is valid and easy for the user to determine. As a result, the Fuzzy SMRGT method is easier to implement and more reliable than other methods described in the literature. The new procedure employs the physical cause-and-effect relationship. As a result, it can be generalized and applied to any basin or region.

The following is the organization of the manuscript: The second section of this report provides an overview of the area under investigation and discusses the datasets that were provided by the General Directorate of State Hydraulic Works and the Turkish State Meteorological Service (TSMS). In Section 3, the author demonstrates the extensive scope of the necessary process and analyses that can be carried out utilizing Simple Membership Functions and the Fuzzy Rules Generation Technique. These are two of the tools that are discussed (SMRGT). The most important findings from our research are summarized in the fourth section, along with a discussion of the results of the processing and hydrological analysis performed on the study area. In Section 5, we present some generalizations and interpretations regarding the findings as a whole.

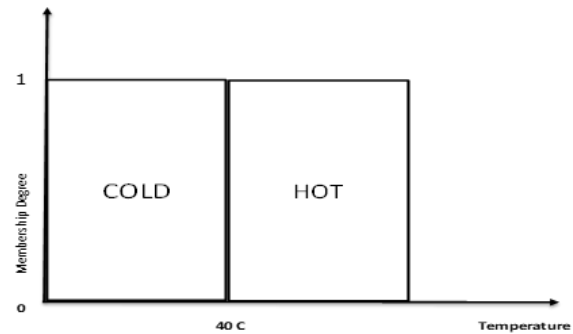


Figure 1. Classical set.

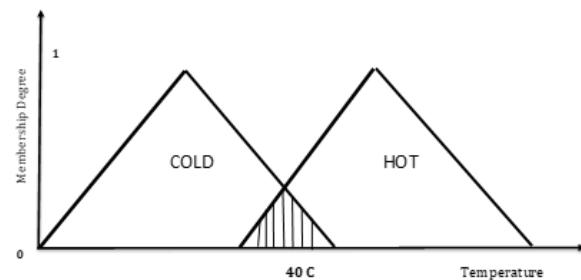


Figure 2. Fuzzy set.

## 2. Method

The first step in all hydrological studies is to collect the necessary data, such as Current measurements,

evaporation, precipitation, temperature, etc. The hydrological processes must be as natural as possible. Therefore, it is necessary to provide sufficient tools and measurements. Latitudes 36–38 degrees north and longitudes 30–31 degrees east define the boundaries of the study area. It is one of the ten sub-basins that make up the Antalya Basin. According to observations of the river's flow made over a prolonged period, the Aksu has an annual average flow of 94.98 hm<sup>3</sup>. The Mediterranean Sea forms the southern boundary of the basin, while the sub-basins Korkuteli and Duden Stream make up the western boundary. The closed Konya Basin can be seen from the northeast, the Buyuk Menderes Basin and the Akarcayi Basin can be seen from the north, and the Koprucayi Sub-basin can be seen from the east. A Mediterranean climate and a continental climate coexist in the Aksu stream basin. Both of these climates are distinct from one another. The northern portion of the basin is characterized by the continental climate of Central Anatolia, which is characterized by hot, dry summers and cold, snowy winters. In contrast, the southern portion of the basin is characterized by a Mediterranean climate. The dataset containing information on precipitation, temperature, humidity, land use, and slope in the Aksu River Basin over a long period (1990-2020) was used in this study.

In hydrological design, watershed management, and other types of research, it is helpful to make accurate predictions of the flow coefficient rate. The development of more accurate models has widely used various methods; however, improving the accuracy of predictions is still a pressing issue for decision-makers in a wide range of fields. In virtually every fuzzy system, the primary concern is determining how to construct the membership functions (MFs) and fuzzy rules (FRs) so that the system generates the most accurate results possible. The creation of membership functions (MFs) and fuzzy rules (FRs) are the two aspects of a data-based fuzzy model that are considered to be of the utmost significance. After the MF types have been chosen, the problem then becomes one of optimizing the number of MFs and FRs as well as their logic and the shape they take. The construction of MFs and the simple generation of FRs has recently seen the development of a large number of methods and algorithms, including genetic algorithms (GA) [9–16], the combined use of GAs and artificial neural networks (ANNs) [17, 18], ANNs [19–23], Kalman filters [24], probability measurement [25–31], and a great number of others. Many academics have proposed methods for modifying or optimizing only the number of MFs [9-10,19,20,24-33], while others present methods for identifying only the FRs [21-23]. In addition, there were very few works that attempted to optimize both the MFs and the FRs at the same time [11–18]. The studies that were discussed earlier, with a few notable exceptions, do not contribute to the joint determination of FRs and MFs. In addition, many researchers are hesitant to use these methods because of how difficult it

is to put them into practice. As a direct result of this, the methods of trial and error continue to be favored. Thus, the purpose of this study is to provide assistance to individuals who have difficulty determining the number, shape, and logic of the MFs and FRs in any fuzzy system by presenting a new fuzzy method. The new fuzzy technique that has been presented in this study is solely based on a select few primary numbers and that applies to all MFs of both the input and output variables. The key numbers were selected in accordance with the MF shape (triangular, trapezoidal, etc.) and the defuzzification technique (centroid, maximum membership degree, etc.). The SMRGT method was first introduced by [8], the Mamdani fuzzy system was selected as an operator, and has been utilized successfully in numerous types of research, including those conducted by [34-40]. As a result, they concluded that this new method for determining membership functions (MFs) and fuzzy rules (FRs) is reliable. For effective results with the new method presented in this study, the following steps can be summarized:

- i. The independent and dependent variables that affect the current event have been selected. The independent variables serve as inputs to the fuzzy system, while the dependent variables serve as outputs. This study was designed with five inputs (precipitation, temperature, humidity, slope, and land use) and one output see Figure 3. These variables should be bounded by a certain range. Thus, the maximum and minimum values must be determined. These ranges can be as broad as desired based on the current event. Equation 1 can be used to calculate the  $X_R$  value.

$$X_R = (X_{max}) - (X_{min}) \quad (1)$$

- ii. There must be at least three temporary membership functions defined for each independent variable. A large number of membership functions decreases the error of the model [41] but increases the program load (processing volume). This study employed five MFs labelled as Very low, Low, Medium, High, and Very high.
- iii. The membership functions (MFs) were designed to be triangular. The initial and final membership functions should be right-angled triangles, while the middle membership functions should be isosceles triangles [8]. A fuzzy system is valid for data distributed between the key values of the first and last MFs for each independent variable.
- iii. For each variable, the key values (K1, K2... KN) and core value (Ci) of the membership functions, the unit width (UW), the symmetrically extended unit width (EUW), and the value (O) of the two intersecting neighbour membership functions are determined. Furthermore, the number of right-angled triangles (nu) in the triangular fuzzy set was determined.

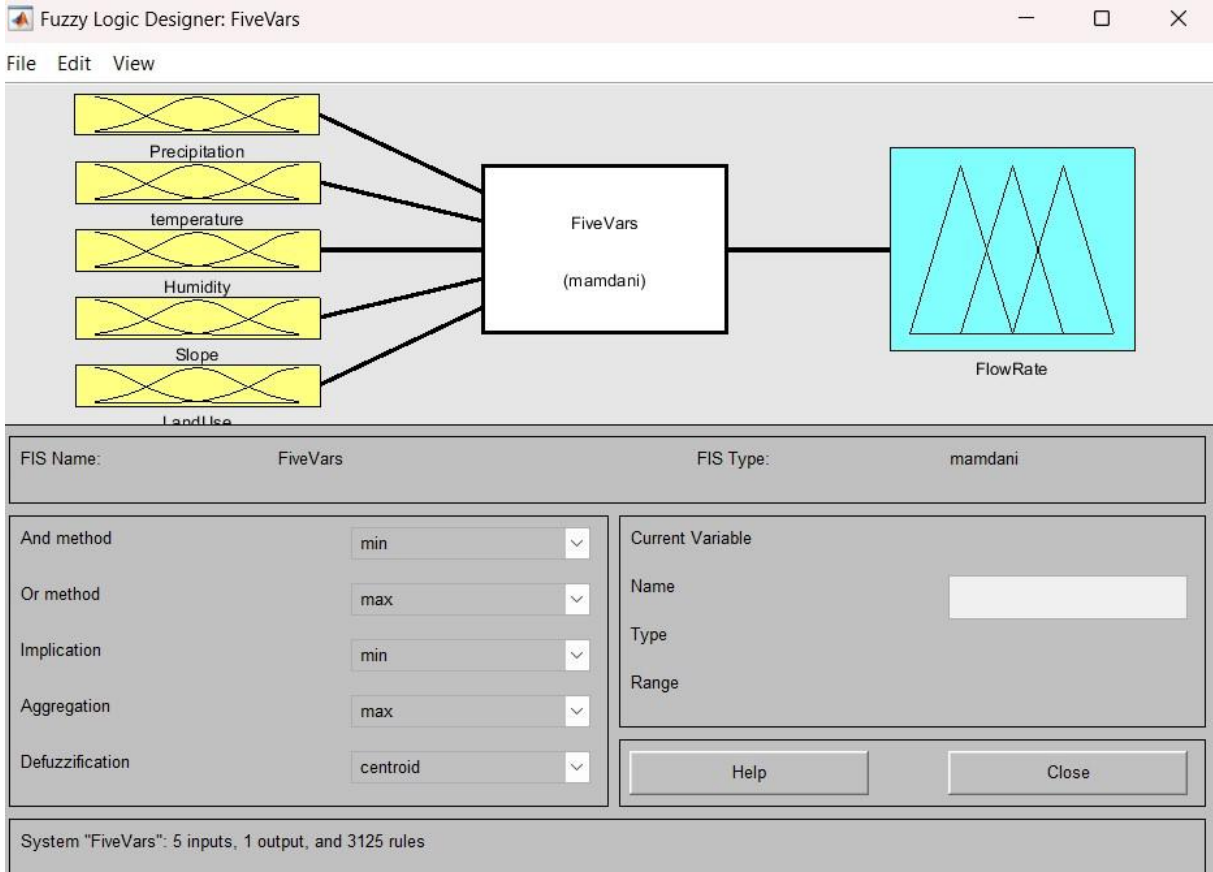


Figure 3. View of the inputs and output.

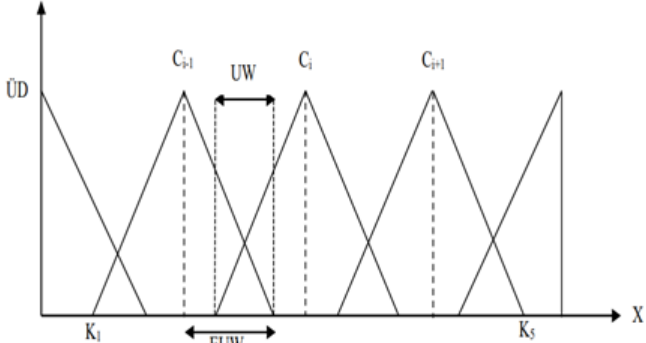


Figure 4. Core values, key values, and unit width for the model.

$$UW = \frac{XR}{nu} \quad (2)$$

$$O = \frac{UW}{2} \quad (3)$$

$$EUW = \left(\frac{XR}{nu}\right) + O \quad (4)$$

$$Ci = K3 = \left(\frac{XR}{2}\right) + Xmin \quad (5)$$

$$K4 = Ci + 1 = \left(\frac{(Ci - Xmin)}{2}\right) + Xmin \quad (6)$$

$$K2 = Ci - 1 = Xmax - \left(Xmax - \frac{Ki}{2}\right) \quad (7)$$

$$K1 = Xmin + \left(\frac{EUW}{3}\right) \quad (8)$$

$$K5 = Xmax - \frac{EUW}{3} \quad (9)$$

- ii. It was decided that the number of key values for each independent variable should equal the number of MFs. These are the inputs to the fuzzy model. It is advantageous to select the same number of membership functions (MFs) as fuzzy rules for the outputs (FRs).
- iii. The fuzzy rules base is determined by considering relevant physical conditions such as "IF," "AND," and "THEN." (see Figure 5) Package program (MATLAB) was set to include the fuzzy set. In total, 3125 rules were set for this study.
- iv. Using calibration data, the input and output data files for the relevant package program were prepared. Using the test data, identical and instantaneous input and output files are generated. Consequently, two data files were generated for each calibration and test phase: one for input and one for output. Using the corresponding package program, the fuzzy system was then developed. A simple subprogram was utilized to execute and evaluate the program. If the output membership functions are excessively intertwined, they must be reduced by combining two or more functions into one [8], and [42].

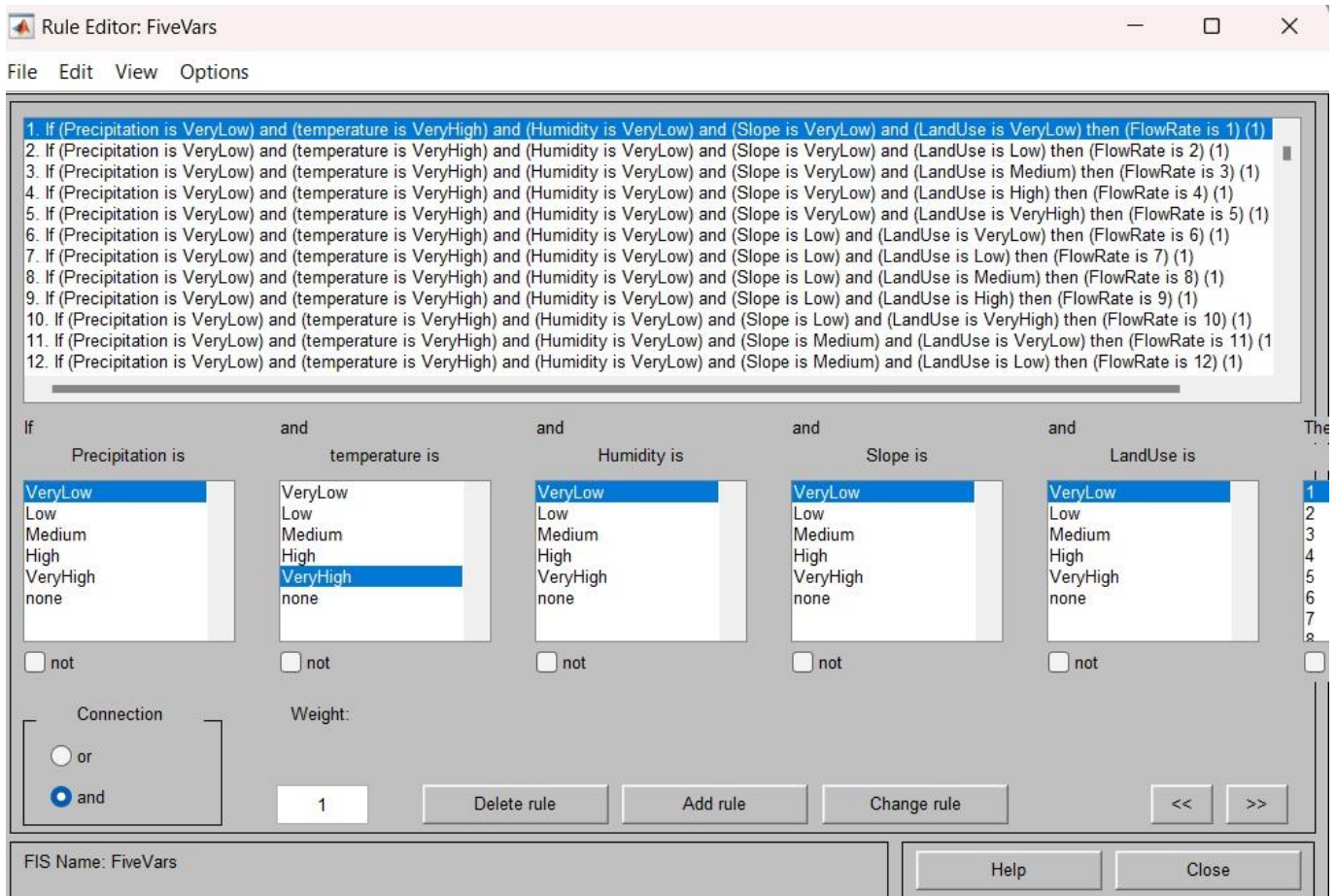


Figure 5. Fuzzy rules set for the model.

### 3. Results

The flow coefficient value of the study area was attempted to be determined. Both the MATLAB computer program and the fuzzy logic module were utilized to accomplish this. The SMRGT method was used to make the decisions regarding the input and output variables in order to achieve the most accurate result possible. The centroid method was chosen to serve as the defuzzification system, and specific formulas were utilized in order to ascertain both the input and the output key values. Table 1 provides a listing of the most significant values for each variable. To resolve the unique equation that, based on basin characteristics, calculates the flow coefficient, a specialist is sought out for assistance. The extent to which the available independent variables had an impact on the results of the model was determined in a manner that was specific to each variable. The SMRGT method dictates that the model output (flow coefficient) for this investigation should be equal to the number of rules, which in this case is 3125. When there is no precipitation, the minimum and maximum value ranges for the flow coefficient are changed to 0 and 1, respectively. These values are used to calculate the flow coefficient. The impact of precipitation, temperature, humidity, slope and land use on the flow coefficient was evaluated differently.

Where P is the precipitation (mm), T is the temperature (°C), H is humidity (%), S is the slope, LU is land use, and a is the flow coefficient. The flow coefficient reached its maximum value of (1) when the precipitation

was 2000 mm (very high), the temperature was 0° C (very low), the humidity was 100% (very high), the slope was 90° (very high), and the land use was 100% (Very high) see Figure 6. When the precipitation was 200 millimetres, which is a very low value, the temperature was 50 degrees Celsius, which is a very high value, the humidity was 0%, which is a very low value, the slope was 0 degrees, which is a very low value, and the land use was 0% (Very low).

Table 1. Key values of each variable.

	X <sub>R</sub>	K <sub>2</sub>	K <sub>3</sub>	K <sub>4</sub>	K <sub>1</sub>	K <sub>5</sub>
P	1800	650	1100	1550	312.5	1887.5
T	50	12.5	25	37.5	3.125	46.88
H%	100	25	50	75	6.25	93.75
S	90	22.5	45	67.4	5.625	84.375
LU	100	25	50	75	6.25	93.75
a	1	0.125	0.5	0.25	0	1*

\*(The last key value of the output is K<sub>3125</sub>)

Statistical parameters such as minimum (X<sub>min</sub>), mean (X<sub>m</sub>), maximum (X<sub>max</sub>), standard deviation (σ), coefficient of variation (C<sub>v</sub>), coefficient of skewness (C<sub>s</sub>), and correlation coefficient (r) were used to compare the model's output with the data in order to test the model's ability to accurately predict the outcomes of future events. Many types of errors include Mean Absolute Relative Error (also abbreviated as MARE), Mean Square Error (also abbreviated as MSE), Mean Absolute Error (also abbreviated as MAE), and Root

Mean Square Error (RMSE). The results of the statistical comparison are shown in Table 2. In addition, graphical representations of the comparison were created using a

scatter diagram and a series graph (see Figure 7, and Figure 8).

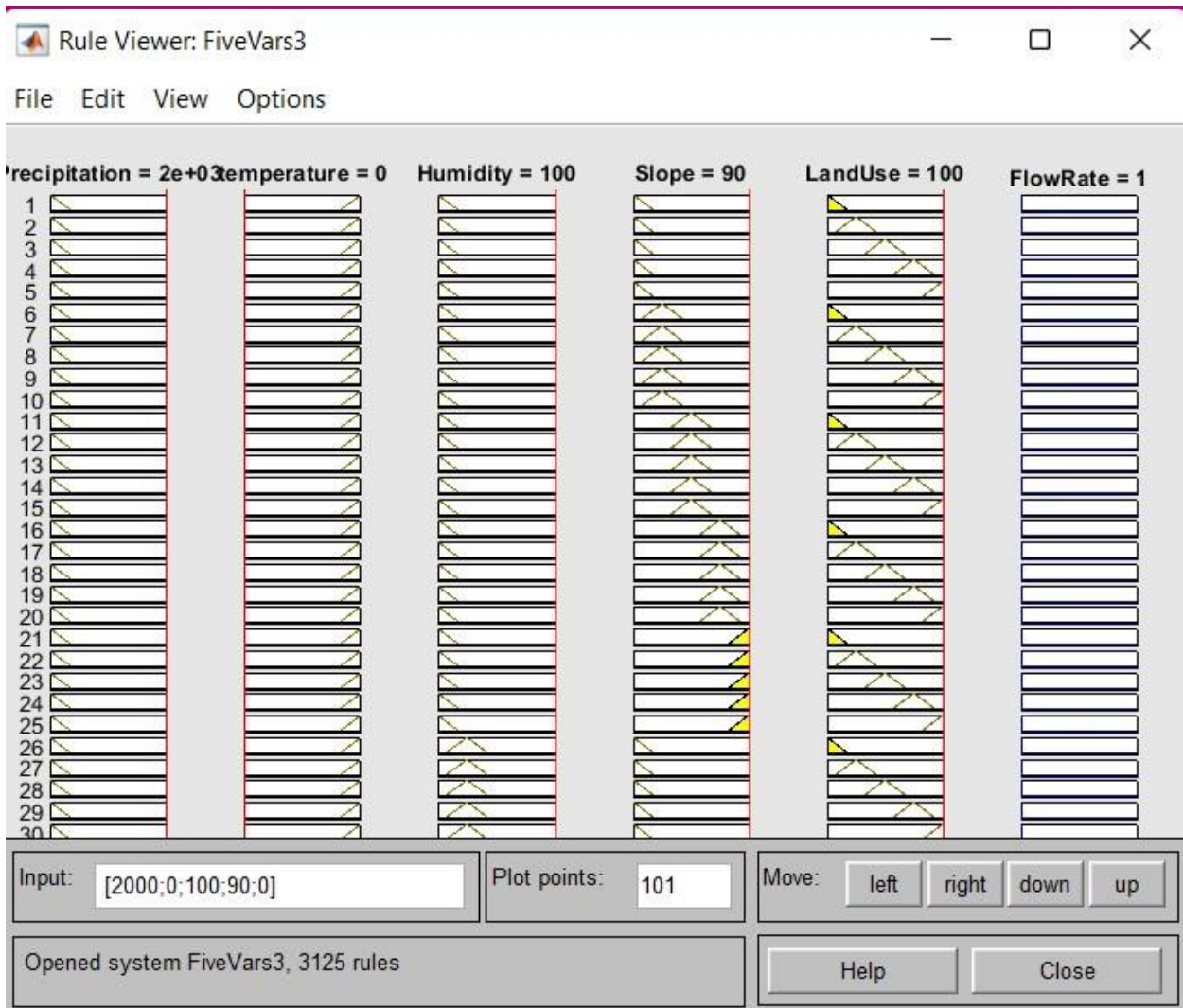


Figure 6. MATLAB view of the fuzzy rules.

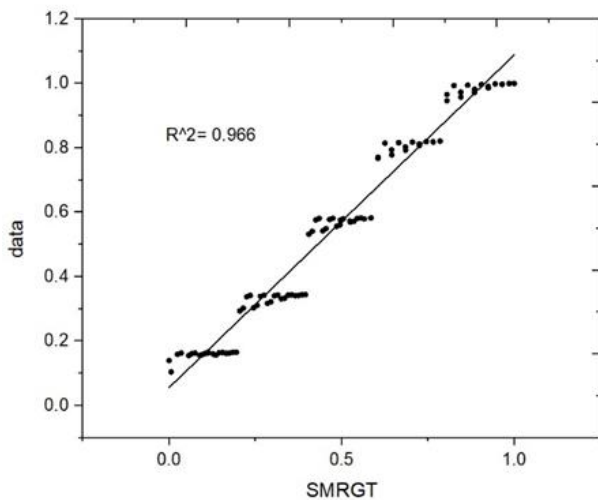


Figure 7. The scatter diagram of data and SMRGT.



Figure 8. Series graph of the data and SMRGT.

**Table 2.** Comparison between data and model.

Statistical Parameters & Errors	Data	Model
Max.	1.00	1.00
Min.	0.10	0.00
Mean	0.57	0.50
Standard Deviation	0.304	0.288
Skewness	-0.008514	-0.00291
Coefficient of Variance	0.532	0.577
Correlation Coefficient	0.966	
Mean Square Error	0.91 %	
Mean Absolute Error	11 %	
Mean Absolute Relative Error	18.3 %	
Root Mean Square Error	9.3 %	

**4. Discussion**

In this paper, a fuzzy logic approach was used to model the flow coefficient. In addition, a straightforward membership function and a fuzzy rule generation technique known as SMRGT were incorporated into the fuzzy modelling process. The fact that the flow coefficient value is dependent on the input data demonstrates that

the model is not only mathematically accurate but also physically accurate. This is supported in the literature by [35,37,39,40], among other references. The relationship that exists between the output variable and the variables that were used to create it, is statistically significant in both directions. There is a positive correlation between flow coefficient and precipitation, humidity, slope, and land use; however, there is an inverse correlation between flow coefficient and temperature. It can be seen from the scatter plot that the regression line crosses the horizontal axis at an angle that is approximately 45 degrees. To put it another way, the model does not generate predictions that routinely deviate from the data that has been collected. The fact that the coefficient of determination is so high ( $R^2 = 0.966$ ) suggests that the statistical relationship that exists between the model and the data can be expressed in a mathematical manner. Figure (9-11) illustrate how the model result—a dependent variable called the flow coefficient—varies in three dimensions as a function of the model's independent variables (Amount of rainfall, temperature, and humidity, as well as slope and land use). This variation is shown in three-dimensional space.

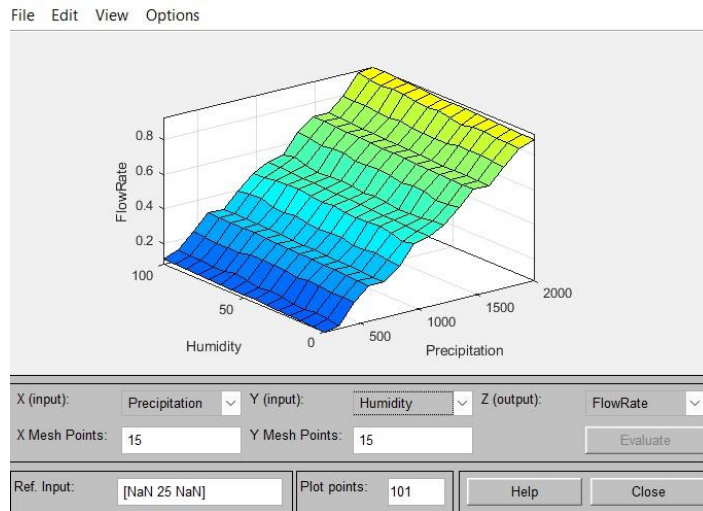


**Figure 9.** Variation of output as a function of inputs (P&H).

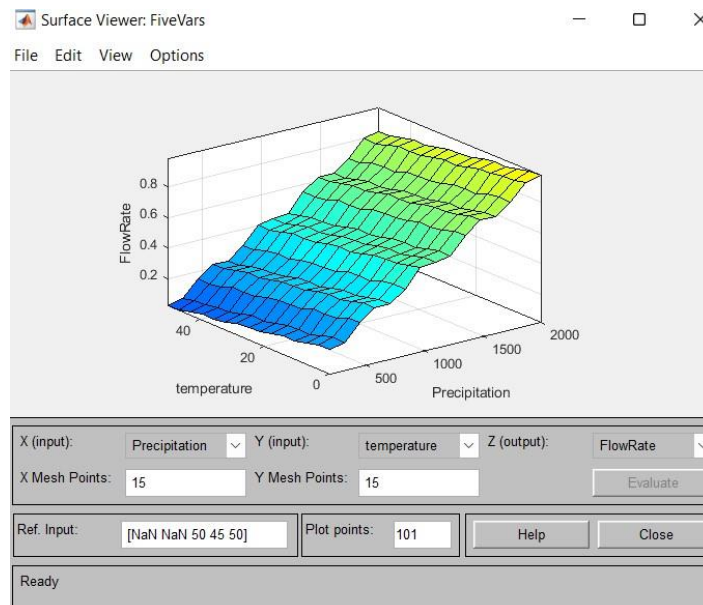


**Figure 10.** Variation of output as a function of inputs (P&T).

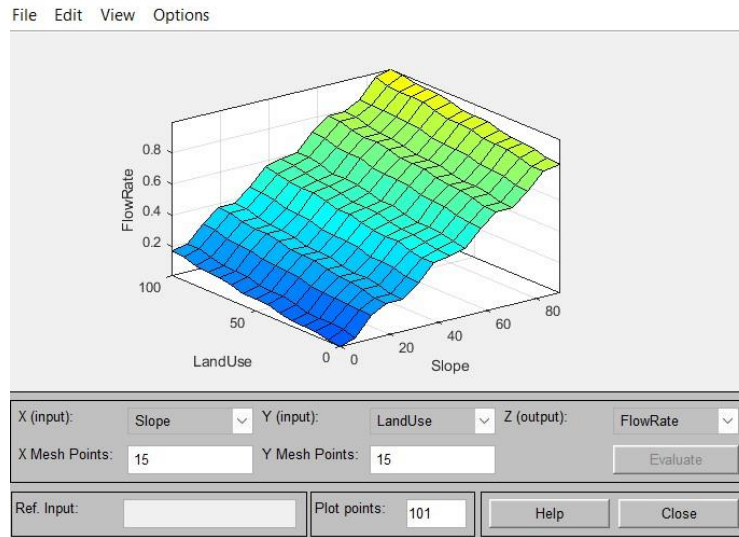


**Figure 11.** Variation of output as a function of inputs (S&LU).

## 5. Conclusion

The concept of fuzzy logic has the potential to be practical when applied to the analysis of conventional, less complicated systems. For certain kinds of issues, for instance, giving very specific responses is not always necessary. A solution that is approximative but quick can be particularly useful in generating initial design decisions, as an initial assessment in a more precise numerical process to reduce computational costs, or in the many instances where the inputs to the problem are unclear, ambiguous, or not understood at all. This is especially true in situations where the inputs to a problem are unclear, ambiguous, or not understood at all. It has been determined that when calculating flow coefficients, it is necessary to take into account all aspects of the study area. These must include the weather conditions, the land use, and the properties of the soil instead of relying on the information that can be found in prefabricated tables. The use of fuzzy logic in the study of hydrological phenomena, such as precipitation and flow, is essential because these phenomena are inherently fraught with uncertainty. The fuzzy SMRGT method makes it possible to calculate the flow coefficient in a precise and straightforward manner. The model was successful in determining the flow coefficient rate as evidenced by its impartiality and linearity in scatter diagrams, high determination and correlation coefficients between the data and the model's estimation, lowness in the mean absolute relative error of the models, and similarity between statistical characteristics of the data and the model's estimations. Calculating membership functions, their shapes, and the number of variables that are involved can all be done with a reasonable amount of ease. The SMRGT technique, on the other hand, applies to any basin or region because it takes into account the physical cause-and-effect relationship. The role of the trial-and-error method is reduced significantly as a result of the new method. SMRGT is not only quick and simple to use, but it also produces more reliable results. When it comes to modelling the flow coefficient, many people believe that the fuzzy SMRGT method and other similar physics-based modelling techniques ought to be used more

frequently because it gives the opportunity to reflect an expert's opinion on the model in comparison to other methods that have been described in the literature. In addition, it has been determined that a relatively limited number of studies have been carried out in order to get an accurate reading of the flow coefficient.

## Acknowledgement

The authors would like to express their gratitude to Prof. Dr. Zeynel Fuat TOPRAK. His exceptional qualities of intellect and character have consistently and effectively nurtured a sense of curiosity and passion for scientific inquiry in the field of educational research

## Author contributions

**Ayse Yeter Gunal:** Conceptualization, Methodology, Software, Writing-Reviewing and Editing. **Ruya Mehdi:** Data curation, Writing-Original draft preparation, Software, Validation.

## Conflicts of interest

The authors declare no conflicts of interest.

## References

1. Zadeh, L. A. (1965). Fuzzy sets. *Information and control*, 8(3), 338-353. [https://doi.org/10.1016/S0019-9958\(65\)90241-X](https://doi.org/10.1016/S0019-9958(65)90241-X)
2. Erdem, F. (2022). Risk assessment with the fuzzy logic method for Ankara OIZ environmental waste water treatment plant. *Turkish Journal of Engineering*, 6(4), 268-275. <https://doi.org/10.31127/tuje.975623>
3. Öztürk, A., Allahverdi, N., & Saday, F. (2022). Application of artificial intelligence methods for bovine gender prediction. *Turkish Journal of Engineering*, 6(1), 54-62. <https://doi.org/10.31127/tuje.807019>
4. Freksa, C. (1992). Temporal reasoning based on semi-intervals. *Artificial intelligence*, 54(1-2), 199-227. [https://doi.org/10.1016/0004-3702\(92\)90090-K](https://doi.org/10.1016/0004-3702(92)90090-K)

5. Mamdani. (1977). Application of fuzzy logic to approximate reasoning using linguistic synthesis. *IEEE transactions on computers*, 100(12), 1182-1191.  
<https://doi.org/10.1109/TC.1977.1674779>
6. Sen, Z. (2009). *Fuzzy logic and hydrological modeling*. CRC Press. ISBN: 978-1-4398-0939-6
7. Zadeh, L. A. (1971). Quantitative fuzzy semantics. *Information sciences*, 3(2), 159-176.  
[https://doi.org/10.1016/S0020-0255\(71\)80004-X](https://doi.org/10.1016/S0020-0255(71)80004-X)
8. Toprak, Z. F. (2009). Flow discharge modeling in open canals using a new fuzzy modeling technique (SMRGT). *CLEAN–Soil, Air, Water*, 37(9), 742-752.  
<https://doi.org/10.1002/clen.200900146>
9. Kissi, M., Ramdani, M., Tollabi, M., & Zakarya, D. (2004). Determination of fuzzy logic membership functions using genetic algorithms: application to structure–odor modeling. *Journal of molecular modeling*, 10, 335-341.  
<https://doi.org/10.1007/s00894-004-0200-2>
10. Kim, J. W., Kim, B. M., & Kim, J. Y. (1998). Genetic algorithm simulation approach to determine membership functions of fuzzy traffic controller. *Electronics Letters*, 34(20), 1982-1983.  
<https://doi.org/10.1049/el:19981369>
11. Mondelli, G., Castellano, G., Attolico, G., & Distanto, C. (1998, April). Parallel genetic evolution of membership functions and rules for a fuzzy controller. In *International Conference on High-Performance Computing and Networking* (pp. 922-924). Berlin, Heidelberg: Springer Berlin Heidelberg.  
<https://doi.org/10.1007/BFb0037234>
12. Chen, S. M., & Chen, Y. C. (2002). Automatically constructing membership functions and generating fuzzy rules using genetic algorithms. *Cybernetics & Systems*, 33(8), 841-862.  
<https://doi.org/10.1080/01969720290040867>
13. Wu, C. J., & Liu, G. Y. (2000). A genetic approach for simultaneous design of membership functions and fuzzy control rules. *Journal of Intelligent and Robotic Systems*, 28, 195-211.  
<https://doi.org/10.1023/A:1008186427312>
14. Wu, S., Er, M. J., & Gao, Y. (2001). A fast approach for automatic generation of fuzzy rules by generalized dynamic fuzzy neural networks. *IEEE transactions on fuzzy systems*, 9(4), 578-594.  
<https://doi.org/10.1109/91.940970>
15. Inoue, H., Kamei, K., & Inoue, K. (1998). Automatic generation of fuzzy rules using hyper-elliptic-cone membership functions by genetic algorithms. *Journal of Intelligent & Fuzzy Systems*, 6(1), 65-81.
16. Kim, M. W., Ryu, J. W., Kim, S., & Lee, J. G. (2003). Optimization of fuzzy rules for classification using genetic algorithm. In *Advances in Knowledge Discovery and Data Mining: 7th Pacific-Asia Conference, PAKDD 2003*, Seoul, Korea, April 30–May 2, 2003 Proceedings 7 (pp. 363-375). Springer Berlin Heidelberg. [https://doi.org/10.1007/3-540-36175-8\\_36](https://doi.org/10.1007/3-540-36175-8_36)
17. Pal, T., Pal, N. R., & Pal, M. (2003). Learning fuzzy rules for controllers with genetic algorithms. *International Journal of Intelligent Systems*, 18(5), 569-592.  
<https://doi.org/10.1002/int.10104>
18. de Castro, P. A., & Camargo, H. A. (2004). A study of the reasoning methods impact on genetic learning and optimization of fuzzy rules. In *Advances in Artificial Intelligence–SBIA 2004: 17th Brazilian Symposium on Artificial Intelligence*, Sao Luis, Maranhao, Brazil, September 29–October 1, 2004. Proceedings 17 (pp. 414-423). Springer Berlin Heidelberg. [https://doi.org/10.1007/978-3-540-28645-5\\_42](https://doi.org/10.1007/978-3-540-28645-5_42)
19. Rutkowska, D. (1998). On generating fuzzy rules by an evolutionary approach. *Cybernetics & Systems*, 29(4), 391-407.  
<https://doi.org/10.1080/019697298125669>
20. Lin, C. J., & Ho, W. H. (2005). An asymmetry-similarity-measure-based neural fuzzy inference system. *Fuzzy Sets and Systems*, 152(3), 535-551.  
<https://doi.org/10.1016/j.fss.2004.11.001>
21. Kim, J. H., Seo, J., & Kim, G. C. (1996). Estimating membership functions in a fuzzy network model for part-of-speech tagging. *Journal of Intelligent & Fuzzy Systems*, 4(4), 309-320.
22. Leng, G., McGinnity, T. M., & Prasad, G. (2005). An approach for on-line extraction of fuzzy rules using a self-organising fuzzy neural network. *Fuzzy sets and systems*, 150(2), 211-243.  
<https://doi.org/10.1016/j.fss.2004.03.001>
23. Besada-Juez, J. M., & Sanz-Bobi, M. A. (2002). Extraction of fuzzy rules using sensibility analysis in a neural network. In *Artificial Neural Networks—ICANN 2002: International Conference Madrid, Spain, August 28–30, 2002 Proceedings 12* (pp. 395-400). Springer Berlin Heidelberg.  
[https://doi.org/10.1007/3-540-46084-5\\_64](https://doi.org/10.1007/3-540-46084-5_64)
24. Jin, Y., & Sendhoff, B. (2003). Extracting interpretable fuzzy rules from RBF networks. *Neural Processing Letters*, 17, 149-164.  
<https://doi.org/10.1023/A:1023642126478>
25. Simon, D. (2002). Sum normal optimization of fuzzy membership functions. *International Journal of Uncertainty, Fuzziness and Knowledge-Based Systems*, 10(04), 363-384.  
<https://doi.org/10.1142/S0218488502001533>
26. Singpurwalla, N. D., & Booker, J. M. (2004). Membership functions and probability measures of fuzzy sets. *Journal of the American statistical association*, 99(467), 867-877.  
<https://doi.org/10.1198/016214504000001196>
27. Dempster, A. P. (2004). Membership functions and probability measures of fuzzy sets: comment. *Journal of the American Statistical Association*, 99(467), 882-885.
28. Zadeh, L. A. (2004). Membership functions and probability measures of fuzzy sets: comment. *Journal of the American Statistical Association*, 99(467), 880-882.
29. Lindley, D. V. (2004). Membership functions and probability measures of fuzzy sets: comment. *Journal of the American Statistical Association*, 99(467), 877-880.
30. Laviolette, M. (2004). Membership functions and probability measures of fuzzy sets: comment. *Journal of the American Statistical Association*, 99(467), 879-881.

31. Singpurwalla, N. D., & Booker, J. M. (2004). Membership functions and probability measures of fuzzy sets. *Journal of the American statistical association*, 99(467), 867-877. <https://doi.org/10.1198/016214504000001196>
32. Sancho-Royo, A., & Verdegay, J. L. (1999). Methods for the construction of membership functions. *International Journal of Intelligent Systems*, 14(12), 1213-1230. [https://doi.org/10.1002/\(SICI\)1098-111X\(199912\)14:12<1213::AID-INT3>3.0.CO;2-5](https://doi.org/10.1002/(SICI)1098-111X(199912)14:12<1213::AID-INT3>3.0.CO;2-5)
33. Chen, J. E., & Otto, K. N. (1995). Constructing membership functions using interpolation and measurement theory. *Fuzzy Sets and systems*, 73(3), 313-327. [https://doi.org/10.1016/0165-0114\(94\)00322-X](https://doi.org/10.1016/0165-0114(94)00322-X)
34. Altas, E., Aydin, M. C., & Toprak, Z. F. (2017). Determination of Water Surface profile in Open Canal Using a New Fuzzy Modeling Technique (SMRGT), *International Conference on Water Resource and Environmental (WRE 2107)*, July 26 – 29, 2017, Qingdao – China.
35. Coskun, C. (2014). Automated fuzzy model generation and an analysis of the proposed method. *International Journal of Open Problems in Computer Science and Mathematics*, 238(1397), 1-13.
36. Toprak, Z. F., Songur, M., Hamidi, N., & Gulsever, H. (2013). Determination of losses in water-networks using a new fuzzy technique (SMRGT). *AWERProcedia Information Technology & Computer Science*, 3(2013), 833-840.
37. Karakaya, D. (2018). Modelling of flow coefficient with fuzzy SMRGT method. Master's Thesis, Dicle University
38. Yalaz, S., Atay, A., Toprak, Z. F. (2013). Fuzzy Linear Regression for Time-Related Data with Fuzzy SMRGT Method, *Mathematics Symposium*, Diyarbakır, 1-7.
39. Bayri, G., (2018). Classification of Soils with Simple Membership Functions and Fuzzy Rules Generation Technique (SMRGT). Master's Thesis, Bitlis Eren University.
40. Şevgin, F., & fuat TOPRAK, Z. (2021). Meteorolojik Akış Katsayısının Bulanık SMRGT Yöntemi ile Belirlenmesi: Murat Havzası Örneği. *Dicle Üniversitesi Mühendislik Fakültesi Mühendislik Dergisi*, 12(2), 401-409. <https://doi.org/10.24012/dumf.844325>
41. Toprak, Z. F. (2004). Determination of Longitudinal Dispersion Coefficients in Natural Channel Using Fuzzy Logic Method. PhD Thesis, Istanbul Technical University
42. Toprak, Z. F. (2017). The Advantages of SMRGT Method In Modelling Hydrological Events. *International Conference on Water Resource and Environment (WRE 2017)*, July 26 – 29, Qingdao – China



© Author(s) 2024. This work is distributed under <https://creativecommons.org/licenses/by-sa/4.0/>



### Prediction of elevation points using three different heuristic regression techniques

Vahdettin Demir\*<sup>1</sup>, Ramazan Doğu<sup>1</sup>

<sup>1</sup>KTO Karatay University, Department of Civil Engineering, Türkiye, vahdettin.demir@karatay.edu.tr, rdogu27@gmail.com

Cite this study: Demir, V., & Doğu, R. (2024). Prediction of elevation points using three different heuristic regression techniques. Turkish Journal of Engineering, 8 (1), 56-64

#### Keywords

M5-Tree  
MARS  
LSSVR  
Elevation Point  
Google Earth Pro

#### Research Article

DOI:10.31127/tuje.1257847

Received:28.02.2023

Revised: 14.04.2023

Accepted:17.04.2023

Published:15.09.2023



#### Abstract

The aim of this study is to estimate the digital elevation model, which is the most important data of the projects and needed in the engineering project, using latitude and longitude information of the elevation points and three different heuristic regression techniques. As the study area, an area with mid-level elevations, located in the Marmara region, and covering a part of the intersection of Edirne, Kırklareli and Tekirdağ provinces was chosen. In the study, the estimations were investigated for three different sized areas, and these areas are square areas with the dimensions of 1x1 km, 10x10 km and 100x100 km, respectively. A total of 3500 elevation points were used in the study, and this number is constant in all areas, and 60% of these points were used in the testing phase and 40% in the training phase. The models used in the study are M5 model tree (M5-tree), multivariate adaptive regression curves (MARS) and Least Square Support Vector Regression (LSSVR). The results of the models were evaluated according to three different comparison criteria. These, coefficient of determination ( $R^2$ ), Mean Absolute Error (MAE) and Root Mean Square Error (RMSE) were used. When the modeling results are examined; M5-Tree regression method gave the best results (1), LSSVR method was better than MARS methods (2), The most successful input data was found in datasets using X and Y coordinates information, and the worst results were found in datasets using X coordinates (3). As the study area increased, the model performance did not improve (4). The least error was obtained in the modeling of 1x1 km area, and the highest  $R^2$  was obtained from the modeling of 10x10 km area (5). It was concluded that the M5-tree method is a very successful method in elevation modeling.

#### 1. Introduction

The data of the heights (elevation) of the land points are used in many areas. However, measuring all points in the field is difficult and costly. Therefore, various mathematical-statistical methods and more modern techniques such as machine learning are used to estimate elevation points [1].

Disaster risk assessment, agriculture, forestry, watershed management, urban and rural planning, transportation planning, etc. numerous fields make use of numerical models created from land locations. These models serve as the foundation for engineering study projects [2-4]. Information about the surface and the subsurface can be processed, analyzed, and visually presented using digital surface models [5].

Important studies in the literature in recent years; Demir and Keskin [1], estimated elevations in Samsun Mert River Basin using X and Y coordinate information and three different Artificial Neural Networks and IDW

and Kriging interpolation techniques. Demir and Çubukçu [5], estimated elevation points in a similar study area (Samsun Mert River Basin) using M5 model tree (M5-tree) and multivariate adaptive regression curves (MARS) heuristic regression methods. The results were compared with the regression methods. In the literature on surface modeling, there are also studies on the use of regression or artificial neural network methods on mathematical-theoretical surfaces [6-8].

For other important studies in the literature, a search was made on the Scopus database with the keywords "machine AND learning, AND elevation AND point AND estimation" and 27 studies were found. The relationship map of the keywords in these studies was obtained in the VOSviewer software (Figure 1).

In Figure 1, it is seen that methods such as deep learning and artificial neural networks and keywords such as remote sensing, 3D point cloud, classification is more prominent. Especially deep learning and artificial neural networks methods and similar machine learning

methods are used successfully in solving many engineering problems [9–20]. In addition, when the years of these publications are examined, it is seen that they are between 2020 and 2022. It is seen that this situation is among the studies that have been researched in recent years and the keywords researched are included in current studies. This study differs from the literature in terms of the changing field of the study area.

In this study, elevation estimations were made using latitude and longitude information of points obtained by remote sensing and three different heuristic regression techniques (M5-tree, MARS and LSSVR). A region with moderate (flat-mountainous area with mid-level elevations) heights (Z) was chosen as the study area. Predictions were made separately for three different sized areas and compared.

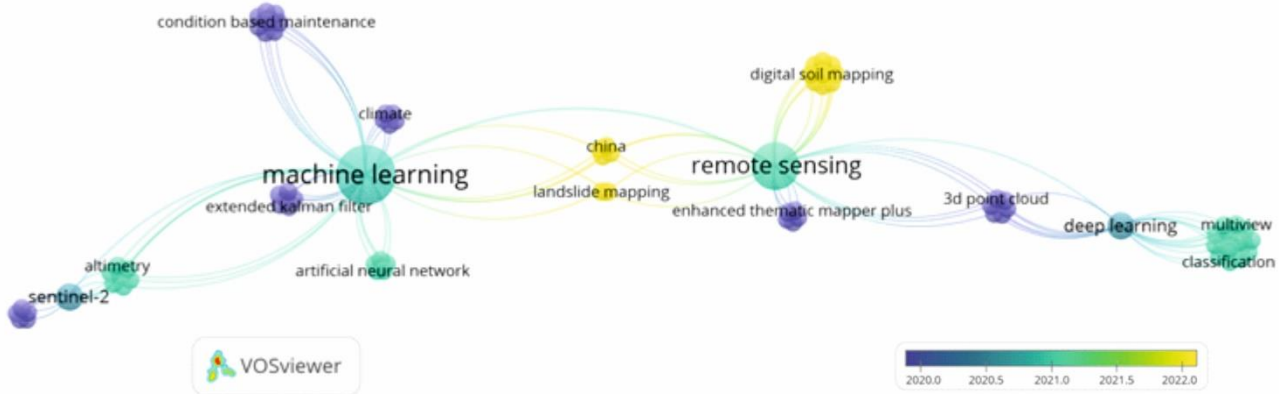


Figure 1. The relationship of the keywords of the similar studies.

2. Material and Method

The study area is located in the Marmara region of Türkiye, the region at the intersection of Kırklareli, Edirne and Tekirdağ provinces was selected, and data were obtained for three different sized areas. These areas are 1x1 km, 10x10 km and 100x100 km square areas. The data were obtained with the help of Google-Earth Pro. The following study can be examined for the methodology used in obtaining the data [21]. The study area is shown in Figure 2.

In Figure 2, areas of three different sizes are represented by square polygons. In choosing this area as the model area, the distinction in the classification of

heights was considered. The height points within these square areas are shown in Figure 3. Hassan et al. [22], areas with a height difference of up to 0.06-5 meters are considered as flat-mountainous. In this study, the estimations were made in a flat-mountainous region.

In Figure 3, it is seen that the points are randomly distributed. The reason why this distribution is preferred is to ensure that the models give unbiased and non-memorizing predictions. Points that go out of the study area are not included in the modeling. Statistical information about the data is given in Table 1-3. The flowcart of the study is shown in Figure 4.

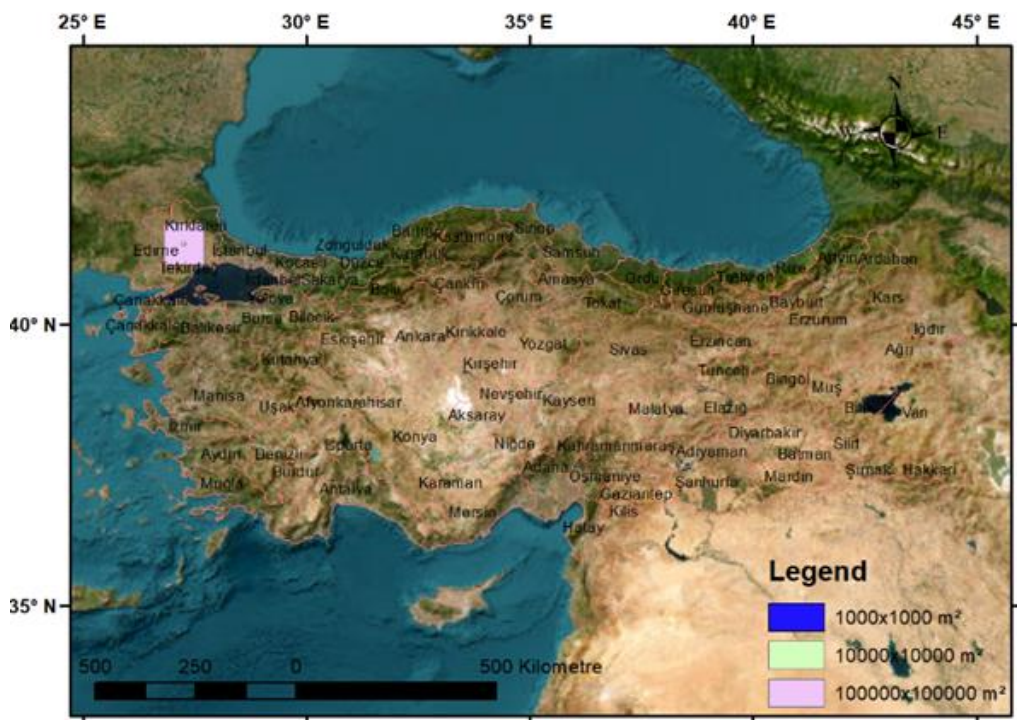


Figure 2. Study area.



Figure 3. Elevation points.

Table 1. Statistical indicators of model data for 1x1 km area.

Data Set Variable	Training			Testing		
	Latitude	Longitude	H	Latitude	Longitude	H
Number of Data	2100	2100	2100	1400	1400	1400
Maximum Value (m)	27.25	41.373	37.888	27.25	41.373	37.505
Minimum Value (m)	27.241	41.366	33	27.241	41.366	33
Average (m)	27.245	41.369	35.27	27.245	41.369	35.269
Standard Deviation	0.003	0.002	0.834	0.003	0.002	0.829
Skewness Coefficient	0.022	0.16	-0.083	-0.011	0.075	-0.092

Table 2. Statistical indicators of model data for 10x10 km area.

Data Set Variable	Training			Testing		
	Latitude	Longitude	H	Latitude	Longitude	H
Number of Data	2100	2100	2100	1400	1400	1400
Maximum Value (m)	27.296	41.416	109.000	27.296	41.413	97.504
Minimum Value (m)	27.198	41.332	31.092	27.196	41.332	31.759
Average (m)	27.245	41.365	52.114	27.246	41.366	52.698
Standard Deviation	0.028	0.021	14.188	0.028	0.021	14.123
Skewness Coefficient	-0.005	0.265	0.722	-0.064	0.197	0.587

Table 3. Statistical indicators of model data for 100x100 km area.

Data Set Variable	Training			Testing		
	Latitude	Longitude	H	Latitude	Longitude	H
Number of Data	2100	2100	2100	1400	1400	1400
Maximum Value (m)	27.739	41.797	644.837	27.729	41.777	462.810
Minimum Value (m)	26.743	40.995	16.022	26.748	41.001	17.000
Average (m)	27.262	41.316	131.044	27.249	41.309	128.260
Standard Deviation	0.273	0.210	69.874	0.277	0.207	66.079
Skewness Coefficient	-0.124	0.372	1.581	-0.066	0.410	1.304

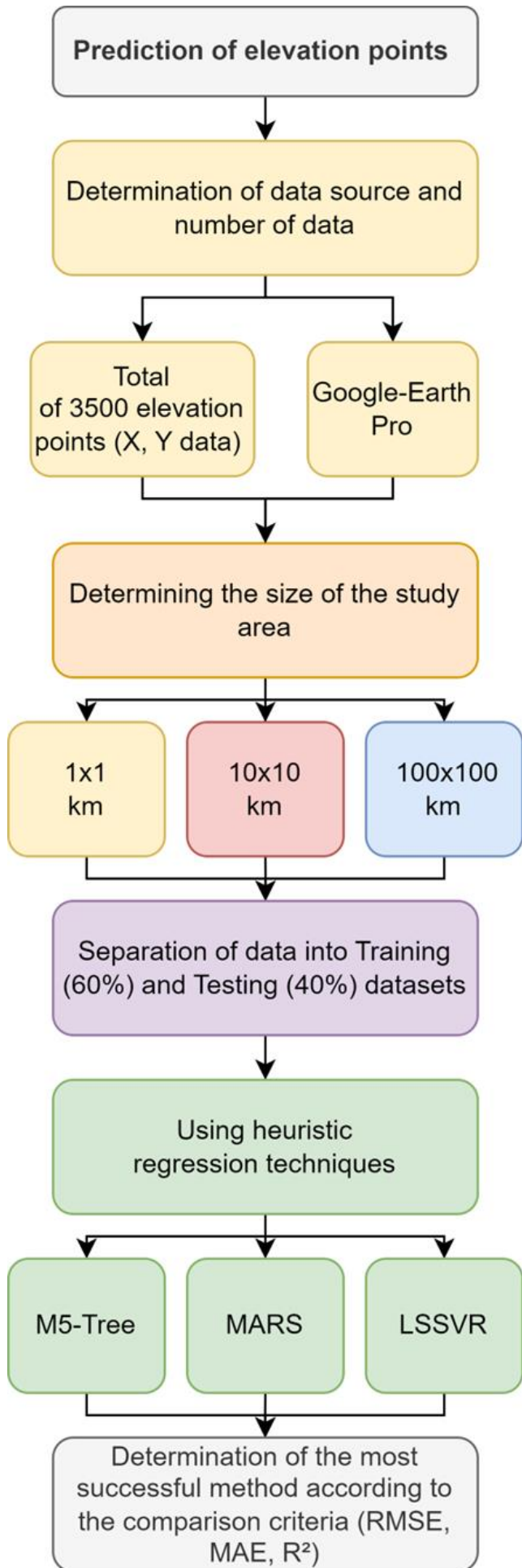


Figure 4. Flow chart of the study.

### 2.1. M5-Tree

The M5 model tree algorithm is a new regression method developed by Quinlan in 1992 [23]. The M5 model tree is better than other decision tree models used for categorical data. The model also gives successful predictions in numerical data [24].

The M5 model fits the model in two steps. The data are divided into sets in the first stage and created a decision tree. The splitting of the decision tree is based on calculating the predicted reduction in this error as a result of evaluating each attribute at the node and utilizing the standard deviations of the class values that reach a node as measurements of the error at the nodes [25]. The formulation of the standard deviation reduction (SDR) is as follows.

The formulation of the standard deviation reduction (SDR) is shown in Equation 1.

$$SDR = sd(T) - \sum \frac{|T_i|}{|T|} sd(T_i) \quad (1)$$

In Equation 1,  $T_i$  is the subset of examples that have the  $i^{th}$  possible outcome of the set, SD is the standard deviation, and T is a set of examples that reach the node.

### 2.2. Multivariate Adaptive Regression Splines (MARS)

The MARS is a type of regression analysis developed by Friedman [26]. This method is one of the non-parametric regression techniques, which is an extension of linear models.

It explains the complex nonlinear relationship between the model, estimation method and dependent variables. The MARS algorithm consists of two steps, forward and backward. It selects a set of suitable input variables with the forward step algorithm [27]. With the backward step algorithm, it eliminates unnecessary variables in the pre-selected set. This method also increases the accuracy of the predictions. The function is drawn from variable X to the new variable Y by two base functions or both variable values defined at the deviation point across the input range in Equation 2-3 [28].

$$Y = \max(0, X - c) \quad (2)$$

$$Y = \max(0, c - X) \quad (3)$$

Here c represents the threshold (lower limit) value. MARS model is used especially in financial affairs management system, time series data in engineering and in many fields [5,29-33].

### 2.3. Least Square Support Vector Regression (LSSVR)

LSSVR is an extended version of the support vector regression (SVR) model by Suykens and Vandewalle [34]. In this study, the optimal mapping function between inputs and outputs of LSSVR is used to estimate with statistically randomly distributed x and y values for z

values. It performs this operation with a nonlinear relationship function with a multidimensional feature space. The regression function can be formulated in Equation 4.

$$y(x) = w^T \varphi(x) + b \quad (4)$$

Here  $y$  is the value obtained in  $x$ ,  $w$  is the coefficient vector,  $\varphi$  is the mapping function,  $b$  is the bias term obtained by minimizing the upper bound of the generalization error [34].

### 3. Results

In all areas, 3500 elevation points were used for the study; 60% of these points were used for testing, and 40% were used for training. This amount remains constant across all places. The M5-tree, MARS, and LSSVR

models were employed in the study. The models' outputs were assessed using three different comparison metrics. These included the Root Mean Square Error (RMSE), Mean Absolute Error (MAE), and Coefficient of Determination ( $R^2$ ) in Equation 5-7. In addition, three different input combinations were tried in the modeling; (i) X (1 input); (ii) Y (1 input); (iii) X, Y (2 inputs). Model performance is evaluated as more successful with the RMSE and MAE values approaching the minimum and the  $R^2$  value approaching 1.

The observed and predicted height in the above equations is denoted by  $Z$ .  $N$  stands for the amount of data. The training and testing results of the three models are given in Table 4. The flow chart of the study is given below. Figure 5 and Figure 6 shows the scatter plots of the most successful training and test results for each method.

$$RMSE = \frac{1}{n} \sum_{i=1}^n \sqrt{(Z_{\text{predicted}} - Z_{\text{measured}})^2} \quad (5)$$

$$MAE = \frac{1}{n} \sum_{i=1}^n |Z_{\text{predicted}} - Z_{\text{measured}}| \quad (6)$$

$$R^2 = \frac{\sum_{i=1}^n (Z_{i \text{ measured}} - \overline{Z_{i \text{ measured}}})^2 \cdot (Z_{i \text{ predicted}} - \overline{Z_{i \text{ predicted}}})^2}{\sum_{i=1}^n (Z_{i \text{ measured}} - \overline{Z_{i \text{ measured}}})^2 \cdot \sum_{i=1}^n (Z_{i \text{ predicted}} - \overline{Z_{i \text{ predicted}}})^2} \quad (7)$$

**Table 4.** Results of the training and test phase.

Model	Region/Area	Input	Training			Testing		
			RMSE	MAE	$R^2$	RMSE	MAE	$R^2$
M5-Tree	1x1 km	X	0.702	0.548	0.292	0.854	0.689	0.043
		Y	0.572	0.422	0.530	0.745	0.576	0.237
		X and Y	0.187	0.116	<b>0.950</b>	0.312	0.199	<b>0.861</b>
	10x10 km	X	12.434	9.564	0.232	15.006	11.915	0.008
		Y	7.574	5.243	0.715	9.430	6.765	0.566
		X and Y	2.400	1.502	<b>0.971</b>	4.198	2.770	<b>0.913</b>
	100x100 km	X	58.617	41.965	0.296	69.241	51.917	0.041
		Y	43.657	29.724	0.610	54.212	39.644	0.368
		X and Y	16.415	10.672	<b>0.945</b>	25.032	18.244	<b>0.857</b>
MARS	1x1 km	X	0.787	0.646	0.111	0.793	0.654	0.086
		Y	0.722	0.583	0.251	0.723	0.594	0.239
		X and Y	0.695	0.561	<b>0.307</b>	0.686	0.557	<b>0.316</b>
	10x10 km	X	13.980	11.180	0.029	13.890	11.276	0.035
		Y	9.004	6.848	0.597	8.950	6.941	0.599
		X and Y	8.703	6.615	<b>0.624</b>	8.588	6.675	<b>0.631</b>
	100x100 km	X	65.767	49.845	0.114	63.067	48.677	0.092
		Y	52.698	39.518	0.431	51.263	39.277	0.400
		X and Y	47.154	33.864	<b>0.545</b>	46.824	34.069	<b>0.503</b>
LSSVR	1x1 km	X	0.807	0.664	0.065	0.802	0.664	0.065
		Y	0.747	0.604	0.198	0.739	0.606	0.206
		X and Y	0.560	0.440	<b>0.552</b>	0.568	0.452	<b>0.533</b>
	10x10 km	X	14.036	11.256	0.022	13.842	11.254	0.049
		Y	9.093	6.947	0.589	9.019	7.023	0.592
		X and Y	5.013	3.622	<b>0.875</b>	5.174	3.748	<b>0.866</b>
	100x100 km	X	66.069	50.381	0.106	63.238	48.993	0.087
		Y	53.081	39.725	0.423	51.678	39.675	0.392
		X and Y	27.196	20.750	<b>0.849</b>	27.954	21.387	<b>0.822</b>

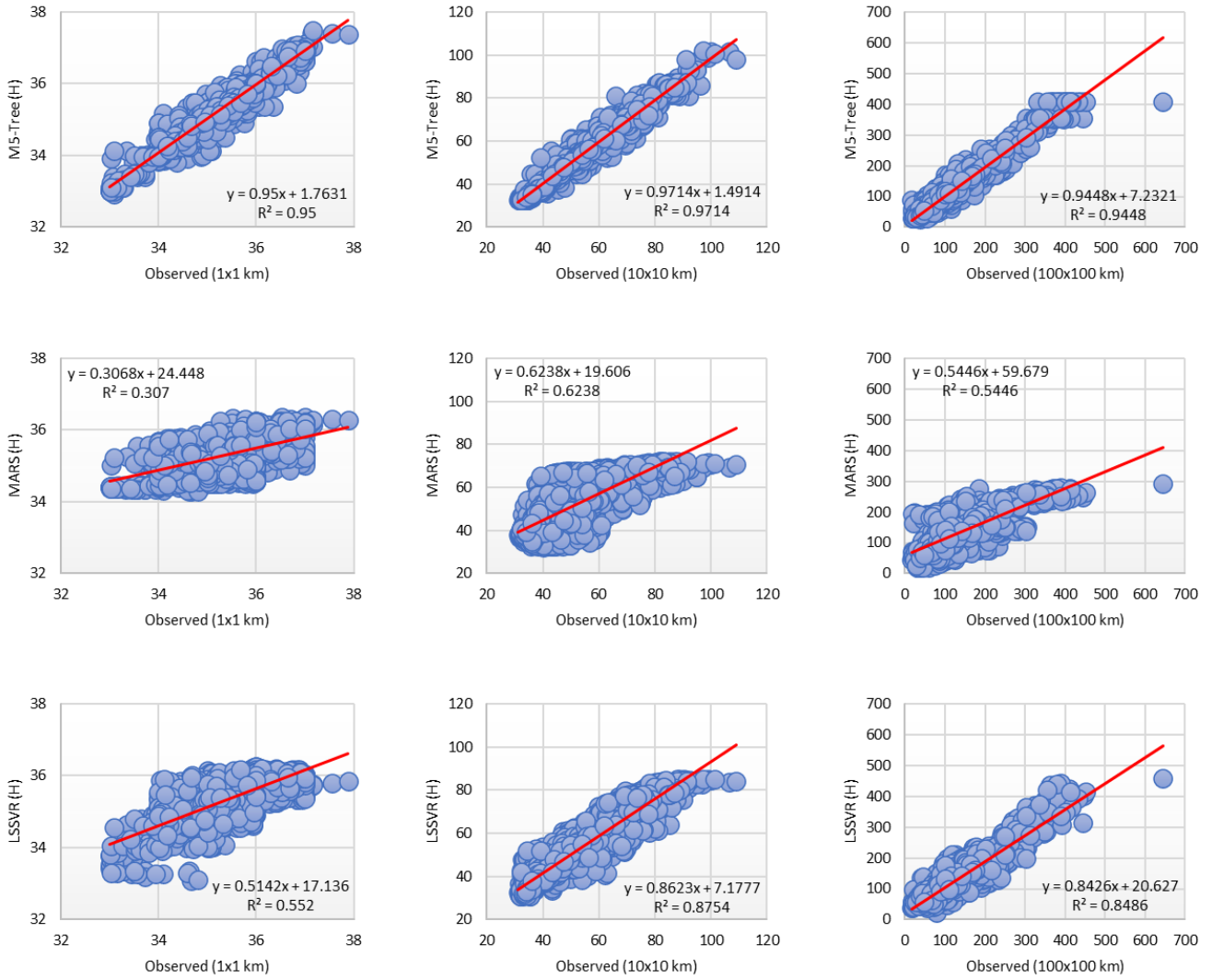


Figure 5. Scatter plots of best models for training phase.

In Table 4, the results of the most successful training phase were obtained in the data package using two inputs. The lowest error values and the highest R<sup>2</sup> value were obtained in the M5-tree method during the training phase, followed by LSSVR, and the more unsuccessful model was determined as MARS. Considering X and Y coordinate inputs, more successful results were observed in input sets using Y coordinate information. When the results are evaluated in terms of areas, the most successful results were observed in areas of 10x10 km. According to the coefficient of determination, this situation is similar in all models. According to the RMSE criterion, the models that give the least error are the models in which points in 1x1 km areas are used. The reason for this is that the points are closer to each other than other areas. As a result, the training has been more successful. Depending on the area growth, the prediction performance decreases as the points move away from each other.

When the results in the test phase were examined, the most successful results (considering the RMSE) were observed in the M5-tree method as in the training phase, in 1x1 km areas and in models using X and Y input data sets. Then, LSSVR and MARS methods made successful predictions. The highest coefficient of determination was observed in areas of 10x10 km, as in the training phase.

#### 4. Discussion

As a result of the modeling, the most successful results were obtained in the 1x1 km area where the area is the least. In this model, both X and Y coordinates information are used. In addition, it has been observed that Y coordinates information gives more successful results in the study area than X coordinates information. In this study, modeling was done on fixed points (3500 units) but increasing sizes. It is seen that the error value increases depending on the increasing areas. For this reason, for more successful results in larger areas, either by increasing the ratios of the training-test datasets or with new measurements, the points should be added.

The effect of the number of data can be investigated by changing the training and testing rates. However, in any case, the increase in the number of training data sets means not that the model performance will always increase [35]. In addition, with point compaction, lower resolution raster data can be compressed with similar models and higher resolution (pixel size) models can be obtained.

Models were run on a computer with 12<sup>th</sup> Gen Intel(R) Core (TM), i7-12700H, 2.30 GHz, 64 GB RAM and 6 GB graphics card and the modeling times were compared, MARS and M5-tree yielded modeling results

quite recently (average of 5 sec). But the LSSVR model took a lot of time (average 1 hour). The kernels of LSSVR contain two modification parameters ( $\gamma$ ,  $\alpha$ ). In order to obtain the optimum of these parameters, cycles were established for these parameters from 1 to 100 and it was observed that the most successful results (100,1) were generally observed in coefficient pairs. Therefore, the

method took more time. As a result of the study, it has been determined that MARS and M5-Tree are more advantageous because they do not have any model parameters. Although the results of the LSSVR model are close to the M5-tree, faster and more successful results can be obtained with a hybrid optimization technique.

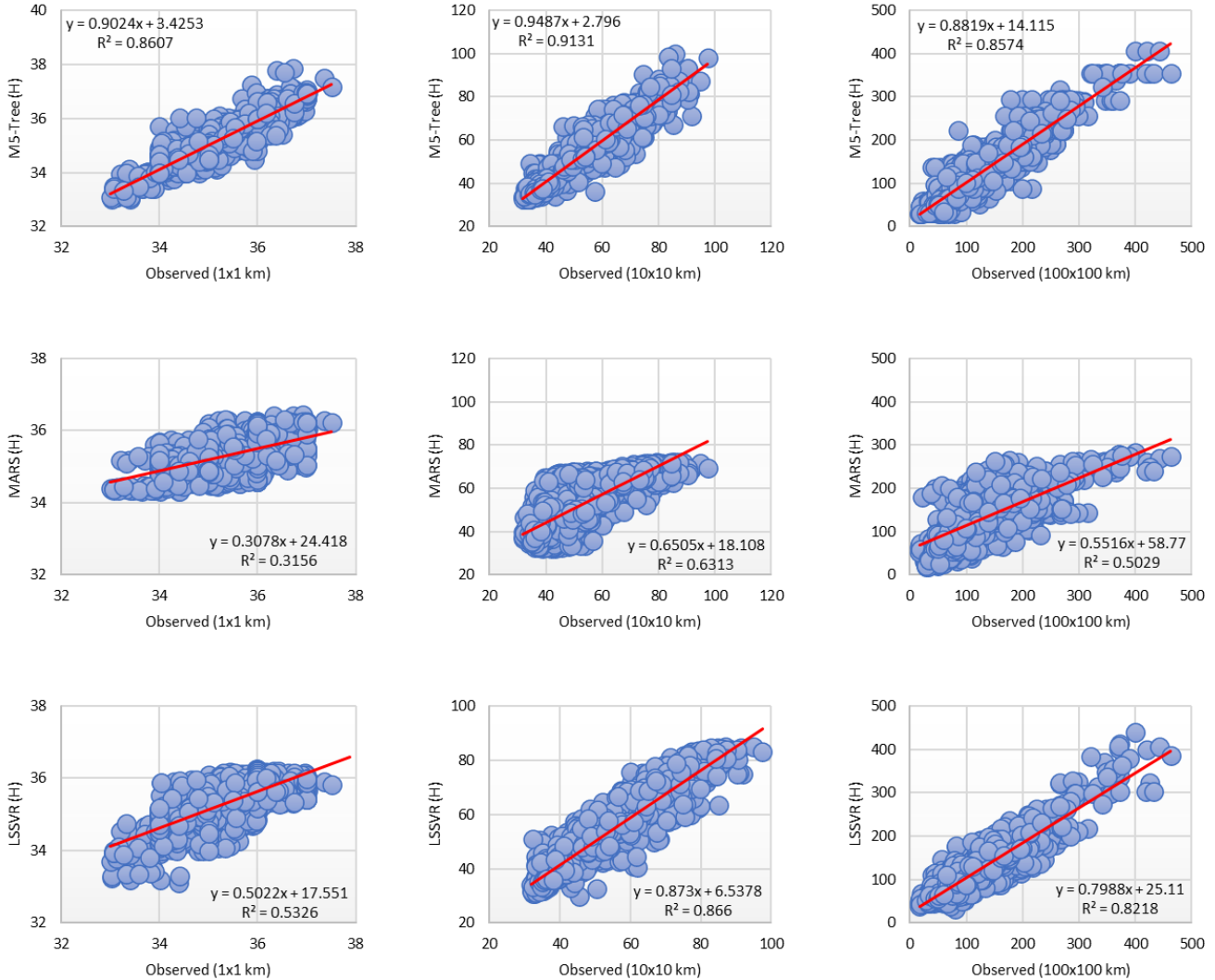


Figure 6. Scatter plots of best models for testing phase.

### 5. Conclusion

In this study, the estimation of the elevation points in a flat-mountainous area where a fixed number of data is randomly distributed over three different sized areas was performed. Three different models were used in the study: M5-tree, MARS and LSSVR. The training and testing rates in the models are 60% and 40%, respectively, and the performance of three different input types in the models was investigated. These are 1-only X coordinates, 2-only Y coordinates, and 3-both X and Y coordinates information are used. In the study, a total of 3500 points belonging to the fields were obtained from the Google earth pro database and the study areas are 1x1 km, 10x10 km and 100x100 km, respectively. When the results are examined;

- The most successful results in models were obtained as a result of using 2-input data sets.
- Models using Y location information are more successful than models using X location information. Therefore, it is important to minimize these coordinate errors.
- Increasing the area did not increase the model performance.
- Although the coefficient of determination is highest in areas of 10x10 km, the lowest errors were detected in areas of 1x1 km.
- As a result of the study, the most successful method is M5-Tree, followed by LSSVR and MARS methods.

The limits of this study are as follows, using the same number of data sets in areas of different sizes, making predictions and comparisons using three different heuristic regression techniques, using X and Y location

information as input data in the models, providing the data source in Google earth pro software with remote sensing techniques.

In future studies, results for different fields will be investigated using different training and testing rates and different methods. In addition, the effect of the change in the topography of the study area on the performance will be investigated.

### Acknowledgement

The authors thank KTO Karatay University and TÜBİTAK.

### Funding

This study is supported by the application numbered **1919B012107905** within the scope of the **2209-A** University Students Research Projects Support Program 2021-2, carried out by the **TÜBİTAK** Scientist Support Programs Presidency (BİDEB).

### Author contributions

**Vahdettin Demir:** Writing-Reviewing, Methodology, Application, Editing, **Ramazan Doğu:** Methodology, Application.

### Conflicts of interest

The authors declare no conflicts of interest.

### References

- Demir, V., & Ulke Keskin, A. (2020). Height Modelling with Artificial Neural Networks (Samsun\_Mert River Basin). *Gazi Journal of Engineering Sciences*, 6(1), 54-61. <https://dx.doi.org/10.30855/gmbd.2020.01.05>
- Sahin, İ., Yakar, M. (2008). Farklı kaynaklardan elde edilen sayısal yükseklik modellerinin ortofoto doğruluğuna etkilerinin araştırılması. *Harita Dergisi*, 74(140), 45-59.
- Yakar, M. (2009). Digital elevation model generation by robotic total station instrument. *Experimental Techniques*, 33, 52-59. <https://doi.org/10.1111/j.1747-1567.2008.00375.x>
- Yakar, M., Yilmaz, H. M., & Yurt, K. (2010). The effect of grid resolution in defining terrain surface. *Experimental Techniques*, 34, 23-29. <https://doi.org/10.1111/j.1747-1567.2009.00553.x>
- Demir, V., & Çubukçu, E. A. (2021). Sezgisel Regresyon Teknikleri ile Sayısal Yükseklik Modellenmesi. *Avrupa Bilim ve Teknoloji Dergisi*, (24), 484-488. <https://doi.org/10.31590/ejosat.916012>
- Çakır, L. (2013) Sayısal Yükseklik Modellerinde Polinomlar ve Yapay Sinir Ağları Yöntemlerinin Karşılaştırılması. In Proceedings of the Türkiye Ulusal Fotogrametri ve Uzaktan Algılama Birliği VII. Teknik Sempozyumu (TUFUAB'2013), 23-25 Mayıs 2013, 1-4, Trabzon, Türkiye.
- Çakır, L. (2015) Sayısal Yükseklik Modellerinde Klasik ve Esnek Hesaplama Yöntemlerinin Karşılaştırılması. In Proceedings of the TMMOB Harita ve Kadastro Mühendisleri Odası, 15. Türkiye Harita Bilimsel ve Teknik Kurultayı, 25--28 Mart 2015, 1-6, Ankara, Türkiye
- Konakoglu, B., Çakır, L., & Gökalp, E. (2016). 2D coordinate transformation using artificial neural networks. *The International Archives of the Photogrammetry, Remote Sensing and Spatial Information Sciences*, 42, 183-186. <https://doi.org/10.5194/isprs-archives-XLII-2-W1-183-2016>
- Biyik, M. Y., Atik, M. E., & Duran, Z. (2023). Deep learning-based vehicle detection from orthophoto and spatial accuracy analysis. *International Journal of Engineering and Geosciences*, 8(2), 138-145. <https://doi.org/10.26833/ijeg.1080624>
- Çubukçu, E. A., Demir, V., & Sevimli, M. F. (2023). Modeling of annual maximum flows with geographic data components and artificial neural networks. *International Journal of Engineering and Geosciences*, 8(2), 200-211. <https://doi.org/10.26833/ijeg.1125412>
- Demiryeye, İ., & Ulukavak, M. (2022). Derin öğrenme tabanlı iyonosferik TEC tahmini. *Geomatik*, 7(2), 80-87. <https://doi.org/10.29128/geomatik.870773>
- Demirgöl, T., Demir, V., & Sevimli, M. F. (2023). Model-Ağacı (M5-tree) yaklaşımı ile HELIOSAT tabanlı güneş radyasyonu tahmini. *Geomatik*, 8(2), 124-135. <https://doi.org/10.29128/geomatik.1137687>
- Kotan, B., & Erener, A. (2023). PM10, SO2 hava kirlenmelerinin çoklu doğrusal regresyon ve yapay sinir ağları ile sezonsal tahmini. *Geomatik*, 8(2), 163-179. <https://doi.org/10.29128/geomatik.1158565>
- Tasdemir, S., & Ozkan, I. A. (2019). ANN approach for estimation of cow weight depending on photogrammetric body dimensions. *International Journal of Engineering and Geosciences*, 4(1), 36-44. <https://doi.org/10.26833/ijeg.427531>
- Uncuoglu, E., Citakoglu, H., Latifoglu, L., Bayram, S., Laman, M., Ilkentapar, M., & Oner, A. A. (2022). Comparison of neural network, Gaussian regression, support vector machine, long short-term memory, multi-gene genetic programming, and M5 Trees methods for solving civil engineering problems. *Applied Soft Computing*, 129, 109623. <https://doi.org/10.1016/j.asoc.2022.109623>
- Bayram, S., & Çitakoğlu, H. (2023). Modeling monthly reference evapotranspiration process in Turkey: application of machine learning methods. *Environmental Monitoring and Assessment*, 195(1), 67. <https://doi.org/10.1007/s10661-022-10662-z>
- Zeybekoglu, U. (2018). Forecasting of Annual Mean Rainfall Using Artificial Neural Network and Wavelet Components: Case of Study Sinop Forecasting of Annual Mean Rainfall Using Artificial Neural Network and Wavelet Components: Case of Study Sinop. In Proceedings of the 1. International Technological Sciences and Design Symposium, 1700-1709, Giresun Türkiye.

18. Hezarani, A. B., Zeybekoğlu, U., & Keskin, A. Ü. (2021). Hydrological and meteorological drought forecasting for the Yesilirmak river basin, Turkey. *Sürdürülebilir Mühendislik Uygulamaları ve Teknolojik Gelişmeler Dergisi*, 4(2), 121-135. <https://doi.org/10.51764/smutgd.993792>
19. Öztürk, A., Allahverdi, N., & Saday, F. (2022). Application of artificial intelligence methods for bovine gender prediction. *Turkish Journal of Engineering*, 6(1), 54-62. <https://doi.org/10.31127/tuje.807019>
20. Gülgün, O. D., & Hamza, E. R. O. L. (2020). Classification performance comparisons of deep learning models in pneumonia diagnosis using chest x-ray images. *Turkish Journal of Engineering*, 4(3), 129-141. <https://doi.org/10.31127/tuje.652358>
21. Demir, V., & Doğu, R. (2022). Creating digital elevation model with Google Earth Pro. *Advanced Engineering Days (AED)*, 4, 78-80.
22. Hassan, O., Elnazeer, E., & Zomrawi, N. (2015). Application of Artificial Neural Network for Height Modelling. *International Journal of Recent and Innovation Trends in Computing and Communication*, 3(3), 1374-1377.
23. Quinlan, J. R. (1992) Learning with Continuous Classes. *Proceedings of Australian Joint Conference on Artificial Intelligence*, Hobart 16-18 November 1992, 343-348.
24. Mitchell, T. M. (1997). *Machine learning*. McGraw-Hill Science, ISBN: 0070428077
25. Srivastava, R., Tiwari, A. N., & Giri, V. K. (2019). Solar radiation forecasting using MARS, CART, M5, and random forest model: A case study for India. *Heliyon*, 5(10), e02692. <https://doi.org/10.1016/j.heliyon.2019.e02692>
26. Friedman, J. H. (1991). Multivariate adaptive regression splines. *The annals of statistics*, 19(1), 1-67. <https://doi.org/10.1214/aos/1176347963>
27. De Andrés, J., Lorca, P., de Cos Juez, F. J., & Sánchez-Lasheras, F. (2011). Bankruptcy forecasting: A hybrid approach using Fuzzy c-means clustering and Multivariate Adaptive Regression Splines (MARS). *Expert Systems with Applications*, 38(3), 1866-1875. <https://doi.org/10.1016/j.eswa.2010.07.117>
28. Sharda, V. N., Patel, R. M., Prasher, S. O., Ojasvi, P. R., & Prakash, C. (2006). Modeling runoff from middle Himalayan watersheds employing artificial intelligence techniques. *Agricultural water management*, 83(3), 233-242. <https://doi.org/10.1016/j.agwat.2006.01.003>
29. Yaseen, Z. M., Kisi, O., & Demir, V. (2016). Enhancing long-term streamflow forecasting and predicting using periodicity data component: application of artificial intelligence. *Water resources management*, 30, 4125-4151. <https://doi.org/10.1007/s11269-016-1408-5>
30. Adnan, R. M., Petroselli, A., Heddami, S., Santos, C. A. G., & Kisi, O. (2021). Comparison of different methodologies for rainfall-runoff modeling: machine learning vs conceptual approach. *Natural Hazards*, 105, 2987-3011. <https://doi.org/10.1007/s11069-020-04438-2>
31. Kisi, O., Parmar, K. S., Soni, K., & Demir, V. (2017). Modeling of air pollutants using least square support vector regression, multivariate adaptive regression spline, and M5 model tree models. *Air Quality, Atmosphere & Health*, 10, 873-883. <https://doi.org/10.1007/s11869-017-0477-9>
32. Bera, P., Prasher, S. O., Patel, R. M., Madani, A., Lacroix, R., Gaynor, J. D., ... & Kim, S. H. (2006). Application of MARS in simulating pesticide concentrations in soil. *Transactions of the ASABE*, 49(1), 297-307. <https://doi.org/10.13031/2013.20228>
33. Sephton, P. (2001). Forecasting recessions: can we do better on MARS?. *Federal Reserve Bank of St. Louis*, 83, 39-49.
34. Suykens, J. A., & Vandewalle, J. (1999). Least squares support vector machine classifiers. *Neural processing letters*, 9, 293-300. <https://doi.org/10.1023/A:1018628609742>
35. Çubukçu, E. A., Demir, V., & Sevimli, M. F. (2022). Digital elevation modeling using artificial neural networks, deterministic and geostatistical interpolation methods. *Turkish Journal of Engineering*, 6(3), 199-205. <https://doi.org/10.31127/tuje.889570>



© Author(s) 2024. This work is distributed under <https://creativecommons.org/licenses/by-sa/4.0/>



## Comparison of CNN-based methods for yoga pose classification

Vildan Atalay Aydın \*<sup>1</sup> 

<sup>1</sup>Izmir Demokrasi University, Department of Computer Engineering, Türkiye, vildan.atalayaydin@idu.edu.tr

Cite this study: Aydın, V. A. (2024). Comparison of CNN-based methods for yoga pose classification. Turkish Journal of Engineering, 8 (1), 65-75

### Keywords

Image classification  
Wavelet transform  
Deep learning  
Yoga posture  
CNN

### Research Article

DOI: 10.31127/tuje.1275826

Received:02.04.2023

Revised: 07.05.2023

Accepted:11.05.2023

Published:15.09.2023



### Abstract

Yoga is an exercise developed in ancient India. People perform yoga in order to have mental, physical, and spiritual benefits. While yoga helps build strength in the mind and body, incorrect postures might result in serious injuries. Therefore, yoga exercisers need either an expert or a platform to receive feedback on their performance. Since access to experts is not an option for everyone, a system to provide feedback on the yoga poses is required. To this end, commercial products such as smart yoga mats and smart pants are produced; Kinect cameras, sensors, and wearable devices are used. However, these solutions are either uncomfortable to wear or not affordable for everyone. Nonetheless, a system that employs computer vision techniques is a requirement. In this paper, we propose a deep-learning model for yoga pose classification, which is the first step of a quality assessment and personalized feedback system. We introduce a wavelet-based model that first takes wavelet transform of input images. The acquired subbands, i.e., approximation, horizontal, vertical, and diagonal coefficients of the wavelet transform are then fed into separate convolutional neural networks (CNN). The obtained probability results for each group are fused to predict the final yoga class. A publicly available dataset with 5 yoga poses is used. Since the number of images in the dataset is not enough for a deep learning model, we also perform data augmentation to increase the number of images. We compare our results to a CNN model and the three models that employ the subbands separately. Results obtained using the proposed model outperforms the accuracy output achieved with the compared models. While the regular CNN model has 61% and 50% accuracy for the training and test data, the proposed model achieves 91% and 80%, respectively.

## 1. Introduction

Especially with the lockdowns caused by the Covid-19 pandemic, people started to tend towards exercises such as yoga and pilates that they can perform at home. Even though, when performed right, the health benefits of such exercises are undeniable, incorrect moves are known to cause serious injuries. Therefore, there is a need for an expert to give feedback to the exerciser. Nonetheless, since not everyone has time or money to attend a class, and the pandemic is the reason for exercising at home in the first place, the need for an expert's opinion is replaced with the requirement of a user application. With the help of an application, the exercisers can upload a picture of themselves performing a pose, and receive feedback on either the correctness or the quality of their asana.

Kinect cameras [1], wearable devices [2], Internet of Things (IoT) [3], and smart mats/pants are used for

action recognition during exercises. However, these devices might be expensive or uncomfortable to wear during practice. As a result, researchers take advantage of computer vision techniques such as action recognition, pose estimation, and image classification. Several studies exploit deep learning and transfer learning methods in order to do so.

Deep learning is a powerful technique in many recent research areas. Researchers have also adopted deep learning methods in yoga pose classification. As an example, Jain et al. [4] design a 3D Convolutional Neural Network (CNN) to exploit the spatial-temporal relationship among Yoga poses for a real-time video dataset. Since the architecture of state-of-art image classifiers such as VGG and ImageNet is based on feature extraction by downsizing, these classifiers require high-resolution images. Therefore, Gochoo et al. [5] propose a privacy-preserving classification method for low-resolution images using deep learning. They utilize a

feature-preserving architecture for 16x16 images, with variable ReLU slopes and a custom loss function.

A large number of studies in yoga pose classification make use of pose estimation together with deep learning. Some studies propose pose estimation and feedback generation using extraction of body joints (e.g., OpenPose) and finding differences in angles between the expert's and the user's pose [6, 7]. An angle-likelihood mechanism is also used by [8]. The authors propose a coarse-to-fine algorithm to classify yoga poses by first training a DenseNet classifier to predict image class at a coarse level. Later, a pre-trained pose estimator is employed to find noisy keypoints from input images to generate joint angles of the human body. Finally, to predict the pose class, a K-Nearest Neighbors classifier is trained on the pose vectors generated using the joint angles and the output probability vector of DenseNet. Moreover, Wu et al. [9] propose a yoga pose grading system by first extracting the keypoints of a human skeleton and later training with contrastive triplet examples. Garg et al. [10] utilize MediaPipe library to skeletonize input images and later compare several deep learning methods with and without the skeletonization process to conclude that VGG16 outperforms others if images are not skeletonized, and their proposed deep learning method performs best when skeletonized. On the other hand, Swain et al. [11] also use MediaPipe library for keypoint extraction. Features of keypoints are extracted via CNN, and Long-Short Term Memory (LSTM) layer is used to understand the sequence of video frames for predictions. In a similar method, Rishan et al. [12] propose a technique that uses OpenPose to detect keypoints and employ CNN, Long Short Term Memory (LSTM), and SoftMax regression for classification. Furthermore, Yadav et al. [13] propose another model that uses OpenPose to extract keypoints. The authors collect a video dataset for six Yoga poses and later employ CNN and LSTM to extract keypoint features and obtain temporal predictions, respectively.

When the amount of data at hand is not enough for a deep learning solution, transfer learning comes into play. Long et al. [14] proposed a yoga posture coaching system based on transfer learning. They compared VGG16, VGG19, MobileNet, MobileNetV2, InceptionV3, and DenseNet201 for classification and concluded that the MobileNet model was optimal on their collected dataset consisting of 14 different yoga postures performed by eight participants 10 times each. On the other hand, Chasmai et al. [15] propose using transfer learning, AlphaPose, to be specific, to extract the human body keypoints for human pose estimation. Later, a random forest classifier is trained for the classification of an in-house collected video dataset of yoga poses.

While some studies work on publicly available datasets and some use their in-house generated ones, some of them create challenging datasets for yoga pose classification. Verma et al. [16] propose a large-scale challenging dataset including pose diversity, object occlusion, and viewpoints for 82 yoga pose classes. The dataset has a fine-grained hierarchical structure that separates classes by body posture variations. The authors compare Resnet, DenseNet, MobileNet, and ResNext models on their proposed dataset and conclude

that DenseNet-201 outperforms other models. Moreover, Yadav et al. [17] creates a video dataset including 5484 videos in 82 classes of yoga poses. They also propose an architecture with three parallel components which use the part affinity fields model, optical flow, and raw RGB videos to classify yoga asanas. Finally, Li et al. [18] introduce a 3D yoga pose dataset with 117 classes, including 3792 action samples where each sample consists of an RGB image, a human skeleton, a pose label, and a quality score for both action recognition and activity quality assessment. The authors also provide a two-stream adaptive graph CNN to recognize and access the poses.

Image classification is a process where deep learning is widely and successfully used to categorize images. There are two main types of classification, namely, supervised and unsupervised. While supervised classification uses a training set of data to predict classes for new images, unsupervised classification clusters images based on their characteristics without the need for a training dataset. Image classification has numerous application areas, including but not limited to medical applications [19], object recognition and detection, face recognition, and image segmentation, to name a few [20]. Lu and Weng [21] provide a review of image classification methods, especially in the remote sensing area. For a successful classification of remote sensing data, the authors advise employing multiple features and a suitable classification technique.

Deep learning techniques are employed effectively in image classification [22, 23], as in many other areas [24]. An interested reader can find a detailed review of the application of convolutional neural networks (CNN) to image classification task in [25]. In their paper, the authors provide an explanation of the CNN architecture, their development and early successes, and their application to image classification by reviewing over 300 publications. Su et al. [26] also provide a comprehensive work on the robustness of several deep learning methods for image classification. Due to the fact that the accuracy metric is used as a comparison technique for classification methods and the lack of robustness of these methods are studied in the literature, the authors compare 18 models using more robust comparison metrics, including distortion, success rate, and transferability of adversarial examples. They conclude that the empirical distortion metrics scale linearly with the logarithm of the error; model architecture is more important than its size; and increasing the depth of the architecture only slightly affects robustness.

Wavelets have also been employed in many areas such as super-resolution, image registration, video coding, etc. [27–34] due to their nature of local extraction of spectral and temporal information of images.

Wavelet-based methods are applied to image classification problem successfully. As an example, Li et al. [35] propose replacing the max pooling, strided-convolution, and average pooling layers with Discrete Wavelet Transform in order to reduce the noise-prone nature of CNNs. They decompose the feature maps into low- and high-frequency subbands. Later, the high-frequency subbands are dropped to avoid the noise included, and low-frequency subbands with the

information on the basic data structures in images are fed into the next layers. Their comparisons on ImageNet [36] and ImageNet-C [37] confirm that their proposed wavelet-based method outperforms state-of-the-art techniques.

Image classification is widely used in medical applications in order to help experts in diagnostic radiology and disease detection. Wavelet-based deep learning methods are also used in medical image classification tasks. For example, Mallick et al. [38] propose a deep wavelet-autoencoder-based neural network architecture for brain MRI image classification. The paper aims to build a system for cancer detection using image classification. The authors use the deep wavelet autoencoder for image compressing in order to combine the properties of feature reduction and image decomposition of the autoencoder and wavelet decomposition, respectively. They use the autoencoder together with a Deep Neural Network for brain MRI image classification. Their comparisons prove that the proposed wavelet-based method outperforms existing classifiers based on accuracy.

Khatami et al. [39] also propose a wavelet decomposition method for medical X-ray image classification. Their proposed method employs the approximation (low-pass) subbands of the wavelet decomposition only, and provide promising results on disease detection.

Said et al. [40] combine wavelet network with deep learning for first supervised and later unsupervised classification. They experiment on COIL-100 and MNIST datasets to present that the proposed work outputs promising results.

Even though wavelet-based deep learning is widely and effectively used in medical image classification literature, its benefits have not yet been exploited for yoga pose classification. Motivated by the conclusion made by Fujieda et al. [41] on wavelet-CNN for texture classification which stated that the wavelet-CNN achieves higher accuracy results together with having a lower number of parameters than conventional CNN models, our goal in this paper is to explore the effects of wavelet transform on a CNN-based image classification technique applied to yoga pose images. Several deep-learning methods use the wavelet transform for numerous vision problems [30, 42, 43]. To the best of our knowledge, this study is the first attempt to employ wavelet transform-based deep learning in yoga pose classification. Inspired by the work of Serte and Demirel [44], instead of classifying original images, we perform wavelet transform on the images to obtain wavelet subbands. Later, our model is trained using the subbands only. Predictions obtained with approximation, horizontal, and vertical subbands are later fused together in order to achieve the final classes of images. We compare our results to a CNN model trained on the original data to conclude that the proposed method overperforms the CNN model.

The paper is organized as follows. In Section 2, we introduce the methodology proposed. We represent the results obtained in Section 3, discuss the application areas of our method in Section 4, and finally, concluding remarks are provided in Section 5.

## 2. Method

In this section, we introduce our proposed model for yoga pose classification.

Inspired by the work of Serte and Demirel [44], we investigate the effect of wavelet transform on classifying yoga poses. In their paper, Serte and Demirel [44] proposes taking wavelet transform of input skin lesion images and training their transfer learning (i.e., ResNet) models on two sets of data. The first dataset consists of the original skin images, together with one-level approximation, horizontal and vertical wavelet subbands; while the second dataset includes the original images together with approximation coefficients on the first, second, and third decompositions. Their proposed method outperforms the method based only on the original image dataset. The authors also present a method that uses Gabor wavelets in [43], which decomposes the image data into seven directional wavelet subbands.

In this paper, we propose a CNN model that is trained on only the wavelet subbands instead of a combination with the original data. Our goal is to demonstrate that training on the wavelet subbands only results in higher accuracy than training on the original yoga pose images. Unlike Serte and Demirel's work in [44], our model does not use the original images in training; instead, it employs one-level approximation, horizontal, vertical, and diagonal detail coefficients. The probabilities obtained for all subbands are later fused to reach the final classification of the images, as [44].

In Figure 1, we demonstrate the proposed wavelet CNN model for yoga pose classification. As seen in the figure, we first decompose input images into wavelet coefficients, i.e., approximation, horizontal, vertical, and diagonal subbands. Later, each subband dataset is fed into a separate CNN to be trained. After the training step, prediction scores for all subbands are fused together in order to achieve the final output class [44]. The sum of probabilities formula used is given in Equation 1.

$$s_i = \frac{\sum_{j=1}^n s_{ij}}{\sum_{i=1}^c \sum_{j=1}^n s_{ij}} \quad (1)$$

where  $s$  represents the score,  $c$  is the number of classes, and  $n$  is the number of CNN models.

We also show the CNN model used to predict the 5 yoga classes in Figure 2. We utilize a 3x3 convolution kernel in the convolution layer. Our previous work on the comparison of activation functions for yoga pose classification shows that the ReLU function outperforms the tanh and leaky ReLU functions widely used in CNN models for image classification [45]. The ReLU function acquires higher accuracy in less time compared to the methods mentioned before. Therefore, we employ the ReLU activation function in this work as well. After each pooling layer with max pooling, we employ a dropout layer which helps prevent the overfitting problem in many optimization tasks. Finally, one of the five classes is predicted for each input after a fully connected layer. When the prediction probability for each subband is achieved, the probabilities are fused in order to obtain the final class prediction for each input image.

For our studies, we used a dataset for yoga classification provided in Kaggle [46]. A set of example images is presented in Figure 3. The dataset consists of RGB images in 5 classes, i.e., Downdog, Goddess, Plank, Tree, and Warrior, with varying numbers of images for each class. While the training dataset has 1081 images in total, including 223 images for downdog, 180 for goddess, 266 for plank, 160 for tree, and 252 for warrior

pose; the test dataset contains 470 in total, 97 images for downdog, 80 for goddess, 115 for plank, 69 for tree, and 109 for warrior pose. We separate our training dataset into two parts for training and validation by reserving 20% of the training set for validation.

The next section will display the results obtained using the proposed method.

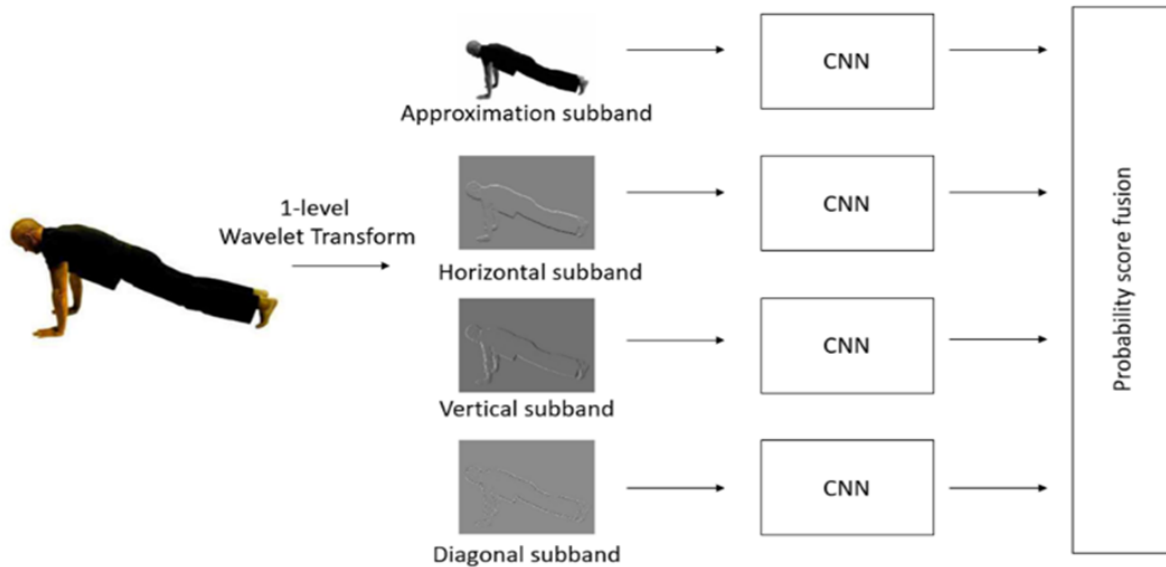


Figure 1. Proposed wavelet CNN model for yoga pose classification.

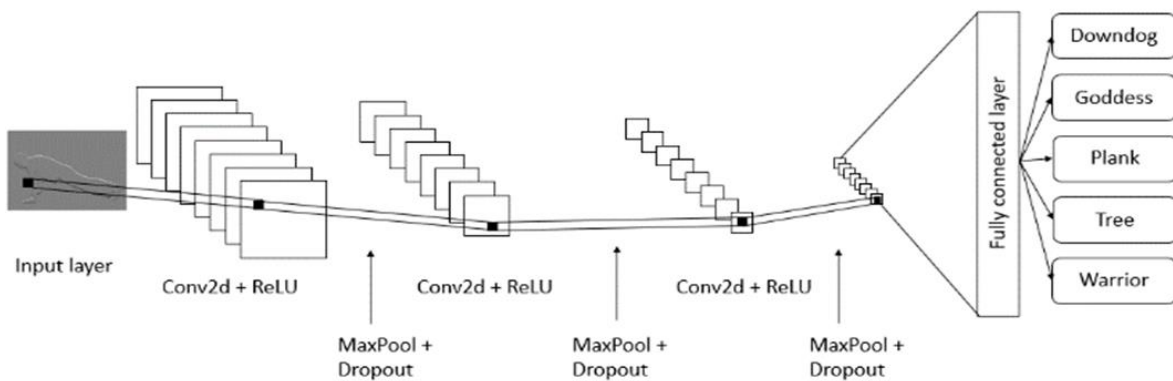


Figure 2. CNN model.

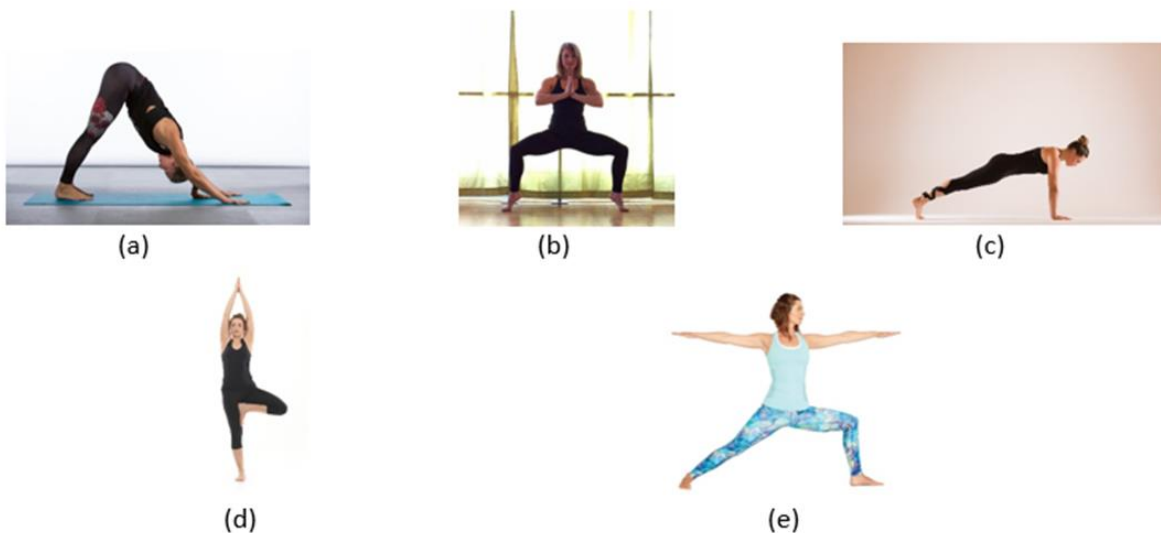


Figure 3. Sample images in training dataset (a) Downdog (b) Goddess (c) Plank (d) Tree (e) Warrior.

### 3. Results

We demonstrate the results using the proposed method in this section.

The experiments are run on MATLAB R2021a on a laptop computer with 8 GB RAM and a single CPU @1.60 GHz. The goal of this paper is to compare the accuracy results obtained using the proposed combined method to a CNN-based method and the subbands separately, instead of a comparison on the time consumption. Since the proposed method requires training on all four subbands, including the first level approximation, horizontal, vertical, and diagonal coefficients of the wavelet transform, the runtime of the proposed

combined method is higher than the training times for each subband separately.

Since this work aims to demonstrate the effect of wavelet transform on yoga pose classification, we do not employ a transfer learning-based method. Therefore, the dataset used in this study must be augmented to increase the number of images. Only horizontal flip is used in data augmentation. When the employed dataset is investigated more in detail, one can see that the images do not rotate. However, as in [Figure 4](#), horizontally flipped images exist. Therefore, we apply horizontal flip for data augmentation but not rotation. The augmentation step is not applied to validation and test datasets.



**Figure 4.** Horizontally flipped images from the dataset.

All images are resized to 224x224 before training. Since Discrete Wavelet Transform (DWT) is a 2D transform, all input data is converted to grayscale before the training step, and DWT is applied later.

Due to the fact that we employ wavelet transform in this work, we have four separate sets of data for each class mentioned above. Meaning, our training dataset for the approximation subband, as an example, has 1081 images in total for all classes, and the test dataset has 470 images, as well as the horizontal, vertical, and diagonal datasets.

We demonstrate the accuracy and loss graphs generated in MATLAB in [Figure 5-9](#). [Figure 5](#) presents the accuracy and loss results for the CNN model in [Figure 2](#), while [Figure 6](#) demonstrates the accuracy and loss results for approximation, [Figure 7](#) shows horizontal, [Figure 8](#) displays vertical, and finally, [Figure 9](#) presents diagonal subbands, separately. Investigating the graphs, one can see that the CNN model does not provide highly accurate results when used alone because the dataset is not large enough for a deep learning method. The approximation subband, like the regular CNN model applied to the original images, also has limitations on achieving high accuracies, since the approximation subband is actually a low-resolution version of the original ones. Due to the fact that the horizontal, vertical, and diagonal subbands consist of the details in the images, compared to the approximation subbands and the original images, these subbands have higher accuracy and lower loss results.

[Table 1](#) summarizes the obtained results using the proposed method compared to the CNN model and the subbands separately. For the comparison to be fair, we use the same model for CNN, shown in [Figure 2](#), for all models. For the CNN model, all images are resized to 224x224x3, and data augmentation is also employed with a horizontal flip.

One can see from [Table 1](#) that, the combined (i.e., proposed) model outperforms the CNN model, and the model's using approximation, horizontal, vertical, and diagonal subbands one by one separately. Since the approximation subband is a low-resolution representation of the original images, the accuracy achieved using only the approximation subband cannot match the results obtained with the CNN model. We can observe that the detail subbands, i.e., the horizontal, vertical, and diagonal ones, have higher accuracies than the CNN and approximation counterparts because the high-frequency subbands have detailed information on images. While the accuracy results achieved using the subbands separately are not high enough, we can see that the combination of the probabilities achieved with the subbands provides a promising outcome.

[Table 2](#) demonstrates the comparison of the proposed method to the transfer learning methods based on the accuracy results of the training data. It can be observed from the table that the proposed technique outperforms the transfer learning methods of ResNet18, ResNet50, and GoogleNet. All compared transfer learning models are fed the original images as input and the same data augmentation step is also applied before training.

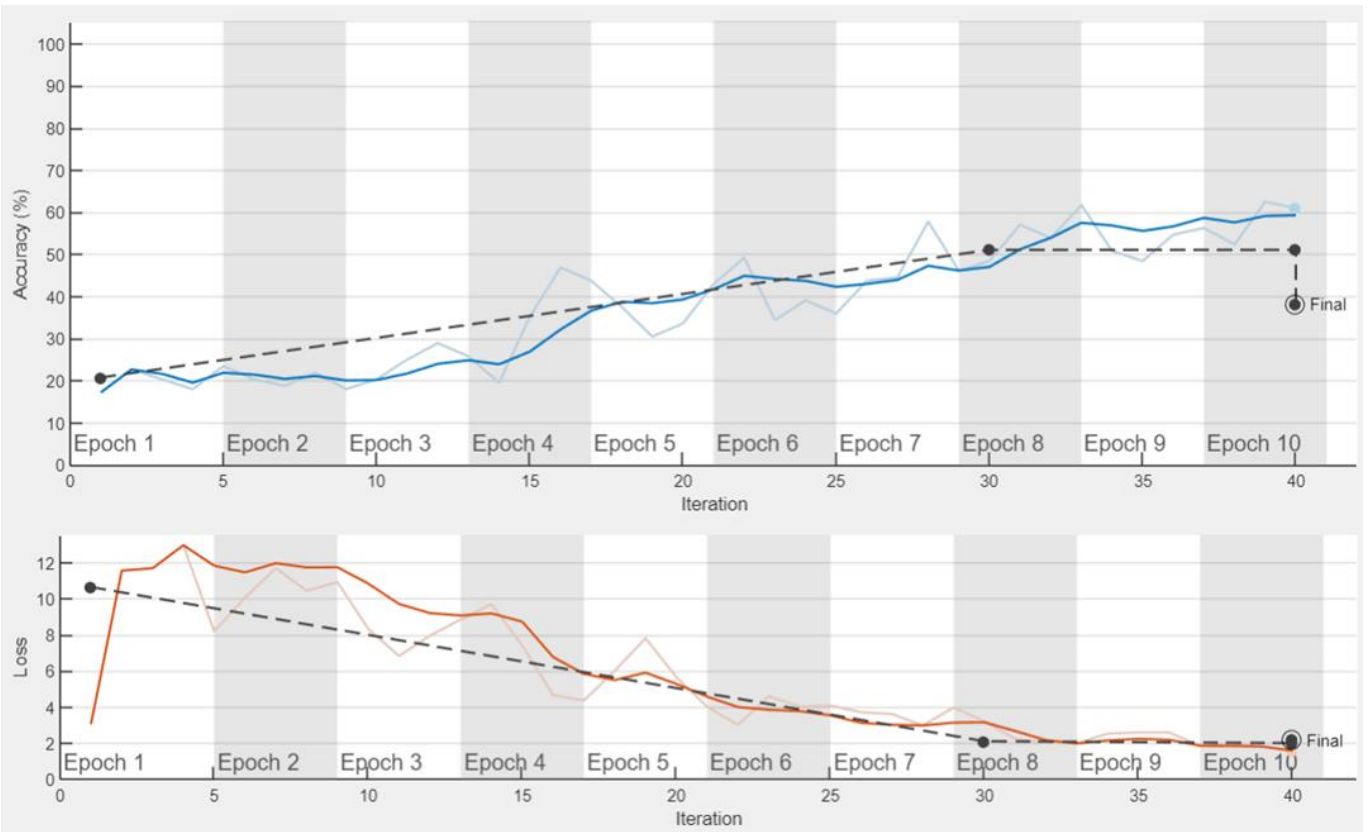


**Figure 5.** Accuracy and loss graphs for the CNN model.

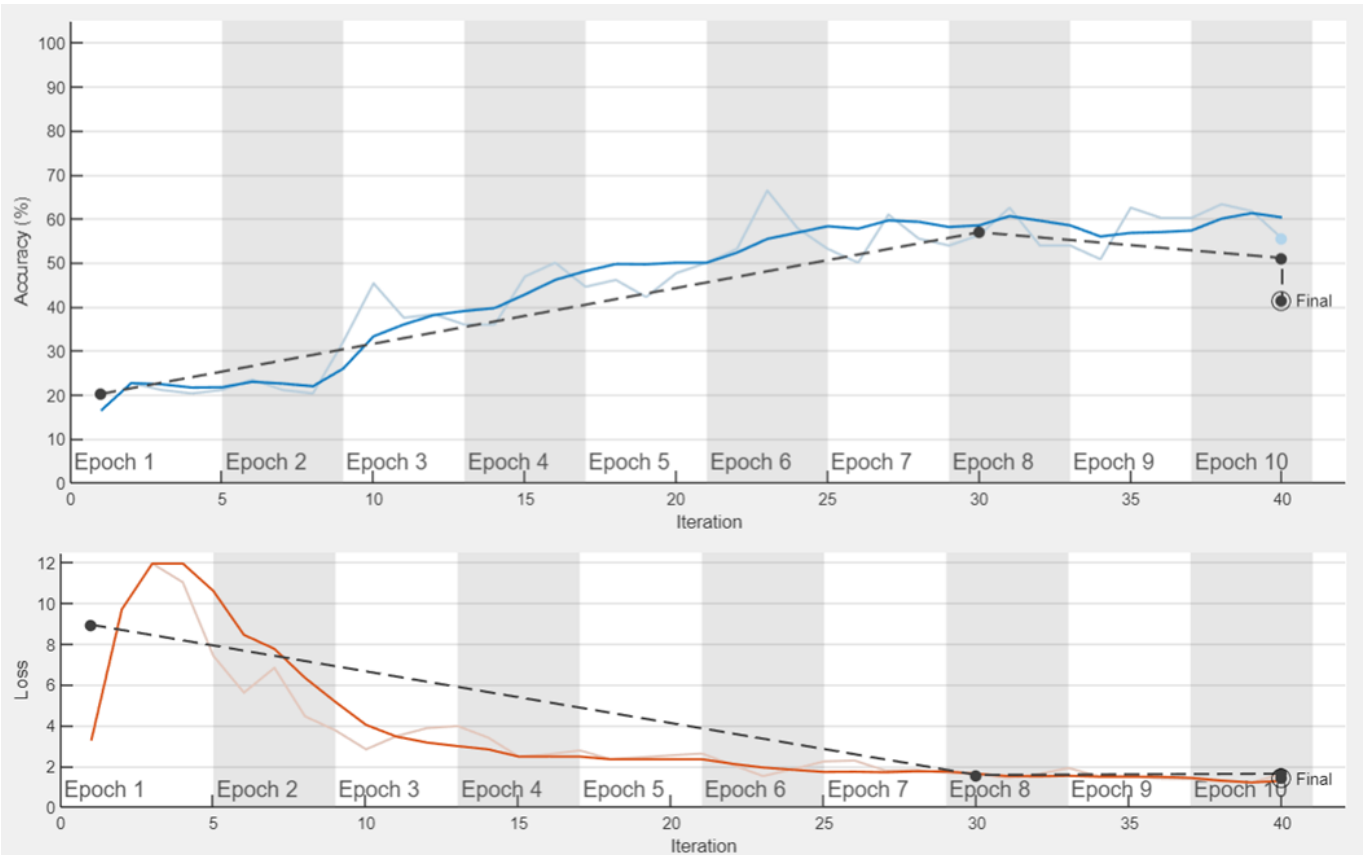


**Figure 6.** Accuracy and loss graphs for approximation subband.

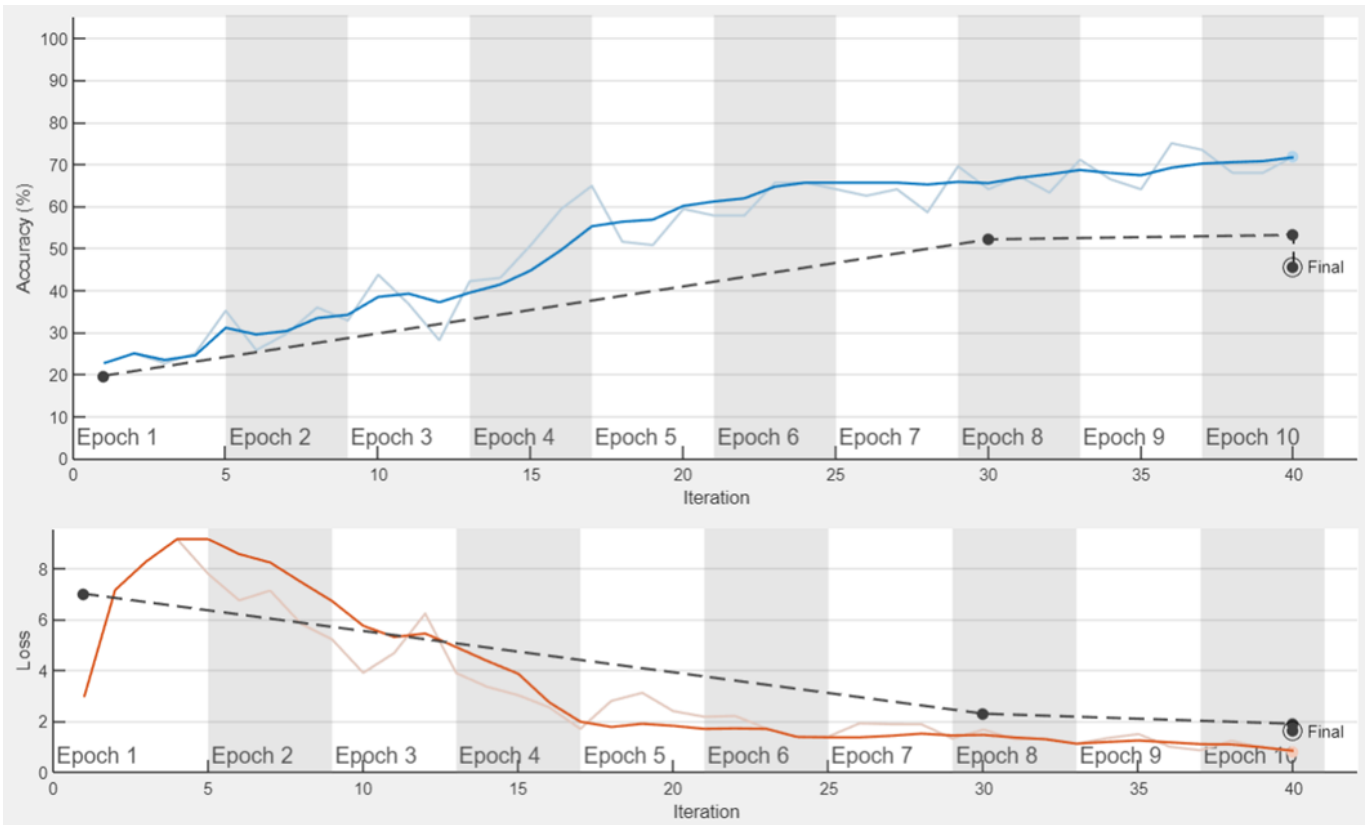


**Figure 7.** Accuracy and loss graphs for horizontal subband.

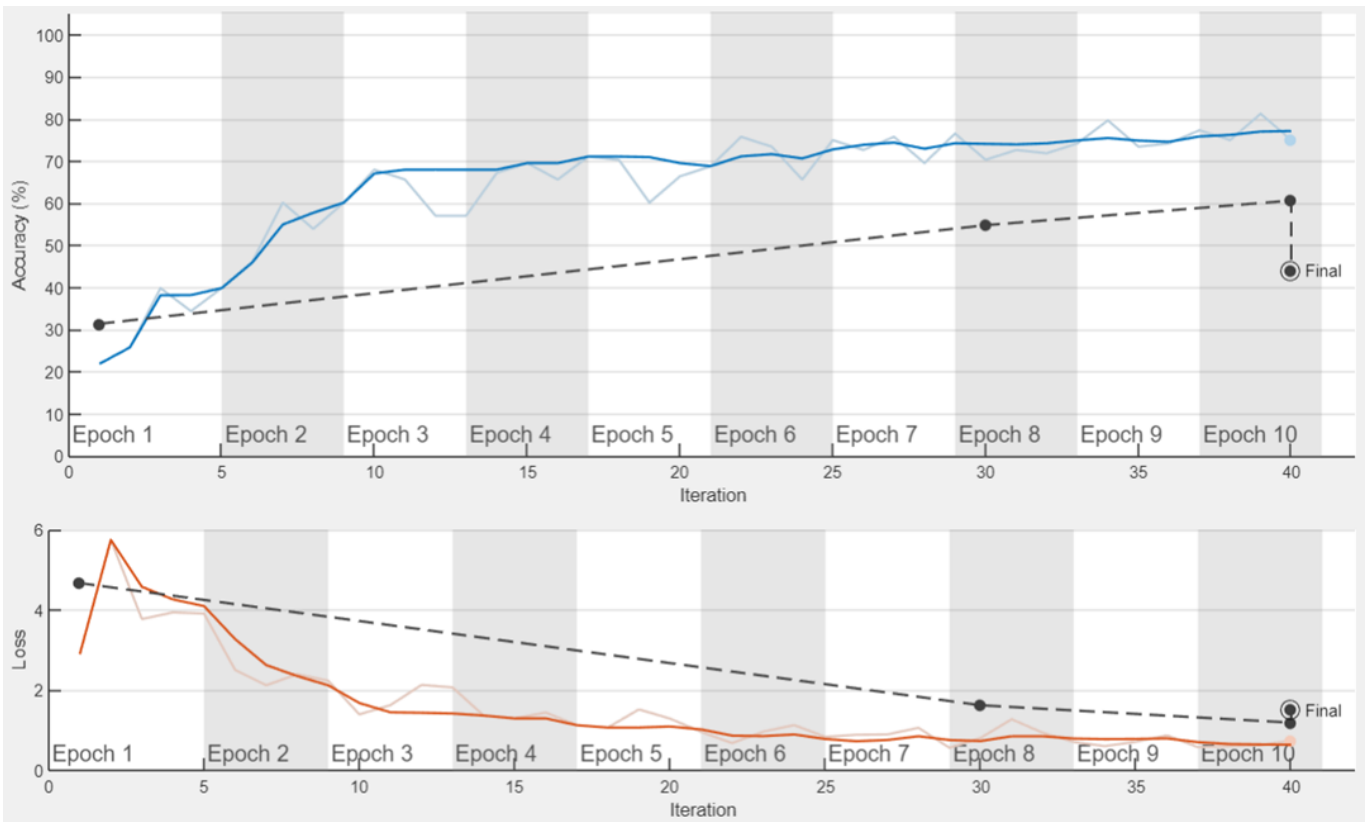


**Figure 8.** Accuracy and loss graphs for vertical subband.

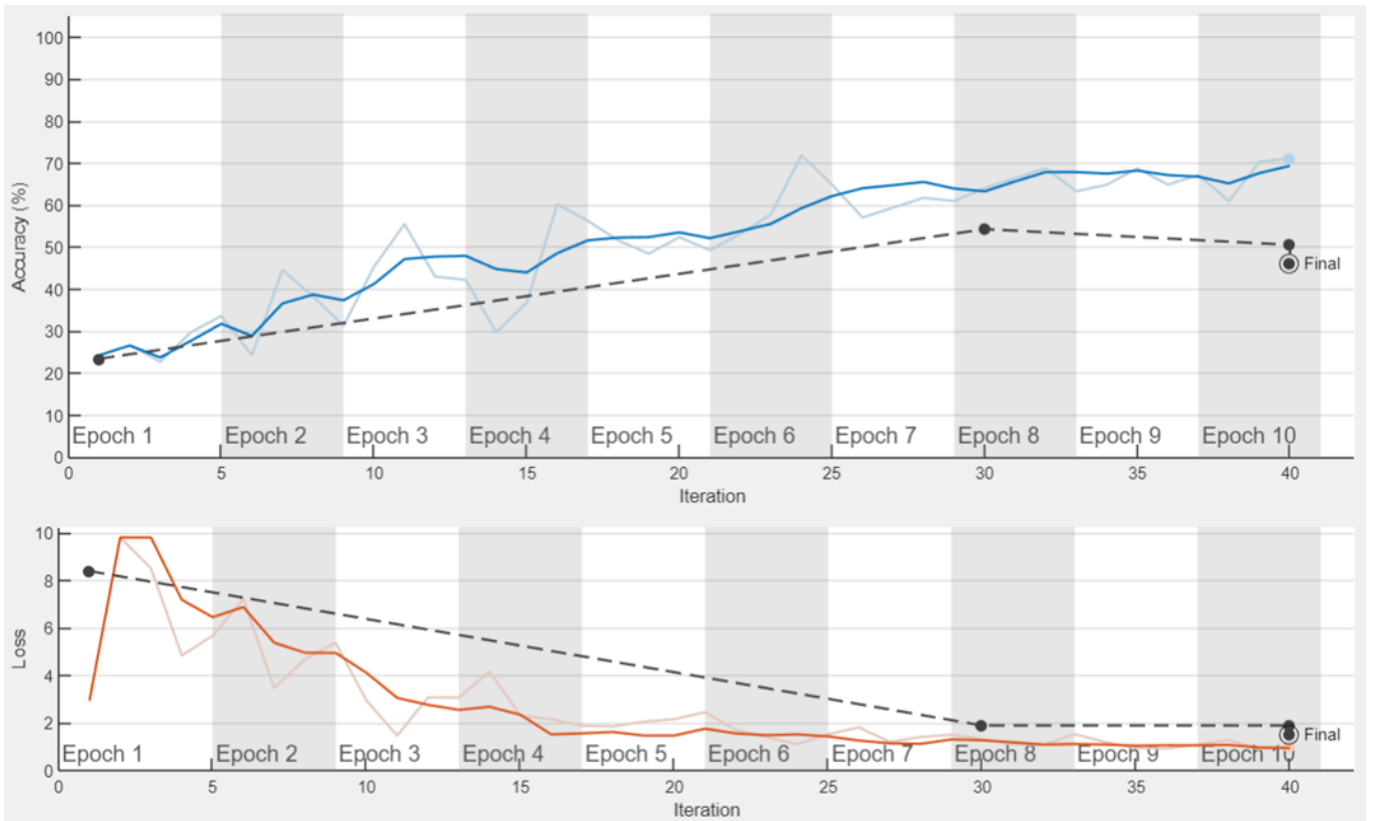


**Figure 9.** Accuracy and loss graphs for diagonal subband.

**Table 1.** Accuracy results obtained with the proposed method compared to a CNN model and the CNN model applied to the subbands separately.

Model	Training data	Test data
CNN	0.61	0.51
Approx.	0.55	0.51
Horizontal	0.72	0.53
Vertical	0.75	0.61
Diagonal	0.71	0.51
Proposed	0.91	0.8

**Table 2.** A comparison between transfer learning methods and the proposed model.

Model	Training data
ResNet18	0.80
ResNet50	0.83
GoogleNet	0.86
Proposed	0.91

#### 4. Discussion

This paper investigates the effects of employing wavelet subbands on a deep learning-based yoga pose classification problem. The proposed method aims at increasing the accuracy results obtained with a regular CNN method by employing wavelet subbands.

Even though the proposed CNN-based method outperforms the compared methods and does have promising results, since each subband of wavelet transform is fed into separate CNNs and the methodology is not parallelized, it requires higher run time compared to regular CNN, which is applied on the original images.

However, since wavelet subband images have lower resolution compared to the original images, and each subband is separately fed into CNNs, employing parallelization would decrease the runtime to allow for the proposed method to be effectively used in real-time applications.

The proposed method can also be employed in 3D pose estimation. Chen and Ramanan [47] argue that instead of predicting 3D poses from image measurements, it is more accurate to use 2D pose estimation with 3D mocap libraries. They experiment with off-the-shelf 2D pose estimation systems to prove their argument. Our proposed 2D pose estimation system can also be used in such scenarios.

The proposed system is the first step of a personalized feedback system. As in the previously mentioned publications, the image classification method can be incorporated into a feedback-providing application where the users either upload their pictures or perform their asanas in front of a camera to rate their performance.

Misclassification of images occurs due to the fact that some poses look alike, as shown in Figure 10. The image on the left is in the Warrior dataset, while the one on the right is in Goddess. One can see the similarity between poses, which results in misclassified images in the datasets. Incorporating skeletonization and angle-likelihoods into the proposed method would decrease the rate of misclassified images as in previously mentioned publications.



**Figure 10.** Misclassified images from the dataset.

## 5. Conclusion

Yoga is an ancient exercise performed by people for its many benefits. Although it helps gain strength in the body and mind, and its benefits are innumerable when performed correctly, an inaccurate move can cause serious health problems. With the increase in the number of people exercising at home after the COVID-19 pandemic, the need for systems to determine whether the poses are done correctly has increased. Since the commercial products produced are not accessible by everyone; computer vision methods such as image classification came in handy. In this paper, we propose a wavelet-based CNN model for yoga pose classification. To the best of our knowledge, this work is the first attempt at exploring the effects of wavelet decomposition in the yoga pose detection problem. Since wavelet transform exhibits the details in images, as expected, decomposing images into wavelet subbands to train the models, in fact, increases the accuracy compared to the one acquired by training on the original images. We propose first decomposing input images into wavelet subbands, later these subbands are fed into separate CNN models. When the output probabilities for each subband are achieved, we fuse the probability results in order to find the final prediction of the yoga pose class for an input image. Demonstrated results outperform the training outcomes achieved using the original images or the separate subbands while having promising accuracy percentages. Since the datasets used are not large enough for a deep learning method to have high accuracies, the next step of this work will include employing a transfer learning method to increase the accuracy results obtained in this paper.

## Conflicts of interest

The authors declare no conflicts of interest.

## References

1. Chang, C. W., Da Nian, M., Chen, Y. F., Chi, C. H., & Tao, C. W. (2014, August). Design of a Kinect sensor based posture recognition system. In 2014 Tenth International Conference on Intelligent Information Hiding and Multimedia Signal Processing (pp. 856-859). IEEE. <https://doi.org/10.1109/IIH-MSP.2014.216>
2. Wang, J., Huang, Z., Zhang, W., Patil, A., Patil, K., Zhu, T., ... & Harris, T. B. (2016, December). Wearable sensor based human posture recognition. In 2016 IEEE International conference on big data (big data) (pp. 3432-3438). IEEE. <https://doi.org/10.1109/BigData.2016.7841004>
3. Gochoo, M., Tan, T. H., Huang, S. C., Batjargal, T., Hsieh, J. W., Alnajjar, F. S., & Chen, Y. F. (2019). Novel IoT-based privacy-preserving yoga posture recognition system using low-resolution infrared sensors and deep learning. *IEEE Internet of Things Journal*, 6(4), 7192-7200. <https://doi.org/10.1109/JIOT.2019.2915095>
4. Jain, S., Rustagi, A., Saurav, S., Saini, R., & Singh, S. (2021). Three-dimensional CNN-inspired deep learning architecture for Yoga pose recognition in the real-world environment. *Neural Computing and Applications*, 33, 6427-6441. <https://doi.org/10.1007/s00521-020-05405-5>
5. Gochoo, M., Tan, T. H., Alnajjar, F., Hsieh, J. W., & Chen, P. Y. (2020, October). Lownet: Privacy preserved ultra-low resolution posture image classification. In 2020 IEEE International Conference on Image Processing (ICIP) (pp. 663-667). IEEE. <https://doi.org/10.1109/ICIP40778.2020.9190922>
6. Anand Thoutam, V., Srivastava, A., Badal, T., Kumar Mishra, V., Sinha, G. R., Sakalle, A., ... & Raj, M. (2022). Yoga pose estimation and feedback generation using deep learning. *Computational Intelligence and Neuroscience*, 4311350. <https://doi.org/10.1155/2022/4311350>
7. Kumar, D., & Sinha, A. (2020). Yoga pose detection and classification using deep learning. *International Journal of Scientific Research in Computer Science, Engineering and Information Technology*, 6 (6), 160-184. <https://doi.org/10.32628/CSEIT206623>

8. Dittakavi, B., Bavikadi, D., Desai, S. V., Chakraborty, S., Reddy, N., Balasubramanian, V. N., ... & Sharma, A. (2022). Pose tutor: an explainable system for pose correction in the wild. In Proceedings of the IEEE/CVF Conference on Computer Vision and Pattern Recognition (pp. 3540-3549).
9. Wu, Y., Lin, Q., Yang, M., Liu, J., Tian, J., Kapil, D., & Vanderbloemen, L. (2021, December). A computer vision-based yoga pose grading approach using contrastive skeleton feature representations. *Healthcare*, 10(1), 36. <https://doi.org/10.3390/healthcare10010036>
10. Garg, S., Saxena, A., & Gupta, R. (2022). Yoga pose classification: a CNN and MediaPipe inspired deep learning approach for real-world application. *Journal of Ambient Intelligence and Humanized Computing*, 1-12. <https://doi.org/10.1007/s12652-022-03910-0>
11. Swain, D., Satapathy, S., Acharya, B., Shukla, M., Gerogiannis, V. C., Kanavos, A., & Giakovis, D. (2022). Deep Learning Models for Yoga Pose Monitoring. *Algorithms*, 15(11), 403. <https://doi.org/10.3390/a15110403>
12. Rishan, F., De Silva, B., Alawathugoda, S., Nijabdeen, S., Rupasinghe, L., & Liyanapathirana, C. (2020, December). Infinity yoga tutor: Yoga posture detection and correction system. In 2020 5th International conference on information technology research (ICITR) (pp. 1-6). IEEE. <https://doi.org/10.1109/ICITR51448.2020.9310832>
13. Yadav, S. K., Singh, A., Gupta, A., & Raheja, J. L. (2019). Real-time Yoga recognition using deep learning. *Neural Computing and Applications*, 31, 9349-9361. <https://doi.org/10.1007/s00521-019-04232-7>
14. Long, C., Jo, E., & Nam, Y. (2022). Development of a yoga posture coaching system using an interactive display based on transfer learning. *The Journal of Supercomputing*, 78, 5269–5284. <https://doi.org/10.1007/s11227-021-04076-w>
15. Chasmai, M., Das, N., Bhardwaj, A., & Garg, R. (2022). A View Independent Classification Framework for Yoga Postures. *SN computer science*, 3(6), 476. <https://doi.org/10.1007/s42979-022-01376-7>
16. Verma, M., Kumawat, S., Nakashima, Y., & Raman, S. (2020). Yoga-82: a new dataset for fine-grained classification of human poses. In Proceedings of the IEEE/CVF conference on computer vision and pattern recognition workshops (pp. 1038-1039).
17. Yadav, S. K., Singh, G., Verma, M., Tiwari, K., Pandey, H. M., Akbar, S. A., & Corcoran, P. (2022). YogaTube: a video benchmark for Yoga action recognition. In 2022 International Joint Conference on Neural Networks (IJCNN) (pp. 1-8). IEEE. <https://doi.org/10.1109/IJCNN55064.2022.9892122>
18. Li, J., Hu, H., Li, J., & Zhao, X. (2022). 3D-Yoga: A 3D Yoga Dataset for Visual-Based Hierarchical Sports Action Analysis. In Proceedings of the Asian Conference on Computer Vision (pp. 434-450).
19. Fu, Y., Lei, Y., Wang, T., Curran, W. J., Liu, T., & Yang, X. (2020). Deep learning in medical image registration: a review. *Physics in Medicine & Biology*, 65(20), 20TR01. <https://doi.org/10.1088/1361-6560/ab843e>
20. Yang, W., Zhang, X., Tian, Y., Wang, W., Xue, J. H., & Liao, Q. (2019). Deep learning for single image super-resolution: A brief review. *IEEE Transactions on Multimedia*, 21(12), 3106-3121. <https://doi.org/10.1109/TMM.2019.2919431>
21. Lu, D., & Weng, Q. (2007). A survey of image classification methods and techniques for improving classification performance. *International journal of Remote sensing*, 28(5), 823-870. <https://doi.org/10.1080/01431160600746456>
22. Gülgün, O. D., & Hamza, E. R. O. L. (2020). Classification performance comparisons of deep learning models in pneumonia diagnosis using chest x-ray images. *Turkish Journal of Engineering*, 4(3), 129-141. <https://doi.org/10.31127/tuje.652358>
23. Zeybek, M. (2021). Classification of UAV point clouds by random forest machine learning algorithm. *Turkish Journal of Engineering*, 5(2), 48-57. <https://doi.org/10.31127/tuje.669566>
24. Öztürk, A., Allahverdi, N., & Saday, F. (2022). Application of artificial intelligence methods for bovine gender prediction. *Turkish Journal of Engineering*, 6(1), 54-62. <https://doi.org/10.31127/tuje.807019>
25. Rawat, W., & Wang, Z. (2017). Deep convolutional neural networks for image classification: A comprehensive review. *Neural computation*, 29(9), 2352-2449. [https://doi.org/10.1162/neco\\_a\\_00990](https://doi.org/10.1162/neco_a_00990)
26. Su, D., Zhang, H., Chen, H., Yi, J., Chen, P. Y., & Gao, Y. (2018). Is Robustness the Cost of Accuracy?--A Comprehensive Study on the Robustness of 18 Deep Image Classification Models. In Proceedings of the European conference on computer vision (ECCV), 631-648.
27. Aydin, V. A., & Foroosh, H. (2017, September). Motion compensation using critically sampled dwt subbands for low-bitrate video coding. In 2017 IEEE International Conference on Image Processing (ICIP), 21-25. <https://doi.org/10.1109/ICIP.2017.8296235>
28. Aydin, V. A., & Foroosh, H. (2017). In-band sub-pixel registration of wavelet-encoded images from sparse coefficients. *Signal, Image and Video Processing*, 11, 1527-1535. <https://doi.org/10.1007/s11760-017-1116-5>
29. Aydin, V. A., & Foroosh, H. (2018). A linear well-posed solution to recover high-frequency information for super resolution image reconstruction. *Multidimensional Systems and Signal Processing*, 29, 1309-1330. <https://doi.org/10.1007/s11045-017-0499-3>
30. Huang, H., He, R., Sun, Z., & Tan, T. (2017). Wavelet-srnet: A wavelet-based cnn for multi-scale face super resolution. In Proceedings of the IEEE international conference on computer vision (pp. 1689-1697).
31. Le Moigne, J., Campbell, W. J., & Crompton, R. F. (2002). An automated parallel image registration technique based on the correlation of wavelet features. *IEEE Transactions on Geoscience and Remote Sensing*, 40(8), 1849-1864. <https://doi.org/10.1109/TGRS.2002.802501>

32. Postalcioglu, S., Erkan, K., & Bolat, E. D. (2005). Comparison of wavenet and neuralnet for system modeling. In Knowledge-Based Intelligent Information and Engineering Systems: 9th International Conference, KES 2005, Melbourne, Australia, September 14-16, 2005, Proceedings, Part II 9 (pp. 100-107). Springer Berlin Heidelberg. [https://doi.org/10.1007/11552451\\_14](https://doi.org/10.1007/11552451_14)
33. Postalcioglu, S., & Becerikli, Y. (2007). Wavelet networks for nonlinear system modeling. *Neural Computing and Applications*, 16, 433-441. <https://doi.org/10.1007/s00521-006-0069-3>
34. Robinson, M. D., Toth, C. A., Lo, J. Y., & Farsiu, S. (2010). Efficient Fourier-wavelet super-resolution. *IEEE Transactions on Image Processing*, 19(10), 2669-2681. <https://doi.org/10.1109/TIP.2010.2050107>
35. Li, Q., Shen, L., Guo, S., & Lai, Z. (2020). Wavelet integrated CNNs for noise-robust image classification. In *Proceedings of the IEEE/CVF Conference on Computer Vision and Pattern Recognition*, 7245-7254.
36. Deng, J., Dong, W., Socher, R., Li, L. J., Li, K., & Fei-Fei, L. (2009, June). Imagenet: A large-scale hierarchical image database. In *2009 IEEE conference on computer vision and pattern recognition*, 248-255. <https://doi.org/10.1109/CVPR.2009.5206848>
37. Hendrycks, D., & Dietterich, T. (2019). Benchmarking neural network robustness to common corruptions and perturbations. *arXiv preprint arXiv:1903.12261*. <https://doi.org/10.48550/arXiv.1903.12261>
38. Mallick, P. K., Ryu, S. H., Satapathy, S. K., Mishra, S., Nguyen, G. N., & Tiwari, P. (2019). Brain MRI image classification for cancer detection using deep wavelet autoencoder-based deep neural network. *IEEE Access*, 7, 46278-46287. <https://doi.org/10.1109/ACCESS.2019.2902252>
39. Khatami, A., Nazari, A., Beheshti, A., Nguyen, T. T., Nahavandi, S., & Zieba, J. (2020, July). Convolutional neural network for medical image classification using wavelet features. In *2020 International Joint Conference on Neural Networks (IJCNN)*, 1-8. <https://doi.org/10.1109/IJCNN48605.2020.9206791>
40. Said, S., Jemai, O., Hassairi, S., Ejbali, R., Zaid, M., & Amar, C. B. (2016, October). Deep wavelet network for image classification. In *2016 IEEE International conference on systems, man, and cybernetics (SMC)*, 000922-000927. <https://doi.org/10.1109/SMC.2016.7844359>
41. Fujieda, S., Takayama, K., & Hachisuka, T. (2017). Wavelet convolutional neural networks for texture classification. *arXiv preprint arXiv:1707.07394*. <https://doi.org/10.48550/arXiv.1707.07394>
42. Postalcioglu, S. (2022). Design of Automatic Tool for Diagnosis of Pneumonia Using Boosting Techniques. *Brazilian Archives of Biology and Technology*, 65, e22210322.
43. Serte, S., & Demirel, H. (2019). Gabor wavelet-based deep learning for skin lesion classification. *Computers in biology and medicine*, 113, 103423. <https://doi.org/10.1016/j.compbiomed.2019.103423>
44. Serte, S., & Demirel, H. (2020). Wavelet-based deep learning for skin lesion classification. *IET Image Processing*, 14(4), 720-726. <https://doi.org/10.1049/iet-ipr.2019.0553>
45. Aydin, V. A. (2022). CNN Tabanlı Yoga Pozu Sınıflandırmasında Aktivasyon Fonksiyonu Karşılaştırması. In *Proceedings of IES'22 International Engineering Symposium, Engineering Applications in Industry*, 117-122. <https://www.kaggle.com/datasets/niharika41298/yoga-poses-dataset>
47. Chen, C. H., & Ramanan, D. (2017). 3d human pose estimation= 2d pose estimation+ matching. In *Proceedings of the IEEE conference on computer vision and pattern recognition* (pp. 7035-7043).



© Author(s) 2024. This work is distributed under <https://creativecommons.org/licenses/by-sa/4.0/>



## Counterface soil type and loading condition effects on granular/cohesive soil – Geofom interface shear behavior

Tanay Karademir \*<sup>1</sup> 

<sup>1</sup>Istanbul Bilgi University, Department of Civil Engineering, Türkiye, [tanay.karademir@bilgi.edu.tr](mailto:tanay.karademir@bilgi.edu.tr)

Cite this study:

Karademir, T. (2024). Counterface soil type and loading condition effects on granular/cohesive soil – Geofom interface shear behavior. Turkish Journal of Engineering, 8 (1), 76-91

### Keywords

Geofoams  
Interface shear  
Granular soils  
Cohesive soils  
Loading conditions

### Research Article

DOI: 10.31127/tuje.1279304

Received:07.04.2023

Revised: 08.05.2023

Accepted:15.05.2023

Published:15.09.2023



### Abstract

Soil – geofom interfaces have been studied through an extensive experimental program by performing multiple series of interface shear tests using two different granular soils (i.e. beach sand and construction material sand) and one cohesive soil (i.e. bentonite clay) as well as a soil mixture containing 75% sand and 25% clay by dry weight at distinct loading conditions (i.e. normal stresses ( $\sigma$ ): 25, 100, 250; low, moderate, high loading conditions, respectively). Using the shear stress versus horizontal displacement curves obtained, some important engineering design parameters including peak shear stress, residual shear stress, interface sensitivity (i.e., peak/residual ratio) and displacement required to reach peak stress have been determined and the variations in those interface mechanical properties as a function of loading condition and counterface soil type have been investigated. It was shown that the peak as well as residual shear stresses increased with an increase in normal stress for all the interface systems tested. Further, the granular soil (sand) interfaces demonstrated relatively larger frictional strengths (both peak and residual) as compared to both the cohesive soil (clay) interface and the sand/clay admixture soil interface. Additionally, the higher the angularity of granular soil particles became, the larger the interface shear strengths (peak and residual), when sheared against gefoams, developed in light of experimental results attained as a result of interface shear tests on different material combinations. For comparison, the detected peak strength at average for the construction material sand, the beach sand, and the sand/clay admixture soil interfaces as compared to the bentonite clay interface were improved 59.8%, 43.4%, and 20.3%, respectively. Additionally, the detected residual strength at average for the construction material sand, the beach sand, and the sand/clay admixture soil interfaces as compared to the bentonite clay interface were improved 53.9%, 28.6%, and 15.4%, respectively.

## 1. Introduction

The primary function of the gefoams consists of providing; i) lightweight fill for construction on soft ground (i.e., embankment), ii) relatively stiff base for subgrade installation below a highway (i.e., roadway, runway foundation), bridge approach (i.e., abutment backfill), and iii) slope stabilization for retaining structures. In those applications, the gefoams are in direct contact with soils and this interaction results in development of an interface where likelihood of a failure to initiate is higher. For this reason, the frictional resistance and the type of shear response mobilizing at these soil – geofom interfaces control the stability of composite system, and hence, govern the integrity of the infrastructure.

The sole and/or the mutual mechanical behavior (i.e., tensile, compressive, and shear) of soil (i.e., granular and cohesive) and/or geosynthetics (e.g., geofom and geomembrane) in infrastructural applications have always attracted the attention of researchers. In this regard, the laboratory and/or the in-situ tests are performed to further evaluate their stand-alone/independent or integrated responses against the induced stresses and strains. To this end, the behavior of expanded polystyrene (EPS) geofom under triaxial loading conditions was examined by Padade and Mandal [1]. Besides, the behavior of EPS geofom in true triaxial compression tests was studied by Leo et al. [2]. Moreover, the behavior of EPS geofom in stress-controlled cyclic uniaxial tests was reported by Trandafir

et al. [3]. Additionally, the interface shear strength of EPS-concrete elements of various configurations was investigated by Özer and Akay [4] that shearing resistance between the EPS and precast concrete was found to be higher than that of the flat EPS-EPS interface owing to the improvement of the interface shear behavior as a result of interlocking and the modification of shear mechanism taking place at the interface of EPS-precast concrete from purely frictional to frictional-adhesional. Furthermore, the shear strength properties of compacted high plasticity clay soils based on different laboratory tests were examined by Yilmaz and Türköz [5]. A number of twenty high plasticity soil samples were used and the geotechnical identification tests including direct shear as well as unconfined compression tests were performed such that the shear strength properties of the samples prepared by compression in their compaction characteristics were determined to further evaluate effective shear strength and total shear stress parameters. Further, the geomechanical properties of fiber reinforced cohesive soils were investigated by Ertuğrul and Canogullari [6]. It has been observed that the strength of soil was improved with increasing density of the fibers up to a certain level based on the percentage of added fiber. The performed statistical analysis revealed that the improvement of strength in soil is a function of fiber density, LL/PL ratio (LL: liquid limit; PL: plastic limit). Moreover, the effect of silica fume on the undrained strength parameters of dispersive soils was studied by Öztürk and Türköz [7]. As such, the dispersibility behavior of the soil samples prepared was determined by the crumb test in adding silica fume to improve the soil properties for which the soil specimens mixed with silica fume at different proportions ranging from 0% up to 30% by 5% increments in mass proportion were compacted by using the standard proctor test so that the dispersibility potential of the prepared specimens was evaluated through the crumb tests. Additionally, the strength properties of soil samples were assessed by conducting unconsolidated undrained (UU) triaxial tests. As a result, it was observed that the dispersibility feature of the soil samples was treated and the strength properties were improved accordingly depending on the silica fume content.

Furthermore, geofabric, produced from expanded polystyrene (EPS), has been employed over 45 years in geotechnical applications for the enormous extent of diverse infrastructural projects requires lightweight fill material including highways, railways, airport runways, embankments, bridge abutments, earth retaining structures (i.e., retaining walls), slope stabilization, structural foundation fills, building fills, plaza decks, stadium seating, utility protection and compressible. Among the most versatile lightweight materials available in the industry, geofabric – having predictable material behavior – is an engineered product unlike the other lightweight fill materials that can be variable in composition. Additionally, geofabric is an ultra-lightweight such that it only weighs about 1% weight of soil or rock. Further, the physical properties of geofabric will not degrade (i.e., non-biodegradable) assuring long term performance and durability in engineered geotechnical applications. In those various

infrastructural applications aforementioned, the geofabrics utilized are in direct contact and interaction with the surrounding soils as those kinds of systems are in composite nature composed of synthetic polymeric materials (i.e., geofabric) and natural soils (i.e., sand, silt, clay mixtures).

The physical, index and mechanical properties as well as material characteristics of synthetics can be controlled and predetermined as opposed to that of natural soils. Moreover, an interaction zone, called interface, between two dissimilar materials will develop such that the mechanical behavior in terms of strength, durability (load-bearing capacity and long-term resistance, respectively) will be governed by the shearing mechanisms and the mobilized frictional properties along the contact surface. To this end, soil – geofabric interface shear behavior plays a critical role in controlling stability, steadiness, and long-lasting performance of those diverse geotechnical applications.

## 2. Geofabrics: Lightweight Fill Applications

In lightweight fill applications, the geofabrics are employed principally as specified for providing opportunity; (i) in replacing heavy fill materials to reduce settlement, (ii) safely support super-structural (i.e. overlying structure) loading without over-stressing the underlying soils and to reduce differential movement, (iii) in site development on weak and poor load-bearing foundation soils by reducing the load on underlying compressible soils to minimize deformation, (iv) reduction of lateral pressure on vertical walls as well as improves slope stability by means of stabilization, (v) reduction of induced stress or load on underground structures and/or utilities (i.e. underlying structures and services), (vi) cost-effective solutions where conventional construction methods have failed or demonstrated sub-standard performance. As such, the typical engineering approaches in design and the traditional techniques in construction practices aim to develop an operational mechanism to work for resisting the forces of nature. On the other hand, the design methodology and the implementation of the project using geofabrics goal to mobilize a functional execution in order to work with the forces of nature in resolving structural fill challenges such that the geofabrics utilized in the infrastructural applications reduce the forces acting on a structure (i.e., retaining walls) or foundation soil (i.e. embankments) instead of reinforcing them to withstand the forces that would exist without geofabric inclusion and/or substitution [8 – 10].

Although, the literature especially on the mechanical behavior (i.e., material response under compression) of geofabrics employed infrastructural applications appears in the 1970s, an organized technical knowledge can be found in Horvath [11] where the generic term “geofabric” was proposed to describe rigid-plastic-foams utilized in geotechnical applications. In this regard, this polymeric synthetic material (geofabric) is now recognized as a category of geosynthetics. Seismic response (i.e., dynamic behavior) was first studied extensively by Bathurst and Alfaro [12], and additionally, the results of a finite element method (FEM) study on the seismic

response attracted attention presented by Pelekis et al. [13] pointing out that a substantial decrease in seismic earth pressures acting on a retaining structure (i.e., cantilever type retaining wall) protected by a layer of geofoam placed at the wall – backfill interface. Since then, a remarkable amount of research work has been published concerning with mechanical behavior of geofoams including static and dynamic loading conditions such as Zarnani and Bathurst [14]. On the other hand, a combined response analysis of soil – geofoam composite systems have not received sufficient interest in the studies, and thus, a comprehensive and detailed examination in regards to geofoam – surrounding soil contact behavior and resulting interaction mechanisms is required. However, soil – geofoam composite systems, subjected to the action of both static and dynamic loads in the aforementioned geotechnical projects, require rigorous analysis (proper and neat) as well as organized (elaborate and comprehensive) modeling to accomplish proper engineering design of the relevant technical works prior to applying in the field. To this end, in order to achieve this engineering process, the mechanical behavior of geofoam, in particular, the interaction mechanism at the contact surface (i.e., interface shear behavior) with counterface soils needs to be known extensively and evaluated precisely so as that the frictional response could exactly be predicted. Within this scope, a laboratory testing program has been conducted to examine soil – geofoam interface shear behavior under the influence of different loading conditions as well as the effect of counterface soil type as being course or fine grained at the contact surface (i.e., interface).

### 3. Laboratory Testing Program

The laboratory testing program consists of four series of shear tests on four different composite interface systems comprised of geofoam counterfaced against distinct soils. The physical properties as well as characteristics of the tested material will be described in this section along with some detailed information

provided on testing device and experimental procedures, and additionally, further explanation given on the test matrix.

#### 3.1. Geofoam characteristics and soil physical properties

The geofoam utilized in the entire experimental program is a polymeric material produced from expanded polystyrene (EPS). As such, the EPS geofoam is foam plastic, that is, thermoplastic closed-cell polymer based building and infrastructure material manufactured from hard foam blocks of polystyrol granules. Further, geofoams, being glassy foam based polymeric materials, exhibit visco-elastic behavior when subjected to load application. Therefore, the compressive stress at 1%, 2%, 5%, and 10% strains (i.e., deformations) is measured and reported instead of compressive strength. To this end, the physical and mechanical properties of the EPS geofoam utilized throughout the entire laboratory experimental program are listed in Table 1. This type of geofoam possessing relatively high density and intact material characteristics was intentionally selected owing to the fact that this is a generally preferred geosynthetic material for the design of infrastructural projects as well as for the construction of relevant geotechnical applications containing geofoam and surrounding soil interfaces which involves in the interaction of granular and/or cohesive soil versus geofoam over the entire extent of contact area between those counterface materials that is exactly being the scope of this research study. As per polymeric material characteristics, the geofoam used in the entire testing program possesses relatively larger bearing capacity properties such that the resultant amount of compressive deformation mobilized due to compressive forces/stresses is generally marginal. This shows that the material inherent ability in terms of the generated compressive resistance against loading for the geofoam is very considerable, remarkable and significant compared to the other infrastructural construction materials such as natural soil.

**Table 1.** Physical and mechanical properties of EPS Geofoam used in testing program.

Physical and Mechanical Properties	Density (kg/m <sup>3</sup> )	Compressive Resistance (kPa), min. at 2% deformation	Compressive Resistance (kPa), min. at 5% deformation	Compressive Resistance (kPa), min. at 10% deformation	Flexural Strength (kPa), min
Geofoam	20	60	80	100	150

Furthermore, although the EPS geofoams possess relatively high strength as compared to most of the construction materials, it has very low density attained by expanding and compressing various closed air (gas) filled cells.

Moreover, two types of poorly graded granular soil were selected to be used as a specimen for the interface shear tests in the experimental program. The physical and index properties (Table 2) of sand specimens are similar to each other whereas the construction material sand composed of grains (i.e., particles) possessing angular features in comparison to that of beach sand possessing subrounded features. This was purposefully

intended to examine the influence of sand particle shape and geometry on the developed interface shear behavior and on the mobilized frictional strength characteristics such as engineering design parameters including peak shear stress, residual shear stress, interface sensitivity and displacement to peak. The test methods followed to determine those required physical and index properties of granular soils used in the experimental program are listed in Table 2 for clarification. Further, both beach sand and construction material sand soils are classified as SP (poorly graded sand) according to Unified Soil Classification System (USCS). Additionally, the bentonite clay used in the experimental program is classified as

high plasticity clay (CH) based on USCS. The construction material sand (75%)/bentonite (25%) clay admixture soil can be classified as poorly graded sand with clay (SP-

SC) per USCS, accordingly. Furthermore, the mean grain size ( $D_{50}$ ) and the effective particle size ( $D_{10}$ ) for the tested bentonite clay are 79  $\mu\text{m}$  and 46  $\mu\text{m}$ , respectively.

**Table 2.** Physical and index properties of granular soils used in testing program.

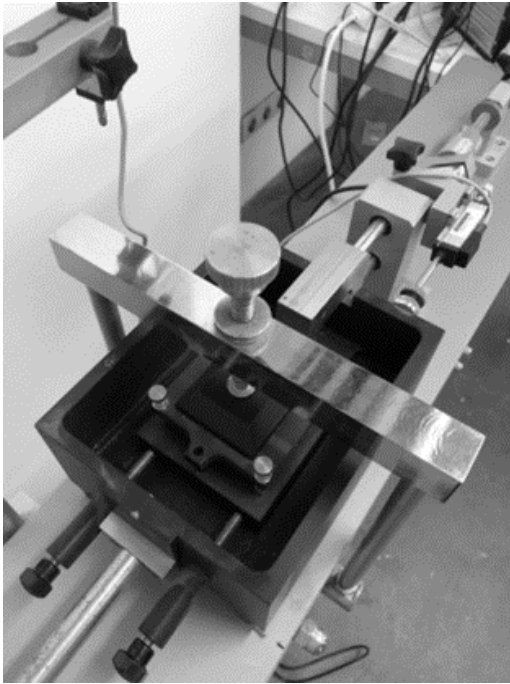
Sand Properties	$D_{50}$ (mm)	$C_u^a$	$C_c^b$	$G_s^c$	$e_{max}^d$	$e_{min}^e$	$D_r^{d,e}$
Beach Sand	0.34	2.30	0.91	2.67	0.73	0.57	69.8% $\pm$ 1.8%
Construction Material Sand	0.39	2.37	0.96	2.68	0.82	0.68	70.1% $\pm$ 1.7%

**Note:** <sup>a</sup> $C_u = D_{60}/D_{10}$ ; <sup>b</sup> $C_c = D_{30}^2/(D_{10} * D_{60})$ ; <sup>c</sup>ASTM D854 [15]; <sup>d</sup>ASTM D4253 [16]; <sup>e</sup>ASTM D4254 [17]

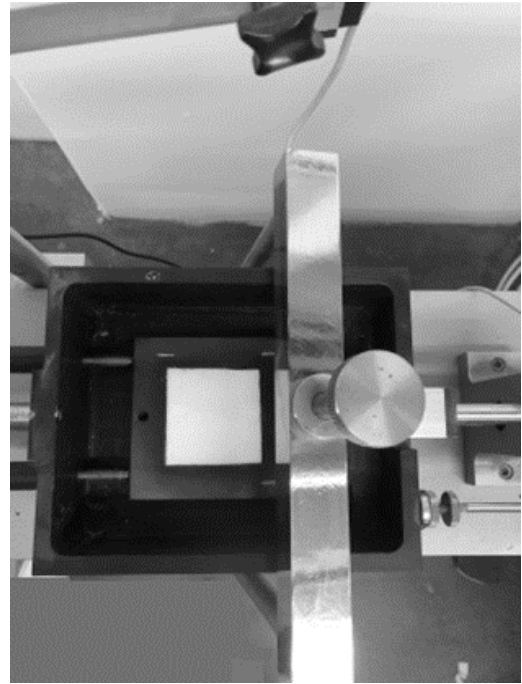
**3.2. Testing device and experimental procedures: Specimen preparation**

A strain-controlled interface device (Figure 1) has been used to perform shear tests in which frictional response and engineering strength as well as deformation properties of different soil versus geofoam interfaces have been measured and detected so that the frictional characteristics of contact surfaces for composite layered systems between geofoams and distinct soil types including granular, cohesive and mixed soils have been investigated. The experimental program was conducted under dry conditions. The tests were performed at a constant strain rate (i.e., constant lateral

speed) such that the rate of lateral displacement was set as 0.1 mm/min and it was allowed to up to a total horizontal displacement of 10 mm. This shearing speed (i.e., loading speed) was selected intentionally to observe the essential and accurate interface shear response and frictional resistance behavior both in cohesive soil and granular soil interface systems. The shear force and both lateral as well as vertical displacements were measured by employing a load cell and linear displacement transducers (LVDTs), respectively. The measurement data was logged and recorded into a computer through a controller program enabling analog-digital communication in between the sensors and the computer.



(a)



(b)

**Figure 1.** Testing device and shear box.

The geofoam specimens were cut and prepared by utilizing a hot wire equipment and placed at the bottom half of the shear box. Further, the soil specimens, placed at the top half, were prepared in dry form by applying air pluviation technique to attain the same relative density for the specimens for achieving same denseness or concentration in the box. Thereafter, the shear box was closed by a cap on which a LVDT is located to measure vertical displacement during the test progress. Afterwards, the normal load was applied and the test process was initiated by facilitating horizontal displacement at a constant lateral speed.

**3.3. Test matrix**

The laboratory experimental program consists of 12 interface shear tests at various loading conditions ranging from 25 kPa up to 250 kPa to observe the shear behavior at low, medium and high stress levels, respectively (Table 3).

Four different composite systems including two different granular materials such as beach sand and construction material sand as well as one cohesive soil (bentonite clay) and a soil mixture composed of 75% sand and 25% clay were formed (constituted) to

investigate the influence of soil type – counterfaced with geof foam – on the developed interface response and frictional characteristics including strength and

deformation properties. The laboratory program test matrix provided in Table 3 presents the details and the extent of the experimental study.

**Table 3.** Laboratory program test matrix.

Materials Tested	Beach Sand	Construction Material Sand	Clay (Bentonite)	75% Construction Material Sand and 25% Clay (Bentonite)
Geofoam	Beach Sand vs. Geofoam ( $\sigma = 25$ kPa)	Construction Mat. Sand vs. Geofoam ( $\sigma = 25$ kPa)	Clay (Bentonite) vs. Geofoam ( $\sigma = 25$ kPa)	75% Cons.Mat. Sand 25% Bentonite Clay vs. Geofoam ( $\sigma = 25$ kPa)
Geofoam	Beach Sand vs. Geofoam ( $\sigma = 100$ kPa)	Construction Mat. Sand vs. Geofoam ( $\sigma = 100$ kPa)	Clay (Bentonite) vs. Geofoam ( $\sigma = 100$ kPa)	75% Cons.Mat. Sand 25% Bentonite Clay vs. Geofoam ( $\sigma = 100$ kPa)
Geofoam	Beach Sand vs. Geofoam ( $\sigma = 250$ kPa)	Construction Mat. Sand vs. Geofoam ( $\sigma = 250$ kPa)	Clay (Bentonite) vs. Geofoam ( $\sigma = 250$ kPa)	75% Cons.Mat. Sand 25% Bentonite Clay vs. Geofoam ( $\sigma = 250$ kPa)

#### 4. Experimental Investigations

The experimental findings will be presented in two subsections for which in the foremost one, the shear stress versus horizontal displacement curves obtained for different interface systems at distinct loading conditions will be demonstrated to expand the understanding on the characteristics of the observed interface behavior, and additionally, in the latter one, the frictional properties regarding to some important engineering design parameters including peak shear stress, residual shear stress, interface sensitivity (i.e. peak/residual ratio) and displacement required to reach peak stress determined as a result of the measured interface shear response curves will be presented. Further, the change in the values of those interface mechanical properties as a function of loading condition and counterface soil type will be shown.

##### 4.1. Interface test results: Shear response

The shear responses of different interface systems including the counterface materials such as bentonite clay, bentonite clay/construction material sand admixture, beach sand, and construction material sand at various normal loading conditions are demonstrated in Figures 2, 3, and 4 for the normal stress levels of 25 kPa, 100 kPa, and 250 kPa, respectively.

The measured shear stress increases with an increase in normal stress regardless of the material combinations at the interface. As such, the shear stress versus displacement envelope (i.e., curve), showing load versus deformation behavior, enlarges with an increase in normal stress by locating at upper space of shear stress versus displacement plots for all the interface systems comprised of either granular or cohesive soils or soil mixtures. Furthermore, additional important particular detail observed in the developed shear stress versus displacement curves is that the displacement softening behavior is exhibited for all the interface systems tested such that a reduction in shear stress is displayed indicating strength reduction with continued displacement develops at geof foam and soil contact surfaces. This is attributed to the shearing mechanism

mobilizing when a continuum material (geof foam) is counterfaced with particulate material (soil).

The largest shear stress versus displacement curves is observed at the interface of construction material sand compared to that of the interface of bentonite clay at which the smallest shear stress – displacement curves are shown regardless of the magnitude of loading applied onto the interface. In-between, the interface of beach sand demonstrates higher shear stress versus displacement curves (envelopes) compared to that of the soil mixture including 75% construction material sand and 25% bentonite clay by dry weight. This indicates that although the content of cohesive soil is less than the content of construction material sand by one-third, the clay initiates to predominate the interface behavior at the contact surface resulting in a reduction in frictional strength of the construction materials sand even below of the beach sand in the light of the diminishing (i.e. decrement) displayed in the curves of soil mixture in comparison to the curves of pure construction material sand due to addition of bentonite clay. Further, gradually progressive curves are observed for all the interface systems tested in such a way that, instead of sharp peak transformation, smoother transition develops at peak stages for soil – geof foam composite layered systems.

Further, although the physical and index properties of sand specimens were similar to each other, the construction material sand composed of grains (i.e. particles) possessing angular features in comparison to that of beach sand possessing subrounded features. This was purposefully intended to examine the influence of sand particle shape and geometry on the developed interface shear behavior and on the mobilized frictional strength characteristics such as engineering design parameters including peak shear stress, residual shear stress, interface sensitivity and displacement to peak. As shown in Figures 2-4, regardless of loading condition either low, medium, or high, the construction material sand specimens were able indent and plough through counterface geof foam surface owing to greater interlocking features of particles which resulted in obtaining relatively higher frictional resistances (i.e., larger shear strengths) at the interface during shearing displacement.

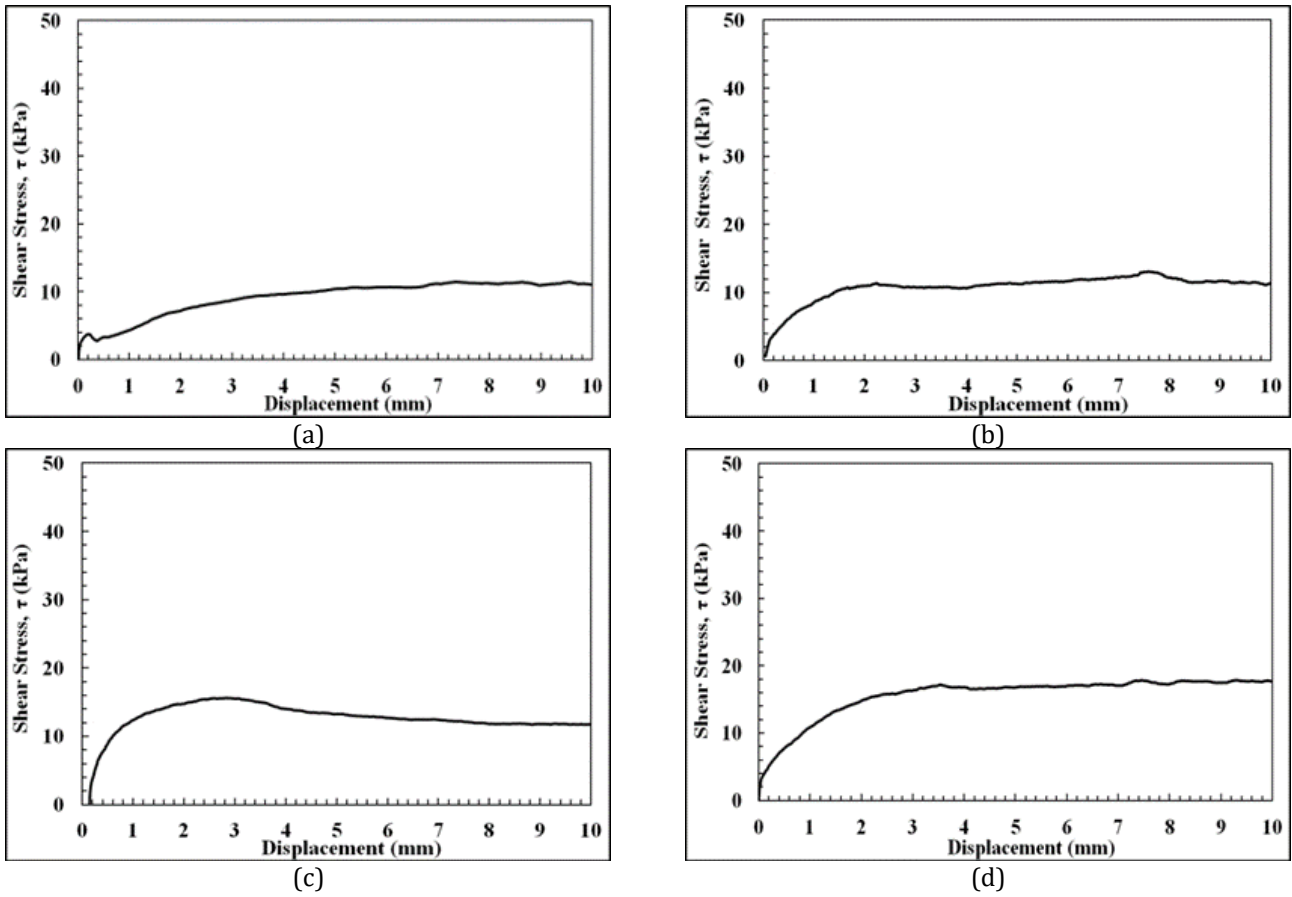


**Figure 2.** Shear response of different interface systems at 25 kPa normal stress level: **(a)** Bentonite clay; **(b)** Bentonite clay/construction material sand admixture; **(c)** Beach sand; **(d)** Construction material sand.

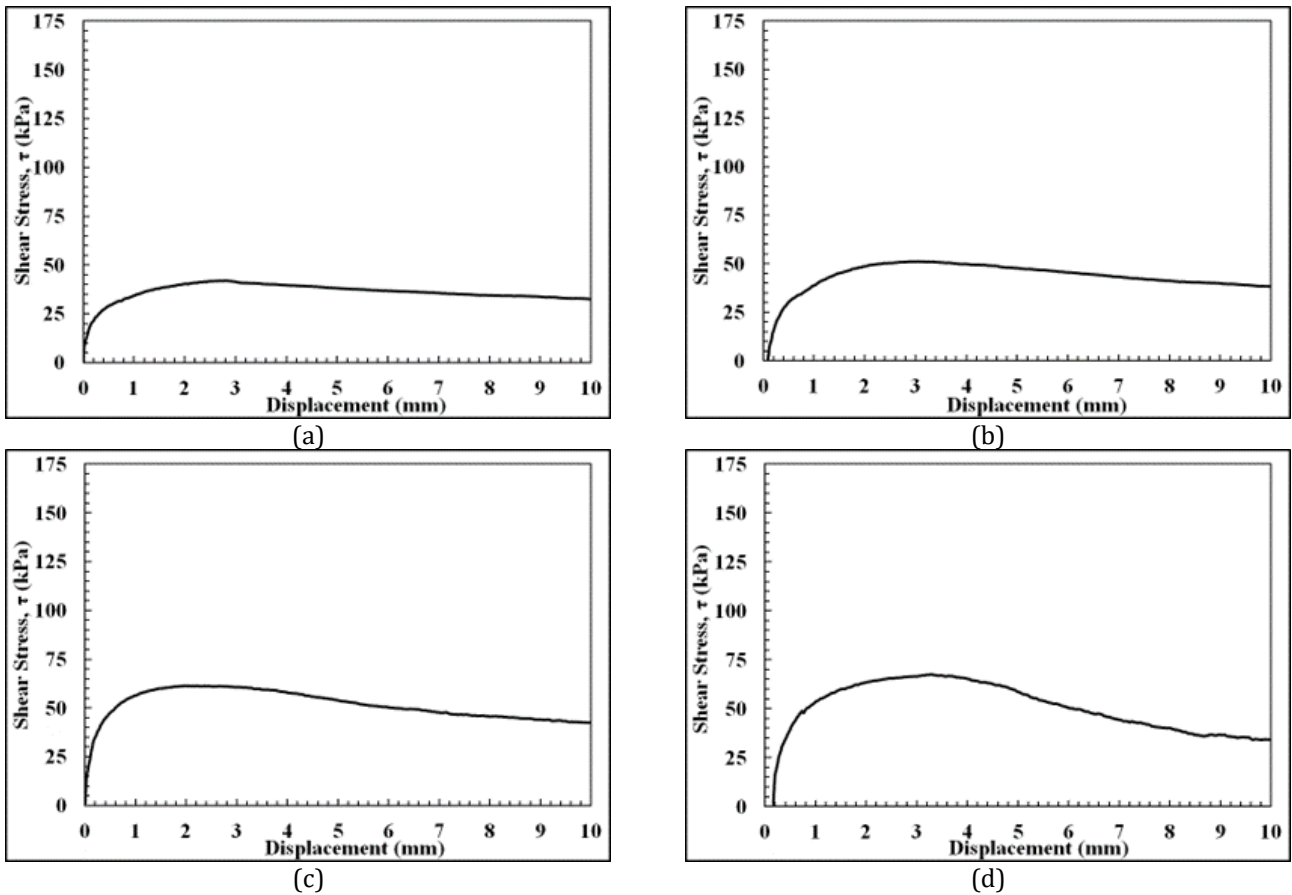


**Figure 3.** Shear response of different interface systems at 100 kPa normal stress level: **(a)** Bentonite clay; **(b)** Bentonite clay/construction material sand admixture; **(c)** Beach sand; **(d)** Construction material sand.

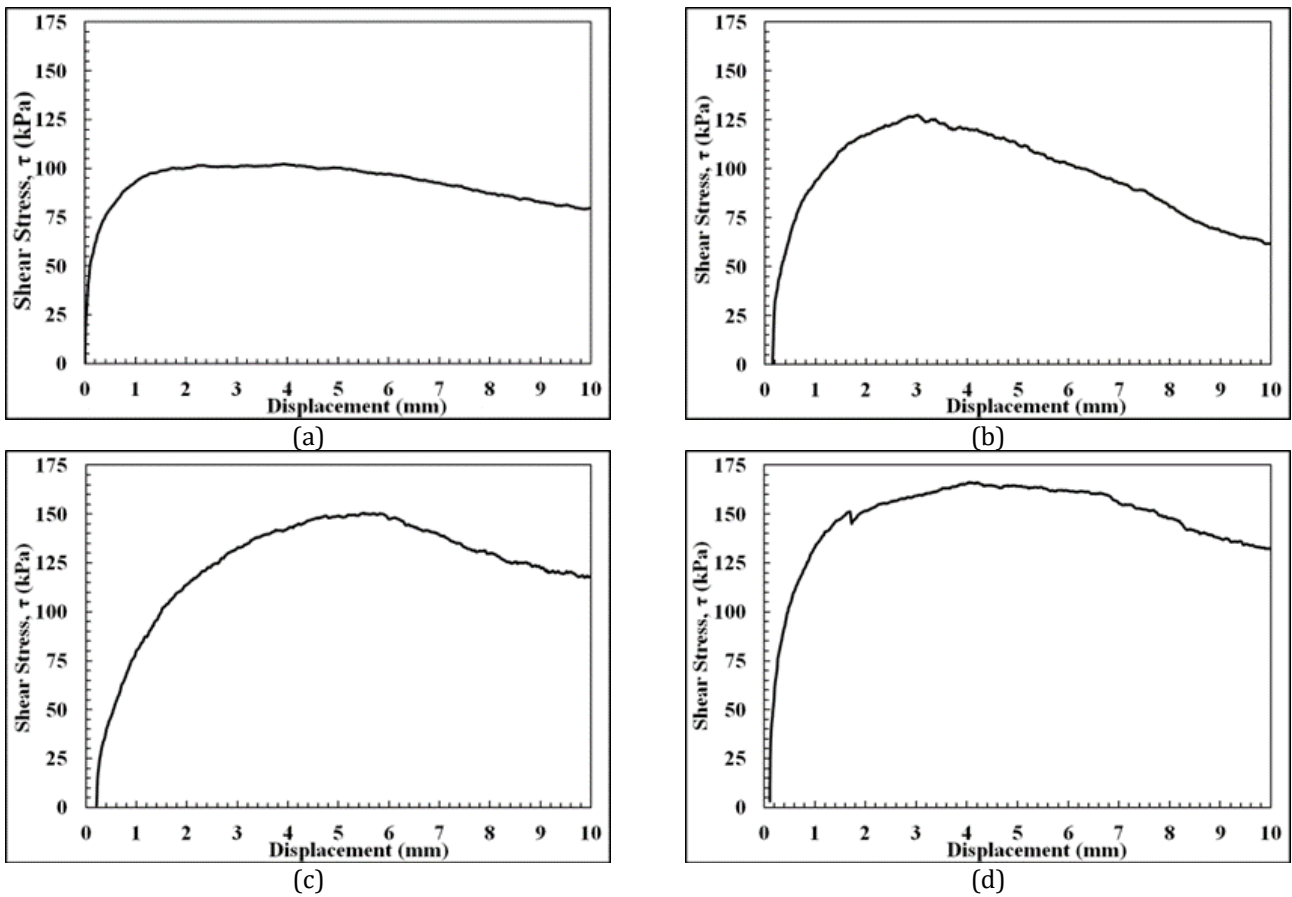


**Figure 4.** Shear response of different interface systems at 250 kPa normal stress level: **(a)** Bentonite clay; **(b)** Bentonite Clay/Construction material sand admixture; **(c)** Beach sand; **(d)** Construction material sand.

Moreover, the variation in vertical displacement during shearing for bentonite clay, bentonite clay/construction material sand admixture, beach sand, construction material sand interfaces are presented in Figures 5a, 5b, and 5c for various loading conditions (i.e., low, medium, high) including 25 kPa, 100 kPa, and 250 kPa, respectively. The surface topography of the man-made surface (i.e., a geosynthetic surface) was quantitatively linked to the stress and volume change behavior of the interface systems for the development of insightful interface behavior models in which the two general end-member conditions for the behavior of interfaces between soil and a man-made construction material (i.e., polymeric geosynthetics) were earlier defined in the literature [18-20]. The first condition was when the size of soil grains was large with respect to the asperity height and spacing on the construction material surface (e.g., a sand grain contacting a smooth geosynthetic surface). Experimental results for dense sand specimens against smooth geomembranes from Dove and Frost [20] indicated that soil volume changes were small and the soil above the interface did not participate in the shear process. These interface systems were referred to as nondilative as exhibited in the testing program by the interface system of bentonite clay as well as bentonite clay and construction material sand admixture soil. Further, it was showed that peak strength of nondilative interface systems was controlled by particle contact conditions which, in turn, are principally controlled by material hardness and surface roughness of the bodies at the scale of the contact. Moreover, the

second end member condition was defined as the situation in which there occurs significant volume changes and interface strength can reach frictional resistance levels as great as, or greater than the soil internal shear strength. These interface systems were referred to as dilative as exhibited in the testing program by the interface system of construction material sand as well as beach sand. Additionally, it is evident that it is possible to observe the occurrence of an infinite number of states between the nondilative and dilative conditions at particulate – continua contact surfaces. In light of the discussion provided herein, the variation in vertical displacement at the interface plotted against horizontal displacement for normal stress levels of 25, 100 and 250 kPa (Figures 5a, 5b and 5c, respectively) shows that the cohesive soil and its admixture soil – continua (i.e. geofilm) interface displayed relative contraction as shearing progresses due to the mobilization of increased frictional shear strength taking place at the interface at all loading conditions including low, medium, high normal stress levels of 25 kPa, 100 kPa, and 250 kPa, respectively. On the other hand, the variation in vertical displacement at the interface plotted against horizontal displacement for normal stress levels of 25, 100 and 250 kPa (Figures 5a, 5b and 5c, respectively) shows that the construction material sand and the beach sand– continua (i.e., geofilm) interface displayed relative dilation as shearing progresses due to larger resistance of the counterface material against the sand particles during the course of shearing in the tests with a greater contribution of the plowing effect mobilized mechanism

at the interface during shear such that sand grains in the interface were able to penetrate deeper into the surface of the geofoam. The sand specimen experienced a relative volumetric expansion to overcome the greater shear resistance of the counterface geofoam due to occurrence of deeper plowing of the grains during shear displacement. In addition, a relatively larger volumetric

dilation compared to that at the beach sand interface system was exhibited at the construction material sand interface system as a result of the angular features of the particles of construction material sand leading to greater penetration/embedment of grains into and plow through counterface geofoam surface.

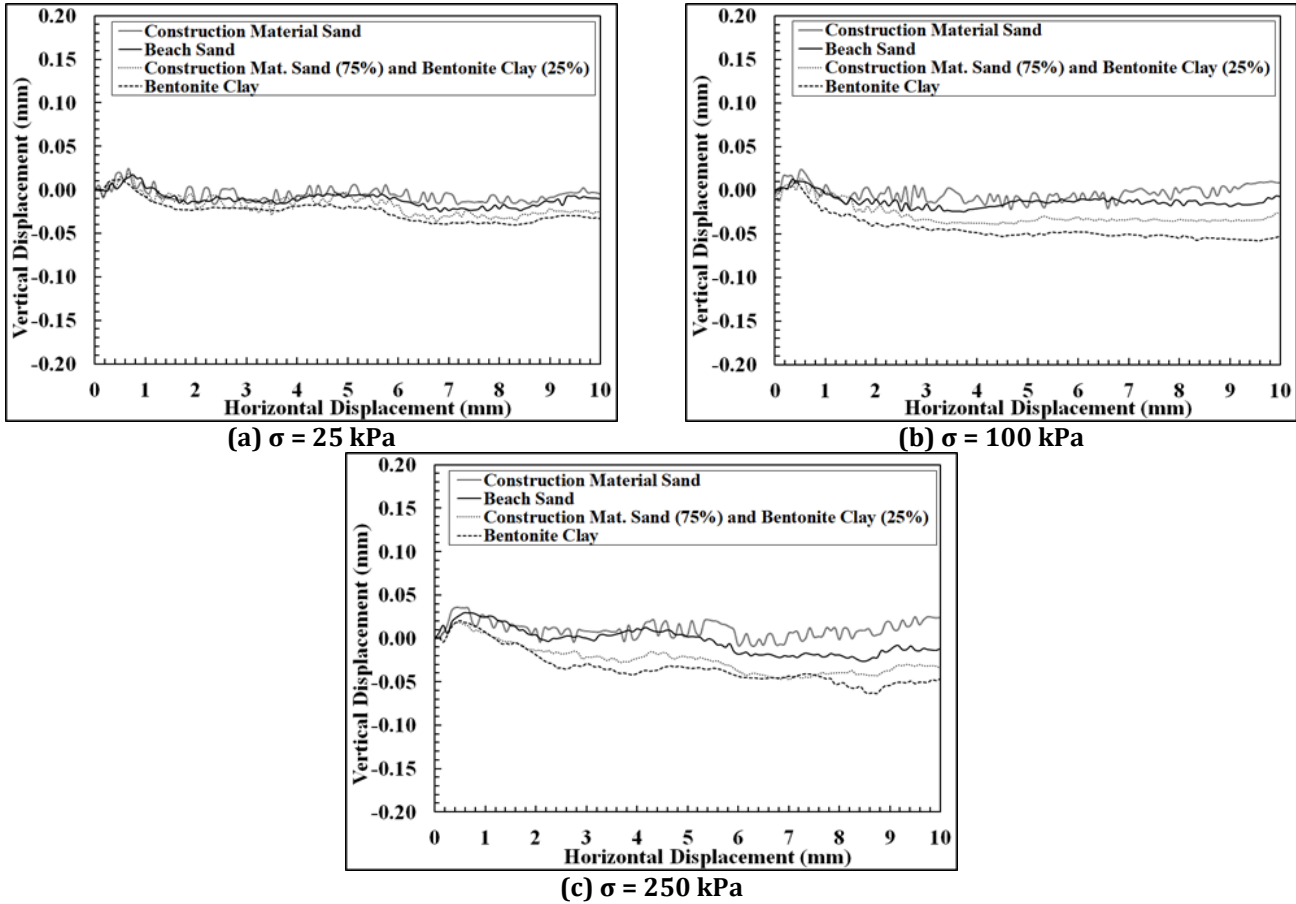


**Figure 5.** The variation in vertical displacement during horizontal displacement mobilized in interface shear tests at different normal loading conditions: **(a)** 25 kPa; **(b)** 100 kPa; **(c)** 250 kPa.

**4.2. Frictional properties: Engineering design parameters**

The characterization of shear response of geofoam – soil interfaces involve in determination of the frictional properties. These interface mechanical properties regard to some important engineering design parameters including peak shear stress, residual shear stress, interface sensitivity (i.e., peak/residual ratio) and displacement required to reach peak stress investigated as a result of the measured shear response curves. Figure 6 shows the frictional strength and deformation properties of the different soil versus geofoam interface systems tested in the entire experimental program. At all normal stress levels including 25 kPa, 100 kPa and 250 kPa, the greatest peak shear strength ( $\tau_{Peak}$ ) was obtained in the interface system of construction material sand followed by beach sand, soil mixture (75% sand and 25% clay) and bentonite clay in a decreasing order of the measured magnitude of  $\tau_{Peak}$  at the interface. Similarly, the construction material sand interface system exhibited the largest residual shear strength ( $\tau_{Residual}$ ) mobilized that is followed by a sequential decrease in the

measured values for the magnitudes of  $\tau_{Residual}$  attained in the interface system of beach sand, soil mixture (75% sand and 25% clay) and bentonite clay. Therefore, among the interface systems tested, the lowest values of both  $\tau_{Peak}$  and  $\tau_{Residual}$  were observed in the cohesive soil (bentonite clay) interface at all loading conditions; low, moderate and high stress levels. Consequently, the granular material interfaces displayed larger frictional resistance when counterfaced with geofoams as compared to that of cohesive soil interfaces not only for the peak state but also for the residual state of the interface in the circumstances when subjected to shear displacement or lateral deformation under the action of mechanical loading.

Moreover, comparing different interface systems, the trend for  $\tau_{Peak}$  and  $\tau_{Residual}$  were similar such that the difference in the measured values for different counterface materials (granular, cohesive soil or mixture) were largest at 250 kPa normal stress level, whereas were lowest at 25 kPa normal stress (Figures 6a and 6b). In order to assess load versus deformation characteristics of interfaces for composite layered systems, an engineering parameter being displacement

required to reach peak shear strength was also determined for the different interface systems tested. The highest values were observed in the interface of construction material sand regardless of the magnitude of loading followed by the interface system being its mixture with bentonite clay (75% construction material

sand and 25% bentonite clay). For the interfaces of pure bentonite clay as well as pure beach sand, the almost similar values were attained with an exception of high normal stress level of 250 kPa where the bentonite clay interface displayed slightly (marginally) greater values of displacement to peak (Figure 6c).

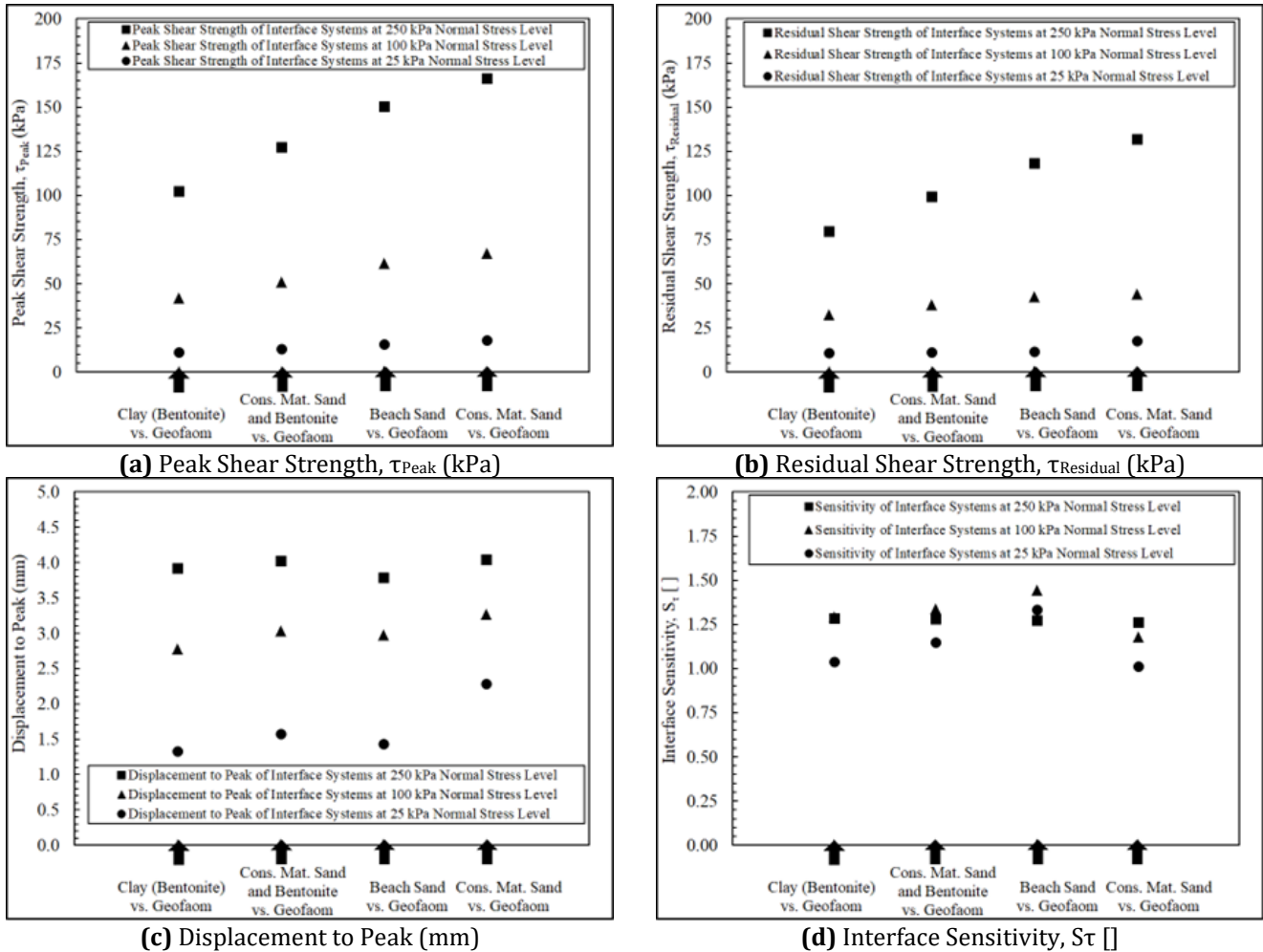


Figure 6. Frictional strength and deformation properties of different soil vs. Geof foam interface systems.

Furthermore, the interface sensitivity that is the ratio of peak shear strength with respect to residual shear strength ( $S_r = \tau_{Peak}/\tau_{Residual}$ ) was computed for all interface systems. This is a very important interface mechanical property, gauging deterioration of frictional resistance, and thus, allowing to quantify the amount and magnitude of strength reduction at the interface with the continued displacement in order to evaluate the degree of strain softening behavior mobilized at the contact surface of geof foam – soil composite layered systems. The more or less analogous sensitivity values were attained at 250 kPa high normal stress level for all the interface systems tested. On the other hand, at low and moderate stress levels of 25 kPa and 100 kPa, respectively, the highest sensitivity was observed in the interface system of beach sand whereas the lowest sensitivity was depicted in that of construction material sand. A trivial (very minor) difference in the sensitivities for the interface system of bentonite and soil mixture (sand and clay) was observed at 25 kPa and 100 kPa loading conditions as well (Figure 6d).

### 5. Further Analysis on Test Results

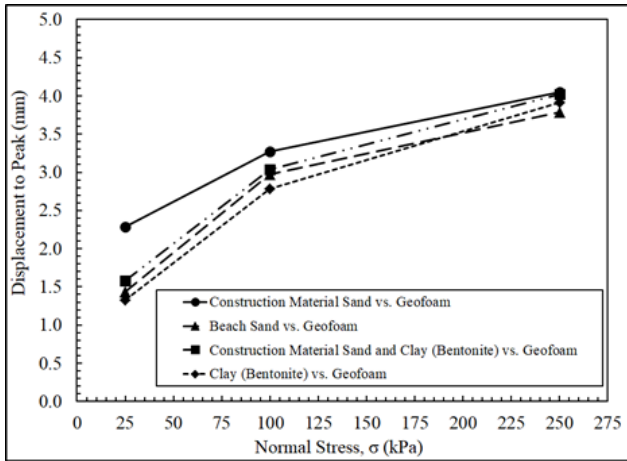
A further comparative analysis on test results was performed to extend understanding on the general interface behavior and shear response. To this end, the displacement required to reach peak interface strength being an important and decisive frictional property for the distinct interface systems tested was determined and the variation of which with increasing normal stress ( $\sigma$ ) was plotted and presented in Figure 7a.

Similar behaviors were observed for the tested different systems in consideration such that the displacements necessitated arriving to peak strength conditions increased at a relatively higher rate from low loading conditions ( $\sigma = 25$  kPa) until medium loading conditions ( $\sigma = 100$  kPa), and thereafter, the rate of this increment became lower and the increase in displacement to peak maintained up to the largest loading conditions ( $\sigma = 250$  kPa). This shows that, regardless of counterface soil type (sand and/or clay), the peak strength conditions could be obtained at greater shearing displacements at soil – geof foam interfaces.

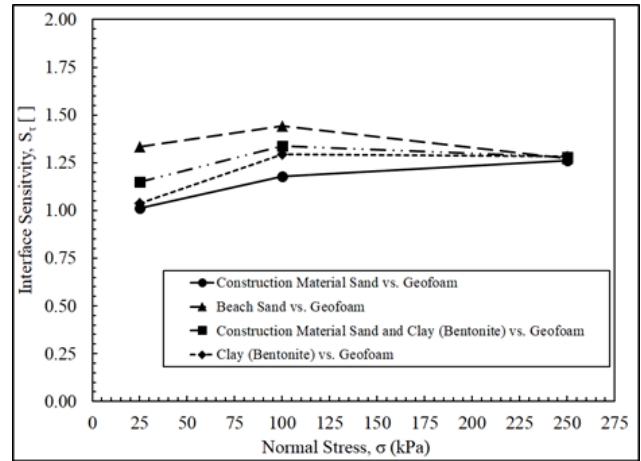
Further, this is attributed to the larger confinement/restraint of the interface at greater normal stresses (i.e.,  $\sigma > \sim 100$  kPa).

The change in another critical frictional property for assessing shearing response of soil – geofabric interfaces being interface sensitivity ( $S_\tau$ ) with respect to a change in normal stress is shown in Figure 7b. In general, an increase in the detected values of  $S_\tau$  is displayed for all the interface systems tested from low normal stress level of 25 kPa up to medium normal stress level of 100 kPa, however, beyond which the detected values of  $S_\tau$  up to high normal stress level of 250 kPa decreased slightly

(i.e., trivial reductions are exhibited) for the construction material and clay as well as the beach sand interface systems; maintained approximately constant for the pure clay interface system; and increased marginally for the pure construction material sand interface system. The contrary response observed in the last interface system is attributed to the mechanism of ploughing of angular construction material sand particles through counterface geofabric surface as a result of shearing displacement developed at the interface which results in mobilization of greater residual strengths at continued larger displacements.



(a) Displacement to Peak

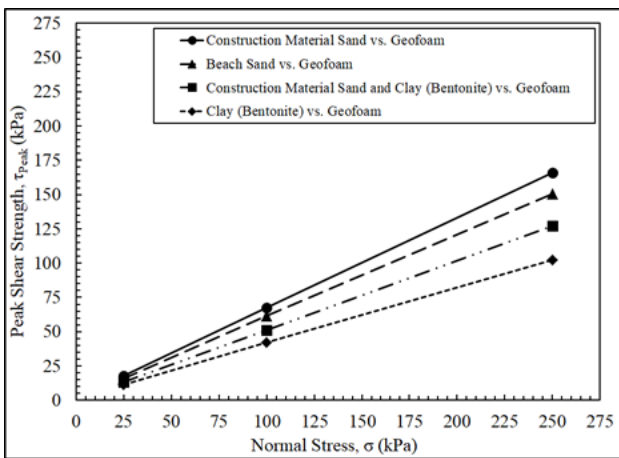


(b) Interface Sensitivity

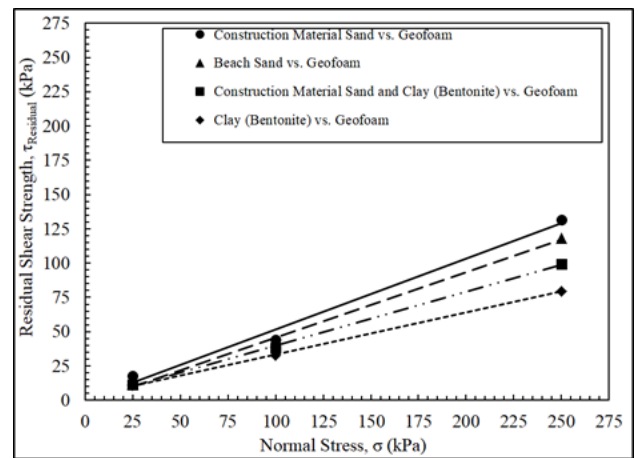
Figure 7. The variation in Displacement to Peak (a) and Interface Sensitivity (b) with respect to normal stress.

Based on Mohr-Coulomb criterion, the resulting linear peak strength as well as residual strength failure envelopes from interface shear tests performed on a variety of distinct soil – geofabric systems under different load conditions over a large range of normal stresses from 25 kPa up to 250 kPa are presented in Figures 8a and 8b, respectively. The linear Coulomb-type failure envelopes (Figure 8), generated using least square fit method, were drawn through the data points for a range of normal stresses expected in the field in such a way that

those failure envelopes are defined in terms of two interface shear strength parameters which are the interface friction angle ( $\delta$ ) representing its inclination in the shear stress versus normal stress space; and adhesion ( $\alpha$ ) representing the intercept of the failure envelope with the shear stress axis so that the stability of any slope containing a soil – geofabric interface can be evaluated using these interface shear strength parameters (i.e., frictional properties of interface response).



(a) Peak Strength



(b) Residual Strength

Figure 8. Peak Strength (a) and Residual Strength (b) Failure Envelopes for different interface systems.

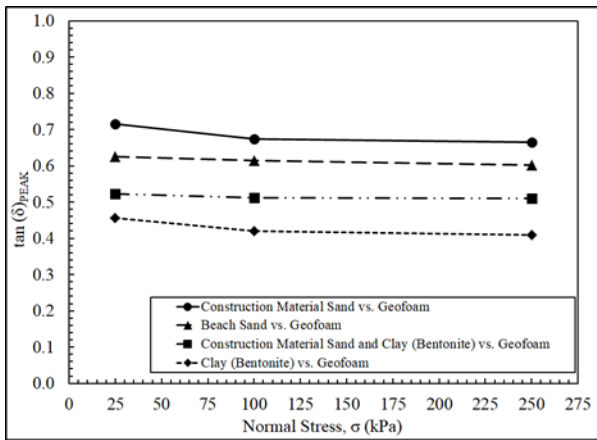
The plots in Figure 8, providing good straight line fits for all the interface systems tested, were developed on a purpose to capture variations in granular soil and/or cohesive soil versus geofabric interface shear behavior as

a function of normal stress levels ranging from low loading conditions to very high loading conditions. All the tested soil (granular and/or cohesive) – geofabric composite interface systems clearly exhibited both linear

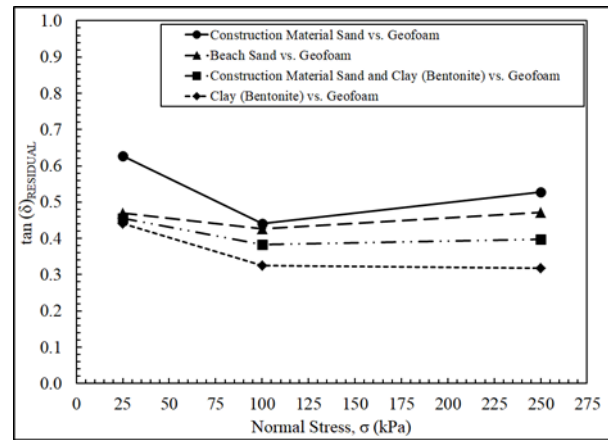
peak and residual strength envelopes over the entire range of normal stresses applied in the laboratory experimental program. Furthermore, it is evident from a comparison of the strength envelopes that the construction material sand system yielded the highest both peak and residual shear strengths, while the bentonite clay system displayed the lowest both peak and residual shear strength over the entire range of normal stresses from 25 kPa up to 250 kPa. The beach sand system exhibited relatively larger both peak and residual shear strengths as compared to that of an admixture soil system including construction material sand and bentonite clay. This is due to the existence of bentonite clay in the admixture leading to reduction of interface frictional resistance sheared against geofoam.

Moreover, among all the interface systems tested, the greatest slope both in peak and residual failure envelopes were obtained in construction material sand interface, while the smallest slope in peak as well as residual envelopes were exhibited by the bentonite clay interface. Furthermore, the slope of both peak and residual failure envelopes for the beach sand interface were larger than that of the admixture soil interface including construction material sand and bentonite clay. Regardless of strength condition; peak or residual, the failure envelopes of construction material sand located at the highest location in shear stress versus normal stress space followed by the order of beach sand, admixture soil, and bentonite clay, respectively.

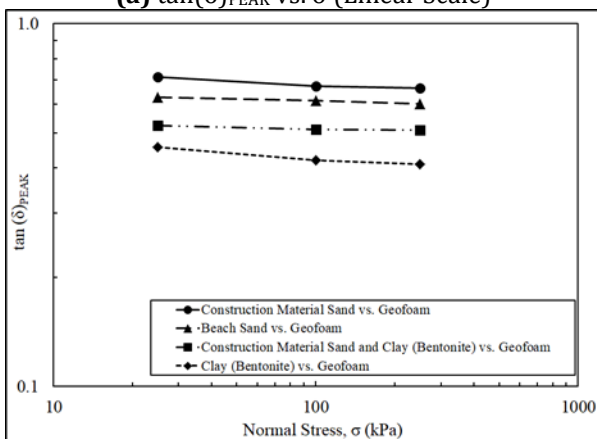
The coefficient of friction ( $\tan(\delta)$ ) versus normal stress plotted on both linear and logarithmic scale as shown in Figures 9a, 9c for peak state and Figures 9b, 9d for residual state, respectively. As evidently seen in Figure 9, the peak coefficient of friction ( $\tan(\delta)_{\text{Peak}}$ ) for all the tested granular and/or cohesive soil – geofoam interface systems decreased with normal stress at low normal stress levels up to ~100 kPa that is consistent with Hertzian contact theory [18, 19]. Further, under high normal stress levels beyond ~100 kPa up to ~250 kPa, the peak coefficient of friction ( $\tan(\delta)_{\text{Peak}}$ ) became more or less constant and remained in this fashion until the greatest loading condition of 250 kPa. The residual coefficient of friction ( $\tan(\delta)_{\text{Residual}}$ ) for all the tested systems decreased with normal stress at low normal stresses up to ~100 kPa. On the other hand, under high normal stresses beyond ~100 kPa up to ~250 kPa, the residual coefficient of friction ( $\tan(\delta)_{\text{Residual}}$ ) increased considerably for granular soil (construction sand and beach sand) interface systems, while remained approximately constant for cohesive soil (bentonite clay) and its admixture soil (bentonite clay and sand) interface systems. This increase is evidently observed particularly in the plot generated using logarithmic scales on both axes (Figure 9d). This is attributed to the higher interbedding occurring between the counterfaces at larger normal loads and is considered to be the influence of the ploughing effect that is often detected at granular material versus planar surface interfaces as previously noted by Dove and Frost [20].



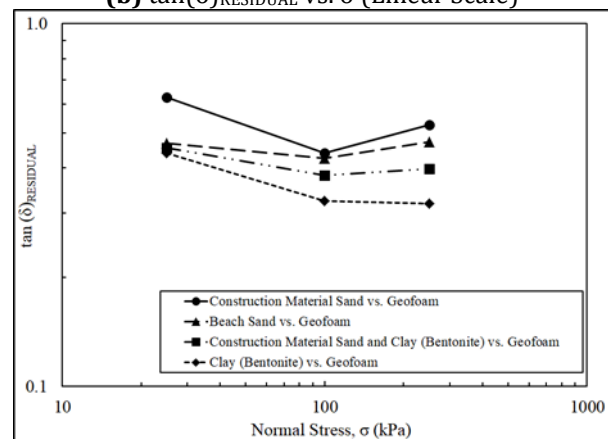
(a)  $\tan(\delta)_{\text{PEAK}}$  VS.  $\sigma$  (Linear Scale)



(b)  $\tan(\delta)_{\text{RESIDUAL}}$  VS.  $\sigma$  (Linear Scale)



(c)  $\tan(\delta)_{\text{PEAK}}$  VS.  $\sigma$  (Logarithmic Scale)



(d)  $\tan(\delta)_{\text{RESIDUAL}}$  VS.  $\sigma$  (Logarithmic Scale)

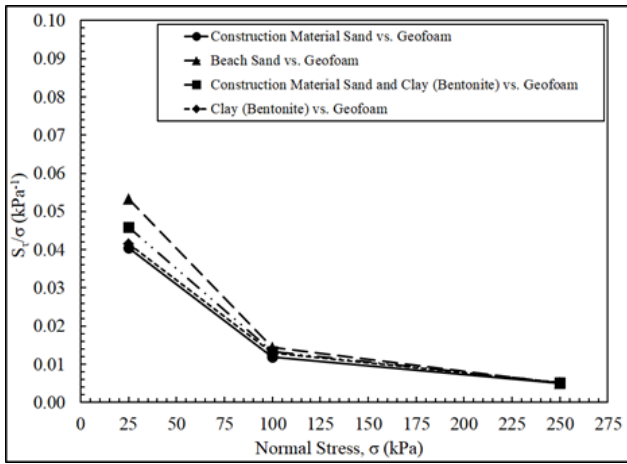
Figure 9. The Change in Interface Strength Parameters; Peak as well as Residual Coefficient of Frictions as a function of Normal Stress on Linear Scale (a), (b) and on Logarithmic Scale (c), (d).

### 6. Comparative Discussions on Experimental Findings

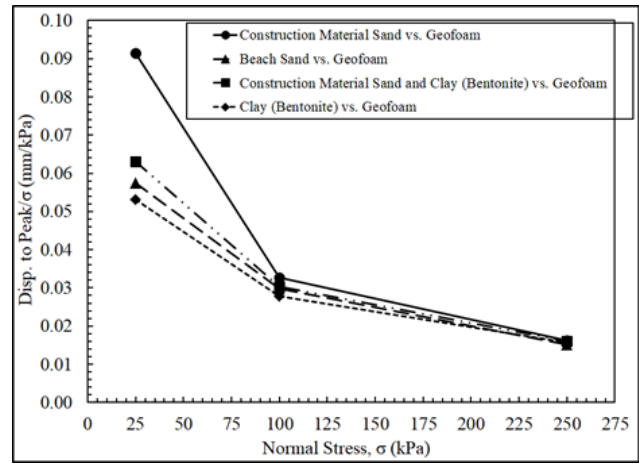
The variation in normalized interface engineering design parameters including normalized sensitivity as well as normalized displacement to peak as a function of normal stress are presented in Figures 10a and 10b, respectively.

As earlier described in Section 4.2., the post-peak strength loss exhibited by an interface can be quantified with a ratio called interface sensitivity ( $S_{\tau}$ ) between peak and residual shear strengths. As such, the differences between the peak stress state relative to the residual stress response of the tested granular and/or cohesive soil versus geofabric interface systems as a function of loading condition can quantitatively be measured and explicitly demonstrated by the interface sensitivity ( $S_{\tau}$ ) normalized with normal stress ( $\sigma$ ) (Figure 10a). For all the tested interface systems, the normalized sensitivity

( $S_{\tau}/\sigma$ ) decreased significantly and sharply at a higher rate with increasing normal stress from 25 kPa until 100 kPa beyond which the rate of this decrease reduced, but the slight decrement in the value of the normalized sensitivity ( $S_{\tau}/\sigma$ ) maintained up to the largest normal stress level of the testing program (250 kPa). This indicates for granular and/or cohesive soil – geofabric interfaces that a substantial reduction (i.e., about 70% to 75% decrease) was exhibited from low level to medium level loading conditions, while a marginal reduction (i.e., about 20% to 25% decrease) was displayed from medium level up to high level loading conditions in the detected value of  $S_{\tau}/\sigma$ , respectively. Consequently, it is noted that the amount of reduction in frictional strength/resistance of both granular and cohesive soil – geofabric interface systems from peak state to residual state when normalized with the magnitude of normal stress applied during shearing became trivial and minor with increasing normal loading.



(a) Normalized Sensitivity



(b) Normalized Displacement to Peak

**Figure 10.** The variation in normalized interface engineering design parameters; normalized sensitivity (a) as well as normalized displacement to peak (b) as a function of normal stress

The displacement required to reach peak strength state as normalized with the magnitude of normal stress level during shearing process as a function of loading conditions is shown in Figure 10b. As similar to the normalized sensitivity, a sharp decrease with a high rate of reduction (with a very high rate of reduction particularly for construction material sand system) was observed in the detected value of normalized displacement to peak parameter from low loading conditions of 25 kPa until medium loading conditions of 100 kPa beyond which a considerable decrease with a relatively smaller rate of reduction is followed up until large loading conditions of 250 kPa. It is remarkable that the largest amount of reduction in the value of normalized displacement to peak parameter from 25 kPa until 100 kPa was exhibited by the construction material sand interface system (i.e., about 65%) as compared to those of the other interface systems (i.e., ranging about between 40% to 45%) tested. All the systems including granular and/or cohesive soil – geofabric interfaces displayed similarly equivalent subsidiary decreases (i.e., minor) in the values of displacement to peak parameters from 100 kPa up to 250 kPa (i.e., reductions about 30%). This points out and specifies that the necessary

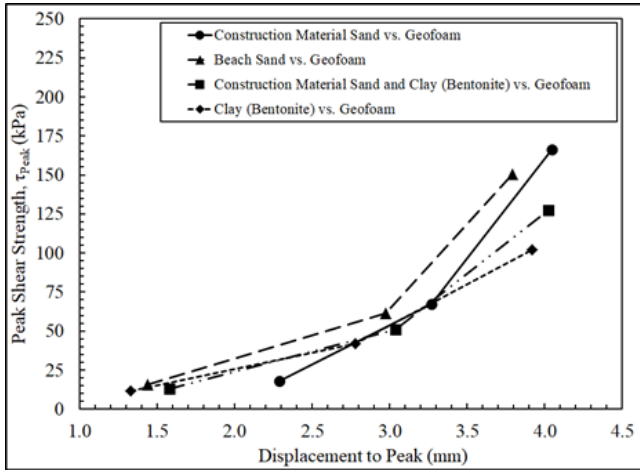
displacement required to be mobilized at the interface during shearing when normalized with the magnitude of applied normal load demonstrates a continuous decrease in the measured value as a function of normal stress level. Additionally, the observed behavior in construction sand interface system is different than those of the other systems due to angular features of soil grains (i.e., sand particles).

Furthermore, the variation in two critical interface strength engineering design parameters including peak shear strength and interface sensitivity with respect to displacement to peak are presented in Figures 11a and 11b, respectively. Among all the tested systems, the construction material sand interface evidently showed a distinct behavior with increasing displacement to peak.

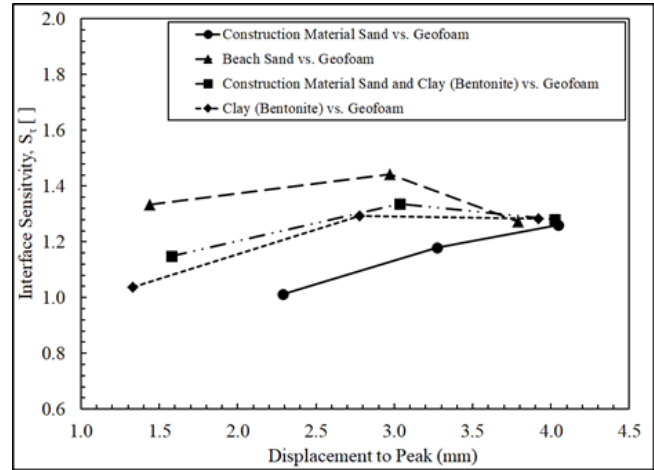
The relationship between peak shear strength ( $\tau_{Peak}$ ) and displacement to peak parameter as shown in Figure 11a is a two stage behavior that was observed for all the systems tested along with a continuous increase in the resultant magnitude of peak shear strength with respect to the measured amount of displacement necessitated to arrive/reach to peak frictional resistance state. The increase in the detected resultant value of peak shear strength comprised of small slope increment for the

displacements from around 1.5 mm until around 3.0 mm; and large slope increment for the displacements from around 3.0 mm up to 4.0 mm. This shows that relatively larger displacements are necessary for the mobilization of higher peak frictional resistances during shearing to generate peak strength state at the interface of both granular and/or cohesive soil – geofabric interfaces. This is attributed to the characteristics of shearing mechanisms that develops particulate soil – planar

continuum geosynthetic interfaces such that the mobilized shear strength results from the relative contributions of the soil particle shearing mechanism including sliding and rolling or ploughing along or into, respectively, the counterface geosynthetic (i.e., geofabric) surface. The sliding and/or ploughing forces combine together to produce total frictional resistance at the interface against shear displacement [21, 22].



(a)  $\tau_{Peak}$  vs. Displacement to Peak



(b)  $S_{\tau}$  vs. Displacement to Peak

**Figure 11.** The relationship between  $\tau_{Peak}$  (a) as well as  $S_{\tau}$  (b) and displacement to peak.

The variation in interface sensitivity ( $S_{\tau}$ ) with respect to displacement to peak, as presented in Figure 11b, depicts evidently more or less similar behaviors for all the systems tested with an exception of construction material sand interface. For the other interface systems tested, an increase in the resultant detected values of  $S_{\tau}$  exhibited starting at the displacements from about 1.5 mm until about 3.0 mm beyond which the increment has ended by displaying a saturation plateau and the trend in the variation of  $S_{\tau}$  has become lateral by maintaining approximately constant in the resultant detected values of  $S_{\tau}$ . However, for construction material sand interface system, a continued rise in the resultant detected values of  $S_{\tau}$  was demonstrated over the entire range of the displacements from about 2.0 mm up to about 4.0 mm. A very minor/trivial decrease in the rate of increment for the resultant values of  $S_{\tau}$  was seen at about 3.0 mm displacement being roughly the half way between the departure (2.0 mm) and the arrival (4.0 mm) displacements. The distinct behavior observed in the interface system of construction material sand is due to angular sharp features of soil particles/grains that result in the mobilization of ploughing at the interface [23, 24] whereas the shearing mechanism, in general, is predominated by sliding and/or rolling over the areal extent of the other interface systems tested including beach sand comprised of rounded smooth granular features and bentonite clay consist of cohesive platy-like very fine particles.

The inter-relationship between peak shear strength ( $\tau_{Peak}$ ) as well as residual shear strength ( $\tau_{Residual}$ ) and interface sensitivity ( $S_{\tau}$ ) is presented in Figures 12a and 12b, respectively. It is clearly seen from the comparison of Figure 12a with Figure 12b that, for the selected interface systems, both the peak shear strength and the

residual shear strength displayed similar behaviors as a function of increased sensitivity. This indicates that the test measurements are robust, consistent and precise regardless of the counterface materials existed at the interface during shearing including granular and/or cohesive soil and geosynthetic geofabric.

For the construction material sand interface system, the peak as well as residual shear strength increased at a slower rate with increasing sensitivity from  $S_{\tau}=1.00$  until  $S_{\tau}=1.20$ , and subsequently, the rate of this increase has become faster and greater by depicting a sharp rise up to the highest recorded sensitivity of the system ( $S_{\tau}=1.20$ ) in the experimental program.

As opposed to that of construction material sand system, the other interface systems including smooth rounded beach sand, cohesive bentonite clay and its admixture with sand displayed similar trends in behavior. As such, the resultant measured values of both peak shear strength ( $\tau_{Peak}$ ) and residual shear strength ( $\tau_{Residual}$ ) with increasing interface sensitivity ( $S_{\tau}$ ) showed lower rate increase from  $S_{\tau}=1.35$  until  $S_{\tau}=1.45$ ; from  $S_{\tau}=1.05$  until  $S_{\tau}=1.30$ ; from  $S_{\tau}=1.15$  until  $S_{\tau}=1.35$  for beach sand interface, bentonite clay interface and its admixture with sand system, respectively; and thereafter, an inversely proportional behaviors were observed for all three interface systems in consideration up to the largest magnitude of both  $\tau_{Peak}$  and  $\tau_{Residual}$  frictional resistances measured for the corresponding interface systems. This is attributed to the modification of shearing mechanism mobilized over the entire areal extent of the interface due to shear displacement from sliding/rolling to ploughing at greater normal stress conditions particularly above 100 kPa, and as a result of which the induced and recorded greater shear stresses at

peak as well as residual state on to the counterface material during shearing displacement [25 – 27].

To sum up, in addition to counterface soil type either granular or cohesive and/or their admixtures, the level of loading conditions either low, medium, high will certainly and significantly influence the resultant frictional behavior exhibited at the interface of composite systems (i.e., granular and/or cohesive soil versus geosynthetic geofabric) during the course of shear displacement mobilized and progressed over the overall extent of contact area of counterface materials.

Consequently, in design and application of such composite layered systems, the selection of counterface materials and their compatibility play a critical and crucial role as per implementation of engineering activities for the development of infrastructural facilities in geotechnical profession. In this regard, the compatibility and/or interaction of counterface materials is of importance for proper development of strength at the interface that is vital for the durability of infrastructural facility.

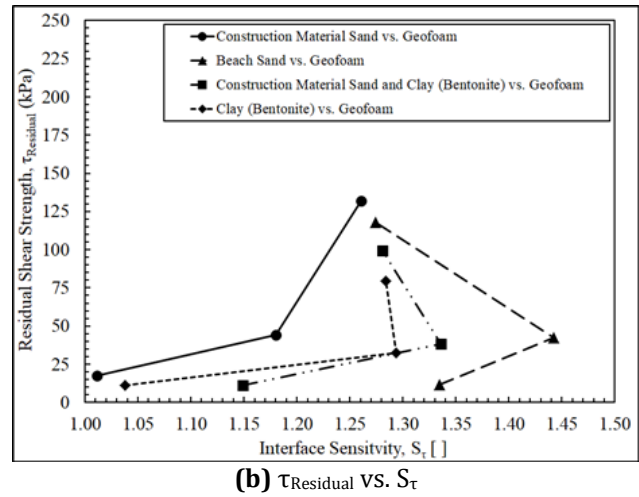
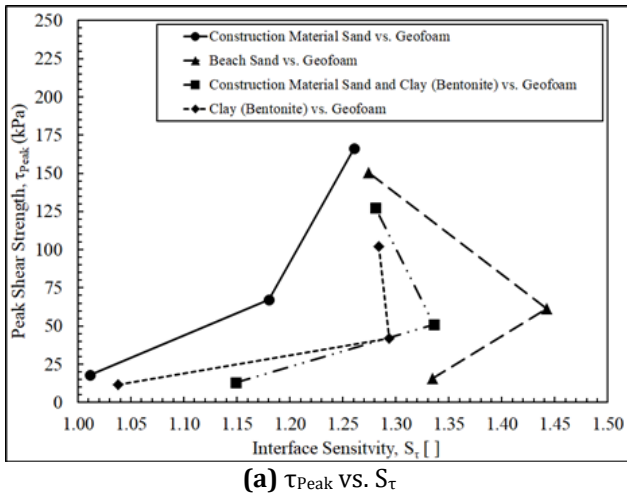


Figure 12. The inter-relationship between  $\tau_{Peak}$  (a) as well as  $\tau_{Residual}$  (b) and  $S_t$ .

### 7. Conclusion

The frictional resistance and the type of shear response mobilizing at soil – geofabric interfaces control the stability of composite layered systems, and hence, govern the integrity of the infrastructure constructed using geofabrics counterfaced with soils. To this end, soil – geofabric interfaces were studied through an extensive experimental program by performing multiple series of interface shear tests using two different granular soils (i.e., beach sand and construction material sand) and one cohesive soil (i.e., bentonite clay) as well as a soil mixture containing 75% sand and 25% clay by dry weight at distinct loading conditions (i.e., normal stresses: 25, 100, 250; low, moderate, high loading conditions, respectively). The following principle key conclusions are drawn based on the attained test results and experimental findings as well as in light of further comparative analysis conducted on experimental investigations:

- Regardless of counterface soil type (sand and/or clay), the peak strength conditions could be obtained at greater shearing displacements at soil – geofabric interfaces. This is attributed to the larger confinement/restraint of the interface at greater normal stresses (i.e.,  $\sigma > \sim 100$  kPa).
- The resultant detected values of interface sensitivity ( $S_t$ ) for the construction material sand system displayed a continued increase over the entire range of loading conditions (25 kPa– 250 kPa). This contrary response observed in the construction material sand interface is attributed

to the mechanism of ploughing of angular construction material sand particles through counterface geofabric surface as a result of shearing displacement developed at the interface which results in mobilization of greater residual strengths at continued larger displacements.

- All the tested soil (granular and/or cohesive) – geofabric composite interface systems clearly exhibited both linear peak and residual strength envelopes over the entire range of normal stresses applied in the laboratory experimental program.
- Furthermore, the construction material sand system yielded the highest both peak and residual shear strengths, while the bentonite clay system displayed the lowest both peak and residual shear strength over the entire range of normal stresses from 25 kPa up to 250 kPa. The beach sand system exhibited relatively larger both peak and residual shear strengths as compared to that of an admixture soil system including construction material sand and bentonite clay. This is due to the existence of bentonite clay in the admixture leading to reduction of interface frictional resistance sheared against geofabric.
- Moreover, among all the interface systems tested, the greatest slope both in peak and residual failure envelopes were obtained in construction material sand interface, while the smallest slope in peak as well as residual envelopes were exhibited by the bentonite clay interface.
- The peak coefficient of friction ( $\tan(\delta)_{Peak}$ ) for all the tested granular and/or cohesive soil – geofabric interface systems decreased with normal

stress at low normal stress levels up to ~100 kPa that is consistent with Hertzian contact theory. Further, under high normal stress levels beyond ~100 kPa up to ~250 kPa, the peak coefficient of friction ( $\tan(\delta)_{\text{Peak}}$ ) became more or less constant and remained in this fashion until the greatest loading condition of 250 kPa.

- The residual coefficient of friction ( $\tan(\delta)_{\text{Residual}}$ ) for all the tested systems decreased with normal stress at low normal stresses up to ~100 kPa. On the other hand, under high normal stresses beyond ~100 kPa up to ~250 kPa, the residual coefficient of friction ( $\tan(\delta)_{\text{Residual}}$ ) increased considerably for granular soil (construction sand and beach sand) interface systems, while remained approximately constant for cohesive soil (bentonite clay) and its admixture soil (bentonite clay and sand) interface systems. This is attributed to the higher interbedding occurring between the counterfaces at larger normal loads and is considered to be the influence of the ploughing effect that is often detected at granular material versus planar surface interfaces.
- To sum up, in addition to counterface soil type either granular or cohesive and/or their admixtures, the level of loading conditions either low, medium, high will certainly and significantly influence the resultant frictional behavior exhibited at the interface of composite systems (i.e. granular and/or cohesive soil versus geosynthetic geof foam) during the course of shear displacement mobilized and progressed over the overall extent of contact area of counterface materials.
- Consequently, in design and application of such composite layered systems, the selection of counterface materials and their compatibility play a critical and crucial role as per implementation of engineering activities for the development of infrastructural facilities in geotechnical profession. In this regard, the compatibility and/or interaction of counterface materials is of importance for proper development of strength at the interface that is vital for the durability of infrastructural facility.

### Conflicts of interest

The authors declare no conflicts of interest.

### References

1. Padade, A. H., & Mandal, J. N. (2012). Behavior of expanded polystyrene (EPS) geof foam under triaxial loading conditions. *Electronic Journal of Geotechnical Engineering*, 17, 2542-2553.
2. Leo, C. J., Kumruzzaman, M., Wong, H., & Yin, J. H. (2008). Behavior of EPS geof foam in true triaxial compression tests. *Geotextiles and Geomembranes*, 26(2), 175-180. <https://doi.org/10.1016/j.geotexmem.2007.10.005>
3. Trandafir, A. C., Bartlett, S. F., & Lingwall, B. N. (2010). Behavior of EPS geof foam in stress-controlled cyclic uniaxial tests. *Geotextiles and Geomembranes*, 28(6), 514-524. <https://doi.org/10.1016/j.geotexmem.2010.01.002>
4. Tolga Özer, A., & Akay, O. (2022). Interface shear strength of EPS-concrete elements of various configurations. *Journal of Materials in Civil Engineering*, 34(6), 04022102. [https://doi.org/10.1061/\(ASCE\)MT.1943-5533.0004251](https://doi.org/10.1061/(ASCE)MT.1943-5533.0004251)
5. Yilmaz, B., & Türköz, M. (2022). Determination of shear strength parameters of compacted high plasticity clay soils based on different laboratory tests. *Turkish Journal of Engineering*, 6(4), 313-319. <https://doi.org/10.31127/tuje.1004043>
6. Ertuğrul, Ö. L., & Canoğulları, F. D. (2021). An investigation on the geomechanical properties of fiber reinforced cohesive soils. *Turkish Journal of Engineering*, 5(1), 15-19. <https://doi.org/10.31127/tuje.651222>
7. Öztürk, O., & Türköz, M. (2022). Effect of silica fume on the undrained strength parameters of dispersive. *Turkish Journal of Engineering*, 6(4), 293-299. <https://doi.org/10.31127/tuje.1001413>
8. Horvath, J. S. (1995). *Geof foam Geosynthetic*, published by Horvath Engineering, PC, Scarsdale, New York, USA.
9. Horvath, J. S. (1996). The compressible inclusion function of EPS geof foam: an overview. In *Proceedings of international symposium on eps (expanded polystyrol) construction method (EPS Tokyo'96)*, 72-81.
10. Horvath, J. S. (1997). The compressible inclusion function of EPS geof foam. *Geotextiles and Geomembranes*, 15(1-3), 77-120. [https://doi.org/10.1016/S0266-1144\(97\)00008-3](https://doi.org/10.1016/S0266-1144(97)00008-3)
11. Horvath, J. S. (1992). New developments in geosynthetics; 'lite' products come of age. *Standardization News*, 20(9), 50-53.
12. Bathurst, R. J. (1997). Review of seismic design, analysis and performance of geosynthetic reinforced walls, slopes and embankments, Keynote Lecture. In *Proceedings of the International Symposium on Earth Reinforcement (Vol. 2, pp. 887-918)*. Balkema.
13. Pelekis, P. C., Xenaki, V. C., & Athanasopoulos, G. A. (2000, October). Use of EPS geof foam for seismic isolation of earth retaining structures: results of an FEM study. In *Proceedings of the 2nd European geosynthetics conference, Bologna, Italy (pp. 15-18)*.
14. Zarnani, S., & Bathurst, R. J. (2007). Experimental investigation of EPS geof foam seismic buffers using shaking table tests. *Geosynthetics International*, 14(3), 165-177.
15. ASTM D854 (2016). *Standard Test Methods for Specific Gravity of Soil Solids by Water Pycnometer*. ASTM, West Conshohocken, PA.
16. ASTM D4253 (2019). *Standard Test Methods for Maximum Index Density and Unit Weight of Soils Using a Vibratory Table*. ASTM, West Conshohocken, PA.
17. ASTM D4254 (2016). *Standard Test Methods for Minimum Index Density and Unit Weight of Soils and*

- Calculation of Relative Density. ASTM, West Conshohocken, PA.
18. Johnson, K. L. (1982). One hundred years of Hertz contact. *Proceedings of the Institution of Mechanical Engineers*, 196(1), 363-378. [https://doi.org/10.1243/PIME\\_PROC\\_1982\\_196\\_03\\_9\\_02](https://doi.org/10.1243/PIME_PROC_1982_196_03_9_02)
  19. Johnson, K. L. (1985). *Contact Mechanics*, Cambridge University Press, Cambridge, UK.
  20. Dove, J. E., & Frost, J. D. (1999). Peak friction behavior of smooth geomembrane-particle interfaces. *Journal of Geotechnical and Geoenvironmental Engineering*, 125(7), 544-555.
  21. Frost, J. D., & Han, J. (1999). Behavior of interfaces between fiber-reinforced polymers and sands. *Journal of geotechnical and geoenvironmental engineering*, 125(8), 633-640. [https://doi.org/10.1061/\(ASCE\)1090-0241\(1999\)125:8\(633\)](https://doi.org/10.1061/(ASCE)1090-0241(1999)125:8(633))
  22. Frost, J. D., DeJong, J. T., & Recalde, M. (2002). Shear failure behavior of granular-continuum interfaces. *Engineering Fracture Mechanics*, 69(17), 2029-2048. [https://doi.org/10.1016/S0013-7944\(02\)00075-9](https://doi.org/10.1016/S0013-7944(02)00075-9)
  23. O'rourke, T. D., Druschel, S. J., & Netravali, A. N. (1990). Shear strength characteristics of sand-polymer interfaces. *Journal of Geotechnical Engineering*, 116(3), 451-469. [https://doi.org/10.1061/\(ASCE\)0733-9410\(1990\)116:3\(451\)](https://doi.org/10.1061/(ASCE)0733-9410(1990)116:3(451))
  24. Birhan, A., & Negusse, D. (2014). Effects of confinement on the stress-strain behavior of EPS geofilm. In *Ground Improvement and Geosynthetics* (pp. 536-546). <https://doi.org/10.1061/9780784413401.05>
  25. Khan, M. I., & Meguid, M. A. (2018). Experimental investigation of the shear behavior of EPS geofilm. *International Journal of Geosynthetics and Ground Engineering*, 4, 1-12. <https://doi.org/10.1007/s40891-018-0129-7>
  26. Özer, A. T., & Akay, O. (2021). Shear strength characteristics of interlocked EPS-block geofilm-sand interface. *Geosynthetics International*, 28(5), 521-540. <https://doi.org/10.1680/jgein.21.00009>
  27. Meguid, M. A., & Khan, M. I. (2019). On the role of geofilm density on the interface shear behavior of composite geosystems. *International Journal of Geo-Engineering*, 10(6), 1-18. <https://doi.org/10.1186/s40703-019-0103-9>



© Author(s) 2024. This work is distributed under <https://creativecommons.org/licenses/by-sa/4.0/>



## Optimal power flow analysis with circulatory system-based optimization algorithm

Hüseyin Bakır \*<sup>1</sup> 

<sup>1</sup>Dogus University, Department of Electronics and Automation, Türkiye, hbakir@dogus.edu.tr

Cite this study: Bakır, H. (2024). Optimal power flow analysis with circulatory system-based optimization algorithm. Turkish Journal of Engineering, 8 (1), 92-106

### Keywords

Optimal power flow  
Metaheuristic algorithms  
Power system planning  
Optimization

### Research Article

DOI: 10.31127/tuje.1282429

Received:13.04.2023

Revised: 25.05.2023

Accepted:29.05.2023

Published:15.09.2023



### Abstract

Optimal power flow (OPF) is a challenging optimization problem with a large number of variables and constraints. To overcome the OPF issue, high-performance optimization algorithms are needed. In this direction, this paper has been centered on the optimization of the OPF with the circulatory system-based optimization (CSBO) algorithm. The performance of the algorithm was evaluated on the IEEE 57- and 118-bus power networks for the optimization of non-convex OPF objectives, i.e., fuel cost, power loss, voltage deviation, and enhancement of voltage stability. The solution quality of CSBO is compared with state-of-the-art metaheuristic algorithms such as Artificial Rabbits Optimization (ARO), African Vultures Optimization Algorithm (AVOA), and Chaos Game Optimization (CGO). Based on the OPF results, it is seen that the best fuel cost and voltage deviation results are calculated to be 41666.2344 \$/h and 0.5871 p.u with the CSBO algorithm for the IEEE 57-bus power system. The CSBO algorithm obtained the best objective function results for the IEEE 118-bus power network with a fuel cost of 134934.3140 \$/h and a power loss of 16.4688 MW. In conclusion, the present paper reports that the CSBO is a powerful and efficient metaheuristic algorithm to solve the OPF problem.

## 1. Introduction

In today's world, the energy crisis is undoubtedly one of the major problems. With the increasing standard of living, population, and industrialization, energy is needed more and more day by day. The problems that arise from energy increasing demand affect the economy, environment, and social life, that is, every stage of sustainable development in a negative way [1]. The optimal use of available energy resources plays a vital role in alleviating these problems.

The optimal power flow (OPF) is of great importance for the cost-effective and reliable operation of electrical networks [2]. OPF minimizes the selected optimization objective subject to a variety of equality and inequality constraints [3]. In order to achieve the optimal network configuration generally the settings of the independent variables such as the active power of generation units, tap setting of the transformers, the output of shunt VAR compensators, and terminal voltages at generator buses are optimized [4, 5].

OPF is a non-convex optimization problem with high computational complexity [4, 5]. Solving the OPF problem is a challenging task for power system

researchers [6]. To cope with this, it has been observed that various metaheuristic optimization algorithms have been successfully applied to the solution of the OPF problem. For instance, Houssein et al. [7] obtained the OPF solutions of the IEEE 30-bus power system using an enhanced equilibrium optimizer (EEO). In another study, Ramesh et al. [8] used an improved mayfly algorithm (IMA) to solve the OPF problem under different load conditions. Premkumar et al. [9] presented a comparative performance analysis of ESHADE, SHADE-SFS, and SHADE-SAP algorithms in solving the OPF problem. In the study, simulation studies were carried out on two power systems (IEEE 30- and IEEE 118-bus) to demonstrate the effectiveness of the algorithms. The findings revealed that ESHADE designed with the superiority of feasible solution (SFS) and self-adaptive penalty (SAP) methods gives more successful OPF results compared to the SHADE-SFS, and SHADE-SAP. Kaur and Narang [10] obtained OPF solutions for IEEE 30-, 57-, and 118-bus test systems using invasive weed optimization improved by the space transformation search method. Bakır et al. [11] used the fitness-distance balance-based stochastic fractal search (FDB-SFS) algorithm for solving OPF configured with renewable energy sources and

voltage source converters. Sonmez et al. [12] achieved OPF solutions for the IEEE 30-bus power network using improved artificial ecosystem optimization with a fitness-distance balance strategy. Abd El-Sattar et al. [13] used the powerful variant of the salp swarm algorithm to obtain the optimal operation configuration of three IEEE power networks. Jangir et al. [14] proposed the many-objective teaching-learning-based optimizer (MaOTLBO) to obtain the OPF solutions of the IEEE 30-bus power system. The authors evaluated the performance of the proposed algorithm with optimization of the power loss, voltage stability index, fuel cost, voltage deviation, and emission objectives. The results showed that MaOTLBO offers better OPF solutions compared to MOEA/D-DR and NSGA-III algorithms. Pandya et al. [15] formulated a multi-objective OPF problem in the presence of renewable power (wind, solar PV, small-hydro). The authors proposed the multi-objective equilibrium optimizer (MOEO) to solve the OPF problem incorporating renewable power. Considering the IEEE 30-bus power system results are together, it is seen that the proposed algorithm is more successful than the competitor optimizers in terms of the quality of Pareto-optimal solutions and their distribution. Premkumar et al. [16] developed the many-objective gradient-based optimizer (MaOGBO) to solve multi-objective OPF problems of IEEE 30-, 57- and 118-bus power systems. In the study, the authors considered fuel cost, voltage stability, emission, voltage deviation, and active-reactive power loss objectives. The results obtained from the OPF case studies showed that the proposed algorithm is an effective method for solving multi-objective OPF problems of large-scale power systems.

From the literature survey, it can be observed that power system researchers have investigated the efficiency of various metaheuristic algorithms in the solution of the OPF problem. Findings obtained from the literature works showed that OPF solution quality is directly related to the exploration and balanced search capabilities of optimizers. Accordingly, it can be said that high-performance optimization algorithms are required to obtain high-quality solutions to the OPF problem. In this regard, testing novel metaheuristic algorithms in the solution of the OPF problem will be beneficial. This topic deserves further investigation. With this point of view, this paper has centered on the solution to the OPF problem with circulatory system-based optimization (CSBO) [17]. In the study, fuel cost, real power loss, enhancement of voltage stability, and voltage deviation objectives are optimized. Simulation studies are performed on IEEE 57- and 118-bus power networks. The obtained OPF solutions from the CSBO algorithm were compared with up-to-date metaheuristic algorithms such as Artificial Rabbits Optimization (ARO) [18], African Vultures Optimization Algorithm (AVOA) [19], and Chaos Game Optimization (CGO) [20].

The main contributions of the study can be summarized as follows:

- Application of CSBO algorithm to the solution of single and multi-objective OPF problems for the first time.

- Comparative performance analysis of CSBO with state-of-the-art metaheuristic algorithms such as ARO, AVOA, and CGO.
- Optimization of fuel cost, power loss, voltage deviation, and voltage stability enhancement objectives on IEEE 57- and 118-bus power networks.
- Wilcoxon signed-rank test is applied to evaluate algorithm performance.

The remaining sections of the paper are structured as follows: Section 2 gives the definition of the OPF problem. In this direction, the dependent variables, independent variables, and constraints of the OPF problem are introduced. The optimization model of the CSBO algorithm is elaborated in Section 3. Section 4 summarizes and discusses the simulation results of the OPF case studies. Finally, conclusions of the study are presented in Section 5.

## 2. Formulation of OPF Problem

OPF is defined as the minimization of the selected objective function subject to various equality and inequality constraints. The optimization model of the OPF can be written as shown in Equation (1) [21, 22].

$$\begin{aligned} & \text{Minimize } O(s, c) \\ & \text{subject to } \begin{cases} g(s, c) = 0 \\ h(s, c) \leq 0 \end{cases} \end{aligned} \quad (1)$$

where  $O$  shows the objective function,  $s$  and  $c$  are the dependent and independent variable vectors of the OPF problem.  $g(s, c)$  and  $h(s, c)$  represent the set of equality and inequality constraints.

### 2.1. Dependent variables

The active power of the swing bus ( $P_{g_{swing}}$ ), the voltage value of the load bus ( $V_l$ ), the reactive power of the generator bus ( $Q_g$ ), and the transmission line loading ( $S_L$ ) are the dependent variables. Equation (2) gives the dependent variables vector ( $s$ ). In the equation,  $NPQ$ ,  $NG$ , and  $NL$  show the number of load buses, generator buses, and transmission lines.

$$s = [P_{g_{swing}}, V_{l_1} \dots V_{l_{NPQ}}, Q_{g_1} \dots Q_{g_{NG}}, S_{L_1} \dots S_{L_{NL}}] \quad (2)$$

### 2.2. Independent variables

Equation (3) gives the independent variables vector ( $c$ ) of the OPF problem

$$c = [P_{g_2} \dots P_{g_{NG}}, V_{g_1} \dots V_{g_{NG}}, Q_{c_1} \dots Q_{c_{NC}}, T_1 \dots T_{NT}] \quad (3)$$

where  $P_g$  is the active power of generation units except the swing generator,  $V_g$  represents the voltage magnitude of the generator buses.  $Q_c$  and  $T$  indicate the output of shunt VAR compensators and the tap setting of transformers, respectively.  $NT$  and  $NC$  represent the number of transformers and shunt VAR compensators.

### 2.3. OPF constraints

Active and reactive power balance Equations (4-5) are the equality constraints of the OPF problem [22].

#### 2.3.1. Equality constraints

$$P_{g_m} - P_{d_m} - V_m \sum_{n=1}^{NB} V_n [G_{mn} \cos(\delta_m - \delta_n) + B_{mn} \sin(\delta_m - \delta_n)] = 0 \quad \forall m \in NB \quad (4)$$

$$Q_{g_m} - Q_{d_m} - V_m \sum_{n=1}^{NB} V_n [G_{mn} \sin(\delta_m - \delta_n) + B_{mn} \cos(\delta_m - \delta_n)] = 0 \quad \forall m \in NB \quad (5)$$

where  $P_d$  and  $Q_d$  indicate active and reactive power demands.  $G_{mn}$  and  $B_{mn}$  are conductance and susceptance between bus  $m$  and bus  $n$ .  $NB$  shows the number of buses.

$$FC(P_g) = \sum_{i=1}^{NG} p_i + r_i P_{g,i} + w_i P_{g,i}^2 \quad (13)$$

#### 2.3.2. Inequality constraints

The following inequality constraints (Equations 6-12) are considered to ensure the secure operation of power systems.

- Generator constraints

$$P_{g,k}^{min} \leq P_{g,k} \leq P_{g,k}^{max} \quad \forall k \in NG \quad (6)$$

$$Q_{g,k}^{min} \leq Q_{g,k} \leq Q_{g,k}^{max} \quad \forall k \in NG \quad (7)$$

$$V_{g,k}^{min} \leq V_{g,k} \leq V_{g,k}^{max} \quad \forall k \in NG \quad (8)$$

- Shunt capacitor constraints

$$Q_{c,k}^{min} \leq Q_{c,k} \leq Q_{c,k}^{max} \quad \forall k \in NC \quad (9)$$

- Transformer constraints

$$T_k^{min} \leq T_k \leq T_k^{max} \quad \forall k \in NT \quad (10)$$

- Security constraints

$$V_{l,k}^{min} \leq V_{l,k} \leq V_{l,k}^{max} \quad \forall k \in NPQ \quad (11)$$

$$|S_{L,k}| \leq S_{L,k}^{max} \quad \forall k \in NL \quad (12)$$

### 2.4. Objective functions

In the study, single and multi-objective OPF objectives were optimized. Multi-objective OPF problems are converted into single-objective optimization by weighting the objective functions and solved in that way.

#### 2.4.1. Single-objective OPF objectives

- Fuel cost

Fuel cost minimization is widely used objective function in OPF problems. Mathematically, the fuel cost objective function can be written as follows [22]:

where  $P_{g,i}$  shows the active power of  $i$ -th generator in MW.  $p_i$ ,  $r_i$ , and  $w_i$  represent the cost coefficients of the same generator.

- Voltage deviation

Voltage deviation is one of the most important indicators that reflects the voltage quality of the network. The voltage deviation objective function is formulated as the cumulative deviation of all load buses from the nominal value (1 p.u) [22].

$$VD = \left( \sum_{m=1}^{NPQ} |V_{l_m} - 1| \right) \quad (14)$$

- Power loss

Real power loss is inevitable in power systems due to the inherent resistance of transmission lines. The real power loss objective function can be modeled as follows [22]:

$$P_{loss} = \sum_{p=1}^{NL} G_{p,ij} [V_i^2 + V_j^2 - 2 V_i V_j \cos(\delta_{ij})] \quad (15)$$

- Enhancement of voltage stability

The L-index value of the load buses is an important indicator of voltage stability. This index takes values between 0 and 1. If the value of the L-index is close to 0, the power system is stable, and when it is 1, voltage collapse occurs. The L-index value of the  $j$ -th bus ( $L_j$ ) is calculated using Equation 16 [22]:

$$L_j = \left| 1 - \sum_{i=1}^{NG} F_{ji} \frac{V_i}{V_j} \right| \quad j = 1, 2, \dots, NPQ \quad (16)$$

The objective function of system stability can be formulated using Equation 17 [22]:

$$L_{max} = \max(L_j) \quad \text{where } j = 1, 2, \dots, NPQ \quad (17)$$

### 2.4.2. Multi-objective OPF objectives

- Optimization of both fuel cost and voltage deviation

The objective function including simultaneous optimization of fuel cost and voltage deviation is given in Equation (18). In the equation, the value of the weight coefficient is set to  $\lambda_{VD}=100$  [22].

$$O(s, c) = \sum_{i=1}^{NG} (p_i + r_i P_{g,i} + w_i P_{g,i}^2) + (\lambda_{VD} \times VD) \quad (18)$$

$$O(s, c) = \sum_{i=1}^{NG} (p_i + r_i P_{g,i} + w_i P_{g,i}^2) + (\lambda_L \times L_{max}) \quad (19)$$

### 3. Circulatory System-based Optimization

Circulatory system-based optimization (CSBO) is a bio-inspired optimization algorithm with a high convergence performance developed by Ghasemi et al. in 2022 [17]. The optimizer is inspired by the function of the body's blood vessels and mimics the pulmonary and systematic circulation to perform the optimization task. Its simple structure, easy applicability, and lack of user-defined parameters are important advantages. The optimization steps of the CSBO algorithm are described in detail below.

- Initialization

An initial population of blood particles is generated as shown in Equation (20). In that equation,  $N$  and  $D$  show

$$X_i^{new} = X_i + K_{i1} \times p_i \times (X_i - X_1) + K_{23} \times p_i \times (X_3 - X_2) \quad (21)$$

$$K_{ij} = \frac{f(X_j) - f(X_i)}{|f(X_j) - f(X_i)| + \epsilon} = \begin{cases} 1 & f(X_i) \leq f(X_j) \\ -1 & f(X_i) > f(X_j) \\ 0 & f(X_i) = f(X_j) \end{cases} \quad (22)$$

where  $K_{ij}$  indicates the direction of movement of the blood mass.  $p_i$  determines the amount of displacement. It takes a value between 0 and 1.

- Blood mass flow in the pulmonary circulation

The CSBO algorithm ranks the blood population at each iteration and directs the population's weakest solution candidates to the pulmonary circulation system (Equation 23).

$$X_i^{new} = X_i + \left(\frac{randn}{iter}\right) \times randc(1, D), i = 1:Nr \quad (23)$$

where  $randn$  shows the random normal number.  $iter$  represents the current iteration number.  $randc$  represents Cauchy probability distribution function. In this phase,  $p_i$  is updated based on the number of the weakest population ( $Nr$ ) (Equation 24).

- Optimization of both fuel cost and enhancement of voltage stability

Equation (19) gives the objective function used in the simultaneous optimization of both fuel cost and enhancement of voltage stability. In that equation, the value of the weight coefficient is set to  $\lambda_L=100$  [22].

the numbers of population size and design parameters. The position of the blood particles in the search space ( $X_i = [x_{i1}, x_{i2}, \dots, x_{iD}]$ ) represents a possible solution to the optimization problem.

$$P = \begin{bmatrix} X_1 \\ \vdots \\ X_N \end{bmatrix} = \begin{bmatrix} x_{11} & \cdots & x_{1D} \\ \vdots & \ddots & \vdots \\ x_{N1} & \cdots & x_{ND} \end{bmatrix}_{N \times D} \quad (20)$$

- Movement of blood particles in veins

This step of the circulation cycle determines the new position of the  $i$ -th blood particle ( $X_i^{new}$ ) using the particle's current position and fitness value (Equation 21).

$$p_i = rand(1, D), i = 1:Nr \quad (24)$$

- Blood mass flow in the systematic circulation

The remainder of the blood particles in the population ( $Nl = N-Nr$ ) enters the pulmonary circulation (Equation 25).

$$X_{i,j}^{new} = X_{1,j} + p_i \times (X_{3,j} - X_{2,j}) \quad (25)$$

In the systematic circulation, the value of  $p_i$  is updated as shown in Equation 26:

$$p_i = \frac{f(X_i) - f_{worst}}{f_{best} - f_{worst}}, i = 1:Nl \quad (26)$$

The search process lifecycle steps (movement of blood particles in the veins, pulmonary circulation, and systematic circulations) of the CSBO algorithm continue

until the termination criterion is met. The pseudocode of the CSBO algorithm is given in Figure 1 [17].

```

1. Begin
2. Create a random initial blood population ( $P$ ) as shown in Equation (20)
3. Calculate  $p_i$  using Equations (24) and (26)
4. iter  $\leftarrow$  0
5. FEs  $\leftarrow$  N
6. while FEs  $\leq$  maxFEs do
7.   iter  $\leftarrow$  iter + 1
8.   Step 1: Movement of blood particle in the veins
9.   for  $i=1:N$  do
10.    Calculate  $K_{i1}$  and  $K_{23}$  using Equation (22)
11.    Create a new blood particle using Equation (21)
12.    Update the new position of  $i$ -th blood particle
13.    FEs = FEs + 1
14.   end for
15.   Step 2: Pulmonary Circulation
16.   for  $i=1:Nr$  do
17.     for  $j=1:D$  do
18.       if rand > 0.9
19.         Apply pulmonary circulation using Equation (23)
20.       else
21.          $X_{i,j}^{new} = X_{i,j}$ 
22.       end if
23.     end for
24.     FEs = FEs + 1
25.     Calculate  $p_i$  using Equation (24)
26.   end for
27.   Step 3: Systematic Circulation
28.   for  $i=1:Nl$  do
29.     Apply systematic circulation using Equation (25)
30.     Update the new position of  $i$ -th blood particle
31.     Calculate  $p_i$  using Equation (26)
32.     FEs = FEs + 1
33.   end for
34.   Update the best solution
35. end while
36. Display the best solution

```

Figure 1. Pseudocode of CSBO algorithm.

Figure 2 gives the steps followed to solve the OPF problem with CSBO and other competitive optimization algorithms.

#### 4. Results and Analysis

This section presents a comparative performance analysis of the CSBO and other well-known optimization algorithms (ARO, AVOA, and CGO) in solving the OPF problem. The performance of the algorithms is tested for optimization of non-convex OPF objectives i.e., fuel cost, voltage deviation ( $VD$ ), enhancement of voltage stability (L-index), and real power loss ( $P_{loss}$ ). OPF case studies performed on IEEE 57- and 118-bus power systems are summarized in Table 1.

Data for IEEE 57- and 118-bus power networks are taken from [17, 23]. All algorithms were coded in MATLAB R2016a [24] software and simulation studies were performed on PC with 11th Gen Intel (R) Core (TM)

i5-1135G7 @ 2.40 GHz /16 GB RAM/x64-based processor. MATPOWER 7.1 [23, 25] package program was used for OPF power flow calculations. For each OPF case study, the optimization algorithms were run 30 times. The algorithms were run using the settings given in their original article. The maximum number of fitness function evaluations (maxFEs) was used as the termination criterion of the metaheuristic search process. The maxFEs value for OPF case studies on IEEE 57- and 118-bus power networks are set to 42000 and 300000, respectively.

Table 1. Configuration of OPF case studies.

Case no	IEEE 57-bus system			IEEE 118-bus system	
	Fuel Cost	$VD$	L-index	Fuel Cost	$P_{loss}$
Case-1	●				
Case-2	●	●			
Case-3	●		●		
Case-4		●			
Case-5				●	
Case-6					●

#### 4.1. Simulation results of OPF case studies

- Case-1: Optimization of fuel cost

In this case, the fuel cost of the IEEE 57-bus power system is optimized. The results of the fuel cost objective function obtained by metaheuristic optimization algorithms are given in Table 2. As can be seen from the table, the fuel cost value is calculated to be 41666.2344 \$/h, 41668.8301 \$/h, 41676.0759 \$/h, and 41668.1817 \$/h by CSBO, ARO, AVOA, and CGO algorithms, respectively. Based on the numerical data, it is seen that the CSBO method offered the best fuel cost value. To put it more clearly, the CSBO algorithm yielded a profit of 9.8415 \$/h, 2.5957 \$/h, and 1.9473 \$/h in fuel cost compared to the results of the AVOA, ARO, and CGO methods.

- Case-2: Optimization of both fuel cost and voltage deviation

Case-2 handles the simultaneous minimization of the fuel cost and voltage deviation objectives on an IEEE 57-bus power system. In the present OPF case, objective functions are weighted and transformed into a single-objective optimization framework as shown in Equation (18). Considering the simulation results given in Table 2, it is seen that the CSBO algorithm reaches the best fitness value with 41774.4578, while AVOA gives the worst result with 41780.1955. The fuel cost and voltage deviation objective function values obtained with CSBO are 41697.22 \$/h and 0.7723 p.u, respectively.

- Case-3: Optimization of both fuel cost and enhancement of voltage stability

In Case 3, simultaneous optimization of the both fuel cost and enhancement of voltage stability (L-index) on an IEEE 57-bus power system is studied. In this OPF case,

objective functions are weighted and converted into a single-objective optimization as shown in Equation (19). As can be seen in Table 2, the fitness value of Case-3 is obtained to be 41693.9633, 41696.7465, 41701.7993, and 41695.6204 by CSBO, ARO, AVOA, and CGO algorithms, respectively. Accordingly, CSBO gave the best

result, followed by CGO. In addition, ARO and CGO algorithms have obtained competitive results. The fuel cost and L-index objective function values were calculated to be 41666.10 \$/h and 0.2785 for the CSBO algorithm.

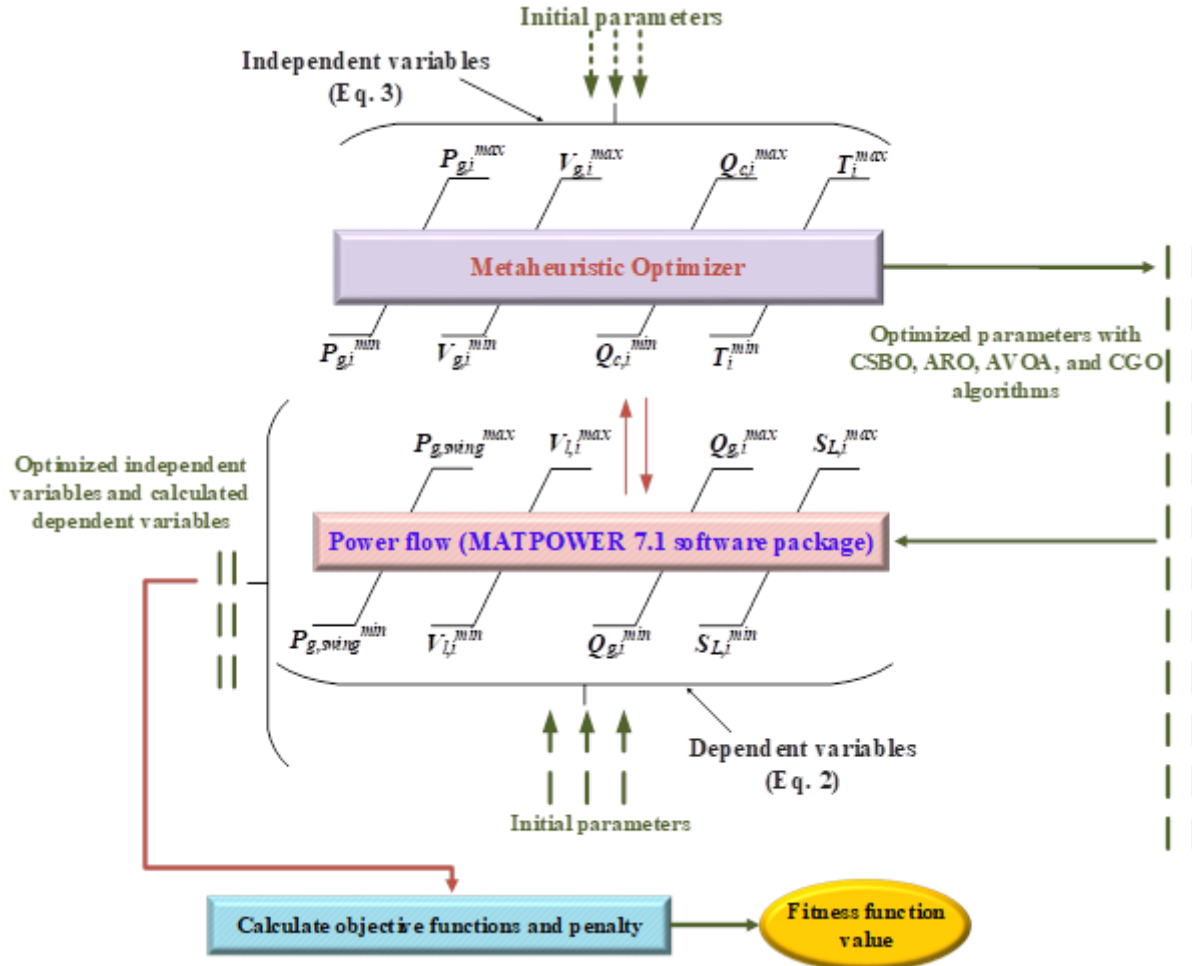


Figure 2. A flowchart for application of metaheuristic optimization algorithms to OPF problem.

- Case-4: Optimization of voltage deviation

Case-4 minimizes the voltage deviation of load buses in the IEEE 57-bus power network. As seen in Table 2, the voltage deviation value obtained by CSBO, ARO, AVOA, and CGO algorithms is 0.5871 p.u, 0.6151 p.u, 0.6329 p.u, and 0.6014 p.u, respectively. It is clear that the CSBO algorithm reached the best result, followed by CGO. In other words, CSBO reduced the voltage deviation by 4.5521%, 7.2365%, and 2.3777% compared to the ARO, AVOA, and CGO algorithms.

- Case-5: Optimization of fuel cost

This case aims to minimize the fuel cost of the IEEE 118-bus system. Based on the results given in Table 2, the fuel cost value is calculated to be 134934.3140 \$/h, 135023.4711 \$/h, 134985.7415 \$/h, and 135149.3384 \$/h for CSBO, ARO, AVOA, and CGO algorithms, respectively. From the numerical results, it is noticed that the CSBO method offered the best fuel cost value. To be more specific, the CSBO algorithm yielded a profit of

89.1571 \$/h, 51.4275 \$/h, and 215.0244 \$/h in fuel cost compared to the results of the ARO, AVOA, and CGO algorithms.

- Case-6: Optimization of active power loss

In Case-6, active power loss minimization of the IEEE 118-bus power system is performed. As can be seen from Table 2, the power loss objective function value is calculated to be 16.4688 MW, 17.3497 MW, 21.9025 MW, and 19.2740 MW by CSBO, ARO, AVOA, and CGO algorithms, respectively. Considering the numeric results, it is noticed that the CSBO offered the lowest active power loss value of 16.4688 MW. In other words, CSBO reduced the power loss by 5.0773%, 24.8085%, and 14.5543% compared to the ARO, AVOA, and CGO algorithms.

Given the results of OPF case studies are together, it is observed that the solution quality of the CSBO algorithm is superior compared to its competitors. The optimum parameter settings obtained with CSBO algorithm are given in Tables 3-5.

### 4.2. Convergence analysis

This subsection analyzes the convergence performance of metaheuristic algorithms for OPF case studies on IEEE 57- and 118-bus power systems. In this context, convergence curves were drawn to show the variation of the fitness value over the number of maxFES. Figure 3 gives the convergence curves of CSBO, ARO, AVOA, and CGO algorithms. Considering the convergence curves for the OPF case studies carried out on the IEEE 57-bus power system (Figure 3 a, b, c, d), it is seen that the CSBO and CGO algorithms exhibit a more successful search performance than their competitors. The convergence speed and solution quality of these two algorithms are impressive. On the other hand, it is seen that the ARO and AVOA algorithms cannot successfully converge to the global optimum. The underlying reason behind it is thought to be the premature convergence problem of these algorithms. From the convergence curves for the OPF case studies performed on the IEEE 118-bus power system (Figure 3 e, f), it is observed that the CSBO algorithm converges rapidly and produces better results than the compared ones.

### 4.3. Box-Plots

Box plots were prepared to observe the fitness value obtained by the algorithms over 30 independent runs. Each box plot includes the minimum, average, and maximum values of fitness value. A narrow box shows

that the algorithm exhibits a robust search performance. Figure 4 shows box plots of CSBO, ARO, AVOA, and CGO algorithms for OPF case studies. As is seen in the figure, the CSBO algorithm exhibited a stable and robust search performance in the optimization of OPF problems.

### 4.4. Statistical analysis

Performance metrics (minimum, mean, maximum, and standard deviation) calculated using data obtained from 30 runs are not sufficient to reveal the overall search performance of algorithms. In this context, statistical analysis of data is inevitable. This study applies Wilcoxon statistical test [35] for pairwise comparison between algorithms. Table 6 gives the Wilcoxon test results between CSBO and competitive algorithms. Considering ARO vs CSBO statistical test result for Case-1 (1/464), it is seen that ARO achieved a better fitness value than the CSBO algorithm for only run 1. In the remaining OPF cases, the fitness value of CSBO is better than ARO in all runs. Given the AVOA vs CSBO statistical test result, it is observed that the CSBO algorithm gave better OPF results compared to AVOA in all runs. Based on the CGO vs CSBO statistical test results for Case-3 and Case-4 (2/463), it is seen that CGO obtained a better fitness value than the CSBO algorithm for only run 2. In other OPF case studies, the CSBO algorithm is superior to CGO. In a nutshell, the Wilcoxon test results confirmed that the CSBO algorithm achieved better quality results than its competitors.

**Table 2.** Simulation results obtained from 30 runs.

Algorithm	Metric	Case-1	Case-2	Case-3	Case-4	Case-5	Case-6
CSBO	Best	<b>41666.2344</b>	<b>41774.4578</b>	<b>41693.9633</b>	<b>0.5871</b>	<b>134934.3140</b>	<b>16.4688</b>
	Mean	41667.3685	41774.9323	41694.9648	0.5925	134953.0728	16.9596
	Worst	41670.0940	41775.6829	41697.0897	0.6063	134984.2226	17.4696
	Std. Dev.	1.0878	0.3915	0.8563	0.0046	14.5031	0.2769
ARO	Best	41668.8301	41778.1130	41696.7465	0.6151	135023.4711	17.3497
	Mean	41673.4410	41784.0492	41701.5898	0.6524	135108.9051	18.7526
	Worst	41681.4971	41793.9520	41707.6488	0.7139	135260.7873	21.8958
	Std. Dev.	3.1497	4.8270	2.7930	0.0201	56.7417	0.9142
AVOA	Best	41676.0759	41780.1955	41701.7993	0.6329	134985.7415	21.9025
	Mean	41706.4203	41794.0997	41728.6458	0.7158	135143.2439	31.3293
	Worst	41764.5797	41813.8279	41782.6629	1.1610	135617.5325	45.3612
	Std. Dev.	22.5228	9.3521	19.2953	0.0936	156.7355	5.4363
CGO	Best	41668.1817	41775.6618	41695.6204	0.6014	135149.3384	19.2740
	Mean	41692.2616	41782.2631	41715.7907	0.6201	135253.7785	20.5832
	Worst	41771.7204	41825.9333	41759.5148	0.6798	135748.6388	23.3513
	Std. Dev.	23.5681	9.5836	19.8783	0.0193	106.5352	0.9733

### 4.5. Literature comparison

In this study, it has been observed that OPF solutions obtained with CSBO are of higher quality than ARO, AVOA, and CGO methods. However, the success of the CSBO algorithm against other literature studies is unknown. To clarify this state, the OPF solutions obtained by CSBO are compared with the available literature. The comparative results are given in Table 7. Given that all the results are together, it is noticed that the CSBO algorithm offered better-quality solutions than the literature studies.

### 5. Conclusion

This paper presents a comparative performance analysis of the metaheuristic algorithms in the optimization of single and multi-objective OPF problems. In this direction, CSBO, ARO, AVOA, and CGO algorithms are applied to obtain OPF solutions of IEEE 57- and 118-bus power systems. In the study, the fuel cost, voltage deviation, active power loss, and enhancement of voltage stability objectives are optimized. In the IEEE 57-bus power system, CSBO achieved 1.9473 \$/h and 2.3777% better results in terms of fuel cost and voltage deviation objectives compared to the CGO algorithm, which

exhibited the second-best performance. The CSBO algorithm reduced the fuel cost and power loss of the IEEE 118-bus power system by 51.4275 \$/h and 5.0773%, respectively. Considering the simulation results, it is seen that the CSBO algorithm obtained the best results for all OPF case studies under study. Convergence curves, box plots, and Wilcoxon statistical

test results showed that the CSBO algorithm exhibited a better convergence success compared to other optimizers considered in the study. The obtained OPF solutions from CSBO are compared with the literature studies and it is observed that the proposed algorithm gives better solutions.

**Table 3.** Optimum solutions of CSBO algorithm for IEEE 57-bus OPF case studies.

Parameters	Min	Max	Case-1	Case-2	Case-3	Case-4
$P_{G_{g_1}}$ (MW)	0	576	142.7350	142.6349	142.8443	352.9668
$P_{g_2}$ (MW)	30	100	89.2764	88.3179	89.3849	32.3379
$P_{g_3}$ (MW)	40	140	45.0011	45.0339	44.9871	134.2231
$P_{g_6}$ (MW)	30	100	70.7775	71.6483	70.8617	30.5596
$P_{g_8}$ (MW)	100	550	460.6593	460.3545	460.4950	272.6486
$P_{g_9}$ (MW)	30	100	96.9825	97.8728	96.8019	99.8451
$P_{g_{12}}$ (MW)	100	410	360.2274	360.5228	360.2750	348.9024
$Q_{g_1}$ (MVar)	-140	200	43.1142	40.8621	44.7284	-40.4167
$Q_{g_2}$ (MVar)	-17	50	49.9947	49.9932	49.9931	49.6062
$Q_{g_3}$ (MVar)	-10	60	30.9278	34.8576	35.6592	59.9374
$Q_{g_6}$ (MVar)	-8	25	-7.8592	-3.9786	-7.6921	-7.9544
$Q_{g_8}$ (MVar)	-140	200	53.6284	72.5680	49.7739	43.9786
$Q_{g_9}$ (MVar)	-3	9	8.9982	8.9983	8.9993	8.9826
$Q_{g_{12}}$ (MVar)	-150	155	60.1086	45.6496	58.3601	154.9041
$V_1$ (p.u)	0.95	1.10	1.0635	1.0333	1.0670	1.0081
$V_2$ (p.u)	0.95	1.10	1.0611	1.0317	1.0647	1.0064
$V_3$ (p.u)	0.95	1.10	1.0534	1.0272	1.0573	1.0165
$V_6$ (p.u)	0.95	1.10	1.0589	1.0427	1.0602	1.0019
$V_8$ (p.u)	0.95	1.10	1.0757	1.0627	1.0753	1.0214
$V_9$ (p.u)	0.95	1.10	1.0500	1.0285	1.0507	1.0107
$V_{12}$ (p.u)	0.95	1.10	1.0511	1.0191	1.0525	1.0392
$Q_{c18}$ (MVar)	0	20	7.9183	5.4348	8.4539	0.0436
$Q_{c25}$ (MVar)	0	20	13.7033	16.0706	13.1343	18.8307
$Q_{c53}$ (MVar)	0	20	12.3686	15.5759	12.0256	19.9985
$T_{19}$ (p.u)	0.90	1.10	0.9518	1.0443	0.9293	1.0425
$T_{20}$ (p.u)	0.90	1.10	1.0112	0.9529	1.0396	0.9447
$T_{31}$ (p.u)	0.90	1.10	1.0086	0.9902	1.0096	0.9691
$T_{35}$ (p.u)	0.90	1.10	1.0535	0.9325	1.0469	1.0986
$T_{36}$ (p.u)	0.90	1.10	0.9801	1.0999	0.9768	1.0190
$T_{37}$ (p.u)	0.90	1.10	1.0327	1.0219	1.0314	1.0022
$T_{41}$ (p.u)	0.90	1.10	0.9955	1.0181	0.9952	0.9948
$T_{46}$ (p.u)	0.90	1.10	0.9609	0.9390	0.9599	0.9195
$T_{54}$ (p.u)	0.90	1.10	0.9128	0.9000	0.9128	0.9000
$T_{58}$ (p.u)	0.90	1.10	0.9790	0.9671	0.9817	0.9310
$T_{59}$ (p.u)	0.90	1.10	0.9639	0.9648	0.9673	0.9831
$T_{65}$ (p.u)	0.90	1.10	0.9753	0.9850	0.9763	1.0184
$T_{66}$ (p.u)	0.90	1.10	0.9388	0.9369	0.9398	0.9000
$T_{71}$ (p.u)	0.90	1.10	0.9738	0.9699	0.9743	0.9631
$T_{73}$ (p.u)	0.90	1.10	0.9919	0.9983	0.9924	1.0017
$T_{76}$ (p.u)	0.90	1.10	0.9627	0.9425	0.9689	0.9087
$T_{80}$ (p.u)	0.90	1.10	1.0004	1.0078	1.0041	0.9920
Fuel Cost (\$/h)	-	-	<b>41666.2344</b>	<b>41697.22</b>	<b>41666.10</b>	48524.40
$P_{loss}$ (MW)	-	-	14.8593	15.5851	14.8500	20.3134
$VD$ (p.u)	-	-	1.7033	<b>0.7723</b>	1.7059	<b>0.5871</b>
L-index	-	-	0.2789	0.2930	<b>0.2785</b>	0.3008

**Table 4.** Optimum solutions of CSBO algorithm for Case-5.

Parameters	Bounds	Values	Parameters	Values	Parameters	Values
$P_{g_1}$ (MW)	30-100	30.0000	$V_{g_1}$ (p.u)	1.0341	$Q_{c5}$ (MVar)	24.9998
$P_{g_4}$ (MW)	30-100	30.0002	$V_g$ (p.u)	1.0594	$Q_{c34}$ (MVar)	0.1247
$P_{g_6}$ (MW)	30-100	30.0000	$V_{g_6}$ (p.u)	1.0531	$Q_{c37}$ (MVar)	0.0017
$P_{g_8}$ (MW)	30-100	30.0001	$V_{g_8}$ (p.u)	1.0404	$Q_{c44}$ (MVar)	3.5609
$P_{g_{10}}$ (MW)	165-550	315.8477	$V_{g_{10}}$ (p.u)	1.0483	$Q_{c45}$ (MVar)	18.8540
$P_{g_{12}}$ (MW)	55.5-185	67.3771	$V_{g_{12}}$ (p.u)	1.0489	$Q_{c46}$ (MVar)	0.0002
$P_{g_{15}}$ (MW)	30-100	30.0000	$V_{g_{15}}$ (p.u)	1.0455	$Q_{c48}$ (MVar)	7.0132
$P_{g_{18}}$ (MW)	30-100	30.0000	$V_{g_{18}}$ (p.u)	1.0474	$Q_{c74}$ (MVar)	24.9925
$P_{g_{19}}$ (MW)	30-100	30.0000	$V_{g_{19}}$ (p.u)	1.0455	$Q_{c79}$ (MVar)	24.9999
$P_{g_{24}}$ (MW)	30-100	30.0002	$V_{g_{24}}$ (p.u)	1.0587	$Q_{c82}$ (MVar)	24.9442
$P_{g_{25}}$ (MW)	96-320	152.2763	$V_{g_{25}}$ (p.u)	1.0718	$Q_{c83}$ (MVar)	13.0013
$P_{g_{26}}$ (MW)	124.2-414	220.4765	$V_{g_{26}}$ (p.u)	1.08288	$Q_{c105}$ (MVar)	24.8915
$P_{g_{27}}$ (MW)	30-100	30.0000	$V_{g_{27}}$ (p.u)	1.0506	$Q_{c107}$ (MVar)	24.8057
$P_{g_{31}}$ (MW)	32.1-107	32.1000	$V_{g_{31}}$ (p.u)	1.0465	$Q_{c110}$ (MVar)	24.9997
$P_{g_{32}}$ (MW)	30-100	30.0000	$V_{g_{32}}$ (p.u)	1.0489	$T_8$ (p.u)	0.9857
$P_{g_{34}}$ (MW)	30-100	30.0000	$V_{g_{34}}$ (p.u)	1.0496	$T_{32}$ (p.u)	1.0644
$P_{g_{36}}$ (MW)	30-100	30.0000	$V_{g_{36}}$ (p.u)	1.0474	$T_{36}$ (p.u)	0.9804
$P_{g_{40}}$ (MW)	30-100	30.00000	$V_{g_{40}}$ (p.u)	1.0339	$T_{51}$ (p.u)	0.9858
$P_{g_{42}}$ (MW)	30-100	30.0006	$V_{g_{42}}$ (p.u)	1.0360	$T_{93}$ (p.u)	0.9810
$P_{g_{46}}$ (MW)	35.7-119	35.7000	$V_{g_{46}}$ (p.u)	1.0524	$T_{95}$ (p.u)	1.0013
$P_{g_{49}}$ (MW)	91.2-304	161.7616	$V_{g_{49}}$ (p.u)	1.0618	$T_{102}$ (p.u)	0.9653
$P_{g_{54}}$ (MW)	44.4-148	44.4039	$V_{g_{54}}$ (p.u)	1.0418	$T_{107}$ (p.u)	0.9431
$P_{g_{55}}$ (MW)	30-100	30.0000	$V_{g_{55}}$ (p.u)	1.0415	$T_{127}$ (p.u)	0.9895
$P_{g_{56}}$ (MW)	30-100	30.0007	$V_{g_{56}}$ (p.u)	1.0414	Fuel Cost (\$/h)	<b>134934.3140</b>
$P_{g_{59}}$ (MW)	76.5-255	124.7872	$V_{g_{59}}$ (p.u)	1.0598	VD (p.u)	2.9658
$P_{g_{61}}$ (MW)	78-260	122.7446	$V_{g_{61}}$ (p.u)	1.0616	$P_{loss}$ (MW)	57.8922
$P_{g_{62}}$ (MW)	30-100	30.0000	$V_{g_{62}}$ (p.u)	1.0569	$P_{G_{69}}$ (Swing Bus)	370.0572
$P_{g_{65}}$ (MW)	147.3-491	289.0389	$V_{g_{65}}$ (p.u)	1.0622		
$P_{g_{66}}$ (MW)	147.6-492	288.9684	$V_{g_{66}}$ (p.u)	1.0731		
$P_{g_{70}}$ (MW)	30-100	30.0004	$V_{g_{69}}$ (p.u)	1.0701		
$P_{g_{72}}$ (MW)	30-100	30.0000	$V_{g_{70}}$ (p.u)	1.0554		
$P_{g_{73}}$ (MW)	30-100	30.0001	$V_{g_{72}}$ (p.u)	1.0625		
$P_{g_{74}}$ (MW)	30-100	30.0008	$V_{g_{73}}$ (p.u)	1.0597		
$P_{g_{76}}$ (MW)	30-100	30.0001	$V_{g_{74}}$ (p.u)	1.0420		
$P_{g_{77}}$ (MW)	30-100	30.0000	$V_{g_{76}}$ (p.u)	1.0233		
$P_{g_{80}}$ (MW)	173.1-577	348.5164	$V_{g_{77}}$ (p.u)	1.0480		
$P_{g_{85}}$ (MW)	30-100	30.0003	$V_{g_{80}}$ (p.u)	1.0562		
$P_{g_{87}}$ (MW)	31.2-104	31.2000	$V_{g_{85}}$ (p.u)	1.0600		
$P_{g_{89}}$ (MW)	212.1-707	384.3456	$V_{g_{87}}$ (p.u)	1.0759		
$P_{g_{90}}$ (MW)	30-100	30.0000	$V_{g_{89}}$ (p.u)	1.0723		
$P_{g_{91}}$ (MW)	30-100	30.0000	$V_{g_{90}}$ (p.u)	1.0573		
$P_{g_{92}}$ (MW)	30-100	30.0002	$V_{g_{91}}$ (p.u)	1.0622		
$P_{g_{99}}$ (MW)	30-100	30.0000	$V_{g_{92}}$ (p.u)	1.0612		
$P_{g_{100}}$ (MW)	105.6-352	177.4768	$V_{g_{99}}$ (p.u)	1.0582		
$P_{g_{103}}$ (MW)	42-140	42.0007	$V_{g_{100}}$ (p.u)	1.0605		
$P_{g_{104}}$ (MW)	30-100	30.0001	$V_{g_{103}}$ (p.u)	1.0578		
$P_{g_{105}}$ (MW)	30-100	30.0002	$V_{g_{104}}$ (p.u)	1.0531		
$P_{g_{107}}$ (MW)	30-100	30.0000	$V_{g_{105}}$ (p.u)	1.0507		
$P_{g_{110}}$ (MW)	30-100	30.0000	$V_{g_{107}}$ (p.u)	1.0441		
$P_{g_{111}}$ (MW)	40.8-136	40.8000	$V_{g_{110}}$ (p.u)	1.0529		
$P_{g_{112}}$ (MW)	30-100	30.0000	$V_{g_{111}}$ (p.u)	1.0619		
$P_{g_{113}}$ (MW)	30-100	30.0000	$V_{g_{112}}$ (p.u)	1.0442		
$P_{g_{116}}$ (MW)	30-100	30.0001	$V_{g_{113}}$ (p.u)	1.0555		
			$V_{g_{116}}$ (p.u)	1.0600		

**Table 5.** Optimum solutions of CSBO algorithm for Case-6.

Parameters	Bounds	Values	Parameters	Values	Parameters	Values
$P_{g_1}$ (MW)	30-100	69.6586	$V_{g_1}$ (p.u)	1.0418	$Q_{c5}$ (MVar)	18.8284
$P_{g_4}$ (MW)	30-100	30.0001	$V_g$ (p.u)	1.0566	$Q_{c34}$ (MVar)	0.0007
$P_{g_6}$ (MW)	30-100	30.3765	$V_{g_6}$ (p.u)	1.0527	$Q_{c37}$ (MVar)	0.0006
$P_{g_8}$ (MW)	30-100	30.0081	$V_{g_8}$ (p.u)	1.0375	$Q_{c44}$ (MVar)	4.6913
$P_{g_{10}}$ (MW)	165-550	165.0001	$V_{g_{10}}$ (p.u)	1.0451	$Q_{c45}$ (MVar)	17.7797
$P_{g_{12}}$ (MW)	55.5-185	134.5671	$V_{g_{12}}$ (p.u)	1.0514	$Q_{c46}$ (MVar)	24.9838
$P_{g_{15}}$ (MW)	30-100	87.3883	$V_{g_{15}}$ (p.u)	1.0502	$Q_{c48}$ (MVar)	7.47022
$P_{g_{18}}$ (MW)	30-100	30.0006	$V_{g_{18}}$ (p.u)	1.0501	$Q_{c74}$ (MVar)	24.9999
$P_{g_{19}}$ (MW)	30-100	60.1661	$V_{g_{19}}$ (p.u)	1.0496	$Q_{c79}$ (MVar)	24.9971
$P_{g_{24}}$ (MW)	30-100	30.0002	$V_{g_{24}}$ (p.u)	1.0579	$Q_{c82}$ (MVar)	24.9465
$P_{g_{25}}$ (MW)	96-320	96.0000	$V_{g_{25}}$ (p.u)	1.0671	$Q_{c83}$ (MVar)	10.9260
$P_{g_{26}}$ (MW)	124.2-414	124.2000	$V_{g_{26}}$ (p.u)	1.0546	$Q_{c105}$ (MVar)	24.9992
$P_{g_{27}}$ (MW)	30-100	48.4661	$V_{g_{27}}$ (p.u)	1.0525	$Q_{c107}$ (MVar)	0.15651
$P_{g_{31}}$ (MW)	32.1-107	62.2590	$V_{g_{31}}$ (p.u)	1.0519	$Q_{c110}$ (MVar)	18.5319
$P_{g_{32}}$ (MW)	30-100	37.1864	$V_{g_{32}}$ (p.u)	1.0518	$T_8$ (p.u)	0.98264
$P_{g_{34}}$ (MW)	30-100	65.6885	$V_{g_{34}}$ (p.u)	1.0462	$T_{32}$ (p.u)	1.04261
$P_{g_{36}}$ (MW)	30-100	55.2984	$V_{g_{36}}$ (p.u)	1.0435	$T_{36}$ (p.u)	0.97987
$P_{g_{40}}$ (MW)	30-100	99.9999	$V_{g_{40}}$ (p.u)	1.0403	$T_{51}$ (p.u)	0.98036
$P_{g_{42}}$ (MW)	30-100	99.9987	$V_{g_{42}}$ (p.u)	1.0387	$T_{93}$ (p.u)	1.00009
$P_{g_{46}}$ (MW)	35.7-119	81.1353	$V_{g_{46}}$ (p.u)	1.0364	$T_{95}$ (p.u)	0.99712
$P_{g_{49}}$ (MW)	91.2-304	142.2017	$V_{g_{49}}$ (p.u)	1.0349	$T_{102}$ (p.u)	0.97309
$P_{g_{54}}$ (MW)	44.4-148	147.9995	$V_{g_{54}}$ (p.u)	1.0294	$T_{107}$ (p.u)	0.96532
$P_{g_{55}}$ (MW)	30-100	70.3444	$V_{g_{55}}$ (p.u)	1.0289	$T_{127}$ (p.u)	0.96915
$P_{g_{56}}$ (MW)	30-100	99.9989	$V_{g_{56}}$ (p.u)	1.0288	Fuel Cost (\$/h)	155741.09
$P_{g_{59}}$ (MW)	76.5-255	254.1118	$V_{g_{59}}$ (p.u)	1.0282	$VD$ (p.u)	2.5323
$P_{g_{61}}$ (MW)	78-260	78.0000	$V_{g_{61}}$ (p.u)	1.0289	$P_{loss}$ (MW)	<b>16.4688</b>
$P_{g_{62}}$ (MW)	30-100	64.0547	$V_{g_{62}}$ (p.u)	1.0276	$P_{G_{69}}$ (Swing Bus)	3.4037
$P_{g_{65}}$ (MW)	147.3-491	147.3110	$V_{g_{65}}$ (p.u)	1.0349		
$P_{g_{66}}$ (MW)	147.6-492	147.6050	$V_{g_{66}}$ (p.u)	1.0362		
$P_{g_{70}}$ (MW)	30-100	30.0007	$V_{g_{69}}$ (p.u)	1.0419		
$P_{g_{72}}$ (MW)	30-100	30.0001	$V_{g_{70}}$ (p.u)	1.0439		
$P_{g_{73}}$ (MW)	30-100	30.0012	$V_{g_{72}}$ (p.u)	1.0567		
$P_{g_{74}}$ (MW)	30-100	96.1758	$V_{g_{73}}$ (p.u)	1.0499		
$P_{g_{76}}$ (MW)	30-100	99.9328	$V_{g_{74}}$ (p.u)	1.0413		
$P_{g_{77}}$ (MW)	30-100	99.9809	$V_{g_{76}}$ (p.u)	1.0314		
$P_{g_{80}}$ (MW)	173.1-577	286.763	$V_{g_{77}}$ (p.u)	1.0429		
$P_{g_{85}}$ (MW)	30-100	32.2496	$V_{g_{80}}$ (p.u)	1.0488		
$P_{g_{87}}$ (MW)	31.2-104	31.2013	$V_{g_{85}}$ (p.u)	1.0554		
$P_{g_{89}}$ (MW)	212.1-707	212.1151	$V_{g_{87}}$ (p.u)	1.0733		
$P_{g_{90}}$ (MW)	30-100	99.9387	$V_{g_{89}}$ (p.u)	1.0645		
$P_{g_{91}}$ (MW)	30-100	30.0060	$V_{g_{90}}$ (p.u)	1.0569		
$P_{g_{92}}$ (MW)	30-100	30.0003	$V_{g_{91}}$ (p.u)	1.0593		
$P_{g_{99}}$ (MW)	30-100	39.7779	$V_{g_{92}}$ (p.u)	1.0543		
$P_{g_{100}}$ (MW)	105.6-352	105.6001	$V_{g_{99}}$ (p.u)	1.0508		
$P_{g_{103}}$ (MW)	42-140	42.0015	$V_{g_{100}}$ (p.u)	1.0519		
$P_{g_{104}}$ (MW)	30-100	32.9776	$V_{g_{103}}$ (p.u)	1.0531		
$P_{g_{105}}$ (MW)	30-100	52.5637	$V_{g_{104}}$ (p.u)	1.0507		
$P_{g_{107}}$ (MW)	30-100	57.7776	$V_{g_{105}}$ (p.u)	1.0504		
$P_{g_{110}}$ (MW)	30-100	30.01218	$V_{g_{107}}$ (p.u)	1.0506		
$P_{g_{111}}$ (MW)	40.8-136	40.80305	$V_{g_{110}}$ (p.u)	1.0538		
$P_{g_{112}}$ (MW)	30-100	51.60743	$V_{g_{111}}$ (p.u)	1.0628		
$P_{g_{113}}$ (MW)	30-100	30.00222	$V_{g_{112}}$ (p.u)	1.0502		
$P_{g_{116}}$ (MW)	30-100	74.5478	$V_{g_{113}}$ (p.u)	1.0563		
			$V_{g_{116}}$ (p.u)	1.0326		

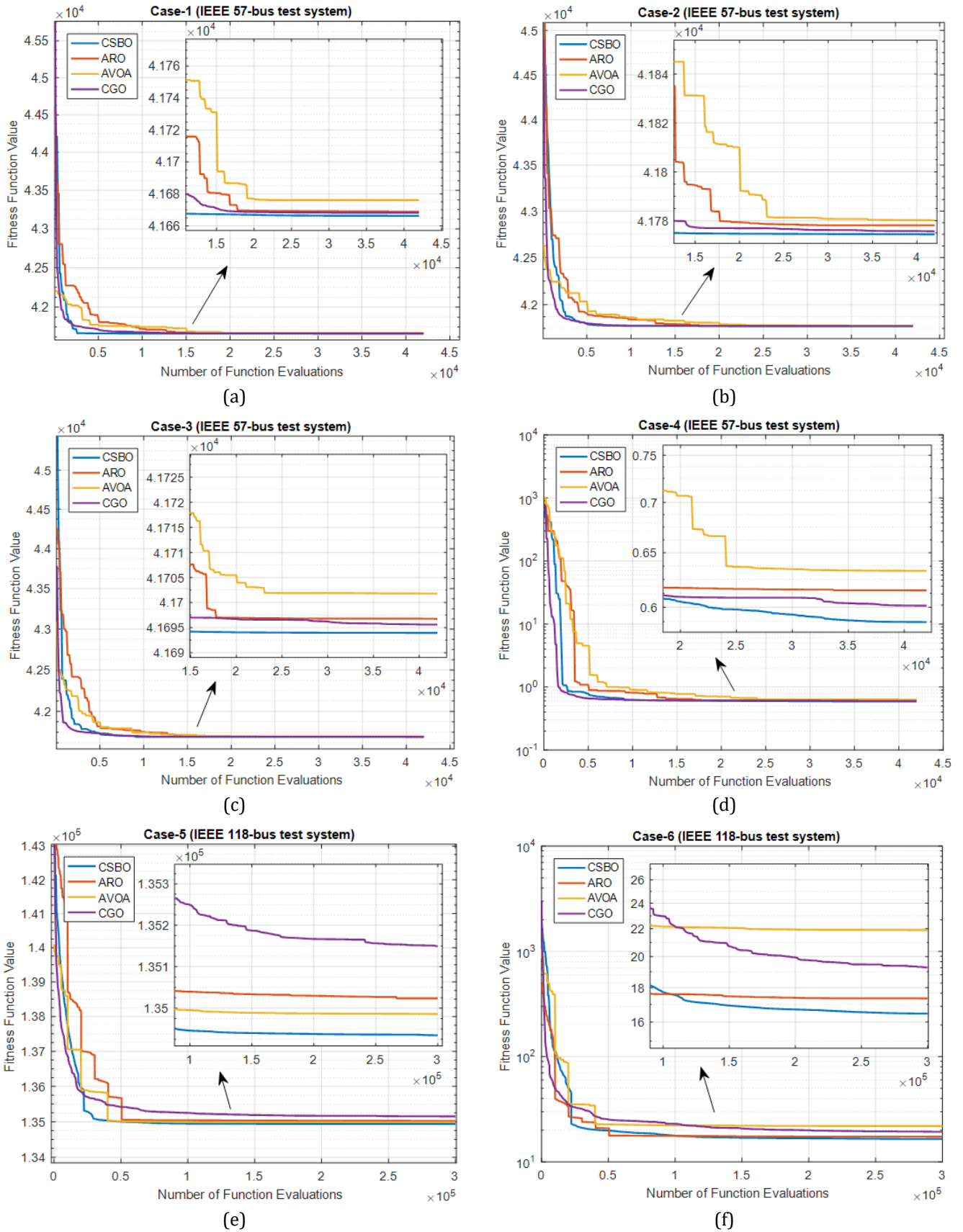
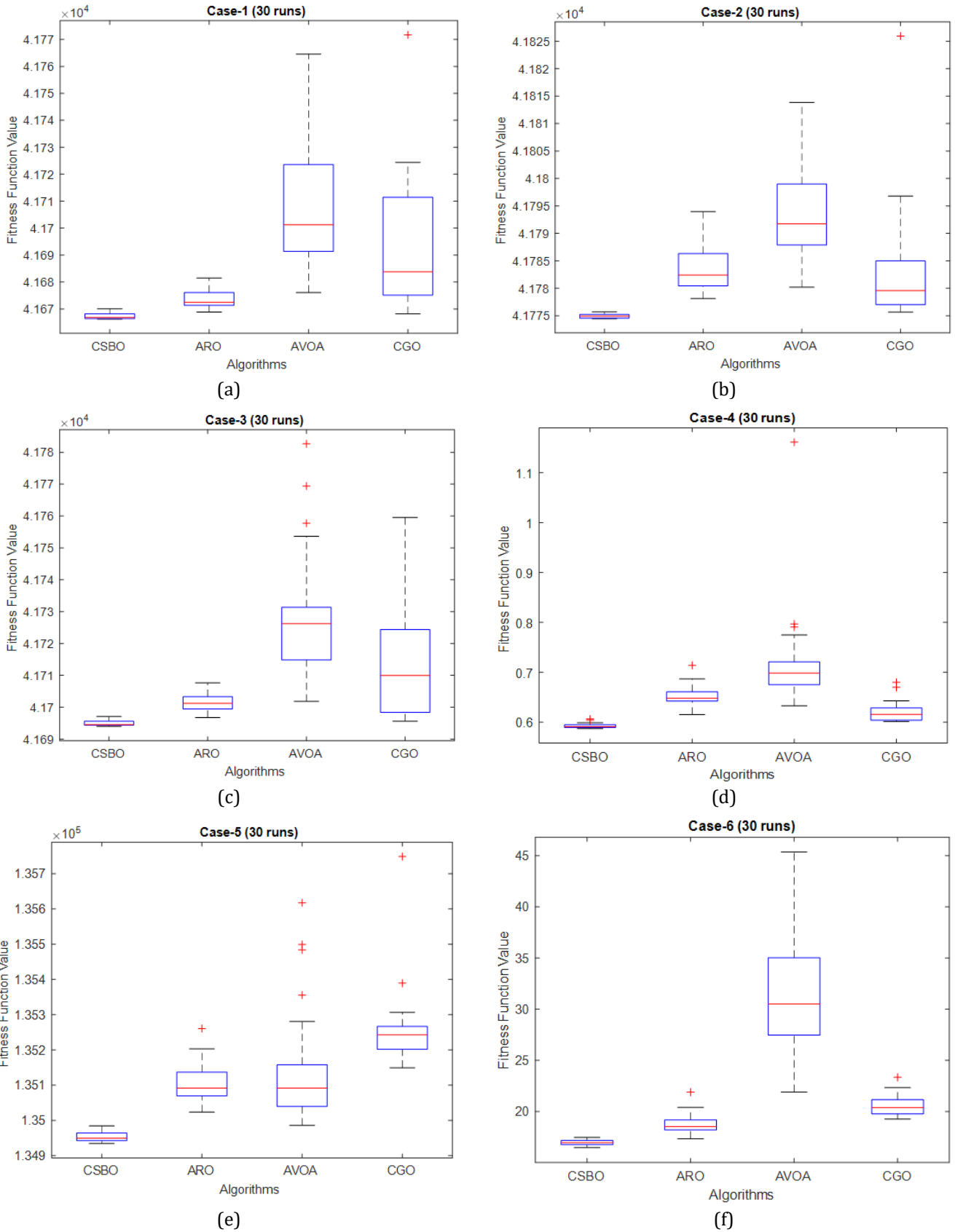


Figure 3. Convergence curves: (a) Case-1, (b) Case-2, (c) Case-3, (d) Case-4, (e) Case-5, (f) Case-6.



**Figure 4.** Box-plots for (a) Case-1, (b) Case-2, (c) Case-3, (d) Case-4, (e) Case-5 (f) Case-6.

**Table 6.** Wilcoxon test results.

Problem Cases	ARO vs CSBO			AVOA vs CSBO			CGO vs CSBO		
	R+	R-	p-value	R+	R-	p-value	R+	R-	p-value
Case-1	1	464	1.92 x 10 <sup>-6</sup>	0	465	1.73 x 10 <sup>-6</sup>	0	465	1.73 x 10 <sup>-6</sup>
Case-2	0	465	1.73 x 10 <sup>-6</sup>	0	465	1.73 x 10 <sup>-6</sup>	0	465	1.73 x 10 <sup>-6</sup>
Case-3	0	465	1.73 x 10 <sup>-6</sup>	0	465	1.73 x 10 <sup>-6</sup>	2	463	2.12 x 10 <sup>-6</sup>
Case-4	0	465	1.73 x 10 <sup>-6</sup>	0	465	1.73 x 10 <sup>-6</sup>	2	463	2.12 x 10 <sup>-6</sup>
Case-5	0	465	1.73 x 10 <sup>-6</sup>	0	465	1.73 x 10 <sup>-6</sup>	0	465	1.73 x 10 <sup>-6</sup>
Case-6	0	465	1.73 x 10 <sup>-6</sup>	0	465	1.73 x 10 <sup>-6</sup>	0	465	1.73 x 10 <sup>-6</sup>

**Table 7.** Comparison of the CSBO algorithm with literature studies.

Case no.	Algorithms	Best Fitness	Fuel Cost	$P_{loss}$	VD	L-index
Case-1	CSBO	<b>41666.23</b>	41666.23	14.8593	1.70336	0.2789
	SP-DE [22]	41667.82	41667.82	14.9090	1.54367	0.28123
	ECHT-DE [22]	41670.56	41670.56	14.9479	1.50319	0.28886
	SF-DE [22]	41667.85	41667.85	14.8864	1.64209	0.27971
	DE [26]	41682	41682	NA	NA	NA
	MSA [27]	41673.72	41673.72	15.0526	1.5508	0.28392
	ICBO [28]	41697.33	41697.33	15.5470	1.3173	0.27760
	DSA [29]	41686.82	41686.82	NA	1.0833	0.24353
	APFPA [30]	41628.75 <sup>a</sup>	41628.75 <sup>a</sup>	14.0470	3.5571 <sup>a</sup>	NA
	MICA-TLA [31]	41675.05	41675.05	15.0149	1.6161	NA
	ARCBBO [32]	41686	41686	15.3769	NA	NA
LTLBO [33]	41679.55	41679.55	15.1589	NA	NA	
Case-2	CSBO	<b>41774.45</b>	41697.22	15.5851	0.7723	0.2930
	SP-DE [22]	41774.75	41697.50	15.5897	0.7725	0.29228
	ECHT-DE [22]	41776.48	41694.82	15.5806	0.81659	0.29198
	SF-DE [22]	41775.09	41697.52	15.5616	0.77572	0.29262
	MSA [27]	41782.80	41714.98	15.9214	0.6782	0.29533
	MFO [27]	41786.66	41718.87	16.2189	0.6780	0.29525
	DSA [29]	41775.60	41699.40	NA	0.7620	0.2471
	MICA-TLA [31]	42013.08	41959.18	19.909	0.5390	NA
Case-3	CSBO	<b>41693.96</b>	41666.10	14.8500	1.7059	0.2785
	SP-DE [22]	41696.54	41668.45	15.012	1.60803	0.28092
	ECHT-DE [22]	41699.25	41671.09	15.0275	1.56188	0.28152
	SF-DE [22]	41695.55	41667.53	14.8963	1.61174	0.28022
	MSA [27]	41703.48	41675.99	15.0026	1.7236	0.27481
	MFO [27]	41707.66	41680.19	15.1026	1.7245	0.27467
	DSA [29]	41785.05	41761.22	NA	1.0573	0.2383
Case-4	CSBO	<b>0.5871</b>	48524.40	20.3134	0.58710	0.3008
	SP-DE [22]	0.59267	45549.49	18.4275	0.59267	0.30052
	ECHT-DE [22]	0.60416	46813.22	19.0821	0.60416	0.3008
	SF-DE [22]	0.59584	45246.02	18.4697	0.59584	0.30135
	DE [26]	0.5839 <sup>b</sup>	NA	NA	0.5839 <sup>b</sup>	NA
	KHA [34]	0.5810 <sup>b</sup>	42006.44	NA	0.5810 <sup>b</sup>	NA
Case-5	APFPA [30]	0.8909	43485.93	12.1513	0.8909	NA
	CSBO	<b>134934.3</b>	134934.3	57.8922	2.9658	NA
Case-6	SP-DE [22]	135055.7	135055.7	60.9596	1.0715	NA
	CSBO	<b>16.4688</b>	155741.09	16.4688	2.5323	NA
	SP-DE [22]	17.6946	155724.9	17.6946	0.8663	NA

<sup>a</sup>Load bus voltage constraint is violated, <sup>b</sup>Limits for shunt compensators are violated.

**Conflicts of interest**

The authors declare no conflicts of interest.

**References**

1. Aydin, M. (2016). Enerji verimliliğinin sürdürülebilir kalkınmadaki rolü: Türkiye değerlendirmesi. *Yönetim Bilimleri Dergisi*, 14(28), 409-441.
2. Akdag, O. (2022). A improved Archimedes optimization algorithm for multi/single-objective optimal power flow. *Electric Power Systems Research*, 206, 107796. <https://doi.org/10.1016/j.epsr.2022.107796>

3. Li, S., Gong, W., Wang, L., & Gu, Q. (2022). Multi-objective optimal power flow with stochastic wind and solar power. *Applied Soft Computing*, 114, 108045. <https://doi.org/10.1016/j.asoc.2021.108045>
4. Elattar, E. E., & ElSayed, S. K. (2019). Modified JAYA algorithm for optimal power flow incorporating renewable energy sources considering the cost, emission, power loss and voltage profile improvement. *Energy*, 178, 598-609. <https://doi.org/10.1016/j.energy.2019.04.159>
5. Akbari, E., Ghasemi, M., Gil, M., Rahimnejad, A., & Andrew Gadsden, S. (2022). Optimal power flow via teaching-learning-studying-based optimization algorithm. *Electric Power Components and Systems*,

- 49(6-7), 584-601.  
<https://doi.org/10.1080/15325008.2021.1971331>
6. Bakir, H., Guvenc, U., & Kahraman, H. T. (2022). Optimal operation and planning of hybrid AC/DC power systems using multi-objective grasshopper optimization algorithm. *Neural Computing and Applications*, 34(24), 22531-22563.  
<https://doi.org/10.1007/s00521-022-07670-y>
  7. Houssein, E. H., Hassan, M. H., Mahdy, M. A., & Kamel, S. (2023). Development and application of equilibrium optimizer for optimal power flow calculation of power system. *Applied Intelligence*, 53(6), 7232-7253.  
<https://doi.org/10.1007/s10489-022-03796-7>
  8. Ramesh, S., Verdú, E., Karunanithi, K., & Raja, S. P. (2023). An optimal power flow solution to deregulated electricity power market using meta-heuristic algorithms considering load congestion environment. *Electric Power Systems Research*, 214, 108867.  
<https://doi.org/10.1016/j.epsr.2022.108867>
  9. Premkumar, M., Kumar, C., Dharma Raj, T., Sundarsingh Jebaseelan, S. D. T., Jangir, P., & Haes Alhelou, H. (2023). A reliable optimization framework using ensembled successive history adaptive differential evolutionary algorithm for optimal power flow problems. *IET Generation, Transmission & Distribution*, 17(6), 1333-1357. <https://doi.org/10.1049/gtd2.12738>
  10. Kaur, M., & Narang, N. (2023). Optimal Power Flow Solution Using Space Transformational Invasive Weed Optimization Algorithm. *Iranian Journal of Science and Technology, Transactions of Electrical Engineering*, 1-27. <https://doi.org/10.1007/s40998-023-00592-y>
  11. Bakır, H., Guvenc, U., Duman, S., & Kahraman, H. T. (2023). Optimal power flow for hybrid AC/DC electrical networks configured with VSC-MTDC transmission lines and renewable energy sources. *IEEE Systems Journal*, 17(3), 3938 – 3949.  
<https://doi.org/10.1109/JSYST.2023.3248658>
  12. Sonmez, Y., Duman, S., Kahraman, H. T., Kati, M., Aras, S., & Guvenc, U. (2022). Fitness-distance balance based artificial ecosystem optimisation to solve transient stability constrained optimal power flow problem. *Journal of Experimental & Theoretical Artificial Intelligence*, 1-40.  
<https://doi.org/10.1080/0952813X.2022.2104388>
  13. Abd El-sattar, S., Kamel, S., Ebeed, M., & Jurado, F. (2021). An improved version of salp swarm algorithm for solving optimal power flow problem. *Soft Computing*, 25, 4027-4052.  
<https://doi.org/10.1007/s00500-020-05431-4>
  14. Jangir, P., Manoharan, P., Pandya, S., & Sowmya, R. (2023). MaOTLBO: Many-objective teaching-learning-based optimizer for control and monitoring the optimal power flow of modern power systems. *International Journal of Industrial Engineering Computations*, 14(2), 293-308.  
<https://doi.org/10.5267/j.ijiec.2023.1.003>
  15. Pandya, S. B., Ravichandran, S., Manoharan, P., Jangir, P., & Alhelou, H. H. (2022). Multi-objective optimization framework for optimal power flow problem of hybrid power systems considering security constraints. *IEEE Access*, 10, 103509-103528.  
<https://doi.org/10.1109/ACCESS.2022.3209996>
  16. Premkumar, M., Jangir, P., Sowmya, R., & Elavarasan, R. M. (2021). Many-objective gradient-based optimizer to solve optimal power flow problems: analysis and validations. *Engineering Applications of Artificial Intelligence*, 106, 104479.  
<https://doi.org/10.1016/j.engappai.2021.104479>
  17. Ghasemi, M., Akbari, M. A., Jun, C., Bateni, S. M., Zare, M., Zahedi, A., ... & Chau, K. W. (2022). Circulatory System Based Optimization (CSBO): An expert multilevel biologically inspired meta-heuristic algorithm. *Engineering Applications of Computational Fluid Mechanics*, 16(1), 1483-1525.  
<https://doi.org/10.1080/19942060.2022.2098826>
  18. Wang, L., Cao, Q., Zhang, Z., Mirjalili, S., & Zhao, W. (2022). Artificial rabbits optimization: A new bio-inspired meta-heuristic algorithm for solving engineering optimization problems. *Engineering Applications of Artificial Intelligence*, 114, 105082.  
<https://doi.org/10.1016/j.engappai.2022.105082>
  19. Abdollahzadeh, B., Gharehchopogh, F. S., & Mirjalili, S. (2021). African vultures optimization algorithm: A new nature-inspired metaheuristic algorithm for global optimization problems. *Computers & Industrial Engineering*, 158, 107408.  
<https://doi.org/10.1016/j.cie.2021.107408>
  20. Talatahari, S., & Azizi, M. (2021). Chaos game optimization: a novel metaheuristic algorithm. *Artificial Intelligence Review*, 54, 917-1004. <https://doi.org/10.1007/s10462-020-09867-w>
  21. Mohamed, A. A. A., Mohamed, Y. S., El-Gaafary, A. A., & Hemeida, A. M. (2017). Optimal power flow using moth swarm algorithm. *Electric Power Systems Research*, 142, 190-206.  
<https://doi.org/10.1016/j.epsr.2016.09.025>
  22. Biswas, P. P., Suganthan, P. N., Mallipeddi, R., & Amaratunga, G. A. (2018). Optimal power flow solutions using differential evolution algorithm integrated with effective constraint handling techniques. *Engineering Applications of Artificial Intelligence*, 68, 81-100.  
<https://doi.org/10.1016/j.engappai.2017.10.019>
  23. Zimmerman, R.D., Murillo-Sánchez, C.E., Thomas, R.J., (2023). *Matpower*.  
<http://www.pserc.cornell.edu/matpower>.
  24. MATLAB, T. U. S. G. (2022). Natick, Massachusetts: The MathWorks Inc.
  25. Zimmerman, R. D., Murillo-Sánchez, C. E., & Thomas, R. J. (2010). MATPOWER: Steady-state operations, planning, and analysis tools for power systems research and education. *IEEE Transactions on power systems*, 26(1), 12-19.  
<https://doi.org/10.1109/TPWRS.2010.2051168>
  26. Shaheen, A. M., Farrag, S. M., & El-Sehiemy, R. A. (2017). MOPF solution methodology. *IET Generation, Transmission & Distribution*, 11(2), 570-581.  
<https://doi.org/10.1049/iet-gtd.2016.1379>
  27. Mohamed, A. A. A., Mohamed, Y. S., El-Gaafary, A. A., & Hemeida, A. M. (2017). Optimal power flow using

- moth swarm algorithm. *Electric Power Systems Research*, 142, 190-206. <https://doi.org/10.1016/j.epsr.2016.09.025>
28. Boucekara, H. R., Chaib, A. E., Abido, M. A., & El-Sehiemy, R. A. (2016). Optimal power flow using an Improved Colliding Bodies Optimization algorithm. *Applied Soft Computing*, 42, 119-131. <https://doi.org/10.1016/j.asoc.2016.01.041>
29. Abaci, K., & Yamacli, V. (2016). Differential search algorithm for solving multi-objective optimal power flow problem. *International Journal of Electrical Power & Energy Systems*, 79, 1-10. <https://doi.org/10.1016/j.ijepes.2015.12.021>
30. Mahdad, B., & Srairi, K. (2016). Security constrained optimal power flow solution using new adaptive partitioning flower pollination algorithm. *Applied Soft Computing*, 46, 501-522. <https://doi.org/10.1016/j.asoc.2016.05.027>
31. Ghasemi, M., Ghavidel, S., Rahmani, S., Roosta, A., & Falah, H. (2014). A novel hybrid algorithm of imperialist competitive algorithm and teaching learning algorithm for optimal power flow problem with non-smooth cost functions. *Engineering Applications of Artificial Intelligence*, 29, 54-69. <https://doi.org/10.1016/j.engappai.2013.11.003>
32. Kumar, A. R., & Premalatha, L. (2015). Optimal power flow for a deregulated power system using adaptive real coded biogeography-based optimization. *International Journal of Electrical Power & Energy Systems*, 73, 393-399. <https://doi.org/10.1016/j.ijepes.2015.05.011>
33. Ghasemi, M., Ghavidel, S., Gitizadeh, M., & Akbari, E. (2015). An improved teaching-learning-based optimization algorithm using Lévy mutation strategy for non-smooth optimal power flow. *International Journal of Electrical Power & Energy Systems*, 65, 375-384. <https://doi.org/10.1016/j.ijepes.2014.10.027>
34. Roy, P. K., & Paul, C. (2015). Optimal power flow using krill herd algorithm. *International Transactions on Electrical Energy Systems*, 25(8), 1397-1419. <https://doi.org/10.1002/etep.1888>
35. Derrac, J., García, S., Molina, D., & Herrera, F. (2011). A practical tutorial on the use of nonparametric statistical tests as a methodology for comparing evolutionary and swarm intelligence algorithms. *Swarm and Evolutionary Computation*, 1(1), 3-18. <https://doi.org/10.1016/j.swevo.2011.02.002>



© Author(s) 2024. This work is distributed under <https://creativecommons.org/licenses/by-sa/4.0/>



## Solution-based fabrication of copper oxide thin film influence of cobalt doping on structural, morphological, electrical, and optical properties

Samed Çetinkaya<sup>\*1</sup> 

<sup>1</sup>Mersin University, Department of Medical Services and Techniques, Türkiye, samedcetinkaya@mersin.edu.tr

Cite this study:

Çetinkaya, S. (2024). Solution-based fabrication of copper oxide thin film influence of cobalt doping on structural, morphological, electrical, and optical properties. Turkish Journal of Engineering, 8 (1), 107-115

### Keywords

Chemical bath deposition  
Copper  
Cobalt  
Doping  
Activation energy

### Research Article

DOI: 10.31127/tuje.1290655

Received:01.05.2023

Revised: 02.06.2023

Accepted:06.06.2023

Published:15.09.2023



### Abstract

In this study, Cobalt (Co) doped Copper Oxide (CuO) films at different concentrations were deposited on glass substrates, using the Chemical Bath Deposition (CBD) method. The films were characterized by Field Emission Scanning Electron Microscopy (FESEM), X-Ray Diffraction (XRD), Ultra Violet-Visible Spectroscopy (UV-Vis.) and two-point contact method. The FESEM images showed that nanoplates formed increased in size and voids on the films surface decreased with increasing Co concentration. The XRD patterns revealed an increase in crystallite size with increasing (from 14.40 to 18.60 nm) Co concentration and no secondary phase was formed. The Energy-dispersive X-ray spectroscopy (EDS) spectra showed the presence of Co in the film composition with increasing concentration. The results of UV-Vis. spectroscopy showed that band gap values could be changed with Co doping and thus the CuO band gap could be adjusted with the Co doping. The temperature-dependent current-voltage measurement results obtained with the two-point contact method showed that activation energy levels increased (from 0.134 to 0.232 eV) with increasing Co concentration. It was also observed that the conductivity increased with increasing temperature.

## 1. Introduction

The decreasing fossil-based fuel reserves in the face of increasing energy demand has increased the interest in researching renewable alternative energy sources. Among the renewable energy sources, the most efficient and renewable energy source is solar energy [1]. Various materials have been developed to generate electricity from solar energy. Among them, nano-structured materials are widely used in this field due to their unique and interesting properties. These properties (such as electronic, magnetic, optical and structural properties) are characteristic of the nano-structured materials used and can be improved [2]. The surface properties of these structures affect their physical and chemical properties. For example, the photoconductivity properties of these structures vary depending on the surface area/volume ratio of the nanostructured material used and/or the porous structures on the surface. For this reason, these structures have been classified in the literature with various definitions such as nano-particles, nano-plates, nano-tubes, nano-rods, nano-flowers, and nano-spheres

[3]. Nano-structured materials with such different morphologies can be produced by doping various elements. Nanostructured materials are of great interest to researchers because they exhibit interesting properties in different applications as a result of the doping of transition metal oxides.

Among them, copper oxide (CuO) is an important transition metal oxide that exhibits p-type electrical conductivity and has a limited band gap and is a semiconductor with monoclinic crystal structure ( $E_g=1.2-1.8$  eV) [4-6]. CuO is a nanotechnological material with gas sensors, biosensors, chemical sensors, solar cell absorber, high temperature ( $T_c$ ) superconductors, lithium-ion batteries and catalysts applications [7]. In order for this material to be used in such a variety of fields, it must be produced in a cost-effective and environmentally friendly manner. Various deposition methods have been developed to fabricate for doped and undoped CuO nanostructures for instances; electrochemical deposition [8,9], physical vapor deposition [10,11], sol gel immersion [12,13] and sol-gel pin coating [14,15] deposition, radio frequency

sputtering deposition [16,17] and chemical bath deposition [17,18]. The chemical bath deposition method (CBD) offers many advantages for the production of thin films, including simplicity, proportional control of elements, cost-effectiveness, and deposition feasibility on large-area substrates. Many studies are being conducted to improve the performance of nanostructured materials such as CuO. In the literature, there are many studies conducted with the doping of different transition metals (such as Mn, Co and Fe) to improve the characteristics of semiconductors [19-21].

Transition metals (TMs) have high density, good conductivity and high melting-boiling temperatures [22-25]. Among these, Cobalt is preferred in studies due to its good effects on magnetic, hardness and electrical resistance [26,27]. CuO is an exciting semiconducting material with interesting structural and optical properties.

The effects of TMs-doping to the morphological, structural, and optical properties of the CuO films was reported in the literature.

In addition, The TMs- doped CuO thin films have attracted the attention of researchers for its applications in spintronic and ferromagnetism interactions [28,29].

According to the literature records we obtained as a result of our research, the effect of Co doping on the optical, structural, morphological and electrical properties of CuO films has not been studied yet by using the chemical bath deposition method.

In this study, it was aimed to determine the effect of Co doping concentration on the morphology, crystal structure, optical and electrical properties of CuO nano-structured films obtained by using chemical bath deposition method. Also, with this study, it is aimed to develop environmentally friendly materials and cost-effective methods for applications such as gas sensors, solar cells, catalysts, high temperature superconductors by improving the electrical and optical properties of CuO under the doping effect of cobalt ions.

## 2. Method

Doped and undoped CuO thin films were deposited using the CBD method on cleaned substrates following the established procedure [30]. Copper (II) Acetate Monohydrate ( $\text{Cu}(\text{CH}_3\text{COO})_2 \cdot \text{H}_2\text{O}$ ) ( $\geq 98\%$ ) (0.1 M) and Cobalt(II) Chloride Hexahydrate ( $\text{CoCl}_2 \cdot 6\text{H}_2\text{O}$ ) ( $\geq 98\%$ ) metal salts was used as starting solutions for Cu and Co, respectively. All chemicals used in the experiment were supplied by Merck KGaA. The films were deposited on standard microscope slides (7.5 cm \* 2.5 cm). Chemical cleaning of the substrates has been completed by reference to previous studies as previous established procedure [20].

Copper (II) Acetate Monohydrate ( $\text{Cu}(\text{CH}_3\text{COO})_2 \cdot \text{H}_2\text{O}$ ) ( $\geq 98\%$ ) (0.1 M) was mixed with distilled water (double distilled water) as solvent in a 100 mL beaker to store pure CuO thin films. The solution was stirred to the obtain homogeneous solution at room temperature during 10 min.

Aqueous ammonia was added to the starting solution to adjust the pH ( $\sim 10$ ) of the solution. After the previously cleaned substrates were immersed in the bath

solution, the temperature of the solution was adjusted to  $\sim 90$  °C.

( $\text{Cu}(\text{OH})_2$ ) compound, which is formed by adding too much ammonia, turns into CuO with increasing temperature and starts to be stored on the substrate). After 20 minutes, the substrates removed from the solution were washed with double distilled water and left to dry at room conditions. This process was applied in the same way for the films to be deposited with cobalt added to the starting solution (atomic percent ratio (at. %) as 1, 3 and 5). Doped and undoped CuO thin films obtained after deposition were heat treated for 1 hour in an ash furnace (MKF106, Miprolab) at 573 K. According to the contribution ratio in the article, the samples are labelled as S0: undoped, S1: 1 at. %, S3: 3at. % and S5: 5at. % respectively.

Crystallographic structures of the films were investigated by X-Ray Diffraction (Rigaku Smartlab, X-Ray Diffractometer, Tokyo, Japan, X-ray diffraction device,) and  $\text{Cu K}\alpha$  radiation in  $0.01^\circ$  steps ( $\lambda = 1, 54059$  Å). The atomic ratios of the elements were determined using energy dispersion spectroscopy (EDS) (FEI EDS nova nano, NYSE, USA). The morphological and topological properties of the films were determined using Field emission scanning electron microscopy (FESEM, ZEISS EVO-LS10, NTS, Munich, Germany) The electrical properties of the samples were determined using a home-made Labview program-controlled voltage source computer interface with a precision multimeter (GW Instek, New Taipei, Taiwan) and a programmable power supply (GW Instek, New Taipei, Taiwan) using the two-point probe method with a temperature range of 300-500 K. Optical absorption spectra of pure and Co-doped CuO films were obtained using UV-Vis. Spectrophotometer (PerkinElmer) in the wavelength range of 200-1100 nm.

## 3. Results

The diffraction patterns of Co-doped and undoped CuO films as a result of X-ray diffraction spectrophotometer measurement are given in Figure 1. All the diffraction peaks match the monoclinic CuO (ICCD: 801916) phase, and no foreign peaks and/or a secondary phase were observed. It had been observed that these results are compatible with the literature. This can be interpreted as proof that Co doping penetrates into the CuO crystal lattice [30-32].

In Figure 1, it was seen that all films have the preferential orientation ( $\bar{1}11$ ) and (111). Apart from these, (110), ( $\bar{2}02$ ), (020), (202), ( $\bar{1}13$ ), (022), (113), (311) and (004) peaks were also detected. In addition, it was observed that the ( $\bar{1}11$ ) and (111) peak positions did not undergo a large shift in the peak positions with the contribution of Co. Table 1 clearly shows that the microstrain is directly proportional to the dislocation density and inversely proportional to the crystal size.

Dislocations are irregularities in a crystal that occur due to lattice mismatch from one part of the crystal to the other. These irregularities cause defects and strains in the crystal structure. Table 1 showed that the strains and strains in the crystal structure of the produced films were smaller compared to the undoped films. Also, D the

crystal size;  $\epsilon$ , micro strain;  $\rho$ , defect density and  $d$ , distance between planes are calculated and given in [Table 1](#). The positions of the peaks did not show a significant shift as the Co contribution had no or negligible effect on the strains in the lattice. Also, no extra peaks representing any copper-cobalt phase were detected, ultimately proving that this method can reliably produce samples in a single phase. In addition, since the ionic radii of  $\text{Co}^{+2}$  (0.74 Å) and  $\text{Cu}^{+2}$  (0.73 Å) are very close to each other,  $\text{Co}^{+2}$  can easily settle in the spaces left by the  $\text{Cu}^{+2}$  ion [30].

$$D = \frac{K\lambda}{\beta \cos \theta} \quad (1)$$

Here  $\lambda$ ; is the wavelength of X-ray radiation,  $K$ ; (fixed with a value of 0.94 not greater than 1) correction factor,  $\theta$ ; is the Bragg diffraction angle and  $\beta$ ; is the width of the half-maximum of a vertex is the angular value of the vertices at full width [20].

Defective place density, which gives the number of defects in the structure, can be calculated with the following [Equation 2](#) [20].

$$\delta = \frac{1}{D^2} \quad (2)$$

A low value of the defect location density indicates the presence of crystallized wells. The micro strain ( $\epsilon$ ) of the films can be calculated using [Equation 3](#) [20].

$$\epsilon = \frac{\beta \cos \theta}{4} \quad (3)$$

Here;  $\beta$  is the full width half maximum and  $\theta$  is the diffraction angle. The micro strain is caused by the ion diameter between the guest (Co, doping) element and the host (Cu, doped) element. However, since the ionic diameters of these two elements are very close to each other, it is thought that there is no significant change.

The crystallite size values listed in [Table 2](#) increased from 14.40 nm to 18.60 nm with increasing Co doping. According to [Table 1](#), the increase in cobalt concentration increases the crystallite dimensions. It is seen that the increase in the crystallite size causes a decrease in the band gap. It was found that the increase in cobalt concentration caused the formation of other phase peaks of monoclinic CuO. This increase in peak density can be attributed to the increase in the crystallinity of the films.

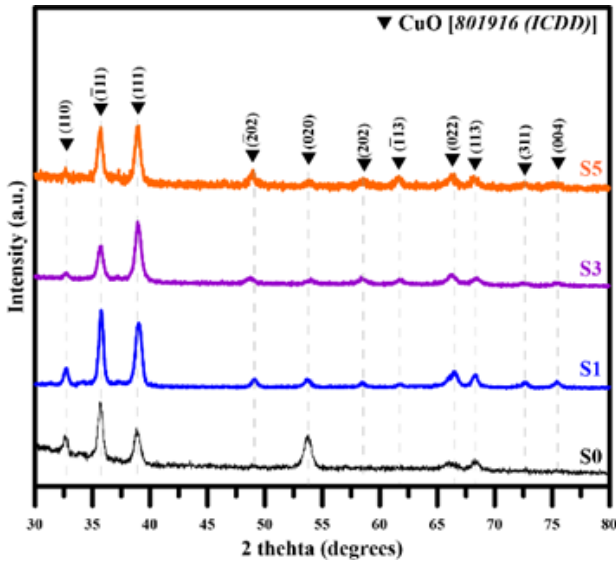


**Figure 1.** Diffraction patterns of Co-doped and undoped CuO films (S0: undoped, S (1-5): Co-doped CuO films).

The mean crystallite size ( $D$ ) was calculated from the full width ( $\beta$ ) of the half-maximum of a peak using the Scherrer formula, using [Equation 1](#).

**Table 1.** Some structural parameters obtained and calculated from the films ( $D$ , crystal size;  $\epsilon$ , micro strain;  $\rho$ , defect density;  $d$ , interplane spacing).

Samples	(111)		(111)		(020)		$D$ (nm)	$\epsilon$ ( $10^{-4}$ )	$\rho$ ( $10^{15} \text{ cm}^{-2}$ )
	$2\theta$ ( $^\circ$ )	$d$ (Å)	$2\theta$ ( $^\circ$ )	$d$ (Å)	$2\theta$ ( $^\circ$ )	$d$ (Å)			
S0	35,672	2,510	38,810	2,318	53,670	1,707	14,40	29,19	4,91
S1	35,735	2,511	39,000	2,308	53,770	1,704	16,00	23,28	4,22
S3	35,676	2,514	38,920	2,312	54,050	1,695	17,20	23,25	4,19
S5	35,669	2,515	38,875	2,315	53,870	1,700	18,60	23,09	4,14

**Table 2.** Variation of CuO:Co films on atomic doping ratio percentages, crystallite sizes and optical band gaps.

Samples	Atomic contribution ratio (%)	Crystallite Size (nm)	Forbidden energy gap (eV)
S0	0	14,40	1,64
S1	1	16,00	1,55
S3	3	17,20	1,52
S5	5	18,60	1,44

FESEM surface morphology images of Co-doped and undoped CuO films are given in [Figure 2](#) and EDS spectrum is given in [Figure 3](#). As can be seen in [Figure 2](#), it was observed that the surface properties of CuO films changed significantly as a function of Co concentration. It was observed that the Co concentration had a significant effect on the shape and size of the nanostructures. It was found that the undoped CuO film has a regular and homogeneous distribution of micron-sized plates, on the

other hand, these plates increase in size (from ~200nm to ~800nm) with the increase of Co concentration, and agglomerated heaps are formed on the film surface. In addition, it was observed that the gaps between the nano-sized plates decreased with the increase in the amount of Co.

Here, it has been reported by researchers in the literature that the increase in grain size may have a positive contribution to the conductivity mechanism as it

will create less obstacle for the charge carriers [30,31]. Figure 3 shows the chemical composition analysis result using the EDS spectrum of Co-doped and undoped CuO films. In the EDS spectrum, it was observed that there are peaks of Cu, Co and O elements. In Figure 3, it is clearly

seen that the Co element enters the CuO matrix with the increase in the doping ratio. It can be interpreted by considering the obtained structural measurement (XRD) results that Co doping has a significant effect on the characteristic properties of CuO films.

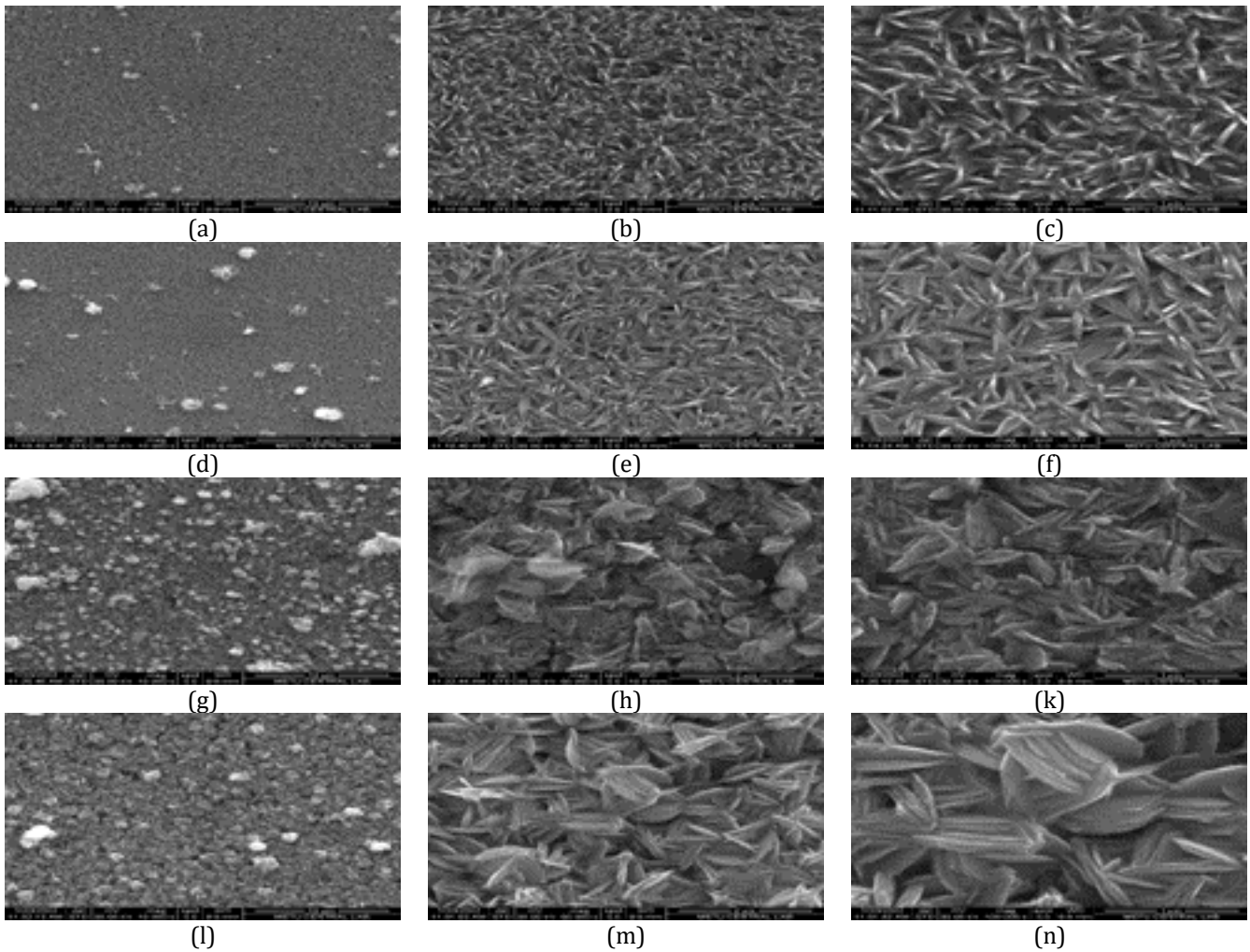


**Figure 2.** (a) 10kX, (b) 50kX and (c) 100kX, S0 coded samples; (d) 10kX, (e) 50kX and (f) 100kX belong to the S1 coded samples; FE-SEM surface morphology images of (g) 10kX, (h) 50kX and (k) 100kX and (l) 10kX, S3 coded samples, (m) 50kX and (n) 100kX, S5 coded samples.

The optical properties of the films were calculated using the absorption spectra collected by UV-Vis. spectrophotometer. Tauc plots of the allowed band gap of the films as a function of Co contribution are given in Figure 4. Equation 4 was used to obtain the band gap values.

$$ahv = C(hv - E_g)^m \quad (4)$$

where C is a constant, a is the optical absorption coefficient and  $m = 1/2$  for direct allowed transition semiconductors. The point where the linear part of the Tauc plots shown in Figure 4 intersects the hv axis gives the band gap values of the films [33-35].

The calculated band gap of the forbidden energy of the films for S0-S5 at atomic concentrations of Co element, respectively; S0: 1.64, S1: 1.55, S3: 1.52, and S5: 1.44 eV. The results are consistent with the literature [20]. Moreover, the change in band gap values versus Co doping is shown in Figure 4. It is seen that the  $E_g$  values

of the films decrease with increasing Co concentration. This narrowing in the allowed band gap according to the additive concentration can be interpreted as a result of the band gap and crystallite size being inversely proportional to each other (Table 2). Similar behavior, Bayansal et al. [20] reported with the relationship they obtained as a result of cobalt doping. Bayansal et al. [20] reported this as the result of an effect that can be seen in nanoparticles due to the quantum confinement effect. Consequently, a change in particle and/or crystallite size directly affects the optical properties. As a result, Co doping has shown that it can be used to regulate the  $E_g$  of CuO films.

In order to find the electrical activation energies of the impurity levels, the conductivity-temperature characteristics of the samples were investigated in the 300-500 K temperature range by using the software prepared using LabVIEW graphical programming language and programmable precision multimeter (GW Instek 8261A) and voltage source (GW Instek 4303S) equipment. Conductive spring contact tips to be used in

two contact methods are used in FEIN brand and scientific circuit conductivity test (ICT) processes. These are gold-plated contact tips with a diameter of 0.6mm, low contact resistance, and stable measurement between -45° and +200°C. Contact tips can be made to contact the surface of the films directly or by taking an Ohmic contact. Here, ohmic contacts are formed on the surface of the films with silver conductive paste in order to increase the conductivity on the contact surface. Contributions from the contacts have been calibrated

and eliminated to be minimized by software. According to the solid state theory of semiconductors, the temperature dependence of the dark electrical resistance of a semiconductor with one or more impurity levels is given by Equation 5 [39].

$$R(T) = R_0 e^{\frac{E_g}{2kT}} + \sum_{(i=1)}^n R'_{0,i} e^{\frac{\Delta E_i}{kT}} \quad (5)$$

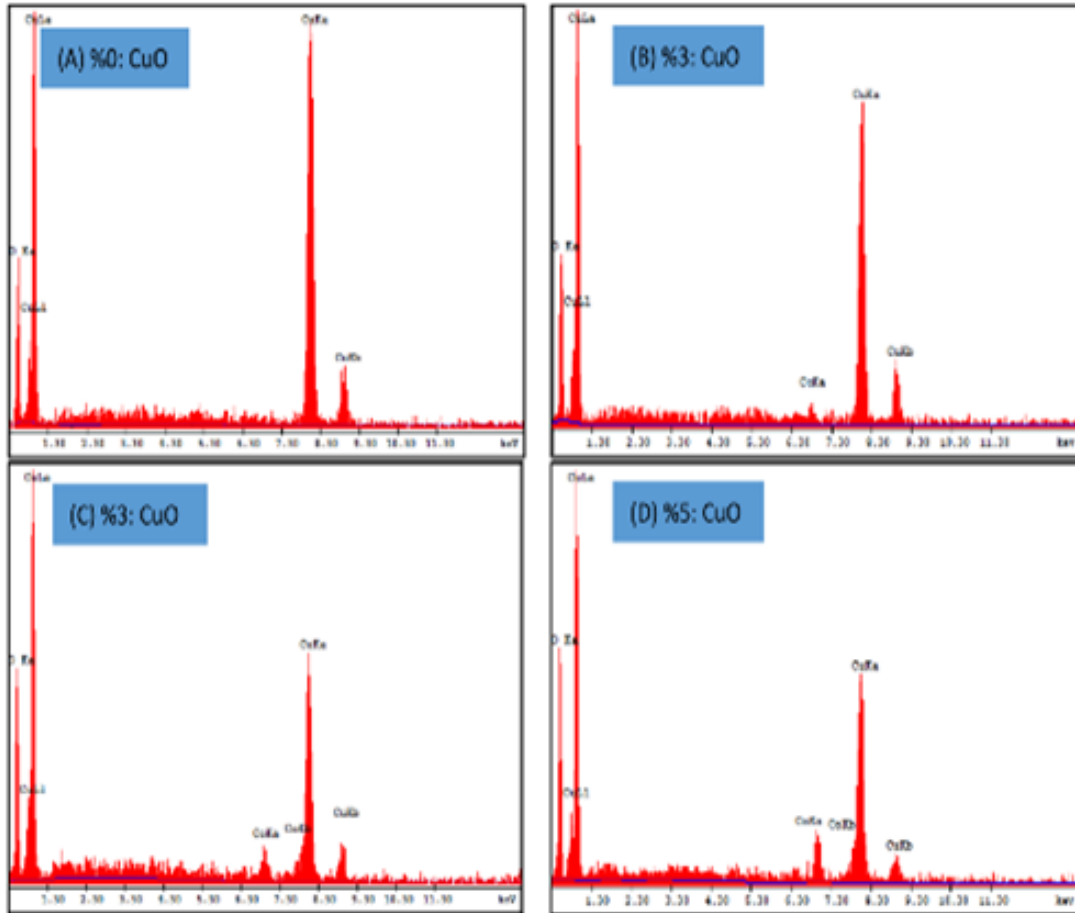


Figure 3. Energy dispersion X-ray spectroscopy (EDS) spectra of (a) S0, (b) S1, (c) S3 and (d) S5 coded samples.

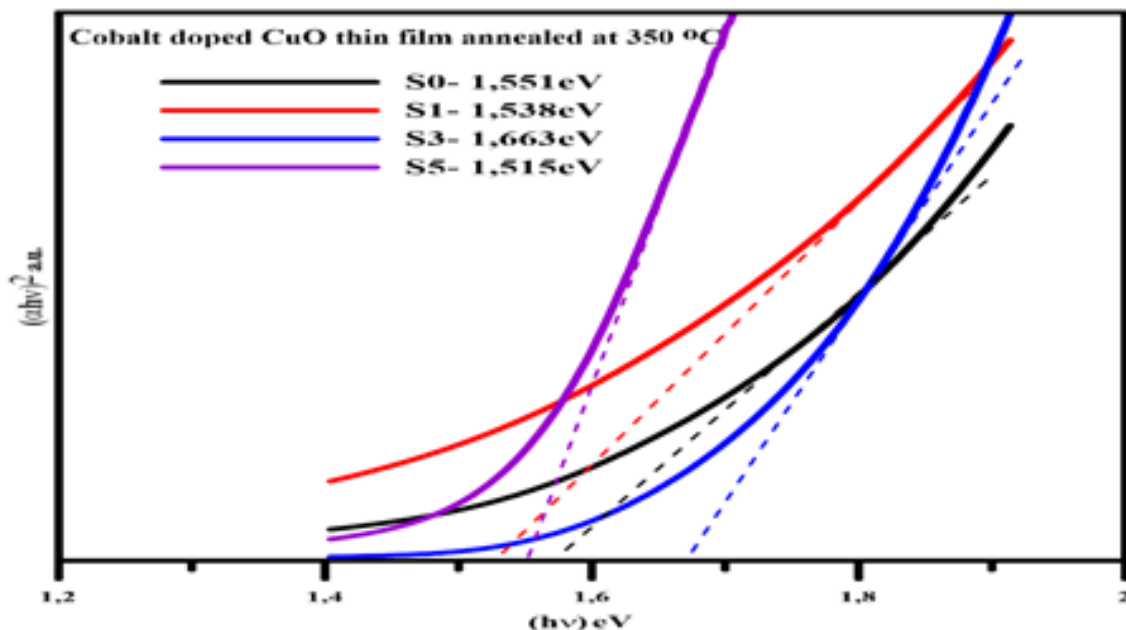


Figure 4. Direct-allowed bandgap energy values of Co-doped and undoped CuO thin films.

Here, the constants  $R_0$  and  $R_{(0,i)}$  define the temperature-dependent forbidden band gap energy,  $E_g$  the impurity level ionization energy,  $k$  the Boltzmann constant, and  $T$  the absolute temperature in Kelvin. In the temperature range region of 300-390 K, the overall electrical conductivity of a semiconductor is suppressed by the charge carriers produced by the ionization of impurity levels, and therefore the second term in Equation 5 dominates in this temperature range. With the increase towards high temperatures, the variation of the resistance of the semiconductor with temperature changes through band-to-band electronic transitions. Under these conditions, charge carriers acquire sufficient thermal energy to switch between bands [36]. According to the information above, they can be considered as independent values in the temperature ranges corresponding to the two terms appearing in Equation 5. Therefore, a series of linear trends appear, showing the band gap of the forbidden energy and a range of impurity levels (band gap states) in that gap. The slope of these linear regions formed, the electrical conductivity for a semiconductor such as CuO, is governed by the ionization of charge carriers at impurity levels in the investigated temperature range [37].

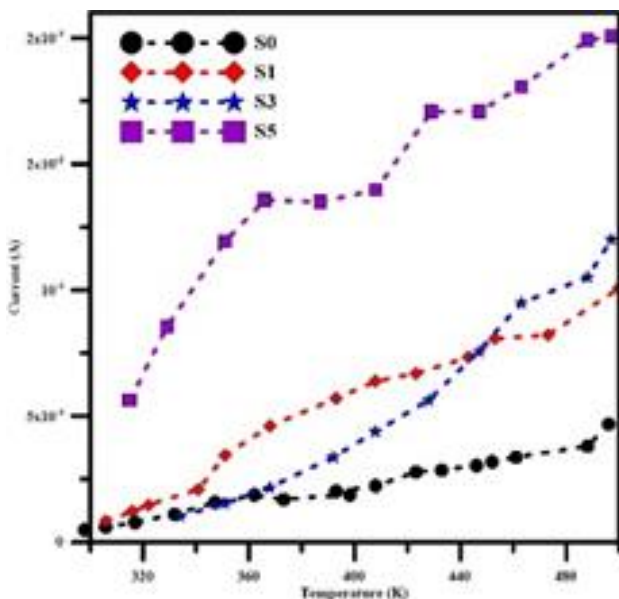
Therefore, the second term in Equation 5 is more dominant in R-T dependence. Upon increasing the temperature in the outer conductivity region, a decrease in electrical resistance (corresponding to a lower temperature range) is expressed by Equation 6 [36].

$$T = \sum_{(i=1)}^n R'_{(0,i)} \exp \left( \frac{\Delta E_i}{k R(T)} \right) \quad (6)$$

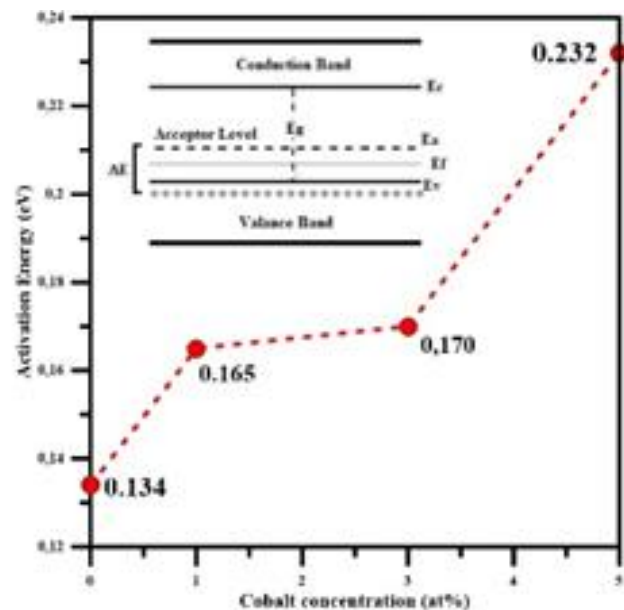
Only one linear region was detected in Co-doped and undoped CuO thin films, and an impurity level could be calculated for each sample. Using Equation 7, it can be written as [36];

$$\Delta E = k \frac{d(\ln R(T))}{d\left(\frac{1}{T}\right)} \quad (7)$$

Figure 5a shows the changes in the current depending on the temperature in the films (S0, S1, S3, and S5). By calculating the ionization energy values of the pollution (impurity) level against the Co additive concentration, S0: 0.134; S1: 0.165; S3: 0.17 and S5: 0.232 eV. Also, the change in activation energy values versus cobalt additive concentration is given in Figure 5b. The activation energy level represents the energy difference between the acceptor level and the valence band in the inner drawing shown in the graph in Figure 5b. Thus, the amount of energy required for the charge carriers located in these intermediate levels (pollution/impurity) between the valence and conductivity energy levels to pass into the conduction band and contribute to the electrical conductivity can be calculated using the temperature-dependent current voltage measurement technique. Thermally activated band conductivity is defined by Equation 6. Activation energy for thermally activated band conductivity; The majority depends on the charge carrier concentration and the impurity energy levels. The change in charge carrier concentration changes the Fermi energy level in the  $E_g$  energy range, resulting in an increase or decrease in the activation energy [38]. When the calculated forbidden energy band gap ( $E_g$ ) values of the samples are examined, it is observed that the  $E_g$  values decrease (Figure 4) and the activation energy level values (Figure 5b) increase with the increase in the amount of doping. As Nguyen et al. reported in their study, this contradicts their interpretation of Donor-type load bearers. Because the CuO semiconductor used in our study has p-type electrical conductivity. For this reason, it can be interpreted that the increase in carrier concentration will decrease the Fermi energy level in the  $E_g$  energy range and this may cause an increase in the activation energy. Thus, it can be said that the results are compatible with the literature.



(a)



(b)

Figure 5. Variations of (a) current with temperature and (b) impurity levels with Co concentration.

According to the results obtained are compatible with the experimental results of XRD and FESEM analyzes (Figure 1 and Figure 2) because, according to these results, it is seen with the results of both methods that the crystallite and grain sizes increase with increasing Co concentration. As the crystallite size increases, the grain sizes increase, the contact surface areas between the grains increase, and therefore the gaps at the grain boundaries decrease. As a result, the scattering of carriers at grain boundaries is reduced [39]. As a result of this decrease, the number of load carriers participating in the transmission increases. Similar results were reported by Patil et al. [40]. The calculated activation energies are much smaller than the optical band gap energy ( $\ll E_g/2$ ), which can be interpreted as the transmission of charge carriers from the valence band to the acceptor level [38].

#### 4. Discussion

According to the results obtained valuable information given as below;

- ❖ According to X-ray diffraction spectrum data, it was determined that CuO and CuO:Co films have monoclinic crystal structure. It was determined that Co atoms penetrated CuO well and the preferential orientation of ( $\bar{1}11$ ) and (111) did not change with the increase in Co doping concentration. The increase in cobalt concentration increases the crystallite size. It is seen that the increase in crystallite size causes an increase in the activation energy values depending on the thermal conductivity together with the band gap. The crystallite size of undoped CuO (14.40 nm) increased with doping and the highest crystal size was calculated as 18.60 nm for the film with the highest Co concentration (S5).
- ❖ According to the FESEM images, a structure consisting of dense void-free nano-sized plates was seen. It was observed that the surface morphologies of the films changed depending on the Co concentration. It was observed that the gaps between the nano-sized plates decreased with the increase in the amount of Co. It has been observed that the average dimensions of these structures vary between 200-800 nm. It has been interpreted that Cu and Co elements have different atomic radii (Co: 167 pm; Cu: 157 pm) and electronegativity (Co: 1.88; Cu: 1.90) and the free surface energy and thermodynamic equilibrium states have an effect on the growth of CuO crystals. It was observed that the peaks of Cu, Co and O elements were observed in the EDS spectrum, and the change in the spectrum with Co concentration was clearly seen.
- ❖ Examining the optical behavior, it was determined that Co-doping was dominant on  $E_g$  of CuO films. This situation is directly related to the surface morphologies of the films produced. Because a change in particle/crystallite size directly affects the optical properties. The calculated band gap of the films was calculated as S0: 1.64, S1: 1.55, S3: 1.52 and S5: 1.44 eV for S0-S5, respectively, according to the atomic concentrations of Co element.
- ❖ It has been determined that Co doping, which has a significant effect on its electrical properties, increases the activation energy values. Activation energy values, S0: 0.14; S1: 0.16; S3: 0.17 and S5: 0.23 eV. It was found that as a result of the formation of larger nano-sized plates with the increase of the additive amount, the gaps between these nanostructures decreased. Since these gaps act as scattering centers for charge carriers, the increase in conductivity value is directly related to the surface morphology.

#### 5. Conclusion

In this study, CuO films doped with CuO and atomic additive ratio (1.0; 3.0; 5.0%at.) were deposited on glass substrates by using chemical bath deposition technique. The effects of Co concentration in CuO host on structural, morphological, optical and electrical properties were investigated in detail.

Thus, according to all data obtained from XRD, FESEM and Optical band measurement results, it was observed that each of the structural, morphological and optical parameters had significant effects on the electrical behavior of Cobalt doped CuO thin films. The research results show that some physical parameters of the CuO can be easily controller via doping Cobalt.

#### Conflicts of interest

The authors declare no conflicts of interest.

#### References

1. Mishra, A. K., & Pradhan, D. (2021). Hierarchical urchin-like cobalt-doped CuO for enhanced electrocatalytic oxygen evolution reaction. *ACS Applied Energy Materials*, 4(9), 9412-9419. <https://doi.org/10.1021/acsaem.1c01632>
2. Kerli, S., & Kavgacı, M. (2021). Bakır oksit ince filmlere bor katkısının metil mavisi üzerindeki fotokatalitik etkisinin araştırılması. *Journal of Boron*, 6(2), 283-289. <https://doi.org/10.30728/boron.797645>
3. Yetim, N. K., Aslan, N., Sarioğlu, A., Sarı, N., & Koç, M. M. (2020). Structural, electrochemical and optical properties of hydrothermally synthesized transition metal oxide (Co<sub>3</sub>O<sub>4</sub>, NiO, CuO) nanoflowers. *Journal of Materials Science: Materials in Electronics*, 31, 12238-12248. <https://doi.org/10.1007/s10854-020-03769-x>
4. Johan, M. R., Suan, M. S. M., Hawari, N. L., & Ching, H. A. (2011). Annealing effects on the properties of copper oxide thin films prepared by chemical deposition. *International Journal of Electrochemical Science*, 6(12), 6094-6104.
5. Bayansal, F., Şahin, O., & Çetinkara, H. A. (2020). Mechanical and structural properties of Li-doped CuO thin films deposited by the successive ionic layer adsorption and reaction method. *Thin Solid Films*, 697, 137839. <https://doi.org/10.1016/j.tsf.2020.137839>

6. Diachenko, O., Kováč Jr, J., Dobrozhan, O., Novák, P., Kováč, J., Skriniarova, J., & Opanasyuk, A. (2021). Structural and optical properties of CuO thin films synthesized using spray pyrolysis method. *Coatings*, 11(11), 1392. <https://doi.org/10.3390/coatings11111392>
7. Alzaid, M., Sajjad, M., Ali, K., Jamil, Y., Akbar, L., Sattar, A., Rizwan, A., Suhale, A., Ahmad, H., Nouman, C. M., Ghani, M. U., & Umair, A. (2020). Enhanced structural and optical properties of copper oxide for solar cell applications. *Journal of Ovonic Research Vol*, 16(6), 405-412.
8. Sadale, S. B., Patil, S. B., Teli, A. M., Masegi, H., & Noda, K. (2022). Effect of deposition potential and annealing on performance of electrodeposited copper oxide thin films for supercapacitor application. *Solid State Sciences*, 123, 106780. <https://doi.org/10.1016/j.solidstatesciences.2021.106780>
9. Dhanasekaran, V., Mahalingam, T., Chandramohan, R., Rhee, J. K., & Chu, J. P. (2012). Electrochemical deposition and characterization of cupric oxide thin films. *Thin Solid Films*, 520(21), 6608-6613. <https://doi.org/10.1016/j.tsf.2012.07.021>
10. Huang, M. L., Lu, S. G., Zhou, J. J., Luo, B. S., & Li, Y. H. (2022). Metallic coloration with Cu/CuO coating on polypropylene nonwoven fabric via a physical vapor deposition method and its multifunctional properties. *The Journal of The Textile Institute*, 113(7), 1345-1354. <https://doi.org/10.1080/00405000.2021.1928995>
11. Mahana, D., Mauraya, A. K., Pal, P., Singh, P., & Muthusamy, S. K. (2022). Comparative study on surface states and CO gas sensing characteristics of CuO thin films synthesised by vacuum evaporation and sputtering processes. *Materials Research Bulletin*, 145, 111567. <https://doi.org/10.1016/j.materresbull.2021.111567>
12. Musa, A. M. M., Farhad, S. F. U., Gafur, M. A., & Jamil, A. T. M. K. (2021). Effects of withdrawal speed on the structural, morphological, electrical, and optical properties of CuO thin films synthesized by dip-coating for CO<sub>2</sub> gas sensing. *AIP Advances*, 11, 115004. <https://doi.org/10.1063/5.0060471>
13. Salam, S., Jose, B., Raphael, R., & Anila, E. I. (2021, February). Synthesis and characterisation of copper oxide thin films by double dip method. In *IOP Conference Series: Materials Science and Engineering*, 1070(1), 012011. <https://doi.org/10.1088/1757-899X/1070/1/012011>
14. Kabir, M. H., Ibrahim, H., & Billah, M. M. (2021, February). Effect of stabilizer on sol ageing for CuO thin films synthesized by sol-gel spin coating technique. In *AIP Conference Proceedings*, 2324, 030007. <https://doi.org/10.1063/5.0037501>
15. Baturay, S., Candan, I., & Ozaydin, C. (2022). Structural, optical, and electrical characterizations of Cr-doped CuO thin films. *Journal of Materials Science: Materials in Electronics*, 33(9), 7275-7287. <https://doi.org/10.1007/s10854-022-07918-2>
16. Wu, J., Gao, Q., Wei, G., Xiu, J., Li, Z., & Liu, H. (2021). Optical properties and laser-induced breakdown spectroscopy analysis of Al-or Co-doped CuO thin films prepared on glass by radio-frequency magnetron sputtering. *Thin Solid Films*, 722, 138572. <https://doi.org/10.1016/j.tsf.2021.138572>
17. Patwary, M. A. M., Ohishi, M., Saito, K., Guo, Q., Yu, K. M., & Tanaka, T. (2021). Effect of Nitrogen Doping on Structural, Electrical, and Optical Properties of CuO Thin Films Synthesized by Radio Frequency Magnetron Sputtering for Photovoltaic Application. *ECS Journal of Solid State Science and Technology*, 10(6), 065019. <https://doi.org/10.1149/2162-8777/ac0a98>
18. Reyes-Vallejo, O., Escorcia-García, J., & Sebastian, P. J. (2022). Effect of complexing agent and deposition time on structural, morphological, optical and electrical properties of cuprous oxide thin films prepared by chemical bath deposition. *Materials Science in Semiconductor Processing*, 138, 106242. <https://doi.org/10.1016/j.mssp.2021.106242>
19. Babu, M. H., & Podder, J. (2021). Bond length controlling opto-structural properties of Mn doped CuO thin films: an experimental and theoretical study. *Materials Science in Semiconductor Processing*, 129, 105798. <https://doi.org/10.1016/j.mssp.2021.105798>
20. Bayansal, F., Taşköprü, T., Şahin, B., & Çetinkara, H. A. (2014). Effect of cobalt doping on nanostructured CuO thin films. *Metallurgical and Materials Transactions A*, 45, 3670-3674. <https://doi.org/10.1007/s11661-014-2306-1>
21. Chaudhary, M., Singh, M., Kumar, A., Gautam, Y. K., Malik, A. K., Kumar, Y., & Singh, B. P. (2021). Experimental investigation of Co and Fe-Doped CuO nanostructured electrode material for remarkable electrochemical performance. *Ceramics International*, 47(2), 2094-2106. <https://doi.org/10.1016/j.ceramint.2020.09.042>
22. Singh, P., Singh, R. K. & Kumar, R. (2021). Journey of ZnO quantum dots from undoped to rare-earth & transition metal-doped & their applications. *RSC Advance*, vol. 11, pp. 2512-2545. <https://doi.org/10.1039/D0RA08670C>
23. Qamar, M. A., Javed, M., Shahid, S., & Sher, M. (2022). Fabrication of g-C<sub>3</sub>N<sub>4</sub>/transition metal (Fe, Co, Ni, Mn and Cr)-doped ZnO ternary composites: Excellent visible light active photocatalysts for the degradation of organic pollutants from wastewater. *Materials Research Bulletin*, 147, 111630. <https://doi.org/10.1016/j.materresbull.2021.111630>
24. Wang, B., Iqbal, J., Shan, X., Huang, G., Fu, H., Yu, R., & Yu, D. (2009). Effects of Cr-doping on the photoluminescence and ferromagnetism at room temperature in ZnO nanomaterials prepared by soft chemistry route. *Materials Chemistry and Physics*, 113(1), 103-106. <https://doi.org/10.1016/j.matchemphys.2008.07.031>
25. Zhang, S. G., Wen, L., Li, J. L., Gao, F. L., Zhang, X. W., Li, L. H., & Li, G. Q. (2014). Plasmon-enhanced ultraviolet photoluminescence from highly ordered ZnO

- nanorods/graphene hybrid structure decorated with Au nanospheres. *Journal of Physics D: Applied Physics*, 47(49), 495103. <https://doi.org/10.1088/0022-3727/47/49/495103>
26. Vinoth, S., Arulanantham, A. M. S., Saravanakumar, S., Rimal Isaac, R. S., Soundaram, N., Chidhambaram, N., ... & AlFaify, S. (2021). Enriched optoelectronic properties of cobalt-doped ZnO thin films for photodetector applications. *Journal of Materials Science: Materials in Electronics*, 32, 27060-27072. <https://doi.org/10.1007/s10854-021-07077-w>
  27. Babu, M. M. H., Podder, J., Tofa, R. R., & Ali, L. (2021). Effect of Co doping in tailoring the crystallite size, surface morphology and optical band gap of CuO thin films prepared via thermal spray pyrolysis. *Surfaces and Interfaces*, 25, 101269. <https://doi.org/10.1016/j.surfin.2021.101269>
  28. Bahoosh, S. G., Apostolov, A. T., Apostolova, I. N., & Wesselinowa, J. M. (2012). Theory of phonon properties in doped and undoped CuO nanoparticles. *Physics Letters A*, 376(33), 2252-2255. <https://doi.org/10.1016/j.physleta.2012.05.042>
  29. Babu, M. H., Podder, J., Dev, B. C., & Sharmin, M. (2020). p to n-type transition with wide blue shift optical band gap of spray synthesized Cd doped CuO thin films for optoelectronic device applications. *Surfaces and interfaces*, 19, 100459. <https://doi.org/10.1016/j.surfin.2020.100459>
  30. Yuksel, M., Pennings, J. R., Bayansal, F., & Yeow, J. T. (2020). Effect of B-doping on the morphological, structural and optical properties of SILAR deposited CuO films. *Physica B: Condensed Matter*, 599, 412578.
  31. Marotti, R. E., Giorgi, P., Machado, G., & Dalchiele, E. A. (2006). Crystallite size dependence of band gap energy for electrodeposited ZnO grown at different temperatures. *Solar Energy Materials and Solar Cells*, 90(15), 2356-2361. <https://doi.org/10.1016/j.solmat.2006.03.008>
  32. Oh, J., Ryu, H., & Lee, W. J. (2019). Effects of Fe doping on the photoelectrochemical properties of CuO photoelectrodes. *Composites Part B: Engineering*, 163, 59-66. <https://doi.org/10.1016/j.compositesb.2018.11.041>
  33. Du, Y., Gao, X., & Meng, X. (2019). Preparation and characterization of single-phased n-type CuO film by DC magnetron sputtering. *Physica B: Condensed Matter*, 560, 37-40. <https://doi.org/10.1016/j.physb.2019.02.037>
  34. Thi, T. V., Rai, A. K., Gim, J., & Kim, J. (2014). Potassium-doped copper oxide nanoparticles synthesized by a solvothermal method as an anode material for high-performance lithium ion secondary battery. *Applied surface science*, 305, 617-625. <https://doi.org/10.1016/j.apsusc.2014.03.144>
  35. Tauc, J., & Mentel, A. (1972). States in the gap. *Journal of non-crystalline solids*, 8, 569-585. [https://doi.org/10.1016/0022-3093\(72\)90194-9](https://doi.org/10.1016/0022-3093(72)90194-9)
  36. Erat, S., Braun, A., Çetinkaya, S., Yildirimcan, S., Kasapoğlu, A. E., Gür, E., ... & Ocakoglu, K. (2021). Solution-Processable Growth and Characterization of Dandelion-like ZnO: B Microflower Structures. *Crystals*, 12(1), 11. <https://doi.org/10.3390/cryst12010011>
  37. Bayansal, F., Çetinkara, H. A., Kahraman, S., Çakmak, H. M., & Güder, H. S. (2012). Nano-structured CuO films prepared by simple solution methods: plate-like, needle-like and network-like architectures. *Ceramics International*, 38(3), 1859-1866. <https://doi.org/10.1016/j.ceramint.2011.10.011>
  38. Nguyen T. T. H., Qui, T. L., Xuan, N. D., Hanh, N., Chinh, D. H. & Lin, V. D. (2005). Preparation and Characterization of Cobalt Doped ZnO Films. *Proceedings of The Eighth German-Vietnamse Seminar on Physics and Engineering*, Erlangen, April 3-8, 2005.
  39. Lee, J. H., Ko, K. H., & Park, B. O. (2003). Electrical and optical properties of ZnO transparent conducting films by the sol-gel method. *Journal of crystal growth*, 247(1-2), 119-125. [https://doi.org/10.1016/S0022-0248\(02\)01907-3](https://doi.org/10.1016/S0022-0248(02)01907-3)
  40. Jundale, D., Pawar, S., Chougule, M., Godse, P., Patil, S., Raut, B., ... & Patil, V. (2011). Nanocrystalline CuO thin films for H<sub>2</sub>S monitoring: microstructural and optoelectronic characterization. *Journal of Sensor Technology*, 1(2), 34-36. <https://doi.org/10.4236/jst.2011.12006>



© Author(s) 2024. This work is distributed under <https://creativecommons.org/licenses/by-sa/4.0/>



## Investigating best algorithms for structural topology optimization

Sohayb Abdulkerim\*<sup>1</sup> 

<sup>1</sup> Gaziantep University, Department of Aerospace Engineering, Türkiye, karim@gantep.edu.tr

Cite this study: Abdulkerim, S. (2024). Investigating best algorithms for structural topology optimization. Turkish Journal of Engineering, 8 (1), 116-126

### Keywords

Interior Point Method  
Topology Optimization  
Finite Element  
Plane Stress

### Research Article

DOI: 10.31127/tuje.1298508

Received: 17.05.2023

Revised: 19.06.2023

Accepted: 21.06.2023

Published: 03.01.2024



### Abstract

This study investigates the topology optimization problem using various optimization approaches, taking inspiration from the 99-line MATLAB code developed by Sigmund. The educational MATLAB code is based on the Solid Isotropic Material with Penalization (SIMP) model of the artificial material density method. The objective is to minimize the compliance function with a weight constraint, with the design variables being the densities of all elements. The aim is to identify a more efficient optimization technique as an alternative to the commonly used optimality criteria algorithm provided by other MATLAB built-in tools. Two types of optimization algorithms are examined: gradient-based methods such as Interior-Point, Sequential Quadratic Programming (SQP), and Active-Set, as well as metaheuristic methods including the Genetic Algorithm. The results are verified and validated by comparing them with existing literature, demonstrating good agreement. Performance assessments are conducted to compare the results obtained from these algorithms in terms of quality and computational efficiency. The numerical findings indicate that the interior-point method outperforms the other investigated methods, although the optimality criteria algorithm remains the most efficient for solving topology optimization problems.

## 1. Introduction

Over the past two decades, the topology optimization problem has been investigated by many researchers. The purpose of the optimization, in general, is to find the optimum layout or the optimum distribution of the material to meet the design requirements, with minimum weight and cost. Therefore, research centers and industrial sectors are increasingly attracted to implementing this technique because it helps to find competitive constructions in various fields such as bridges, cars, and aerospace structures. Topology optimization expanded in several disciplines, including a combination of structures, acoustic, fluid flow, heat transfer, material design, and aero-elasticity [1].

The topology optimization aims at minimizing the structure objective function within constraints.

However, the type of the objective function and the constraints depends greatly on the type of the problem that needs solved. More specifically, in some applications, the weight is the most crucial parameter; therefore, the objective function focuses on minimizing the compliance within weight limits [2].

While in vibration problems, avoiding resonance is the most important problem. The objective function, in this case, is to adjust the natural frequency of the structure within an acceptable range [1].

Accordingly, in fixed-wing air vehicles, the wing flutter problem is always of big interest to aerospace designers. Increasing the vibration modes separation is another type of objective function. Constraints could be varied depending on the type of problem such as weight, strength, or heat [3].

Similarly, to the objective functions, constraints, and the boundary of the design variables; the optimization numerical approach is an important issue affecting the computational efficiency and the quality of the results.

Optimality Criteria (OC) is a classical optimization tool for solving topology problems, It was first used by the Australian Michel in 1904 [4]. Bendsoe and Sigmund offer a definitive review of the topology optimization and OC problem for newcomers to the topic [5].

Besides OC, so many different types of approaches are found in the literature. However, this paper is not focused on reviewing the topology optimization as many

works in this field have done, such as review papers by [2,4,6-9].

In brief, Rozvany [4], compared numerical methods of structural topology between Evolutionary Structural Optimization (ESO), (or Sequential Element Rejections and Admissions) and SIMP. He found that the latter is a rigorously derived gradient method and requires fewer iterations. Furthermore, there is a wide range of applications.

In addition, he reported that the disadvantage of SIMP is that the global optimum is not always found. While some recently published papers that focused on the ESO method found significant fundamental flaws, fully heuristic behavior, and computational inefficiency [4]. A different categorization of the topology optimization problem was made by Eschenauer et al. [7]. They included 425 references in their review and divided the topology problem into two different kinds of topology, namely the material or microstructure technique and the geometrical or macrostructure technique.

Rozvany [8] found that the OC is the oldest technique and most popular method. However, the disadvantage of OC is that may not yield a minimum weight design even for simple stress constraints. He examined and discussed alternative methods such as "hard-kill" methods, ESO, or the Adaptive Biological Growth (ABG) method as well as Generalized Stress Design (GSD) method [8].

He added that methods that rely on minimizing compliance may lead to a locally optimal solution. While Zero-order methods such as ESO are computationally efficient if a rapid design improvement is needed without necessarily finding the best solution [8]. Differently, the optimization problem methods were categorized into two types, analytical and numerical methods, by Zargham et al. [2] in their paper review. The numerical methods were also classified into three sub-classifications: direct methods, such as mathematical programming; indirect methods, such as optimality criteria; and lastly metaheuristic methods, such as Genetic Algorithms (GA). They compared various algorithms in vibration problems and discussed the performance of algorithms such as the Global Convergent Method of Moving Asymptotes (GCMMA) algorithm, which was employed simultaneously to optimize for static loads and random excitations. In addition, the level-set method, was first used in 2005, showed promise for future applications. The most popular method applied was the SIMP. Lastly, they found that GA is easy to use but computationally inefficient [2]. This agrees with the conclusion of Hajel and Lee 1995 [4].

GA was also implemented by Cardillo et al. [10] to solve multi-objective topology optimization using hybridization of partial solutions and also was compared with the OC algorithm. It is reported that optimization based on OC is more efficient than GA from a computational point of view in spite of the fact that GA has a higher capability in finding the global optimal solution.

Literature regarding topology optimization, highlighting the development from 2000 to 2012, was surveyed by Joshua et al. [1]. Who also divided the problem into four categories as follows [1]: density-based method (SIMP), Hard-kill methods evolutionary

ESO, Boundary variation methods (Level set and phase field), and then finally a new biologically inspired method based on cellular division rules.

Sivapuram and Picelli [11] demonstrated the possibility of using the Integer Linear Programming (ILB) method to solve the topology optimization problems using binary variables, the constraints, and objective functions are linearized using Taylor's first-order approximation.

In the same subject, Hassani and Hinton [6] focused their review on topology optimization homogenization theory.

Educationally, Challis et al. [12] introduced a simple MATLAB code, 129 lines, inspired by the educational paper 99-line-code work by Sigmund [13]. The code implements the level set method. The educational report 88 line code by Andreassen et al. [14] which also was inspired by the 99-line code by Sigmund [13] where the improvement was made by pre-allocating arrays and vectoring loops. A Benchmark case study for 7500 elements was introduced. In their code, the Heaviside filter was used.

Talischi et al. [12] used a MATLAB tool to solve topology optimization. The finite element mesh was established using unstructured polygonal finite element meshes.

In order to reduce the computational time, Parallel programming was used by several researchers and found an efficient solution [1].

Wang et al. [15] used an enhanced the Genetic Algorithm (GA) to solve topology optimization using discrete variable density void/solid elements. The enhancement depended on the knowledge of the topology optimization problem. In order to solve element connectivity problems, an image-processing-based connectivity analysis was developed and implemented.

Wang et al. [15] also introduced a comparison between the enhanced GA with the SIMP method. They concluded that GA generates better solutions but with higher computational costs.

Another optimization method is the Conservative Convex Separable Approximations (CCSA). Introduced by Svanberg [16], it is capable of solving nonlinear inequality constraints. It was applied to a very large number of design variables. Talischi et al. [12] implemented a MATLAB code to solve topology optimization using unstructured polygonal finite element meshes. Technical Description of the Method of Moving Asymptotes (MMA) first described and implemented by [17]. The SIMP method is first introduced by [5,18]. Several different approaches such as OC methods, Sequential Linear Programming (SLP) methods or the MMA by Svanberg [17] and others.

It was found that involving methods, such as Interior-Point, Sequential Quadratic Programming, SQP, or Active-Set method, as an optimization scheme is possible to solve topology optimization.

Based on the literature review, it is worthwhile to test the efficiency and compare these methods in solving the topology optimization problem. Therefore, in the first section, a statement of the standard topology optimization problem will be defined. Then, a brief definition of the used scheme is introduced. Definitions

of two case studies found in the literature will be illustrated with graphical results. The next chapter presents the numerical analysis of those two cases using the tested schemes coded by MATLAB and followed by discussions and conclusions.

**2. Statement of the standard topology optimization problem:**

Consider domain structure modeled using the well-known finite element method as shown in Equation 1:

$$\{F\} = [K]\{U\} \tag{1}$$

where,  $[K]$  is the global stiffness matrix,  $\{U\}$  is nodal displacement vector,  $\{F\}$  is nodal applied forces. After applying the boundary conditions, the displacement vector can be calculated as shown in Equation 2:

$$\{U\} = [K]^{-1}\{F\} \tag{2}$$

Assuming  $x_e$  is the density of the element (e), and then the compliance function  $C(x)$  as a function of the densities penalized by the power law can be calculated as shown in Equation 3:

$$C(x) = \sum_{e=1}^N x_e^p U_e^T k_e U_e \tag{3}$$

where,  $N$  is the total number of elements,  $p$  is the penalty parameter, and equal to 3 as a typical value used by others,  $U_e$  is the nodal displacements vector of the element (e),  $k_e$  is the local stiffness matrix of the element (e).

The total volume of the structure as a function of the artificial densities of the elements can be calculated as shown in Equation 4:

$$V(x) = \sum_{e=1}^N x_e \cdot v_e \tag{4}$$

Thus, the standard topology optimization using the SIMP method can be determined as shown in Equation 5:

$$\left[ \begin{array}{l} \text{minimize } C(x) \\ \text{subject to } \left\{ \begin{array}{l} \sum_{e=1}^N x_e \cdot v_e \geq fV_o \\ LB \leq X \leq UB \end{array} \right. \end{array} \right] \tag{5}$$

where,  $V_o$  is the base volume,  $f$  the fraction of the weight (volumetric fraction), LB and UB are the lower and upper bound of the densities respectively; LB values are normally taken as 0.003 instead of zero values in order to avoid singularity in the calculation of the global stiffness matrix while UB values are unities. Obviously, the objective function is nonlinear. While the constraints are linear inequalities.

The gradient function can be calculated as shown in Equation 6:

$$\frac{\partial C(x)}{\partial x} = \sum_{e=1}^N p \cdot x_e^{p-1} U_e^T k_e U_e \tag{6}$$

Some schemes can perform better if the hessian function is provided, which can be derived from the gradient function by derivative respect to density variables as shown in Equation 7:

$$\frac{\partial^2 C(x)}{\partial x^2} = \sum_{e=1}^N (p - 1) \cdot x_e^{p-2} U_e^T k_e U_e \tag{7}$$

**3. Optimization algorithms**

In order to compare the efficiency of different optimization schemes, this study investigated two categories of optimizers: gradient-based algorithms and heuristic methods. The first category, gradient-based algorithms, includes 'Interior-point', 'SQP' (Sequential Quadratic Programming), 'SQP-legacy', and 'active-set'. These algorithms utilize gradient information to guide the optimization process towards the optimal solution. On the other hand, the second category comprises heuristic methods or non-gradient-based approaches, with the genetic algorithm being one of the prominent examples. Heuristic methods employ techniques inspired by natural processes or behaviors to explore the solution space without relying on explicit gradient information. By examining both gradient-based and heuristic methods, this study aims to provide insights into their respective strengths and weaknesses in solving topology optimization problems.

It is important to give a brief description of these schemes. The 'Interior-point' algorithm is an optimization algorithm used to solve nonlinear convex problems that are subject to nonlinear inequality constraints. It was first utilized by John von Neumann in 1948 for linear programming [19]. During the 1960s, it gained popularity for solving nonlinear constrained objective functions and was pioneered by Fiacco and McCormick [19]. Over the years, from 1979 to 2003, the method underwent significant development and became the most efficient and reliable method for solving large-scale problems. The 'Interior-point' algorithm is widely available in software packages such as MATLAB, among others. Notably, it has demonstrated high efficiency in handling spar matrix problems [20–22].

To enable the implementation of various optimization algorithms, a general MATLAB subroutine was developed. The subroutine is structured as follows:

```
function [X,FVAL,EXITFLAG,OUTPUT,LAMBDA,GRAD,
elapsedTime]=runfmincon(strMethod)
global nelx nely volfrac
% linear constraints
A = []; b = [];
Aeq = []; beq = [];
% initial guess
```

```

x0(1:nely*nex) = volfrac;
lb(1:nely*nex)=0.001;
ub(1:nely*nex)=1.0;
% nonlinear constraints
nonlincon = @nlcon;
options =
optimoptions('fmincon','Algorithm','strMethod ...
    , 'ConstraintTolerance',1e-6 ...
    , 'StepTolerance',1e-6 ...
    , 'FunctionTolerance',1e-6 ...
    , 'OptimalityTolerance',1e-10 ...
    , 'MaxFunctionEvaluations',1000000 ...
    , 'MaxIterations',1000 ...
    , 'SpecifyObjectiveGradient',false ...
    , 'SpecifyConstraintGradient',false ...
);

tic;
% Call fmincon to run the optimization using the specified
algorithm
[X,FVAL,EXITFLAG,OUTPUT,LAMBDA,GRAD,
elapsedTime] = ...

fmincon(@objectiveMAC,x0,A,b,Aeq,beq,lb,ub,nonlincon,o
ptions);
elapsedTime= toc;
x = reshape(X,[nely,nex]);
end

```

The code provides a general MATLAB subroutine for implementing the optimization algorithms. The subroutine sets up the necessary constraints, initializes the variables, and defines the options for the optimization algorithm using optimoptions. The fmincon function is then called with the objective function objectiveMAC, the initial guess x0, and other parameters. Finally, the solution is reshaped into a matrix x based on the dimensions specified by nely and nex.

To use the routine, the value of the strMethod parameter has to be set to one of the available options: 'Interior-Point', 'sqp', 'sqp-Legacy', or 'Active-Set', depending on the desired optimization method. For example; the following two lines:

```

strMethod='SQP';
[X,FVAL,EXITFLAG,OUTPUT,LAMBDA,GRAD]=runfmincon
(strMethod);

```

is used to utilize the SQP algorithm. By incorporating those lines of code, users can harness the capabilities of those algorithms to optimize their objective functions, subject to the specified constraints. The subroutine encapsulates the necessary functionalities, including constraint handling and option settings, to facilitate the application of the SQP algorithm in MATLAB.

**3.1. Sequential quadratic programming (SQP)**

Sequential Quadratic Programming (SQP) is a popular optimization algorithm widely used to solve optimization problems where the objective function needs to be minimized or maximized, subject to

nonlinear inequality constraints. It is considered one of the most effective approaches in optimization due to its ability to handle a wide range of problems efficiently [22-24]. The SQP algorithm operates by iteratively solving a series of quadratic sub-problems that approximate the original nonlinear optimization problem. At each iteration, the algorithm constructs a quadratic model of the objective function and the nonlinear constraints around the current iterate. The quadratic model is then minimized or maximized to obtain a new iterate, which is expected to improve the objective function value while satisfying the constraints [22-24].

The quadratic sub-problems in SQP involve solving a quadratic programming (QP) sub-problem at each iteration, which is a mathematical programming problem with a quadratic objective function and linear constraints. These QP sub-problems are typically easier to solve compared to the original nonlinear problem, allowing for efficient convergence towards the optimal solution [22-24].

One of the advantages of SQP is its ability to handle both small and large-scale optimization problems. It is particularly suitable for problems with nonlinear inequality constraints, where it can effectively handle the nonlinearity and provide feasible solutions that satisfy the constraints [22-24].

Overall, SQP is a powerful optimization algorithm that combines the benefits of quadratic programming and sequential approximation techniques. Its iterative nature, quadratic model generation, and effective handling of nonlinear constraints make it a widely used method for solving optimization problems in various fields, including engineering, economics, finance, and operations research [22-24]. A detailed explanation of the SQP algorithm can be found in the textbook by Fletcher [23,24].

**3.2. SQP-Legacy**

SQP-Legacy is a variant of the Sequential Quadratic Programming (SQP) algorithm. It shares similarities with the SQP algorithm in terms of its approach and methodology. However, SQP-Legacy is typically characterized by longer computation times and higher memory requirements compared to the standard SQP algorithm. Despite these considerations, SQP-Legacy can still be a valuable optimization approach in certain scenarios [25]. For example, it may be preferred when compatibility with legacy code or systems is a priority. Additionally, in cases where the problem size is relatively small or the computational resources are not a major constraint, SQP-Legacy can provide satisfactory results [25].

It's important to note that SQP-Legacy should be used judiciously, considering the specific requirements and constraints of the optimization problem at hand. If computational efficiency and faster convergence are critical, it may be worthwhile to explore alternative optimization algorithms or more recent versions of SQP. Nonetheless, SQP-Legacy remains a viable option that can be employed effectively in appropriate situations, leveraging its established methodology and capabilities

for solving optimization problems with nonlinear inequality constraints [25].

### 3.3. Active-Set

Active-Set is an optimization algorithm used to solve the optimization problem within inequality constraints. If an objective function is subject to inequality constraints,  $L_i(x) \geq 0$ , given a point  $x$  in the solution space, if any constraint satisfies an equality,  $L_i(x) = 0$ , it is called active at  $x$ . Thus the solution can be developed as follows: first solve the equality constraint defined by the active-set, then compute the Lagrange multipliers, then constraints with negative Lagrange multipliers are removed, then search for infeasible constraints, repeat the previous steps until enough approaching the final solution with negligible change [21].

The Active-Set algorithm effectively combines the concepts of feasibility and optimality to find the optimal solution within the inequality constraints. By iteratively adjusting the active set based on the current point's active constraints and Lagrange multipliers, the algorithm seeks to optimize the objective function while satisfying the inequality constraints [21]. The textbook Numerical Optimization by Jorge Nocedal and Stephen J. Wright 2006 explained this technique in more details [21].

### 3.4. Genetic Algorithm

The Genetic Algorithm (GA) is a heuristic optimization algorithm based on the principles of evolutionary theory, specifically the concepts of natural selection and genetic inheritance [26]. In this method, a population of random solutions, often referred to as individuals, is generated and evaluated based on their fitness or objective function value. Each individual represents a potential solution to the optimization problem [26].

The GA mimics the process of biological evolution by allowing the individuals to evolve and reproduce through a selection process. This selection process involves competition among individuals, where the fittest individuals have a higher chance of reproducing and passing on their genetic information to the next generation. This concept is commonly referred to as the "survival of the fittest." [26].

The Genetic Algorithm was first introduced by John Holland in 1970 and has since become a widely used optimization technique. In the book "Genetic Algorithm" by Kramer [27], detailed explanations of the algorithm's principles and implementation are provided [26].

In this work, GA programming is tested using the MATLAB built-in function, gamultiobj. This tool allows for the optimization of a user-defined objective function. Both nonlinear equality and non-equality constraints are allowed. Additionally, upper, and lower bounds are possible to set for the state variables.

## 4. Code Validation

### 4.1. Case Study 1

For comparison with the existing literature, two case studies were conducted in this report. The first case study, originally reported by Sigmund [13], involved a cantilever beam modeled using finite element plane stress analysis. The beam was clamped from the left side, as shown in Figure 1. The mesh used for this analysis consisted of 32 elements horizontally and 20 elements vertically. In Sigmund's study, a volume fraction of 0.4, a power penalty of 3, and a filter radius size of 1.2 were employed. The optimization algorithm used in this case study was coded in MATLAB following Sigmund's 99-line code. The results obtained from this code are presented in Figure 1.

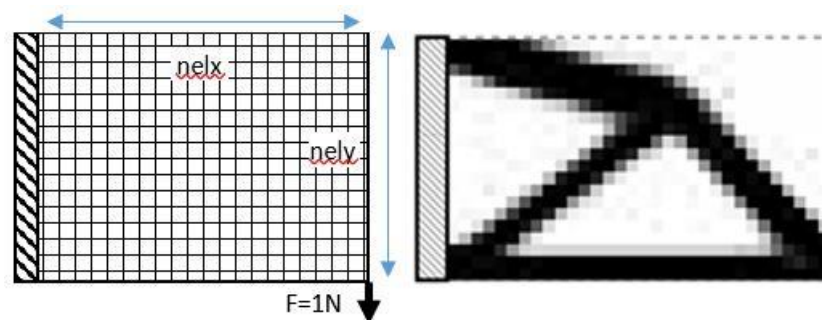


Figure 1. Case study 1, the topology optimization results of a cantilever beam and concentrated load by Sigmund [10]

Additionally, Sigmund [13], suggested other possible optimization methods such as Sequential Linear Programming (SLP) and the Method of Moving Asymptotes (MMA). However, in this work, a different family of optimization algorithms was implemented using the MATLAB package and the 'fmincon' function. These algorithms are gradient-based schemes and have been briefly described in the introduction chapter. The purpose of using these algorithms was to verify their

performance and identify the most efficient schemes for the two case studies conducted in this report.

Aguilar et al. [28] conducted a similar case study as depicted in Figure 2. The study involved a plate with dimensions of 40 x 30 cm and a meshing density of 32x24 using isoperimetric plane stress elements. The optimization method employed in their study was the Genetic Algorithm (GA). The results obtained using the GA for this case study are also presented in Figure 2.

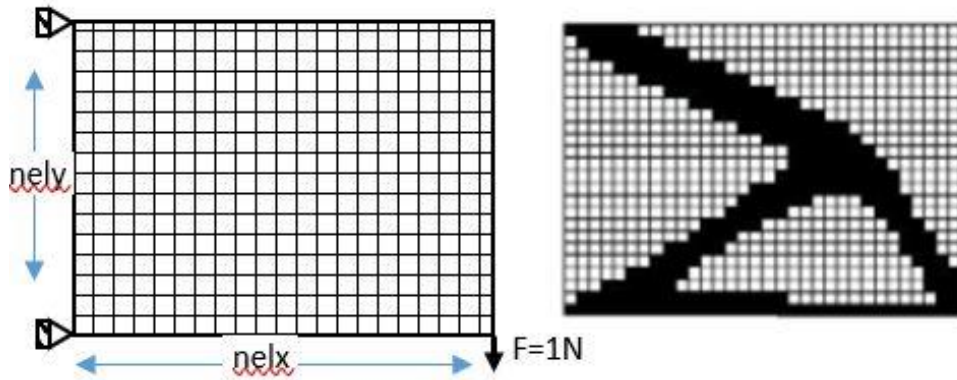


Figure 2. Case study 1 for the beam that introduced by Aguilar et al. [25], [26].

#### 4.2. Case Study 2

The second case study, as presented by Sigmund [13] and Andreassen et al. [14] is illustrated in Figure 3. The figure displays the right-hand half of a simply supported beam subjected to a downward load at the top-central point. Due to the symmetry around the vertical axis at the

central line, only one half of the beam was analyzed to obtain the results. The density distributions depicted in the figure were generated using the following parameters: a mesh with 60 elements, consisting of 20 elements in the horizontal direction and 20 elements in the vertical direction; a filter radius of  $r_{min} = 1.5$ ; and the volumetric ratio was 0.5.

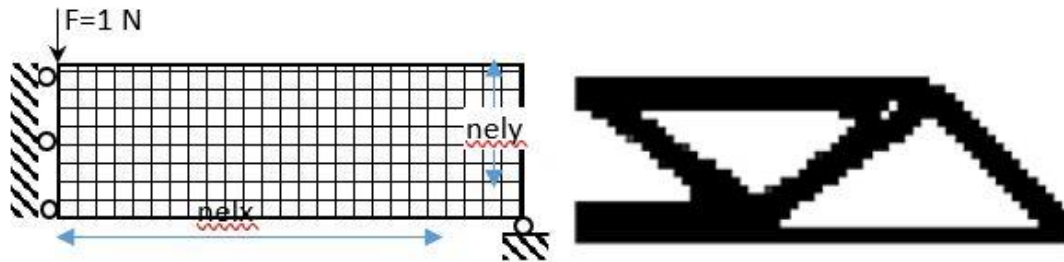


Figure 3. Case study 2, MATLAB 88-lines code case study results by Andreassen et al. [11] and by Sigmund [10].

### 5. Results

The numerical results of the two case studies were replicated in this study using six different algorithms implemented in MATLAB code, as described in detail in Appendix A. The computational costs, measured in terms of computation elapsed time, were compared to assess the quality of the results. The quality of the results was evaluated using grayscale graphs, where higher density regions were represented by black color.

For the Genetic Algorithm (GA), the following parameter values were chosen: a Crossover Fraction of 0.8000, a Population Size of 200, and Uniform Mutation with a value of 0.0500. The fitness function utilized in the GA was the same as the one employed in all the other algorithms. It is worth noting that, unlike other routines, this particular routine does not require a gradient function.

#### 5.1. Case Study 1

The results of Case Study 1, which focused on a beam modeled using the finite element method with plane stress state, are presented in Figure 4. The beam was subjected to specific boundary conditions, where all nodes along the left-hand edges were assigned constrained degrees of freedom. Furthermore, a unity vertical force was applied to the bottom right node to induce loading.

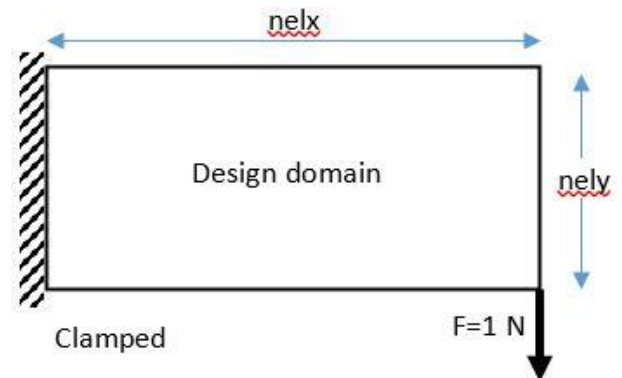


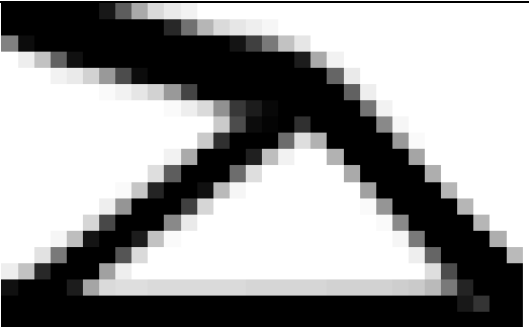
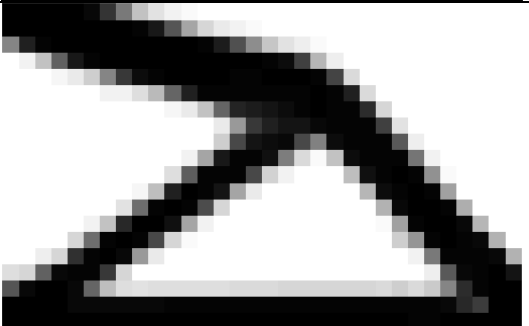
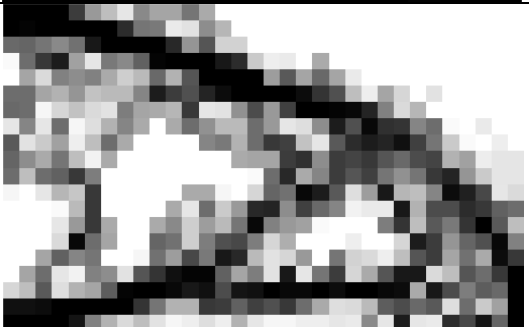
Figure 4. Base structure of a clamped beam subjected to load at the tip.

The following parameters were utilized for Case Study 1: a tolerance of  $1e-6$  for constraints, a tolerance of  $1e-10$  for optimality, and a total of  $(nel * nely) = (32 \times 20 = 512)$  four-node elements in the plane stress analysis. The boundary condition was specified as  $fixeddofs = [1:2*(nely+1)]$ , and the applied force was identified as  $F(2*(nelx+1)*(nely+1),1)=-1.0$ . The volume fraction was set to 0.4. It is worth noting that the absolute values of dimensions and loads did not affect the density distributions, so unity dimensions and loads were considered. Table 1 presents the results obtained from different optimization algorithms for Case Study 1. The

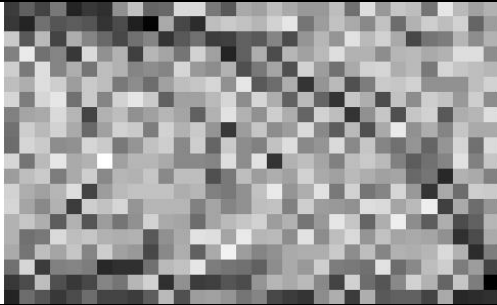
first column indicates the name of the algorithm, the second column displays the computational elapsed time using a desktop computer (the same computer for all cases), the third column denotes the number of iterations, and the fourth column shows the value of the

objective function. The fifth column provides the count of objective function calculations. Specifically, Table 2 lists the results of the genetic algorithm scheme, including the number of generations and the count of objective function calculations.

**Table 1.** The analysis results of case study 1 using different optimization algorithms.

Method	Time [sec]	Iteration	Objective Function	Function Count	Results
Optimality criteria by 99-line code Sigmund [10]	2.14	71	57.35	71	
Interior Point	10	48	59.9	30801	
Sequential quadratic programming SQP	51	17	106	10984	
SQP-Legacy	63	18	104	11630	
Active-set	4420	74	263	47627	

**Table 2.** The analysis results of case study 1 using genetic algorithm.

Method	Time [sec]	Generations	Objective Function	Function Count	Results
Genetic Algorithm	3060	663	230	132801	

By inspecting the graphical results of the density distribution in the domain, it is evident that there is a good agreement with the results shown by others, which validates the MATLAB code and the implementation of the optimization tools. However, some methods did not perform as well due to the nature of this type of application. A comparative analysis of the results can be seen in Table 1 and Table 2.

The interior-point method stands out due to its superior performance in terms of both result quality and computational efficiency. It achieves a low objective function value of 59.9, which is very close to the value calculated by the optimal configuration (OC) as 57. Additionally, the elapsed time for the interior-point method is the lowest at 10 seconds. The SQP method also yields relatively close results, with an elapsed time of 51 seconds and an objective function value of 106. However, the objective function value is approximately 60% higher compared to the interior-point method. On the other hand, the results of the Active-Set and Genetic Algorithm methods are significantly poorer.

For instance, the genetic algorithm takes 3060 seconds to reach an objective function value of 230, which is much higher (worse) than the minimum achieved by the interior-point method. Similarly, the Active-Set method performs poorly in terms of computational costs and reaching a minimum. To facilitate further comparisons, another case will be analyzed and presented next.

### 5.2 Case Study 2

The results of Case 2, depicted in Figure 3, are presented here, involving a simply supported beam that is symmetric about a vertical axis at the midpoint and loaded downward at the central point-top. MATLAB optimization tools were used with the following data: a mesh of (nelxnely) = (60x20 = 1200) elements in the horizontal and vertical directions, a filter radius of rmin = 1.5, and a volumetric ratio of 0.5. The boundary conditions were defined as fixeddofs = union([1:2:2(nely+1)], [2\*(nelx+1)\*(nely+1)]), and the applied force was given as F(2,1) = -1.

The results obtained through optimization using the same set of techniques are summarized in Table 3 and Table 4. The quality of the algorithm results is illustrated using grayscale graphs, with the highest density represented as black. The tables include the name of the

optimization algorithm in the first column, the computational elapsed time on a normal desktop computer in the second column, the number of iterations in the third column, and the value of the objective function in the fourth column. The fifth column indicates the number of objective function calculations. The results of the genetic algorithm are presented separately in Table 2.

Expectedly, the numerical results for Case Study 2 once again demonstrate that the Interior Point algorithm outperformed the other tested algorithms in terms of computational efficiency and achieving global optimization results. However, it is worth noting that the OC method is still faster and produces better results.

### 6. Conclusion

In conclusion, this work focused on solving the topology optimization problem for domain structures using MATLAB and built-in optimization tools. The approach followed the structural modeling similar to Sigmund’s 99-line code (2001), utilizing the finite element plane-stress method and compliance as the objective function. The densities of the elements were considered as design variables, and the power law was used to weigh the densities.

Several optimization algorithms, including Interior-Point, SQP, SQP-legacy, Active-Set, and Genetic Algorithm, were implemented in MATLAB for comparison and validation. Two case studies from the literature were reproduced using these methods, and the results were compared with published results. Overall, the obtained results showed good agreement with the literature.

Among the tested algorithms, the Interior-Point method demonstrated superior performance in terms of both computational efficiency and result quality. It achieved acceptable results with reasonable computational effort required. On the other hand, the Genetic Algorithm exhibited low computational efficiency, and the Active-Set method yielded the worst results both in terms of computational expense and result quality.

It was observed that providing analytical gradient and Hessian functions reduced the number of iterations required for convergence. However, it is important to note that some methods, especially heuristic approaches like the Genetic Algorithm, do not rely on gradient

functions. Therefore, for problems where gradient functions are unavailable, it is advisable to use heuristic approaches.

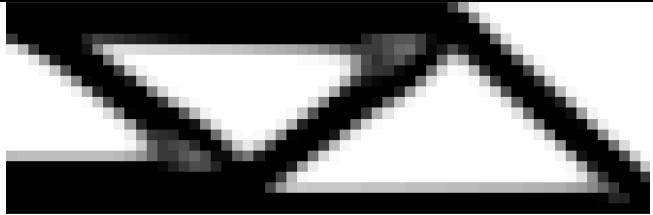
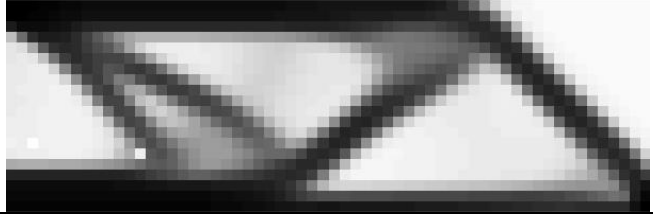
In summary, this study successfully implemented and validated various optimization algorithms for topology optimization of domain structures. The Interior-Point method emerged as the most efficient and effective approach, while the Genetic Algorithm and Active-Set method showed limitations. The findings highlight the

importance of considering algorithm selection and availability of gradient functions when solving topology optimization problems.

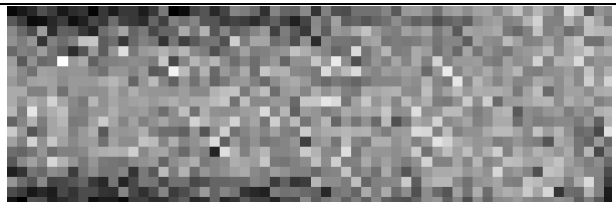
**Conflicts of interest**

The authors declare no conflicts of interest.

**Table 3.** The analysis results of case study 2 using different optimization algorithms.

Method	Time [sec]	Iteration	Objective Function	Function Count	Results
Optimality criteria by 99-line code Sigmund [10]	7	94	203	94	
Interior Point	31.6	41	288	49318	
Sequential quadratic programming SQP	341	7	416	8463	
SQP-Legacy	258	7	416	8463	
Active-set	2037	190	345	57585	

**Table 4.** The analysis results of case study 2 using genetic algorithm.

Method	Time [sec]	Generations	Objective Function	Function Count	Results
Genetic Algorithm	10004	688	562	137801	

## References

1. Deaton, J. D., & Grandhi, R. V. (2014). A survey of structural and multidisciplinary continuum topology optimization: post 2000. *Structural and Multidisciplinary Optimization*, 49, 1-38. <https://doi.org/10.1007/s00158-013-0956-z>
2. Zargham, S., Ward, T. A., Ramli, R., & Badruddin, I. A. (2016). Topology optimization: a review for structural designs under vibration problems. *Structural and Multidisciplinary Optimization*, 53, 1157-1177. <https://doi.org/10.1007/s00158-015-1370-5>
3. Bendsoe, M. P. (1989). Optimal shape design as a material distribution problem. *Structural optimization*, 1, 193-202. <https://doi.org/10.1007/BF01650949>
4. Rozvany, G. I. (2009). A critical review of established methods of structural topology optimization. *Structural and multidisciplinary optimization*, 37, 217-237. <https://doi.org/10.1007/s00158-007-0217-0>
5. Bendsoe, M. P., & Sigmund, O. (2003). *Topology optimization: theory, methods, and applications*. Springer Science & Business Media.
6. Hassani, B., & Hinton, E. (1998). A review of homogenization and topology optimization I—homogenization theory for media with periodic structure. *Computers & Structures*, 69(6), 707-717. [https://doi.org/10.1016/S0045-7949\(98\)00131-X](https://doi.org/10.1016/S0045-7949(98)00131-X)
7. Eschenauer, H. A., & Olhoff, N. (2001). Topology optimization of continuum structures: a review. *Applied Mechanics Reviews*, 54(4), 331-390. <https://doi.org/10.1115/1.1388075>
8. Rozvany, G. I. N. (2001). Stress ratio and compliance-based methods in topology optimization—a critical review. *Structural and Multidisciplinary Optimization*, 21, 109-119. <https://doi.org/10.1007/s001580050175>
9. Tiismus, H., Kallaste, A., Vaimann, T., & Rassõlkin, A. (2022). State of the art of additively manufactured electromagnetic materials for topology optimized electrical machines. *Additive Manufacturing*, 55, 102778. <https://doi.org/10.1016/j.addma.2022.102778>
10. Cardillo, A., Cascini, G., Frillici, F. S., & Rotini, F. (2013). Multi-objective topology optimization through GA-based hybridization of partial solutions. *Engineering with Computers*, 29, 287-306. <https://doi.org/10.1007/s00366-012-0272-z>
11. Sivapuram, R., & Picelli, R. (2018). Topology optimization of binary structures using integer linear programming. *Finite Elements in Analysis and Design*, 139, 49-61. <https://doi.org/10.1016/j.finel.2017.10.006>
12. Talischi, C., Paulino, G. H., Pereira, A., & Menezes, I. F. (2012). PolyTop: a Matlab implementation of a general topology optimization framework using unstructured polygonal finite element meshes. *Structural and Multidisciplinary Optimization*, 45, 329-357. <https://doi.org/10.1007/s00158-011-0696-x>
13. Sigmund, O. (2001). A 99 line topology optimization code written in Matlab. *Structural and multidisciplinary optimization*, 21, 120-127. <https://doi.org/10.1007/s001580050176>
14. Andreassen, E., Clausen, A., Schevenels, M., Lazarov, B. S., & Sigmund, O. (2011). Efficient topology optimization in MATLAB using 88 lines of code. *Structural and Multidisciplinary Optimization*, 43, 1-16. <https://doi.org/10.1007/s00158-010-0594-7>
15. Wang, S. Y., Tai, K., & Wang, M. Y. (2006). An enhanced genetic algorithm for structural topology optimization. *International Journal for Numerical Methods in Engineering*, 65(1), 18-44. <https://doi.org/10.1002/nme.1435>
16. Svanberg, K. (2002). A class of globally convergent optimization methods based on conservative convex separable approximations. *SIAM Journal on Optimization*, 12(2), 555-573. <https://doi.org/10.1137/S1052623499362822>
17. Svanberg, K. (1987). The method of moving asymptotes—a new method for structural optimization. *International Journal for Numerical Methods in Engineering*, 24(2), 359-373. <https://doi.org/10.1002/nme.1620240207>
18. Bendsoe, M. P., & Sigmund, O. (1999). Material interpolation schemes in topology optimization. *Archive of Applied Mechanics*, 69, 635-654. <https://doi.org/10.1007/s004190050248>
19. Dantzig, G. B., & Thapa, M. N. (2003). *Linear programming: Theory and extensions (Vol. 2)*. New York: Springer.
20. Jansen, B. (2013). *Interior point techniques in optimization: Complementarity, sensitivity and algorithms (Vol. 6)*. Springer Science & Business Media.
21. Nocedal, J., & Wright, S. J. (Eds.). (1999). *Numerical optimization*. New York, NY: Springer New York.
22. Forsgren, A., Gill, P. E., & Wright, M. H. (2002). Interior methods for nonlinear optimization. *SIAM Review*, 44(4), 525-597. <https://doi.org/10.1137/S0036144502414942>
23. Dubois, T. (2013). EASA Requires A380 Structural Inspection for Cracking. <https://www.ainonline.com/aviation-news/air-transport/2013-11-11/easa-requires-a380-structural-inspection-cracking>
24. Singal, R. K., Gorman, D. J., & Forgues, S. A. (1992). A comprehensive analytical solution for free vibration of rectangular plates with classical edge conditions: Experimental verification. *Experimental Mechanics*, 32, 21-23. <https://doi.org/10.1007/BF02317979>
25. Hauser, F., Häberle, M., Merling, D., Lindner, S., Gurevich, V., Zeiger, F., Frank, R., & Menth, M. (2023). A survey on data plane programming with p4: Fundamentals, advances, and applied research. *Journal of Network and Computer Applications*, 212, 103561. <https://doi.org/10.1016/j.jnca.2022.103561>
26. Kramer, O. (2017). *Genetic Algorithm Essentials*, Springer International Publishing, Cham.

27. Kramer, O. (2017). Genetic algorithms (pp. 11-19). Springer International Publishing.
28. Madeira, J. A., Rodrigues, H. C., & Pina, H. (2006). Multiobjective topology optimization of structures using genetic algorithms with chromosome repairing. *Structural and Multidisciplinary Optimization*, 32, 31-39. <https://doi.org/10.1007/s00158-006-0007-0>



© Author(s) 2024. This work is distributed under <https://creativecommons.org/licenses/by-sa/4.0/>



## Drought analysis based on SPI and RDI drought indices in the Burdur Basin

Nazire Göksu Soydan Oksal<sup>1</sup> , Neslihan Beden<sup>\*2</sup> 

<sup>1</sup> Mersin University, Department of Civil Engineering, Türkiye, [gokussoydan@mersin.edu.tr](mailto:gokussoydan@mersin.edu.tr)

<sup>2</sup> University of Samsun, Department of Meteorological Engineering, Samsun, Türkiye, [neslihan.beden@samsun.edu.tr](mailto:neslihan.beden@samsun.edu.tr)

Cite this study:

Soydan Oksal, N. G., & Beden, N. (2024). Drought analysis based on SPI and RDI drought indices in the Burdur Basin. *Turkish Journal of Engineering*, 8 (1), 127-138

### Keywords

Drought  
Drought Analysis  
SPI  
RDI  
Burdur Basin

### Research Article

DOI: 10.31127/tuje.1326875

Received: 13.07.2023

Revised: 28.10.2023

Accepted: 30.10.2023

Published: 05.01.2024



### Abstract

Drought is the most complex of the recurrent extreme weather events and is defined as a natural disaster with severe environmental, economic, and agricultural impacts resulting from a significant decrease in the average rainfall recorded in an area and the average rainfall recorded in the same place. Droughts have become more frequent and severe in many parts of the world, including Türkiye, due to global warming and climate change (increasing temperatures and changing precipitation patterns). Water resources and the agricultural sector are most severely affected by droughts. In this study, drought analyses of the Burdur Basin, located in the Aegean region, one of Türkiye's seven geographical regions, were carried out. For drought analysis, annual average total precipitation, annual maximum temperature, annual minimum temperature, and annual average temperature data of 17238 Burdur and 17892 Tefenni meteorological observation stations were used. Both meteorological and agricultural drought analyzes are included in the analysis of droughts. Standard Precipitation Index (SPI) and Reconnaissance Drought Index (RDI) methods were used to determine meteorological and agricultural drought, respectively. SPI and RDI values were obtained for 1-, 3-, 6- and 12-month time periods, and the severity, size, and distribution of dry and humid periods were determined for both stations separately. When the results of both methods were examined, severe droughts were observed in the study area in 1973, 1978, 1981, and 2017.

## 1. Introduction

Natural disasters triggered by climate change, such as droughts, floods, sea level rise, and extreme weather events, are quite common in Türkiye. Especially water resources and the agriculture sector are seriously affected by droughts. Drought; It is defined as a natural disaster with serious environmental, economic, and agricultural effects that occurs as a result of the precipitation recorded in a region falling significantly below the average recorded in the same region [1, 2].

Drought, which is defined as one of the greatest natural disasters humanities has faced, has started to occur more frequently and severely over time with climate change [3]. Determining the drought severity for a particular region according to time and place is important in taking precautions in planning and managing water resources.

According to the variables used, drought can be grouped under four main headings: meteorological, hydrological, agricultural, and socio-economic [4-6]. Meteorological drought, one of these four groups, can be

defined as the need for water due to the inadequacy of precipitation [7]. While hydrological drought, which is related to the effect of precipitation periods, is defined as the lack of soil and groundwater as a result of long-term precipitation deficiency, agricultural drought is expressed as the situation that occurs after meteorological drought and before hydrological drought and where there is not enough moisture in the roots of plants [8]. The presence of meteorological drought creates hydrological drought, and the formation of hydrological drought creates agricultural drought. At the end of all these, socio-economic famine drought is mentioned in the region where the drought occurs. Researchers have done many studies on drought. Inan et al., [9] applied the annual drought analysis of 16 stations in the Black Sea Region with Standard Precipitation Index (SPI) and Percentage of Normal Index (PNI). It is stated in the study that the stations showed normal and above drought levels. Çitakoğlu and Coşkun [10] investigated the short-term meteorological droughts with hybrid machine learning models using monthly precipitation data of Sakarya Meteorological Station. It is

stated in the study that the hybrid models used together with the pre-processing techniques were found to be more successful than the stand-alone models. Coşkun and Çitakoğlu [11] predicted the meteorological drought of Sakarya province for 1, 3, and 6-month time scales by using SPI. By using long short-term memory (LSTM), they concluded that drought time series do not need to be subjected to pre-processing techniques.

In this study the meteorological drought analysis of Burdur basin is investigated by using SPI and RDI method for 1-, 3-, 6- and 12- months' time scales. The annual average total precipitation, annual maximum temperature, annual minimum temperature, and annual average temperature data of 17238 Burdur and 17892 Tefenni meteorological observation stations between 1963-2021 were used. As a result of the study, the drought of the basin was evaluated temporally and the drought characteristics of the stations were determined. In this study, it is aimed to compare the SPI method, which analyzes drought using only precipitation data, and the RDI method, which uses minimum and maximum temperature parameters in addition to precipitation. Thus, it was aimed to determine the effect of temperature on drought in the region.

**2. Method**

**2.1. Study Area**

Burdur Basin, one of Türkiye's 25 basins, is a small, closed basin compared to other basins surrounded by Antalya and the Western Mediterranean Basins (Figure 1). Burdur Basin, which covers approximately 1% of Türkiye's surface area, has a precipitation area of 8,764 km<sup>2</sup>. The basin is under the influence of a transitional climate between the continental and Mediterranean climates. The annual average precipitation is 446.0 mm/m<sup>2</sup>, and the annual average temperature is 12°C [12].

**2.2. Climate Data**

Climate data is used in modeling to analyze climate change, trend analysis, and time-dependent atmospheric

behaviors and to be prepared for disasters such as drought and flood [13,14]. At the same time, these data depend on analyzing extreme values, numerical model applications, and climate change projections to reduce disaster risk and climatic risk effects. For the Burdur Basin drought analysis, the data of the 17238 Burdur and 17892 Tefenni meteorological observation stations of the General Directorate of Meteorology has been used. The annual average total precipitation, annual maximum temperature, annual minimum temperature and annual average temperature observation data were used in the analysis. General information about the study area is given in Table 1.

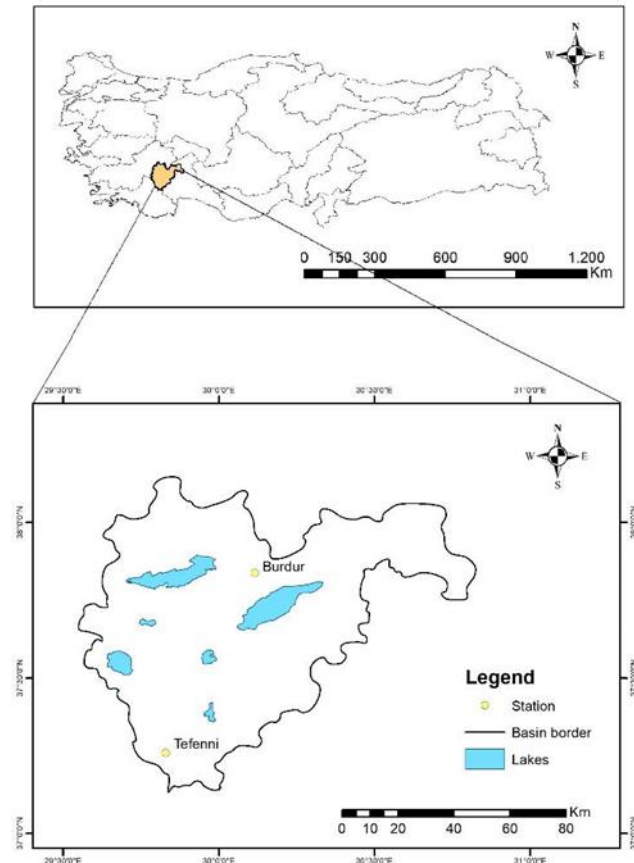


**Figure 1.** Burdur Basin location map.

**Table 1.** General information of the meteorological stations.

Station No	Station Name	Latitude	Longitude	Altitude (m)	Year	P <sub>avg</sub> (mm)	T <sub>min</sub> (°C)	T <sub>max</sub> (°C)
17238	Burdur	37° 43' 00.0"	30° 18' 00.0"	957	1963-2021	420.1	-6.2	36.2
17892	Tefenni	37° 19' 00.0"	29° 46' 00.0"	1142	1963-2021	466.9	-9.1	35.1

**2.3. Standard Precipitation Index (SPI)**

The Standard Precipitation Index (SPI) method evaluates drought severity by calculating the lack of precipitation for different time series in rainy and dry periods [15]. The SPI method, which uses only precipitation data as input data, is one of the most widely used methods in determining meteorological drought [16]. While positive values calculated with this method determine the severity of rainy periods, negative values indicate the severity of drought [17]. While calculating the SPI, the gamma distribution is first applied to the long-term precipitation data. The calculated values are

replaced in the formula given in Equation 1 to calculate the SPI.

$$SPI_{ij} = \frac{x_{ij} - x_{im}}{\sigma_i} \tag{1}$$

where  $x_{ij}$  is the precipitation in month  $j$  of the year (in mm), and  $x_{im}$  and  $\sigma_i$  are the mean and standard deviation, respectively. SPI values can be calculated for different time scales, such as short-term 1-, 3-, month, and long-term 6- and 12-month. The intensity values given in Table 2 can be used to classify drought [16, 18].

### 2.4. Reconnaissance Drought Index (RDI)

The reconnaissance drought index (RDI) is a drought analysis method that uses the potential evapotranspiration (PET) value and precipitation data. Minimum temperature and maximum temperature data are used to calculate PET values. In determining the RDI, it is first referred to as the initial value of the RDI. It is presented collectively using a monthly time step and calculated using Equation 2 for each month, season, or year of the hydrological year [17].

$$a_k^{(i)} = \frac{\sum_{j=1}^k P_{ij}}{\sum_{j=1}^k PET_{ij}} \quad (2)$$

where  $P_{ij}$  and  $PET_{ij}$  are  $i$  by hydrological year, respectively.  $j$  of the year are precipitation and PET values for the month, and  $N$  is the total number of years of available data. The second Normalized RDI ( $RDI_n$ ) is calculated each year using Equation 3. Here,  $\bar{a}_k$  parameter is the arithmetic mean of  $a_k$  values calculated for  $N$  years of data.

$$RDI_n^{(i)} = \frac{a_k^i}{\bar{a}_k} - 1 \quad (3)$$

In the standardized RDI ( $RDI_{st}$ ) calculation, the expression given in Equation 4 follows a procedure similar to that used for calculating the SPI.

$$RDI_{st(k)}^{(i)} = \frac{y_k^i - \bar{y}_k}{\hat{\sigma}_{y_k}} \quad (4)$$

where  $y_k$  is calculated with  $\ln \ln a_k^{(i)}$  while  $\bar{y}_k$  and  $\hat{\sigma}_{y_k}$  denote the arithmetic mean and standard deviation of  $y_k$  respectively.

The intensity values given in Table 2 can be used to classify drought [16, 18].

**Table 2.** Severity classification for SPI and RDI.

Drought Classification	SPI/RDI
Extremely wet (EW)	$2 \leq \text{SPI/RDI}$
Severely wet (SW)	$1.5 \leq \text{SPI/RDI} < 2$
Moderately wet (MOW)	$1.0 \leq \text{SPI/RDI} < 1.5$
Mildly wet (MW)	$1.0 \leq \text{SPI/RDI} < 0$
Mild drought (MD)	$0 \leq \text{SPI/RDI} < -1.0$
Moderate drought (MOD)	$-1.0 \leq \text{SPI/RDI} < -1.5$
Severe drought (SD)	$-1.5 \leq \text{SPI/RDI} < -2$
Extreme drought (ED)	$\text{SPI/RDI} \leq -2$

### 3. Results

In this study, SPI and RDI index values were calculated, and drought analyzes were carried out using the annual average precipitation, maximum average, and minimum average temperature data observed between 1963-2021 of 17238 Burdur and 17892 Tefenni stations in the Burdur basin. By obtaining the temporal

distributions of the SPI and RDI values obtained from 1-, 3-, 6- and 12-month time scales, it is possible to determine the conditions of EW, SW, MOW, MW and MD, MOD, SD, ED according to the drought severity classification given in Table 2. The number of occurrences and the percentages of dry and rainy periods observed in the study area were determined. Besides, according to the SPI and RDI values obtained for Burdur and Tefenni stations, the duration and time of the most severe drought period between 1963-2021 were determined, and the driest year between these years was determined.

### 3.1. Drought Analysis of Burdur Station

#### 3.1.1. Drought analysis based on SPI

The temporal distribution of SPI values in the 1-, 3-, 6- and 12-month periods calculated using the monthly average precipitation data between 1963-2021 at Burdur station is given in Figure 2-5. According to Figure 2-5, as the period increases, the frequency of occurrence of dry periods also increases. As a result of the analysis, the highest droughts for the 1-, 3-, 6- and 12-month periods were seen in 1973, 1978, 1981, and 2017, respectively. The rainiest periods were experienced in 1991, 1997, and 2004, respectively.

In Figure 6, the percentages of occurrence of drought classes are given according to the SPI values obtained at the Burdur station. According to Figure 6, in the period examined at Burdur station, mild drought and mildly wet periods are experienced in general. As the time period increased, the percentage of mildly drought periods that occurred increased. In addition, as the time period increases, the percentages of occurrence of extremely drought periods decrease, while the percentages of occurrence of extremely wet periods increase.

The duration, intensity, and maximum occurrence values of the arid values obtained by SPI in the 1-, 3-, 6- and 12-month periods between 1963-2021 at Burdur station are given in Table 3. According to Table 3, it was clearly seen that the drought severity and duration increased as the period increased. However, with the increase of the period, it is seen that the highest drought value between 1963-2021 decreased in absolute terms. The maximum drought for the 1-, 3-, 6-, and 12-month periods occurred in 1973, 1978, 1981, and 2017, respectively.

#### 3.1.2. Drought analysis based on RDI

The temporal distribution of SPI values in the 1-, 3-, 6- and 12-month periods calculated using the monthly average precipitation data between 1963-2021 at Burdur station is given in Figure 2-5. According to Figure 2-5, as the period increases, the frequency of occurrence of dry periods also increases. As a result of the analysis, the highest droughts for the 1-, 3-, 6- and 12-month periods were seen in 1973, 1978, 1981, and 2017, respectively. The rainiest periods were experienced in 1991, 1997, and 2004, respectively.

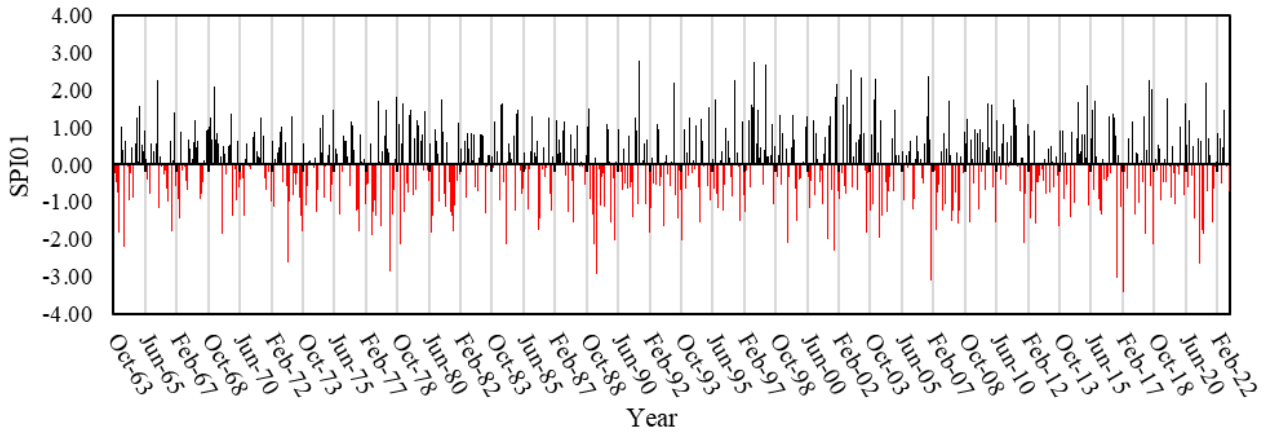


Figure 2. Temporal distribution of Burdur station SPI01 values.

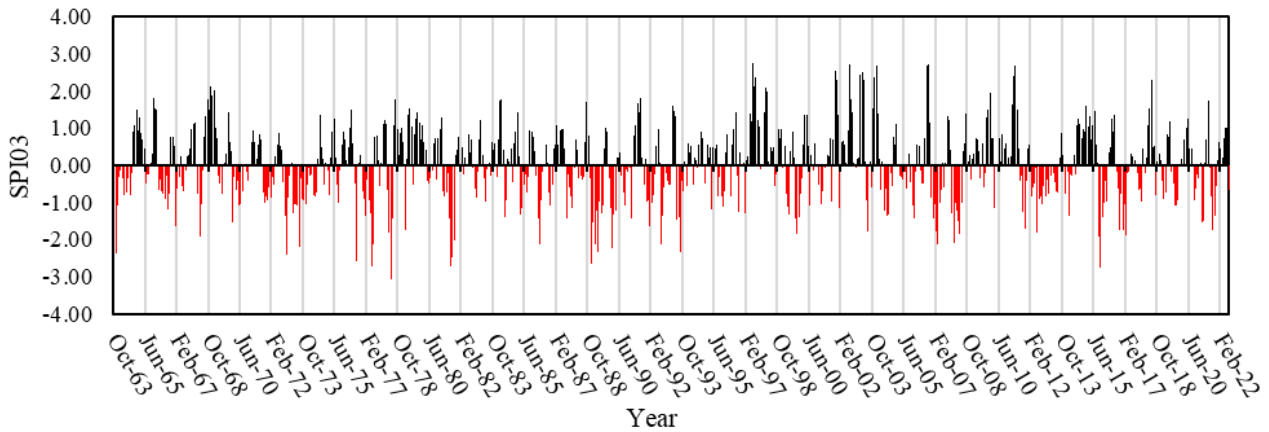


Figure 3. Temporal distribution of Burdur station SPI03 values.

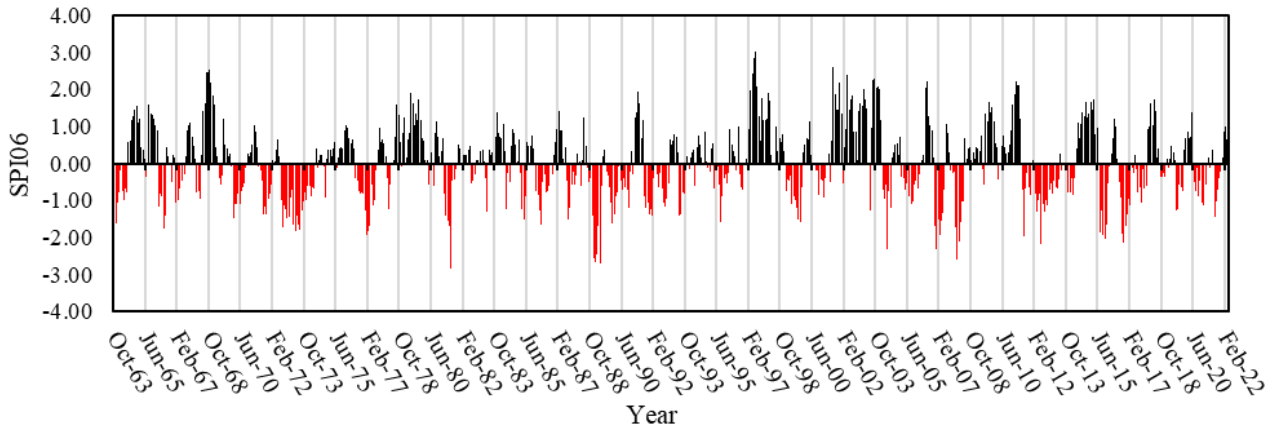


Figure 4. Temporal distribution of Burdur station SPI06 values.

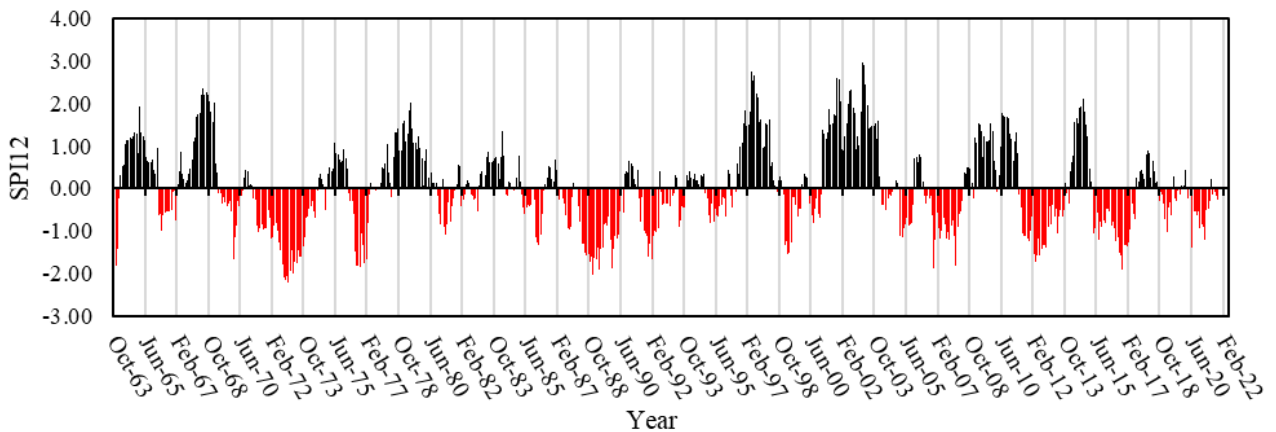
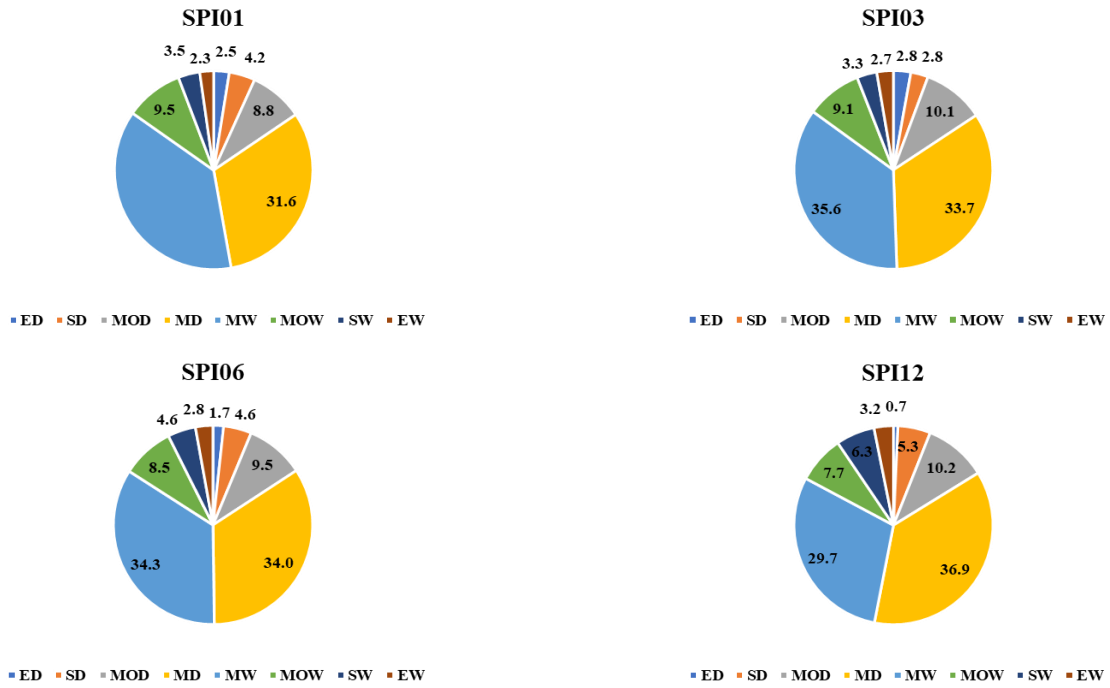


Figure 5. Temporal distribution of Burdur station SPI12 values.



**Figure 6.** Occurrence percentages of drought classes (SPI) at Burdur station.

**Table 3.** Duration, severity and maximum occurrence values (SPI) of drought at Burdur station.

Period	Severity	Time (Month)	Start	Finish	Pick Value	Pick Time
SPI01	-6.52	6	Dec.06	May.07	-3.41	Feb.17
SPI03	-13.6	9	Jan.89	Sep.89	-3.07	Jul.78
SPI06	-25.5	22	Dec.72	Sep.74	-2.86	Nov.81
SPI12	-46.3	41	Jan.72	May.75	-2.23	Nov.73

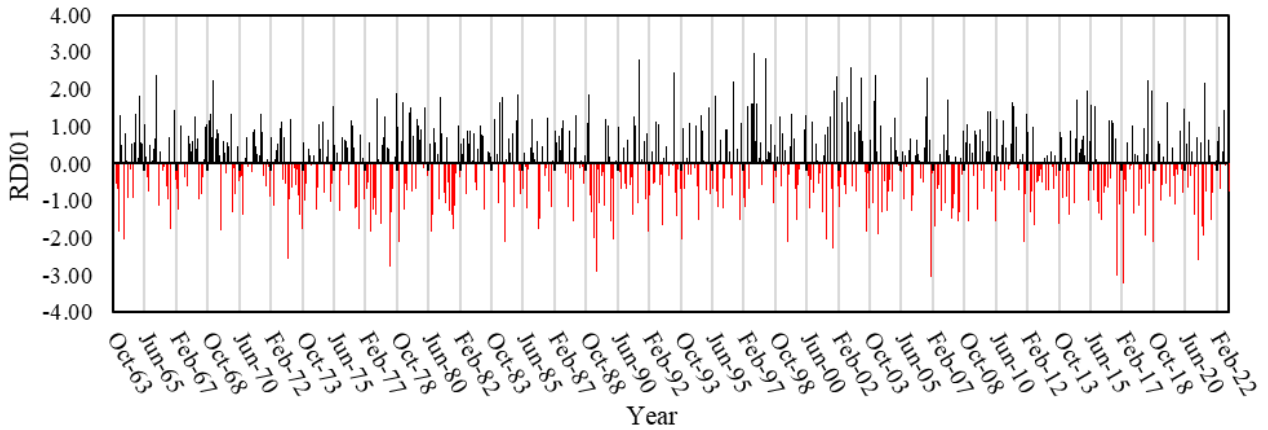


**Figure 7.** Temporal distribution of Burdur station RDI01 values.

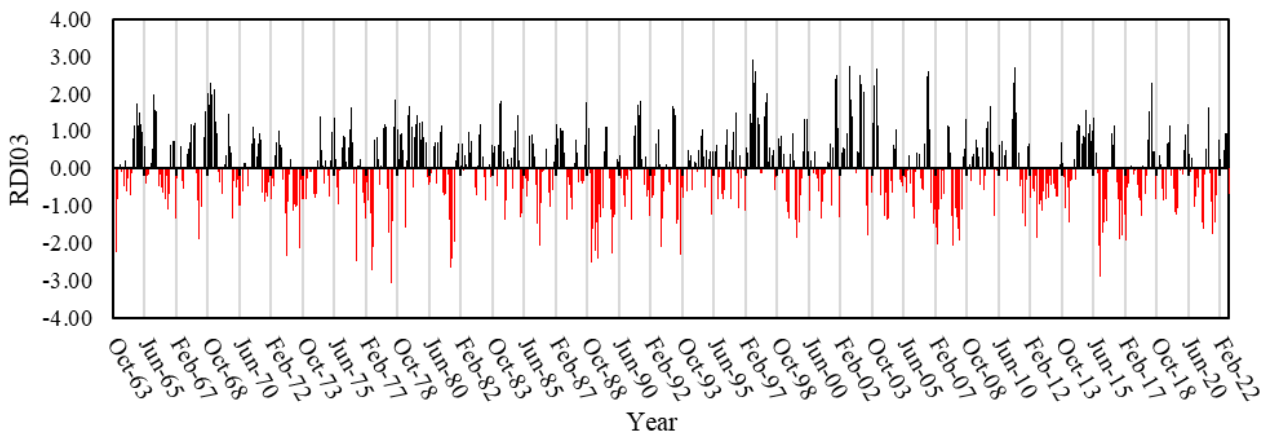


**Figure 8.** Temporal distribution of Burdur station RDI03 values.

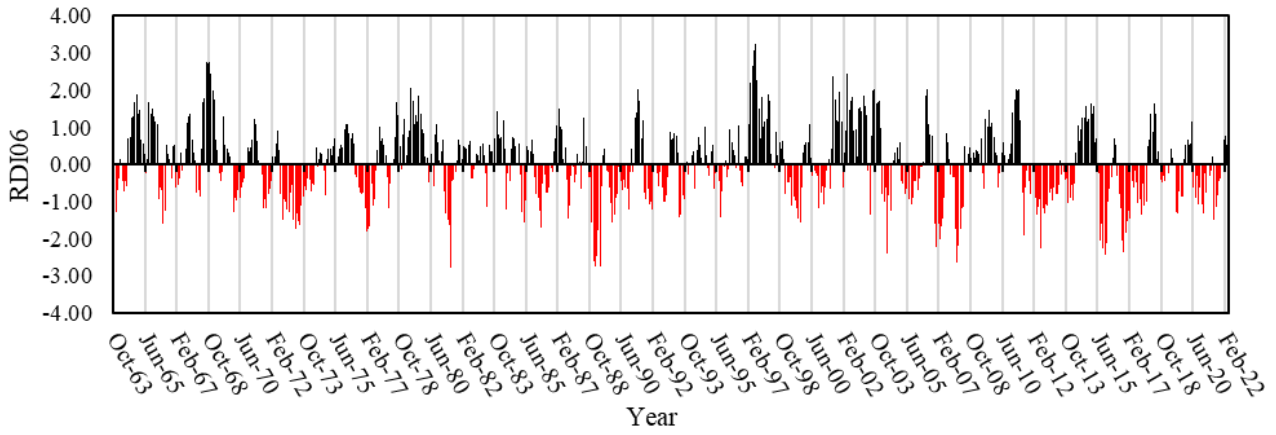


Figure 9. Temporal distribution of Burdur station RDI06 values.

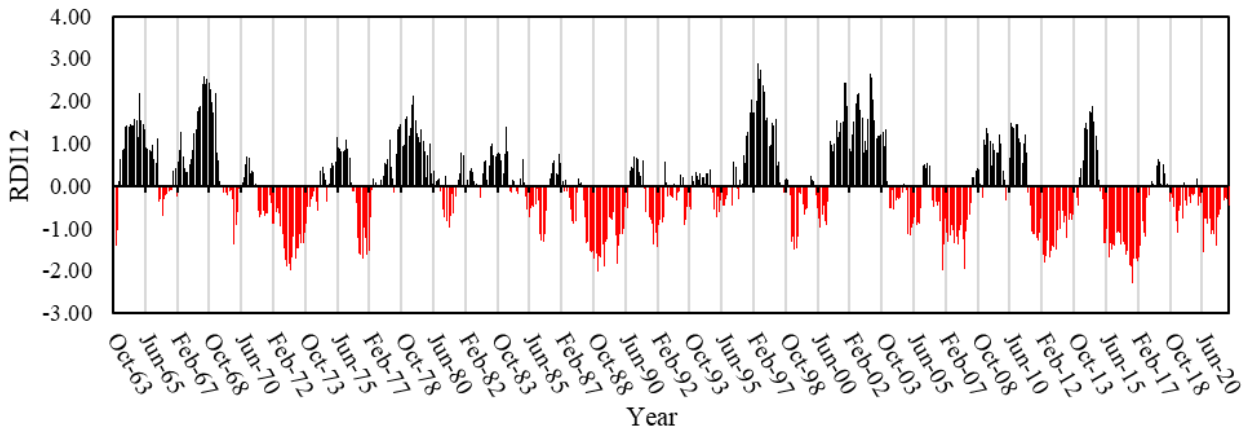


Figure 10. Temporal distribution of Burdur station RDI12 values.

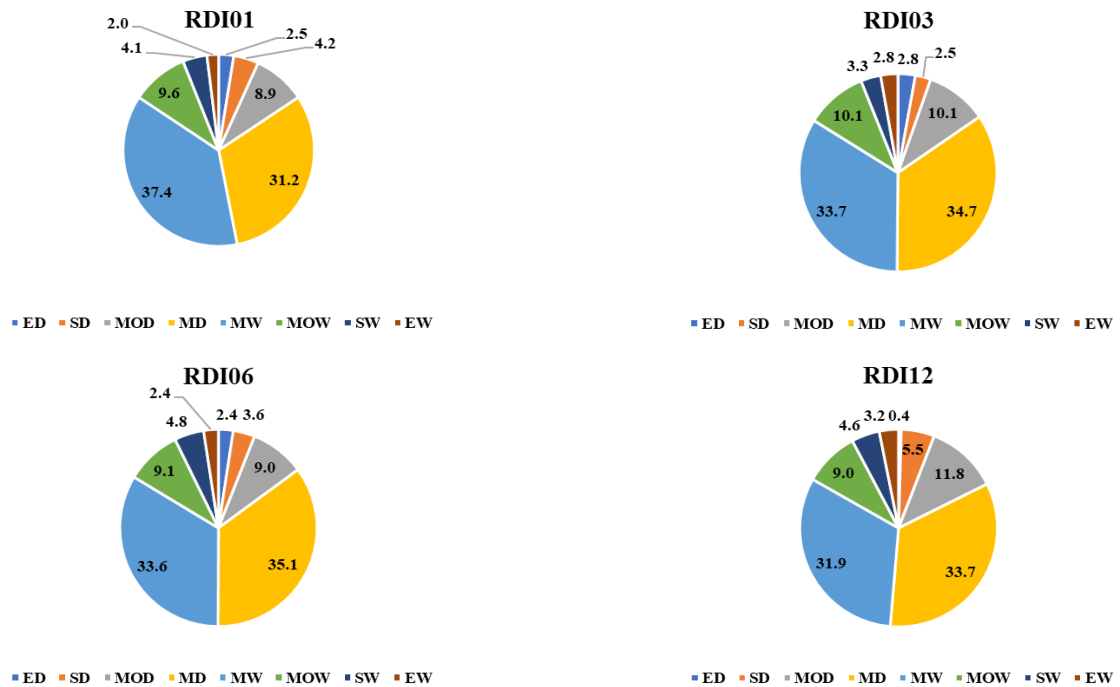


Figure 11. Occurrence of drought classes at Burdur station (RDI).

Table 4. Duration, severity and maximum occurrence values (RDI) of drought at Burdur station.

Period	Severity	Time (Month)	Start	Finish	Pick Value	Pick Time
RDI01	-10.01	10	Dec.88	Sep.89	-3.25	Feb.17
RDI03	-13.7	9	Jan.89	Sep.89	-3.07	Jul.78
RDI06	-21.7	22	Dec.72	Sep.74	-2.79	Nov.81
RDI12	-40.1	32	Jan.16	Jul.18	-2.30	Sep.17

The temporal distribution of RDI values in the 1-, 3-, 6- and 12-month periods calculated using the monthly average precipitation, maximum average, and minimum average temperature data between 1963-2021 at Burdur station is given in Figure 7-10. When the Figure 7-10 are examined, it is seen that while the drought intensity decreases as the period increases, the drought period increases. The highest drought SPI results for the 1-, 3-, and 6-month periods were seen in 1973, 1978, 1981, and 2017, similar to the results. For the 12 months, the driest year was determined as 2017. The rainiest periods were experienced in 1997 and 1998, respectively.

In Figure 11, the percentages of occurrence of drought classes are given according to the RDI values obtained at the Burdur station. As can be seen from the figures, mild drought and mildly wet drought classes are generally experienced in Burdur station, according to the drought occurrence percentages obtained with RDI, similar to the SPI percentages. As the period increased, an increase was observed in the percentage of mild drought periods, while the percentages of occurrence of extreme drought periods decreased.

The duration, intensity, and maximum occurrence values of the arid values obtained by RDI in the 1-, 3-, 6- and 12-month periods between 1963-2021 at Burdur station are given in Table 4. According to the Table 4, it was clearly seen that the severity and duration of drought increased as the period increased. However, it is seen that the highest drought value of the period decreased in absolute terms. The maximum drought for the 1-, 3-, and 6-month periods is the same as the SPI and occurred in July 1978, November 1981, September 2017, and February 2017, respectively. For the 12 months, the maximum drought was observed in September 2017. When the values calculated by SPI and RDI in 1-, 3-, 6- and 12-month time periods were examined in general, it was observed that 1973, 1978, 1981, and 2017 were generally dry.

### 3.2. Drought Analysis of Tefenni Station

#### 3.2.1. Drought analysis based on SPI

When the temporal distributions of the 1-, 3-, 6- and 12-month periods of the SPI values calculated using the monthly average precipitation data between 1963-2021 at Tefenni station are examined (Figure 12-15), it is seen that the period of the dry periods increases as the period increases. In addition, it is understood from the Figure 12-15 that the value of the maximum dry and rainy period decreases with the increase of the period. For the 1-, 3-, 6-, and 12-month periods, the highest droughts were observed in 1989, 2017, and 2021, respectively. The wettest periods were observed in December 2001 in the 1-, 3-, and 6-month periods and in January 1966 in the 12-month period.

According to the results of SPI analysis made with Tefenni station data, the percentages of occurrence of drought classes are given in Figure 16. Accordingly, when all periods are considered at Tefenni station, it is seen that mild drought and mildly wet drought classes are predominantly experienced according to the percentages of drought formation obtained with SPI. As the period increased, there was a decrease in the percentage of mild drought periods, while the percentages of extreme drought periods in general decreased. However, as the period increased, there was an increase in the moderate drought and moderately wet periods.

The duration, intensity, and maximum occurrence values of the arid values obtained by SPI in the 1-, 3-, 6- and 12-month periods between 1963-2021 at Tefenni station are given in Table 5. According to the Table 5, it was clearly seen that the drought severity and period increased as the period increased. However, it is observed that the highest drought value occurring in 1-, 3-, 6- and 12-month periods decreased in absolute terms. For the 1-, 3-, 6-, and 12-month periods, the maximum drought occurred in June 1989, January 1990, February 2017, and September 2021, respectively. In general, it was observed that a dry period started at the end of 1988.

**Table 5.** Duration, severity and maximum occurrence values (SPI) of drought at Tefenni station.

Period	Severity	Time (Month)	Start	Finish	Pick Value	Pick Time
SPI01	-11.7	10	Dec.88	Sep.89	-3.32	Feb.17
SPI03	-17.8	10	Jan.89	Oct.89	3.88	Sep.22
SPI06	-44.5	35	Jan.89	Nov.91	-3.36	Jul.89
SPI12	-79.2	59	Mar.89	Jan.94	-2.80	Jan.90

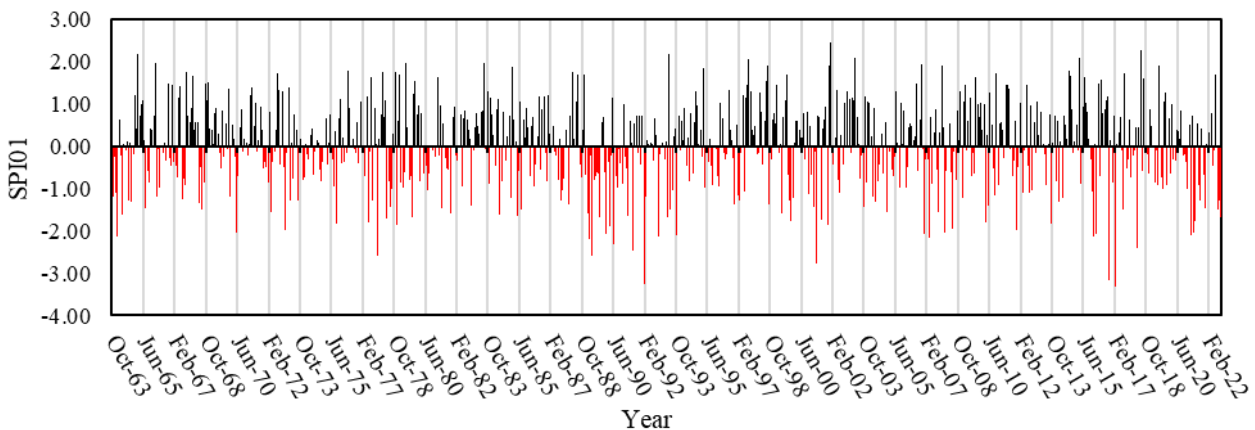


**Figure 12.** Temporal distribution of Tefenni station SPI01 values.

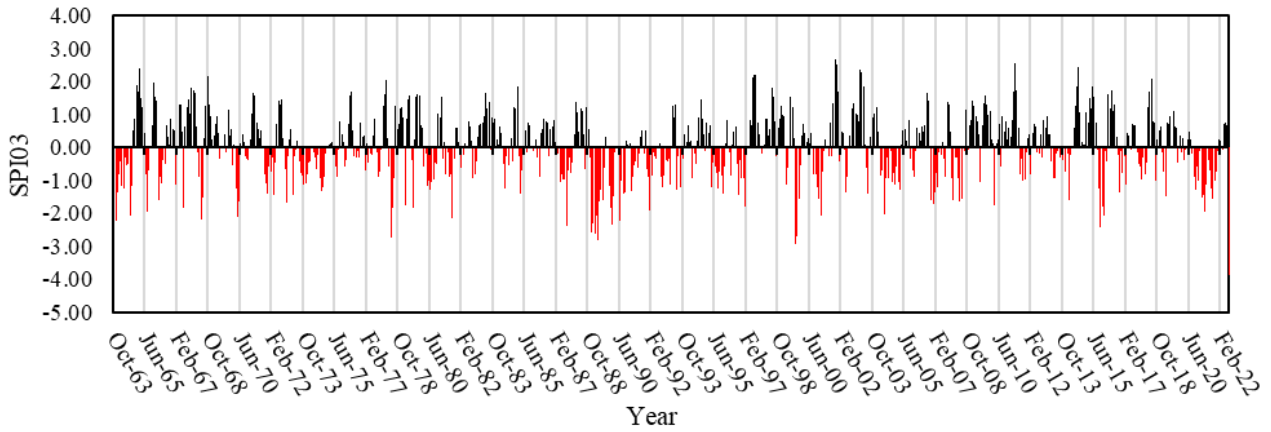


Figure 13. Temporal distribution of Tefenni station SPI03 values.

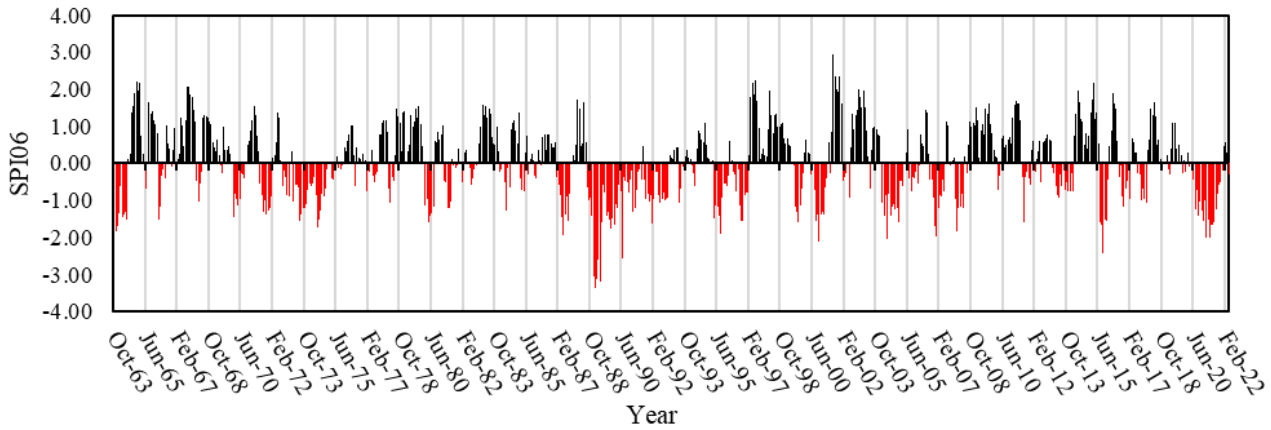


Figure 14. Temporal distribution of Tefenni station SPI06 values.

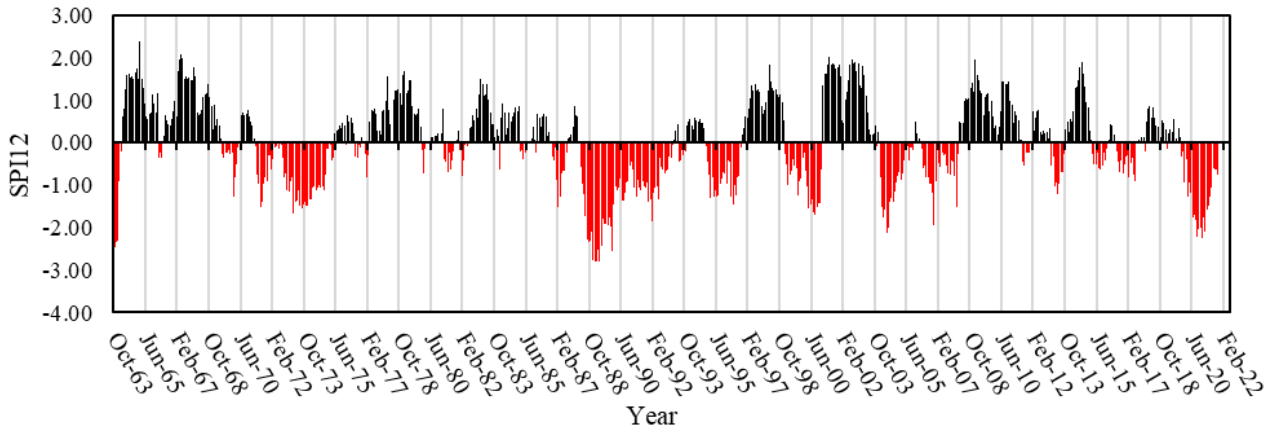


Figure 15. Temporal distribution of Tefenni station SPI12 values.

### 3.2.2. Drought analysis based on RDI

The temporal distribution of the RDI values calculated using the monthly average precipitation data between 1963-2021 at Tefenni station for 1-, 3-, 6- and 12-month periods is given in Figure 17-20. According to Figure 17-20, as in all periods and all drought indices, it is seen that the period of dry periods increases as the period increases. In addition, it was observed that the value of the maximum dry and rainy period decreased with the increase of the period. The highest drought for the 1-, 3-, 6-, and 12-month periods was seen in 1989, 2017, and 2021, respectively, similar to the SPI index. According to the RDI and SPI indexes, the date of the maximum drought at Tefenni station was the same. The

wettest periods were observed in December 2001 in the 1- and 6-month periods and in January 1966 and June 2011 in the 3- and 12-month periods, respectively.

The duration, intensity, and maximum occurrence values of the arid values obtained by RDI in the 1-, 3-, 6- and 12-month periods between 1963-2021 at Tefenni station are given in Table 6. According to Table 6, drought severity and duration increase as the period increases. However, it is observed that the highest drought value occurring in 1-, 3-, 6- and 12-month periods decreased in absolute terms. For the 1-, 3-, 6-, and 12-month periods, the maximum drought occurred in June 1989, January 1990, February 2017, and September 2021, respectively. In general, a dry period started at the end of 1988.

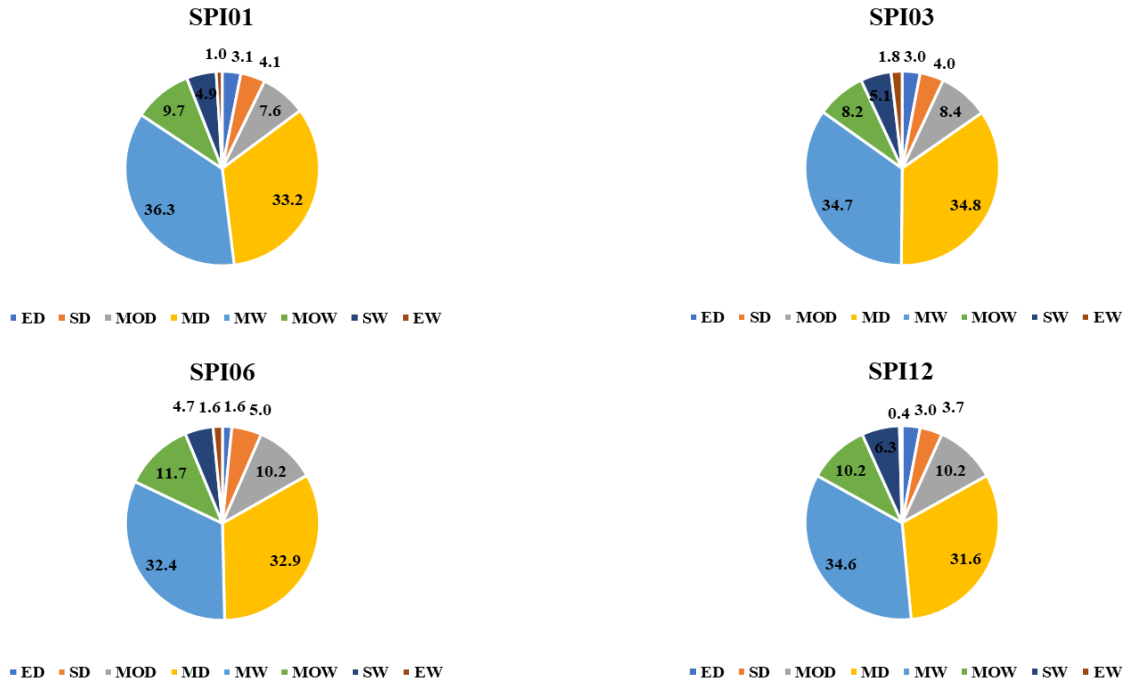


Figure 16. Occurrence percentages of drought classes (SPI) at Tefenni station.

Table 6. Duration, severity and maximum occurrence values (RDI) of drought at Tefenni station.

Period	Severity	Time (Month)	Start	Finish	Pick Value	Pick Time
RDI01	-11.56	10	Dec.88	Sep.89	-3.15	Feb.17
RDI03	-17.35	10	Jan.89	Oct.89	-3.87	Sep.22
RDI06	-43.15	35	Jan.89	Nov.91	-3.34	Jul.89
RDI12	-73.51	59	Mar.89	Jan.94	-2.79	Jan.90

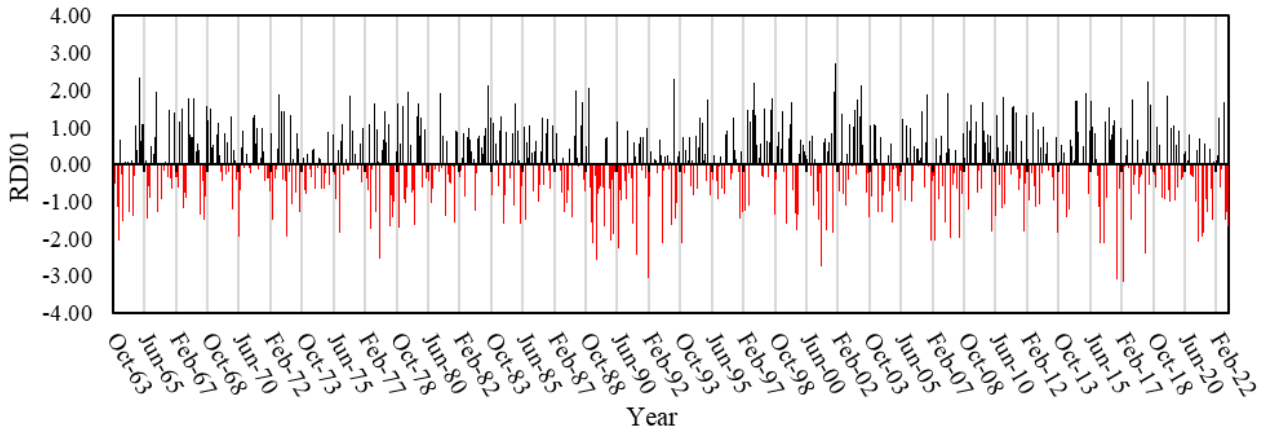


Figure 17. Temporal distribution of Tefenni station RDI01 values.

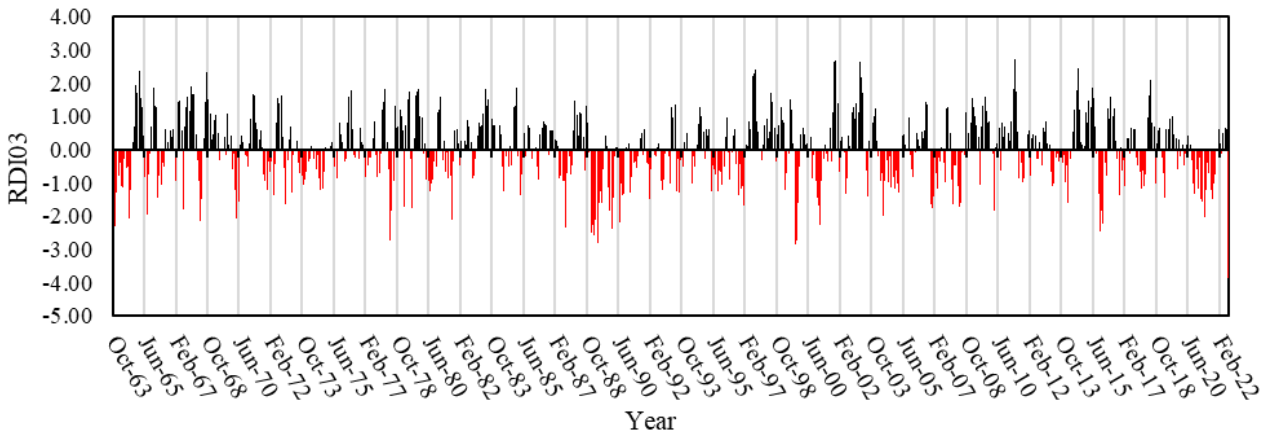


Figure 18. Temporal distribution of Tefenni station RDI03 values.

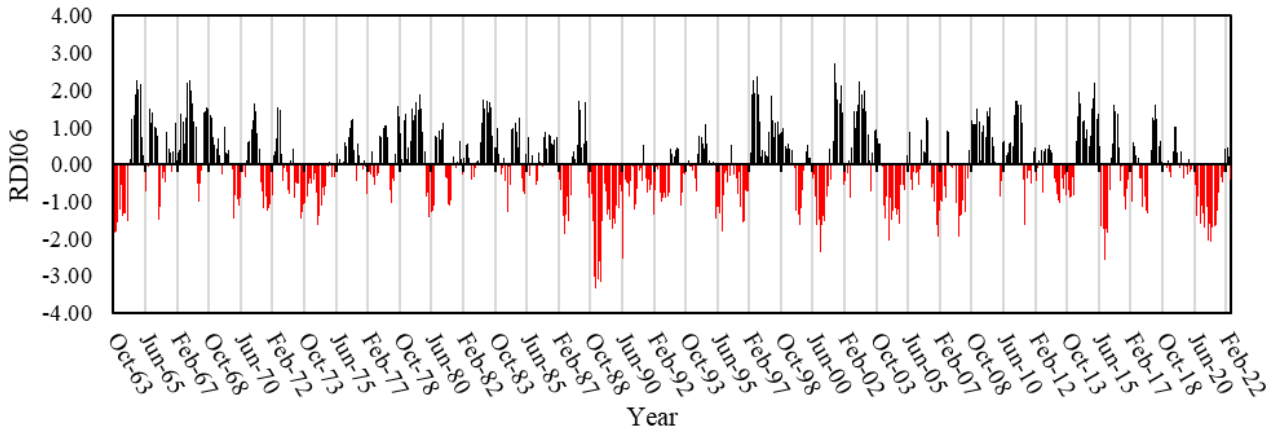


Figure 19. Temporal distribution of Tefenni station RDI06 values.

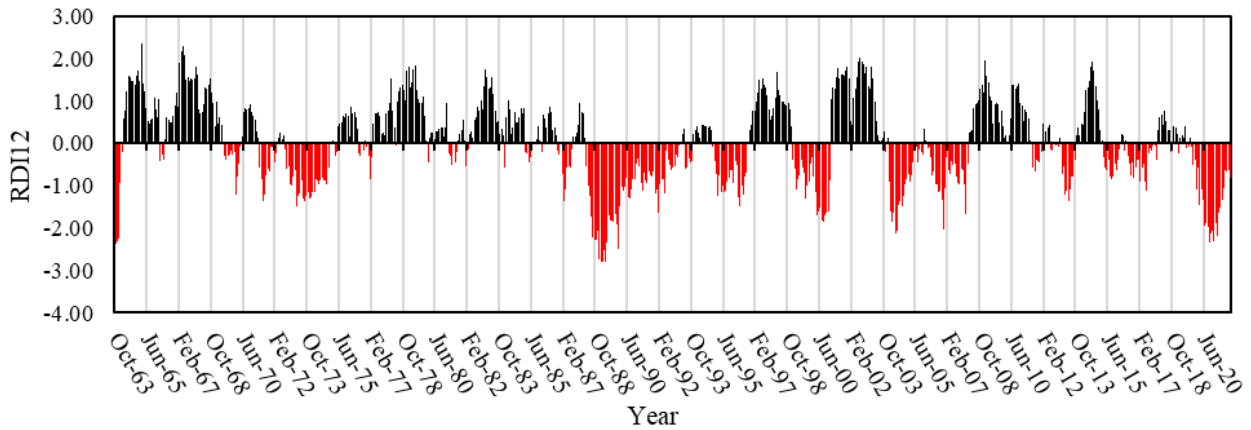


Figure 20. Temporal distribution of Tefenni station RDI12 values.

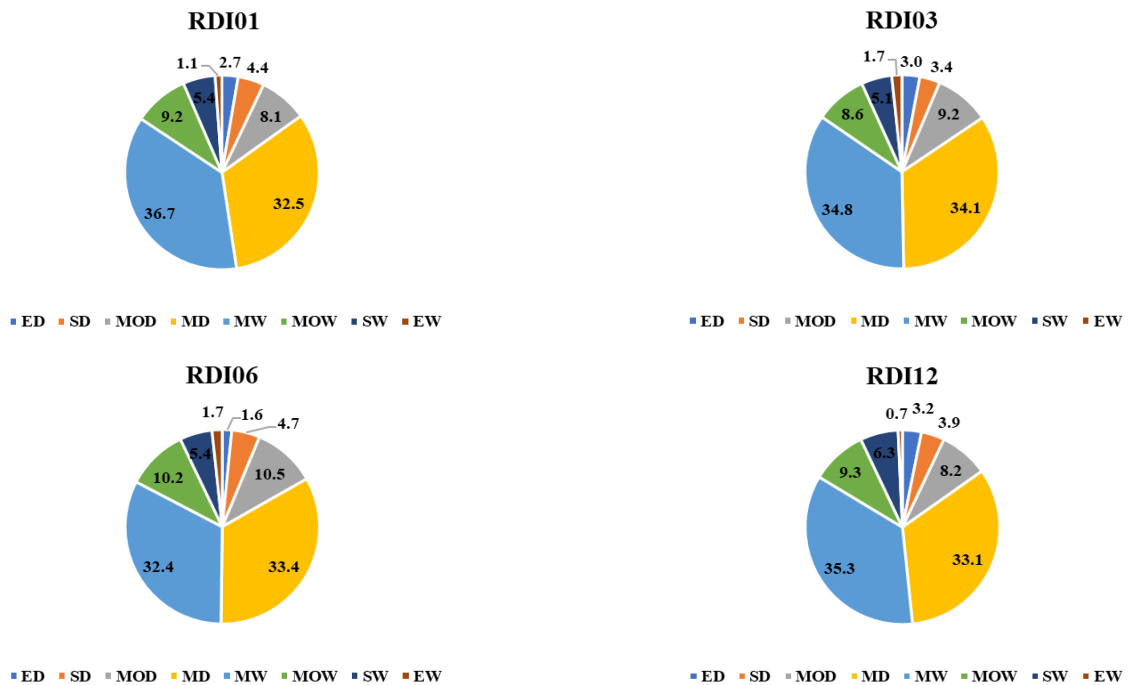


Figure 21. Occurrence percentages of drought classes (RDI) at Tefenni station.

#### 4. Discussion

This study conducted meteorological and agricultural drought analysis in the Burdur Basin in the Aegean

Region. For this purpose, meteorological and agricultural droughts for 1963-2021 were analyzed using the average precipitation, average minimum and maximum temperatures observed in Burdur No. 17238 and Tefenni

No. 17892 in the Burdur Basin. By applying Standard Precipitation Index (SPI) and Exploratory Drought Index (RDI) methods to the data sets, respectively, the severity, size, and distribution of dry and humid periods were determined by the SPI and RDI values calculated for 1-, 3-, 6- and 12-month periods.

When the SPI results are examined, the number of extreme drought months observed between 1963-2021 was 6, 9, 22, and 41 for the Burdur station in 1-, 3-, 6- and 12-month periods, respectively; 10, 10, 35 and 59 respectively for Tefenni station. In the examined period, maximum droughts for 1-, 3-, 6- and 12-month periods were experienced in Burdur station in July 1978, November 1973, November 1981, and February 2017, and at Tefenni station in June 1989, January 1990, February 2017 and September 2021.

When the RDI results are examined, the number of extreme drought months observed between 1963-2021 was 10, 9, 22, and 32 for the Burdur station in 1-, 3-, 6- and 12-month periods, respectively; 10, 10, 35 and 59 respectively for Tefenni station. In the examined period, maximum droughts for 1-, 3-, 6- and 12-month periods were experienced at Burdur station in July 1978, November 1981, September 2017, and February 2017, and at Tefenni station in June 1989, January 1990, February 2017 and September 2021.

When the values calculated by SPI and RDI were examined in general, it was observed that the years 1973, 1978, 1981, and 2017 were generally dry in the study area.

## 5. Conclusion

As a result of the analysis, the severity and duration of droughts in the Burdur basin have increased in recent years, and meteorological drought; agricultural drought has been observed. In order to combat the devastating effects of the drought disaster in the Burdur Basin, which is an important area for our country in terms of water resources, it will be beneficial to regularly monitor the variability in climatological data and develop local policies that will ensure the effective management of water resources. In addition, determining hydrological droughts and precipitation trends for the same region will be an important resource for water management studies.

## Author contributions

**Nazire Göksu Soydan Oksal:** Conceptualization, Methodology, Original draft preparation and Editing.

**Neslihan Beden:** Data curation, Methodology, Writing-Reviewing and Editing.

## Conflicts of interest

The authors declare no conflicts of interest.

## References

1. Kundzewicz, Z. W., & Robson, A. (2000). Detecting trend and other changes in hydrological data. *World Climate Programme Data and Monitoring, WCDMP – 45*
2. Beşel, C., & Kayikci, E. T. (2020). Investigation of Black Sea mean sea level variability by singular spectrum analysis. *International Journal of Engineering and Geosciences*, 5(1), 33-41. <https://doi.org/10.26833/ijeg.580510>
3. Ojha, S. S., Singh, V., & Roshni, T. (2021). Comparison of meteorological drought using SPI and SPEI. *Civil Engineering Journal*, 7(12), 2130-2149. <http://dx.doi.org/10.28991/cej-2021-03091783>
4. Zarch, M. A. A., Sivakumar, B., & Sharma, A. (2015). Droughts in a warming climate: A global assessment of Standardized precipitation index (SPI) and Reconnaissance drought index (RDI). *Journal of Hydrology*, 526, 183-195. <https://doi.org/10.1016/j.jhydrol.2014.09.071>
5. Surendran, U., Kumar, V., Ramasubramoniam, S., & Raja, P. (2017). Development of drought indices for semi-arid region using drought indices calculator (DrinC)—a case study from Madurai District, a semi-arid region in India. *Water Resources Management*, 31, 3593-3605. <https://doi.org/10.1007/s11269-017-1687-5>
6. An, S., Park, G., Jung, H., & Jang, D. (2022). Assessment of future drought index using SSP scenario in Rep. of Korea. *Sustainability*, 14(7), 4252. <https://doi.org/10.3390/su14074252>
7. Mishra, A. K., & Singh, V. P. (2010). A review of drought concepts. *Journal of Hydrology*, 391(1-2), 202-216. <https://doi.org/10.1016/j.jhydrol.2010.07.012>
8. Wilhite, D. A., & Glantz, M. H. (1985). Understanding: The Drought Phenomenon: The Role of Definitions. *Water International*, 10, 111-120.
9. İnan, B., Demir, V., & Sevimli, M. F. (2021). Drought analysis of Black Sea Region by standardized precipitation index (SPI) and percent of normal index (PNI). *Advanced Engineering Days (AED)*, 1, 8-10.
10. Citakoglu, H., & Coşkun, Ö. (2022). Comparison of hybrid machine learning methods for the prediction of short-term meteorological droughts of Sakarya Meteorological Station in Turkey. *Environmental Science and Pollution Research*, 29(50), 75487-75511. <https://doi.org/10.1007/s11356-022-21083-3>
11. Coşkun, Ö., & Citakoglu, H. (2023). Prediction of the standardized precipitation index based on the long short-term memory and empirical mode decomposition-extreme learning machine models: The Case of Sakarya, Türkiye. *Physics and Chemistry of the Earth, Parts A/B/C*, 131, 103418. <https://doi.org/10.1016/j.pce.2023.103418>
12. SYGM, (2019). Burdur Havzası Taşkın Yönetim Planı. Ankara: Türkiye Cumhuriyeti Tarım ve Orman Bakanlığı.
13. Ünel, F. B., Kuşak, L., Yakar, M., & Doğan, H. (2023). Coğrafi bilgi sistemleri ve analitik hiyerarşi prosesi

- kullanarak Mersin ilinde otomatik meteoroloji gözlem istasyonu yer seçimi. *Geomatik*, 8(2), 107-123. <https://doi.org/10.29128/geomatik.1136951>
14. Demir, V., & Keskin, A. Ü. (2022). Yeterince akım ölçümü olmayan nehirlerde taşkın debisinin hesaplanması ve taşkın modellemesi (Samsun, Mert Irmağı örneği). *Geomatik*, 7(2), 149-162. <https://doi.org/10.29128/geomatik.918502>
15. Mohamed, M. J., Cemek, B., Küçüktopcu, E., Omar, A. A., & Hassan, S. M. (2022). Drought Analysis in Somalia Using GIS-Based on Reconnaissance Drought Index (RDI) and Standardized Precipitation Index (SPI). *African Journal of Climate Change and Resource Sustainability*, 1(1), 62-75. <https://doi.org/10.37284/ajccrs.1.1.981>
16. Beden, N., Demir, V., & Keskin, A. Ü. (2020). Samsun İlinde SPI ve PNI Kuraklık İndekslerinin Eğilim Analizi. *Dokuz Eylül Üniversitesi Mühendislik Fakültesi Fen ve Mühendislik Dergisi*, 22(64), 107-116. <https://doi.org/10.21205/deufmd.2020226411>
17. Gümüş, V., Başak, A., & Oruç N. (2016). Standartlaştırılmış yağış indeksi (SYİ) yöntemi ile Şanlıurfa istasyonunun kuraklık analizi. *Harran Üniversitesi Mühendislik Dergisi*, 1(1), 36-44.
18. Tsakiris, G., Pangalou, D., & Vangelis, H. (2007). Regional drought assessment based on the Reconnaissance Drought Index (RDI). *Water Resources Management*, 21, 821-833. <https://doi.org/10.1007/s11269-006-9105-4>



© Author(s) 2024. This work is distributed under <https://creativecommons.org/licenses/by-sa/4.0/>



## Cotton yield estimation using several vegetation indices

Bakhtiyar Babashli <sup>\*1</sup>, Aytaj Badalova <sup>1</sup>, Ramis Shukurov <sup>2</sup>, Agil Ahmadov <sup>3</sup>

<sup>1</sup> National Aviation Academy, Aerospace Faculty, Azerbaijan, bakhtiyar.babashli@gmail.com, badalova-aytac60@rambler.ru

<sup>2</sup> Mil Experiment Station, Azerbaijan, ramis.shukur@gmail.com

<sup>3</sup> Azercosmos, Azerbaijan, aqil1964@gmail.com

Cite this study:

Babashli, B., Badalova, A., Shukurov, R., & Ahmadov, A. (2024). Cotton yield estimation using several vegetation indices. *Turkish Journal of Engineering*, 8 (1), 139-151

### Keywords

Cotton  
Yield  
Vegetation indices  
Biomass  
Satellite images

### Research Article

DOI: 10.31127/tuje.1346353

Received:19.08.2023

Revised: 21.11.2023

Accepted:26.11.2023

Published:07.01.2024



### Abstract

Accurate yield estimation before harvest is important for farmers and researchers to optimize field management and increase productivity. The purpose of this study is to develop efficient cotton plant productivity using field studies and satellite imagery. Nitrogen (N) fertilizer is an important nutrient in plant development, and when suboptimal amounts are applied, it can cause yield reductions. Different vegetation indices were employed to analyze the dynamics and yield of cotton plants, with a primary focus on the Red, Near-Infrared (NIR), and Red Edge bands derived from satellite imagery. The objective was to assess the nitrogen content in the plants. The present study involved a comparative analysis of various vegetation indicators in relation to cotton plant production. The productivity of the cotton plant was assessed by employing the indices that exhibited the most influence. The analysis revealed that the MCARI index exhibited the worst weaknesses, while the CLRE index demonstrated the main performance. The productivity of each index was computed, and it was observed that the CLRE index exhibited the closest proximity to the average productivity of 34.48 cents per hectare (cent/ha). Similar results have been observed in other indices. The MCARI index exhibits a distinct value of 32.08 in comparison to the others indices. The results of this study illustrate the potential of satellite imaging in monitoring cotton yield, hence offering valuable theoretical and technological assistance for estimating cotton production in agricultural areas.

## 1. Introduction

Agriculture plays a crucial role in the global economy, and as the world's population grows, the need for agricultural products increases [1]. Cotton belongs to the genus *Gossypium* L. of Malvaceae family [2]. The cotton industry is of great national economic importance in terms of employment of the population and the development of the textile industry. Cotton is among the most cultivated plants in the world [3]. Today, the most developed countries in the world are engaged in cotton production. Countries such as the USA, Israel, Turkey, China, and India receive quite a lot of income from this field. China, India and the United States are the top three producers of cotton in the world [4-5]. Cotton growing in Pakistan, Uzbekistan and Turkey is developing at a high pace. Along with the development of cotton cultivation in these countries, the textile industry is also expanding.

Crop growth and productivity are the combined effects of the environment, water, soil, nitrogen and other

components. This makes product evaluation difficult and often inaccurate. Currently, evaluation of cotton plant productivity plays an important role for agriculture [6]. Conventionally, cotton yield is estimated based on the number of bolls per unit area. However, cotton yield varies according to field irrigation and fertilization. Many researchers have tried to develop different methods to increase the accuracy of productivity estimation [7-9].

The traditional yield survey method relies on the experience of farmers or professionals, which is time-consuming, laborious and uncertain. Recent studies have shown that technological progress can play a crucial role in achieving sustainable intensification in agriculture [10]. In recent years, remote sensing technology has been widely applied in agriculture [11]. At present, relevant scientists also offer various methods for predicting cotton yield.

Quan Xu significantly contributed to the enhancement of precision agriculture by conducting an evaluation of cotton productivity in China [12]. The study introduced a

novel approach named SENP (Seedling Emergence and Number of Peaches) that leverages the capabilities of Amazon Web Services (AWS). The assessment of cotton productivity was conducted utilizing high-resolution data collected by an Unmanned Aerial Vehicle (UAV), the U-Net model of deep learning and Sentinel-2 data. It is demonstrated that estimating cotton condition from Normalized difference vegetation index (NDVI) data collected over a specific time is imprecise. The utilization of predominantly time series data has demonstrated that NDVI is a more effective method for monitoring cotton development. The experiment's results indicate that utilizing cotton emergence and growth data is a suitable approach for estimating yield. The reliability and excellent accuracy of the SENP-based cotton yield estimation model have been proven through validation using the real crop. Therefore, a digital platform has been developed utilizing Amazon Web Services (AWS) and ENVI Services Engine (ESE) measure cotton production online. This platform aims to offer valuable data for regional agricultural management and macro-level decision-making, leveraging the benefits of cloud computing. Accuracy of precision achieved in the experiment was 93.88%, recall rate was found to be 97.87% and F value calculated 95.83%.

Guanwei Shi employed a new method to estimate cotton yield by utilizing the density of open Cotton boll Pixels (DCP) derived from unmanned aerial vehicles (UAVs) [13]. Correlation analysis was employed to compare the performance of several indexes. A performance indicator that demonstrates excellence and an index that measures profitability, both obtained from empirical field research, are conceptualized. The study area is partitioned into three distinct regions, each characterized by varying datasets obtained from drone-based observations and traditional field surveys. The findings of the study indicate a significant relationship between the DCP and crop yield, as evidenced by a Pearson correlation coefficient of 0.84. The Random Forest (RF) technique had superior performance in estimating revenue, as evidenced by its average R-squared (R<sup>2</sup>) value of 0.77 and relative root mean squared error (RMSE) value of 7.5%.

Ping Lang investigated the most significant VIs and CVs for Xinjiang Province district-level cotton productivity estimation [14]. The researcher discovered that the vegetation indices (VIs) pertaining to canopy structure, chlorophyll content, and moisture coefficient of variation (CV) were the primary determinants influencing the growth of cotton. The individual employed various regression methodologies to estimate cotton yield. The study acquired annual (April-September) and monthly averages of MODIS and Sentinel-2 photos pertaining to cotton fields from 2012 to 2019. A total of 14 satellite VIs were computed to forecast fertility. Monthly data was utilized for the purpose of predicting cotton production prior to harvest and examining the temporal progression of cotton growth. Climatic variables are extensively employed in the estimation of crop productivity. The findings of the study indicate that the Long Short-Term Memory (LSTM) model exhibited the highest performance, as evidenced by an R<sup>2</sup> value of 0.76, a Root Mean Square Error (RMSE)

of 150 kg/ha, and a relative Root Mean Square Error (RMSE) of 8.67%. The study showcased the viability of county-level yield estimation and early forecasting in extensive cotton fields through the integration of satellite imagery and environmental data.

Compared to traditional methods, remote sensing methods are more economical and effective when it comes to cotton yield monitoring [15-16]. Nitrogen (N) is a major nutrient that directly affects plant behavior [17-18]. Both N deficiency and N excess have negative effects on plant development, yield, and fiber quality [19-20]. Insufficient N supply often leads to reduced leaf area and reduced leaf photosynthesis and biomass production, resulting in reduced yield and unsatisfactory fiber quality [21-23]. VIs used in yield calculations are designed to increase sensitivity to vegetation characteristics while minimizing confounding factors such as soil background reflectance, directional, and atmospheric effects [24-25].

The implementation of satellite remote sensing has been widely used in agricultural research. The utilization of satellite data to calculate VIs has emerged as a prevalent approach in predicting crop yields [26]. VIs has the capability to characterize biotic attributes, including vegetation structure, chlorophyll concentration, and nitrogen content. Various VIs, such as the (NDVI), Enhanced Vegetation Index (EVI), and Near Infrared Reflectance of Vegetation (NIR), have been employed in studies to elucidate the fluctuations in yields of wheat, cotton, corn, rice, and soybeans [27-28]. Even though VIs is useful in predicting cotton production, environmental conditions should also be taken into account as a component that affects yield.

The objective of this research is to assess productivity of the cotton plant by determining the growth level (biomass) with the VI based on ground and satellite data. VIs is considered the main factor in agriculture to calculate the biomass of vegetation in cultivated areas.

## 2. Method

The focus of this study related to the cotton fields located within Beylagan district (Figure 1). Beylagan district has boundaries with the Agjabadi, Zardab, Fuzuli, and Imishli districts of the Republic of Azerbaijan, as well as the Islamic Republic of Iran [29]. Azerbaijan, the nation and former Soviet republic is geographically bounded by the Caspian Sea and the Caucasus Mountains, encompassing territories spanning the continents of Asia and Europe. The geographical location of this entity is situated in the central region of the country, and it is encompassed within the Mil-Mugan Economic Region. The district spans between longitudes 47.46°E and 47.94°E, and latitudes 39.57°N and 40.14°N. The district covers an area of 1.13 thousand square kilometers. Beylagan is the city in the center.

The scope of this study encompasses cultivated cotton fields spanning across 14 villages, occupying a total arable land area of 59,893 hectares. Based on statistical data, it can be observed that the financial backing for planted cotton fields primarily stems from three firms, namely "MTK IK" LLC, "Azer Pambig" LLC, and "P-Agro" LLC [30].

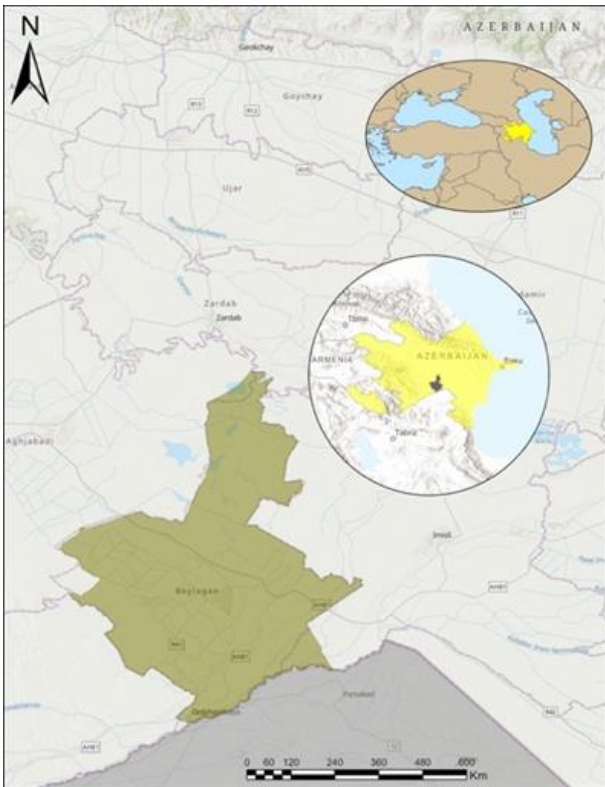


Figure 1. Study area.

### 2.1. Data

At the initial stage, Azersky/SPOT-7 (Satellite Pour l'Observation de la Terre-7) satellite images taken in periods covering different vegetation stages of cotton were used in the research area [31-32]. SPOT 7 is an Azerbaijan's first commercial high-resolution earth observation satellite. It was launched on 30 June 2014 and ceased operations on 17 March 2023. On December 2, 2014, the name was changed to 'Azersky'. It was providing a consistent stream of high-resolution, wide-swath data. The Panchromatic imagery exhibited a

resolution of 1.5 meters, whereas the Multispectral imagery showed a resolution of 6 meters. The imaging system consisted of 1 panchromatic band and 4 multispectral bands, specifically capturing data in the green, blue, red, and near-infrared wavelengths. The shown landscape exhibited a range of dimensions, with a minimum extent of 60 kilometers by 60 kilometers and a maximum extent of 60 kilometers by 600 kilometers. The satellite was deployed in a Sun-synchronous circular orbit at an altitude of 694 km.

Based on the controlled classification algorithm of satellite images, cotton fields were identified in the area [33-34]. Hancong [35] calculated the percentage of cotton area using satellite imagery. By dividing the number of cotton pixels by the total area of the field, they obtained the percentage of cotton area that was strongly correlated with yield. The methodology consists of two main data sources (Figure 2). Satellite images and field research data were used. The image used is the main phase of the plant in the growing season [36]. NDVI was produced based on a satellite image of the study area acquired on August 17, 2022 (Figure 3) to separate the cotton fields [37-38].

Five stationary observation sites were chosen using NDVI images to assess the development state of the cotton fields in the study area (Figure 4). Thus, the stationary areas to be researched cover approximately 2350 ha of cotton cultivation area, which is up to 27% of the total cotton cultivation area. Cotton plantations are categorized into three distinct classes based on their level of development. Weak, medium and high levels of productivity. Field study was conducted in each of the five pre-determined permanent observation areas, following the approved sequence of activities inside the specific cotton fields of the respective areas. The agricultural enterprises in the local area supplied farmers with a range of cultivars, including BA-440, Flash, Lodos, May 344, ADN-123, Ganja-114 and Ganja-160.

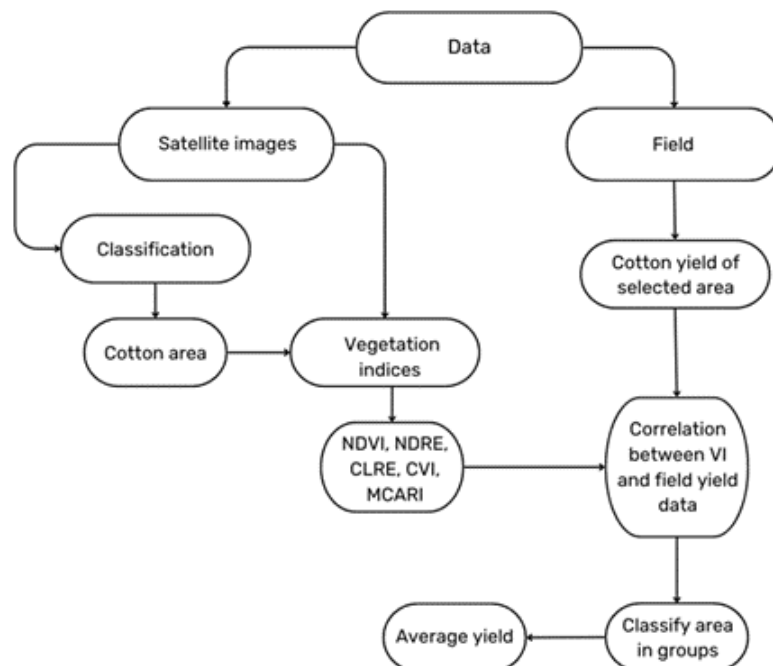


Figure 2. Productivity modeling based on remote sensing and field survey data.

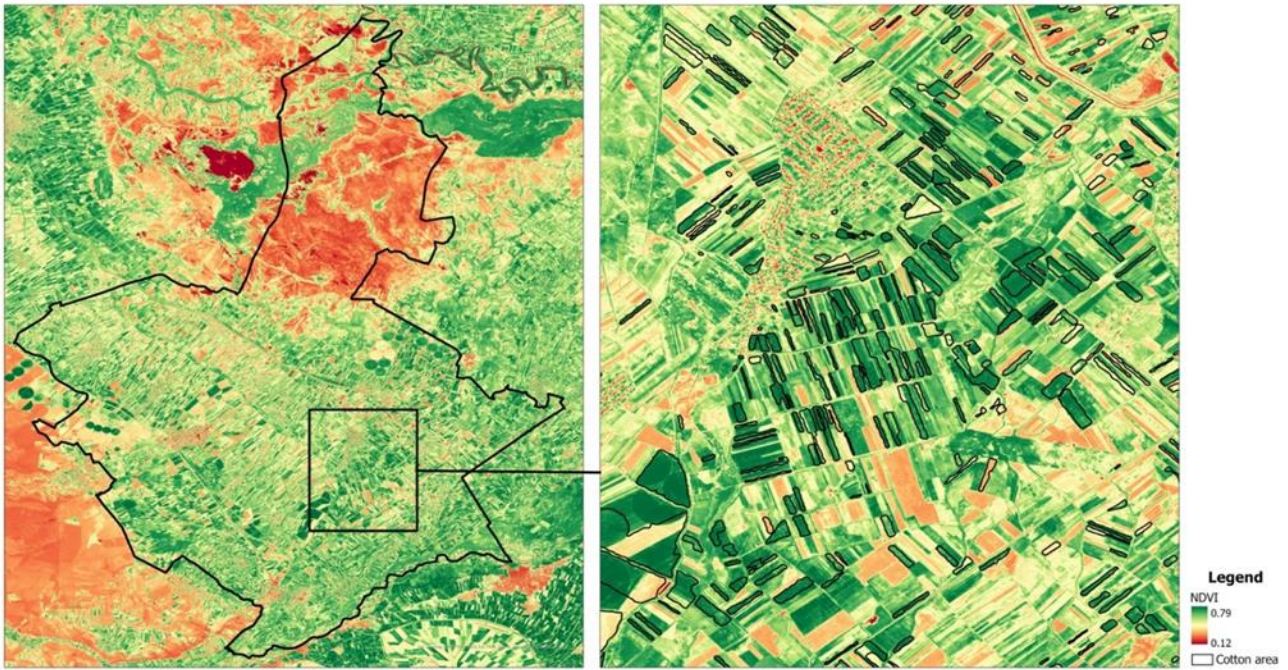


Figure 3. NDVI image of the study area.

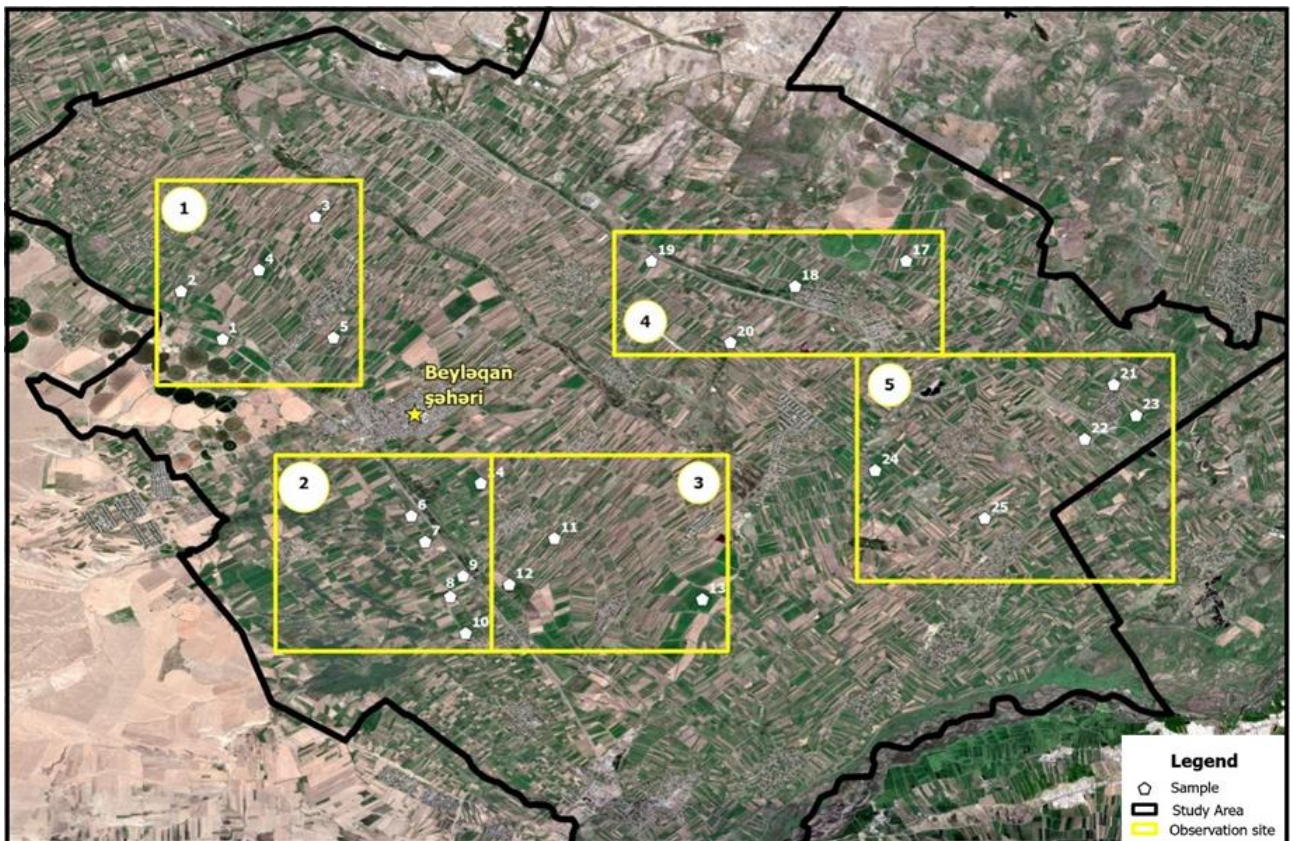


Figure 4. Selected stationary observation sites.

The study involved the random selection of a 1-meter row of plant bushes within a designated region spreading 20-25 meters. The objective was to determine the quantity of plant bushes in this row, as well as the number of productive cotton bolls that were older than 30-35 days, within these bushes. However, it should be noted that the repetition of the same activities was carried out in a diagonal manner with 30-50 meters, depending on the size of the field. The determination and record of both the plant count and boll count were

conducted at a minimum of three distinct locations along a single diagonal within each field. Additionally, this process was repeated on the other diagonal in two separate samples. For an example, the product of 219.6 grams of cotton per meter and the row length of 11111.1 meters yields a value of 2440 kg or 24.4 centners per hectare. In each group, a diagonal assessment was conducted across three samples to determine the number of plants within a one-meter radius and the corresponding count of bolls capable of producing crop.

Subsequently, cotton samples were obtained from the opened bolls and quantified by weight using an electronic scale. Multiple independent experiments were done on predetermined regions, referred to as stationary zones (Table 1).

Nowadays, the evaluation of plant production primarily relies on the utilization of satellite remote sensing data. The Sentinel-2 satellite was employed due to the absence of a red edge capability in the Azersky satellite. Multispectral sensors (MSI) with 13 spectral bands and varying spatial resolutions (10, 20, 60 m) are installed on board the twin satellites Sentinel-2, A and B. This provides novel prospects for the monitoring of agricultural activities at both regional and global scales. The utilization of the Sentinel-2 satellite has facilitated the conduction of time-series analysis for monitoring agricultural development and studying productivity.

**Table 1.** Statistical analysis of field research results.

Study area	Number of samples	Biological productivity cent/ha
1	5	35.1
2	5	43.2
3	5	35.9
4	6	36.6
5	5	34.5
6	6	41.1
7	6	45.4
8	6	36.4
9	6	45.3
10	6	44.4
11	6	31.0
12	6	33.7
13	6	31.8
14	5	33.1
15	6	32.1
16	5	36.8
17	5	29.8
18	6	30.8
19	5	32.7
20	5	32.9
21	6	30.3
22	6	34.7
23	5	30.5
24	6	42.4
25	5	31.2
Sum	139	33.5 cent/ha

## 2.2. Vegetation indices

The most used indices for vegetation use red and near-infrared (NIR) reflectance or brightness data [39]. For this purpose, some VIs such as NDVI, Chlorophyll vegetation index (CVI), Modified Chlorophyll Absorption in Reflectance Index (MCARI), Normalized Difference Red-Edge (NDRE), Chlorophyll Red Edge Index (Clre) and The Green Normalized Difference Vegetation Index (GNDVI) have been used.

Various VIs is employed in the computation of cotton yield (Table2). NDVI indicates that in healthy vegetation where there is a lot of green foliage, most of the visible light that hits it is absorbed, while NIR light is mainly reflected by the plant [40-41]. Unhealthy vegetation with little or no green foliage reflects most of the visible light, absorbing more NIR light [42-43]. Strong correlations are observed between NDVI measurements and plant biomass, total green area, spikeless green area, and above-ground nitrogen content [44-46]. The calculation procedure of NDVI is as follows [47-48]. CVI has an increased sensitivity to the chlorophyll content of leaf cover [49]. It is used early to mid-crop growth cycle for a wide range of soil and crop conditions by analyzing a large set of synthetic data obtained using a leaf surface contrast model. The increased sensitivity of the index to leaf chlorophyll concentration is due to the effective normalization of different LAI values obtained by applying red and green colors. MCARI measures the depth of chlorophyll absorption and is very sensitive to changes in leaf area index and chlorophyll concentration [50-51]. MCARI values are not affected by lighting conditions, background reflection from soil and other observed non-photosynthetic materials.

Using the Normalized Difference Red-Edge (NDRE) Red edge parameter, a measurement that is not strongly absorbed by the uppermost layers of leaves allows for better information about plants at a later stage [52-53]. These include poor watering, disease, improper fertilizer use, or identifying pests.

Clrededge was developed to estimate the chlorophyll content of leaves using the ratio of reflectance in the near-infrared (NIR) and red-edge bands [54]. Chlorophyll is a good indicator of a plant's production potential. Additionally, it can be utilized to get insight on the nutrient status of plants, the presence of water stress, the prevalence of diseases, and other related factors.

**Table 2.** Vegetation indices formula.

Index	Formula	Reference
NDVI	$(\text{NIR} - \text{RED}) / (\text{NIR} + \text{RED})$	[40]
CVI	$(\text{NIR} * (\text{RED} / (\text{GREEN} * \text{GREEN})))$	[49]
MCARI	$((\text{RE} - \text{RED}) - 0.2 * (\text{RE} - \text{GREEN})) * (\text{RE} + \text{RED})$	[50]
NDRE	$(\text{RE} - \text{RED}) / (\text{RE} + \text{RED})$	[52]
CLRE	$(\text{NIR} - \text{RE}) / 1$	[54]
GNDVI	$(\text{NIR} - \text{Green}) / (\text{NIR} + \text{Green})$	[55]

GNDVI provides an indicator for quantifying the level of "greenness" or photosynthetic activity shown by crops [55]. The vegetation index (VI) under consideration is extensively employed for assessing water and nitrogen absorption inside the crop canopy. The results provided

by this index exhibit variation within the range of -1 to 1. Values within the range of -1 to 0 are indicative of the existence of water or exposed soil. The utilization of this measure is primarily observed throughout the intermediate and final phases of the crop cycle. GNDVI is

a quantitative measure that utilizes the near infrared and green band wavelengths within the electromagnetic spectrum.

CLRE enhances vegetation detection in areas with little vegetation cover by utilizing the difference between the NIR and red edge bands. It can be used to monitor vegetation change in dry and semi-arid locations. The NDRE is calculated using the nir and red edge bands. The NDRE system is intended for observing the depth of dense vegetation. This makes it an excellent instrument for monitoring densely planted crops such as coffee, corn, cotton, grapes, sunflowers, and others. CVI estimates chlorophyll concentration in plants using the ratio of NIR and red bands. It can be used to monitor plant health and detect nutritional deficits in crops. MCARI reacts to chlorophyll content in the leaf and ground reflectance. In general, high MCARI readings suggest a poor chlorophyll concentration in the leaf. MCARI has a deficit in forecasting low chlorophyll concentrations, which is exacerbated by the influence of the soil signal. The Nir and red bands are used to calculate NDVI. The density and greenness of vegetation in a field can be measured using NDVI. Dense green vegetation is a good general sign of crop health under the proper conditions and at the right time of year. However, cotton is a unique plant, it produces varied results when calculating productivity. The NDVI is primarily used to calculate the degree of photosynthesis in plants. As a

result, the healthier and denser the plant tissues are, the more energy they absorb while also reflecting the NIR spectrum. Vegetation covers have indicators ranging from 0.3 to 0.8 (tall and dense plants) as biomass increases. MCARI is the proportion of the green, Nir and red bands.

According to the field samples collected to determine the biological productivity and the calculations made, the productivity of the cotton fields was divided into 3 classes according to the following up criteria:

Poorly developed, up to 60-62 cones per meter:  
 $61 \times 4.5^{**} = 180 \text{ g} \times 11111^* = \text{up to } 31 \text{ cent/ha}$

Medium developed, up to 65-70 cones per meter:  
 $67 \times 4.5 = 225 \times 11111 = \text{up to } 34 \text{ cent/ha}$

Strongly developed, up to 75-80 cones per meter:  
 $80 \times 4.5 = 363 \times 11111 = \text{up to } 40 \text{ cent/ha}$

\* 11111 - row length in 1 hectare.

\*\* 4.5 – average cotton weight from field data

Based on statistical indicators, 2350 hectares of the 9122 ha of cotton area planted in the region formed the scope of our research, and the biological productivity of cotton was studied in 139 samples in those areas. This includes one sample for every 16.9 hectares of cotton.

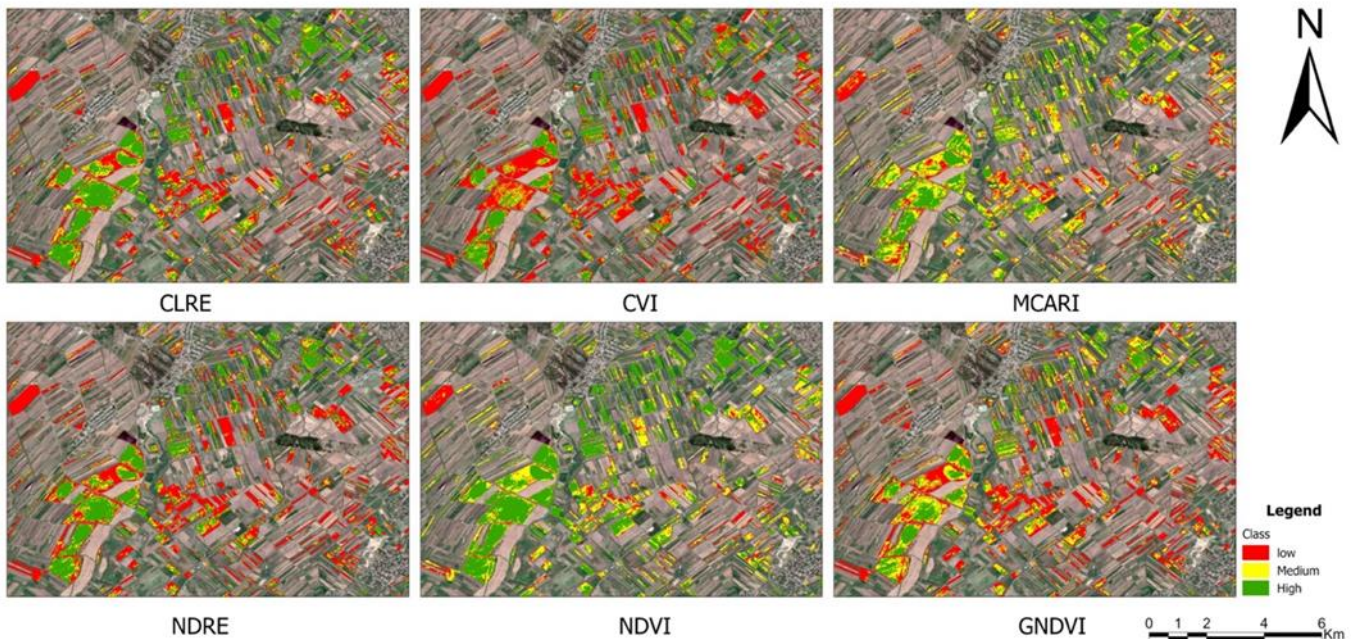


**Figure 5.** Development levels of vegetation indices.

The most critical phase in cotton irrigation is the second vegetation irrigation. If the second vegetation irrigation of cotton is not carried out on time, we can face a 25-40 percent decrease in yield. The maximum consumption of water by the plant falls during the period of flowering and ripening. In this period, the lack of water leads to a sharp decrease in the yield and its quality. During the period of mass ripening, cotton shows relatively little demand for water shortage. The total water used for crop production in a cotton field consists

of the part absorbed by the plant and the part that evaporates from the soil. If we consider the total amount of water used by the field as 100%, then the water used by the plant (for transpiration) will be 60-80% and the water evaporated from the soil will be 20-40%. The more fertile the soil and the higher the applied agrotechnical measures, the less the amount of water that will be used for evaporation, and the more efficient its use by the plant will be. Irrigation mode and volume of cotton should be organized based on the biological

characteristics of cotton varieties and the conditions of agrotechnics. Experiments show that increasing the density of the cotton plant increases the total amount of water consumed by the cotton field. This is related to the increase of dry mass and leaf area in the same unit area, which should be considered when determining the irrigation rate. The variety of irrigation also depends on the distance between rows. NDVI is mainly used in the calculation of biomass density. It is observed that the correlation relationship between biomass and productivity is not high. For this reason, measuring the amount of nitrogen in plants is a more reliable way to determine the condition of crops. Based on the results of the field samples and the values of the VIs, the cotton

fields were divided into 3 classes, and the development group was determined by using the classified satellite images of the areas belonging to each class (Figure 5).

**3. Results**

NDVI measurements produce different results while calculating cotton plant yield during the vegetation season by the biomass technique, hence other indices were examined in the project while accounting for the data mentioned above. It is clear from the graph that CVI, MCARI, NDRE, CLrededge and NDVI indices have more influence factors during the growing season (Figure 6). Therefore, in addition to the NDVI index, the CVI, MCARI, NDRE, and CLrededge indexes were utilized.

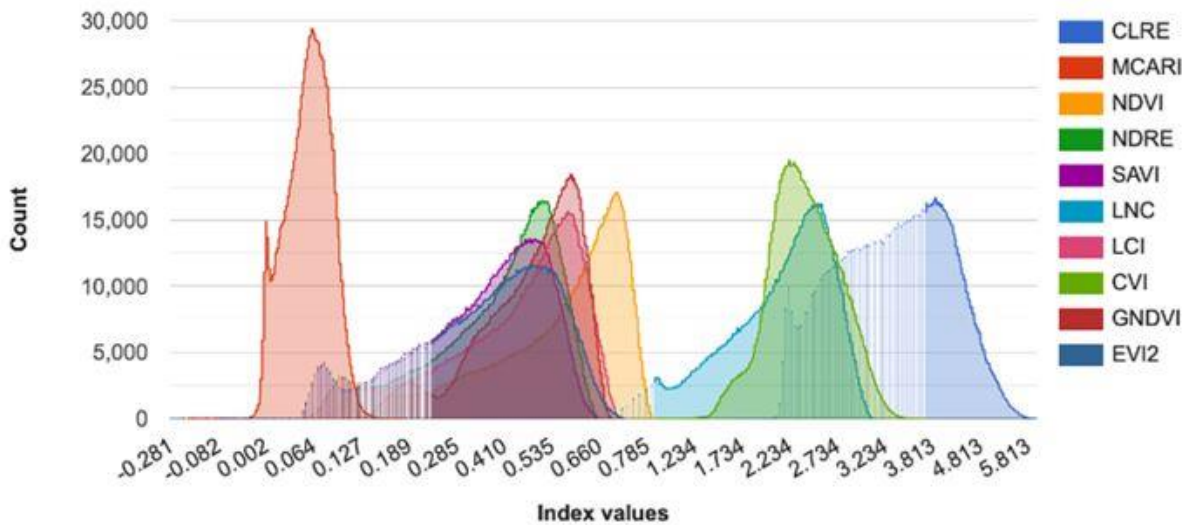


**Figure 6.** Comparison of different vegetation indices on cotton fields.

The graph provides evidence indicating that CVI exhibits a higher level of sensitivity in relation to cotton fields. Simultaneously, MCARI has a higher level of sensitivity in comparison to other alternatives. The values of NDVI, NDRE, and CLRE exhibit a high degree of similarity. Distribution percentages and "Impact index" (Ti) coefficient were calculated based on the values of VIs

selected according to the obtained indicators and the state of development (Table 3). As we defined earlier, weak areas were considered as 31 cent/ha, medium areas as 34 cent/ha and strong areas as 40 cents/ha. As a result of the observations, the weakest areas are observed in the MCARI, and the strongest areas are observed in the CLRE index (Figure 7).

**Table 3.** Vegetation indices results.

	Level of development	Values	Area*	Impact index**, Ti
NDVI	Low	< 0.66	4901.4 ha	53.68 %
	Mid	0.66 - 0.72	2887.18 ha	31.6 %
	High	> 0.72	1342.77 ha	14.7 %
NDRE	Low	< 0.52	5175.64 ha	56.06 %
	Mid	0.52 - 0.55	1529.56 ha	16.7 %
	High	> 0.55	2438.73 ha	26.7 %
MCARI	Low	< 0.07	6522.41 ha	71.33 %
	Mid	0.07 - 0.09	2292.76 ha	25.07 %
	High	> 0.09	328.72 ha	3.59 %
CVI	Low	< 2.5	5768.76 ha	63.09 %
	Mid	2.5 – 2.6	1161.93 ha	12.71 %
	High	> 2.6	2213.28 ha	24.2 %
CLRE	Low	< 4	4214.11 ha	46.09 %
	Mid	4 – 4.34	2096.26 ha	22.93 %
	High	> 4.34	2833.6 ha	30.99 %
GNDVI	Low	< 0.55	2639.27 ha	28.59 %
	Mid	0.55 – 0.6	2339.95 ha	25.34 %
	High	> 0.6	4253.53 ha	46.07 %

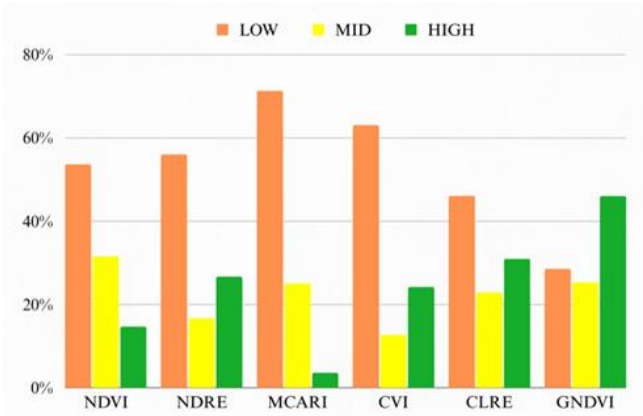


**Figure 7.** Grouping of various vegetation indices on cotton fields.

Based on the impact indices, the generalized Sylvester-transfer matrix equation [56] can be used to calculate the average biological productivity for the region as shown in Equation 1.

$$MBio = Mlow * Tlow + Mmid * Tmid + Mhigh * Thigh \quad (1)$$

Cotton harvested from cultivated fields yielded an average of 34.4 cents per hectare in 2022 [57]. The various VIs yielded diverse outcomes. Among the indices considered, the CLRE index had a level of production that closely approximated the average value of 34.48 (Figure 8). Similar values have been obtained for other indices. The MCARI index exhibits a distinct value in comparison to the remaining indices.

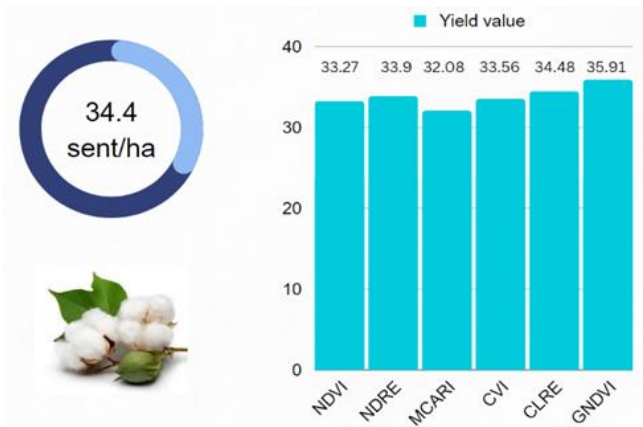


**Figure 8.** Average cotton yield of vegetation indices.

#### 4. Discussion

The objective of this work is to forecast the yield of cotton by utilizing VIs that are derived from satellite imagery. One notable advantage associated with the utilization of satellites for plant monitoring is the capacity for remote control, which consequently leads to reduced maintenance expenses.

A total of six VIs were chosen for the purpose of conducting a comprehensive assessment of vegetation within the designated experimental region, as indicated in Table 3. The calculation of VIs was performed by utilizing multispectral reflectance measurements taken at certain wavelengths, including the visible, near-

infrared, and red-edge regions. The range of lengths has been employed in several applications within the field of precision agriculture, ranging from to plant counting, growth tracking, and chlorophyll measurement.

Currently, the assessment of plant productivity is carried out mainly based remote sensing data. The red edge band is used to measure chlorophyll levels. The Sentinel-2 satellite was utilized because the Azersky satellite does not have a red edge band. The fundamental issue with these techniques is that Sentinel images' resolution is low for some uses. Nevertheless, Sentinel images are sufficient for vegetation monitoring.

The primary objective of our initial experiment was to examine the significance of various satellite data and VIs in the assessment of cotton yield. After conducting a screening process on a sample of 10 variables of interest (VIs), a total of six VIs were chosen for further analysis. They exhibit a heightened sensitivity for cotton fields compared to other individuals. Similar to the majority of crops, reflectance exhibits its maximum values throughout the infrared range, while displaying relatively minimal absorption within the green range and total absorption within the red range. According to Meng et al. (2017), VIs has proven to be a successful approach in the monitoring of crop development and yield.

NDVI is extensively employed for assessing crop health. However, it is important to note that the calculated productivity of different crop types using the NDVI index may yield varying results. According to a study conducted by [58], it has been observed that high NDVI values throughout the developmental phase of cotton do not necessarily correlate with high productivity. The timely implementation of irrigation practices has a significant impact on plant development in regions where it is not promptly executed. If the crops receive further irrigation from underground water sources, this simply impacts the growth and maturation of the leaves. During this phase, the growth of the cotton plant is inhibited, resulting in stunted development. Consequently, the assessment of production through the evaluation of NDVI values becomes complex. Hence, the growth of additional leaves does not invariably serve as the main reason for the formation of cones. In the context of cotton fields, there is a notable proximity in values seen between areas characterized by both low and high production. Consequently, this difference leads to different outcomes while calculating productivity. This rationale was employed in further indices apart from NDVI.

Measuring the amount of nitrogen in plants is a more reliable technique to estimate crop condition when calculating biomass density. The classification of cotton fields into three classes was based on the findings from field samples and the analysis of VI values. Subsequently, satellite images were utilized to classify the areas of each class, and the development group was identified (Figure 5).

The analysis involved conducting an overall assessment of the VI values obtained from the sample locations utilized in the field investigation. Each VI possesses distinct values. The graph (Figure 9) illustrates the range of values for the CLRE index, with the minimal value being 3.22 and the highest value being 4.99 du. The

NDVI index ranges from a minimum value of 0.51 to a maximum value of 0.71. Similarly, the NDRE index ranges from a minimum value of 0.38 to a maximum value of 0.6. The MCARI index ranges from a minimum value of 0.03

to a maximum value of 0.09. The CVI index ranges from a minimum value of 2.03 to a maximum value of 2.87. Lastly, the GNDVI index ranges from a minimum value of 0.44 to a maximum value of 0.62.

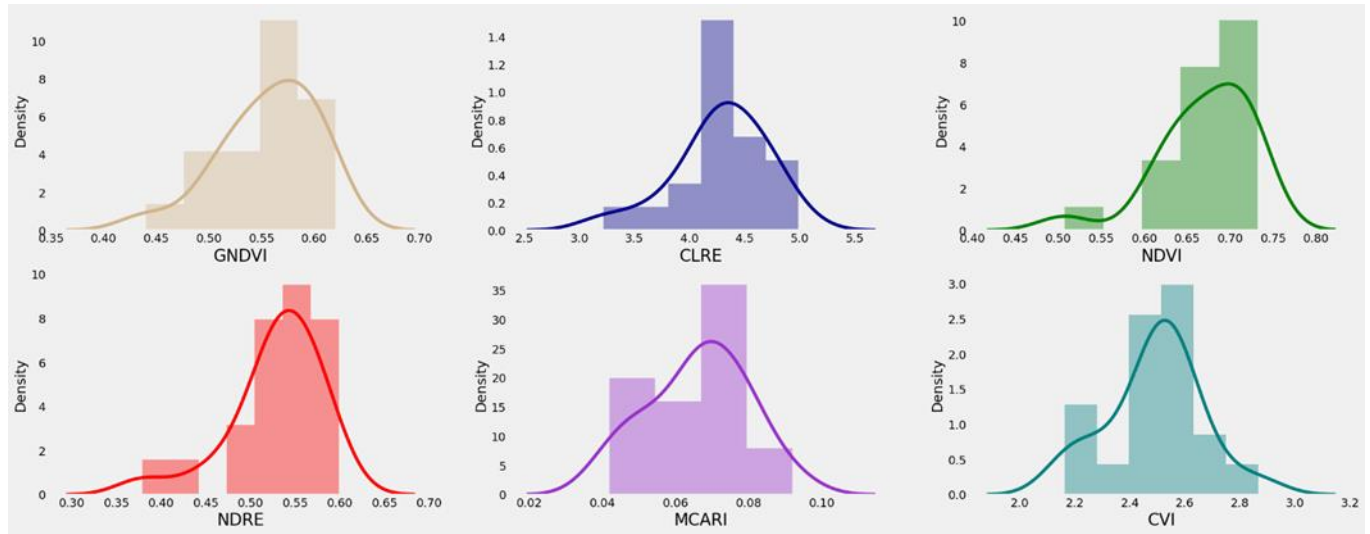


Figure 9. Distribution values of vegetation indices.

In the context of CLRE, low area values classified up to 4, medium areas to 4-4.34, and high area with values over 4.34. The selection criteria for categorizing areas based on NDVI values up to 0.66 were classified as low, areas with NDVI values ranging from 0.66 to 0.72 were classified as medium, and areas with NDVI values greater than 0.72 were classified as high. The selection criteria for NDRE values below 0.52 were classified as low, areas with NDRE values ranging from 0.52 to 0.55 were classified as medium, and areas with NDRE values greater than 0.55 were classified as high. The selection criteria for MCARI involved categorizing areas as low if their values were up to 0.07, if their values were from 0.07 to 0.09 as medium, and high if their values exceeded 0.09. In the context of CVI, regions with a CVI value of up to 2.5 were classified as low areas, while places with CVI values ranging from 2.5 to 2.6 were categorized as medium areas. CVI values over 2.6 were designated as good areas. Lastly, GNDVI areas with values below 0.5 were categorized as low, areas with values ranging from 0.5 to 0.55 were classified as medium, and areas with values above 0.55 were designated as high.

The categorization of cotton fields based on VIs were conducted, taking into consideration the productivity of each field. Based on the data derived from field research, places exhibiting lower levels of performance were categorized as weak, with an average cost of 31 cents per hectare. places demonstrating moderate levels of performance were classified as medium, with an average cost of 34 cents per hectare. Lastly, areas displaying higher levels of performance were designated as strong, with an average cost of 40 cents per hectare. The VIs of the respective locations were compared using the provided data. Therefore, the development groups and intermediate values derived from each index have been identified. Once the identification of each development area was completed, the respective area was quantified and subsequently assigned a percentage value, referred to as the impact index. The average productivity of the

development groups and the region was determined based on data collected from impact and field studies.

According to statistics data, the mean productivity in the region was calculated to be 34.4 cents per hectare. Based on the calculations derived from the CLRE values in our investigation, the productivity observed was found to be near the average value with 34.48 (Figure 8). The analysis reveals that there is no significant difference in the mean productivity achieved across other indices. The MCARI index exhibits a distinct value in comparison to the remaining indices. The primary factor contributing to this phenomenon is the prevalence of underdeveloped regions in MCARI, as depicted in Figure 7. Furthermore, it is evident that there are comparatively few high areas (3.59%), which is the lowest percentage when compared to other indices. The medium areas exhibit a range of 12-31% across all indices.

The occurrence of moderate weather during the months of May and June in 2022 resulted in delays in the vegetation season of plants and restricted their growth. The growing season was extended beyond expectations due to the negative impact of prolonged overcast and foggy days on the cotton plant. The process of maturation and boll opening is experiencing a delay. Additionally, Insufficient exposure to sunlight can also lead to the deterioration of internal organs [59]. All varieties of cotton plants necessitate exposure to shorter daylight periods. While the plant development levels in past years exhibited distinct visibility, the development levels in the current year displayed a notable proximity to one another. Crop yields can fluctuate from year to year due to a combination of various genotypes, management approaches, and extreme weather conditions, including high temperatures, precipitation, floods, and droughts [60]. The precise and punctual assessment of cotton output is crucial to implement efficient agronomic management strategies intended for mitigating potential losses [61]. Due to this factor, there existed distinct variations in the values of the acquired VIs. Furthermore,

the cotton plant's development is adversely impacted by drought conditions and water scarcity.

Nitrogen plays a crucial role in promoting plant development and enhancing productivity. The proper growth and physiological development of cotton are crucial factors to consider [62]. Analyzing the anomalies that have occurred within the cotton fields over the previous five years has revealed various consequences depending on the amount of nitrogen. The categorization led to the identification of areas with excellent, good,

efficient, and poor performance (Figure 10). Poor areas are more visible in 2019 than other years. In 2020, high areas are more dominant. In the year 2022, there is a greater prevalence of fields that are considered medium or good. Upon analyzing the five-year statistical data pertaining to the Beylagan region, it is evident that the agricultural production in the year 2020 surpassed that of previous years, reaching a notable value of 35.5 cents per hectare [30].

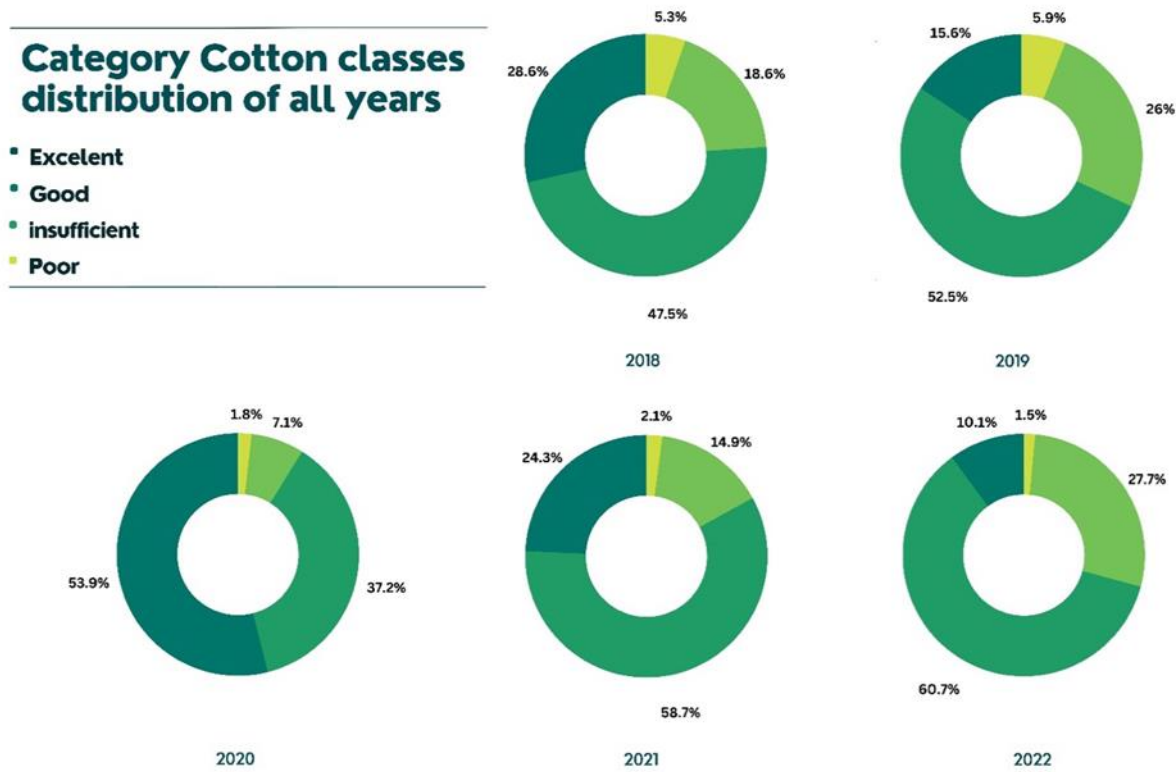


Figure 10. Classification of 5-year cotton fields.

## 5. Conclusion

In this study, satellite imagery was used to monitor cotton yield before harvest. VIs and field samples were used to estimate pre-harvest cotton yield from the images. Since nitrogen plays an important role in aphid development, several VIs have been used to estimate plant height in cotton with high accuracy based on remote sensing data in the visible, NIR and Red Edge regions of the spectrum. VIs extracted from the obtained images and sample yield were significantly correlated and therefore could be used in cotton yield monitoring. This shows us that it is possible to obtain practical and economic solutions with satellite observations.

## Acknowledgement

The author thanks The Mil Experimental Station for the data.

## Author contributions

**Bakhtiyar Babashli:** Conceptualization, Methodology, Software, Collected the data, Performed the analysis,

writing original draft preparation; Writing-Reviewing and Editing. **Aytaj Badalova:** Writing original draft preparation and analysis; **Ramis Shukurov:** Field data collection and preparation data. **Agil Ahmadov:** Contributed data and performed the analysis.

## Conflicts of interest

The authors declare no conflicts of interest.

## References

- Giller, K. E., Delaune, T., Silva, J. V., Descheemaeker, K., van de Ven, G., Schut, A. G., ... & van Ittersum, M. K. (2021). The future of farming: Who will produce our food?. *Food Security*, 13(5), 1073-1099. <https://doi.org/10.1007/s12571-021-01184-6>
- Kim, H. J., & Triplett, B. A. (2001). Cotton fiber growth in planta and in vitro. Models for plant cell elongation and cell wall biogenesis. *Plant physiology*, 127(4), 1361-1366. <https://doi.org/10.1104/pp.010724>
- Ashraf, K. H., & Hanif, M. (2010). Screening of cotton germplasm against cotton leaf curl virus. *Pakistan Journal of Botany*, 42(5), 3327-3342.

4. Ridley, W., & Devadoss, S. (2023). Competition and trade policy in the world cotton market: Implications for US cotton exports. *American Journal of Agricultural Economics*, 105, 1365-1387. <https://doi.org/10.1111/ajae.12370>
5. Aytaç, S., Başbağ, S., Arslanoğlu, F., Ekinçi, R., & Ayan, A. K. (2020). Lif bitkileri üretiminde mevcut durum ve gelecek. *Türkiye Ziraat Mühendisliği IX. Teknik Kongresi Bildiriler Kitabı-1*, 463-491.
6. He, L., & Mostovoy, G. (2019). Cotton yield estimate using Sentinel-2 data and an ecosystem model over the southern US. *Remote Sensing*, 11(17), 2000. <https://doi.org/10.3390/rs11172000>
7. Tariq, A., Siddiqui, S., Sharifi, A., & Shah, S. H. I. A. (2022). Impact of spatio-temporal land surface temperature on cropping pattern and land use and land cover changes using satellite imagery, Hafizabad District, Punjab, Province of Pakistan. *Arabian Journal of Geosciences*, 15(11), 1045. <https://doi.org/10.1007/s12517-022-10238-8>
8. Corwin, D. L., Lesch, S. M., Shouse, P. J., Soppe, R., & Ayars, J. E. (2003). Identifying soil properties that influence cotton yield using soil sampling directed by apparent soil electrical conductivity. *Agronomy Journal*, 95(2), 352-364. <https://doi.org/10.2134/agronj2003.3520>
9. Tran, D. X., Pla, F., Latorre-Carmona, P., Myint, S. W., Caetano, M., & Kieu, H. V. (2017). Characterizing the relationship between land use land cover change and land surface temperature. *ISPRS Journal of Photogrammetry and Remote Sensing*, 124, 119-132. <https://doi.org/10.1016/j.isprsjprs.2017.01.001>
10. Zambon, I., Cecchini, M., Egidi, G., Saporito, M. G., & Colantoni, A. (2019). Revolution 4.0: Industry vs. agriculture in a future development for SMEs. *Processes*, 7(1), 36. <https://doi.org/10.3390/pr7010036>
11. Zhang, D., & Zhou, G. (2016). Estimation of soil moisture from optical and thermal remote sensing: A review. *Sensors*, 16(8), 1308. <https://doi.org/10.3390/s16081308>
12. Ahmad, T., Sud, U. C., Rai, A., & Sahoo, P. M. (2020). An Alternative Sampling Methodology for Estimation of Cotton Yield using Double Sampling Approach. *Journal of the Indian Society of Agricultural Statistics*, 74(3), 217-226.
13. Shi, G., Du, X., Du, M., Li, Q., Tian, X., Ren, Y., ... & Wang, H. (2022). Cotton Yield Estimation Using the Remotely Sensed Cotton Boll Index from UAV Images. *Drones*, 6(9), 254. <https://doi.org/10.3390/drones6090254>
14. Lang, P., Zhang, L., Huang, C., Chen, J., Kang, X., Zhang, Z., & Tong, Q. (2023). Integrating environmental and satellite data to estimate county-level cotton yield in Xinjiang Province. *Frontiers in Plant Science*, 13, 1048479. <https://doi.org/10.3389/fpls.2022.1048479>
15. Pantazi, X. E., Moshou, D., Alexandridis, T., Whetton, R. L., & Mouazen, A. M. (2016). Wheat yield prediction using machine learning and advanced sensing techniques. *Computers and Electronics in Agriculture*, 121, 57-65. <https://doi.org/10.1016/j.compag.2015.11.018>
16. Zhang, J., Huang, Y., Pu, R., Gonzalez-Moreno, P., Yuan, L., Wu, K., & Huang, W. (2019). Monitoring plant diseases and pests through remote sensing technology: A review. *Computers and Electronics in Agriculture*, 165, 104943. <https://doi.org/10.1016/j.compag.2019.104943>
17. Hou, P., Liu, Y., Liu, W., Liu, G., Xie, R., Wang, K., ... & Li, S. (2020). How to increase maize production without extra nitrogen input. *Resources, Conservation and Recycling*, 160, 104913. <https://doi.org/10.1016/j.resconrec.2020.104913>
18. Ekinçi, M., Atamanalp, M., Turan, M., Alak, G., Kul, R., Kitir, N., & Yildirim, E. (2019). Integrated use of nitrogen fertilizer and fish manure: Effects on the growth and chemical composition of spinach. *Communications in Soil Science and Plant Analysis*, 50(13), 1580-1590. <https://doi.org/10.1080/00103624.2019.1631324>
19. Guo, Z., Luo, C., Dong, Y., Dong, K., Zhu, J., & Ma, L. (2021). Effect of nitrogen regulation on the epidemic characteristics of intercropping faba bean rust disease primarily depends on the canopy microclimate and nitrogen nutrition. *Field Crops Research*, 274, 108339. <https://doi.org/10.1016/j.fcr.2021.108339>
20. Dhivya, R., Amalabalu, P., Pushpa, R., & Kavithamani, D. (2014). Variability, heritability and genetic advance in upland cotton (*Gossypium hirsutum* L.). *African Journal of Plant Science*, 8(1), 1-5. <https://doi.org/10.5897/AJPS2013.1099>
21. Onoda, Y., Wright, I. J., Evans, J. R., Hikosaka, K., Kitajima, K., Niinemets, Ü., ... & Westoby, M. (2017). Physiological and structural tradeoffs underlying the leaf economics spectrum. *New Phytologist*, 214(4), 1447-1463. <https://doi.org/10.1111/nph.14496>
22. Lassaletta, L., Billen, G., Grizzetti, B., Anglade, J., & Garnier, J. (2014). 50 year trends in nitrogen use efficiency of world cropping systems: the relationship between yield and nitrogen input to cropland. *Environmental Research Letters*, 9(10), 105011. <https://doi.org/10.1088/1748-9326/9/10/105011>
23. Singh, R. J., & Ahlawat, I. P. S. (2012). Dry matter, nitrogen, phosphorous, and potassium partitioning, accumulation, and use efficiency in transgenic cotton-based cropping systems. *Communications in Soil Science and Plant Analysis*, 43(20), 2633-2650. <https://doi.org/10.1080/00103624.2012.716125>
24. Alganci, U., Ozdogan, M., Sertel, E., & Ormeci, C. (2014). Estimating maize and cotton yield in southeastern Turkey with integrated use of satellite images, meteorological data and digital photographs. *Field Crops Research*, 157, 8-19. <https://doi.org/10.1016/j.fcr.2013.12.006>
25. Liu, Q. S., Li, X. Y., Liu, G. H., Huang, C., & Guo, Y. S. (2016). Cotton area and yield estimation at Zhanhua County of China using HJ-1 EVI time series. In *ITM Web of Conferences*, 7, 09001. <https://doi.org/10.1051/itmconf/20160709001>
26. Bian, C., Shi, H., Wu, S., Zhang, K., Wei, M., Zhao, Y., ... & Chen, S. (2022). Prediction of field-scale wheat yield using machine learning method and multi-spectral UAV data. *Remote Sensing*, 14(6), 1474.

- <https://doi.org/10.3390/rs14061474>
27. Leroux, L., Castets, M., Baron, C., Escorihuela, M. J., Bégué, A., & Seen, D. L. (2019). Maize yield estimation in West Africa from crop process-induced combinations of multi-domain remote sensing indices. *European Journal of Agronomy*, 108, 11-26. <https://doi.org/10.1016/j.eja.2019.04.007>
  28. Elders, A., Carroll, M. L., Neigh, C. S., D'Agostino, A. L., Ksoll, C., Wooten, M. R., & Brown, M. E. (2022). Estimating crop type and yield of small holder fields in Burkina Faso using multi-day Sentinel-2. *Remote Sensing Applications: Society and Environment*, 27, 100820. <https://doi.org/10.1016/j.rsase.2022.100820>
  29. Azərbaycan Respublikası Beyləqan Rayon İcra Hakimiyyəti (2023). Coğrafi mövqeyi. <http://www.beyleqan-ih.gov.az/az/page/13.html>
  30. State Statistical Committee of the Republic of Azerbaijan (2022). Main economic indicators of agricultural enterprises and private owner farms.
  31. Simarmata, N., Nadzir, Z. A., & Agustina, L. K. (2022). Application of Spot6/7 Satellite Imagery for Rice Field Mapping Based on Transformative Vegetation Indices. *Jurnal Geografi*, 14(1), 69. <https://doi.org/10.24114/jg.v14i1.29036>
  32. Ismatova, K. H. R., Badalova, A. N., Ismailov, A. I., Aliyev, Z. H., & Talibova, S. S. (2019). Features of the Use of Aerospace Methods in Soil Science. *Journal of Medical Care Research and Review*, 2(5), 149-154.
  33. De Wit, A. J. W., & Clevers, J. G. P. W. (2004). Efficiency and accuracy of per-field classification for operational crop mapping. *International Journal of Remote Sensing*, 25(20), 4091-4112. <https://doi.org/10.1080/01431160310001619580>
  34. Beriaux, E., Jago, A., Lucau-Danila, C., Planchon, V., & Defourny, P. (2021). Sentinel-1 time series for crop identification in the framework of the future CAP monitoring. *Remote Sensing*, 13(14), 2785. <https://doi.org/10.3390/rs13142785>
  35. Fu, H., Zhao, H., Song, R., Yang, Y., Li, Z., & Zhang, S. (2022). Cotton aphid infestation monitoring using Sentinel-2 MSI imagery coupled with derivative of ratio spectroscopy and random forest algorithm. *Frontiers in Plant Science*, 13, 1029529. <https://doi.org/10.3389/fpls.2022.1029529>
  36. Hübətov, H. S., X. Q. Xəlilov, X. Q. (2012). Pambiq lifinin texnologiyasi.
  37. Zheng, B., Myint, S. W., Thenkabail, P. S., & Aggarwal, R. M. (2015). A support vector machine to identify irrigated crop types using time-series Landsat NDVI data. *International Journal of Applied Earth Observation and Geoinformation*, 34, 103-112. <https://doi.org/10.1016/j.jag.2014.07.002>
  38. Barriere, V., & Claverie, M. (2022). Multimodal crop type classification fusing multi-spectral satellite time series with farmers crop rotations and local crop distribution. *Computer Vision and Pattern Recognition*. <https://doi.org/10.48550/arXiv.2208.10838>
  39. Fridgen, J. L., & Varco, J. J. (2004). Dependency of cotton leaf nitrogen, chlorophyll, and reflectance on nitrogen and potassium availability. *Agronomy Journal*, 96(1), 63-69. <https://doi.org/10.2134/agronj2004.6300>
  40. Ravandi, S. H., & Valizadeh, M. (2011). Properties of fibers and fabrics that contribute to human comfort. *Improving Comfort in Clothing*, 61-78. Woodhead Publishing. <https://doi.org/10.1533/9780857090645.1.61>
  41. Roznik, M., Boyd, M., & Porth, L. (2022). Improving crop yield estimation by applying higher resolution satellite NDVI imagery and high-resolution cropland masks. *Remote Sensing Applications: Society and Environment*, 25, 100693. <https://doi.org/10.1016/j.rsase.2022.100693>
  42. Ramoelo, A., Cho, M. A., Mathieu, R., Madonsela, S., Van De Kerchove, R., Kaszta, Z., & Wolff, E. (2015). Monitoring grass nutrients and biomass as indicators of rangeland quality and quantity using random forest modelling and WorldView-2 data. *International Journal of Applied Earth Observation and Geoinformation*, 43, 43-54. <https://doi.org/10.1016/j.jag.2014.12.010>
  43. Pettorelli, N. (2013). *The normalized difference vegetation index*. Oxford University Press, USA.
  44. Leo, S., Migliorati, M. D. A., Nguyen, T. H., & Grace, P. R. (2023). Combining remote sensing-derived management zones and an auto-calibrated crop simulation model to determine optimal nitrogen fertilizer rates. *Agricultural Systems*, 205, 103559. <https://doi.org/10.1016/j.agsy.2022.103559>
  45. Li, Z., Menefee, D., Yang, X., Cui, S., & Rajan, N. (2022). Simulating productivity of dryland cotton using APSIM, climate scenario analysis, and remote sensing. *Agricultural and Forest Meteorology*, 325, 109148. <https://doi.org/10.1016/j.agrformet.2022.109148>
  46. Mumtaz, F., Tao, Y., de Leeuw, G., Zhao, L., Fan, C., Elnashar, A., ... & Wang, D. (2020). Modeling spatio-temporal land transformation and its associated impacts on land surface temperature (LST). *Remote Sensing*, 12(18), 2987. <https://doi.org/10.3390/rs12182987>
  47. NASA (2000). Normalized Difference Vegetation Index (NDVI). [https://earthobservatory.nasa.gov/features/MeasuringVegetation/measuring\\_vegetation\\_2.php](https://earthobservatory.nasa.gov/features/MeasuringVegetation/measuring_vegetation_2.php)
  48. Dalezios, N. R., Domenikiotis, C., Loukas, A., Tzortzios, S. T., & Kalaitzidis, C. (2001). Cotton yield estimation based on NOAA/AVHRR produced NDVI. *Physics and Chemistry of the Earth, Part B: Hydrology, Oceans and Atmosphere*, 26(3), 247-251. [https://doi.org/10.1016/S1464-1909\(00\)00247-1](https://doi.org/10.1016/S1464-1909(00)00247-1)
  49. Vincini, M., Frazzi, E., D'alessio, P., & Stafford, J. V. (2007). Comparison of narrow-band and broad-band vegetation indexes for canopy chlorophyll density estimation in sugar beet. *Precision agriculture*, 7, 189-196. <https://doi.org/10.3920/978-90-8686-603-8>
  50. Daughtry, C. S., Walthall, C. L., Kim, M. S., De Colstoun, E. B., & McMurtrey Iii, J. E. (2000). Estimating corn leaf chlorophyll concentration from leaf and canopy reflectance. *Remote sensing of Environment*, 74(2), 229-239. [https://doi.org/10.1016/S0034-4257\(00\)00113-9](https://doi.org/10.1016/S0034-4257(00)00113-9)

51. Elfanah, A. M., Darwish, M. A., Selim, A. I., Shabana, M. M., Elmoselhy, O. M., Khedr, R. A., ... & Abdelhamid, M. T. (2023). Spectral reflectance indices' performance to identify seawater salinity tolerance in bread wheat genotypes using genotype by yield\* trait biplot approach. *Agronomy*, 13(2), 353. <https://doi.org/10.3390/agronomy13020353>
52. Barnes, E. M., Clarke, T. R., Richards, S. E., Colaizzi, P. D., Haberland, J., Kostrzewski, M., ... & Moran, M. S. (2000, July). Coincident detection of crop water stress, nitrogen status and canopy density using ground based multispectral data. In *Proceedings of the fifth international conference on precision agriculture*, Bloomington, MN, USA, 1619, 6.
53. Zhang, K., Ge, X., Shen, P., Li, W., Liu, X., Cao, Q., ... & Tian, Y. (2019). Predicting rice grain yield based on dynamic changes in vegetation indexes during early to mid-growth stages. *Remote sensing*, 11(4), 387. <https://doi.org/10.3390/rs11040387>
54. Gitelson, A. A., Viña, A., Ciganda, V., Rundquist, D. C., & Arkebauer, T. J. (2005). Remote estimation of canopy chlorophyll content in crops. *Geophysical research letters*, 32(8), 1-4. <https://doi.org/10.1029/2005GL022688>
55. Kaya, Y., & Polat, N. (2021). Sulu ve kuru tarım alanlarında buğday verim tahmininde bitki örtüsü indekslerinin kullanımı. *Türk Tarım ve Doğa Bilimleri Dergisi*, 8(3), 736-746. <https://doi.org/10.30910/turkjans.864231>
56. Sasaki, N., & Chansangiam, P. (2020). Modified Jacobi-gradient iterative method for generalized Sylvester matrix equation. *Symmetry*, 12(11), 1831. <https://doi.org/10.3390/sym12111831>
57. Azərbaycan Respublikasının Dövlət Statistika Komitəsi (2023). Tarla bitkilərinin əkin sahəsi, məhsul yığımı və məhsuldarlığı.
58. Zhao, D., Reddy, K. R., Kakani, V. G., Read, J. J., & Koti, S. (2007). Canopy reflectance in cotton for growth assessment and lint yield prediction. *European Journal of Agronomy*, 26(3), 335-344. <https://doi.org/10.1016/j.eja.2006.12.001>
59. Sawan, Z. M. (2018). Climatic variables: Evaporation, sunshine, relative humidity, soil and air temperature and its adverse effects on cotton production. *Information processing in agriculture*, 5(1), 134-148. <https://doi.org/10.1016/j.inpa.2017.09.006>
60. Bauer, P., Thorpe, A., & Brunet, G. (2015). The quiet revolution of numerical weather prediction. *Nature*, 525(7567), 47-55. <https://doi.org/10.1038/nature14956>
61. Li, Z., Ding, L., & Xu, D. (2022). Exploring the potential role of environmental and multi-source satellite data in crop yield prediction across Northeast China. *Science of The Total Environment*, 815, 152880. <https://doi.org/10.1016/j.scitotenv.2021.152880>
62. Iqbal, A., Qiang, D., Zhun, W., Xiangru, W., Huiping, G., Hengheng, Z., ... & Meizhen, S. (2020). Growth and nitrogen metabolism are associated with nitrogen-use efficiency in cotton genotypes. *Plant Physiology and Biochemistry*, 149, 61-74. <https://doi.org/10.1016/j.plaphy.2020.02.002>



© Author(s) 2024. This work is distributed under <https://creativecommons.org/licenses/by-sa/4.0/>



## Energy capable protocol for heterogeneous blue brain network

Rajesh Dennison <sup>\*1</sup>, Giji Kiruba Dasebenezer <sup>2</sup>, Ramesh Dennison <sup>3</sup>

<sup>1</sup> Vel Tech Rangarajan Dr. Sagunthala R&D Institute of Science and Technology, Department of Computer Science & Engineering, India, rajeshd936@gmail.com

<sup>2</sup> Satyam College of Engineering and Technology, Department of Electrical and Electronics Engineering, India, d.jijikiruba@gmail.com

<sup>3</sup> Anna University, Department of Computer Science and Engineering, India, ramesh4773@gmail.com

Cite this study:

Dennison, R., Dasebenezer, G. K., & Dennison, R. (2024). Energy capable protocol for heterogeneous blue brain network. Turkish Journal of Engineering, 8 (1), 152-161

### Keywords

Blue Brain  
Broadcasting  
Energy  
Cutoff  
Heterogeneous network

### Research Article

DOI: 10.31127/tuje.1346925

Received:20.08.2023

Revised: 22.11.2023

Accepted:24.11.2023

Published:15.01.2024



### Abstract

The Blue Brain has a wide range of applications, which raises a number of challenging issues. Electronics may continuously monitor their surroundings depending on the real data that their Blue Brain nodes are acquiring by employing situational intelligence based on the Blue Brain environment. The Blue Brain does more than only monitor user behavior when utilizing this technology. Blue Brain is linked to a critical prerequisite for energy-efficient communication methodologies. Through the Blue Brain network, it utilizes the heterogeneity and variety of the interconnected components. Blue Brain nodes that are outsourced and have limited energy resources must utilize less energy. IoT nodes with differing energy levels are frequently dispersed across different geographic regions. The main goal of this work is to provide an energy-efficient Blue Brain framework capable of managing cluster head (CH) selection and Blue Brain node clustering. The appropriate CHs are selected, and an energetic cutoff concept is developed to guarantee that energy is shared equally among the CHs and participating Blue Brain nodes. The proposed concept envisions three different kinds of Blue Brain nodes for a Blue Brain infrastructure: expert, intermediary, and normal Blue Brain nodes. Level 1 Blue Brain nodes are regarded as normal nodes; level 2 nodes are regarded as intermediate Blue Brain nodes; and level 3 nodes are regarded as expert Blue Brain nodes. Level 1 Blue Brain nodes use the least amount of energy. The outcomes of the simulation demonstrate that the recommended strategy outperforms other existing methods.

## 1. Introduction

Over the past ten years, there has been a notable increase in the everyday use of digital gadgets. The "internet of things" (IoT) enables connections between cellular applications, RFID tags, workstations, sensors, and other objects in the environment [1-4]. IoT technology allows these devices to monitor their environment closely and provides situational awareness by using data collected in real time by its Blue Brain nodes.

The Blue Brain not only oversees the products but also monitors the behavior of its owners. Blue Brain is being used more and more in a variety of applications, such as smart home design, health analysis, and environmental observation [5-8]. As such, increasing the effectiveness of real information gathering and communication is a challenging undertaking.

The following categories can be used to group issues about Blue Brain nodes. First, consistency. The networks

bottom layer is actually responsible for ensuring Blue Brain's accuracy; the network layer-routing algorithm must address this problem. One approach is to retransmit information packets, although this increases data transmission delay and slows down efficiency [9]. The second difficulty is the cumulative real-time performance of the Blue Brain networks.

Assuring that any transport system can provide a high degree of resilience with every network Blue Brain node alive and reachable for communication is the final worry [10]. The approach has to decrease the number of CHs because Blue Brain nodes have limited processing and battery life [11-13]. It is necessary to consider each of these issues while developing a new routing method. Real-time environmental monitoring creates another obstacle for the Blue Brain. The Blue Brain nodes might be dispersed throughout many locations. Figure 1 shows the several Blue Brain nodes that can be employed in different scenarios. While such Blue Brains are always monitoring their surroundings, they may not have much

discretion when it comes to battery replacement. As a result, numerous researchers have concentrated on improving the functionality of these Blue Brain nodes by reducing their energy consumption. Furthermore, a number of methods have been developed to lower energy usage and communication latency [14,15].

A lot of specialists think that clustering can lower a Blue Brain networks energy consumption. In the name suggests, Blue Brain nodes are grouped together in clusters. Every cluster selects a CH who will collect information from some of the other cluster members and forward it to a Blue Brain node that serves as a sink. The CH is therefore essential for managing the amount of energy utilized. The current clustering techniques are not able to minimize the overall energy usage of large Blue Brain networks. Figure 2 shows a potential heterogeneous network somewhere at the point of beginning with varying energy levels. Groups of Blue Brain nodes with the lowest energy use are referred to as "regular" Blue Brain nodes. The 'intermediary' Blue Brain nodes use energy in a range between these two, whereas the 'expert' Blue Brain nodes have the highest energy needs.

In this research, concentrates on creating a methodology for reducing Blue Brain node energy utilization and extending system lifetime [16].

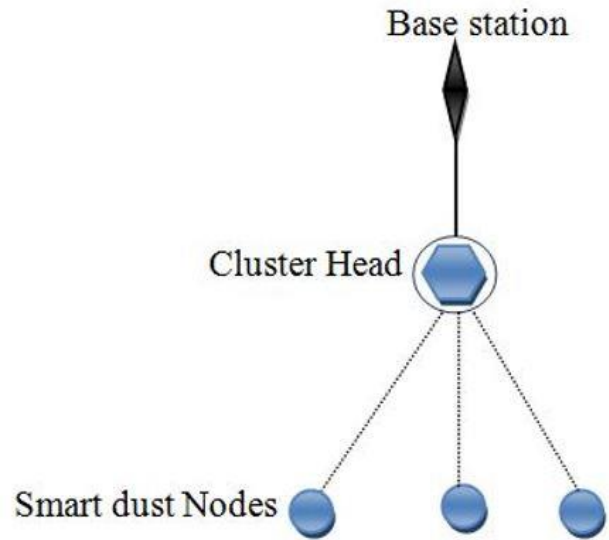


Figure 1. Blue brain architecture.

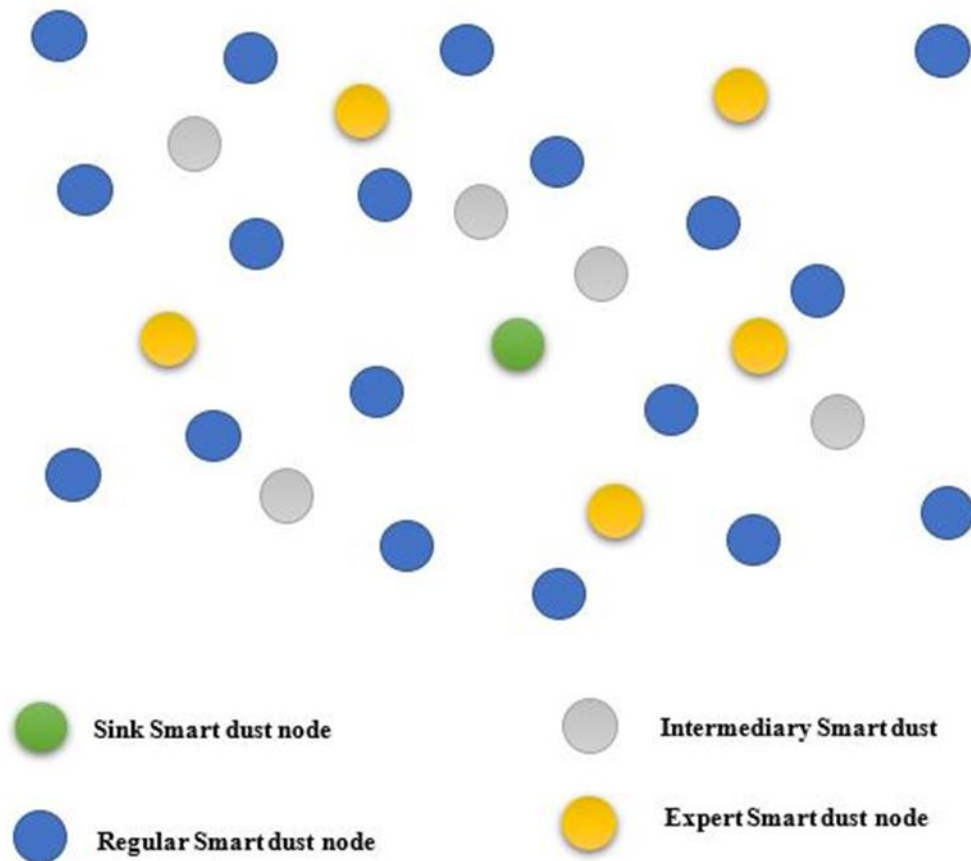


Figure 2. Proposed heterogeneous network architecture.

For the past ten years, researchers have concentrated on developing a real-time information transmission system across the Blue Brain. Most of the discussion has focused on data transmission energy use. The LEACH method, which selects the CH at random, was developed by the authors of [17]. Therefore, every Blue Brain node in the network has an opportunity to be selected as the

CH during the  $1/p$  timestamp. In further cycles, an arbitrary number between 0 and 1 is acquired at arbitrary [18]. The CH will be a Blue Brain node with energy intensity below the threshold [19]. The next CH is determined by grouping non-CH Blue Brain nodes. Only once the cluster has formed does the CH notify the associated nodes via ADV. The nodes transfer this data to

CH during the allotted time-division multiple access (TDMA) session. The primary drawback of the LEACH methodology is its inapplicability non situations involving extensive detection. In a heterogeneous network, certain progressive nodes use more energy than standard nodes [20]. The weighted possibilities are used in the stable election process (SEP) method to select the CHs. It has the advantage of greater consistency and efficiency over the LEACH methodology. A hybrid strategy known as the zonal stable election process (Z-SEP) methodology is recommended by the researchers of [21].

The Z-SEP is divided into three regions: 0, 1, and 2. In Region 0, the nodes are placed in an arbitrary manner. These progressive nodes, which consume a lot of energy, are distributed randomly and equally throughout regions 1 and 2. The Z-SEP uses two distinct broadcasting techniques to provide data to the base station (BS). The first sensor nodes immediately transmit data to the base station. Second, after receiving the data from the sensor nodes, the cluster head sent it to the BS. The CH selected for each cycle is determined by the cutoff value.

## 2. Energy model for blue brain environment

Energy conservation and energy balancing are important considerations while developing a Blue Brain network's routing system. The goal of this research is to develop a routing method that prolongs node lifespans while consuming less energy in networks. To minimize energy loss, we considered the networks variability on

$$\mu_{entire} = k\mu_0(1 - p - q) + kq\mu_0(1 + Q) + kp\mu_0(1 + P) = k\mu_0(1+pP+qQ) \quad (4)$$

Furthermore, take into account the SEP and LEACH methodology models for choosing the CH. Depending upon their chances of choosing the CH, every kind of Blue Brain nodes cutoff is determined. Let S1, S2 and S3 represent the sets of Blue Brain nodes from every kind

$$P_{Re} = P / (1 + pP + qQ) \quad (5)$$

$$T_{K(Re)} = \{ P_{Re} / (1 - [P_{Re} * a \text{mod}(1 / P_{Re})]), 0 \text{ otherwise, if } K(Re) \in S_1 \} \quad (6)$$

$$P_{In} = [P(1+Y)] / (1+pP+qQ) \quad (7)$$

$$T_{K(In)} = \{ P_{In} / (1 - [P_{In} * a \text{mod}(1 / P_{In})]), 0 \text{ otherwise, if } K(In) \in S_2 \} \quad (8)$$

$$P_{ex} = P(1+Q) / (1+pP+qQ) \quad (9)$$

$$T_{K(ex)} = \{ P_{ex} / (1 - [P_{ex} * a \text{mod}(1 / P_{ex})]), 0 \text{ otherwise, if } K(ex) \in S_3 \} \quad (10)$$

$$k(1-p-q) P_{Re} + kpP_{ex} + kqP_{In} = kP \quad (11)$$

The overall possibility of choosing CHs as determined by Equation 11, is identical to a value of a LEACH approach in a heterogeneous network.

The communication protocol for a heterogeneous Blue Brain network is shown in Figure 3. A multipath propagation or free space framework is used to calculate the energy transfer in the heterogeneous environment. The Blue Brain node requires energy to communicate 'n'

three different tiers, depending on the baseline energy of each Blue Brain node. All of the Blue Brain nodes in the network run static systems. It is true that the smallest energy initial stage nodes are called regular Blue Brain nodes, the intermediate energy second tier nodes are called intermediary Blue Brain nodes, and the highest energy third tier nodes are called expert Blue Brain nodes.

Let  $\mu_0$  indicate the starting energy of regular Blue Brain nodes,  $\mu_0(1 + P)$  the beginning energy of expert Blue Brain nodes, and  $\mu_0(1 + P)$  the beginning energy of intermediary Blue Brain nodes. Equations 1-3 reflecting the total amount of energy of the regular, intermediary, and expert Blue Brain nodes.

$$\mu_{Re} = k\mu_0(1 - p - q) \quad (1)$$

$$\mu_{In} = kq\mu_0(1 + Q) \quad (2)$$

$$\mu_{ex} = kp\mu_0(1 + P) \quad (3)$$

The energies of the regular Blue Brain node are denoted by Re in this instance, those of intermediary Blue Brain nodes by In, and those of advanced nodes by An. The networks expert Blue Brain nodes are denoted by the symbol p, and their energy level is P. The networks intermediary Blue Brain is denoted by the letter q, and their energy level is denoted by the formula  $Q = P/2$ ; k denotes the size of the nodes within every category. The entire amount of network energy used is provided as Equation 4.

that were not chosen to serve as the CH. The Blue Brain nodes that should have been chosen are listed here.

Determine the average probabilities of choosing the CHs every cycle using Equations 5-9, and the result is displayed as Equation 10.

bits per package, as can be seen from the communication mechanism illustrated in Equations 12 and 13.

$$\mu_{Tr}(n, r) = \mu_{Tr\_ele}(n) + \mu_{Tr\_amp}(n, r) \quad (12)$$

$$\mu_{Tr}(n, r) = \mu_{ele} \times n + \mu_{fs} \times n \times r^2, r \leq r_0$$

$$\mu_{ele} \times n + \mu_{mp} \times n \times r^4, r > r_0 \quad (13)$$

The terms " $\mu_{fs}$ " and " $\mu_{mp}$ " refer to the amplifiers settings for sending packets in free channels and multipath fading channels, respectively. The Blue Brain nodes energy consumption while transmitting the packet is indicated by the symbol  $\mu_{ele}$ . The Equation 14 is a list of the required energy to obtain the package.

By measuring the amount of energy used during

every cycle, the energy cutoff level for CH selection is calculated. To extend the lifespan of Blue Brain environment, the proposed methodology in Figure 3 calculates energy dissipation cutoff level for any and all kinds of Blue Brain nodes.

$$\mu_{Rc}(n) = \mu_{Rc\_ele}(n) + n\mu_{ele} \quad (14)$$

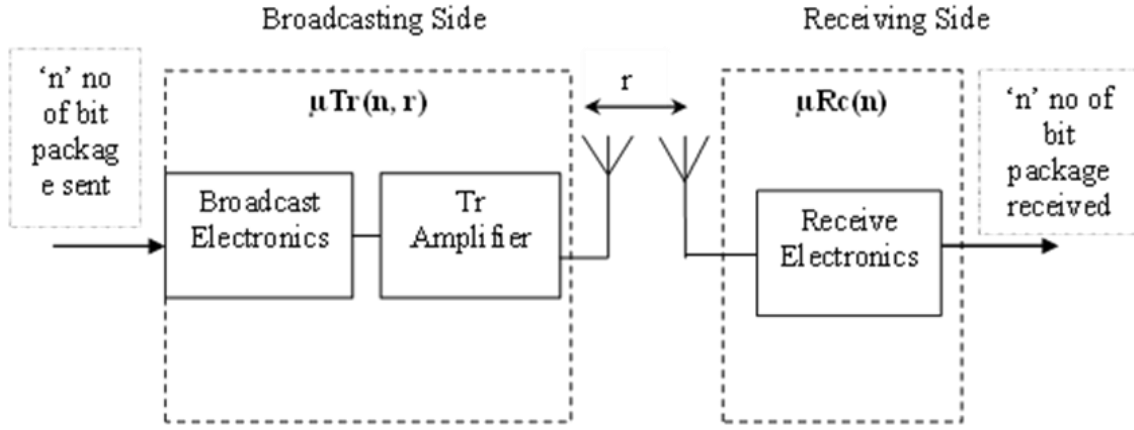


Figure 3. Communication representation for Blue Brain nodes.

### 3. Proposed Methodology (ECHSD)

The Blue Brain nodes use the ADV notification within the cluster to interact with the CH instantly, even before the CH is selected. Once every cycle, the CH and its Blue Brain nodes will switch places. Any type of Blue Brain node that is in close proximity to a sink node uses less energy when sending packets than other types of nodes. Throughout the ensuing rounds, the clusters that were closest to a sink Blue Brain node would retain their CHs and current member Blue Brain nodes. Within a Blue Brain network, the suggested methodology addresses the energy dissipation threshold level for all types of Blue Brain nodes. Based on this threshold level, each clusters CH and member Blue Brain nodes will move on to the next step. The amount of energy left in the CH is calculated at the end of each cycle. If the residual energy value is less than the cutoff point, the network initiates the construction of a new cluster and a new CH election process. The proposed method reduces the energy consumption of both the routing information advertisement and the creation of new CH. Energy requirements for the Blue Brain node and the CH will never be equal. Additional responsibilities for the CH include data collection, consolidation, and forwarding. Hence, compared to the other Blue Brain nodes, the CH will use more energy. Therefore, if the CH really does change into a standard Blue Brain node, the suggested methodology gives the CH a high amplifying energy and gives that particular Blue Brain node a lowered amplifying energy in the cycle that follows.

Let  $s$  denote the overall amount of Blue Brain nodes with in Blue Brain network and  $u$  the proportion of clusters inside it. The CH replenishment count is denoted by the letter  $S$ . The length of the package to be accepted is represented by  $\mu_{nRc}$ , whereas the length of the package to be broadcast is represented by  $\mu_{nTr}$ . In Equation 15 " $\mu S$ " denotes the energy expended for the formation of new clusters and the replacing of cluster heads.

$$\mu S = \{\mu_{nTr} \mu_{Tr} + \mu_{nRc} \mu_{Rc}(CS - 1)\}CS \quad (15)$$

where  $CS = cs$  signifies the size of a cluster and  $\mu_{Tr}$  the amount of energy used to send eight bits of information. The energy required to receive eight bits of information is represented by the symbol  $\mu_{Rc}$ . Calculating the starting energy given to all three categories of nodes regular, intermediary, and expert within the cluster yields the cluster energy usage.  $\mu Z$  denotes the cluster's energy consumption, which is represented as Equations 16-18.

$$\mu Z(Re) = \mu_0 \times cs \quad (16)$$

$$\mu Z(In) = \mu_0(1 - Q) \times cs \quad (17)$$

$$\mu Z(ex) = \mu_0(1 - P) \times cs \quad (18)$$

Depending just on node higher energy across both scenarios the Blue Brain node functioning as Blue Brain node and the CH functioning as CH the energy consumption of every cluster is calculated for a single cycle (Equation 19).

$$\mu C(\delta) = \{(Q\delta - 1) \mu_{nTr} \mu_{Tr} \times \mu_{nRc} \mu_{Rc}\} + \{(Q\delta - 1) \mu_{nTr} \mu_{Tr} + (Q\delta - 1) \mu_{nRc} \mu_{Rc}\} \quad (19)$$

The symbol  $e\mu_{Tr}$  represents the amount of energy used by the Blue Brain node to transport the packages to

the CH. There at CH end, the energy used for data gathering is expressed as  $e(Q-1)\mu_{Rc}$ . Overall energy used

by the CH to the forward data towards the sink Blue Brain node is expressed as  $e(Q-1)_{\mu Tr}$ . If no packets of data are being transmitted or received, the Blue Brain nodes enter a stable state.

The total number of repetitions must be taken into account when determining the energy cutoff value for replacing the CH.  $\alpha$  compute the total cycles in the following manner for the regular, intermediary, and expert Blue Brain nodes (Equation 20-22):

$$\alpha(Re) = \mu C / \mu Z(Re) \times 100 \quad (20)$$

$$\alpha(In) = \mu C / \mu Z(In) \times 100 \quad (21)$$

$$\alpha(ex) = \mu C / \mu Z(ex) \times 100 \quad (22)$$

Equations 19-22 yield the projected energy cutoff value for CH selection, which would be expressed as (Equation 23-24):

$$\mu CO(Re) = \alpha(Re)(\mu n_{Tr} + \mu n_{Rc})_{\mu Tr} \quad (23)$$

$$\mu CO(In) = \alpha(In)(\mu n_{Tr} + \mu n_{Rc})_{\mu Tr} \quad (24)$$

$$\mu CO(ex) = \alpha(ex)(\mu n_{Tr} + \mu n_{Rc})_{\mu Tr} \quad (25)$$

The projected ranges for the expert, intermediary, and regular Blue Brain nodes are represented by  $\mu CO(ex)$ ,  $\mu CO(In)$ , and  $\mu CO(Re)$ . The CH is to be replaced with the suggested energy cutoff model, that maximizes Blue Brain node lifespan and lowers energy use. The energy cutoff model for ECHSD is depicted in Algorithm 1 that attempts to enhance system performance.

**Algorithm 1**

Input:  
 $\mu CO$  indicates the energy threshold value for CH election,  
 $SD_{(n)}$  indicates the set of non-CH Blue Brain nodes,  
 $SD$  indicates the Blue Brain node.  
 $\mu res$  represent CH remaining energy,

CHN indicates the CH number.

Begin

1. for u in 1 to max do
2.  $W = 0$ ;
3. Calculate the possibilities for **Re**, **In** and **ex** by means of the Equations. (5), (7) and (9);
4. Calculate the threshold cost for **Re**, **In** and **ex** by means of the Equations. (6), (8) and (10);
5.  $W = W + 1$ ;
6. if  $G = W$  then
7. High augmentation energy is allocated to  $W$ ;
8. else
9. Low augmentation energy is assigned to  $G$ ;
10. end if
11. for  $\delta$  in 1 to n do
12. Alter the remaining energy  $\mu res$  of the Blue Brain nodes by means of the Equations (13) and (14);
13. Calculate the energy cutoff value for **Re**, **In** and **ex** from Equations (23–25);
14. if  $(\mu res < \mu CO(Re) \&\& \mu res < \mu CO(In) \&\& \mu res < \mu CO(ex))$  then
15. The fresh CH is nominated from  $SD$
16. else
17. Continue the similar CH for further cycle;
18. end if
19. end for
20. end for end

**4. Results**

The ECHSD simulation is conducted using NS2. The 200 m<sup>2</sup> area used for the simulation has 200 Blue Brain nodes evenly spaced out over it. The sink Blue Brain node and other Blue Brain nodes are mobile and have infinite energy. Table 1 lists the variables that are used in the simulation environment. The efficacy of the proposed ECHSD protocol is compared with existing protocols such as LEACH, AHP, and BCSD. The values of x and X are subject to alter based on a variety of factors, while the value of Y remains constant at 0.3.

**Table 1.** Simulation parameters.

Factors	Value
Remoteness among Blue Brain nodes	85m
Energy utilized for data accumulation ( $\mu DA$ )	5nJ/bit
Energy utilized for free space model ( $\mu fs$ )	10 pJ/bit/m <sup>2</sup>
Energy utilized for amplifier ( $\mu amp$ )	100 pJ/bit/m <sup>2</sup>
Packet size	3000 bits
Energy utilized for receiving ( $Rc$ )	0.013 pJ/bit/m <sup>4</sup>
Total energy of the network ( $\mu Tr, \mu Rc$ )	50 J

Utilizing transmission rate, the ECHSD routing protocols effectiveness is evaluated. By enhancing the packet delivery ratio, this refers to the quantity of packages that were effectively delivered. In the initial scenario, the x number is assumed to be 0.1 and the X value to be 1. In the second instance, x is assumed to be 0.2 and X to be 1. The system is divided into three categories: expert Blue Brain nodes (10%), intermediary Blue Brain nodes (30%), and regular Blue Brain nodes. The robustness of the system is depicted in Figure 4 and

5, in which the number of iterations rises till the sensors inevitably collapse. The expert Blue Brain nodes in Figure 4 are assumed to represent 10% of the entire network.

It is discovered that compared to certain other clustering techniques, LEACH has a noticeably shorter network lifespan. The LEACH protocol can be implemented successfully in a homogeneous network but not in a heterogeneous one. Improved results are obtained when comparing the new ECHSD protocol with SEP, Z-SEP, and LEACH approaches. In contrast to the

BCDCP, it shows a 26% increase in network longevity. In Figure 5, 20% of a broadcaster's means algorithm represents expert Blue Brain nodes. The ECHSD protocol

increases the system lifetime by about 34%, especially when compared to BCDCP.

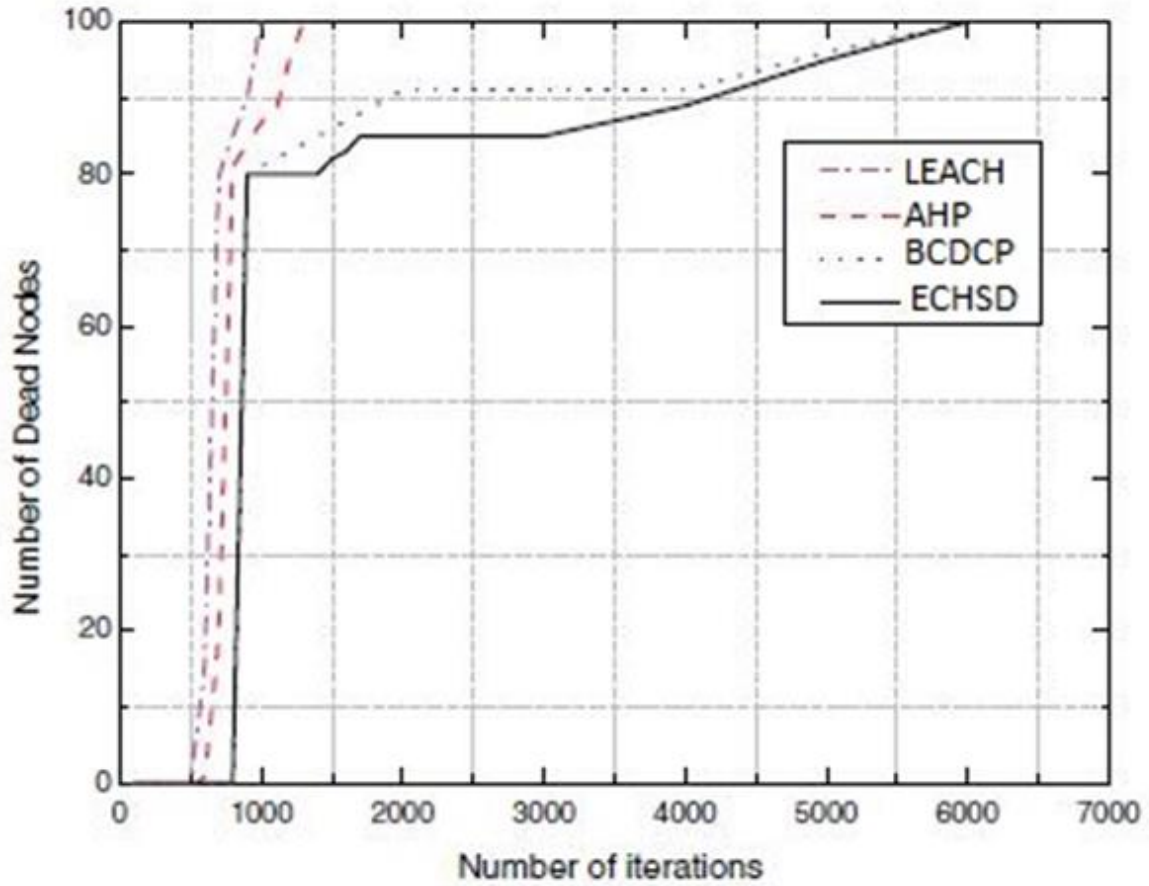


Figure 4. Network duration when x=0.1.

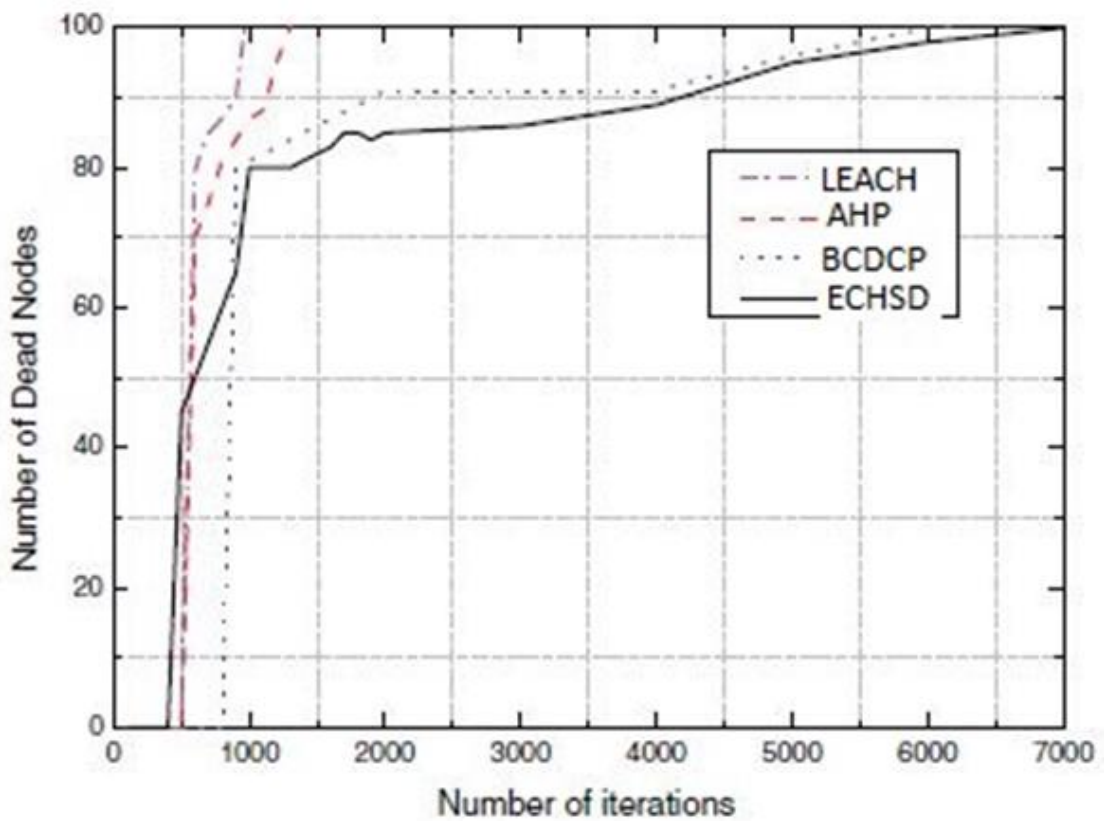


Figure 5. Network duration when x=0.2.

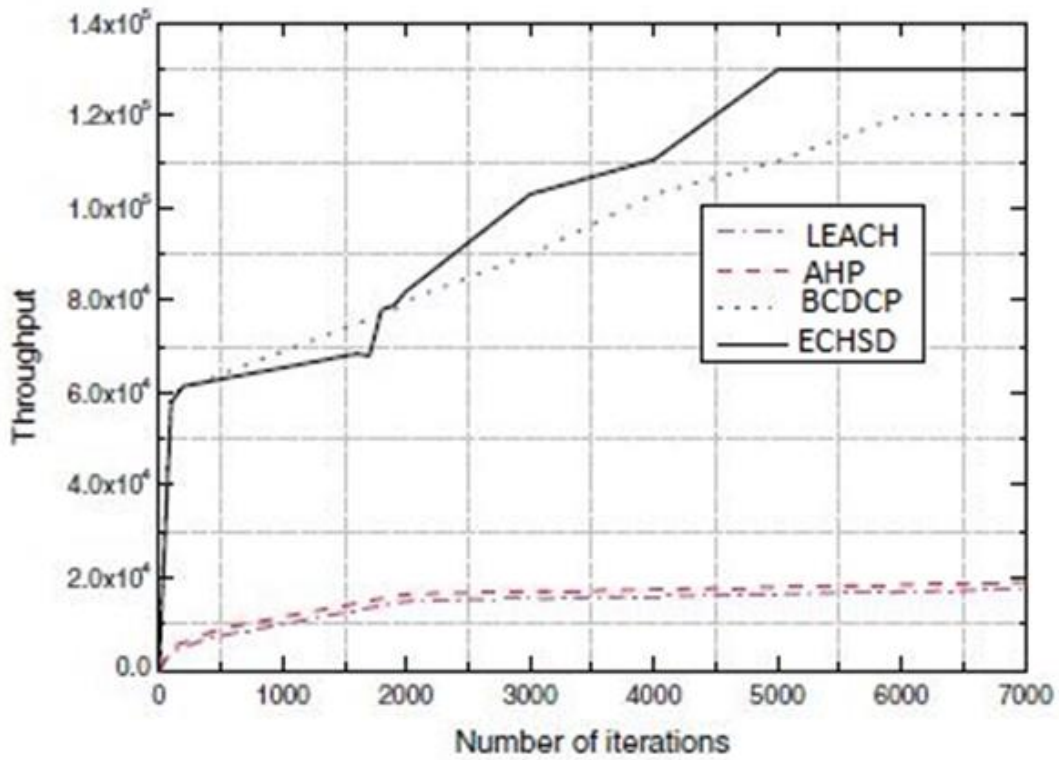


Figure 6. Network throughput when x=0.1.

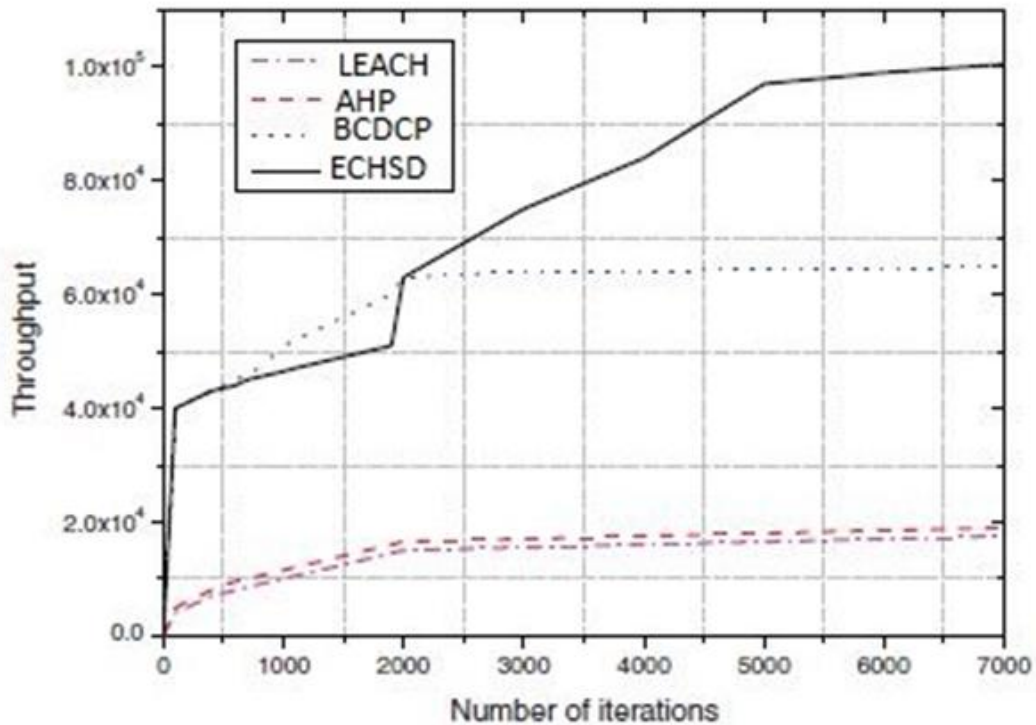


Figure 7. Network throughput when x=0.2.

Figure 6 and 7 show the network throughput that was achieved using the LEACH, AHP, BCDCP, and ECHSD approaches. In the first instance, the recommended routing protocol performed better than other algorithms when 10% of expert Blue Brain nodes were used. In terms of performance, it outperformed the AHP by 65% and the BCDCP by 28%. In the second scenario, where there are 20% more expert Blue Brain nodes, the system

data transmission rate increases. ECHSD experiences a 39% improvement in throughput rate compared to BCDCP. Information gathering amongst Blue Brain nodes depends on CHs. The CHs collect data and forward it to the sink Blue Brain node. Figure 8 and 9 shows the evolution of CHs during each iteration. It has been demonstrated that fewer CHs maintain network power and increase data transmission capacity. With 10% fewer

expert Blue Brain nodes than the LEACH and AHP instances in the first scenario, the ECHSD has less CHs. The ECHSD hits around 10–12 CHs every cycle. In the

second instance of each cycle, the ECHSD attains roughly 6 to 8 CHs using 20% expert Blue Brain nodes.

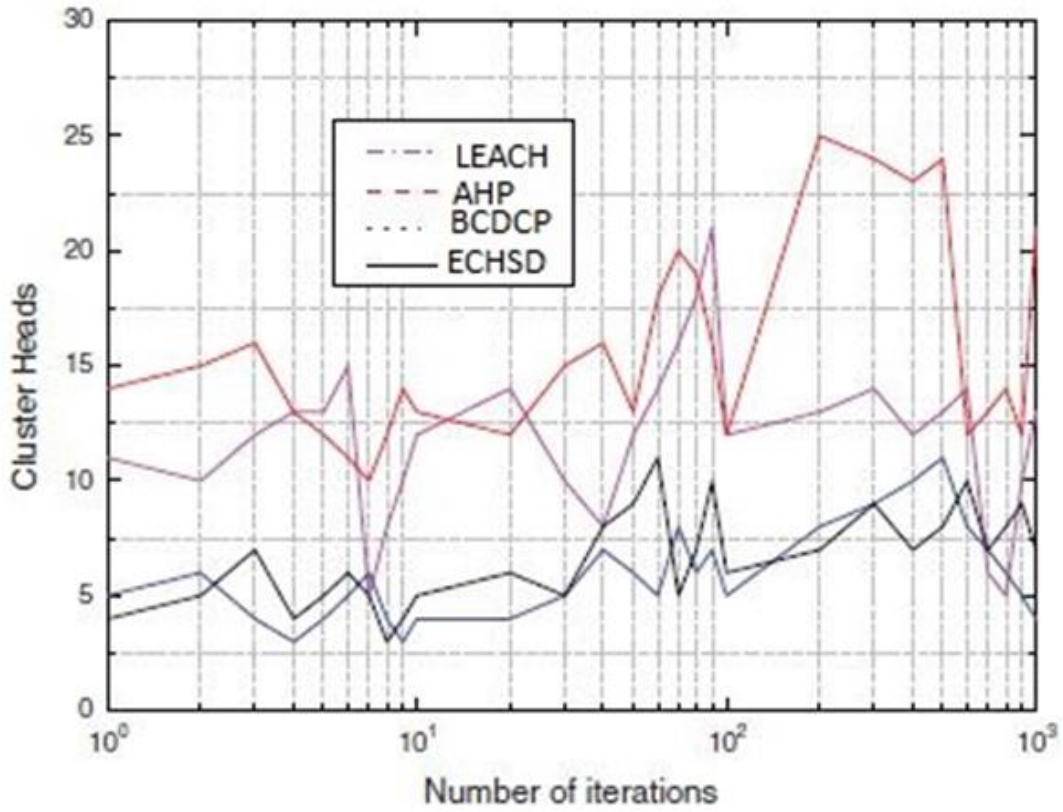


Figure 8. Cluster head amount in particular cycle when x = 0.1.

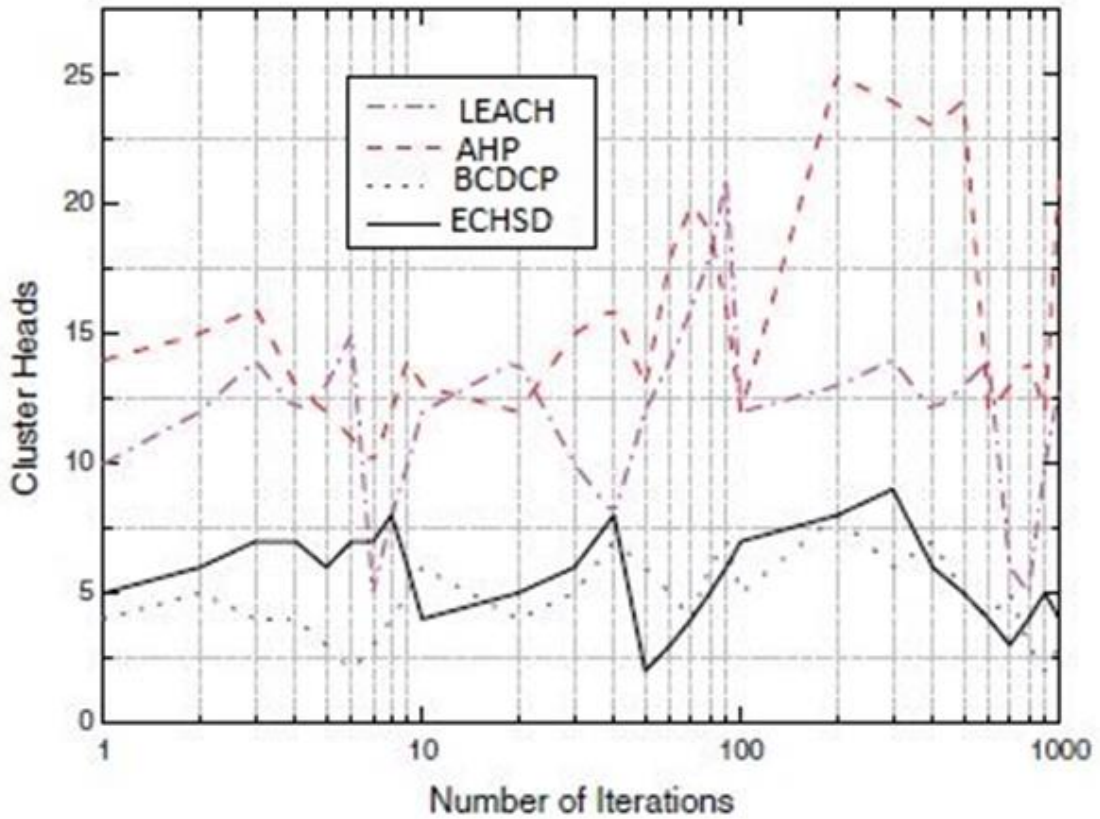


Figure 9. Cluster head amount in particular cycle when x = 0.2.

## 5. Conclusion

An energy-conscious strategy based on a cutoff parameter for a productive Blue Brain environment was used in this study. Current methods, such as the AHP and LEACH protocols, perform poorly in heterogeneous networks and perform best in homogeneous networks. Many energy-constrained Blue Brain nodes inside a real-time context comprise the Blue Brain environment. Even while some devices, such as smart watches and phones, can be recharged, certain Blue Brain nodes have limited power, therefore it's still important to lower their energy requirements. The suggested method divides Blue Brain nodes into three types using different energy cutoff stages. Different amounts of energy are consumed by Blue Brain nodes and CHs that are part of the system. This energy is distributed and managed using the recommended ECHSD protocol. The efficiency of the ECHSD approach is demonstrated by a simulation study in comparison to other existing protocols. Using Blue Brain in real time across large areas is one advantage of the ECHSD approach.

### Author contributions

**Rajesh Dennison:** Conceived of the presented idea, Developed the theory, prepared original manuscript. **Giji Kiruba Dasebenezer:** Performed the computations and verified the analytical methods. **Ramesh Dennison:** Writing-Reviewing and Editing.

### Conflicts of interest

The authors declare no conflicts of interest.

### References

- Rajesh, D., & Kiruba, D. G. (2021). A probability based energy competent cluster based secured ch selection routing EC2SR protocol for smart dust. *Peer-to-Peer Networking and Applications*, 14(4), 1976-1987. <https://doi.org/10.1007/s12083-021-01144-z>
- Škulj, G., Sluga, A., Bračun, D., & Butala, P. (2019). Energy efficient communication based on self-organisation of IoT devices for material flow tracking. *CIRP annals*, 68(1), 495-498. <https://doi.org/10.1016/j.cirp.2019.03.012>
- Huang, Y., Yu, W., Ding, E., & Garcia-Ortiz, A. (2019). EPKF: Energy efficient communication schemes based on Kalman filter for IoT. *IEEE Internet of Things Journal*, 6(4), 6201-6211. <https://doi.org/10.1109/JIOT.2019.2900853>
- Kiruba, D. G., & Benitha, J. (2022). Fuzzy Based Energy Proficient Secure Clustered Routing (FEPSRC) for IOT-MWSN. *Journal of Intelligent and Fuzzy Systems*. 43(6),7633–7645. <https://doi.org/10.3233/JIFS-212014>
- Alhakhbani, N., Hassan, M. M., Ykhlef, M., & Fortino, G. (2019). An efficient event matching system for semantic smart data in the Internet of Things (IoT) environment. *Future Generation Computer Systems*, 95, 163-174. <https://doi.org/10.1016/j.future.2018.12.064>
- Kiruba, D. G., & Benita, J. (2022). A survey of secured cluster head: SCH based routing scheme for IOT based mobile wireless sensor network. *ECS Transactions*, 107(1), 16725. <https://doi.org/10.1149/10701.16725ecst>
- Vankadara, S., & Dasari, N. (2020). Energy-aware dynamic task offloading and collective task execution in mobile cloud computing. *International Journal of Communication Systems*, 33(13), e3914. <https://doi.org/10.1002/dac.3914>
- Kiruba, G. (2022). A comparative study on energy efficient secured clustered approaches for IOT based MWSN. *Suranaree Journal of Science & Technology*, 29(4), 010151
- Mitton, N., Costa, L. H. M., Krishnamachari, B., Pecorella, T., Tahiliani, M., & Puech, N. (2020). Green data collection and processing in smart cities. *Annals of Telecommunications*, 75, 269-270. <https://doi.org/10.1007/s12243-020-00773-4>
- Kiruba, G. B. (2021). Energy capable clustering method for extend the duration of IoT based mobile wireless sensor network with remote nodes. *Energy Harvesting and Systems*, 8(1), 55-61. <https://doi.org/10.1515/ehs-2021-0006>
- Rajab, A. D. (2022). Energy-Efficient Static Data Collector-based Scheme in Smart Cities. *Computers, Materials & Continua*, 72, 2077-2092. <https://doi.org/10.32604/cmc.2022.025736>
- Al-Kaseem, B. R., Taha, Z. K., Abdulmajeed, S. W., & Al-Raweshidy, H. S. (2021). Optimized energy-efficient path planning strategy in WSN with multiple mobile sinks. *IEEE Access*, 9, 82833-82847. <https://doi.org/10.1109/ACCESS.2021.3087086>
- Justus, J. J. & Thirunavukkarasan, M., Dhayalini, K., Visalaxi, G., Khelifi, A., Elhoseny, M. (2022). Type ii fuzzy logic based cluster head selection for wireless sensor network. *Computers, Materials & Continua*, 70(1), 801–816. <https://doi.org/10.32604/cmc.2022.019122>
- Xie, Q., Li, K., Tan, X., Han, L., Tang, W., & Hu, B. (2021). A secure and privacy-preserving authentication protocol for wireless sensor networks in smart city. *EURASIP Journal on Wireless Communications and Networking*, 2021(1), 1-17. <https://doi.org/10.1186/s13638-021-02000-7>
- Sivaram, M., Porkodi, V., Mohammed, A. S., & Karuppusamy, S. A. (2021). Improving Energy Efficiency in Internet of Things using Artificial Bee Colony Algorithm. *Recent Patents on Engineering*, 15(2), 161-168. <https://doi.org/10.2174/1872212114999200616164642>
- Gupta, P., Tripathi, S., & Singh, S. (2021). RDA-BWO: hybrid energy efficient data transfer and mobile sink location prediction in heterogeneous WSN. *Wireless Networks*, 27, 4421-4440. <https://doi.org/10.1007/s11276-021-02678-z>
- Kamarei, M., Patooghy, A., Shahsavari, Z., & Salehi, M. J. (2020). Lifetime expansion in WSNs using mobile data collector: A learning automata approach. *Journal of King Saud University-Computer and Information Sciences*, 32(1), 65-72. <https://doi.org/10.1016/j.jksuci.2018.03.006>

18. Osamy, W., Khedr, A. M., El-Sawy, A. A., Salim, A., & Vijayan, D. (2021). IPDCA: intelligent proficient data collection approach for IoT-enabled wireless sensor networks in smart environments. *Electronics*, 10(9), 997. <https://doi.org/10.3390/electronics10090997>
19. Dande, B., Chen, S. Y., Keh, H. C., Yang, S. J., & Roy, D. S. (2021). Coverage-aware recharging scheduling using mobile charger in wireless sensor networks. *IEEE Access*, 9, 87318-87331. <https://doi.org/10.1109/ACCESS.2021.3088524>
20. Gharaei, N., Al-Otaibi, Y. D., Butt, S. A., Malebary, S. J., Rahim, S., & Sahar, G. (2020). Energy-efficient tour optimization of wireless mobile chargers for rechargeable sensor networks. *IEEE Systems Journal*, 15(1), 27-36. <https://doi.org/10.1109/JSYST.2020.2968968>
21. Choi, H. H., & Lee, K. (2021). Cooperative wireless power transfer for lifetime maximization in wireless multihop networks. *IEEE Transactions on Vehicular Technology*, 70(4), 3984-3989. <https://doi.org/10.1109/TVT.2021.3068345>



© Author(s) 2024. This work is distributed under <https://creativecommons.org/licenses/by-sa/4.0/>



## A lasso regression-based forecasting model for daily gasoline consumption: Türkiye Case

Ertugrul Ayyıldız<sup>\*1</sup>, Mirac Murat<sup>1</sup>

<sup>1</sup> Karadeniz Technical University, Department of Industrial Engineering, Türkiye, [ertugrulayyildiz@ktu.edu.tr](mailto:ertugrulayyildiz@ktu.edu.tr), [miracmurat@ktu.edu.tr](mailto:miracmurat@ktu.edu.tr)

Cite this study: Ayyıldız, E., & Murat, M. (2024). A lasso regression-based forecasting model for daily gasoline consumption: Türkiye Case. Turkish Journal of Engineering, 8 (1), 162-174

### Keywords

Gasoline consumption  
Forecasting  
Lasso regression  
Ridge regression

### Research Article

DOI: 10.31127/tuje.1354501

Received:03.09.2023

Revised: 03.01.2024

Accepted:04.01.2024

Published:16.01.2024



### Abstract

Gasoline is one of the most sought-after resources in the world, where the need for energy is indispensable and continuously increasing for human life today. A shortage of gasoline may negatively affect the economies of countries. Therefore, analysis and estimates about gasoline consumption are critical. Better forecast performance on gasoline consumption can serve the policymakers, managers, researchers, and other gasoline sector stakeholders. This study focuses on forecasting daily gasoline consumption in Türkiye using a lasso regression-based methodology. The methodology involves three main stages: cleaning data, extracting/selecting features, and forecasting future consumption. Additionally, Ridge Regression is employed for performance comparison. Results from the proposed methodology inform strategies for gasoline consumption, enabling more accurate planning and trade activities. The study emphasizes the importance of daily forecasts in deciding import quantities, facilitating timely planning, and establishing a well-organized gasoline supply chain system. Application of this methodology in Türkiye can pave the way for globally coordinated steps in gasoline consumption, establishing efficient gasoline supply chain systems. The findings provide insights for establishing a smooth and secure gasoline collection/distribution infrastructure, offering effective solutions to both public and private sectors. The proposed forecasting methodology serves as a reference for ensuring uninterrupted gasoline supply and maximizing engagement between customers and suppliers. Applied and validated for Türkiye, this methodology can guide global efforts, fostering planned approaches to gasoline consumption and enhancing supply chain systems.

## 1. Introduction

Türkiye's economy is an emerging market economy, as defined by the International Monetary Fund (IMF) [1]. Türkiye has a substantially improved economy. Over the past 20 years, Türkiye globalizes its economy with emerging technologies. The gross domestic product (GDP), which was 272 billion dollars in 2000, tripled in 2022 to 906 billion dollars. Simultaneously, the GDP per capita increased 2.9 times in 2022 compared to 2002, from \$ 3,581 to \$ 10,661 [2]. The change of the GDP per capita and purchasing power parity by years are given in Figure 1 for Türkiye [3]. Türkiye's economy is the world's 19<sup>th</sup>, and Europe's 7<sup>th</sup> largest economy in 2019 [2].

While various energy sources are vital for economic prosperity and technological competitiveness [4], oil and natural gas stand out as the most sought-after resources globally [5], particularly as the world's need for energy is continuously increasing. It is clear that if there is a shortage in the provision of these two resources, the economies of the country, and therefore the world

economy, will be affected. Since the late 19th century, oil, as a primary energy source, has been one of the main factors consumed in parallel with the development of industry and has accelerated its growth, alongside electricity consumption, which has also played an influential role in the growth of economies [6] and has been recognized as another key energy type for end-users. With its much wider usage in the 20th century, oil is indispensable for human life today. Research shows that oil will remain the essential energy source in the medium term.

Three main views are accepted in measuring the linear relationship between oil consumption and economic growth. According to the first view, oil is one of the most important production factors, and oil demand is the primary economic development dynamic. The second view is that both oil consumption and economic growth affect each other, and there is bi-directional variability between the existing variables. According to the third view, it is argued that there is no linear relationship between oil consumption and economic growth [7].

The growing economy and developing technology have increased the need for oil in Türkiye. The demand for oil is increasing daily because of the rapid growth of the economy, particularly within the context of the oil market. Oil is used for transportation, energy, etc. Indeed, in 2019, the amount of oil consumed in Türkiye is over

thirty million liters [8]. More than 90 percent of Türkiye's oil is imported from different countries as Iraq, Russia, Iran, etc. [9]. TÜPRAŞ's (the biggest petroleum refinery holding of Türkiye) yearly amount of exported crude oil and domestic production is given in Figure 2 [10].

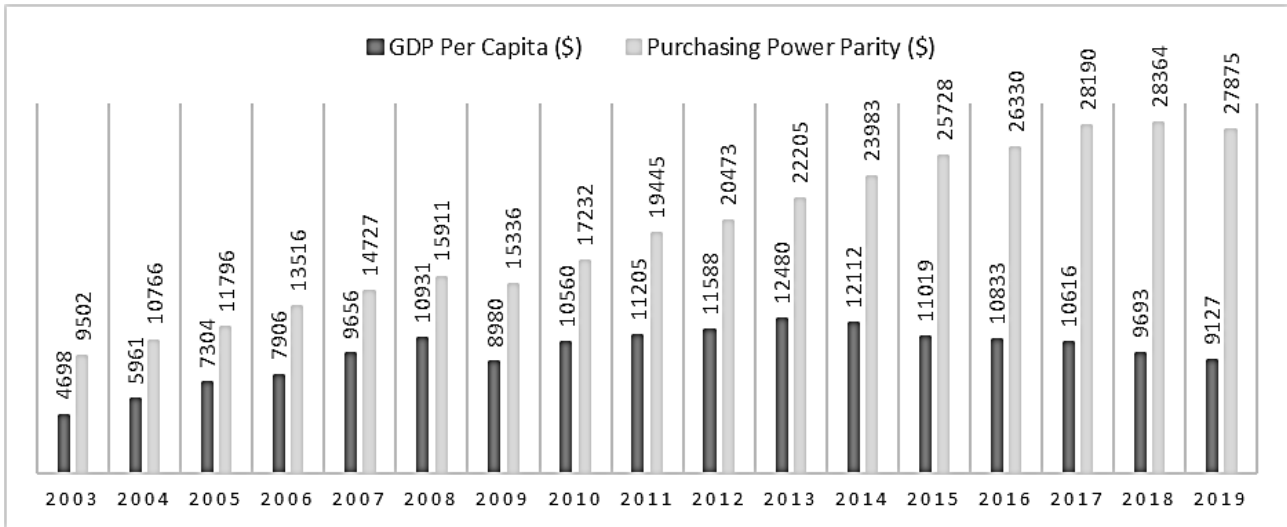


Figure 1. Türkiye's GDP and purchasing parity by years.

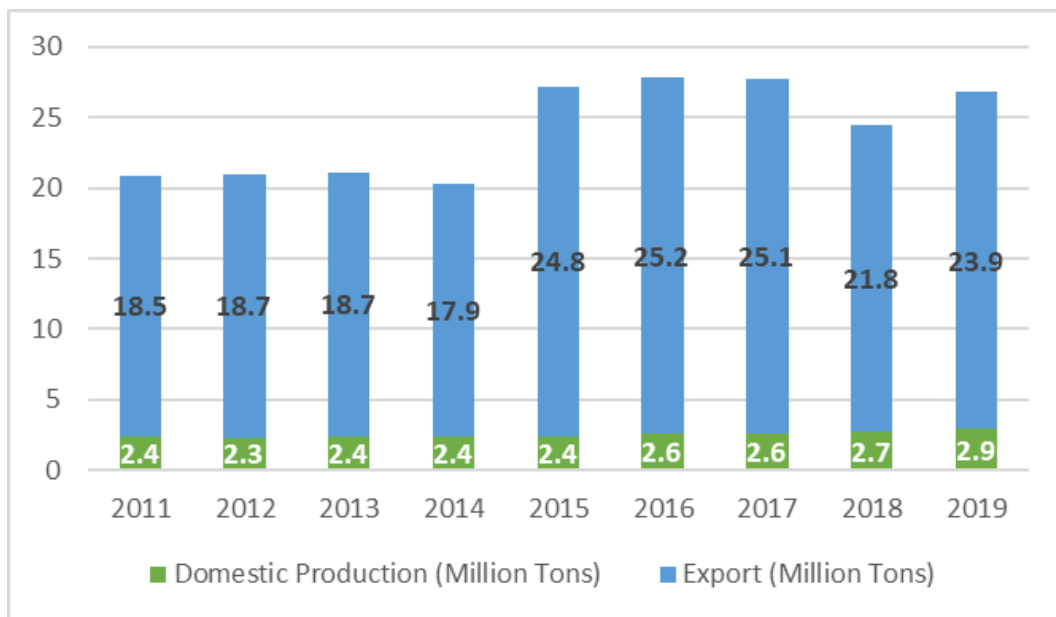


Figure 2. TÜPRAŞ's yearly amount of crude oil supplies by type.

Accurate forecasts help maintain a balance between gasoline supply and demand, allowing for better economic planning. This is important to avoid shortages or surpluses that could disrupt economic activity. Forecasts influence import strategies and trade planning by helping to determine the amount of gasoline to be imported. This is important for Türkiye's economic relations with other countries. Price stability is achieved by understanding and forecasting gasoline consumption trends. This contributes to the Turkish economy, where most of the gasoline consumed is imported, and is particularly important for consumers, businesses, and policymakers in managing inflation and economic fluctuations. Daily forecasts of gasoline consumption

provide a basis for the formulation of energy policies, helping governments set targets and develop strategies to balance energy needs with environmental sustainability. Better forecast performance on oil consumption can serve the policymakers, managers, researchers, and other stakeholders of the oil sector in both Türkiye and the world [11-13].

Researchers and theoreticians have focused on the oil or gasoline consumption forecasting problem and its extensions over the years. Nel and Cooper analyze the relationship between oil consumption and economic growth for countries. They use a logistic curve to predict oil demand for China. They construct projections until 2030 [14]. Azadeh et al. concentrate on forecasting oil

prices in various settings, including noisy, uncertain, and complex environments. Artificial Neural Network (ANN) is integrated with fuzzy regression to determine the best oil price forecast. Different statistical tests are performed to show the validity of the proposed methodology [15]. Narayan and Wong examine the components that affect oil consumption for the territory, located in Australia for twenty years. They determine oil price and income as the most active factors. Income is then estimated to be significantly important for oil consumption, while oil prices are not [16]. Yang et al. propose a forecasting model that includes both a genetic algorithm and the backpropagation neural network to estimate China's oil consumption. They also use a gray model to take advantage of both nonlinear and linear models [17]. Li et al. develop 26 different combination models using a traditional combination method to handle overfitting and improving prediction accuracy. They test regression models, gray theory, and a hybrid model to predict China's oil consumption [18]. Assareh et al. use the genetic algorithm and particle swarm optimization techniques to predict Iran's oil demand. They predict yearly demand using data of 35 years [19]. Lin and Xie focus on oil demand forecasting for the transport sector in China. Multiple factors such as gross domestic product, road condition, oil price, and labor performance are determined, and the forecasting model is proposed. Monte Carlo simulation is also used for risk analysis of the proposed model [20]. Rao and Parikh use the forecasting model based on a time series to forecast the oil demand for India. They perform forecasting for different oil products, such as gasoline, diesel oil, and liquid petroleum. Six different variables are used in the model [21]. Wang and Song examine the different versions of the gray model and propose a novel gray model based on time series. Yearly demand between 1990 and 2017 is used to forecast the next ten years for oil consumption in China [22]. Duan et al. extend the SIGM model with gray theory to forecast China's crude oil consumption. To handle conforming class ratio check, least squares estimation is performed. Particle swarm optimization techniques are also used to achieve better forecasting performance. They use yearly data from 2002 to 2014 to forecast between 2015 and 2020 [23]. Behrang et al. present a novel approach to forecast oil consumption. Gross domestic product, import, export, and population are determined as variables in the forecasting model. Gravitational Search Algorithm is used to forecast oil consumption in Iran, then the Genetic Algorithm and Particle Swarm Optimization are used to compare the proposed model [24]. Minniear evaluates global petroleum product production. Saudi Arabia, Kuwait, Iran, Venezuela, United Arab Emirates, and Iraq are analyzed, and future prediction is made [25]. Al-Qaness et al. improve the adaptive neuro-fuzzy inference system (ANFIS) with a sine-cosine algorithm for forecasting oil consumption. Monthly oil consumption data from 2007 to 2017 from three different countries, as Canada, Germany, and Japan, is used to assess the performance of the proposed methodology. Extensions of ANFIS are used for comparison [26]. Fatima et al. predict oil demand in China using oil prices, oil reserves, oil consumption, and economic growth. Time-series

techniques are used to investigate the linkages between parameters and oil demand in this paper [27]. Yu et al. investigate the relationship between parameters of oil consumption. Popular forecasting methods are applied to forecast oil consumption using Google trends, including big data [28]. Keshavarzian et al. make projections of oil consumption for the road transportation sector [29]. First, vehicle ownership is forecasted using a time series via a nonlinear Gompertz model. Then, specific geographic and demographic variables are implemented into the model for different countries. Yearly data from 1972 to 2008 in 154 countries are used in the study.

Sadri et al. aim to determine gasoline consumption for a period of ten-year using vehicle population, traffic volume, average private vehicles kilometers traveled/capita as input variables with different artificial neural network models [30]. Melikoglu employs semi-empirical models to predict Türkiye's yearly demand for gasoline, diesel, liquefied petroleum gas bioethanol, and biodiesel [31]. Azadeh et al. present a fuzzy mathematical programming-analysis of variance approach to forecasting yearly gasoline consumption of Iran, Kuwait, USA, Canada, and Japan [32]. Sapnken et al. focus on the gasoline consumption of Cameroon. They use linear regression-based forecast methodologies to determine yearly gasoline consumption for two years [33]. Anggarani and Watada aim to develop an accurate harmony search-based forecast model for gasoline consumption forecasting [34]. Chen et al. present a gray fractional FGM (1, 1) model to predict six years' energy consumption for natural gas, crude oil, gasoline, and diesel [35]. Güngör et al. investigate Türkiye's gasoline consumption after pandemic with Autoregressive Integrated Moving Average (ARIMA) models [36]. Wang et al. use single-linear, hybrid-linear, and non-linear time series models to forecast the yearly energy demand of China and India [37]. Wang et al. employ hybrid ARIMA and metabolic nonlinear gray model for forecasting the monthly gas production in the United States [38]. Wang et al. analyze COVID-19 impact on the United States' oil consumption via developed novel ARIMA based forecasting model [39]. Wang et al. investigate the pandemic impact on energy consumption in China via an ARIMA model and show the reduction in energy consumption [40]. Wang et al. employ ARIMA based methodologies to analyze the pandemic impact on carbon emissions [41].

As seen in the studies above, the problem of accurate forecast on oil and its derivatives consumption is one of the - studied topics in the forecasting literature. But there are a limited number of studies on daily gasoline consumption forecasting. Therefore, apart from other studies in the literature, the problem of the forecasting of daily gasoline consumption is discussed in this study. Accurate forecasting performance plays a key role for decision-makers.

This study aims to develop a forecasting strategy for daily gasoline consumption, which is scarce in the literature. For this purpose, a lasso regression-based forecasting methodology is proposed. To the best of our knowledge, lasso regression is used to forecast gasoline consumption for the first time with this study.

This study stands out from the current academic perspective by addressing a specific gap in daily gasoline consumption forecasting research. The primary contribution lies in introducing a forecasting technique based on lasso regression, specifically designed for daily gasoline consumption. This represents a significant innovation in the region, filling existing gaps and providing decision makers with a new and practical tool for effective planning and strategy development in the petroleum sector. Another distinguishing point is that this distribution is the first to survive lasso regression in predicting gasoline consumption. The paper also expands the repertoire of forecasting techniques used in the existing literature to predict gasoline consumption. Beyond the methodological advances, the article emphasizes that the proposed forecasting strategies are presented in a practical manner for decision makers. Accurate daily gasoline consumption forecasts are positioned as indispensable for effective decision making, drawn to the extent of increasing the distribution of oil imports and providing guidance on production.

## 2. Method

Lasso regression is selected as forecasting methodology because it fits the nature of the daily gasoline consumption forecasting problem. Lasso regression is particularly suited to situations with a large number of potential predictor variables because it introduces a penalty term that forces some regression coefficients to be exactly zero to encourage sparse solutions [42]. In the realm of forecasting daily gasoline consumption, numerous factors intrinsic to the components of the time series have influence over the results. It becomes imperative to discern the most pertinent features in this context. Lasso regression is compatible with the goal of isolating the most influential variables in daily gasoline consumption time series data by automatically performing variable selection and feature extraction [43].

Variables for energy consumption prediction often exhibit multicollinearity, i.e. they are highly correlated. Lasso regression handles multicollinearity by selecting one variable from a set of highly correlated variables, making the model more robust [44]. Given the complex dependencies inherent in energy consumption data, this method is well suited to ensure the reliability of the predictive model. The penalty term of lasso regression not only assists in variable selection but also prevents overfitting [45]. Reducing the risk of overfitting provides a more accurate and feasible daily gasoline consumption prediction model [46]. Moreover, Lasso regression but also provides interpretability in terms of variable importance [47]. This is critical in the context of daily gasoline consumption, as policymakers, managers, and researchers need insight into which factors contribute significantly to observed changes. The transparent nature of lasso regression meets the need for an understandable and actionable forecasting model.

The time series forecast in this study is based on extracting prospective features from data. Features are generated by mining both the observations and the time

points. One of these features is "lag" that describes earlier observations in the series [48]. The lag is based on the concept of autocorrelation, which is the similarity between the series and observations as a function of the time lag. Another feature is the tuple of date and/or time components. With these types of features, the unit time in the series can be transferred into ones of a minute of an hour, an hour of a day, a day of a week, a month of a year, etc. The transformation can also be made by considering if a day is a holiday or if there is a special event. Hence, each matching unit time is coded in the same way to capture possible patterns of the series. The last feature used for forecasting is the target encoding that generally calculates averages of identical date features [49]. This distinguishes a forecasting model from any other time series that involves the same time interval and creates an exclusive time series forecasting.

In this study, the forecasting approach used for daily gasoline consumption consists of three main stages: i) preprocessing the data ii) extracting and selecting features iii) forecasting the future of daily gasoline consumption time series via the proposed models, and six basic steps described in following. A detailed description of each step is provided in the following three subsections.

Step 1. Gathering the data for gasoline consumption from the related sources and reformatting the data points to enable forecasting.

Step 2. Deleting and then replacing excessively oscillating and missing values with interpolated values.

Step 3. Evaluating if the time series is stationary or not to form an idea related to possible forecasting performance.

Step 4. Extracting features that depend on the series itself. Creating various historical time series, which are totally-dependent features; and date components, which are semi-dependent, from the original data.

Step 5. Developing an effectively forecasting gasoline consumption model by regularizing it and selecting significant features using Lasso Regression.

Step 6. Forecasting future gasoline consumption through the selected features and developed model.

### 2.1. Extracting features from data

The data used in this study was gathered from the weekly official reports of the Turkish Ministry of Energy and Natural Resources [50]. It has daily observations of the gasoline consumption in Türkiye. Since the data exhibits inconsistencies, such as variations in format, unit discrepancies, and gaps in information sharing because of weekly releases, the data had to be organized. Missing and abnormal observations in the data were rectified by updating them with new values calculated through an interpolation method, considering assumptions about the underlying continuous function.

The forecasting process for gasoline consumption relies on features extracted from the series itself, requiring diverse features that are not necessarily independent of the series. These features can be divided into two groups: totally-dependent features and semi-dependent features. The values of features included in the group of totally-dependent are calculated from the

values of the series itself considering the relevant dates. On the other hand, the values of the features in the semi-dependent group are contingent upon the time points within the time span of the series. These values would be identical if the time spans of two dissimilar time series are the same. Week of year for the fifth time points, for instance, of two time series gasoline consumption vs coal consumption in the same year, would have the same value.

The features extracted as date components from the series fall under the category of semi-dependent. Decomposing the date into independent parts, such as year, month, week, day of the week, and week of the year, has the potential to generate robust predictors. However, these features require systematic transformation owing to their inherent ordered and cyclic nature, since the initial and final data points, akin to the intermediate ones, are interconnected in a sequence, demonstrating the continuous and cyclical nature of time in data analysis. These types of data generally are transformed into two variables that swing back and forth [51].

Calculating average values of the same time units and assigning them for corresponding units creates eventual distinguishing features that fall under totally-dependent. These features that represent data regarding the observations itself, along with their temporal component, are exclusive to the series. Hence, each observation in the series is enriched by average values associated with the time units, such as weekday, week, or month to which it belongs. For instance, if a value named *monthaverage* is to be determined for an observation, this value is calculated by taking the average of the data points only from the months in which that observation is present.

An advance transformation for the date feature is to determine if any observation of the series belongs to an exclusive time of the year, such as a weekend or holiday. This helps to understand the cause for the unusual deviations (within allowed limits) from prior and posterior observations. Such features are also included in the semi-dependent group.

Another group of features is *lags* that represent the relationship between the current and historical observations of the series. Lags, a delayed rendition of the series, are derived exclusively through time shifting, excluding the direct utilization of time values or observation averages from the series. To interpret the structure of a time series, autocorrelation with various lags serves as a valuable criterion. A plot generated through autocorrelations can aid in acquiring a better understanding of the structure of the series, such as the magnitude of seasonality. The Autocorrelation Function (ACF) plot encompasses correlations with all feasible lags, contributing to a comprehensive analysis.

## 2.2. Model development and feature selection

The basic regularization techniques used to forecast gasoline consumption alongside linear regression are ridge regression (RR) and lasso regression (LR).

The Equation 1 for the linear regression model that has an error term ( $e$ ) with an expected value of 0 ( $E[e] = 0$ ) and constant variance ( $Var(e_i) = \sigma^2$ ) is:

$$y = \beta_0 I + X\beta + e \quad (1)$$

where  $y = (y_1, y_2, \dots, y_N)^T$  is the vector of  $N$  observations,  $I$  is the unit matrix, and  $\beta_0$  is the intercept.  $X$  is a  $N \times p$  matrix of features;  $\beta$  is the vector of the regression coefficients of  $p$  features.

Linear regression may cause a model that has poorly determined coefficients with high variance due to complex relationships caused by a large number of features [52]. RR is ideal to solve the issue of determining adequate coefficients and to develop high-quality models with numerous predictors, each having a small effect. RR overcomes this issue by shrinking the coefficients of correlated predictors towards zero and improves the forecasting performance [42].

RR minimizes the loss function given in Equation 2.

$$\text{minimize}_{\beta} \left\{ \frac{1}{2N} \|y - X\beta\|_2^2 + \lambda \|\beta\|_2^2 \right\}, \quad \lambda \geq 0 \quad (2)$$

where  $y = (y_1, y_2, \dots, y_N)^T$  is a  $N \times 1$  dimensional vector that stands for the dependent variable,  $X$  is a  $N \times p$  dimensional matrix whose elements stand for  $p$  independent variables and  $\beta$  is the  $p \times 1$  dimensional vector of coefficients of independent variables.  $\|\cdot\|_2$  indicates the Euclidean distance.  $\|\beta\|_2^2$  is the  $l_2$  norm penalty on  $\beta$  with the tuning parameter of  $\lambda$  that differs LR from ordinary regression analysis [53]. The optimal values for parameters  $\beta$  and  $\lambda$  are determined according to the performance measurement of mean squared error (MSE) acquired cross validation procedure.

The process of feature extraction can produce a large number of so-called features. Some of these features might have a low or no effect on the forecasting performance or might cause overfitting. Therefore, there is a need for a feature selection/reduction to apply effective forecasting [54]. Here, another regularization technique that provides an opportunity for feature selection/reduction, as well as model simplicity and prevention of overfitting, is Least Absolute Shrinkage and Selection (Lasso), i.e. LR [55].

LR was essentially developed to eliminate the disabilities of the least squares method by Tibshirani [56]. However, it recently stands out as one of the methods that improve the forecasting performance in analyzing high-dimensional data [53]. LR is an inbuilt variable selection method, it has the mastery to control the parameters leading to revealing ineffective variables. It shrinks some regression coefficients to make them zero according to Equation 3 given in the Lagrange form [57]. Therefore, the accuracy of predictions and ease of interpretation are enhanced.

$$\text{minimize}_{\beta} \left\{ \frac{1}{2N} \|y - X\beta\|_2^2 + \lambda \|\beta\|_1 \right\}, \quad \lambda \geq 0 \quad (3)$$

where  $\|\cdot\|_1$  is Manhattan distance and  $\|\beta\|_1$  indicates  $l_1$  norm penalty on  $\beta$ .

Lasso regularization forces some coefficients to be zero to vanishing, thus some predictors may completely leave out from the forecasting of the series. The non-zero coefficients sign the effective variables to forecast the

time series. The remaining variables of interest are more powerful to represent the relationship between the parts of the series and itself. Hence, LR produces a more interpretable regression model with only the most relevant and predictive subset of features while the forecasting performance for the time series increases.

### 2.3. Forecasting daily gasoline consumption using the proposed models

The top-performing models from each regression technique are employed to predict the daily gasoline consumption for the test data period, corresponding to the final year of the series. The performance of each model is compared according to the forecasting error. Mean absolute percentage error (MAPE) is a simple comparative measurement that simplifies the intuitive interpretation of the error. Equation 4 gives MAPE between the actual values ( $A$ ), comprising  $n$  observations, and their corresponding forecasted values ( $F$ ).

$$MAPE = \frac{1}{n} \sum_{t=1}^n \frac{(|A_t - F_t|)^2}{A_t} \quad (4)$$

### 3. A real case application for Türkiye

The raw time series used in this study is a six-and-a-

half-year time series that has daily observations recorded in the interval between 2013-06-03 and 2019-12-31 as shown in Figure 3. The series contained missing values, and the missing values were filled using the Piecewise Cubic Hermite Interpolating Polynomial (Pchip) interpolation technique. Pchip proved to be the optimal interpolation method after extensive testing against cubic spline and Akima piecewise cubic Hermite interpolation across 1000 time series, each artificially designed to include missing values. In every iteration, the three techniques were simultaneously assessed for their ability to interpolate the so-called missing values, which were randomly assigned within the longest section of the time series (from 2016-11-21 to 2018-09-07) devoid of missing data. After 1000 trials, Pchip stood out for achieving the majority of best fit performances, especially excelling with non-smooth and widely spaced data [58].

In the series, instances of excessive consumption data were observed during periods of peak consumption, particularly around summer. While it is not believed that these data were inaccurately recorded, a further evaluation was conducted using the quartiles method, which specifically, data points beyond 1.5 interquartile ranges are identified outliers. Figure 3b illustrates the outlier data with the red line. These data points have been replaced with values at the specified thresholds. Consequently, the blue line in Figure 3b is the adjusted time series used to develop forecasting models.

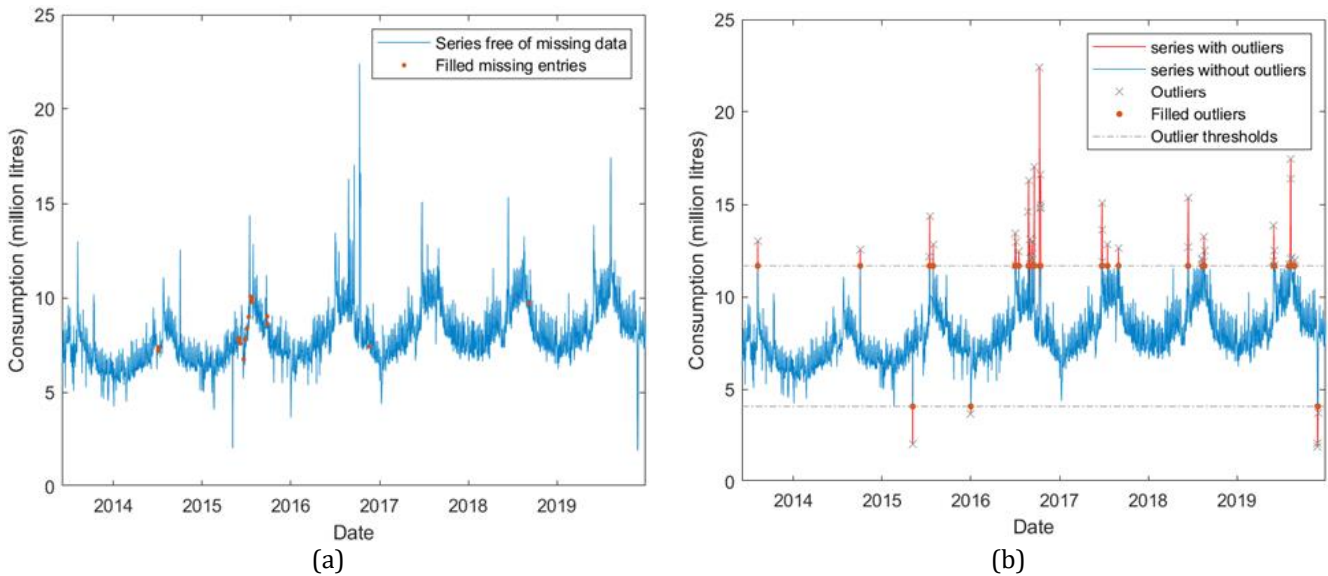
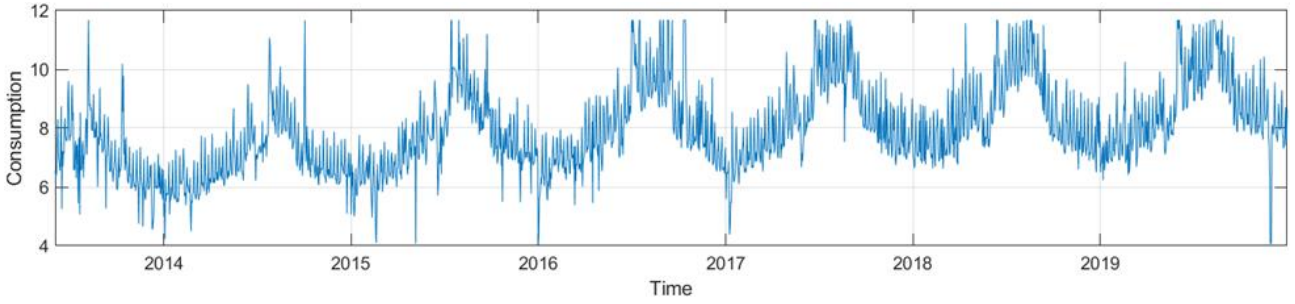


Figure 3. a) Gasoline consumption time series with missing data filled by Pchip technique, b) time series without outliers

The forecasting performance of a time series significantly depends on the presence of stationarity, denoting a consistent mean and variance over time that enhances predictability. In this study, the adjusted time series exhibits non-stationarity, as indicated by the Dickey-Fuller test [59] result with a p-value of 0.3990 at a significance level of 0.05. This non-stationary characteristic, as illustrated in Figure 4, while posing a challenge to conventional methodologies of forecasting, the approach in this study is designed to operate

effectively without the assumption of existing stationarity.

Figure 5 illustrates the correlation values between the series and all possible lags. The plot has sine-like waves, indicating cycles of strong negative and positive correlation, which is a strong sign of seasonality in the time series. Approximately 358 lags after the initial lag, a relatively high correlation of 0.634 occurs again. Thus, it can be simply captured that there is a relationship of a point of time series with past points in the same season that is around a year.



**Figure 4.** Non-stationary time series of consumption.

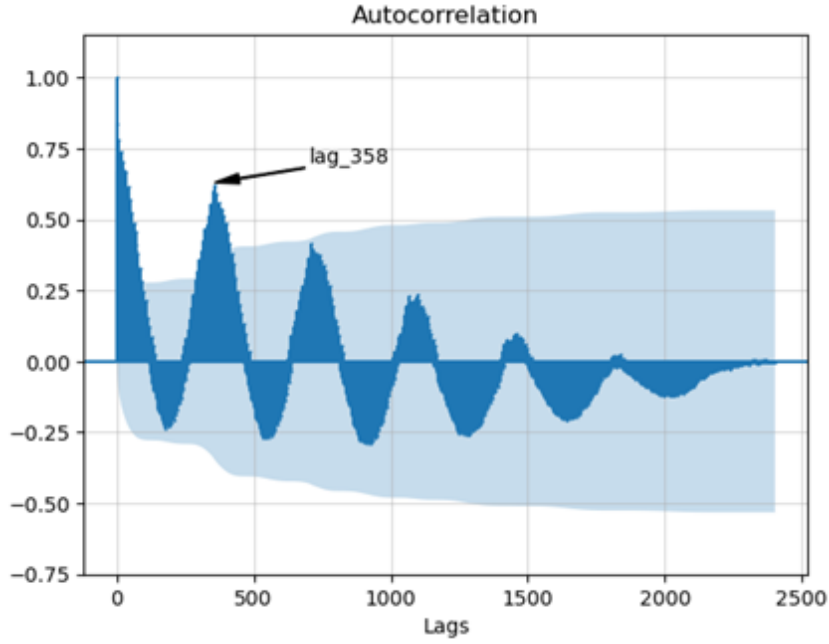


**Figure 5.** The Autocorrelation plot of time series

Once organizing the time series and preparing it for forecasting, a non-random partitioning is applied. Time points corresponding to almost the first year (2013-06-03 and 2014-05-26) are excluded from data due to 358 lags. Subsequently, the preprocessed time series data, now complete and free of missing values, has been divided into three sets: training, validation, and test data. Approximately 20% of the series, representing the last year (data points between 2019-01-01 and 2019-12-31), has been reserved as test data. The training data comprises the initial 75% of the remaining series (data points between 2014-05-27 and 2018-08-04), while the validation data consists of the consecutive 25% (2018-01-01 and 2018-12-31). In terms of proportions, the training, validation, and test data account for

approximately 64%, 17%, and 17% of the entire forecasting dataset, respectively.

The lags with a reasonable correlation ( $\geq 0.6$ ) [60] with the series itself were incorporated as features for the analysis. 26 lags were included as features, almost all comprising delays within the first 45 days. Notably, two of these lags, namely the 351st and 358th, contribute to capturing a yearly seasonal variation in the series.

The data used in the study consists of daily points; it is therefore broken into parts of the day of the week, day of the month, day of the year, week, and month. The transformation for the timestamp of unit time to the daily, weekly, and monthly counterparts are performed according to Equations 5-14, respectively.

$$DayOfWeek_{x_t} = \sin(2 * \pi * WeekDayOfO_t / 7) \# \tag{5}$$

$$DayOfWeek_{y_t} = \cos(2 * \pi * WeekDayOfO_t / 7) \tag{6}$$

$$DayOfMonth_{x_t} = \sin\left(2 * \pi * \frac{MonthDayOfO_t}{\# \text{ of days in the month}}\right) \tag{7}$$

$$DayOfMonth_{y_t} = \cos\left(2 * \pi * \frac{MonthDayOfO_t}{\# \text{ of days in the month}}\right) \tag{8}$$

$$DayOfYear_{x_t} = \sin\left(2 * \pi * \frac{YearDayOfO_t}{\# \text{ of days in the year}}\right) \tag{9}$$

$$DayOfYear_{Y_t} = \cos\left(2 * \pi * \frac{YearDayOfO_t}{\# \text{ of days in the year}}\right) \tag{10}$$

$$Week_{X_t} = \sin(2 * \pi * WeekOfO_t / 52) \tag{11}$$

$$Week_{Y_t} = \cos(2 * \pi * WeekOfO_t / 52) \tag{12}$$

$$Month_{X_t} = \sin(2 * \pi * MonthOfO_t / 12) \tag{13}$$

$$Month_{Y_t} = \cos(2 * \pi * MonthOfO_t / 12) \tag{14}$$

The Equation 5-14 can be summarized as Equation 15-16:

$$\tau_x^t = \sin\left(2 * \pi * \frac{\tau^t}{\rho}\right) \tag{15}$$

$$\tau_y^t = \cos\left(2 * \pi * \frac{\tau^t}{\rho}\right) \tag{16}$$

where,  $\tau^t$  is the corresponding time component to be transformed for the observation  $O_t$  at time step  $t$ .  $\tau_x^t$  and  $\tau_y^t$  are the transformed forms of the time component and  $\rho$  is the number of the time component in a specific time period.  $\rho$  is 52 and 7, for instance, when time components of observation are week and weekday, respectively.

Another type of feature, the unusualness of any timestamp, are being the weekend and holidays. For any observation belongs to weekends or holidays announced by the official government is tagged in a binomial scheme according to whether the day is the weekend/holiday (1) or not (0).

Average values for any week of the year, month of the year, any day of the week, day of the month, and day of the year are calculated for the period represented by training data considering only the training data. On the contrary, the average values for the period represented by the test data are calculated considering both the training and the validation data that is known anymore.

44 different features were formed through the feature extraction phase as predictors. The predictors consist of 12 time-components, 5 averages, and 27 lags that have at least the correlation coefficient of 0.6 with the time series itself. The predictors are given in Table 1.

**Table 1.** The predictors for gasoline consumption forecast model.

Time Components	Lags	Average
dayofweek_x	lag_1	weekday_average
dayofweek_y	from 2 to 16	monthday_average
dayofmonth_x	lag_17	yearday_average
dayofmonth_y	lag_21	week_average
dayofyear_x	lag_23	month_average
dayofyear_y	lag_28	
week_x	lag_29	
week_y	lag_30	
month_x	lag_36	
month_y	lag_35	
is_weekend	lag_351	
is_holiday	lag_358	

When considering the linear relation between all 44 predictors given in Table 1 and the time series, the linear

regression, RR, and LR models have an explanation capacity of approximately 84% on the change of the time series for the test data. The linear regression and RR models, which use all available features, result in more complex equations that can be challenging to interpret. LR, however, generates a more interpretable model while preserving explanation capacity. Hence, it is decided as the forecasting model for the consumption of gasoline. By excluding the other 14 features with zero coefficients, LR produces a model with 30 non-zero coefficient features. The features having a non-zero coefficient are shown in Figure 6. The predictors monthX, monthY, dayOfMonthX, dayOfYearX, dayOfYearY, weekAverage, and Lags of 9, 10, 11, 13, 16, 21, 23, 28 and 29 have no effect on the prediction of gasoline consumption.

The R<sup>2</sup> remains constant (approximately 82%) with the LR for the test data despite a reduction in the number of variables having a non-zero coefficient. Table 2 gives the R<sup>2</sup> values and the MAPE level for training, validation, and test data.

While three regression models have similar performance levels for the partitions of data, LR produces slightly better performance for training and test data, according to the values of both MAPE and R<sup>2</sup>.

Figure 7 shows the forecasting pattern for the validation data of the LR model. The model predictions deviate from actual validation values as a 4.34% MAPE overall. Upper and lower bounds have been drawn according to limit values imposed by train data sign as an outlier observation in the actual data. This is the reason why the prediction error occurred at this level.

Figure 8 shows the forecasting pattern for the test data of the LR model. The prediction error for the test data is recorded at 4.39%. The test data has more outlier values considering the upper and lower bounds imposed by the training data merged by the test data.

As a result of the proposed forecasting methodology, appropriate strategies for gasoline consumption will be developed with the forecasted daily consumption of gasoline and more accurate planning activities will be developed for the countries. By forecasting the daily consumption of gasoline, the gasoline amount that will be imported will be determined, so that the correct planning and timely implementation of gasoline trading will be realized. By means of this proposed forecasting methodology, which is applied and verified for Türkiye, more planned steps can be taken regarding the gasoline consumption in all countries of the world, and hence a gasoline supply chain system can be established.

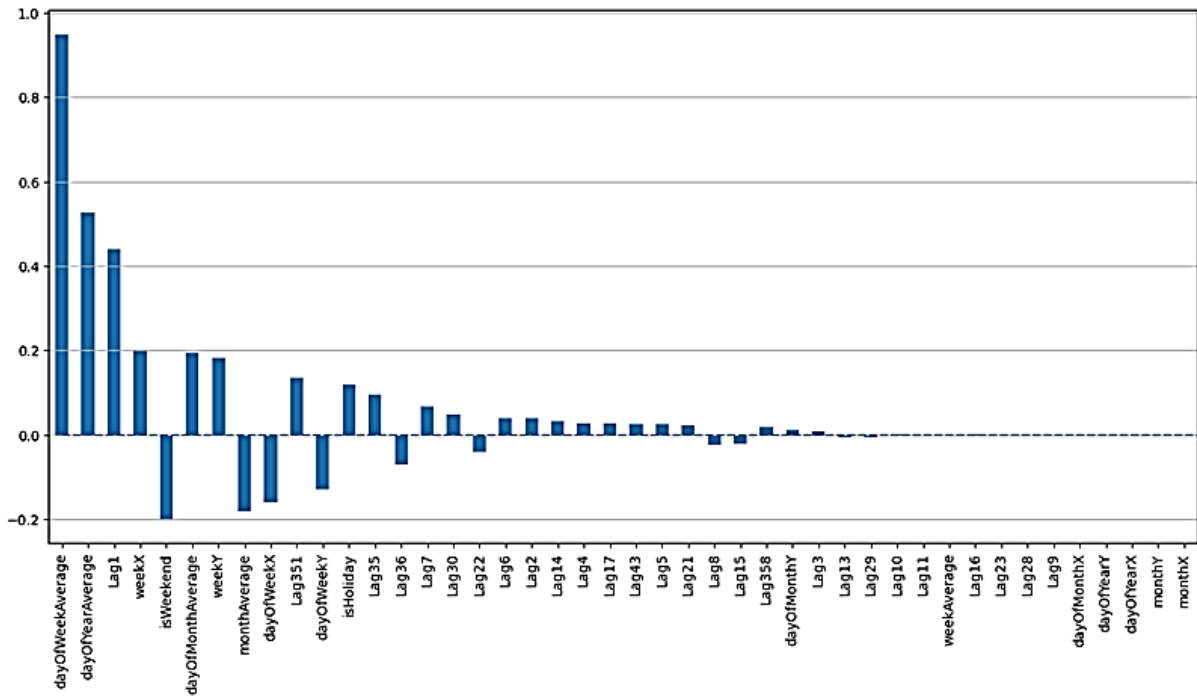


Figure 6. Coefficient of LR model.

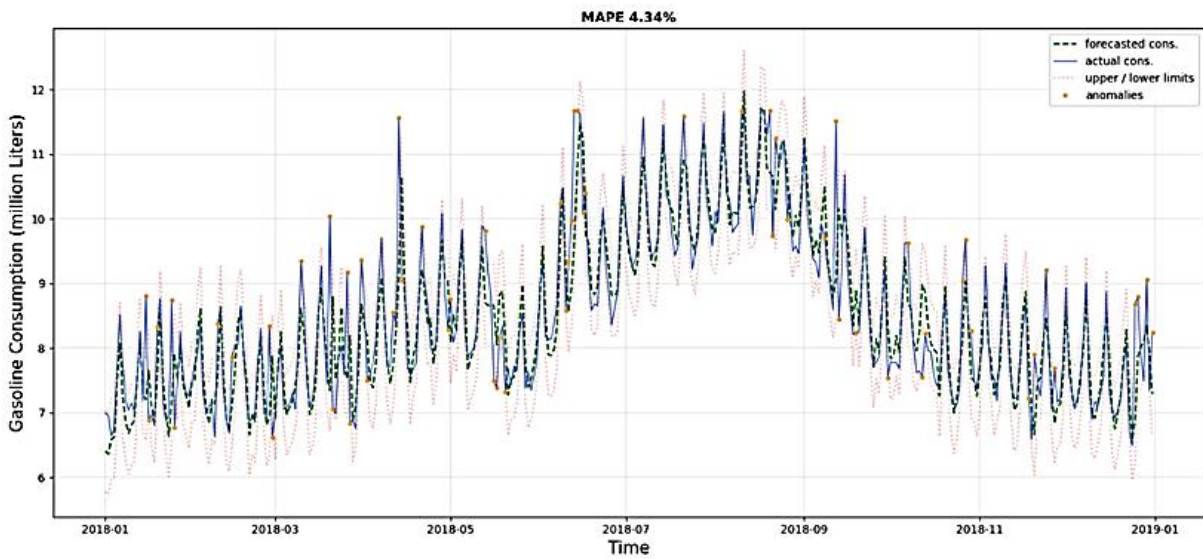


Figure 7. Forecasting pattern for the validation data of the LR model.

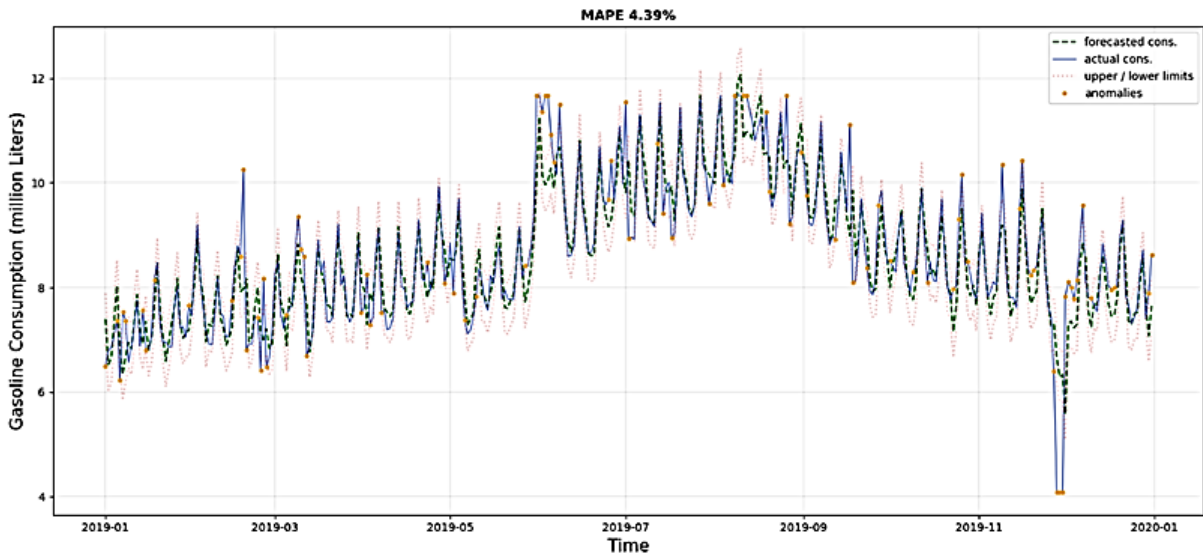


Figure 8. Forecasting pattern for the test data of LR model.

**Table 2.** R<sup>2</sup> and MAPE values of models.

	Linear regression		Ridge regression		Lasso regression	
	R <sup>2</sup>	MAPE	R <sup>2</sup>	MAPE	R <sup>2</sup>	MAPE
Training	0.837	4.68%	0.835	4.68%	0.835	4.67%
Validation	0.828	4.27%	0.826	4.32%	0.826	4.34%
Test	0.841	4.40%	0.839	4.41%	0.839	4.39%

## 5. Policy implications

There is a need to implement a more dynamic policy framework that recognizes the variability in daily gasoline consumption. This includes the use of real-time data to improve accuracy and responsiveness, as well as regular updates and adjustments to forecasting models. To improve the accuracy of daily gasoline consumption forecasts, policymakers should consider incorporating advanced forecasting techniques such as lasso regression. This study shows that lasso regression is a reliable tool for planners and policymakers and demonstrates its effectiveness in this context. To address the environmental impacts of gasoline consumption, environmental considerations must be integrated into the policy framework. In this context, supply chain planning should be aligned with sustainability goals. Using alternative energy sources should be promoted, and environmentally friendly practices should be adopted in the gasoline industry. For the successful implementation of the proposed recommendations, cooperation should be established with the petrol industry, research institutions and environmental organizations. To support the development and implementation of changes, adequate funding should be provided. Policy makers should invest in the necessary technological infrastructure to facilitate the seamless integration of improved forecasting methods into the existing management systems of the gasoline supply chain. Integrating environmental considerations into policy frameworks is consistent with global sustainability goals, helps reduce environmental impacts, and promotes a more sustainable gasoline industry. By increasing policy framework adaptability and working with industry stakeholders, policymakers can contribute to the gasoline sector economic stability by ensuring a flexible and responsive supply chain.

The proposed policy implications aim to address the identified gaps in the current policy and provide practical, cost-effective, and socially acceptable solutions. By implementing these recommendations, policymakers can promote positive change, improve the status quo, and contribute to the overall well-being of society.

## 6. Discussion and Conclusion

Currently, the need for gasoline is increasing day by day. Gasoline is used in almost every industry. Gasoline also has great economic importance. When gasoline consumption continues to have a significant impact on economies worldwide, making accurate forecasts about its consumption is crucial. Such forecasts are essential for implementing necessary actions and developing proper economic strategies for these countries. However,

besides these forecasts, it is crucial to predict the gasoline consumption daily which has a huge impact on the environment is currently considered important to make a quick measure to reduce environmental pollution. In this way, accurate planning can be made in the accomplishment of gasoline supply between the customers and suppliers, and it can create a smooth supply chain system for an indispensable product, like gasoline. The daily gasoline consumption that plays a key role in planning gasoline supply and distribution required for the continuum of public and private sector operations should be forecasted. A dynamic forecasting model that can be used daily, especially for short-term operations, is introduced into the literature. The gasoline consumption for Türkiye is forecasted daily with this model using the last six years of data. For this aim, the daily gasoline consumption in Türkiye is forecasted using lasso regression in this paper. The time series for daily gasoline consumption is analyzed based on the feature extraction technique. The data for daily gasoline consumption is created using official data, then the data is cleaned. For this purpose, the abnormal observations in data are updated with the new values calculated by Pchip interpolation. Subsequently, data is analyzed, and features are selected according to the results of the analysis. After the features are determined, values have complied, and the best lasso regression model is structured with these features. As a result of the study, it is shown that the lasso regression is a useful approach to be used to accurately forecast daily gasoline consumption.

The effectiveness of this approach in achieving accurate daily forecasts is demonstrated through the systematic application of feature extraction techniques, data cleaning, and model structuring using lasso regression. Importantly, the study establishes a critical link between daily gasoline consumption, environmental impact, and supply and distribution system planning. By highlighting the need for daily forecasts, the study contributes to a more comprehensive understanding of the complex dynamics that shape gasoline demand. In addition, the proposed forecasting methodology serves as a guide for building a resilient supply/distribution infrastructure that can more effectively respond to the diverse needs of both the public and private sectors. Through these contributions, this research not only provides practical insights for decision makers but also lays the foundation for future efforts to develop and expand forecasting techniques for a more sustainable and responsive gasoline supply chain.

This study can be a guide to establish a smooth and secure collection/distribution infrastructure on supplying gasoline, giving a more effective response to the public and private sectors. The proposed forecasting methodology can be a reference for the uninterrupted

flow of gasoline supply and solutions where customers and suppliers can be reached at the maximum level.

### 6.1 Limitations and future recommendations

There are some limitations despite the findings of this study. The primary limitation is the use of lasso regression as the forecasting method. Lasso regression has proven to be effective in predicting daily gasoline consumption. However, all possible alternative methods can be explored in this study. Future research could benefit from a comparative analysis of different forecasting approaches, such as artificial neural networks or time series models, to improve the robustness of the forecasts. For future directions, the approach outlined in this study could be expanded by incorporating updated data or employing different forecasting methods. Techniques such as artificial neural networks, ARIMA, and Seasonal ARIMA (SARIMA) could compare with the current results. Together with Autometrics, the General to Specific approach shows promise in improving the accuracy of daily gasoline consumption forecasting and can be used for future studies.

Another limitation is that the study focuses only on gasoline consumption in Türkiye. Generalizing the results to other regions or countries may require caution due to specific economic, environmental, and geopolitical factors affecting gasoline demand. A more comprehensive understanding of the factors influencing daily gasoline consumption could be achieved with a broader data set covering different regions. The generalizability of the findings could be enhanced by expanding the study to include international comparisons. Examining the daily gasoline consumption patterns of different countries or regions will allow for a more detailed understanding of the factors that influence demand and enable the development of more adaptable and globally applicable forecasting models.

Future research could further explore the integration of environmental variables into forecasting models, building on the current study. A more sustainable and environmentally friendly approach to supply chain planning could be achieved by examining the impact of environmental policies, climate factors, or alternative energy sources on daily gasoline consumption.

### Author contributions

**Ertugrul Ayyildiz:** Conceptualization, Methodology, Software, Data curation, Original draft preparation, Validation. **Mirac Murat:** Visualization, Investigation, Writing-Reviewing and Editing.

### Conflicts of interest

The authors declare no conflicts of interest.

### References

- World Economic Outlook (2016). World Economic Outlook, April 2016: Too Slow for Too Long.
- The World Bank (2023). The World Bank in Türkiye. <https://www.worldbank.org/en/country/turkey/overview>
- T.C. Ticaret Bakanlığı (2023). Ekonomik Görünüm Mayıs 2023.
- Ertuğrul, N. A., Bağcı, Z. H., & Ertuğrul, Ö. L. (2018). Aquifer thermal energy storage systems: Basic concepts and general design methods. *Turkish Journal of Engineering*, 2(2), 38-48. <https://doi.org/10.31127/tuje.340334>
- Koyunoğlu, C. (2024). The economic case for blend fuels: A cost-benefit analysis in the European context. *Sustainable Technology and Entrepreneurship*, 3(2), 100060. <https://doi.org/10.1016/j.stae.2023.100060>
- Comert, M., & Yildiz, A. (2021). A novel artificial neural network model for forecasting electricity demand enhanced with population-weighted temperature mean and the unemployment rate. *Turkish Journal of Engineering*, 6(2), 178-189. <https://doi.org/10.31127/tuje.903876>
- Park, S. Y., & Yoo, S. H. (2014). The dynamics of oil consumption and economic growth in Malaysia. *Energy Policy*, 66, 218-223. <https://doi.org/10.1016/j.enpol.2013.10.059>
- Mikayilov, J. I., Mukhtarov, S., Dinçer, H., Yüksel, S., & Aydın, R. (2020). Elasticity analysis of fossil energy sources for sustainable economies: A case of gasoline consumption in Turkey. *Energies*, 13(3), 731. <https://doi.org/10.3390/en13030731>
- PETDER (2019). PETDER Sector Report.
- Aydın, Ü., Peker, H., & Gönülalan, A. U. (2020). Petrol Sektörü. *Türkiye'nin Enerji Görünümü*, 161-214
- Ma, H., & Zhang, Z. (2009). Grey prediction with Markov-Chain for Crude oil production and consumption in China. In *The Sixth International Symposium on Neural Networks (ISNN 2009)*, 551-561. [https://doi.org/10.1007/978-3-642-01216-7\\_58](https://doi.org/10.1007/978-3-642-01216-7_58)
- Wang, Q., & Song, X. (2019). Forecasting China's oil consumption: a comparison of novel nonlinear-dynamic grey model (GM), linear GM, nonlinear GM and metabolism GM. *Energy*, 183, 160-171. <https://doi.org/10.1016/j.energy.2019.06.139>
- Yang, Z. Y., Chai, A. H., Yang, Y. F., Li, X. M., Li, P., & Dai, R. Y. (2016). The semiflexible polymer translocation into laterally unbounded region between two parallel flat membranes. *Polymers*, 8(9), 332. <https://doi.org/10.3390/polym8090332>
- Nel, W. P., & Cooper, C. J. (2008). A critical review of IEA's oil demand forecast for China. *Energy Policy*, 36(3), 1096-1106. <https://doi.org/10.1016/j.enpol.2007.11.025>
- Azadeh, A., Moghaddam, M., Khakzad, M., & Ebrahimipour, V. (2012). A flexible neural network-fuzzy mathematical programming algorithm for improvement of oil price estimation and forecasting. *Computers & Industrial Engineering*, 62(2), 421-430. <https://doi.org/10.1016/j.cie.2011.06.019>
- Narayan, P. K., & Wong, P. (2009). A panel data analysis of the determinants of oil consumption: the

- case of Australia. *Applied Energy*, 86(12), 2771-2775. <https://doi.org/10.1016/j.apenergy.2009.04.035>
17. Yang, Y., Chen, Y., Shi, J., Liu, M., Li, C., & Li, L. (2016). An improved grey neural network forecasting method based on genetic algorithm for oil consumption of China. *Journal of Renewable and Sustainable Energy*, 8(2), 024104. <https://doi.org/10.1063/1.4944977>
  18. Li, J., Wang, R., Wang, J., & Li, Y. (2018). Analysis and forecasting of the oil consumption in China based on combination models optimized by artificial intelligence algorithms. *Energy*, 144, 243-264. <https://doi.org/10.1016/j.energy.2017.12.042>
  19. Assareh, E., Behrang, M. A., Assari, M. R., & Ghanbarzadeh, A. (2010). Application of PSO (particle swarm optimization) and GA (genetic algorithm) techniques on demand estimation of oil in Iran. *Energy*, 35(12), 5223-5229. <https://doi.org/10.1016/j.energy.2010.07.043>
  20. Lin, B., & Xie, C. (2013). Estimation on oil demand and oil saving potential of China's road transport sector. *Energy Policy*, 61, 472-482. <https://doi.org/10.1016/j.enpol.2013.06.017>
  21. Rao, R. D., & Parikh, J. K. (1996). Forecast and analysis of demand for petroleum products in India. *Energy Policy*, 24(6), 583-592. [https://doi.org/10.1016/0301-4215\(96\)00019-5](https://doi.org/10.1016/0301-4215(96)00019-5)
  22. Wang, Q., & Song, X. (2019). Forecasting China's oil consumption: a comparison of novel nonlinear-dynamic grey model (GM), linear GM, nonlinear GM and metabolism GM. *Energy*, 183, 160-171. <https://doi.org/10.1016/j.energy.2019.06.139>
  23. Duan, H., Lei, G. R., & Shao, K. (2018). Forecasting crude oil consumption in China using a grey prediction model with an optimal fractional-order accumulating operator. *Complexity*, 3869619 <https://doi.org/10.1155/2018/3869619>
  24. Behrang, M. A., Assareh, E., Ghalambaz, M., Assari, M. R., & Noghrehabadi, A. R. (2011). Forecasting future oil demand in Iran using GSA (Gravitational Search Algorithm). *Energy*, 36(9), 5649-5654. <https://doi.org/10.1016/j.energy.2011.07.002>
  25. Minniear, M. P. (2000). Forecasting the permanent decline in global petroleum production. *Journal of Geoscience Education*, 48(2), 130-136. <https://doi.org/10.5408/1089-9995-48.2.130>
  26. Al-Qaness, M. A., Abd Elaziz, M., & Ewees, A. A. (2018). Oil consumption forecasting using optimized adaptive neuro-fuzzy inference system based on sine cosine algorithm. *IEEE Access*, 6, 68394-68402. <https://doi.org/10.1109/ACCESS.2018.2879965>
  27. Fatima, T., Xia, E., & Ahad, M. (2019). Oil demand forecasting for China: a fresh evidence from structural time series analysis. *Environment, Development and Sustainability*, 21, 1205-1224. <https://doi.org/10.1007/s10668-018-0081-7>
  28. Yu, L., Zhao, Y., Tang, L., & Yang, Z. (2019). Online big data-driven oil consumption forecasting with Google trends. *International Journal of Forecasting*, 35(1), 213-223. <https://doi.org/10.1016/j.ijforecast.2017.11.005>
  29. Keshavarzian, M., Anaraki, S. K., Zamani, M., & Erfanfard, A. (2012). Projections of oil demand in road transportation sector on the basis of vehicle ownership projections, worldwide: 1972–2020. *Economic Modelling*, 29(5), 1979-1985. <https://doi.org/10.1016/j.econmod.2012.06.009>
  30. Sadri, A., Ardehali, M. M., & Amirnekooei, K. (2014). General procedure for long-term energy-environmental planning for transportation sector of developing countries with limited data based on LEAP (long-range energy alternative planning) and EnergyPLAN. *Energy*, 77, 831-843. <https://doi.org/10.1016/j.energy.2014.09.067>
  31. Melikoglu, M. (2014). Demand forecast for road transportation fuels including gasoline, diesel, LPG, bioethanol and biodiesel for Turkey between 2013 and 2023. *Renewable Energy*, 64, 164-171. <https://doi.org/10.1016/j.renene.2013.11.009>
  32. Azadeh, A., Behmanesh, I., Vafa Arani, H., & Sadeghi, M. H. (2014). An integrated fuzzy mathematical programming-analysis of variance approach for forecasting gasoline consumption with ambiguous inputs: USA, Canada, Japan, Iran and Kuwait. *International Journal of Industrial and Systems Engineering*, 18(2), 159-184. <https://doi.org/10.1504/IJISE.2014.064704>
  33. Sapnken, E. F., Tamba, J. G., Essiane, S. N., Koffi, F. D., & Njomo, D. (2018). Modeling and forecasting gasoline consumption in Cameroon using linear regression models. *International Journal of Energy Economics and Policy*, 8(2), 111-120.
  34. Anggarani, R., & Watada, J. (2012). A gasoline consumption model based on the harmony search algorithm: Study case of Indonesia. *Intelligent Decision Technologies*, 6(3), 233-241. <https://doi.org/10.3233/IDT-2012-0139>
  35. Chen, H., Tong, Y., & Wu, L. (2021). Forecast of energy consumption based on FGM (1, 1) model. *Mathematical Problems in Engineering*, 2021, 1-11. <https://doi.org/10.1155/2021/6617200>
  36. Güngör, B. O., Ertuğrul, H. M., & Soytaş, U. (2021). Impact of Covid-19 outbreak on Turkish gasoline consumption. *Technological Forecasting and Social Change*, 166, 120637. <https://doi.org/10.1016/j.techfore.2021.120637>
  37. Wang, Q., Li, S., & Li, R. (2018). Forecasting energy demand in China and India: Using single-linear, hybrid-linear, and non-linear time series forecast techniques. *Energy*, 161, 821-831. <https://doi.org/10.1016/j.energy.2018.07.168>
  38. Wang, Q., Li, S., Li, R., & Ma, M. (2018). Forecasting US shale gas monthly production using a hybrid ARIMA and metabolic nonlinear grey model. *Energy*, 160, 378-387. <https://doi.org/10.1016/j.energy.2018.07.047>
  39. Wang, Q., Li, S., Zhang, M., & Li, R. (2022). Impact of COVID-19 pandemic on oil consumption in the United States: a new estimation approach. *Energy*, 239, 122280. <https://doi.org/10.1016/j.energy.2021.122280>
  40. Wang, Q., Li, S., & Jiang, F. (2021). Uncovering the impact of the COVID-19 pandemic on energy consumption: New insight from difference between pandemic-free scenario and actual electricity

- consumption in China. *Journal of Cleaner Production*, 313, 127897.  
<https://doi.org/10.1016/j.jclepro.2021.127897>
41. Wang, Q., Li, S., Li, R., & Jiang, F. (2022). Underestimated impact of the COVID-19 on carbon emission reduction in developing countries—a novel assessment based on scenario analysis. *Environmental Research*, 204, 111990.  
<https://doi.org/10.1016/j.envres.2021.111990>
  42. Ogutu, J. O., Schulz-Streeck, T., & Piepho, H. P. (2012). Genomic selection using regularized linear regression models: ridge regression, lasso, elastic net and their extensions. *BMC proceedings*, 6, 1-6.  
<https://doi.org/10.1186/1753-6561-6-S2-S10>
  43. Farvahari, A., Gozashti, M. H., & Dehesh, T. (2019). The usage of lasso, ridge, and linear regression to explore the most influential metabolic variables that affect fasting blood sugar in type 2 Diabetes patients. *Romanian Journal of Diabetes Nutrition and Metabolic Diseases*, 26(4), 371-379.  
<https://doi.org/10.2478/rjdnmd-2019-0040>
  44. Altalbany, S. (2021). Evaluation of ridge, elastic net and lasso regression methods in precedence of multicollinearity problem: A simulation study. *Journal of Applied Economics and Business Studies*, 5(1), 131-142.  
<https://doi.org/10.34260/jaeb.517>
  45. McNeish, D. M. (2015). Using lasso for predictor selection and to assuage overfitting: A method long overlooked in behavioral sciences. *Multivariate Behavioral Research*, 50(5), 471-484.  
<https://doi.org/10.1080/00273171.2015.1036965>
  46. Trivedi, U. B., Bhatt, M., & Srivastava, P. (2021). Prevent overfitting problem in machine learning: a case focus on linear regression and logistics regression. *Innovations in Information and Communication Technologies (IICT-2020) Proceedings of International Conference on ICRHE-2020, Delhi, India: IICT-2020*, 345-349.  
[https://doi.org/10.1007/978-3-030-66218-9\\_40](https://doi.org/10.1007/978-3-030-66218-9_40)
  47. Jovanovic, M., Radovanovic, S., Vukicevic, M., Van Poucke, S., & Delibasic, B. (2016). Building interpretable predictive models for pediatric hospital readmission using Tree-Lasso logistic regression. *Artificial Intelligence in Medicine*, 72, 12-21.  
<https://doi.org/10.1016/j.artmed.2016.07.003>
  48. Jacobson, N. C., Chow, S. M., & Newman, M. G. (2019). The Differential Time-Varying Effect Model (DTVEM): A tool for diagnosing and modeling time lags in intensive longitudinal data. *Behavior Research Methods*, 51, 295-315.  
<https://doi.org/10.3758/s13428-018-1101-0>
  49. Chapman, C. S., Gallivan, J. P., Wood, D. K., Milne, J. L., Culham, J. C., & Goodale, M. A. (2010). Reaching for the unknown: multiple target encoding and real-time decision-making in a rapid reach task. *Cognition*, 116(2), 168-176.  
<https://doi.org/10.1016/j.cognition.2010.04.008>
  50. T.C. Enerji ve Tabii Kaynaklar Bakanlığı (2020). EIGM Raporları
  51. Keogh, E., Chu, S., Hart, D., & Pazzani, M. (2004). Segmenting time series: A survey and novel approach. In *Data mining in time series databases*, 1-21.  
[https://doi.org/10.1142/9789812565402\\_0001](https://doi.org/10.1142/9789812565402_0001)
  52. Pereira, C. V. (2021). Portfolio efficiency with high-dimensional data as conditioning information. *International Review of Financial Analysis*, 77, 101811.  
<https://doi.org/10.1016/j.irfa.2021.101811>
  53. Çınaroğlu, S. (2017). Sağlık harcamasının tahmininde makine öğrenmesi regresyon yöntemlerinin karşılaştırılması. *Uludağ Üniversitesi Mühendislik Fakültesi Dergisi*, 22(2), 179-200.  
<https://doi.org/10.17482/uumfd.338805>
  54. Teixeira, A. L., Leal, J. P., & Falcao, A. O. (2013). Random forests for feature selection in QSPR Models—an application for predicting standard enthalpy of formation of hydrocarbons. *Journal of Cheminformatics*, 5, 1-15.  
<https://doi.org/10.1186/1758-2946-5-9>
  55. Omranian, N., Eloundou-Mbebi, J. M., Mueller-Roeber, B., & Nikoloski, Z. (2016). Gene regulatory network inference using fused LASSO on multiple data sets. *Scientific reports*, 6(1), 20533.  
<https://doi.org/10.1038/srep20533>
  56. Tibshirani, R. (1996). Regression shrinkage and selection via the lasso. *Journal of the Royal Statistical Society Series B: Statistical Methodology*, 58(1), 267-288.  
<https://doi.org/10.1111/j.2517-6161.1996.tb02080.x>
  57. Hastie, T., Tibshirani, R., & Wainwright, M. (2015). *Statistical learning with sparsity: the lasso and generalizations*. CRC Press.
  58. Wang, F., Liu, X., Liu, C., Li, H., & Han, Q. (2018). Remaining useful life prediction method of rolling bearings based on Pchip-EEMD-GM (1, 1) model. *Shock and vibration*, 3013684.  
<https://doi.org/10.1155/2018/3013684>
  59. Kwiatkowski, D., Phillips, P. C., Schmidt, P., & Shin, Y. (1992). Testing the null hypothesis of stationarity against the alternative of a unit root: How sure are we that economic time series have a unit root?. *Journal of Econometrics*, 54(1-3), 159-178.  
[https://doi.org/10.1016/0304-4076\(92\)90104-Y](https://doi.org/10.1016/0304-4076(92)90104-Y)
  60. Mukaka, M. M. (2012). A guide to appropriate use of correlation coefficient in medical research. *Malawi Medical Journal*, 24(3), 69-71.

